Université de Strasbourg

Institut de Physique et Chimie des Matériaux de Strasbourg

Ecole Doctorale de Physique et Chimie-Physique ED182

THÉSE
Discipline : Chimie physique

Multifunctional Complexes for Molecular Devices

Directeur de thése:
Prof. Mario RUBEN

Candidat:
Andrea MAGRÍ

Rapporteurs:
Prof. Heiko WENDE
Prof. Michael MEHRING

Autres membres du jury:
Prof. Nicolas GIUSEPPONE
Dr. Stéphane BELLEMIN-LAPONNAZ
Dr. Valentin Alek DEDIU

December 12th, 2014

I hereby declare that I have developed and written the enclosed thesis completely by myself and I have not reproduced published work without indicating the bibliographic reference.

Andrea Magri

Résumé Substantiel

De nos jours, la micro-électronique est en grande partie basée sur les semi-conducteurs inorganiques tels que le silicium et le germanium. Vers le milieu du siècle dernier, les semi-conducteurs organiques (en anglais: organic semiconductors - OSCs) éveillèrent l'intérêt de la communauté scientifique ainsi que des industriels. En effet, cette nouvelle classe de matériaux est prometteuse, non seulement pour la fabrication de circuits électroniques étendus, à bas cout et imprimables mais aussi pour des applications en opto-électronique. Les OSCs se divisent en deux catégories: d'une part ceux de faible poids moléculaire et d'autre part les polymères. Tous ont en commun d'avoir un système conjugué π sur une chaine formée de structures d'atomes de carbone liés entre eux par des liaisons σ. La structure de la molécule d'éthylène montrée en Figure 1 illustre bien cette caractéristique des OSCs.
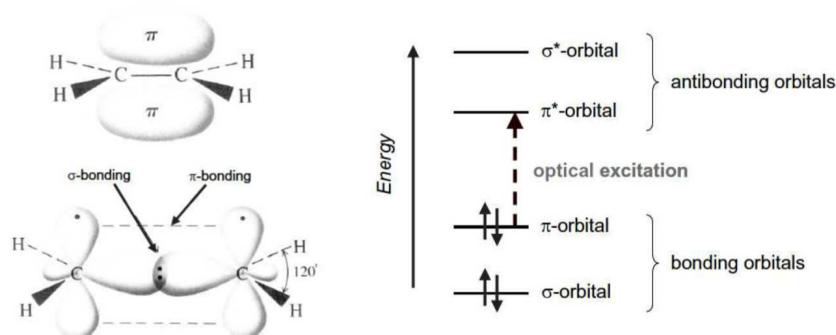

Figure 1: Liaisons σ et π dans l'éthylène, la plus simple molécule présentant un système conjugué π. Les niveaux d'énergie de la molécule ainsi que son niveau d'excitation électronique le plus faible sont indiqués à droite.

Les propriétés optiques des OSCs sont dues aux électrons π qui participent à des transitions $\pi - \pi^*$ ayant lieu dans le système conjugué π délocalisé. Du point de vue des propriétés électroniques, les OSCs sont des isolants intrinsèques. En effet, pour qu'il y ait conduction électronique dans un OSC, des porteurs de charge externes doivent être injectés par des électrodes. Ceux-ci se déplacent dans la couche de matériau organique en passant d'un état localisé à un autre, HO (haute occupée, en anglais: higher occupied molecular orbital - HOMO) et BV (basse vacante, en anglais: lower unoccupied molecular orbital - LUMO), qui sont respectivement l'orbitale liante π et l'orbitale anti-liante π^*. Un des principaux intérêts des OSCs réside dans la possibilité de pouvoir modifier leurs propriétés optiques et électroniques par le biais de modifications chimiques de la chaine carbonée et du système conjugué π.

La molécule de Alq_3 (tris-(8-hydroxyquinoline)aluminum) constitue l'exemple le plus connu parmi les OCSs, en particulier parmi ceux de poids moléculaire faible. Cette molécule est formée par un ion central Al^{3+} chélaté par trois quinolinates bidentées, assurant la neutralité du complexe. Le complexe Alq_3 a deux isomères géométriques: *mer-* et *fac-*Alq_3 (voir Figure 2) qui présentent des propriétés différentes. Mais c'est principalement l'isomère méridional qui se forme lors des synthèses conventionnelles. Ses niveaux énergétiques de HOMO et de LUMO, sa stabilité thermique, sa capacité à former des couches minces ainsi que ses mobilités de porteurs de charge élevée (électrons: 10^{-5}-$10^{-6}\,cm^2\,V^{-1}\,s^{-1}$; trous: 10^{-8}-$10^{-9}\,cm^2\,V^{-1}\,s^{-1}$) font du complexe Alq_3 un OSC utilisé dans de nombreuses applications. Les diodes électroluminescentes organiques (en anglais: organic light emitting devices - OLEDs) constituent l'un des tout premiers champs d'application du complexe Alq_3 en tant que matériau assurant la conduction électrique, l'émission de photons et de matrice. Depuis la première utilisation dans
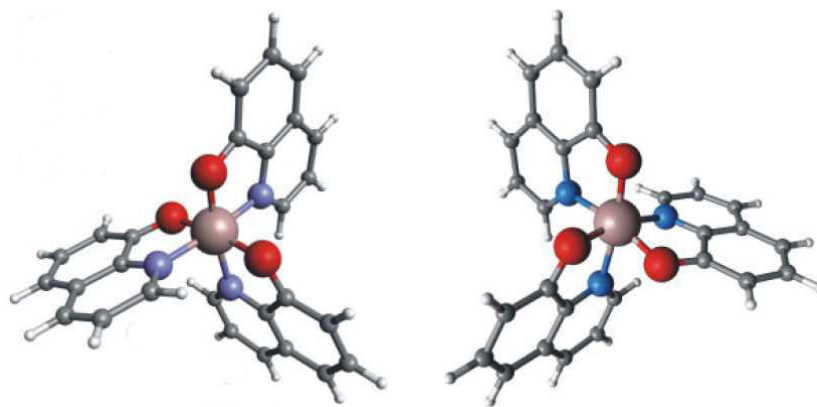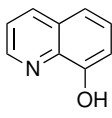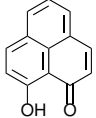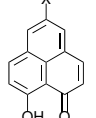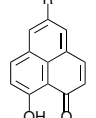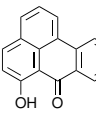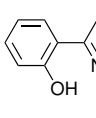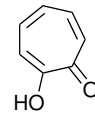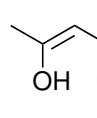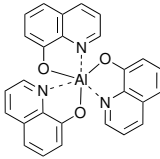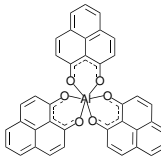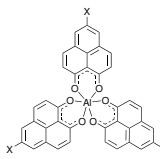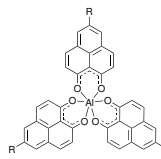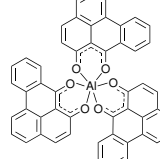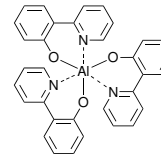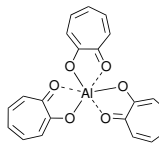
Figure 2: Représentation de la structure moléculaire de l'isomère méridional (*mer*-Alq$_3$) (à gauche) et de celle de l'isomère facial (*fac*-Alq$_3$) (à droite).

ce domaine, le complexe Alq$_3$ ainsi que ses dérivés modifiés chimiquement furent l'objet de nombreuses études afin d'améliorer les performances des OLEDs. Le complexe Alq$_3$ fut utilisé également dans le processus de fabrication de cellules photovoltaïques organiques (en anglais: Organic Photovoltaic - OPVs) comme matériau assurant le transport électronique et le blocage des trous. De plus, ce complexe est, de nos jours, l'un des OSCs les plus étudiés dans le domaine de la spintronique organique. En effet, les dispositifs spintroniques organiques (en anglais: organic spintronic devices - OSPDs) basés sur ce complexe présentent des résultats reproductibles prometteurs. Enfin, la fabrication de transistors organiques à effet de champ (en anglais: organic field-effect transistors - OFETs) ambipolaires et de transistors organiques électroluminescents à effet de champ (en anglais: light-emitting organic field-effect transistor - LE-OFETs) constituent un domaine supplémentaire d'application du complexe Alq$_3$ en tant que matériau actif.

Élaboration, synthèse et caractérisation des OSCs étudiés

Lors de ma thèse, j'ai synthétisé et analysé des OSCs contenant de l'aluminium, afin de comprendre le lien entre la structure chimique et les propriétés opto-élec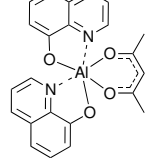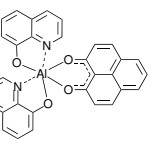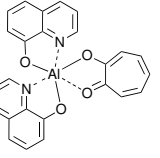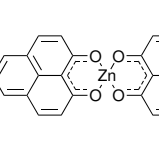troniques. La première étape consista à établir, sélectionner et synthétiser une librairie de ligands pouvant être utilisés dans la fabrication des séries de complexes d'aluminium étudiés (voir Table 1 pour la liste de ces nombreux ligands). Les ligands et les complexes furent caractérisés par spectroscopie et par des méthodes électrochimiques. Le complexe Al(Op)$_3$ (tris-(1-oxo-1H-phenalen-9-olate)aluminum) fut le premier OSC synthétisé lors de mon travail. Ce complexe a une structure symétrique et a des ligands qui présentent un système aromatique étendu par rapport au complexe Alq$_3$. Par la suite, deux séries de dérivés halogenés et substitués du complexe Al(Op)$_3$ furent synthétisées: Al(Op$-$X)$_3$ et Al(Op$-$R)$_3$. De plus, l'extension du système aromatique de Al(Op)$_3$ me permit de former un autre complexe d'aluminium, le complexe Al(Oba)$_3$ (tris-(7-oxo-7H-benzo(de)anthracen-6-olate)aluminum). En raison de leurs caractéristiques structurelles, il me parut intéressant de synthétiser et d'analyser deux autres complexes: le complexe Al(Op$-$py)$_3$ (tris-(2-(pyridin-2-yl)phenolate)aluminum) dont la structure est similaire à celle du complexe Alq$_3$ ainsi que le complexe Al(Trop)$_3$ (tris-(7-oxocyclohepta-1,3,5-trienolate)aluminum) qui lui présente une structure symétrique et trois cycles carbenés insaturés. Trois séries supplémentaires de complexes à ligands mixtes furent obtenues en échangeant un quinolate respectivement par Acac (4-hydroxypent-3-en-2-one), HOp (9-hydroxy-1H-phenalen-1-one) et tropolone

Table 1: Liste des ligands et des (nouveaux) OSCs étudiés. R: phenyl, naphthalenyl, phenylethynynl. X: F, Cl, Br, I.

Hq   HOp   HOp−X   HOp−R   HOba   HOp−py   Trop.   Acac

Alq_3 $Al(Op)_3$ $Al(Op-X)_3$ $Al(Op-R)_3$ $Al(Oba)_3$ $Al(Op-py)_3$

$Al(Trop)_3$ $Al(q_2Acac)$ $Al(q_2Op)$ $Al(q_2Trop)$ $Zn(Op)_2$

(2-hydroxycyclohepta-2,4,6-trien-1-one). Enfin, j'ai synthétisé le complexe plan $Zn(Op)_2$ (bis-(1-oxo-1H-phenalen-9-olate)zinc), le premier d'une série de complexes plans contenant du zinc. Les complexes furent caractérisés par résonance magnétique nucléaire (en anglais: nuclear magnetic resonance - NMR), par analyse élémentaire, par les méthodes de spectrométrie de masse désorption-ionisation laser assistée par matrice-temps de vol (en anglais: matrix assisted lased desorption ionization-time of flight - MALDI-TOF) et ionisation par électronébuliseur-temps de vol (en anglais: electrospray ionization-time of flight - ESI-TOF) ainsi que par diffractométrie de rayons X.

Table 2: Propriétés photo-électroniques des complexes Alq_3 et $Al(Op)_3$ en solution et en couche mince (substrat: quartz), mesures à température ambiante.

Composé	λ^{abs}_{max} [a](ϵ) [nm] ([$M^{-1}\,cm^{-1}$])	λ^{emi}_{max} [b] [nm]	Φ [c]	τ [d] [ns]
Alq_3 solution	385 (1.1×10^4)	517	0.13	16.2
Alq_3 couche mince	393	523	0.17	12.5
$Al(Op)_3$ solution	362 (9.1×10^4)	458	0.027	0.7
$Al(Op)_3$ couche mince	366	583	0.014	7.1

[a] λ^{abs}_{max} = absorption maximum de la première bande de transition $\pi \to \pi^*$ ainsi que son coefficient d'extinction (ϵ).

[b] λ^{emi}_{max} = émission maximum.   [c] Φ = rendement quantique de photoluminescence, determiné en utilisant la molécule de rhodamine 6G comme standard.

[d] τ = durée de vie photonique de luminescence.

Les propriétés photo-physique du complexe $Al(Op)_3$ furent mesurées en solution et lorsqu'il est déposé en couche mince. Ces résultats furent comparés à ceux obtenus pour le complexe Alq_3 (voir Figure 3).

Les analyses montrent que, à l'état solide , le complexe $Al(Op)_3$ forme des excimères et exhibe
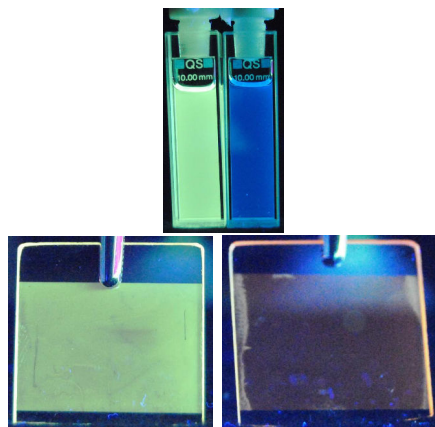
Figure 3: Émission de photons observée pour le complexe Alq$_3$ (jaune) et pour le complexe Al(Op)$_3$ (bleu) sous illumination UV (en solution). Émission de photons observée pour le complexe Alq$_3$ (jaune) et pour le complexe Al(Op)$_3$ (marron) (couche mince). L'émission pour le complexe Al(Op)$_3$ en couche mince est sensiblement décalée par rapport à celle observée en solution due à la formation d'excimères.

par conséquent des propriétés photo-physiques très différentes qu'il soit en solution ($\lambda_{max}^{emi} =$ 458 nm, $\Phi =$ 0.027 et $\tau =$ 0.7 ns) ou bien déposé en couche mince ($\lambda_{max}^{emi} =$ 583 nm, $\Phi =$ 0.014 et $\tau =$ 7.1 ns), comme indiqué dans la Figure 3. Les spectres d'absorption et d'émission des complexes halogènés et substitués Al(Op$-$X)$_3$ et Al(Op$-$R)$_3$ ne montrent que peu de variations par rapport à ceux du complexe Al(Op)$_3$ pur. Un point intéressant à souligner est l'émission phosphorescente ($\approx$600 nm), due à l'effet des atomes lourds, observée pour le complexe Al(Op$-$I)$_3$. Par ailleurs, malgré son substituant massif, le complexe Al(Op$-$p)$_3$ forme des excimères lorsqu'il est déposé en couche mince ($\lambda_{max}^{emi} =$ 537 nm). En raison de son noyau de phenalenyl, le complexe Al(Oba)$_3$ présente des spectres d'absorption et d'émission similaires à ceux du complexe Al(Op)$_3$. De plus, il forme des excimères à l'état solide ($\lambda_{max}^{emi} =$ 591 nm). Au contraire, le complexe Al(Op$-$py)$_3$ qui est insoluble dans tous les solvants, est caractérisé à l'état solide par une émission ($\lambda_{max}^{emi} =$ 445 nm) déplacée vers le bleu par rapport au complexe Alq$_3$ ($\lambda_{max}^{emi} =$ 523 nm). Il résulte de la structure particulière du complexe Al(Trop)$_3$, que ses spectres ne sont pas comparables à ceux des complexes Alq$_3$ et Al(Op)$_3$. Cependant, les bandes d'absorption du complexe Al(Trop)$_3$ purent être identifiées à leur transitions respectives et une émission fluorescente dans le bleu fut détectée ($\lambda_{max}^{emi} =$ 456 nm). Les spectres d'absorption et d'émission des complexes à ligands mixtes Al(q$_2$Acac), Al(q$_2$Op) et Al(q$_2$Trop) sont le résultat de la combinaison des spectres des groupes fonctionnels formant ces complexes. Puisque Acac n'émet pas, l'émission du complexe Al(q$_2$Acac) ($\lambda_{max}^{emi} =$ 512 nm) est pratiquement similaire à celle observée pour le complexe Alq$_3$. En revanche, dans le cas du complexe Al(q$_2$Op) puisque les groupes fonctionnels quinolinate et phenalenyl émettent, le spectre d'émission est une combinaison des spectres des groupes fonctionnels. Les deux groupes fonctionnels peuvent être excités de façon sélective, permettant ainsi d'observer une émission du complexe Al(q$_2$Op) différente suivant la longueur d'onde d'excitation. Le même effet fut observé pour le complexe Al(q$_2$Trop). Cepedant, puisque le domaine d'absorption des groupes fonctionnels quinolinate et tropolonate se superposent, l'excitation sélective d'un seul groupe fonctionnel se revela être impossible dans ce cas. Dans le cas du complexe Zn(Op)$_2$, dernier complexe analysé dans ce travail, les spectres d'absorption et d'émission dérivent des ligands phenalenyl, et ceux, en dépit de la structure plane du complexe.

La réduction électrochimique simple et irréversible du complexe Alq$_3$ a lieu pour des potentiels

Table 3: Potentiels de réduction et niveaux d'énergie HOMO et LUMO pour les OSCs analysés.

Composé	$E_{1/2}^{red}$ [V]	E_{LUMO}[a] [eV]	E_{gap}[b] [eV]	E_{HOMO} [eV]
mer-Alq$_3$	-1.79[c]	-3.01	2.82	-5.83
Al(Op)$_3$	-1.63, -1.84, -2.07	-3.26	2.67	-5.93
Al(Op$-$F)$_3$	-1.52, -1.70, -1.89	-3.35	2.59	-5.94
Al(Op$-$Cl)$_3$	-1.49, -1.68, -1.86	-3.37	2.60	-5.97
Al(Op$-$Br)$_3$	-1.49, -1.68, -1.88	-3.36	2.60	-5.96
Al(Op$-$I)$_3$	-1.50, -1.66, -1.82, -2.01	-3.35	2.58	-5.93
Al(Op$-$p)$_3$	-1.62, -1.79, -2.02	-3.28	2.54	-5.82
Al(Op$-$n)$_3$	-1.57, -1.80, -2.01	-3.33	2.56	-5.89
Al(Op$-$pe)$_3$	-1.55, -1.73, -1.94	-3.31	2.49	-5.80
Al(Oba)$_3$	-1.75, -1.93, -2.15	-3.12	2.68	-5.80
Al(Trop)$_3$	-2.10	-2.78	3.14	-5.92
$pseudofac$-Al(q$_2$Acac)	-1.80[c]	-3.00	2.87	-5.87
$pseudofac$-Al(q$_2$Op)	-1.58, -2.08[c]	-3.31	2.67	-5.98
$pseudomer$-Al(q$_2$Trop)	-2.08	-2.84	3.11	-5.95
Zn(Op)$_2$	-1.50, -1.81, -2.04	-3.38	2.77	-6.15

[a] L'énergie LUMO est déterminée à partir du premier pic de réduction mesuré par le méthode CV.   [b] Le gap HOMO-LUMO est determiné par la bande d'absorption de plus basse énergie du spectre.   [c] Valeur de début de courbe.
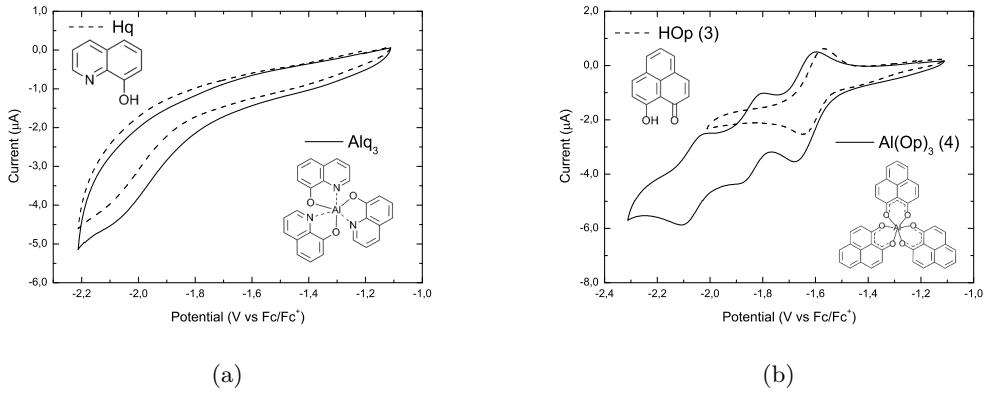

(a)

(b)

Figure 4: (a) Courbe CV cathodique puor Hq et Alq$_3$ dans une solution de DCM mesurée à température ambiante. Électrolyte: TBAPF$_6$. Vitesse de scan: $100\,\mathrm{mV\,s^{-1}}$. (b) Courbe CV cathodique pour HOp et Al(Op)$_3$ dans une solution de DCM mesurée à température ambiante. Électrolyte: TBAPF$_6$. Vitesse de scan:$100\,\mathrm{mV\,s^{-1}}$.

relativement négatifs ($-1.79\,\text{V}$). Ceci contraste avec le complexe $Al(Op)_3$ qui peut subir trois réductions ($-1.63\,\text{V}$, $-1.84\,\text{V}$ et $-2.07\,\text{V}$), chacune quasi-réversible, la première de ces réductions ayant lieu pour un potentiel moins négatif que dans le cas de la molécule de Alq_3. La Figure 4 montre les courbes de voltammétrie cyclique (en anglais: cyclic voltammetry - CV) pour les complexes Alq_3 et $Al(Op)_3$. De part leur similarité structurelle avec le complexe $Al(Op)_3$, le même comportement put être observé pour les complexes halogenés et substitués $Al(Op-X)_3$, $Al(Op-R)_3$ et $Al(Oba)_3$ (voir Table 3). En raison de sa petite structure aromatique, le complexe $Al(Trop)_3$ est réduit pour un potentiel fortement négatif ($-2.10\,\text{V}$). La réduction des complexes $Al(q_2Acac)$, $Al(q_2Op)$ et $Al(q_2Trop)$ est rendue possible grâce leurs groupes fonctionnels électro-actifs. Plus précisément, la réduction du complexe $Al(q_2Acac)$ ($-1.80\,\text{V}$) a lieu sur les quinolinates, celle du complexe $Al(q_2Op)$ ($-1.58\,\text{V}$) sur le phenalenyl et la réduction du complexe $Al(q_2Trop)$ ($-2.08\,\text{V}$) sur le tropolonate. Le complexe $Zn(Op)_2$ est, quant à lui, caractérisé par trois réactions de réduction ($-1.50\,\text{V}$, $-1.81\,\text{V}$ et $-2.04\,\text{V}$) ayant lieu sur les deux phenalenyl et, très probablement, sur le zinc. Les niveaux d'énergie des orbitales HOMO et LUMO furent estimés en se basant sur les caractérisations photo-physiques et electrochimiques. Le complexe $Al(Op)_3$ se caractérise par des niveaux HOMO et LUMO ($-5.93\,\text{eV}$ et $-3.96\,\text{eV}$) plus bas que ceux du complexe Alq_3 ($-5.83\,\text{eV}$ et $-3.01\,\text{eV}$). Les complexes halogenés et substitués $Al(Op-X)_3$ et $Al(Op-R)_3$ présentent des niveaux HOMO et LUMO similaires à ceux du complexe $Al(Op)_3$ (voir Table 3), contrairement au complexe $Al(Oba)_3$ qui lui présente des niveaux d'énergie supérieurs ($-5.80\,\text{eV}$ et $-3.12\,\text{eV}$). Le complexe $Al(Trop)_3$ se singularise en ayant le niveau LUMO le plus elevé ($-2.78\,\text{eV}$) de tous les OSCs ici etudiés, son niveau HOMO ($-5.92\,\text{eV}$) étant comparable à celui du composé $Al(Op)_3$. Les niveaux HOMO et LUMO des complexes à ligands mixtes $Al(q_2Acac)$ ($-5.87\,\text{eV}$ et $-3.00\,\text{eV}$), $Al(q_2Op)$ ($-5.98\,\text{eV}$ et $-3.31\,\text{eV}$) et $Al(q_2Trop)$ ($-5.95\,\text{eV}$ et $-2.84\,\text{eV}$) sont similaires à ceux des complexes Alq_3, $Al(Op)_3$ et $Al(Trop)_3$ respectivement. Malgré sa géométrie différente, le complexe $Zn(Op)_2$ présente des niveaux HOMO et LUMO ($-6.15\,\text{eV}$ et $-3.38\,\text{eV}$) proches de ceux du complexe $Al(Op)_3$.

Étude théorique et résultats expérimentaux préliminaires concernant les (nouveaux) OSCs

En collaboration avec: Dr. Velimir Meded and Pascal Friederich (INT-KIT, Karlsruhe, Germany); Dr. Timo Strunk (Nanomatch, Eggenstein-Leopoldshafen, Germany), Dr. Xiangnan Sun and Prof. Luis E. Hueso (CIC nanoGUNE, Donostia-San Sebastiãqn, Spain); Dr. Valeria Fattori and Dr. Francesca Tinti (ISOF-CNR, Bologna, Italy)

La mobilité des porteurs de charge dans les OSCs fut étudiée en se basant aussi bien sur des méthodes théoriques tout comme sur des méthodes expérimentales. Tout d'abord, les niveaux HOMO et LUMO ainsi que les moments dipolaires des différents OSCs furent calculés pour des systèmes dans le vide (voir Table 4). Les calculs effectués montrèrent que la localisation des orbitales HOMO et LUMO dépend de la symétrie des ligands. Ce phénomène est illustré pour les complexes *mer*-Alq_3 et $Al(Op)_3$ dans la Figure 5. La présence de ligands asymétriques, qui forment les complexes *mer*-Alq_3 and *mer*-$Al(Op-py)_3$, a pour conséquence des orbitales HOMO et LUMO localisées. Ces OSCs présentent ainsi un moment dipolaire élevé ($4.45\,\text{D}$ et $4.79\,\text{D}$ respectivement). En revanche, la présence de ligands symétriques, qui forment les complexes $Al(Op)_3$, $Al(Trop)_3$ et $Al(Acac)_3$, conduit à des orbitales HOMO et LUMO équitablement reparties et donc à un moment dipolaire faible ($0.086\,\text{D}$, $0.12\,\text{D}$, et $0.053\,\text{D}$ respectivement). Les orbitales HOMO et LUMO du complexe à ligands mixtes *pseudofac*-$Al(q_2Acac)$ sont localisées exclusivement sur le groupe fonctionnel quinolinate. Cette configuration contraste avec celle des complexes *pseudofac*-$Al(q_2Op)$ et *pseudomer*-$Al(q_2Trop)$, dont les orbitales HOMO et

LUMO sont reparties alternativement sur les groupes fonctionnels quinolinate et phenalenyle ou tropolonate, ce qui conduit à un moment dipolaire elevé (6.52 D et 5.49 D respectivement).
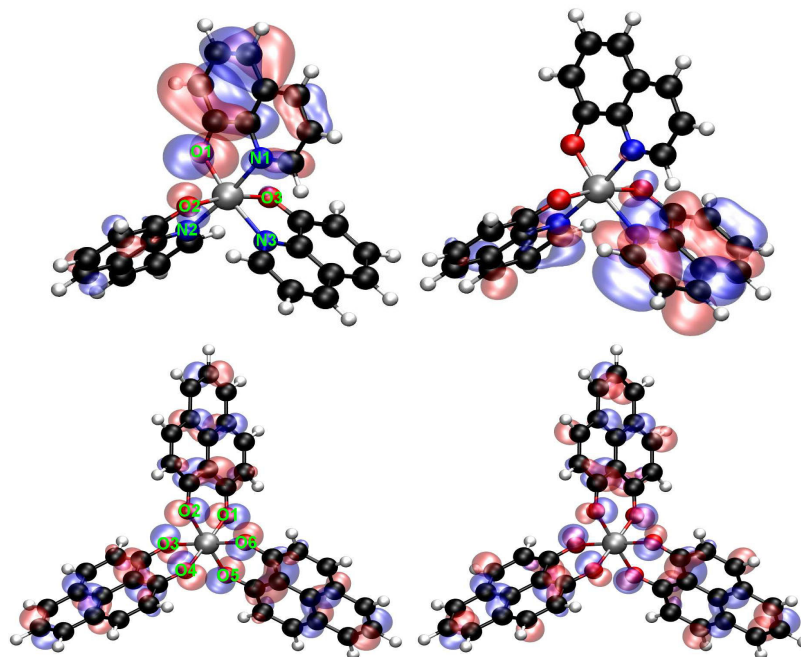

Figure 5: Représentation de la surfaces des orbitales moléculaires HOMO (à gauche) et LUMO (à droite) pour les complexes *mer*-Alq$_3$ (en haut) et Al(Op)$_3$ (en bas).

Par la suite, la morphologie adoptée par les OSCs lorsque ceux-ci sont déposés en couche mince fut determinée en utilisant le code DEPOSIT. Les fonctions de distribution de paire ($g(r)$) purent ainsi être représentées. En raison de sa structure symétrique et peu étendue, le complexe Al(Acac)$_3$ présente la couche la plus ordonnée et la plus dense de tous les OSCs etudiés. De même, les complexes *mer*-Alq$_3$, *mer*-Al(Op$-$py)$_3$ et *pseudofac*-Al(q$_2$Ac) forment des couches minces ordonnées et denses, propriétés liées à leur moment dipolaire élevé et à leur ligands de taille réduite. En revanche, les complexes Al(Op)$_3$ et Al(Trop)$_3$ forment des couches minces désordonnées en raison de leur moment dipolaire négligeable. Les complexes Al(q$_2$Op) et Al(q$_2$Trop) présentent, eux aussi, une structure désordonnée malgré leur moment dipolaire élevé. Ceci s'explique par des groupes fonctionnels phenalenyl et tropolonate volumineux.
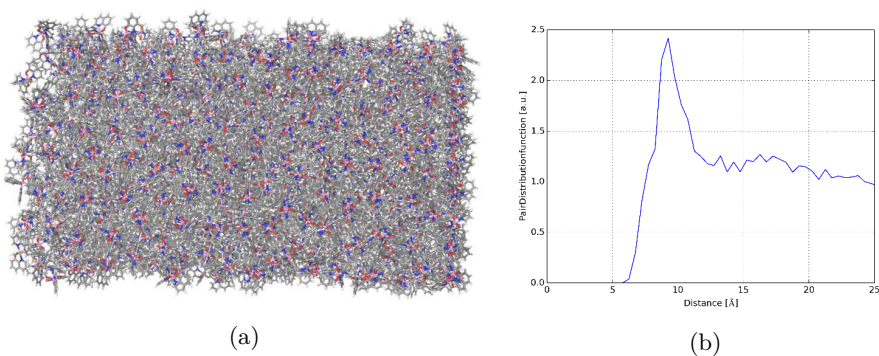

Figure 6: (a) Morphologie du complexe *mer*-Alq$_3$. (b) Fonction de corrélation de paire $g(r)$ pour le complexe *mer*-Alq$_3$.

Table 4: Niveaux HOMO and LUMO, gap HOMO-LUMO et moment dipolaire des OSCs étudiés. Ces valeurs ont été calculées pour des systèmes dans le vide ainsi que pour des systèmes déposés en couche mince.

	Vacuum				Environment			
Composé	E_{HOMO} [eV]	E_{LUMO} [eV]	E_{gap} [eV]	P [a] [D]	E_{HOMO} [eV]	E_{LUMO} [eV]	E_{gap} [eV]	P [b] [D]
mer-Alq$_3$	-5.14	-1.91	3.22	4.45	-5.07	-1.80	3.27	5.55
Al(Op)$_3$	-5.71	-2.41	3.30	0.086	-5.41	-2.22	3.19	1.52
mer-Al(Op$-$py)$_3$	-5.07	-1.55	3.52	4.79	-4.98	-1.40	3.58	5.88
Al(Trop)$_3$	-5.72	-1.79	3.93	0.12	-5.30	-1.56	3.74	1.34
Al(Acac)$_3$	-5.99	-1.19	4.80	0.053	-5.83	-1.09	4.74	0.63
$pseudofac$-Al(q$_2$Acac)	-5.29	-1.74	3.55	1.47	-5.16	-1.67	3.48	2.04
$pseudofac$-Al(q$_2$Op)	-4.99	-2.71	2.28	6.52	-5.02	-2.54	2.49	7.89
$pseudomer$-Al(q$_2$Trop)	-5.09	-2.07	3.02	5.49	-4.97	-1.79	3.18	6.84

[a] Moment dipolaire électrique dans le vide.　　[a] Moment dipolaire électrique lorsque déposé en couche mince.

En utilisant la méthode "Quantum Patch" développée récemment, une série de paramètres microscopiques purent être déterminés pour les couches minces formées par les différents OSCs. Nous nous sommes plus particulièrement intéressés à l'énérgie de désordre ($\sigma(E)$), à l'énergie de réorganisation (λ) et à l'énergie de couplage (J^2r^2). Les valeurs de ces grandeurs ont été utilisées pour calculer les mobilités des porteurs de charge μ dans les OSCs déposés en couches mince (voir liste Table 5). La valeur élevée de la mobilité des porteurs de charge obtenue pour le complexe Al(Acac)$_3$ en utilisant la méthode Quantum Patch indique que cette méthode nécessite encore des ajustements. Cependant, la méthode fournit des résultats tout à fait satisfaisants et en bon accord avec les mesures expérimentales dans le cas des complexes suivants: mer-Alq$_3$, $pseudofac$-Al(q$_2$Acac) et Al(Op)$_3$. Il est cependant nécessaire, pour un calcul réaliste de la mobilité électronique, de prendre en compte la formation d'excimères à l'état solide dans les molécules telles que Al(Op)$_3$. Parmis les OSCs, les complexes mer-Alq$_3$, mer-Al(Op$-$py)$_3$, Al(Trop)$_3$ et $pseudofac$-Al(q$_2$Acac) ont des mobilités électroniques calculées similaires. Leur mobilité de trous, en revanche, présente des variations jusqu'à cinq ordre de magnitude. Les complexes à ligands mixtes $pseudofac$-Al(q$_2$Op) et $pseudomer$-Al(q$_2$Trop) ont quant à eux les mobilité d'électrons et de trous les plus faibles de tous les complexes étudiés.

Table 5: Mobilités des porteurs de charge μ dans les OSCs etudiés (Valeurs calculées avec la méthode "Quantum Patch").

Composé	Mobilité [$\mathrm{cm^2\,V^{-1}\,s^{-1}}$]	
	Trous	électrons
mer-Alq$_3$	3.26×10^{-8}	9.23×10^{-8}
Al(Op)$_3$	1.42×10^{-4}	9.49×10^{-6}
mer-Al(Op$-$py)$_3$	5.67×10^{-7}	6.64×10^{-8}
Al(Trop)$_3$	4.70×10^{-10}	2.62×10^{-8}
Al(Acac)$_3$	8.57×10^{-3}	6.31×10^{-4}
$pseudofac$-Al(q$_2$Acac)	1.59×10^{-5}	4.68×10^{-6}
$pseudofac$-Al(q$_2$Op)	8.32×10^{-12}	2.43×10^{-13}
$pseudomer$-Al(q$_2$Trop)	2.64×10^{-11}	3.27×10^{-10}

Le compléxe $Al(Op)_3$ fut utilisé comme matériau pour fabriquer un transistor en couches minces (en anglais: thin film-transistor - TFT), rendant possible la mesure de la mobilité d'effet de champ. Pour les trous, une mobilité entre 0.6 and $2.1 \times 10^{-6} \, cm^2 \, V^{-1} \, s^{-1}$ a été observée tandis que pour les électrons aucun mobilité ne fut détectée. De plus, le ratio On/Off constaté est d'environ 104 et les tensions seuils se situent entre -35 et $-45 \, V$ pour ce TFT à base de $Al(Op)_3$. En revanche, en ce qui concerne le complexe $Al(Op)_3$, il fut impossible de mesurer une quelconque mobilité de porteurs de charge que ce soit en temps de vol (en anglais: time of flight - TOF) ou bien en spectroscopie d'admittance (en anglais: admittance spectroscopy - AS). Il en résulte que la conception des dispositifs intégrant ces complexes doit encore être optimisée, afin de pouvoir obtenir des résultats probants en utilisant les deux méthodes précédemment citées.

Étude des interfaces hybrides OSCs/Co

En collaboration avec: Dr. Mirko Cinchetti and Nicolas Großmann (Department of Physics and Research center OPTIMAS, University of Kaiserslautern, Kaiserslautern, Germany)

Lors de ma thèse, j'ai étudié le complexe $Al(Op)_3$ dans l'optique de développer une nouvelle génération de OSCs pouvant être utilisés pour fabriquer des interfaces hybrides et exploiter la flexibilité des semi-conducteurs organiques. Puisque les ligands du complexe $Al(Op)_3$ sont de plus grande taille que ceux du complexe Alq_3, la chemisorbtion de ces deux complexes sur une surface de cobalt diffère. Par conséquent, les propriétés dépendantes du spin électronique de l'interface hybride $Co/Al(Op)_3$ diffèrent de celles de l'interface hybride Co/Alq_3. En raison des propriétés électroniques hétérogènes exhibées par les OCSs déposés sur un substrat de cobalt, l'interaction entre le complexe et le substrat ferromagnétique présente une grande diversité, que cela soit dans leur nature ou dans leur intensité. Le type d'interaction affecte directement les propriétés quantiques du spin des électrons et, par conséquence, les applications en spintronique de ces interfaces hybrides.
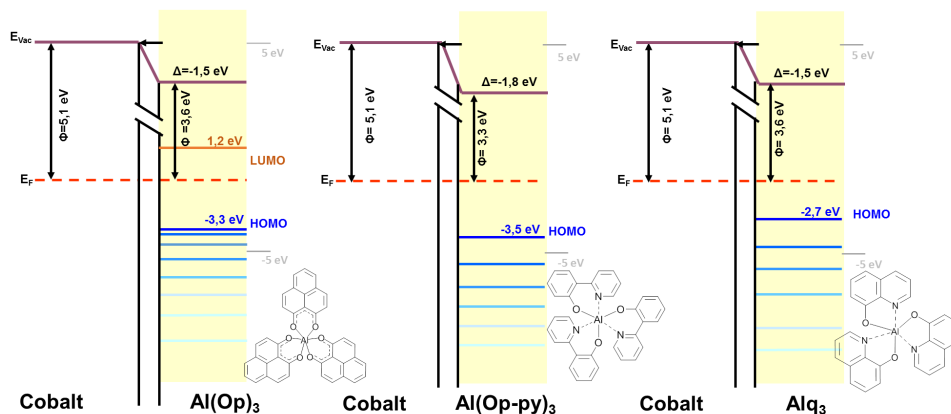

Figure 7: Alignement des niveaux d'énergie pour les interfaces $Co/[5 \, nm] \, Al(Op)_3$ et $Co/[2.8 \, nm]$ $Al(Op-py)_3$. Ces données sont extraites des spectres UPS et 2PPE. L'alignement des niveaux d'énergie pour l'interface Co/Alq_3 est indiqué à titre de comparaison.

L'interface hybride $Co/Al(Op)_3$ fut analysée en utilisant les méthodes de spectroscopie de photoélectrons (en anglais: photoemission spectroscopy - PES) suivantes: la spectroscopie de photoélectrons UV (en anglais: ultraviolet photoemission spectroscopy - UPS), NT-PS (en anglais: near-threshold photoemission spectroscopy) et la spectroscopie de photoélectrons à
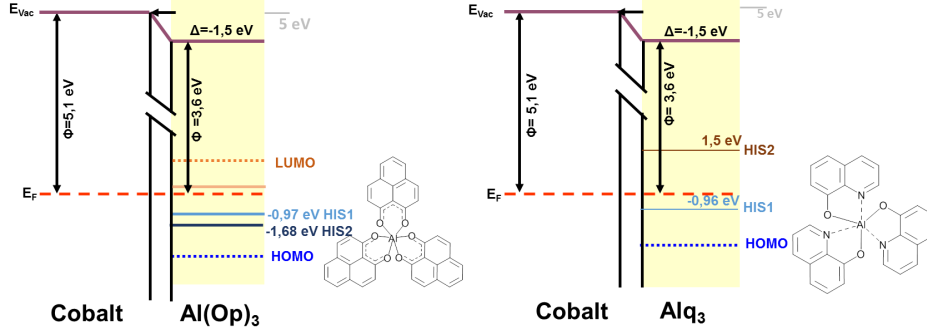
Figure 8: Alignement des niveaux d'énergie pour l'interface Co/[1.5 nm] Al(Op)₃. Ces données sont extraites des spectres NT-PS et 2PPE. L'alignement des niveaux d'énergie pour l'interface Co/Alq₃ est indiqué à titre de comparaison.

deux photons (en anglais: two photon photoemission - 2PPE). Ces analyses permirent de déterminer les propriétés dépendantes directement du spin de cette interface. En plus des analyses de spectroscopie mentionnées précédemment, j'ai effectué des analyses UPS de l'interface hybride Co/Al(Op−py)₃. Les résultats obtenus avec les méthodes d'analyse UPS et 2PPE pour l'interface Co/[5 nm] Al(Op)₃ ainsi que les résultats obtenus pour l'interface Co/[2.8 nm] Al(Op−py)₃ avec la méthode UPS sont présentés et comparés aux resultats obtenus pour l'interface Co/Alq₃ dans la Figure 7. En ce qui concerne l'interface Co/[5 nm] Al(Op)₃, les analyses montrent que huit états d'énergie sont occupés et que le dipôle qui se forme à l'interface est caractérisé par un moment dipolaire d'une valeur de $\Delta= -1.5$ eV. Par ailleurs pour cette interface, les niveaux d'énergie (comptés à partir du niveau de Fermi E_F) sont respectivement de -3.3 eV pour le niveau HOMO et de 1.2 eV pour le niveau LUMO. En ce qui concerne l'interface Co/[2.8 nm]Al(Op−py)₃, le moment dipolaire est de $\Delta= -1.8$ eV et le niveau HOMO de -3.5 eV(compté à partir du niveau de Fermi E_F).

Les résultats fournis par les analyses NT-PS pour l'interface Co/[1.5 nm]Al(Op)₃ sont présentés dans le Figure 8. Les deux états hybrides pour cette interface (en anglais: hybrid interface state - HIS) d'énergie respectives $E - E_F= -0.9$ eV et $E - E_F= -1.6$ eV y sont indiqués. Le HIS1 présente une polarisation du spin (en anglais: spin polarization - SP) 8% plus élevé que celui du cobalt, tandis que le HIS2 est caractérisé par un SP 4% plus bas que celui du cobalt. Les OSCs peuvent être modifiés chimiquement afin de changer les propriétés électroniques des interfaces qu'ils forment avec des métaux. Le niveau HOMO dans le cœur des complexes Al(Op)₃, Al(Op−py)₃ et Alq₃ est respectivement de -3.3 eV, -3.5 eV et -2.7 eV lorsque ces complexes sont déposés sur du cobalt. Les moments dipolaires d'interface des ces trois composés sont quant à eux pratiquement identiques: $\Delta= -1.5$ eV, $\Delta= -1.8$ eV and $\Delta= -1.5$ eV respectivement. Enfin, les mesures 2PPE résolues en spin et en temps montrent qu'aucun état d'énergie d'interface inoccupé (uHISs) n'est présent pour l'interface Co/Al(Op)₃. Cependant, le niveau LUMO du complexe Al(Op)₃ put être détecté lors des mesures. Puisque le niveau LUMO n'est pas influencé par le SP du substrat de cobalt, la durée de vie des électrons spin-up (τe_{up}) et de ceux spin-down (τe_{down}) sont identiques.

Aimants mono-moléculaires à base de phenalenyl

En collaboration avec: Dr. Yanhua Lan (INT-KIT, Karlsruhe, Germany)

J'ai, par ailleurs, analysé les conditions pour lesquelles les ligands HOp chélatent des atomes

paramagnétiques pour former des aimants mono-moléculaires (en anglais: single-molecule magnets - SMMs). Les SMMs ont pour propriété élémentaire de conserver leur magnétisation sur de longues périodes et ce en l'absence de champ magnétique externe. Les lanthanides les plus utilisés pour la fabrication de SMMs sont les suivants: le terbium(III), le dysprosium(III), l'erbium(III)et l'holmium(III). La synthése des complexes à base de dysprosium et de terbium contenant des ligands HOp put être realisée ainsi que la détermination de leurs structures en utilisant les méthodes ^{1}H-NMR, MALDI-TOF et spectrophotométrie UV-Vis. J'ai fait croitre des mono-cristaux de [Dy(Op)$_2$Cl(HOp)(EtOH)] et des mono-co-cristaux de [Dy(Op)$_3$(HOp)] et [Dy(Op)$_3$(EtOH)], permettant de déterminer leur structure moléculaire de façon inéquivoque (voir Table 6).

Table 6: Structure chimique des complexes de lanthanides à base de phenalenyl. Résultats obtenus par diffractométrie de rayons X.

[Dy(Op)$_2$Cl(HOp)(EtOH)]   [Dy(Op)$_3$(HOp)]   [Dy(Op)$_3$(EtOH)]
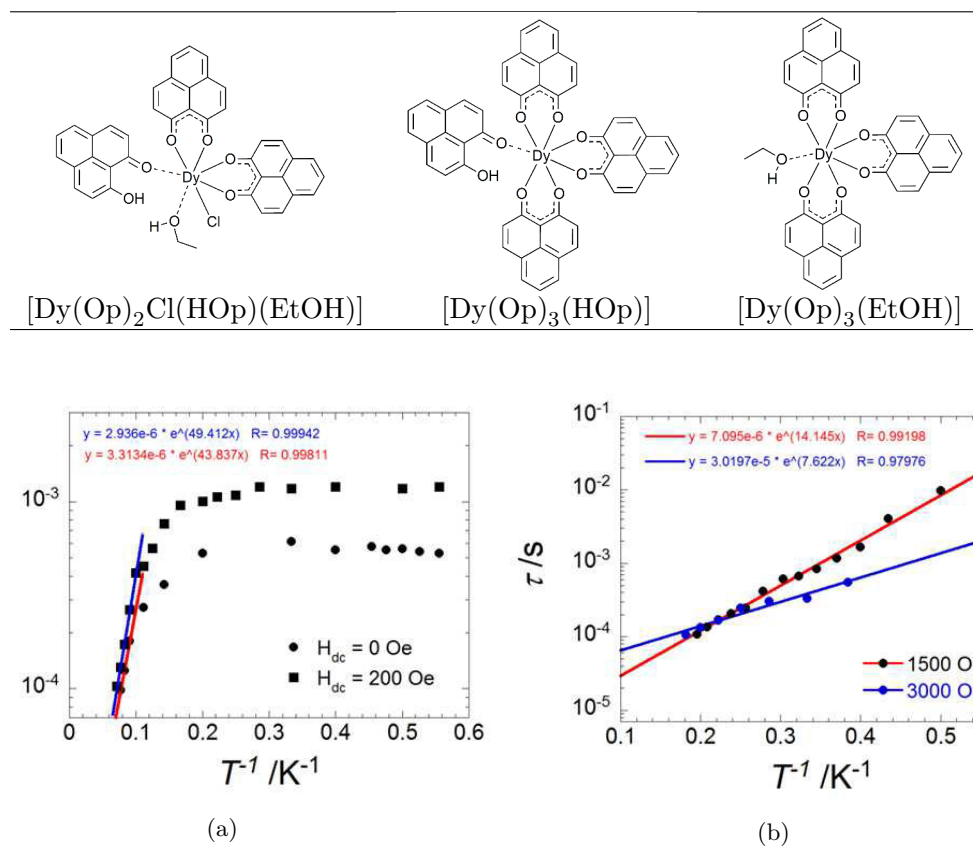
Figure 9: (a) Diagramme d'Arrhenius semi-logarithmique du temps de relaxation τ en fonction de $1/T$ pour le complexe [Dy(Op)$_2$Cl(HOp)(EtOH)]. La susceptibilité magnétique fut mesurée pour un champ magnétique externe nul ainsi que pour un champ statique externe de 200 Oe. La courbe obtenue par régression linéaire pour l'intervalle de température d'activation termique est tracée sur le diagramme.(b) Diagramme d'Arrhenius semi-logarithmique du temps de relaxation τ en fonction de $1/T$ pour le complexe [Dy(Op)$_3$(HOp)]-[Dy(Op)$_3$(EtOH)]. La susceptibilité magnétique fut mesurée pour deux valeurs champs magnétiques externes: 1500 Oe et 3000 Oe. La courbe obtenue par régression linéaire pour l'intervalle de température d'activation termique est tracée sur le diagramme.

Les résultats obtenus lors des mesures des propriétés magnétiques du complexe [Dy(Op)$_2$Cl(HOp)(EtOH)] tendent à montrer que ce complexe est un SMM exhibant, pour un champ statique externe nul,

un barrière anisotropique Δ de $43.8\,\mathrm{K}$ et un temps de relaxation quantique de $\approx 5 \times 10^{-4}\,\mathrm{s}$. Par ailleurs, les même mesures furent répétées en appliquant un champ externe de $200\,\mathrm{Oe}$ et permirent d'observer dans ce cas un barriére anisotropique Δ de $49.4\,\mathrm{K}$ et un temps de relaxation quantique de $\approx 1 \times 10^{-3}\,\mathrm{s}$. Ces résultats permettent de conclure que l'effet tunnel quantique n'est pas très prononcé dans ce composé. Puisque la séparation des deux complexes l'un de l'autre s'avére impossible à réaliser, les mesures des propriétés magnétiques furent réalisées en utilisant les co-cristaux de $[\mathrm{Dy(Op)_3(HOp)}]$ et de $[\mathrm{Dy(Op)_3(EtOH)}]$. Lorsque aucun champ magnétique statique externe n'est appliqué, la susceptibilité ne présente pas de déphasage, ce qui pourrait être du à une forte résonance de l'effet tunnel quantique. Les mesures furent répétées pour des champ magnétique statiques externes de $1500\,\mathrm{Oe}$ et $3000\,\mathrm{Oe}$. Pour un champ magnétique externe de $1500\,\mathrm{Oe}$, le temps de relaxation calculé suit un activé comportement et le gap d'énergie est de Δ $14.1\,\mathrm{K}$ tandis que pour un champ externe de $3000\,\mathrm{Oe}$ la barrière anisotropique Δ est de $7.6\,\mathrm{K}$ lors de la relaxation à haute fréquence. De plus, j'ai pu synthétiser et caractériser d'autres complexes de dysprosium et de terbium. Par exemple, en condition anhydre, j'ai pu obtenir et sublimer des complexes de dysprosium et de terbium à base de phenalenyl. La synthèse de ces composés pourrait permettre de réaliser la déposition de complexes de lanthanides à base de phenalenyl sur des substrats. Cela permettrait ainsi d'ouvrir la porte à leur étude, sous réserve d'obtenir des mono-cristaux condition nécessaire pour connaitre leur structure exacte.

Lors de ma thèse, j'ai conduit et présenté une analyse systématique de nouveaux materiaux OSCs très prometteurs. J'ai pu mettre en évidence ainsi le lien entre la structure chimique et les propriétés électroniques de ces matériaux. La première étape de mon travail consista à synthétiser les OSCs ainsi qu'à caractériser leur structure. Les analyses photo-physiques et électrochimiques réalisées permirent de déterminer les propriétés électroniques de ces nouveaux matériaux. Les résultats obtenus se révélÃrent être en bon accord avec les calculs théoriques. Par ailleurs, les mobilités des porteurs de charge purent être calculées en faisant appel à des méthodes de calcul développées récemment telles que DEPOSIT et Quantum Patch. En ce qui concerne les mesures expérimentales des mobilités, de premiers résultats probants furent obtenus pour le complexe $\mathrm{Al(Op)_3}$ en utilisant la méthode FET. En mÃme temps que l'analyse systématique des complexes OSCs simples, j'ai pu étendre l'analyse à quelques interfaces hybrides OSC/cobalt . Par exemple, l'analyse de la surface hybride $\mathrm{Co/Al(Op)_3}$ par PES montra la formation de HIS.

Parallèlement à mon projet principal, je présente dans ma thèse les premiers résultats obtenus pour des SMMs de lanthanides à base de phenalenyl. Ces résultats préliminaires sont très encourageants puisqu'ils mettent en évidence que les complexes de dysprosium exhibent un comportement caractéristique de SMMs. Par ailleurs, l'obtention de complexes se laissant sublimer ouvre la porte à la déposition de ces molécules sur des substrats par évaporation et, ainsi, à de futures applications en spintronique.

Contents

1. Introduction

I would begin the thesis clarifying what is the meaning of its title: *"Multifunctional Complexes for Molecular Devices"*. Firstly, what is a multifunctional complex?. The Oxford English Dictionary [1] defines *"multifunctional"* as: *"having or fulfilling many functions"*, while the substantive *"complex"* is defined as: *"a substance formed by the combination of simpler substances, especially one in which the bonds between the substances are weaker than or of a different character from those between the constituents of each substance"*. Hence, a coordination compound such as a metal chelate, which can accomplish a variety of functions, can be considered as a *"multifunctional complex"*. Secondly, what is a molecular device? The definition of *"molecular"* is: *"pertaining to, consisting of, or concerned with molecules"*. One of the many definitions of *"device"* is: *"the result of contriving; something devised or framed by art or inventive power; an invention, contrivance; especially a mechanical contrivance (usually of a simple character) for some particular purpose"*. In other words, a molecular device is an invention (a tool or an instrument) based on one, or more molecules developed and built to fulfill specific intentions. In this thesis, we have studied metal complexes belonging to the class of materials known as organic semiconductors (OSCs), which are molecules able to transport charge carriers (electrons and/or holes), but also to exhibit photo- and electro-luminescence, and, as described in the succeeding sections, many more interesting properties.

Around the middle of the last century, the invention of the transistor gave rise to the era of inorganic semiconductors such as silicon and germanium. Contemporaneously, the substitution of vacuum tube based electronics by solid state devices led to the semiconductor microelectronics we experience in our everyday life. The first promise of OSCs was to realize large area, flexible, printed and low cost electronic and optoelectronic devices. First studies on mere conductivity and photoconductivity of anthracene crystals were published in the beginning of the 20th century by Koenigsberger *et al.* and Volmer [2, 3]. With the discovery of electroluminescence (EL) in the 1960s [4, 5], and the work of many researchers, the basic processes involved in optical excitation and charge carrier transport were established [6, 7]. The successful synthesis and controlled doping of conjugated polyacetylene polymers (see Figure 1.1) in the 1970s [8] opened the way for a new class of OSCs, which was awarded with the Nobel Prize in Chemistry in the year 2000. Finally, the demonstration of high-performance OLEDs (Organic Light Emitting Diodes) based on vacuum-deposited molecular films [9, 10] and on conjugated polymers [11, 12] revived the interest in undoped OSCs. Besides OLEDs, OSCs are nowadays implemented in a variety of devices such as organic photovoltaic cells (OPVs) [13, 14], organic spintronic devices (OSPDs) [15] and organic field-effect transistors (OFETs) [16].

"The exciting idea of being able to combine the flexibility and low weight of plastics with the electric properties of metals has stimulated scientists all over the world, resulting in a novel research field bordering physics and chemistry. Various theoretical models and new conductive, but also semi-conductive, polymers followed during the 1980s in the wake of the first discoveries. Today we can see several possible applications. How about electrically luminous plastic that may
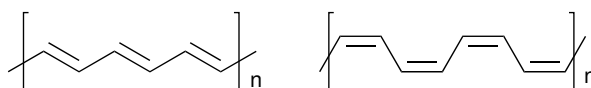
Figure 1.1: Polyacetylene polymers studied in reference [8]. Left: *trans*-polyacetylene. Right: *cis*-polyacetylene.

be used for manufacturing mobile phone displays or the flat television screens of the future? Or the opposite - instead using light to generate electric current: solar-cell plastics that can be unfolded over large areas to produce environmentally friendly electricity. Finally, lightweight rechargeable batteries may be necessary if we are to replace the combustion engines in today's cars with environmentally friendly electric motors - another application where electrical polymers might find use.

In parallel with the development of conducting polymers, there is an ongoing development of what we might call "molecular electronics," where the very molecules perform the same tasks as the integrated circuits we just heard about in the Nobel Prize in Physics, with the difference that these could be made incomparably smaller. In laboratories around the world, scientists are working hard to develop molecules for future electronics. And among test tubes and flasks, and in the interplay between theory and experiment, we may some day again be astonished by something unexpected and fantastic. But this is a different story, and perhaps a different Nobel Prize ..." - Professor Bengt Nordén delivering the Presentation Speech for the 2000 Nobel Prize in Chemistry to Professors Heeger, MacDiarmid and Shirakawa at the Stockholm Concert Hall. Source: [`http://www.nobelprize.org/nobel_prizes/chemistry/laureates/2000/`].
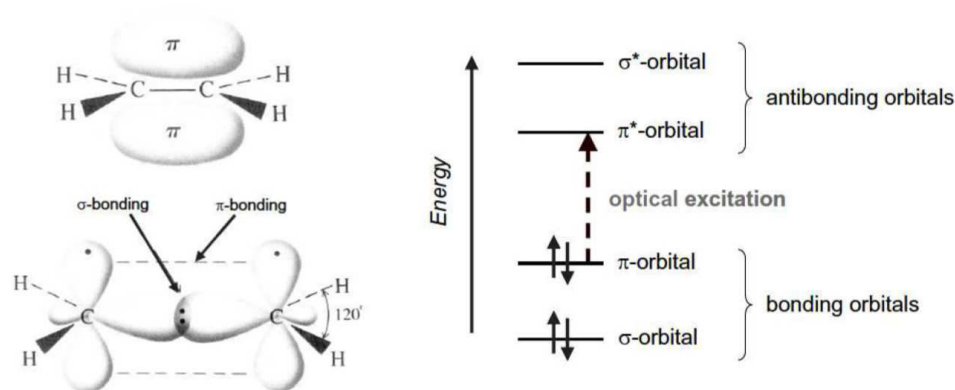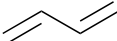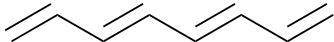
1.1 Organic semiconductors (OSCs)

Figure 1.2: σ- and π-bonds in ethene as an example for the simplest conjugated π-electron system. On the right-hand side are depicted energy levels and lowest electronic excitation of ethene. Source: [17].
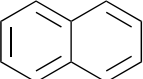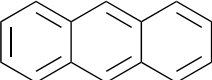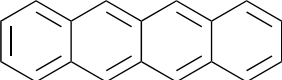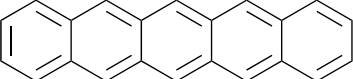
In solid state physic it is convenient to distinguish between three different material classes by means of electrical properties: metals (conductors), semiconductors, and insulators. In general, they are defined by the value of their energy band gap between valence and conduction bands and by the position of the Fermi energy. We will focus on the class of OSCs briefly explaining the main features of these materials (for a review on OSCs see [17–19]).

There are two main classes of OSCs: low molecular weight (small molecules) and polymers.

Both have in common a conjugated π-electron system formed by the p$_z$-orbitals of sp^2-hybridized carbon atoms. The most important difference between the two classes of OSCs is the processing method to form thin films. Low molecular weight OSCs are usually deposited from the gas phase by sublimation or evaporation in vacuum. Polymeric OSCs are processed by solution-based methods such as spin-coating or printing techniques. For both, the controlled growth of high quality films is crucial for the applications in devices [20]. In both classes of OSCs, carbon atoms are bonded with strong σ bonds, which form the backbone of the molecule, and significantly weaker π bonds (see Figure 1.2). As a consequence, the lowest electronic excitation of conjugated molecules are $\pi - \pi^*$ transitions with an energy gap (calculated from the main absorption band) between 185 and 580 nm resulting in absorption and emission ranging from UV to visible wavelengths. As illustrated in Table 1.1, it is possible to tune the energy gap by increasing the degree of conjugation of polyenes and polyacenes. This is an example on how chemistry tools are used to significantly modify the electronic properties of OSCs. The fundamental interaction between different molecules in organic crystals or in amorphous films are the van-der-Waals forces. Hence, due to the weak electronic delocalization between adjacent molecules, electronic and optical properties of isolated molecules are similar to those of molecules in solid state.

Table 1.1: Molecular structure of the first three polyenes and first five polyacenes, together with the wavelength of the main absorption peak. Sources: `http://photonicswiki.org`, [7].

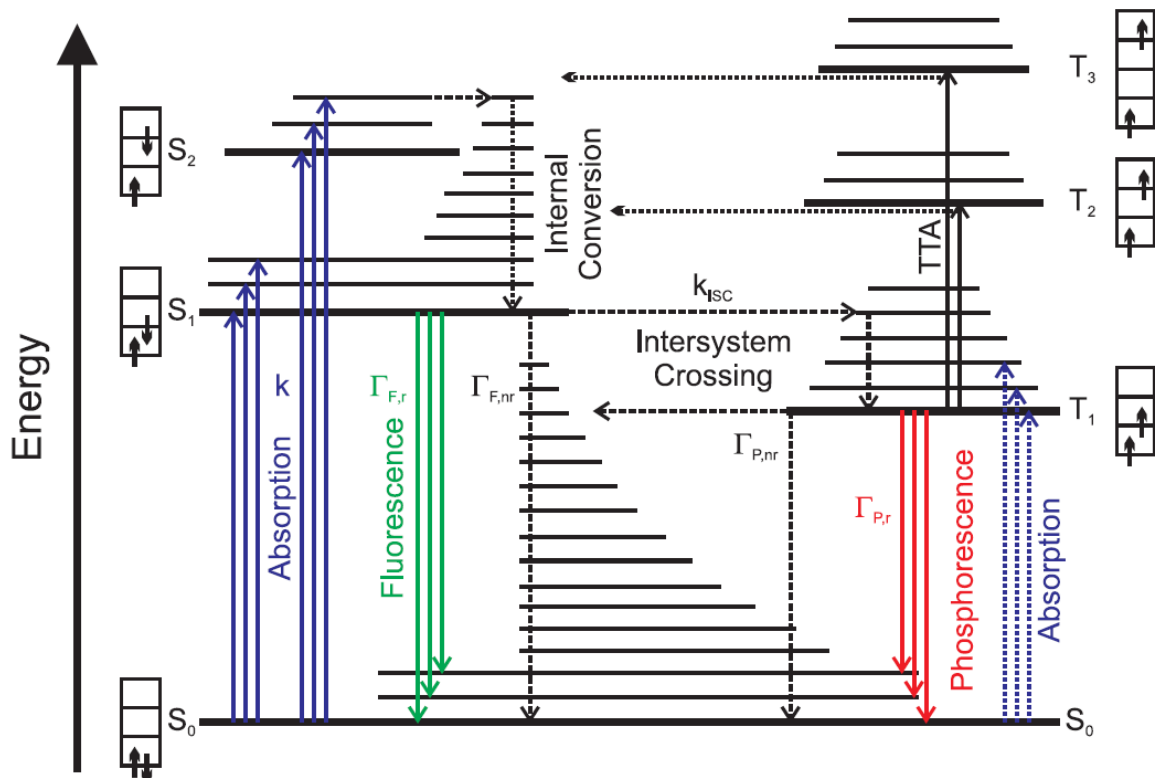| Molecule	Structure	Abs. Max. [nm]
Ethene		185
Butadiene		215
Octatetraene		400
Benzene		255
Naphthalene		315
Anthracene		380
Tetracene		480
Pentacene		580

1.1.1 Optical properties of OSCs

Figure 1.3: Jablonsky diagram of an organic molecule. Left: singlet manifold. Right: triplet manifold. Blue vertical arrows represent absorption processes, green and red vertical arrows represent emission processes, dashed vertical arrows represent radiationless processes, and black solid vertical arrows represent triplet-triplet annihilation processes. Thick horizontal lines are electronic energy levels, and thin horizontal lines are vibronic sublevels. $\Gamma_{F,r}$, $\Gamma_{F,nr}$, $\Gamma_{P,r}$, and $\Gamma_{P,nr}$ are radiative and non-radiative rates of fluorescence and phosphorescence, respectively. k and k_{isc} are rates of absorption and intersystem crossing, respectively. Source: [21].

All the basic optical energy conversion processes of an organic molecule or solid are exemplified in the Jablonsky diagram shown in Figure 1.3. Optical excitation processes take place between the singlet ground state S_0 (HOMO) and singlet excited states S_1 (LUMO), S_2, ... , S_n; singlet states have multiplicity equal to 1. The radiative decay process between S_1 and S_0 is called fluorescence, however, S_1 can experience also non-radiative decays (thermal decay, quenching, ...). Higher singlet excited states undergo a very fast non-radiative internal conversion process to S_1, and thus, normally, no radiative processes are observed between S_2, ... , S_n and S_0 [18]. Triplet states T_n have multiplicity equal to 3, as a result, due to the quantum mechanical selection rules, the radiative decay from triplet states to S_0 (phosphorescence) is strictly forbidden if no spin-orbit coupling is present in the molecule [18]. Triplet emission of molecules constituted from carbon and hydrogen is weak, in contrast, when heavy atoms with a strong spin-orbit coupling are introduced, the phosphorescence process can occur. The triplet state T_1 is formed by intersystem crossing from S_1 rather than by a direct optical excitation S_0-T_1. Intersystem crossing processes are triggered by the spin-orbit coupling resulting in a spin-flip from S_1 to T_1. Higher triplet states are formed by triplet-triplet annihilation processes, in which two triple

states fuse generating a ground state S_0 and higher triplet states $T_2, ... ,T_n$. These states transform in singlet states by intersystem crossing resulting in a delayed fluorescence [22]. Rates of absorption k and radiative Γ_r and non-radiative Γ_{nr} decays depend from the overlap between the wavefunctions of initial i and final f states, which are determined by the transition matrix elements, if one of the three factors is zero, the transition is forbidden with a null probability $P_{i \to f}$ to occur.

$$P_{i \to f}^2 \propto | \langle \Psi_f | \vec{p} | \Psi_i \rangle |^2 \propto \langle \Psi_{el,f} | \vec{p} | \Psi_{el,i} \rangle |^2 \cdot | \langle \Phi_{vib,f} | \Phi_{vib,i} \rangle |^2 \cdot | \langle \chi_{spin,f} | \chi_{spin,i} \rangle |^2 \qquad (1.1)$$

In Equation 1.1, $\vec{p} = e \cdot \vec{r}$ represents the dipole operator and $\vec{M} = | \langle \Psi_f | \vec{p} | \Psi_i \rangle |$ is the transition dipole moment between initial and final states of the molecule. When the parity of the two wavefunctions is different, the transition is allowed. The factor $| \langle \Phi_{vib,f} | \Phi_{vib,i} \rangle |$ takes in account the contribution of vibrations to electronic transitions. The Frank-Condon principle states that only vertical transitions are allowed, and the intensity of the transition is proportional to the overlap between the vibronic wavefunctions of initial and final states. Additionally, higher vibronic states of the first excited electronic state S_1 and higher excited electronic states are coupled, and thus, a fast relaxation process (internal conversion) occurs to the lowest vibronic state of the first excited state S_1 (Kasha's rule). This leads to the characteristic Stokes shift observed between absorption and emission spectra of a molecule. Figure 1.4 illustrates the typical vibronic structure of absorption and emission spectra.
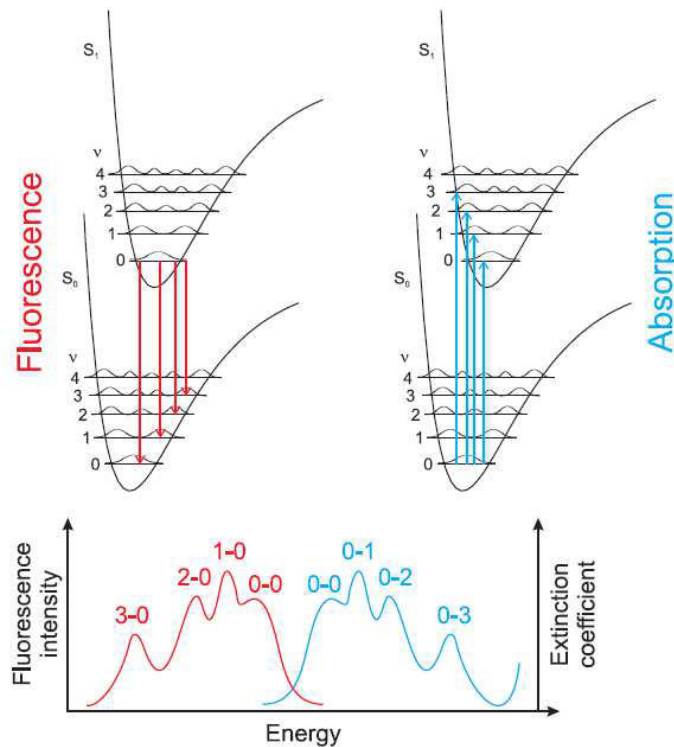

Figure 1.4: Schematic illustration of vibronic transitions (absorption and fluorescence) between S_0 and S_1 in an organic molecule. Source: [21].

The last parameter to take in account, $| \langle \chi_{spin,f} | \chi_{spin,i} \rangle |$, concerns the spin selection rule of an electronic transition. Basically, transitions between spin states with different multiplicities are forbidden. Therefore, only transitions between singlet states, such as fluorescence, are allowed.

However, in case of spin-orbit coupling, induced by heavy atoms, transitions between singlet and triplet states, such as phosphorescence, are allowed.

1.1.2 Electrical properties of OSCs

Macroscopically, the current through a material is given by the charge carrier density n and the carrier drift velocity ν, which can be expressed by the mobility μ and the electric field F [17]:

$$j = qn\nu = qn\mu F \tag{1.2}$$

where, j is the current density and q is the elementary electric charge. In general, the charge carrier mobility exhibits a non-linear behavior and depends on the charge carrier density n, the temperature T, and the electric field F. The intrinsic charge carrier density in a semiconductor is given by:

$$n = N_0 \exp -\frac{E_{gap}}{2k_b T} \tag{1.3}$$

where, N_0 is the density of organic molecules, E_{gap} is the HOMO-LUMO gap, k_b is the Boltzmann constant, and T is the temperature. For a typical organic molecular solid, with E_g= 2.5 eV and N_0= 10×10^{21} cm^{-3}, at room temperature the charge carrier density is n= 1 cm^{-3} (silicon n= 10^{10} cm^{-3}) [17]. As a result, OSCs are characterized by extremely low conductivity if no additional free charge carriers are created. To increase the carrier density in molecular solids, different means can be applied, which are the fundamental processes involved in OSCs-based devices. OLEDs are governed by the injection of charge carriers from electrodes into organic layers. Similarly, in OSPSs, charges (spins) are injected from ferromagnetic electrodes into non-magnetic organic materials. In contrast, in OPVs charge carriers are photogenerated by absorption of light. In OFETs, the density of charge carriers, which are injected from source and drain electrodes, is controlled by the applied gate voltage across the dielectric.
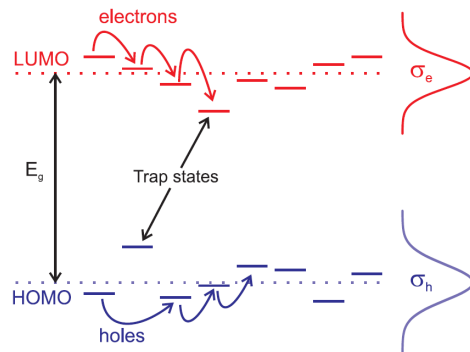

Figure 1.5: Illustration of the hopping transport mechanism. The distribution of the density of HOMO and LUMO states is Gaussian with widths σ_h and σ_e, respectively. Source: [21].

In all these four OSCs-based devices, although taking in account the different mechanisms to inject/generate charge carriers, the charge carrier transport process is similar. In molecular crystals, band transport is observed, whereas in the case of amorphous materials hopping transport prevails (see Figure 1.5). Since nowadays OSCs-based devices are constituted by thin (often amorphous) layers, and since the molecules studied in this thesis are forming amorphous

films, only the hopping mechanism is discussed in the following. The motion of a charge between two localized energy levels under an applied field is described by the hopping transport mechanism [23]. OSCs in amorphous films, due to a statistical alignment of molecules during the film growth, are characterized by distributed energy levels resulting in shifted HOMO and LUMO energies [7, 24–26], as illustrated in Figure 1.5. HOMO and LUMO energies are shifted compared to those of an isolated molecule owing to interactions with the surrounding environment. Considering a statistical number of molecules in an amorphous film, a Gaussian distribution of energy, with typical width (σ_h and σ_e) of 75-100 mV, is assumed [23]. As a result, the hopping of charge carriers must be thermally activated to overcome the energetic barriers between localized states. Lastly, the presence of trap states, which can be a very low LUMO or a very high HOMO, influences the charge transport resulting in low charge carrier mobilities, and thus, poor performance of devices.
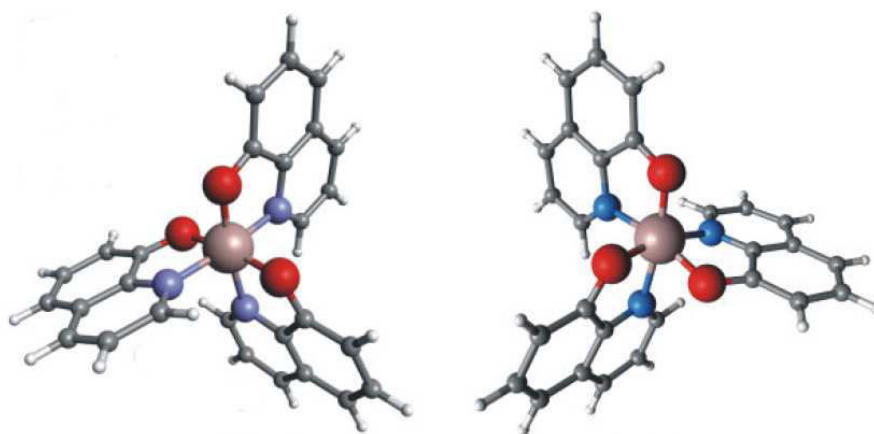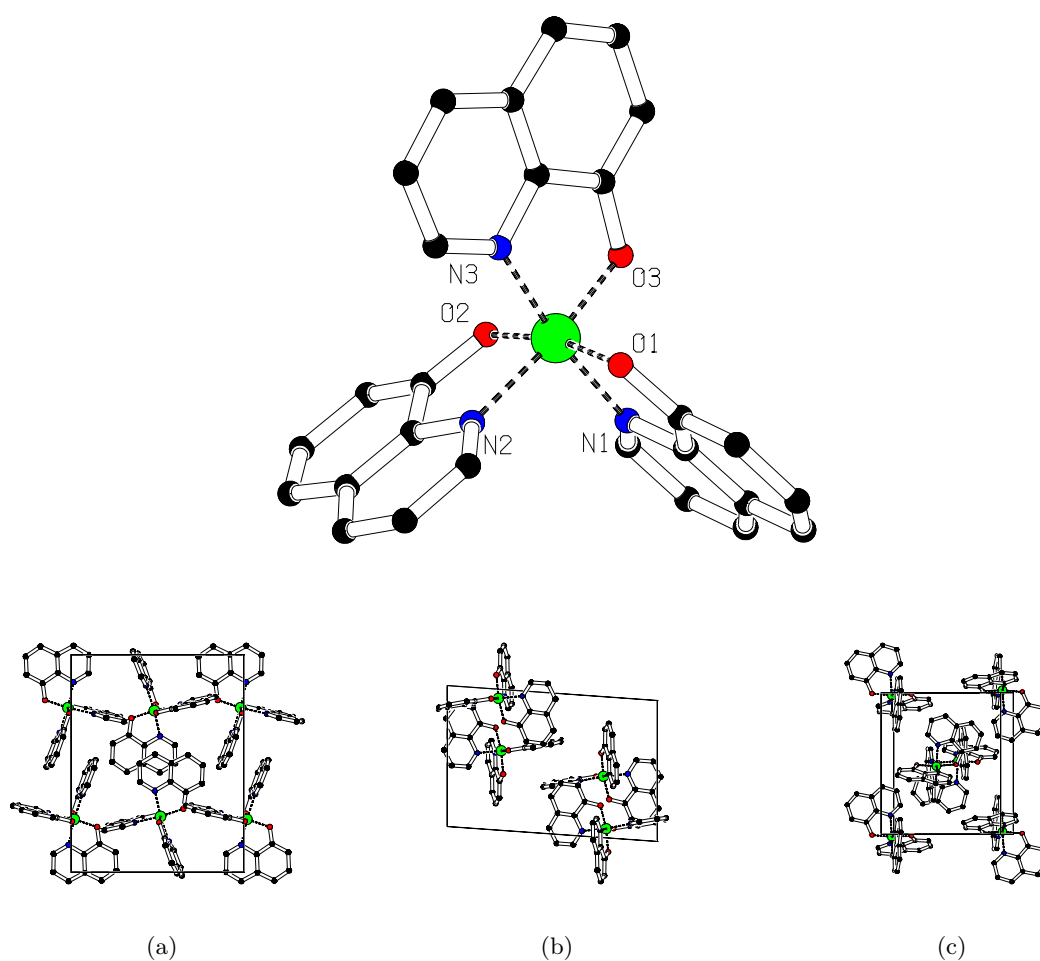
1.2 Tris-(8-hydroxyquinoline)aluminum (Alq₃)

Figure 1.6: Molecular structures of the meridianal isomer (*mer*-Alq₃) on the left hand side, and of the facial isomer (*fac*-Alq₃) on the right end side. Source: [27].

Alq₃ is, beyond any doubt, a multifunctional complex implemented in a multitude of molecular devices. The very first application of quinolin-8-ol metal chelates was in analytical chemistry for the gravimetric determination of metal cations in solution [28]. Since its first application in an electroluminescent device [9], Alq₃ is one of the most widely known OSC [29]. Before describing in detail the applications of Alq₃ in molecular devices, we will focus our attention on the chemical structure of Alq₃, which is at the origin of its properties.
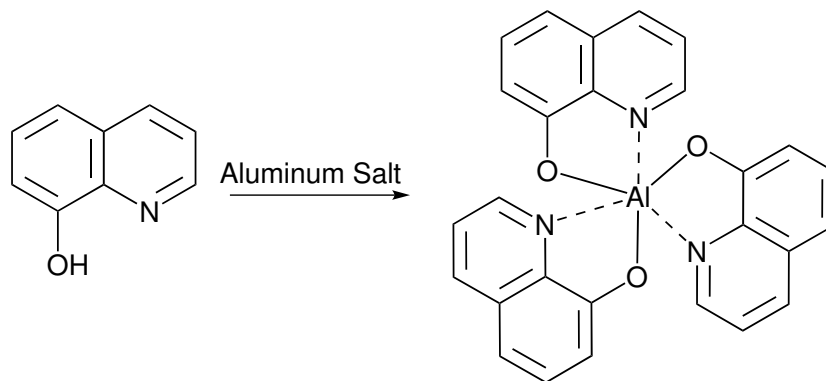
Alq₃ is formed by three bidentate anions, quinolinates, which fill the coordination sites of the central metal ion, Al^{3+}. The resulting net charge of the complex is zero. Alq₃ is also well known to be a MN_3O_3 octahedral complex, where M is a trivalent metal, whereas N and O stand for the nitrogen and oxygen atoms, respectively, in the quinoline ligand. These octahedral complexes can occur in two different geometric isomers, the meridianal and the facial isomer, which are illustrated in Figure 1.6 [27, 30]. In the facial isomer, the three oxygens face the three nitrogens. Diversely, in the meridianal isomer, two oxygens are opposite to each other as well as two nitrogens and one oxygen faces one nitrogen.

The conventional synthesis of Alq₃, from an aluminum salt ($AlCl_3$, $Al(NO_3)_3 \cdot 9\,H_2O$ or $Al(SO_4)_3 \cdot 6\,H_2O$) and quinolin-8-ol (Hq) shown in Scheme 1.1, provides the *mer*-Alq₃ as main product

Figure 1.7: Molecular structure obtained by single crystal X-ray diffraction of *mer*-Alq$_3$. H-atoms and solvent molecules are omitted for clarity. The crystal refinement data is reported in Table C.1. The molecular packing in the single crystal of *mer*-Alq$_3$ is illustrated in (a) yz (b) xz (c) xy perspective. Table: selected bond distances and angles for *mer*-Alq$_3$.

Bond	Length [Å]	Bond angle	Angle [°]	Bond angle	Angle [°]
		mer-Alq$_3$			
Al1-O1	1.8789(10)	O1-Al1-O2	167.98(5)	O2-Al1-N3	95.28(5)
Al1-O2	1.8553(10)	O1-Al1-O3	96.35(5)	O3-Al1-N1	90.17(5)
Al1-O3	1.8384(10)	O1-Al1-N1	82.88(5)	O3-Al1-N2	173.71(5)
Al1-N1	2.0238(12)	O1-Al1-N2	87.99(4)	O3-Al1-N3	84.01(5)
Al1-N2	2.0637(12)	O1-Al1-N3	91.78(5)	N1-Al1-N2	94.90(5)
Al1-N3	2.0421(12)	O2-Al1-O3	94.06(5)	N1-Al1-N3	171.64(5)
		O2-Al1-N1	91.10(5)	N2-Al1-N3	91.33(5)
		O2-Al1-N2	82.14(4)		

Scheme 1.1: Synthesis of *mer*-Alq$_3$. Aluminum salt: AlCl$_3$, Al(NO$_3$)$_3$·9 H$_2$O or Al(SO$_4$)$_3$·6 H$_2$O.

[31]. On the contrary, *fac*-Alq$_3$ has been difficult to isolate for its relatively short lifetime in solution [32]. Nevertheless, by the solid-state synthetic procedure described by Katakura *et al.*, it is possible to efficiently produce the *fac*-isomer [33]. Since *fac*-Alq$_3$ has quite distinct properties compared to those of *mer*-Alq$_3$, it has been extensively studied [27]. The molecular structure of *mer*-Alq$_3$, obtained by single crystal X-ray diffraction, was first reported for single crystals grown in methanol [34] and in ethyl acetate [35]. We have grown single crystals of *mer*-Alq$_3$ in ethanol; the molecular structure obtained by single crystal X-ray diffraction is illustrated in Figure 1.7, in addition, selected bond distances and angles are listed. An intrinsic asymmetry, caused by the positions of the six chelating atoms, characterizes *mer*-Alq$_3$. In detail, O1 faces O2 and N1 faces N3, in contrast, O3 is opposite to N2. This results in an elongation of the bond Al-N2 (2.0637 Å) compared to the bonds Al-N1 and Al-N3 (2.0238 Å and 2.0421 Å, respectively), and a shrinking of the bond Al-O3 (1.8384 Å) compared to the bonds Al-O1 and Al-O2 (1.8789 Å and 1.8553 Å, respectively). In addition, the narrow bite angle of Hq and the electrostatic repulsion between nitrogens and oxygens, induce a distorted octahedral geometry of the six chelating atoms, with bond angles of 82.14°-96.35° and 167.98°-173.71°.

Due to the electron deficient quinoline, Alq$_3$ is characterized by high LUMO and HOMO, ≈ -3.0 eV and ≈ -6.0 eV, respectively [36–38] (-3.01 eV and -5.83 eV experimentally estimated in Section 3.6). As a consequence of its good thermal stability [39], Alq$_3$ can be deposited by vacuum evaporation forming amorphous pinhole-free thin films [40], which are likely containing both the *mer*-Alq$_3$ and *fac*-Alq$_3$ [41]. In addition, Alq$_3$ in amorphous thin film is characterized by electron and hole mobilities of 10^{-5}-10^{-6} cm^2 V^{-1} s^{-1} and 10^{-8}-10^{-9} cm^2 V^{-1} s^{-1}, repetively [42–49]. All these characteristics make Alq$_3$ and ideal material for applications in OSCs-based devices.

1.2.1 Alq$_3$ in OLEDs

OLEDs are devices in which the light emission originates by the radiative recombination of charge carriers in organic layers (for a review on OLEDs see [18]). An elementary OLED can consist of a single organic layer sandwiched between two electrodes [11], however, to improve the device efficiency, multilayer OLEDs, in which each organic layer fulfill a specific function, are preferred. In a simple configuration, an OLED is composed by three organic layers: the electron transport layer (ETL), the hole transport layer (HTL), and the emission layer (ETL). As illustrated in Figure 1.8, the working principle of OLEDs is described by four main processes: (1) injection of electrons from the cathode into the LUMO of the ETL and injection of holes

from the anode into the HOMO of the HTL, (2) transport of the charge carriers through the organic layers, (3) formation of the exciton, and (4) radiative exciton decay and emission of light.
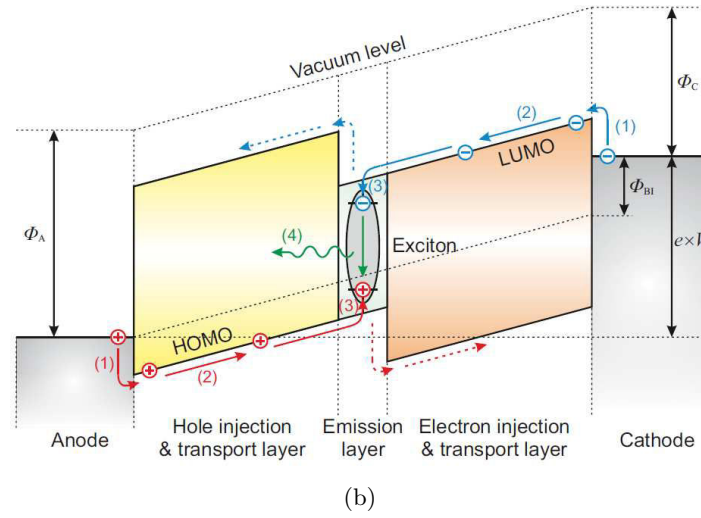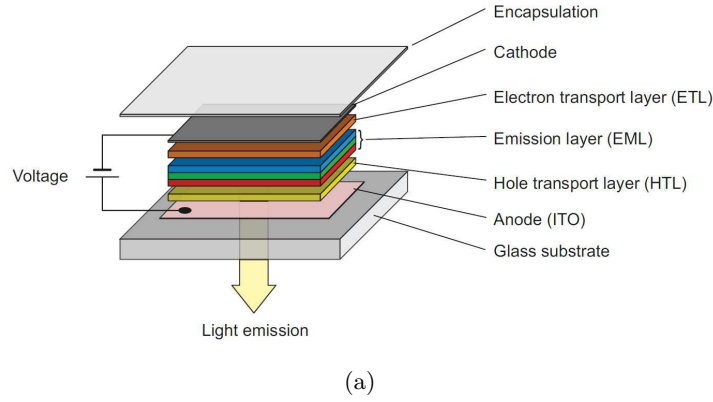

(a)

(b)

Figure 1.8: (a) Simplified illustration of a three-layer OLED. ETL: electron trasport layer, HTL: hole transport layer, and EML: emission layer. To obtain light emission, a voltage must be applied. (b) Schematic energy diagram of a three-layer OLED. The basic processes are illustrated. Electrons are injected from the cathode into the LUMO of the ETL and holes are injected from the anode into the HOMO of the HTL. Subsequently, the charge carriers travel across the organic layers to recombine radiatively in the emission layer. Φ_A and Φ_C are the work functions of the anode and cathode, respectively. Φ_{BI} is the built-in voltage to be overcome by an external voltage V before current can flow in the device. Source: [18].

In the schematic energy diagram shown in Figure 1.8, the barriers for the injection of electrons and holes into the organic materials are illustrated. At first it is important to define the built-in potential Φ_{BI}, which is the difference between the work functions Φ_A and Φ_C of anode and cathode, respectively. As a consequence, to inject charge carriers into the organic layer, it is necessary to apply a voltage V higher than: $V_{BI} = (1/e)(\Phi_A - \Phi_C)$. Additional injection barriers for holes and electrons, Φ_h and Φ_e, respectively, are defined by the Fermi energy of the metals and the HOMO and LUMO of the organic materials. In detail, for holes, $\Phi_h = E_{HOMO} - \Phi_A$, and for electrons, $\Phi_e = E_{LUMO} - \Phi_C$. To minimize the injection barriers, it is fundamental to choose electrodes and organic materials with an as low as possible mismatch between work

function and the energy of HOMO and LUMO.

To measure the performance of OLEDs, the most important parameter is the electroluminescence quantum efficiency η_{EQE}. It is defined as the ratio between the number of emitted photons and injected charges [50]:

$$\eta_{EQE} = \gamma \eta_{S/T} q_{eff} \eta_{out} \tag{1.4}$$

where, γ is the charge balance factor describing what fraction of electrons and holes injected recombine. The fraction of excitons that is allowed to decay radiatively by spin statistic is given by $\eta_{S/T}$. The factor q_{eff} indicates how many spin-allowed excitons decay radiatively. At last, η_{out} is known as the outcoupling factor which measure the fraction of generated photons escaping the device. Another important parameter is the luminous efficacy η_P [lm W^{-1}], which is defined as the luminous flux Φ_L [lm] at given drive conditions (voltage V and current I):

$$\eta_P = \frac{\Phi_L}{VI}; \qquad \Phi_L = K_m \int_{380nm}^{780nm} V(\lambda)\Phi_R(\lambda)d\lambda \tag{1.5}$$

The luminous flux Φ_L quantify the amount of visible light produced by an OLED considering the sensitivity of the human eye. It is calculated by the integration over the whole visible spectra of the spectral flux of radiation Φ_R [W nm^{-1}] and the response curve of the eye (photopic curve) $V(\lambda)$ [51].

(a)

(b)
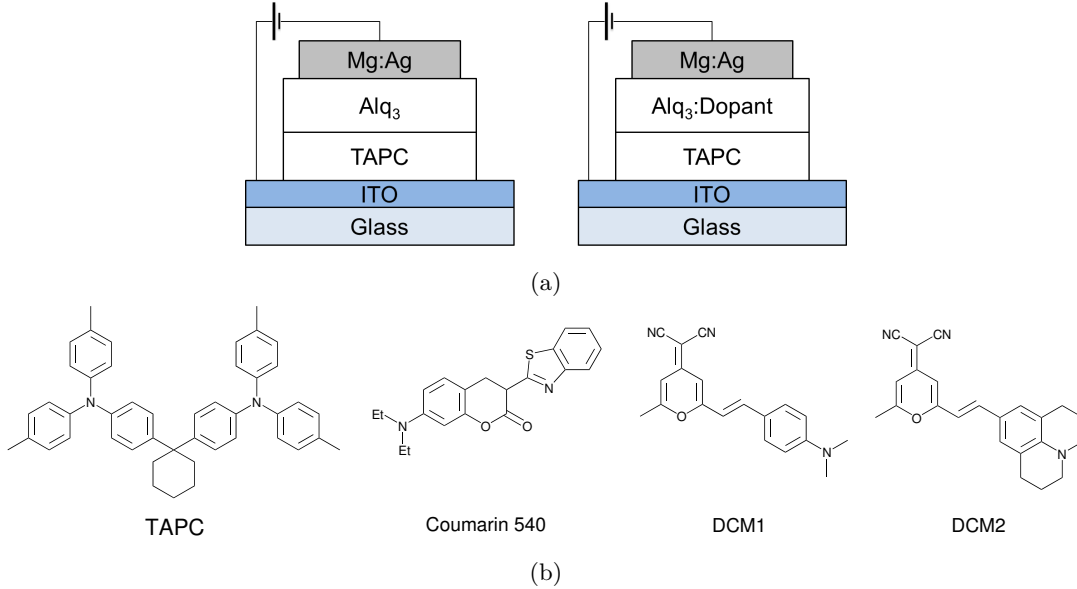
Figure 1.9: (a) Configuration of the first two Alq$_3$-based OLEDs. In the device on the left, Alq$_3$ is the electron-transporting and emitting material, on the right, Alq$_3$ is the electron-transporting and host material. (b) Chemical structure of the hole-transporting material TAPC and of the dopants: Coumarin 540, DMC1 and DCM2. Sources: [9, 10].

In the first demonstration of a double-layer OLED based on low molecular weight OSCs by Tang and VanSlyke, the hole-transporting materials was TAPC (1,1-bis4-[di(*p*-tolyl)amino]-phenylcyclohexane), the electron-transporting and emitting material was Alq$_3$, and the electrodes were ITO (indium tin oxide) and an alloy of silver and magnesium [9]. In this experiment, an external quantum yield η_{EQE} of 1%, a luminous efficacy η_P of 1.5 lm W^{-1}, and

a brightness $>1000\,\text{cd}\,\text{m}^{-2}$ were reported at a driving voltage below $10\,\text{V}$. In a second experiment, Tang and VanSlyke used Alq$_3$ as electron-transporting and host material for fluorescent molecules (Coumarin 540, DMC1 and DCM2) resulting in a two times higher external quantum yield η_{EQE} at an operating voltage below $10\,\text{V}$ [10]. Acting solely as electron-transporting material in an experiment of Kim *et al.*, Alq$_3$ improved the external quantum efficiency η_{EQE} of a bilayer OLED device based on MEH-PPV (poly[2-(2-ethylhexyloxy)-5-methoxy-1,4-phenylenevinylene]) by two orders of magnitude compared to the single-layer device, as a result of the enhanced charge balance [52].
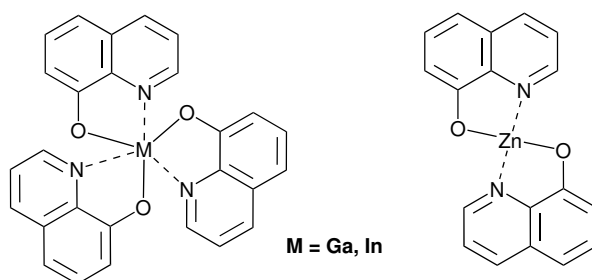
Figure 1.10: Chemical structure of Gaq$_3$ (tris-(8-hydroxyquinoline)gallium) and Inq$_3$ (tris-(8-hydroxyquinoline)indium) on the left hand side and of Znq$_2$ (bis-(8-hydroxyquinoline)zinc) on the right hand side. Sources: [53–57].

Several attempts to improve the properties of Alq$_3$ by structural modifications were made, as an example, other metal chelates containing two or three quinolines were investigated (see Figure 1.10) [53–57]. As emitting material, Gaq$_3$-based devices resulted in similar external quantum yield η_{EQE} and 50% higher luminous efficacy η_P compared to those of Alq$_3$-based devices [53]. On the other hand, Inq$_3$ was superior as electron-transporting material, probably due to its lowered LUMO $\approx -3.4\,\text{eV}$ and improved electron mobility with the increase in size of the central metal ion [54]. OLEDs based on Znq$_2$ yielded a higher luminance $16\,200\,\text{cd}\,\text{m}^{-2}$ and required lowered operating voltages indicating improved electron injection and transport, compared to those of Alq$_3$-based devices [55, 56].
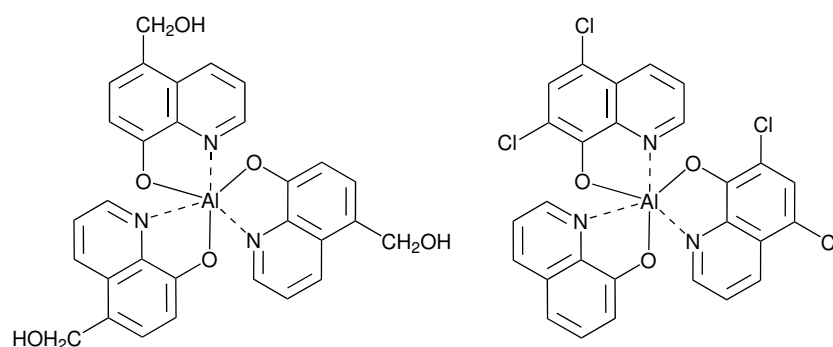
Figure 1.11: Chemical structure of AlOq$_3$ (tris-(5-hydroxymethyl-8-quinolinato)aluminum) on the left hand side and Alq(Clq)$_2$ (bis-(5,7-dichloro-8-quinolinato)-(8-quinolinato)aluminum) on the right hand side. Sources: [58, 59].

Another strategy, exploited to improve the properties of Alq$_3$, was to chemically modify the ligand Hq. Examples among the multitude of reports on structurally modified Alq$_3$ are: AlOq$_3$ and Alq(Clq)$_2$ (see Figure 1.11) [58, 59]. AlOq$_3$ is reported to form super molecular structures in the thin film, due to the hydroxymethyl groups which form hydrogen bonds, yielding luminous

efficacy η_P three times higher than similar Alq$_3$-based OLEDs [58]. Diversely, Alq(Clq)$_2$-based OLEDs showed a red-shifted emission compared to that of Alq$_3$-based devices.
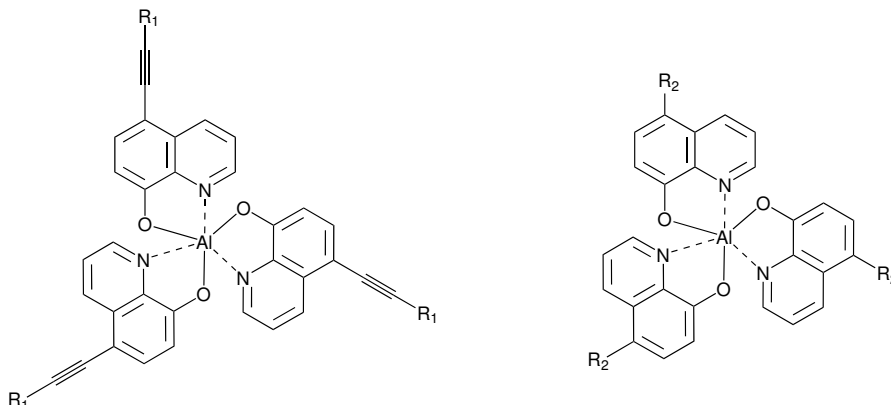

Figure 1.12: Chemical structures of the 5-substituted Alq$_3$. In the left hand side complex the electron-rich and -poor substituents are bonded to the quinolinate by an ethynyl bridge. In the right hand side complex the electron-rich and -poor substituents are directly bonded to the quinolinate. Source: [38].

At last, in a comprehensive work of Montes *et al.*, series of electron-poor and -rich functionalities were used to substitute the 5-position of Hq (see Figure 1.12) [38]. It was found that the HOMO was effectively manipulated while the LUMO was largely unaffected. From the characterization of OLEDs based on modified Alq$_3$'s, the tunability of the electroluminescence spectra was demonstrated with emission ranging from blue to red. However, the external quantum yield η_{EQE} and the maximum ratio between luminance and current density through the device [cd A^{-1}] of the OLEDs were, in the best case, similar, but normally lowered compared to those of OLEDs based on pristine Alq$_3$. The reported examples are only few among the vast number of works on Alq$_3$ derivatives, however, the review of all the literature is exceeding the purpose of this introduction.

1.2.2 Alq$_3$ in OPVs

In organic photovoltaic devices (OPVs) the light energy is directly converted into electrical energy, in a reverse way of what happens in OLEDs (for a review on OPVs [13, 14, 18]). As illustrated in Figure 1.13, OPVs can be made of a single organic thin layer sandwiched between two electrodes (ITO and silver in the figure). Since the work function of the two conductors are different, electrons will flow from the conductor with the highest work function to that with the lowest work function until they reach the same chemical potential. The charge that builds up in the two electrodes generates an electric field across the semiconductor. When light is absorbed by the OSC, an exciton (electron-hole pair) is formed, and the electric field pulls the electrons toward the positive electrode and the holes toward the negative electrode resulting in a net electric current. However, due to the strong binding energy of excitons, single layer OPVs yield poor performance. By adding a second OSC layer, a so-called *pn*-heterojunction is formed. Generally, *p*-type and *n*-type OSCs stand for electron-donating and -accepting organic semiconductors, respectively [61]. When the exciton is formed near the *pn*-heterojunction, the charge separation takes place more efficiently. In detail, electrons can easily transfer from the electron-donating to the electron-accepting material toward the positive electrode, and holes travel in the opposite way to the negative electrode. To further increase the efficiency of OPVs,
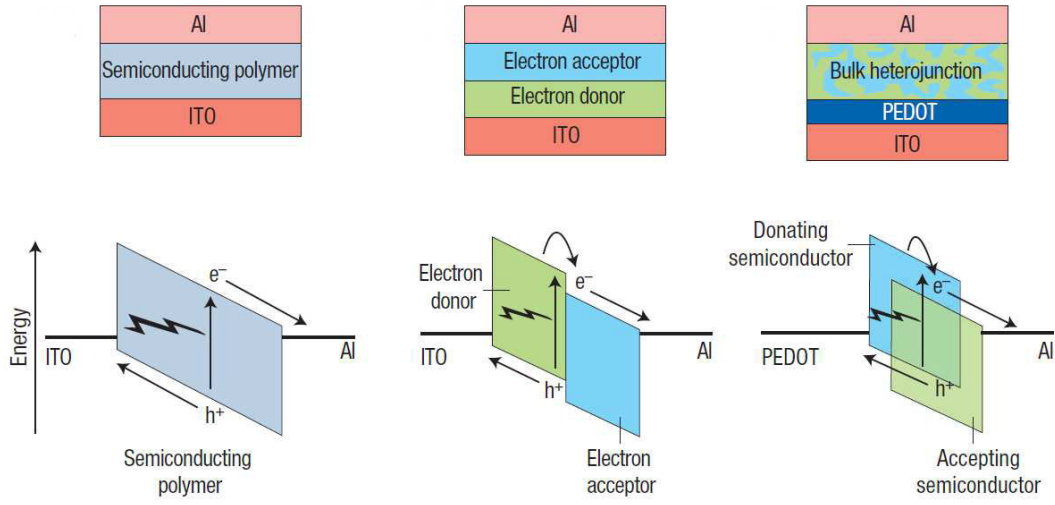
Figure 1.13: Schematic energy band diagram of three types of OPVs. Left: single layer OPV. Center: planar heterojunction OPV. Right: bulk heterojunction OPV (PEDOT: poly(3,4-ethylenedioxythiophene)). Source: [60].
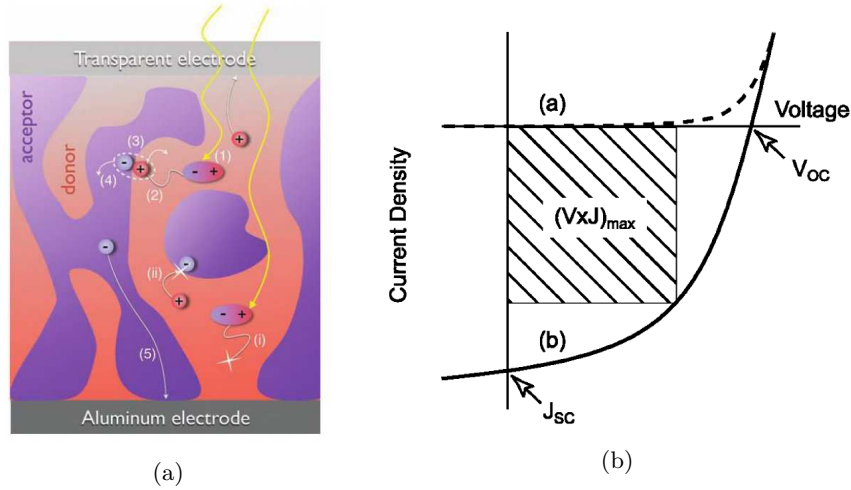

(a)   (b)

Figure 1.14: (a) Schematic representation of the working principle of a bulk heterojunction OPV. Excitons are formed by the absorption of light. At the *pn*-heterojunction excitons dissociate generating holes and electrons, which travel toward negative and positive electrodes, respectively. Source: [18]. (b) Typical J-V curve of OPVs: a, in dark, and b, under illumination. J_{SC} is the short-circuit photocurrent density. V_{OC} is the open circuit voltage. Source: [61].

p- and *n*-OSCs were interpenetrated aiming to extend the *pn*-heterojunction, and thus, favor the charge separation of excitons [62, 63]. The latter type of OPV is called bulk heterojunction cell.

(a)

| C60 | MPc (M=Zn, Cu) | SnCl$_2$Pc | F$_{16}$CuPc |

(b)
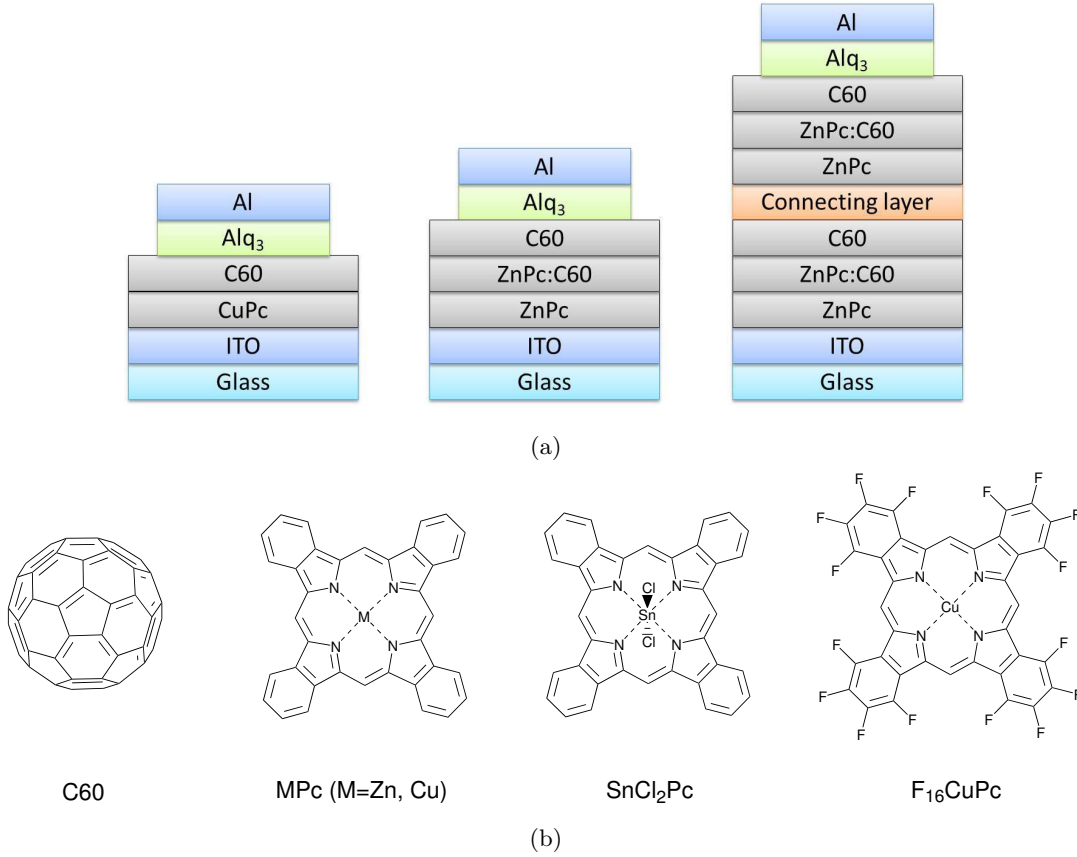
Figure 1.15: (a) Schematic configuration of OPVs including Alq$_3$ as buffer layer. Left OPV: CuPc [30 nm]/C60 [40 nm]/Alq$_3$ [6 nm]. Central OPV: ZnPc [10 nm]/ZnPc:C60 [10 nm]/C60 [10 nm]/Alq$_3$ [5 nm]. Right tandem-OPV: ZnPc [10 nm]/ZnPc:C60 [10 nm]/C60 [10 nm]/Alq$_3$ [5 nm]/connecting layer/ZnPc [10 nm]/ZnPc:C60 [10 nm]/C60 [10 nm]/Alq$_3$ [5 nm]. (b) Chemical structure of the *n*-type OSC: C60 (electron acceptor), *p*-type OSCs: MPc (M=Zn,Cu) (electron donor), and connecting layers: SnCl$_2$Pc and F$_{16}$CuPc. Sources: [64, 65].

The main processes occurring in bulk heterojunction OPVs are illustrated in Figure 1.14: (1) light absorption and excitons generation, (2) diffusion of excitons to the heterojunction, (3) charge transfer of electrons into the electron-accepting material and of holes into the hole-accepting material, (4) exciton dissociation, and (5) holes and electrons transport to the electrodes leading to the photocurrent. Side processes can occur: (i) recombination of excitons before reaching the heterojunction, and (ii) recombination of excitons at the heterojunction. Performance of OPVs is estimated by the power conversion efficiency η_p, which is defined as the ratio between the maximum power P_{max} delivered by the device and the incident power of the light source P_{in}. The maximum power P_{max} is equal to $J_m V_m$, where J_m and V_m are the current and voltage at the maximum power point, respectively.

$$\eta_p = \frac{(J_m V_m)}{P_{in}} = J_{SC} V_{OC} FF / P_{in} \qquad (1.6)$$

where, J_{SC} is the short-circuit photocurrent density, V_{OC} is the open circuit voltage (see Fig-

ure 1.14), and FF is the fill factor. The latter is an indication of the diode quality and is mainly influenced by the charge carrier transport and recombination. Extensive studies on OPVs have been triggered by the demonstration of a planar *pn*-heterojunction based on copper phthalocyanine (CuPc) and perylene sandwiched between ITO and silver electrodes, reported by Tang [66]. A power conversion efficiency η of about 1% and a fill factor FF of 0.65 were recorded under simulated AM2 white light at $75\,\mathrm{mW\,cm^{-2}}$.

OPVs implement active materials such as porphyrins, phthalocyanines, perylenes, fullerenes, polymer hybrid structures and more [13, 14]. However, Alq$_3$ was successfully utilized as buffer layer between cathode and active layer in bulk heterojunction devices [64, 65] (see Figure 1.15). In the work of Song *et al.*, Alq$_3$ was used as electron-transporting and hole-blocking material to carry electrons and, simultaneously, to prevent the leakage of holes to the cathode, resulting in a power conversion efficiency $\eta_p = 2.11\%$ [64]. As a main result, the lifetime of OPVs including Alq$_3$ was $\approx$150 times longer than that of OPVs implementing BCP (2,9-dimethyl-4,7-diphenyl-1,10-phenanthroline), which is the most widely used interfacial layer on the cathode side [13]. The increased stability is attributed to the formation of a superior barrier against oxygen, water molecules, and metal atom diffusion from the cathode to the active layers. Similarly, in the work of Yu *et al.*, Alq$_3$ was introduced between C60 and the aluminum electrode as electron transport layer and, in addition, to avoid the damage of C60 during the deposition of cathode [65]. However, this study aimed to investigate SnCl$_2$Pc and F$_{16}$CuPc (tin phthalocyanine dichloride and copper hexadecafluorophthalocyanine, respectively) as connecting units in tandem cells. Despite the few examples of OPV implementing Alq$_3$, it is clear that, due to its easy processability to form uniform and stable films, and its convenient HOMO and LUMO energy levels, which make Alq$_3$ a good electron-transport and hole-blocking material, Alq$_3$ can be utilized in OPVs.

1.2.3 Alq$_3$ in OSPDs
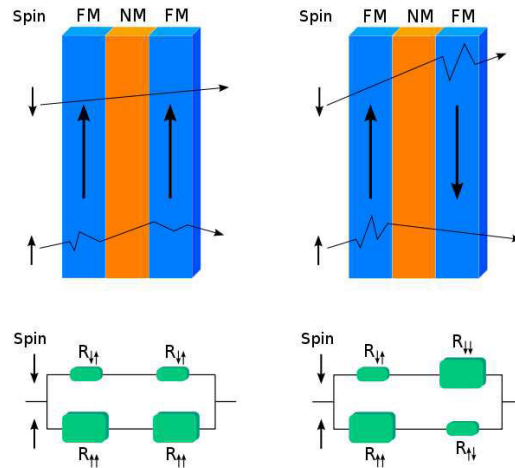
Figure 1.16: Schematic drawing of a spin valve. Ferromagnetic electrodes in parallel configuration on the left hand side, and in antiparallel configuration on the right hand side. Corresponding electrical resistor models illustrated in the bottom. Source: [http://en.wikipedia.org/wiki/Giant_magnetoresistance].

The study of the transport of electrons, depending on the spin degree of freedom, through metallic and semiconducting devices is called spintronics (for a review [15, 18]). Spin valves are

the typical OSPD consisting of, in the simplest form, two ferromagnetic electrodes separated by a nonmagnetic (organic) spacer. Since the electrodes are characterized by two distinct switching fields, the device can switch from a parallel to an antiparallel magnetization configuration applying an external magnetic field. The significant difference between the two configurations is called giant magnetoresistance (GMR) (see Figure 1.16); for the work on GMR, Fert and Gründberg were awarded with the Nobel prize in 2007 [`http://www.nobelprize.org/nobel _prizes/physics/laureates/2007/`]. When a thin layer of insulator is sandwiched between the two ferromagnetic electrodes, the corresponding effect is called tunneling magnetoresistance (TMR) [67, 68]. OSCs represent an interesting material class for spintronics, due to the little spin-orbit coupling of light atoms and the versatility of organic materials [15].
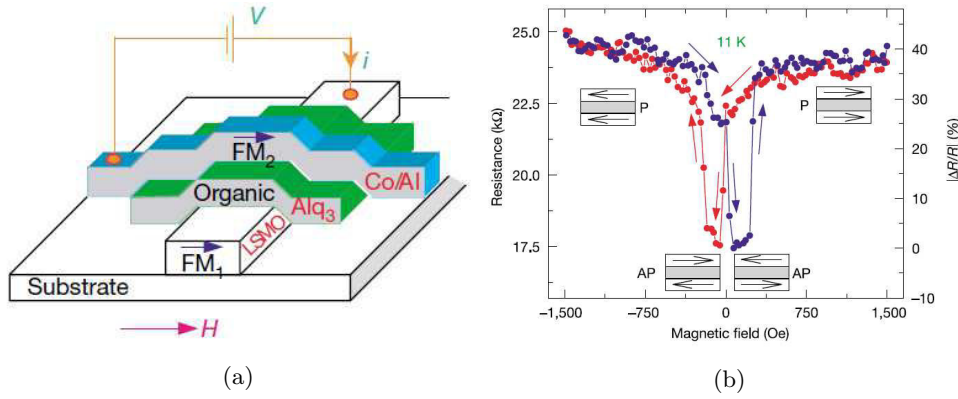
Figure 1.17: (a) Schematic representation of a typical vertical Alq$_3$-based OSPD. Alq$_3$ is sandwiched between LSMO, bottom electrode, and cobalt, top electrode. (b) MR loop of a LSMO [100 nm]/Alq$_3$ [130 nm]/Co [3.5 nm] OSPD measured at 11 K. The magnetization configuration of the electrodes is indicated. Source: [69].

Injection and detection of spin-polarized electrons are the basic processes in OSPDs. In the first demonstration by Dediu *et al.*, spin polarized electrons were injected from LMSO (La$_{0.7}$Sr$_{0.3}$MnO$_3$) ferromagnetic electrodes into an organic layer of sexithiophene (6T) [70]. A strong MR up to 30% was measured on nanostructured planar hybrid junctions LSMO/T-6/LSMO. In addition, spin diffusion length and spin relaxation time in T6 were estimated in about 200 nm and 1 μs, respectively. Among OSCs, Alq$_3$ is the most implemented material in OSPDs, mainly due to its processability, electron mobility, and reproducibility of results [15]. The first example of an Alq$_3$-based OSPD, in which Alq$_3$ was sandwiched between LSMO and cobalt ferromagnetic electrodes in a vertical architecture, was reported by Xiong *et al.* [69] (see Figure 1.17). A MR of ≈40% was measured at 11 K, in addition, the MR was still detectable up to 200 K. Moreover, the device showed an inverse magnetization, in which a lowered MR was detected for an antiparallel magnetization of the electrodes. These results have been confirmed in a reproducible way in several other experiments [71–73].

TMR was detected in Alq$_3$-based OSPD by Barraud *et al.* [74]. A thin layer of Alq$_3$ (2 nm) was sandwiched between LSMO and cobalt ferromagnetic electrodes with a nanoindentation technique, as illustrated in Figure 1.18. As a result, a TMR up to 300% was detected at 2 K. In contrast to the Alq$_3$-based OSPDs previuosly described, which show a negative MR, in this case, a positive MR is observed. In a recent communication by Prezioso *et al.*, Alq$_3$-based OSPDs showed memristance behavior [75]. In few words, the defining property of a memristor is the non-volatile variation of its resistance (memristance), which depends on the history of the applied current or voltage.

(a)

(b)
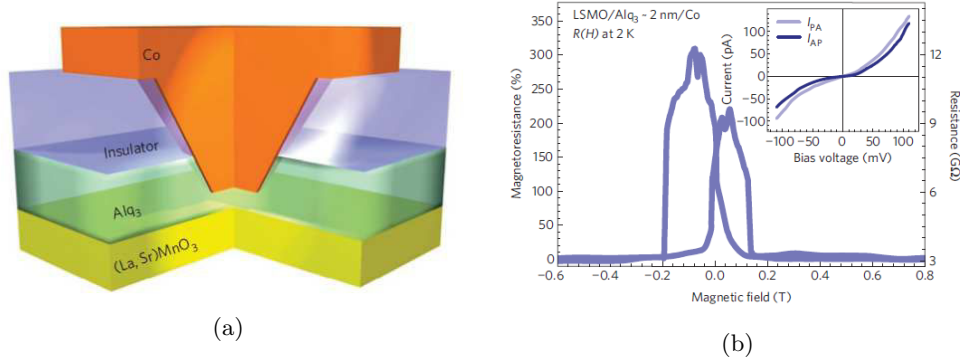
Figure 1.18: (a) Schematic representation of the Alq$_3$-based OSPD device. A nanoindent is realized in the Alq$_3$ layer to control the organic tunnel barrier thickness. The nanohole is then filled with cobalt. LSMO is the bottom electrode and cobalt the top electrode. (b) MR curve of a LSMO/Alq$_3$ [2 nm]/Co OSPD measured at 2 K and −5 mV. In the inset, $I(V)$ curves recorded at 2 K in the parallel (I_{PA}) and antiparallel (I_{AP}) configurations. Source: [74].

In this thesis we have studied phenalenyl-based complexes (Section 3 and Section 6), and thus, the first application of a phenalenyl-based zinc complex (ZMP) in OSPDs, recently published by Raman *et al.*, is reported [76]. In this communication, the authors have measured a negative MR up to 25% at 4.8 K and 15 mV in a Co [8 nm]/ZMP [40 nm]/Co [12 nm] device (see Figure 1.19). The origin of MR is ascribed to the hybridization between the ferromagnetic cobalt surface and the planar structure of ZMP, which creates an anionic radical with a net momentum.

(a)

(b)
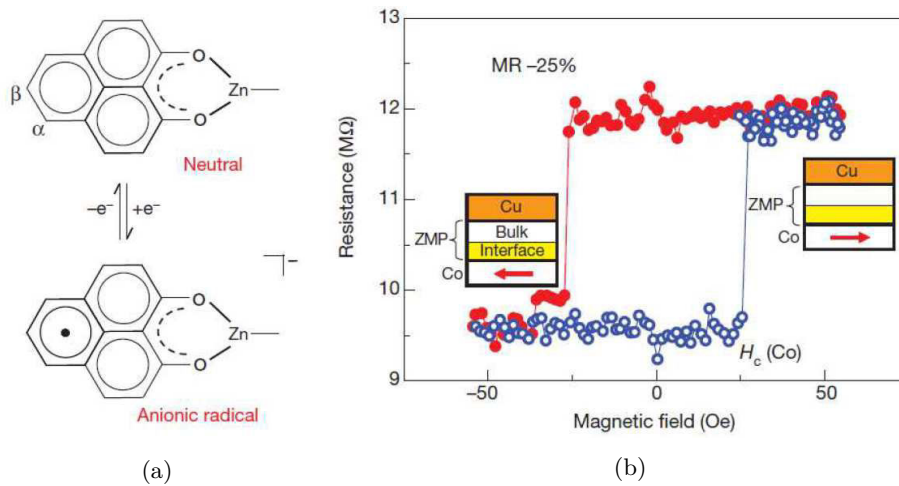
Figure 1.19: (a) Molecular structure of ZMP (zinc methyl phenalenyl) in a neutral state and in an anionic radical. Charge transfer processes through hybridization on the ferromagnetic surface can change the chemical state of the phenalenyl from the neutral state to an anionic radical. (b) MR measurements of a device Co [8 nm]/ZMP [40 nm]/Co [12 nm] recorded at 15 mV after cooling the device to 4.2 K in a magnetic field 550 Oe. The magnetization of cobalt is shown with a red arrow. Source: [76].

1.2.4 Alq$_3$ in OFETs
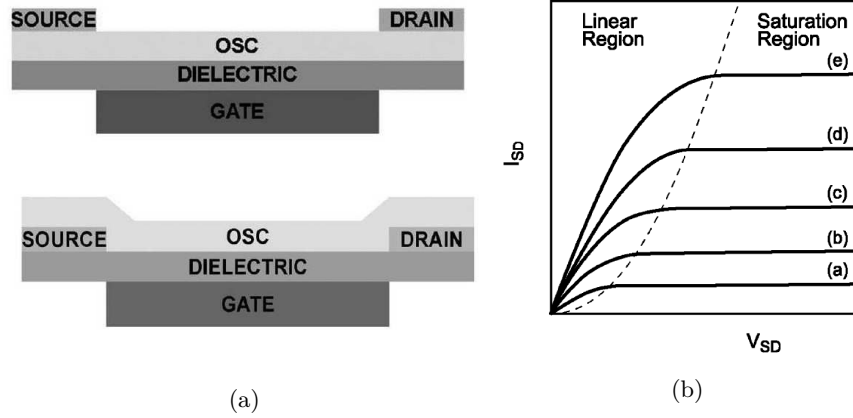
Figure 1.20: (a) Schematic OFET configurations: top contact configuration (top), and bottom contact configuration (bottom). (b) Schematic representation of the source-drain current I_{SD} in function of the source-drain voltage V_{SD} and the gate voltage V_G ($a < b < c < d < e$). Source: [61].

Organic field-effect transistors (OFETs), in the thin film transitor (TFT) architecture, are formed by three conducting electrodes (source, drain and gate), a gate dielectric (insulator), and an OSC as active material (for a review see [16]). Generally, OFETs are built in a top- or bottom-contact configuration, as illustrated in Figure 1.20. Depending on the voltage applied to the gate electrode there are two states in which OFETs can be. The off-state is referred to the state when no voltage is applied to the gate electrode and only small currents flow between source and drain electrodes. In contrast, the on-state is referred to the state when voltage is applied to the gate electrode and there are consistent current flows between source and drain electrodes. In more detail, when a negative voltage is applied to the gate electrode, hole carriers accumulate at the interface between OSC and gate dielectric, and thus, hole currents occur from the source to the drain electrode. This kind of OFET is called *p*-channel device. In the opposite way, a *n*-channel device is characterized by electron currents between source and drain electrodes resulting from the accumulation of electrons at the interface between gate dielectric and OSC induced by a positive voltage applied to the gate electrode. In addition to *p*- and *n*-channel devices (unipolar OFETs), ambipolar OFETs, in which the simultaneous transport of holes and electrons occurs, can be obtained. The best performance is obtained for *p*-channel devices based on single crystals of pentacene, rubrene and copper phthalocyanine [61]. On the contrary, *n*-channel devices display lowered stability and performance with the best results obtained for OFETs based on fullerenes and fullerene derivatives [61]. Due to its relatively low charge carrier mobilities, Alq$_3$ is not among the most implemented OSCs in OFETs. Nonetheless, it was successfully integrated in two specific classes of OFETs: ambipolar OFETs and LE-OFETs (light-emitting OFETs). In few words, LE-OFETs (light-emitting OFETs) combine functions of OLEDs and OFETs. Strictly speaking, electrical switching is enabled by modulation of the current flow between the source and drain electrodes under tuned gate bias voltage, whereas electroluminescence takes place by electron-hole recombination in the transistor channel [77].

In the example reported by Sakanoue *et al.*, Alq$_3$ was utilized as organic material in single-component ambipolar OFETs [78] (see Figure 1.21). The FET electron mobility μ obtained for the *n*-channel device, built with calcium electrodes, was $5.5 \times 10^{-7} \, \text{cm}^2 \, \text{V}^{-1} \, \text{s}^{-1}$ with a thresh-

(a)

(b)
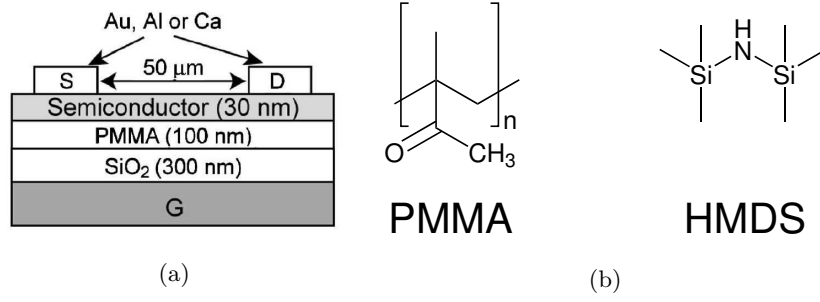
Figure 1.21: (a) Schematic view of the structure of Alq$_3$-based ambipolar OFETs. Alq$_3$-based OFETs were obtained with Ca source and drain electrodes for the *n*-channel device and with a bottom contact configuration with Au/Cr electrodes on a HMDS treated substrate for the *p*-channel device. (b) Chemical structure of PMMA (poly(methyl methacrylate)) and HMDS (hexamethyldisylazane). Source [78].

old voltage V_T of 64 V. To measure the hole mobility, a bottom-contact configuration, with interdigital electrodes of Au/Cr ($L=$ 76 mm, $W=$ 25 μm) on a HMDS (hexamethyldisylazane) treated substrate, was used to enhance the drain current. As a result, for the *p*-channel device, the measured FET electron mobility μ was $1.6 \times 10^{-7}\,\text{cm}^2\,\text{V}^{-1}\,\text{s}^{-1}$ with a threshold voltage V_T of -43 V.
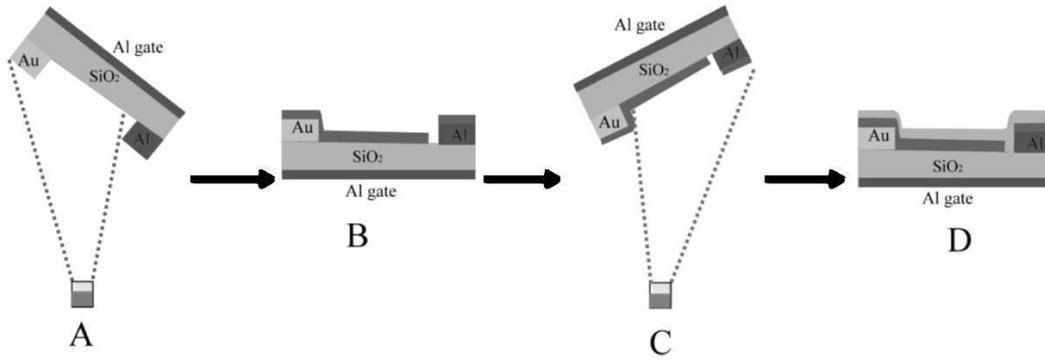
Figure 1.22: Schematic illustration of the laterally arranged heterojunction fabrication process. A: the substrate is tilted with respect to the horizontal plane and pentacene is evaporated resulting in the layer deposition shown in B. C: the substrate is inclined in the opposite direction and Alq$_3$ is evaporated resulting in the final configuration shown in D. Source: [79].

Di *et al.* described LE-OFETs based on laterally arranged heterojunctions formed by pentacene and Alq$_3$ [79]. By implementing the uncommon fabrication strategy illustrated in Figure 1.22, the authors could form heterojunctions between pentacene (chemical structure in Table 1.1) and Alq$_3$. A hole mobility μ between 1.8×10^{-3} and $2.1 \times 10^{-3}\,\text{cm}^2\,\text{V}^{-1}\,\text{s}^{-1}$, a threshold voltage V_T of -10 V, and a on/off current ratio between 10^3 and 10^4 were measured. For electrons, the mobility μ was $1.6 \times 10^{-6}\,\text{cm}^2\,\text{V}^{-1}\,\text{s}^{-1}$, the threshold voltage V_T was 20 V, and the on/off current ratio was 10^3. Additionally, for the device built with gold as source electrode, and lithium fluoride (LiF) as drain electrode, emission of light was detected.

At last, Capelli *et al.* built the first triple-layer hetero-structure LE-OFET illustrated in Figure 1.23. Here, the light-emitting layer, formed by Alq$_3$ doped with DCM1 (chemical structure in Figure 1.9), was inserted between *p*-type (DH-4T) and *n*-type (DFH-4T) layers [80]. In this device, electroluminescence spread over the entire channel was detected. The measured external

(a)

(b)

DH-4T

DFH-4T

(c)
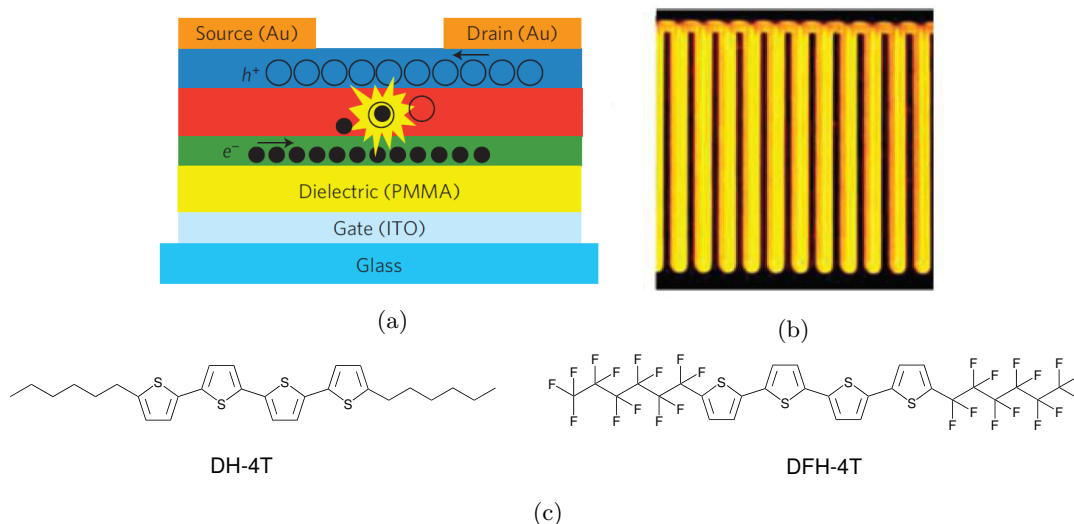
Figure 1.23: (a) Schematic representation of the trilayer LE-OFET device. Field-effect charge transport and light -generation processes are illustrated. (b) Optical micrograph of the light emission from the trilayer LE-OFET ($V_{SD}= V_G= 90$ V). (c) Chemical structure of the *p*-type OSC DH-4T (blue layer) and of the *n*-type OSC DFH-4T (green layer). Source:[80].

quantum efficiency, $\eta_{EQE}= 5\%$, exceeds the best OLED based on the same emitting layer and optimized transport layers ($\eta_{EQE}= 2.2\%$) [81].

1.3 Theoretical and experimental techniques implemented to study the (novel) OSCs

In this thesis we have synthesized and studied a series of (novel) OSCs. Chapter 3 outlines synthetic strategies and characterization results. Firstly, the (novel) OSCs were structurally characterized by means of proton and carbon nuclear magnetic resonance (NMR), matrix-assisted laser desorption/ionization-time of flight (MALDI-TOF), electro-spray ionization-time of flight (ESI-TOF), elemental analysis, and single crystal X-ray diffraction. Secondly, the photophysical and electrochemical properties of the OSCs were determined. The photophysical characterization was carried out measuring absorption, emission and (in some cases) excitation spectra of the (novel) OSCs. Photophysical measurements are fundamental to investigate molecular orbitals and main transitions between ground and excited states of the OSCs. In addition, from the absorption spectra it is possible to estimate HOMO-LUMO gaps. Electrochemical studies, by means of cyclic voltammetry (CV), were performed to measure the reduction potential (electron affinity) of the OSCs, and thus, to evaluate their LUMO energy levels. Moreover, for Alq$_3$ and Al(Op)$_3$ a complete photophysical characterization was carried out to measure the fluorescence quantum yield and the excited state lifetime in solution and in thin film. Lastly, we have determined the HOMO and LUMO energy levels, which are fundamental to assess the possible implementation of the (novel) OSCs in devices. The LUMO energy level was calculated from the reduction potential measured in solution CV, and the HOMO-LUMO gap was estimated from the first absorption band in the absorption spectrum. Knowing the LUMO energy and the HOMO-LUMO gap, the HOMO energy level was computed easily.

1.3.1 Introduction on the theoretical methods

In the first part of Chapter 4, the most interesting OSCs synthesized in Chapter 3 were studied by means of newly developed theoretical methods. A brief introduction on the theoretical methods is given in the following. To start with, all the quantum chemical characterizations in Section 4.2.1 were done with TURBOMOLE [82] on a B3-LYP [83] /SV(P) [84] level of theory.

The atomistic morphologies, presented in Section 4.2.2 were generated with a Monte Carlo based simulated annealing method [85]. The method starts with a set of initial coordinates $\{\vec{r_i}(t_0)\}$ and make use of random guesses for new coordinates $\{\vec{r_i}(t_1)\}$ for one atom. The total energy E_1 of the new system is evaluated and compared to the initial total energy E_0. The new step is accepted to a certain possibility, the Metropolis-criterion in Equation 1.7.

$$\omega(0 \rightarrow 1) = \begin{cases} 1 & \text{if } E_1 \leq E_0 \\ \exp\left(-\frac{E_1 - E_0}{k_b T}\right) & \text{if } E_1 > E_0 \end{cases} \tag{1.7}$$

In the DEPOSIT code, molecules are sequentially added to the simulation box. For each molecule, a certain number of Monte Carlo steps is performed in order to find an energetically favorable position and configuration of the molecule. The deposition is repeated and the final position with the lowest energy is chosen. Afterward, a simulated annealing process is possible to relax the local environment of the new molecule.

Microscopic properties, such as energetic disorder, reorganization energy and electronic coupling, described in Section 4.2.3, were calculated with the Quantum Patch method as described by Friederich *et al.* [86, 87]. These microscopic parameters were used in an analytic Marcus-rate [88] based effective medium approach [89] in order to estimate charge carrier mobilities for electrons and holes for zero-field and low carrier concentration. All quantum chemical calculations involved directly into the multi-scale work-flow, as well as any additional quantum chemical characterization were done with TURBOMOLE [82] on a B3-LYP [83] /SV(P) [84] level of theory. For reorganization energies, a def2-TZVP [90] basis set was used.

When modeling charge transport in disordered organic material, where charges propagate by a succession of leaping processes between neighboring localized sites, the hopping transport formalism is a common starting point. In the case of weakly coupled sites [91] and time scale of local charge reorganization smaller than the time scale of a single hopping process, Marcus theory [88] is widely used for the calculation of charge hopping rates.

$$k_{if} = \frac{2\pi}{\hbar} |J_{if}|^2 \frac{1}{\sqrt{4\pi \lambda_{if} k_B T}} \exp\left(-\frac{(\lambda_{if} + \Delta G_{if})^2}{4\lambda_{if} k_B T}\right) \tag{1.8}$$

where k_{if} is the hopping rate, $\hbar$ is the Plank constant, J_{if} is the electronic coupling, λ_{if} is the reorganization energy, k_B is the Boltzmann factor and ΔG_{if} is the Gibbs free energy difference of initial and final states. Materials specific parameters can be mapped onto transport models, which can then be used for the calculation of charge carrier mobility and other experimentally relevant quantities in master equation approaches [92–94].

In the quantum patch approach, the Hamiltonian operator for a system of N weakly coupled molecules with the total density $n(r)$ is approximated by:

$$\hat{H} = diag(H_1[n_{tot}(\vec{r})], ..., H_N[n_{tot}(\vec{r})]) \tag{1.9}$$

neglecting inter-molecular contributions to kinetic energy and exchange interactions. This approximation is reported in many embedding methods for weakly coupled molecules [95–97]. As a result, under the condition that the total charge density is known, the Hamiltonian for each molecule con be solved separately. To iteratively solve the electronic structure of the system we partition the total charge density $n_{tot}(r)$ into a sum of charge densities of single molecules. To calculate the charge density for the molecule i, the charge densities $n_{j \neq i}(r)$ of the neighboring molecules are replaced by a set of point charges where k is the index of the respective atom at the position $R_{j,k}$.

$$n_{tot}^{\mu}(\vec{r}) = n_i^{\mu}(\vec{r}) + \sum_{j \neq i, k} q_{j,k}^{\mu} \delta(\vec{r} - \vec{R_{j,k}}) \tag{1.10}$$

Intermolecular electrostatic interactions are taken into account by employing partial charges fitted with the Merz-Singh-Kollman scheme (ESP-charges) [98] which are specifically designed to reproduce the electrostatic field of a molecule. The process begins by guessing the initial partial charges $q_{j,k}^0$, using vacuum partial charges, for each molecule, and then, solve the Schrödinger equation for each molecule self-consistently. Subsequently, the partial charges are recalculated on the basis of the new electron densities $n_i^{\mu} = \sum_j |\Phi_{i,j}^{\mu}(r)|^2$ for the molecule i, with Kohn-Sham orbitals $\Phi_{i,j}$. These densities are used in the calculations for the other molecules, such that μ denotes the iteration step. This procedure is iterated for all the molecules in the system of interest until the convergence, as shown in Figure 1.24.
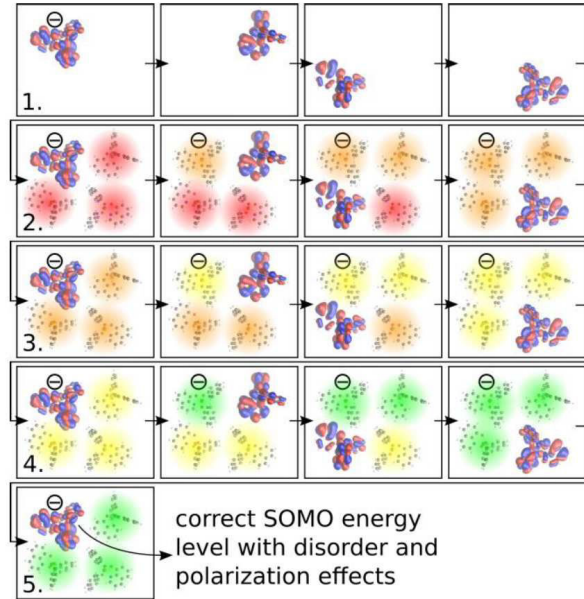
Figure 1.24: Schematic description of the algorithm used for the calculation of energy disorder. In the first step, partial vacuum partial for each molecule are calculated. Afterward, an additional charge is assigned to a certain molecule. Partial charges of this, as well as of the neighboring molecules within a certain cut-off distance, are self-consistently re-evaluated using a cloud of point charges that are iteratively improved until convergence in total energy of the charged molecule is reached. This procedure is repeated for positive and negative additional charges on each molecule in the system.

In order to calculate hopping rates of electrons and holes, as described in Equation 1.8, ΔG_{if} of charged hopping sites is needed as input. In absence of external field and entropic effects,

ΔG_{if} is approximated by the total energy of difference ΔE_{if} between final and initial states [97, 99]. These energy differences are calculated for each pair of hopping sites with the method aforementioned, using an environment of self-consistent point charges surrounding the single monomers. Polaron effects are described by assigning an additional charge to the molecule i, and thus, its vacuum partial charges and the total energy of the system are calculated. Formally, this approach is an approximation of the frozen density embedding method [100–102] including polarization effects due to explicit additional charges in the system. The procedure is repeated by putting an additional charge on the target molecule f of the hopping process. The result is the energy $E_f^-(E_f^+)$, for which the energy differences for electron (hole) transport $\Delta E_{electron}(\Delta E_{hole})$ are computed. These energies differences, averaged over samples of sufficient size, yield the energy disorder distribution $\sigma(\Delta E) = (1/(N_{pairs} - 1) \sum \Delta E^2)^{1/2}$, computed for all the nearest-neighboring pairs in the morphology. To estimate charge carrier mobilities, we employ the analytic solution of the master equation for Marcus rates in a homogeneous medium by Rodin *et al.* (unpublished):

$$\mu = \frac{e\beta}{n\hbar\sqrt{\lambda}} \sqrt{\frac{\pi\beta}{1 + \frac{\beta\sigma^2}{\lambda}}} \exp\left[-\frac{\beta\sigma^2}{4} - \beta\frac{\lambda}{4}\right] M \left\langle J^2 R^2 \right\rangle \tag{1.11}$$

Consistently with our microscopic energy disorder, Rodin *et al.* use a local disorder parameter $\sigma(E)$, which inherently includes energy correlations and show their thusly modified effective medium approach to work well for materials with both strong and weak disorder. $\beta = 1/k_B T$ is the inverse temperature, n the dimension and M the mean number of nearest neighboring molecules. Electronic coupling constants were calculated with a Löwdin orthogonalization method [103], using dimer Fock- and overlap matrices and frontier orbitals of uncharged monomers, within a self-consistently evaluated point charge environment. The inner part of the reorganization energy was calculated in geometry optimizations of charged molecules starting from the optimized geometry of the neutral molecule and *vice versa.*

1.3.2 Introduction on the experimental techniques

In the second part of Chapter 4, we present a preliminary study on the experimental charge carrier mobility of the (novel) OSCs. In particular, we have made use of three methods to determine the mobilities: field-effect transistor (FET), time of flight (TOF), and admittance (impedance) spectroscopy (AS). In the following, a brief description of these methods is given (for a review [61, 104–106]).

Field-effect transistor (FET).

A common measure used to determine the processing speed of FETs is the field-effect mobility, which is the average charge carrier drift velocity per unit electric field. A large field-effect mobility is the key to obtain large on-currents for a given device geometry and gate dielectric [61, 104, 105]. Typical device configuration and source-drain current I_{SD}, in function of source-drain voltage V_{SD} and gate voltage V_G, are illustrated in Figure 1.20. OSCs are essentially electrical insulators, and thus, charge carries are supplied by injection from the source electrode into the organic spacer. The current flow between source and drain electrodes I_{SD} is modulated by gate V_G and source-drain V_{SD} voltages. As illustrated in Figure 1.20, the current I_{SD}, at a given gate voltage V_G, increases almost linearly with increasing source-drain voltage V_{SD} till saturation. In the linear regime the current I_{SD} is calculated by the equation:

$$I_{SD,lin} = \frac{W\mu C_i}{L}(V_G - V_T)V_{SD} \tag{1.12}$$

where, W and L are the channel width and length, respectively, μ is the charge carrier mobility (field-effect mobility), C_i is the capacitance per unit area of the dielectric, and V_T is the threshold voltage, which is the voltage for which the channel conductance is equal to that of the whole semiconducting layer. In other words, the threshold voltage V_T is the gate voltage needed to create a conducting path between source and drain terminals. In the saturation regime the current I_{SD} is described by the equation:

$$I_{SD,sat} = \frac{W\mu C_i}{2L}(V_G - V_T)^2 \tag{1.13}$$

The field effect mobility μ can be calculated from the slope of a linear plot of $I_{SD,sat}^{1/2}$ versus V_G. As an example, a linear plot of $I_{SD,sat}^{1/2}$ versus V_G is illustrated in Figure 4.14 in Section 4.3.1. Moreover, the performance of OFETs is estimated by two additional parameters: threshold voltage V_T and on/off current ratio.

Time of flight (TOF).
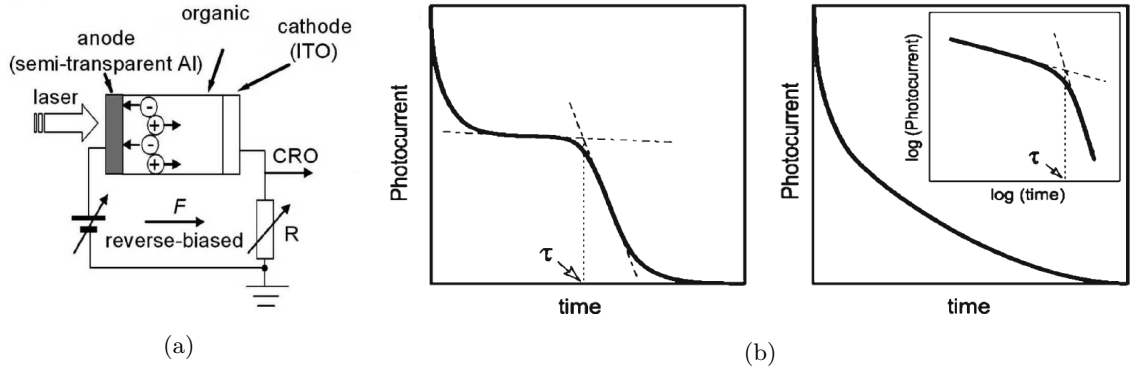
Figure 1.25: (a) Schematic representation of a TOF setup. In the example, the organic material is sandwiched between a semi-transparent Al electrode and a transparent ITO electrode. The carriers are generated near the anode (Al electrode). Under the applied field F, electrons recombine instantaneously at the anode and holes move toward the cathode (ITO electrode). R is representing a resistance (much lower than that of the sample) and CRO is the measuring system (oscilloscope). (b) Typical experimental signal for non-dispersive OSCs on the left. Typical experimental signal for dispersive OSCs on the right, in the inset, double logaritmic plot used to extract the transit time τ. Sources: [61, 106].

TOF is, perhaps, the most general technique to measure charge carrier mobilities of OSCs [107]. In TOF, free charge carriers are photogenerated by a pulsed laser. The mobility is determined by the transit time τ of the leading charge carrier transporting through the organic film. Since charge carriers are photogenerated, the problem of charge injection can be neglected. In a typical TOF experiment, a few μm thick film of OSC is grown between two electrodes (at least one semitransparent). The sample is excited at t_0 photogenerating carriers of both signs (electrons and holes) near one electrode. Depending on the applied field F, one type of carriers recombine instantaneously at the close electrode (electrons in Figure 1.25) generating a spike

in the photocurrent I, whereas the other type of carriers starts moving through the film (holes in Figure 1.25). When the carriers reach the opposite electrode recombine with a drop of the photocurrent I. Illustrative experimental setup and signal are displayed in Figure 1.25. From the transit time τ, the mobility μ [cm^2 V^{-1} s^{-1}] can be derived from: $\mu = (d/(\tau F))$, where d is the thickness of the sample.

Admittance spectroscopy (AS).

(a)   (b)
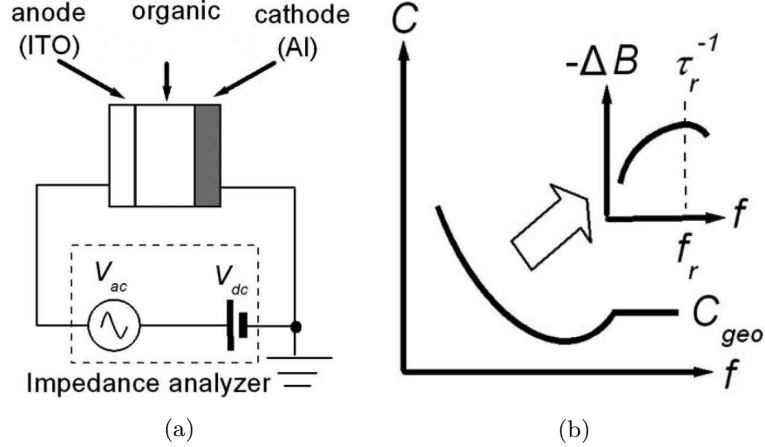
Figure 1.26: (a) Schematic representation of an AS setup. In the example, the organic material is sandwiched between aluminum and ITO electrodes. (b) Typical AS experimental signal. f is the frequency of the applied ac excitation, C is the capacitance, C_{geo} is the geometrical capacitance, $-\Delta B$ is the negative differential capacitance, and τ_r and f_r are the characteristic time and frequency, respectively. Source: [106].

Admittance spectroscopy (AS) is known to be a powerful method to measure charge carrier mobilities [108], moreover, for dispersive materials, it is considered superior to TOF techniques [106]. Illustrative experimental setup, which has a simple structure anode/OSC/cathode, and signal are displayed in Figure 1.26. To measure AS hole mobility, an ohmic contact between anode and OSC is necessary, as well as an electron blocking layer, which prevents the injection of electrons from the cathode. On the contrary, for AS electron mobility, an ohmic contact between cathode and OSC is required, additionally, a hole blocking layer to impede the injection of holes from the anode is crucial. In AS, the relaxation of the charge density of the sample is monitored under a dc biased voltage V_{dc} superimposed with a small ac excitation v_{ac} with frequency f. Experimentally, the ac current response i_{ac} is measured and the complex admittance Y is obtained as $Y(\omega) = i_{ac}/v_{ac} = G + iB = i\omega C$, where $i^2 = 1$, $\omega = 2\pi f$, and G, B, and C are the conductance, susceptance and capacitance, respectively. A convenient way to extract the mobility is to measure the frequency-dependent capacitance by an impedance analyzer, and calculating the negative differential susceptance $-\Delta B = -2\pi f(C - C_{geo})$, where $C_{geo} = \epsilon A/d$ is the geometrical capacitance (ϵ is the permittivity of the OSC, A and d are the active area and thickness of the sample, respectively) [109]. As illustrated in Figure 1.26, by plotting the negative differential susceptance $-\Delta B$ versus the frequency f, a maximum at a distinct frequency $f_r = \tau_r^{-1}$ is obtained. The average transit time is $\tau_{dc} = 0.56\tau_r$. Finally, the charge carrier mobility $\mu = d/\tau_{dc}F = d/0.56\tau_r F$ can be determined (F is the electric field) [106].

1.3.3 Introduction on the photoemission spectroscopy techniques (PES)

In Chapter 5, hybrid interfaces formed by OSCs and cobalt were investigated. In the study, three techniques were implemented: ultraviolet photoemission spectroscopy (UPS), near threshold photoemission spectroscopy (NT-PS), and two-photon photoemission spectroscopy (2PPE). Here, a brief introduction of these techniques is given.

Ultraviolet photoemssion spectroscopy (UPS) and near threshold photoemission spectroscopy (NT-PS).

(a)   (b)
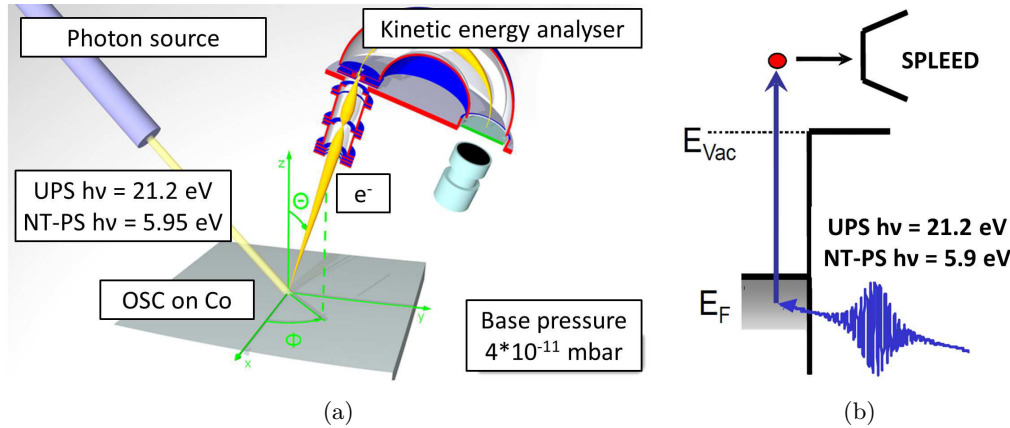
Figure 1.27: (a) Schematic illustration of UPS and NT-PS. The photon sources are a vacuum ultraviolet lamp for UPS and a Ti:sapphire laser for NT-PS. The emitted photoelectrons are energy and spin selected by a spin detector based on spin polarized low-energy electron diffraction mounted on a commercial cylindrical sector analyzer. (b) Conceptual principle of UPS and NT-PS experiments. Electrons are excited by UV photons (21.2 eV or 5.95 eV) above the vacuum energy and leave the sample. The kinetic energy and spin of the electrons is analyzed by a detector (SPLEED).

UPS is based on the measurement of the kinetic energy spectra of photoemitted electrons originating from molecules which have absorbed ultraviolet photons. In other words, UPS measures the ionization potential of molecular orbitals. UPS is, together with XPS (X-ray photoemission spectroscopy), which uses X-ray photons, one of the basic photoemission spectroscopy techniques (PES). Through the simple relation $E_{kin} = h\nu - IP$, where h is the Plank's constant, ν is the frequency of the ionizing light, and IP is the ionization energy, which can be identified as the energy of an occupied molecular orbital (Koopmans' theorem) [110]. UPS determines experimentally the energy of the highest occupied molecular orbitals of molecules absorbed on metal surfaces, in contrast, XPS gives information on the core occupied molecular orbitals. Strictly speaking, the working principle of NT-PS is identical to UPS, the only difference is the photon energy: 21.2 eV for UPS, and 5.95 eV for NT-PS [111, 112]. With the lowered photon energy, NT-PS is capable of probing electronic states close to the Fermi energy E_F. A schematic view of UPS and NT-PS is illustrated in Figure 1.27. In our experiments, we have monitored the changes in the work function and in the energetic position of the molecular orbitals, which give information on the energy level alignment, the spin polarization (SP), and the origin of the electronic states at the interface. In particular, to detect the SP polarization 3.5 nm thin cobalt films were deposited by electron beam epitaxy on a Cu(001) single crystal. Afterwards, the substrate was annealed at 370 K. This results in a metastable tetragonally distorted Co

27

fcc structure with an in-plane magnetic uniaxial anisotropy along the (110) direction of copper [113, 114]. The Co/Cu(001) was then progressively covered with the OSC to form the hybrid interface. The photoemitted electrons were analyzed in a normal emission geometry in an ultrahigh vacuum system equipped with a commercial cylindrical sector energy analyzer (CSA) and a spin detector (SPLEED), which are schematically illustrated in Figure 1.28.
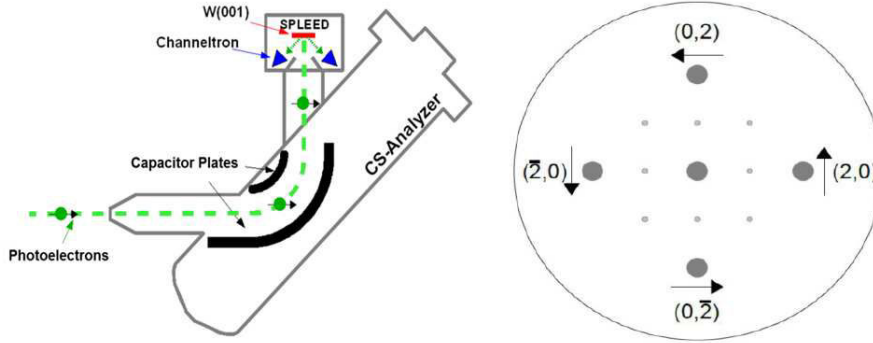
Figure 1.28: Schematic illustration of the CSA (cylindrical sector energy analyzer) and the SPLEED (spin polarized low energy electron detector). Polarized electrons are scattered on the W(001) target and detected by channeltrons positioned at the spin dependent LEED spots of the W(001) surface.

Two-photon photemission (2PPE).
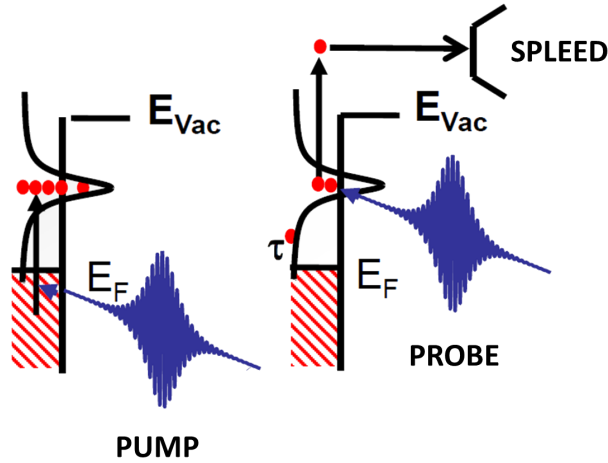
Figure 1.29: Conceptual principle of 2PPE. An electron is excited by a photon (pump) into an intermediate state . By a second photon (probe) the electron is excited above the vacuum energy and photoemitted.

2PPE belongs to the class of PES techniques, however, in contrast to UPS and NT-PS, the photoemission process is caused by the absorption of two photons, namely, pump and probe photon (for a review [115]). As illustrated in Figure 1.29, the first pump photon excites an electron from an occupied state below the Fermi energy E_F to an intermediate state between the Fermi energy E_F and the vacuum energy E_{vac}, subsequently, during the survival time in the

transiently populated intermediate state, this electron can be excited above the vacuum energy E_{vac} by the absorption of the second probe photon.
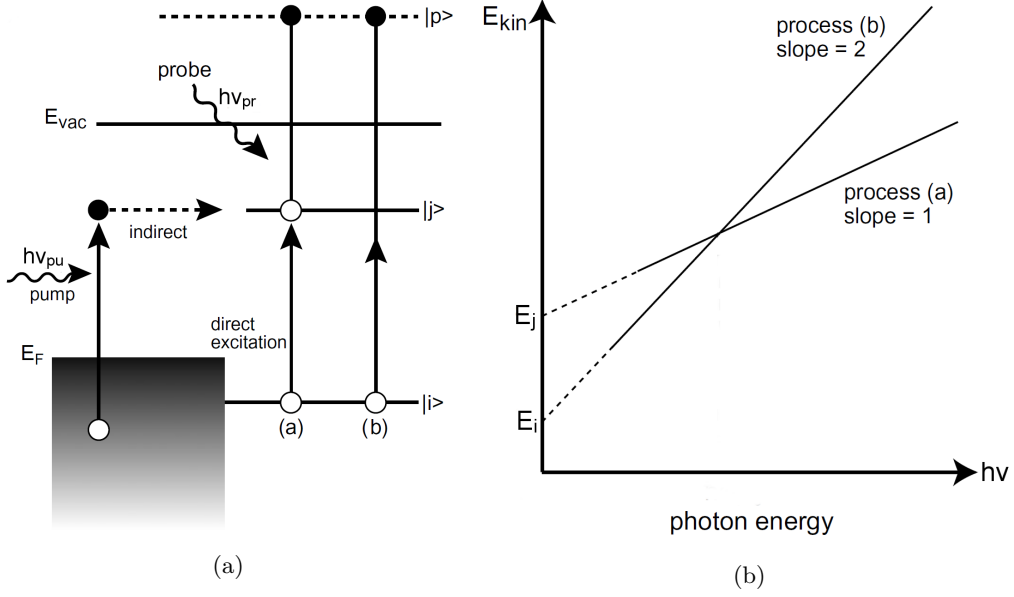
Figure 1.30: (a) Elementary excitation processes in 2PPE. There are two paths leading to the photoemission of the electron above the vacuum energy E_{vac}: a, step-by-step one photon process, and b, and direct two-photon ionization process. (b) Kinetic energy of the photoemittied electrons E_{kin} dependence from the pump and probe photon energy, $h\nu_{pu}$ and $h\nu_{pr}$, respectively. Source: [115].

A 2PPE spectrum represents the energy distribution curve of photoemitted electrons measured in function of their kinetic energy E_{kin} (and emission angle). A peak in the 2PPE spectrum can be assigned to an initial or intermediate state depending on the peak shift relative to the energy of the pump and probe photons $h\nu_{pu}$ and $h\nu_{pr}$, respectively. When a coherent two-photon excitation from an occupied state E_i, below the Fermi energy E_F, brings an electron above the vacuum energy E_{vac}, the kinetic energy of the photoemitted electron is $E_{kin} = h\nu_{pu} + h\nu_{pr} + E_i$ (process (b) in Figure 1.30). On the other hand, when 2PPE is given by two independent processes: transient population of an intermediate state E_j caused by the pump photon with energy $h\nu_{pu}$, and consequent excitation above the vacuum energy E_{vac} caused by the probe photon with energy $h\nu_{pr}$, the kinetic energy of the photoemitted electron is $E_{kin} = h\nu_{pr} + E_j$ (process (a) in Figure 1.30).

In our experiments, the 2PPE technique was used in two modes. In the static mode, which is the 2PPE spectroscopy, the time delay between the two photons is fixed, $\Delta t= 0(1)$ fs, whereas the photon energy was varied between 2.91 and 3.31 eV. In the time-resolved mode, the time delay between the two laser pulses varies from $\Delta t= -9$ to $\Delta t= 9$ ps, whereas the photon energy is tuned to 3.25 eV. In this mode, the determination of the lifetime of hot electrons in the intermediate states populated in the 2PPE process is possible [116]. As illustrated in Figure 1.27 for UPS and NT-PS, the photoemitted electrons were analyzed in a normal emission geometry in an ultrahigh vacuum system equipped with a cylindrical sector energy analyzer (CSA) and a spin detector (SPLEED).

1.4 Single-molecule magnets (SMMs)

Mainly, this thesis is focused on the synthesis and characterization of (novel) OSCs implementing the ligands listed in Table 3.1. These ligands can also easily chelate lanthanides to form stable complexes. Since lanthanides are widely used to form single-molecule magnets (SMMs), we have initiated a study on phenalenyl-based SMMs formed with dysprosium and terbium. Preliminary results are shown in Chapter 6. Here, we present a summary on SMMs and their magnetic characterization, for a review on this class of materials see references [117–121].

(a)

(b)
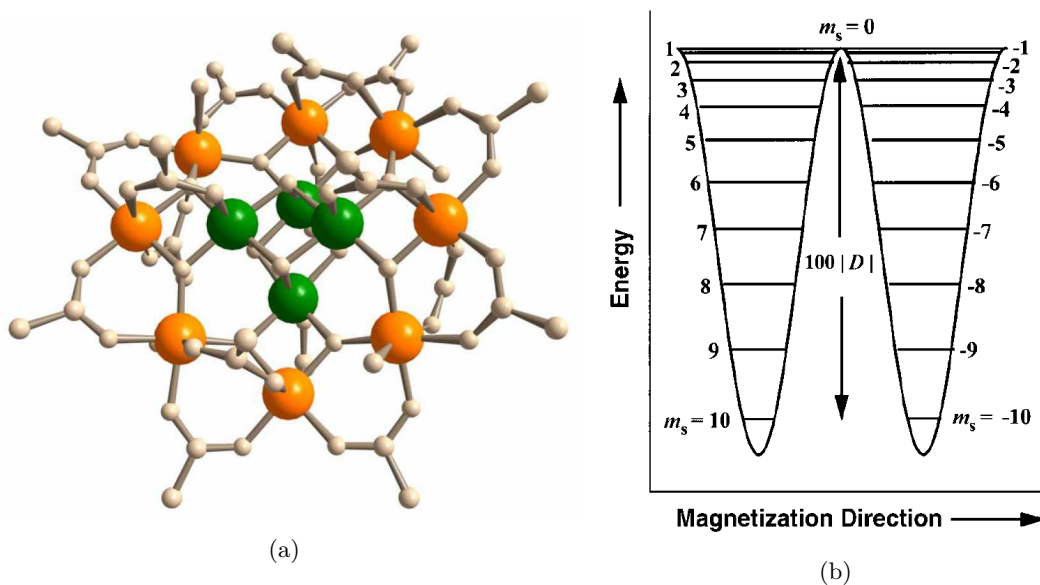
Figure 1.31: (a) Crystal structure of the first SMM $[Mn_{12}O_{12}(OAc)_{16}(H_2O)_4]$ (Mn$_{12}$Ac). The total spin of the molecule is S= 10 given by 4 Mn^{4+} ions, S= 6 (Mn^{4+}: S= 3/2) plus 8 Mn^{3+} ions, S= 16 (Mn^{3+}: S= 2). (b) Plot of the potential energy versus the magnetization for a SMM with S= 10 ground state. The diagram is for zero external magnetic field. Source: [118, 122, 123].

The basic property of SMMs is the capability to retain magnetization for a long period of time in absence of an external magnetic field [122, 123]. In the first famous example, a molecular transition metal coordination compound, namely the famous dodecametallic manganese-acetate cage $[Mn_{12}O_{12}(OAc)_{16}(H_2O)_4]$ (Mn$_{12}$Ac), illustrated in Figure 1.31 [122, 123], could retain its magnetization over years below $2\,K$ [118]. SMMs can be considered as molecular analogues of classic bulk ferromagnets, and thus, in principle, they could have many important technological applications in storage and processing of digital information, and in molecular spintronics [120]. Anyhow, before a real technological application of SMMs, two major problems must be overcome. First, the properties of SMMs are accessible only using liquid helium cooling, and second, depositing and addressing of individual molecules of SMMs on surfaces have been scarcely explored. Two strict prerequisites for a molecule to be a SMM are: a bistable ground state and magnetic anisotropy. For lanthanide ions, with ground electronic terms other than $^1S_0$ and $^8S_{7/2}$, the orbital contribution to the magnetic moment is large and unquenched, and, additionally, ligand field effects are regarded as a small but significant perturbation [117]. In lanthanide-based SMMs, ground state bistability arises from the $[2J+1]$ m_J microstates within the spin-orbit coupled ground term $^{2S+1}L_J$. Metal ions with a large value of microstates m_J are characterized by appreciable magnetic moment. As a consequence of these two prerequi-

sites, the lanthanides most commonly used to form SMMs are: terbium(III), dysprosium(III), erbium(III), and holmium(III) (see Table 1.2).

Table 1.2: Lanthanide(III) ions commonly used in SMMs.

	Tb^{3+}	Dy^{3+}	Ho^{3+}	Er^{3+}
configuration	$4f^8$	$4f^9$	$4f^{10}$	$4f^{11}$
spin-orbit ground term	$^7F_6$	$^6H_{15/2}$	$^5I_8$	$^4I_{15/2}$
free-ion g-value	3/2	4/3	5/4	6/5
χT [cm^3 K mol^{-1}]	11.82	14.17	14.07	11.48

In general, the properties of SMMs are evaluated by measuring three parameters. First, the magnetic blocking temperature T_B is the highest temperature at which a SMM displays hysteresis in plots of magnetization M versus magnetic field H. Second, the coercive magnetic field H_c is the strength of the magnetic field needed to drive the magnetization of an SMM back to zero following saturation. Last, the effective energy barrier to reversal of the magnetization (or anisotropy barrier) U_{eff} (or Δ), is the energy required to convert a SMM back into a simple paramagnet. Due to the strong angular dependence of the 4f orbitals, the electronic structures of Tb(III) and Dy(III) ions possess substantial axial anisotropy.

1.4.1 Magnetic characterization of SMMs

SMMs are generally characterized in crystalline forms using conventional SQUID (superconducting quantum interference device) magnetometers. In the standard experiment, the magnetic susceptibility χ is measured using a very small alternating current (ac) with a magnetic field of about 1-5 Oe across a temperature range between 1-50 K. The frequency ν of the ac field can be varied in the range of 1-1500 Hz resulting in a time dependent magnetic moment, which can be characterized by a relaxation time τ at a given temperature. Since individual SMMs have their own magnetic moment, the magnetization of the SMM will lag behind the driving ac field as it alternates across the sample, and thus, the measured magnetic susceptibility contains a phase shift. By this experiment, the so-called in-phase and out-of-phase susceptibilities, $\chi\prime$ and $\chi\prime\prime$, respectively, are measured.

To identify SMM behavior, the dependence off $\chi\prime$ and $\chi\prime\prime$ versus the temperature is investigated at different frequencies ν. When the temperature decreases, if the plot of $\chi\prime\prime$ gradually increases till a maximum and then decreases at lower temperatures, this indicates that the reversal of the spin has been blocked. Furthermore, changing the ac frequency ν, the maximum in the $\chi\prime\prime(T)$ plot also changes. In contrast, the absence of maxima in the $\chi\prime\prime(T)$ plots, or the lack of frequency dependent $\chi\prime\prime$ in zero fields, originates ambiguity on the SMM behavior. Another experiment implemented to characterize SMMs are the plots of $\chi\prime$ and $\chi\prime\prime$ versus the ac frequency ν at different temperatures. Plots of $\chi\prime\prime(\nu)$ isotherms permit to determine the anisotropy barrier U_{eff}. Strictly speaking, from each $\chi\prime\prime(\nu)$ curve, an average relaxation time τ, at a given temperature T, can be determined. Hence, through the Arrhenius-type relationship:

$$\tau = \tau_0 \exp\frac{U_{eff}}{k_b T} \tag{1.14}$$

the anisotropy barrier U_{eff} can be calculated from the slope of $\ln\tau$ versus T^{-1}. When the graph is linear and τ is temperature dependent, the magnetization in the SMM is relaxing via a thermally assisted mechanism. On the contrary, when τ is temperature independent, the
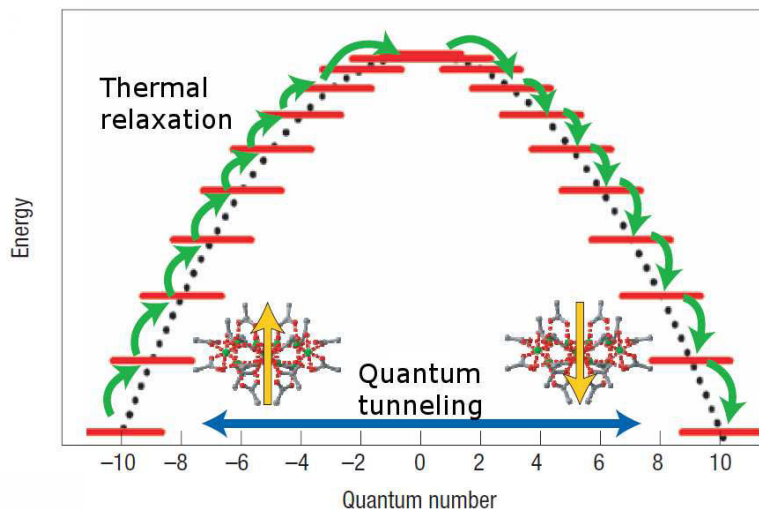
Figure 1.32: Schematic illustration of the relaxation processes of a SMM with a spin ground state S=10. The magnetization reversal can occur via quantum tunneling between energy levels (blue arrow) or by thermal relaxation by climbing up and down all the energy levels (green arrows). Source [120].

relaxation of the magnetization occurs via quantum tunneling (QTM). In many cases, thermal and QTM relaxation of the magnetization take place concurrently, as a result, the Arrhenius plot shows a curvature of $\ln \tau$ versus T^{-1}. A schematic illustration of the relaxation processes is given in Figure 1.32.

1.4.2 Monometallic lanthanide-based SMMs

In our study, we synthesized exclusively mononuclear lanthanide-based SMMs, and thus, a brief overview is given only on this specific class of SMMs. Mononuclear lanthanide-based SMMs show slow relaxation of the magnetization although they contain only one single metal ion (for a review [117]).
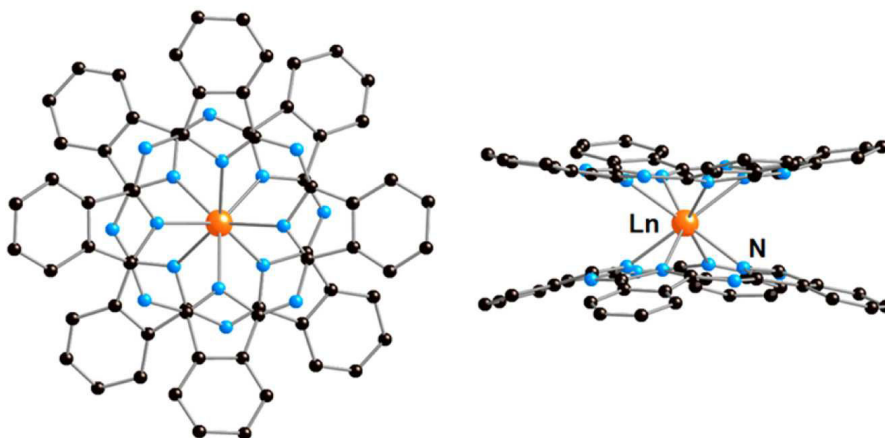
Figure 1.33: Molecular structure of $[LnPc_2]^-$. Hydrogens atoms are omitted. Source: [117].

From the first work of Ishikawa *et al.*, in which SMM behavior was investigated in phthalocya-

<center>(a)   (b)</center>
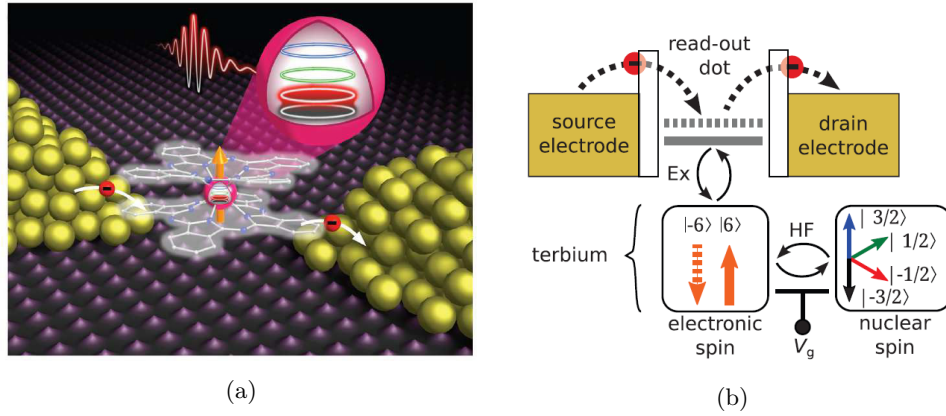
Figure 1.34: (a) Artistic illustration of a nuclear spin qubit transistor based on a single $TbPc_2$ SMM, which is coupled to source, drain, and gate (not shown) electrodes. The four anisotropic nuclear spin states of the Tb^{2+} (colored circles) can be manipulated with an electric field. (b) Schematic illustration of the three coupled subsystem of the transistor. The four-level nuclear spin qubit is hyperfine coupled to an Ising-like electronic spin, which in turn is antiferromagnetic exchange coupled to a readout quantum dot. Source: [124].

<center>(a)   (b)</center>
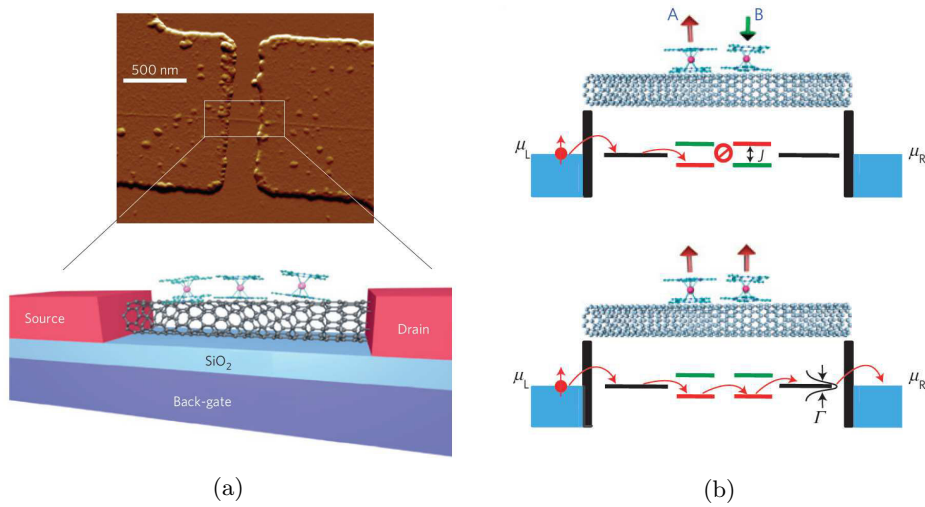
Figure 1.35: (a) Atomic force micrograph and schematic illustration of the $TbPc_2$-based spin valve (hexyl and pyrenyl groups are omitted for clarity). The single-walled carbon nanotube lies on a SiO_2 surface supported by a back gate and is connected to palladium source and drain electrodes. (b) Schematic representation of the mechanism involving two $TbPc_2$ grafted on a single-walled nanotube. Increasing the magnetic field the molecule A switches leading to an antiparallel configuration of the spin valve with lowest conductance. When molecule B switches, the parallel configuration with high conductance is recovered. Source [125].

<center>33</center>

nine complexes [Bu$_4$N][LnPc$_2$] (Ln= Dy, Tb) [126], phthalocyanine-based SMMs are the most widely studied mononuclear lanthanide SMMs. Furthermore, they are seemingly the SMMs with the most potential to be developed for surface deposition, and thus, device applications. The most common molecular structural motif is the double-decker structure, where two phthalocyanine rings sandwich a lanthanide ion with a D_{4d} symmetry and a square-antiprismatic coordination geometry, as illustrated in Figure 1.33. The complex can be a cation, an anion, or uncharged. Phthalocyanine can be substituted using conventional organic chemistry giving rise to a number of derivatives. Phthalocyanine-based SMMs were deposited onto graphene [127], carbon nanotubes [128], copper(111) [129], and more. Among the most interesting results, pristine as well substituted TbPc$_2$ were used in molecular-based transistor to read single-nuclear spin [130], and, in addition, the nuclear spin could be controlled electrically [124] (see Figure 1.34). In an another experiment, spintronic devices with carbon nanotubes as a supramolecular spin valve were built implementing TbPc$_2$ [125] (see Figure 1.35).

Besides phthalocyanines, many ligands have been employed in the synthesis of mononuclear lanthanide SMMs [117]. In the synthesis of SMMs described in Chapter 6, we have implemented a molecule belonging to the class of the β-diketonate ligands, which are widely utilized to form SMMs. The most simple β-diketonate is 4-hydroxypent-3-en-2-one (acac), which is illustrated in Table 3.1. Generally, β-diketonate-based SMMs are of the type [Ln($\beta-$diketonate)$_3$(L)$_n$], where, uncharged ligands L (monodentate or bidentate) complete the coordination sphere of the lanthanide. This results in a neutral complex where the eight coordinating atoms are arranged in a square-antiprismatic geometry.
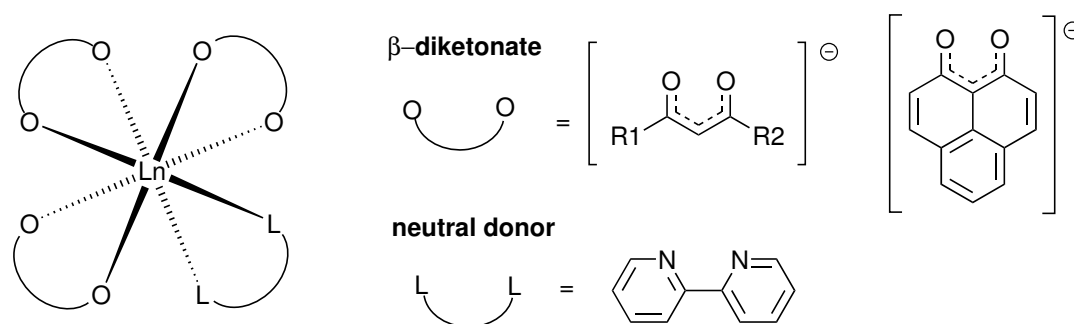
Figure 1.36: Idealized square-antiprismatic structure of [Ln($\beta-$diketonate)$_3$(L)$_n$] complexes. Structures of β-diketonates and of neutral ligands (exemplary, 2,2'-bipyridine) are illustrated.

Figure 1.36 illustrates the structure of [Ln($\beta-$diketonate)$_3$(L)$_n$], the variety of available β-diketonate ligands with R$_1$= R$_2$, but also with R$_1\neq$ R$_2$, and the multitude of neutral ligands, open up to countless SMMs which can be obtained. So far a vast number of β-diketonate-based SMMs was synthesized, however, besides the characterization of the magnetic properties, they were not applied in any device. Therefore, in our study, we aim to synthesize phenalenyl-based lanthanide SMMs to investigate their magnetic properties and eventually to be deposited on surfaces by vacuum evaporation. This would be the first step towards the implementation of such molecules in devices.

2. Aim of the Thesis

In the last two decades, a huge amount of reports related to OSCs has been published. In most cases, the studies aimed to produce materials with enhanced performance in respect to the previously reported OSCs. However, there is still a lack of knowledge about the exact relationship between the molecular structure of an OSC and its electronic properties when it is implemented in devices. Together with our collaborators, we started a study on the low molecular weight class of OSCs. Our work on OSCs can be divided in three main parts:

1. Rational design, synthesis and structural characterization of a series of OSCs utilizing Alq_3 as "leitmotif". Systematic photophysical and electrochemical characterization in solution of the OSCs to determine the influence of the chemical structure on the electronic properties, i.e HOMO and LUMO energy levels.

2. Theoretical and experimental studies on the charge carrier mobility of the (novel) OSCs. Theoretically the OSCs were studied in vacuum and in generated morphologies to determine the charge carrier mobility of electrons and holes. Preliminary experimental measurements have been performed in comparison.

3. Photoemssion spectroscopy studies on the OSCs deposited on cobalt substrates. The spin dependent properties OSC/Co were investigated in comparison with the prototypical Alq_3/Co interface.

In addition, we have synthesized and characterized phenalenyl-based lanthanide complexes. This study aimed to examine the SMM behavior of such molecules and the possible deposition of those materials on substrates for surface studies.

3. Design, Synthesis and Characterization of (novel) OSCs
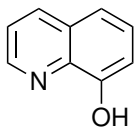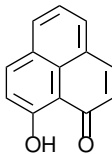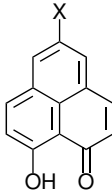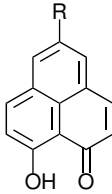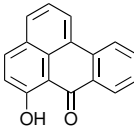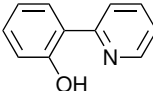
3.1 Introduction

In Section 1.1, the principal characteristics of OSCs are described. All OSCs are based on a backbone formed by carbon atoms bonded through σ bonds and a delocalized π electron system, which derives from the weaker π-electron of the p_z-orbitals of sp^2-hybridized carbon atoms. Alq$_3$ is the most known semiconductor among the class of low molecular weight OSCs. As explained in Section 1.2, Alq$_3$ is formed by three quinolinate ligands chelating the central aluminum atom. Due to the asymmetric structure of Hq, two geometrical isomers, mer-Alq$_3$ and fac-Alq$_3$, can be formed. In addition, the electronic properties of Alq$_3$ are mainly resulting from the ligands. Attempts to ameliorate the electronic properties of Alq$_3$, chemically modifying Hq or substituting the aluminum with other metals, are presented in Section 1.2.1. In this study, we have investigated (novel) OSCs affine to Alq$_3$. Our strategy was to tune the electronic properties (HOMO and LUMO energy levels) of aluminum-based OSCs mutating the following three parameters:

- Extension of the aromatic system

- Symmetry of the ligand

- Symmetry of the complex

The first part of the study was to design and synthesize, when necessary, ligands. Due to their features we selected the ligands listed in Table 3.1, which were utilized to form the aluminum complexes listed in Table 3.2. Additionally, after the report of a phenalenyl-based zinc complex in organic spintronic devices (see Section 1.2.3), we studied a zinc complex for a better understanding of this class of OSCs. The (novel) OSCs were synthesized, purified and structurally characterized by means of elemental analysis, NMR spectroscopy, mass spectrometry, and single crystal X-ray diffraction. In the second part, a photophysical characterization of the ligands and (novel) OSCs in solution is presented. In addition, we have developed a study with Dr. Fattori (ISOF-CNR, Bologna) which investigates the photophysical properties of the complexes evaporated onto quartz substrates. Electrochemical investigations on ligands and (novel) OSCs were carried out to determine the reduction potentials. At last, the HOMO and LUMO energy levels were determined and related to the structure of the ligands and of the (novel) OSCs. The detailed description of the reaction procedures and the analytical characterization of the OSCs as well as of the intermediates are reported in Section 8.2.

Table 3.1: List of ligands used in the synthesis of the (novel) OSCs. Their respective structures and characteristics are described, Hq is added as reference (in the thicker box). X: F, Cl, Br, I. R: phenyl, naphthalenyl, phenylethynynl.

Name	Structure	Characteristics
Hq		• 2 fused aromatic rings • Asymmetric • *mer*- and *fac*-Al complex
HOp		• 3 fused aromatic rings • Symmetric (fast proton transfer) • Symmetric complex
HOp−X		• 3 fused aromatic rings plus halogen • Symmetric (fast proton transfer) • Symmetric complex
HOp−R		• 3 fused aromatic rings plus substituent • Symmetric (fast proton transfer) • Symmetric complex
HOba		• 4 fused aromatic rings • Asymmetric • *mer*- and *fac*-Al complex
HOp−py		• 2 separated aromatic rings • Asymmetric • *mer*- and *fac*-Al complex
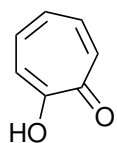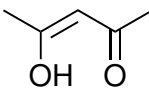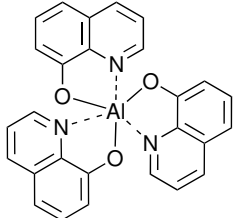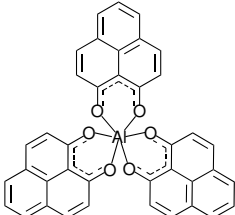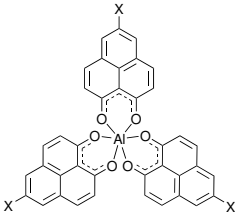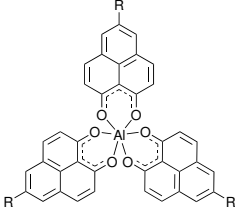
Tropolone		• 1 aromatic ring • Symmetric (fast proton transfer) • Symmetric complex
Acac		• Non-aromatic • Symmetric (fast proton transfer) • Symmetric complex

Table 3.2: List of (novel) OSCs synthesized. Their respective structures and characteristics are described, Alq$_3$ is added as reference (in the thicker box). X: F, Cl, Br, I. R: phenyl, naphthalenyl, phenylethynynl.

Name	Structure	Characteristics
Alq$_3$		• Asymmetric • *mer*- and *fac*-isomer • Homoleptic
Al(Op)$_3$		• Symmetric • No isomers • Homoleptic
Al(Op−X)$_3$		• Symmetric plus halogen • No isomers • Homoleptic
Al(Op−R)$_3$		• Symmetric plus substituent • No isomers • Homoleptic

Al(Oba)$_3$		• Asymmetric • *mer*- and *fac*-isomer • Homoleptic
Al(Op−py)$_3$		• Asymmetric • *mer*- and *fac*-isomer • Homoleptic
Al(Trop)$_3$		• Symmetric • No isomers • Homoleptic
Al(q$_2$Acac)		• Asymmetric • *pseudomer*- and *pseudofac*-isomer • Heteroleptic
Al(q$_2$Op)		• Asymmetric • *pseudomer*- and *pseudofac*-isomer • Heteroleptic
Al(q$_2$Trop)		• Asymmetric • *pseudomer*- and *pseudofac*-isomer • Heteroleptic
Zn(Op)$_2$		• Symmetric (flat) • No isomers • Homoleptic

3.2   Experimental techniques and instrumentation

All the reactions were carried out under argon inert atmosphere using standard Schlenk techniques. All the purchased chemicals and solvents for the synthesis and column chromatography were used as received without any further purification unless otherwise stated. Elemental analysis of carbon, hydrogen, and nitrogen were carried out in a Vario Micro Cube. ^{1}H-NMR and ^{13}C-NMR were recorded in a Bruker FT-NMR Avance III 500 MHz with deuterated solvents as internal standards for proton and carbon signals. MALDI-TOF mass spectrometric data were acquired on a MALDI-TOF Synapt G2-S HDMS with no additional matrix compound other than the sample itself. ESI-TOF mass spectrometric analytical data were acquired on a Bruker microOTOF-Q II equipped with a nanospray source. Single crystal X-ray diffraction data were collected on a STOE IPDS II diffractometer with graphite monochromated Mo Kα radiation (0.710 73 Å). Structure solution and refinement against F^2 were carried out using shelxs and shelxl software. Refinement was performed with anisotropic temperature factors for all non-hydrogen atoms (disordered atoms were refined isotropically); hydrogen atoms were calculated on idealized positions.

Absorption spectra were acquired at room temperature for diluted solutions of the ligands and complexes (8.0×10^{-6} M) on a Cary 500 Scan UV-Vis-NIR spectrophotometer using a 1 cm quartz cell. Photoluminescence, emission and excitation spectra were recorded at room temperature for diluted solutions of the ligands and complexes (8.0×10^{-6} M) on a Cary Eclipse Fluorescence spectrophotometer using a 1 cm quartz cell. The photoluminescence quantum yield in solution was computed using rhodamine 6G as reference [131, 132]. Cyclic voltammetry studies were performed using an Autolab PGSTAT10 potenziostat in a three-electrode single-compartment cell with a glassy carbon working electrode, Ag/AgCl reference electrode, and a platinum wire as auxiliary electrode in an inert argon atmosphere. Tetrabutylammonium hexafluorophosphate (TBAPF$_6$) was used as supporting electrolyte (0.1 M) and DCM was used as solvent (except for the zinc complex). The concentration of the ligands and complexes was 1.0×10^{-4} M; the solutions were degassed with argon prior to the measurements. A scan rate of 100 mV s^{-1} was employed. Ferrocene was used as internal standard to calculate the corrected reduction potential [133]. The evaporation of the OSCs onto quartz substrates was carried out in an Edwards Auto 306 evaporator equipped with a high vacuum chamber (10^{-6} mbar) and a frequency thickness monitor (FTM) to check the evaporation rate. The complexes were grown at a deposition rate of 0.5 nm s^{-1} with a final thickness of 80 nm. The solid state absorption spectra were recorded on a Perkin-Elmer Lamba 900 UV-Vis-NIR spectrophotometer. The solid state photoluminescence spectra were acquired on a Spex Fluorolog 2 (the spectra are corrected to compensate the nonlinear response of the photomultiplier Hamamatsu R28). The photoluminescence quantum yield in thin film was determined using the integrating sphere absolute method [134] on a Spex Fluorolog 2 (the spectra are corrected to compensate the nonlinear response of the photomultiplier Hamamatsu R28). The lifetimes, in solution and solid state, were obtained on a TCSPC (time correlated single photon counter) equipped with a NanoLED source and a Horiba Jobin-Yvon Fluorohub for the data elaboration.

3.3 Synthesis of the (novel) OSCs

3.3.1 Tris-(1-oxo-1H-phenalen-9-olate)aluminum (Al(Op)$_3$) (4)
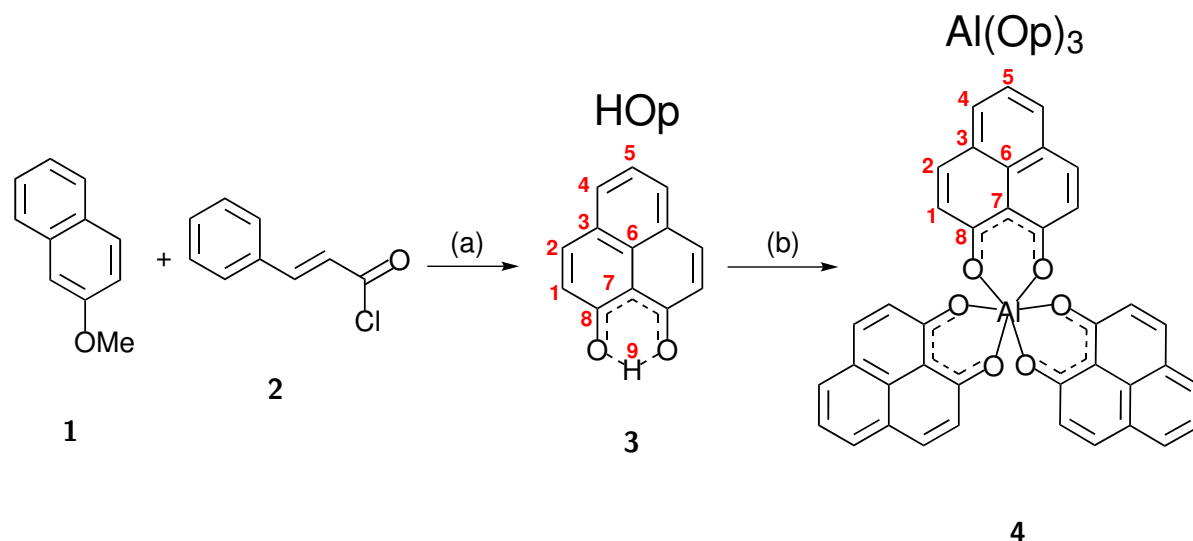
Scheme 3.1: Synthesis of tris-(1-oxo-1H-phenalen-9-olate)aluminum (Al(Op)$_3$) **4**. (a) AlCl$_3$, DCE, reflux, 4h, yield: 86% [135]. (b) AlCl$_3$, toluene, reflux, overnight, yield: 75%. The numbering is shown in red for HOp **3** and Al(Op)$_3$ **4** (on one ligand).

Al(Op)$_3$ **4** is the first molecule to be designed in this study. Its synthesis and implementation in OLEDs was previously reported for commercial applications [136]. The ligand 9-hydroxy-1H-phenalen-1-one (HOp) **3** has been selected for mainly two reasons, which are in contrast to Hq: it is symmetric and it has an extended aromatic system. The symmetry of HOp **3** originates from the characteristic proton tautomerism (or proton transfer) between two degenerate configurations, as illustrated schematically in Figure 3.1. The proton transfer, caused by the strong intramolecular hydrogen bond, has been investigated by several experimental techniques [137–142] and theoretical methods [143–146]. Although HOp **3** is commercially available, an efficient synthesis was described by Koelsch *et al.* [147] and improved by Haddon *et al.* [135]. In the latter approach, illustrated in Scheme 3.1, 2-methoxynaphtalene **1** and cinnamoyl chloride **2** are used as precursors. Several metal chelates of HOp **3** were previously studied by Demura *et al.* [148].
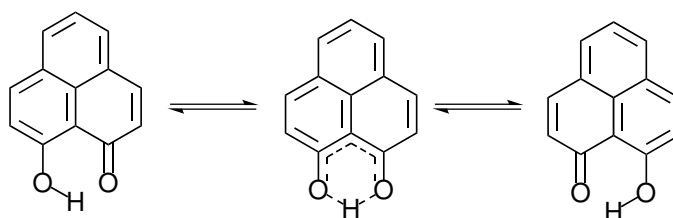
Figure 3.1: Schematic illustration of the proton transfer in HOp **3**.

The aluminum complex Al(Op)$_3$ **4** is formed by the reaction of HOp **3** with an aluminum salt such as AlCl$_3$. After a careful purification by means of column chromatography, sublimation in vacuum and recrystallization, the yield of the reaction is ≈75%. Single crystals of Al(Op)$_3$ **4**
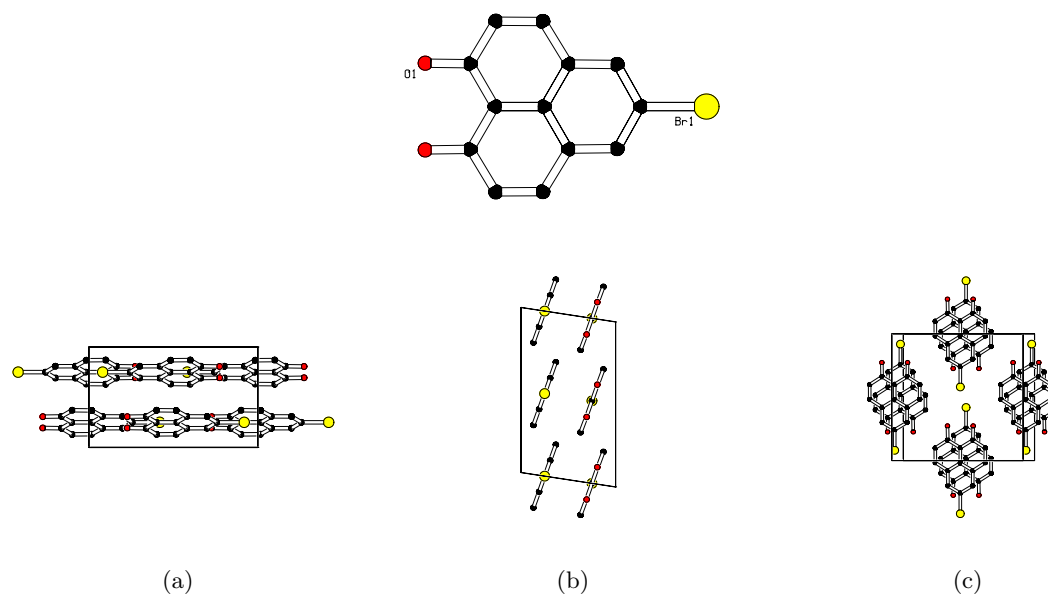
Figure 3.2: Molecular structure obtained by single crystal X-ray diffraction on a single crystal of Al(Op)$_3$ **4**. H-atoms and solvent molecules are omitted for clarity. The crystal refinement data is reported in Table C.2. The molecular packing in the single crystal of Al(Op)$_3$ **4** is illustrated in (a) yz (b) xz (c) xy perspective. Table: selected bond distances and angles for Al(Op)$_3$ **4**.
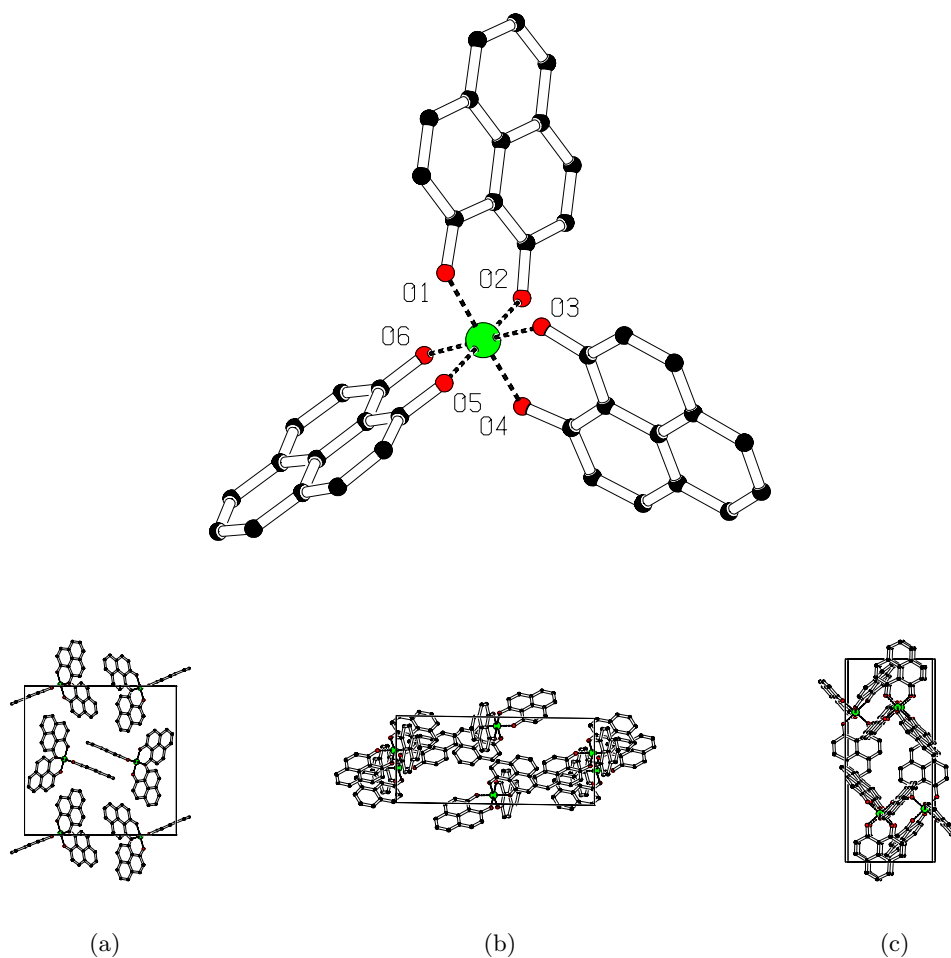
Bond	Length [Å]	Bond angle	Angle [°]	Bond angle	Angle [°]
		Al(Op)$_3$ **4**			
Al1-O1	1.875(2)	O1-Al1-O2	90.99(9)	O2-Al1-O6	88.63(9)
Al1-O2	1.867(2)	O1-Al1-O3	88.77(10)	O3-Al1-O4	91.00(10)
Al1-O3	1.877(2)	O1-Al1-O4	178.34(10)	O3-Al1-O5	87.47(9)
Al1-O4	1.882(2)	O1-Al1-O5	89.48(10)	O3-Al1-O6	178.43(10)
Al1-O5	1.877(2)	O1-Al1-O6	91.68(10)	O4-Al1-O5	92.16(10)
Al1-O6	1.873(2)	O2-Al1-O3	92.86(10)	O4-Al1-O6	88.59(10)
		O2-Al1-O4	87.38(9)	O5-Al1-O6	91.03(10)
		O2-Al1-O5	179.43(10)		

Compound	Resonances [ppm]				
	H1	H2	H4	H5	H9
HOp **3**	7.19	8.11	8.03	7.61	16.05
Al(Op)$_3$ **4**	7.14	8.01	7.96	7.51	-

Figure 3.3: ^{1}H-NMR spectra of HOp **3** and Al(Op)$_3$ **4** in CDCl$_3$. The resonances are marked accordingly to the numbering shown in Scheme 3.1.

were grown by slow evaporation of a chloroform solution at room temperature. The molecular structure obtained by single crystal X-ray diffraction is illustrated in Figure 3.2, in addition, selected bond lengths and angles are listed. The crystal refinement data is reported in Table C.2. As demonstrated by the O-Al-O bond angles, which are all close to 90° or 180°, the six chelating oxygens are arranged in an almost perfect octahedral geometry around the central aluminum atom. Additionally, the bond lengths Al-O are narrowly distributed between 1.867 and 1.882 Å, indicating that the six oxygens are virtually identical, taking in consideration the deformation caused by solvent molecules in the crystal lattice. Al-O distances in Al(Op)$_3$ **4** are comparable to those in *mer*-Alq$_3$, which are reported in Section 1.2. The molecular packing of Al(Op)$_3$ **4** is clearly driven by the $\pi - \pi$ stacking between the flat aromatic ligands. Furthermore, the ligands maintain the aromaticity and flatness after coordinating aluminum. As a result, all the torsion angles of the phenalenyl ligands are close to either 0° or 180°. At last, C-C bonds in the phenalenyl moieties of Al(Op)$_3$ **4** and of HOp **3**, reported by Svensson *et al.* [149], are almost identical between ≈1.35 Å and ≈1.45 Å. This indicates that no major deformations are induced on the phenalenyl ligands by the coordination of aluminum.

Figure 3.3 illustrates the ^{1}H-NMR spectra of HOp **3** and Al(Op)$_3$ **4**. HOp **3** presents five resonances. The first, with a chemical shift of ≈16 ppm (out of the range of the figure), is related to the hydrogen H9 involved in the proton tautomerism described in Figure 3.1 [150]. The high chemical shift indicates that the hydrogen is between the two oxygens rather than being localized on one oxygen. In other words, the proton transfer at room temperature is faster
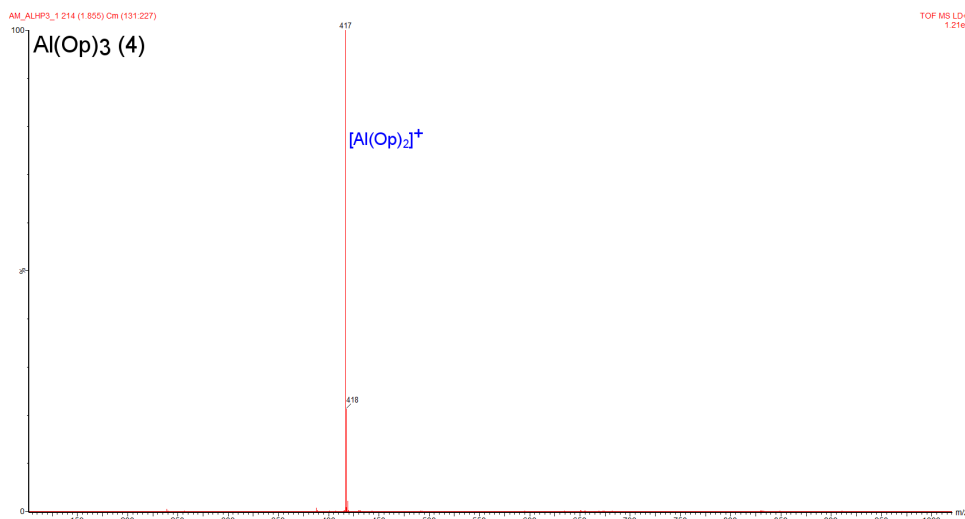
Figure 3.4: MALDI-TOF spectrum of Al(Op)$_3$ **4**. The fragment is marked in the figure.

than the time-scale of the NMR measurement. As a result, HOp **3** is perfectly symmetrical, and thus, it is characterized by four resonances in the aromatic region (H1, H2, H4 and H5). On the contrary, the ^{1}H-NMR spectrum of an asymmetric form of HOp **3**, in which the hydrogen H9 is localized on one oxygen, would result in seven aromatic resonances. Due to the coordination of the aluminum, the four resonances detected for Al(Op)$_3$ **4** (H1, H2, H4 and H5) are observed at slightly lowered chemical shifts. Clearly, this indicates that the three ligands are identical and symmetrical also after the coordination of aluminum. The carbon and hydrogen elemental analysis on the obtained complex, C= 72.29% and H= 4.01%, matches the calculated values, C= 72.00% and H= 4.19%, considering the adsorption of two additional H$_2$O molecules (see Table 3.3). The MALDI-TOF spectrum of Al(Op)$_3$ **4** is illustrated in Figure 3.4. A single peak corresponding to the fragment [Al(Op)$_2$]$^+$ (*m/z*= 417) is detected; the cation is generated during the MALDI process by the elimination of one ligand.

3.3.2 5-Halogenated Al(Op)$_3$: Al(Op−X)$_3$ (6a-d)

Here, the hydrogen in the 5-position of HOp **3** is substituted with the full series of halogen atoms, aiming to modify the electronic properties of HOp **3**, and thus, of Al(Op)$_3$ **4**. This was done to study the effect of the electron-withdrawing character of halogen atoms on the phenalenyl ring. To date, very few reports have been published on symmetrically halogenated HOp **3** derivatives [151, 152]. More importantly, a comprehensive investigation on the symmetrical halogenation effect on the electronic properties of HOp **3** and Al(Op)$_3$ **4** has not been yet reported. Scheme 3.2 illustrates the final step of the synthetic procedure to obtain the halogenated complexes Al(Op−X)$_3$ **6a**–**d** by the reaction of the halogenated ligands HOp−X **5a**–**d** with AlCl$_3$. The detailed procedures to obtain the ligands HOp−X **5a**–**d** are illustrated in Scheme 3.3.

The synthesis of 5-fluoro-9-hydroxy-1H-phenalen-1-one (HOp−F) **5a**, which involves three steps, is unprecedented. In the first step, a cross-coupling reaction between 2-bromo-6-methoxy-naphthalene **7** and ammonia, catalyzed by CuI, was carried out to replace the bromo atom with an amino group [153]. The resulting amino derivative **8** was diazotized, in the presence of HBF$_4$, to obtain the fluorinated methoxynaphtalene **9** [154]. Subsequently, 2-fluoro-6-methoxynaphthalene **9** was reacted with cinnamoyl chloride **2** to form HOp−F **5a**. The

$$Al(Op\text{-}X)_3$$

$$HOp\text{-}X$$

5a–d

6a–d
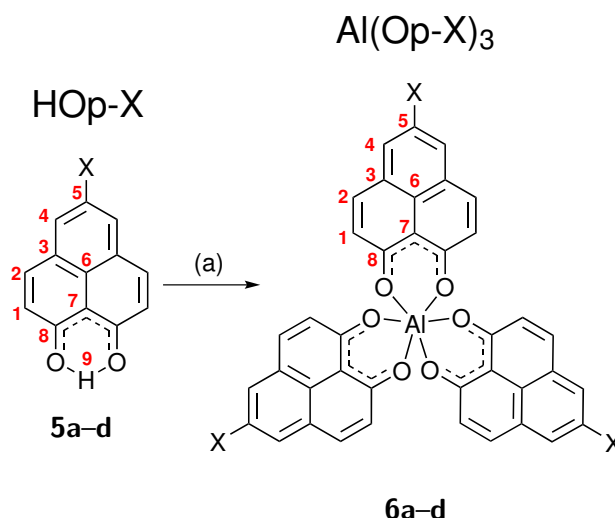
Ref.	Name	Ref.	Name	X
5a	HOp−F	**6a**	Al(Op−F)$_3$	F
5b	HOp−Cl	**6b**	Al(Op−Cl)$_3$	Cl
5c	HOp−Br	**6c**	Al(Op−Br)$_3$	Br
5d	HOp−I	**6d**	Al(Op−I)$_3$	I

Scheme 3.2: Synthesis of the halogenated complexes Al(Op−X)$_3$ **6a–d**. (a) AlCl$_3$, toluene, reflux, overnight, yields: Al(Op−F)$_3$ **6a** 81%, Al(Op−Cl)$_3$ **6b** 83%, Al(Op−Br)$_3$ **6c** 87%, Al(Op−I)$_3$ **6d** 80%. The numbering is shown in red for the halogenated ligands HOp−X **5a–d** and complexes Al(Op−X)$_3$ **6a–d** (on one ligand).

overall yield to obtain HOp−F **5a** is ≈15% and to obtain tris-(5-fluoro-1-oxo-1H-phenalen-9-olate)aluminum (Al(Op−F)$_3$) **6a** it is ≈12%. The synthesis of 5-chloro-9-hydroxy-1H-phenalen-1-one (HOp−Cl) **5b** was previously reported by Nishi *et al.* [151]. 2-Bromo-6-methoxynaphthalene **7** was reacted with CuCl yielding the chloro methoxynaphthalene **10**. HOp−Cl **5b** was formed by the reaction between 2-chloro-6-methoxynaphthalene **10** and cinnamoyl chloride **2**. The total yield of the synthesis of HOp−Cl **5b** is ≈65%. The overall yield to obtain tris-(5-chloro-1-oxo-1H-phenalen-9-olate)aluminum (Al(Op−Cl)$_3$) **6b** is ≈54%. The synthesis of 5-bromo-9-hydroxy-1H-phenalen-1-one (HOp−Br) **5c** was previously described [151]. 2-Bromo-6-methoxynaphthalene **7** was reacted with cinnamoyl chloride **2** to form HOp−Br **5c** with a yield of ≈77%. Tris-(5-bromo-1-oxo-1H-phenalen-9-olate)aluminum (Al(Op−Br)$_3$) **6c** is obtained with an overall yield of ≈67%. The synthesis of 5-iodo-9-hydroxy-1H-phenalen-1-one (HOp−I) **5d** was previously reported by Mochida *et al.* [152]. The procedure involves two steps. In the first step, HOp−Br **5c** was reacted with CH$_3$I in the presence of Ag$_2$O to form the methoxy derivative **11**. In the second step, 5-bromo-9-methoxy-1H-phenalen-1-one **11** was reacted with CuI and KI in DMSO to exchange the bromine atom with iodine. The overall yield to form HOp−I **5d** is ≈56% and to obtain tris-(5-iodo-1-oxo-1H-phenalen-9-olate)aluminum (Al(Op−I)$_3$) **6d** it is ≈45%.

Molecular structures of the halogenated ligands HOp−X (X= Cl, Br and I) **5b–d** are reported in literature [151, 152]. As an example, we have determined the molecular structure of HOp−Br **5c** by single crystal X-ray diffraction (see Figure 3.5). The structure of HOp−Br **5c** presents a plane of symmetry which is perpendicular to the plane of the molecule and splits the ligand
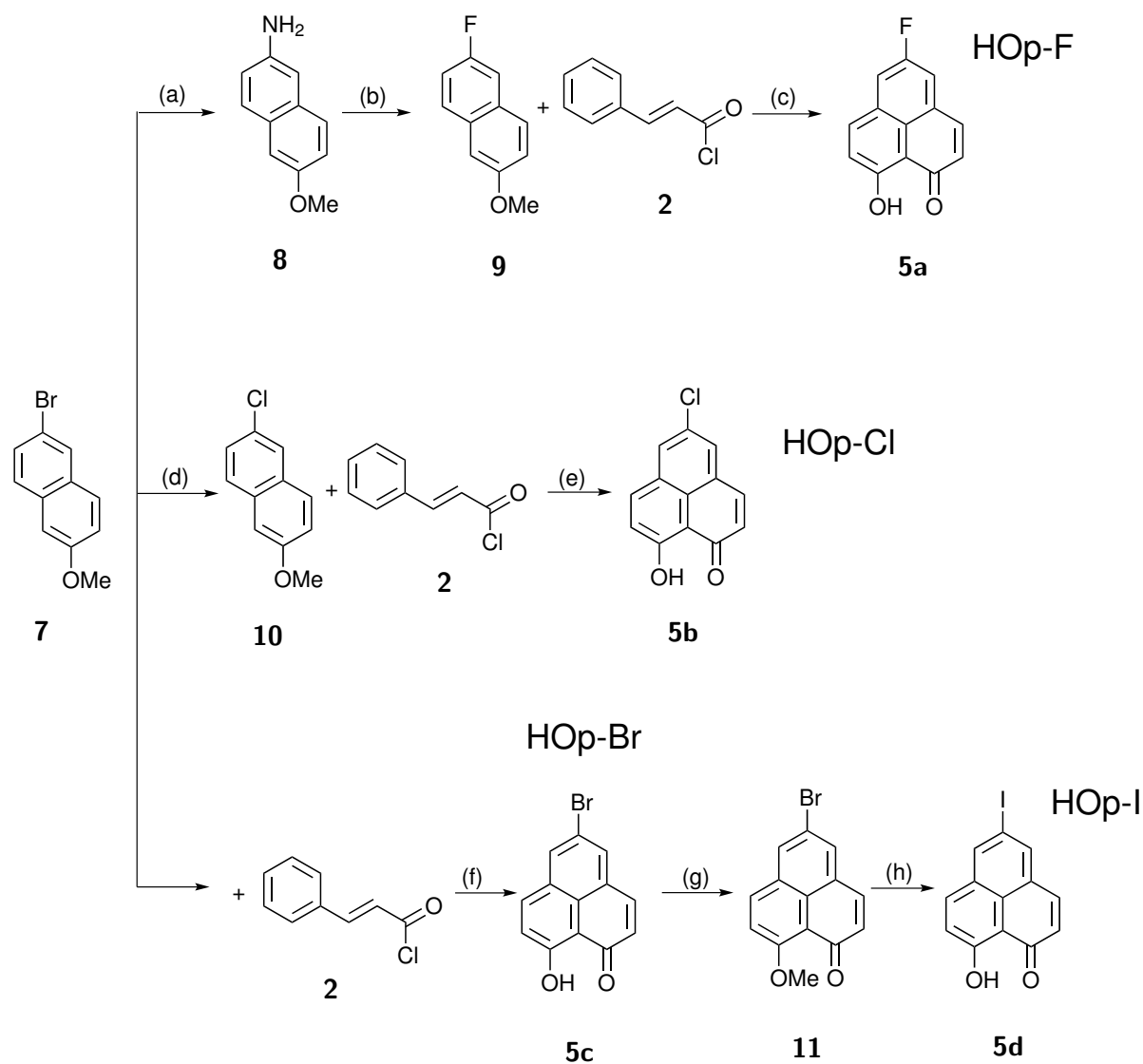
Scheme 3.3: Synthesis of the halogenated ligands HOp−X **5a**–**d**. (a) CuI, Na$_3$PO$_4$, PEG400/NH$_3$(28%), 100 °C, 24 h, yield: 40%. (b.1) HBF$_4$, NaNO$_2$, BF$_4$Na, THF, 0 °C, 1 h. (b.2) Chlorobenzene, reflux, 1 h, yield: 58%. (c) AlCl$_3$, DCE, reflux, overnight, yield: 63%. (d) CuCl, DMF, reflux, 48 h, yield: 85%. (e) AlCl$_3$, DCE, reflux, overnight, yield: 77%. (f) AlCl$_3$, DCE, reflux, overnight, yield: 87%. (g) Ag$_2$O, CH$_3$I, DCM, reflux, 3 h, yield: 96%. (h) CuI, KI, DMSO, reflux, 40 h, yield: 76%.

(a)   (b)   (c)

Figure 3.5: Molecular structure obtained by single crystal X-ray diffraction on a single crystal of HOp−Br **5c**. H-atoms and solvent molecules are omitted for clarity. The crystal refinement data is reported in Table C.3. The molecular packing in the single crystal of HOp−Br **5c** is illustrated in (a) yz (b) xz (c) xy perspective.

in two identical halves. In addition, the C-C bonds in HOp−Br **5c**, 1.351-1.434 Å, are almost identical to those in HOp **3** [149] (see Section 3.3.1). Lastly, the torsion angles are close to 0° and 180° indicating that HOp−Br **5c** is perfectly planar. This indicates that the structure of the phenalenyl ring is mostly unaffected by halogens in the 5 position.

At first, the halogenated ligands HOp−X **5a**–**d** were characterized by means of NMR spectroscopy. The ^{1}H-NMR spectra of the four ligands HOp−X **5a**–**d**, in the aromatic region, are illustrated and compared in Figure 3.6. The ligands are characterized by four resonances. The resonance of the hydrogen H9, which is out of the range of the figure, is fluctuating between 15.80 and 15.87 ppm, however, no clear dependence deriving from the halogen atom is observed. In contrast, the resonances corresponding to the aromatic hydrogens of the phenalenyl experience a considerable shift in relation to the halogen atom. As an example, the shift of the proton H4, which is in the vicinity of the halogen atom, is the most significant. It moves progressively from low to high chemical shift, beginning with the fluoro derivative towards the iodo derivative. In detail, for HOp−F **5a**, the chemical shift of H4 is 7.74 ppm, whereas for HOp−I **5d** it is 8.31 ppm. Due to the coupling between ^{1}H and ^{19}F, the resonance of H4 in HOp−F **5a** is a doublet [155]. Conversely, protons H1 and H2 move from high to low chemical shift going from HOp−F **5a** to HOp−I **5d**. However, the shifts of H1 and H2 are not as appreciable as the shift of H4. In detail, H1 and H2 of HOp−F **5a** are at 7.22 ppm and 8.05 ppm, respectively, whereas in HOp−I **5d** they are at 7.17 ppm and 7.99 ppm, respectively. The same trend is observed in the ^{1}H-NMR spectra of the complexes Al(Op−X)$_3$ **6a**–**d**. As a result, in the ^{1}H-NMR spectra of Al(Op−X)$_3$ **6a**–**d**, illustrated in Figure 3.7, the resonance corresponding to the proton H4 moves from low, 7.68 ppm for Al(Op−F)$_3$ **6a**, to high, 8.24 ppm for Al(Op−I)$_3$ **6d**, chemical shift. In contrast, the resonance of H1 moves from high, 7.17 ppm for Al(Op−F)$_3$ **6a**, to low, 7.11 ppm for Al(Op−I)$_3$ **6d**, chemical shift. Similarly, the resonance of H2 is at 7.96 ppm for Al(Op−F)$_3$ **6a** and at 7.91 ppm for Al(Op−I)$_3$ **6d**.
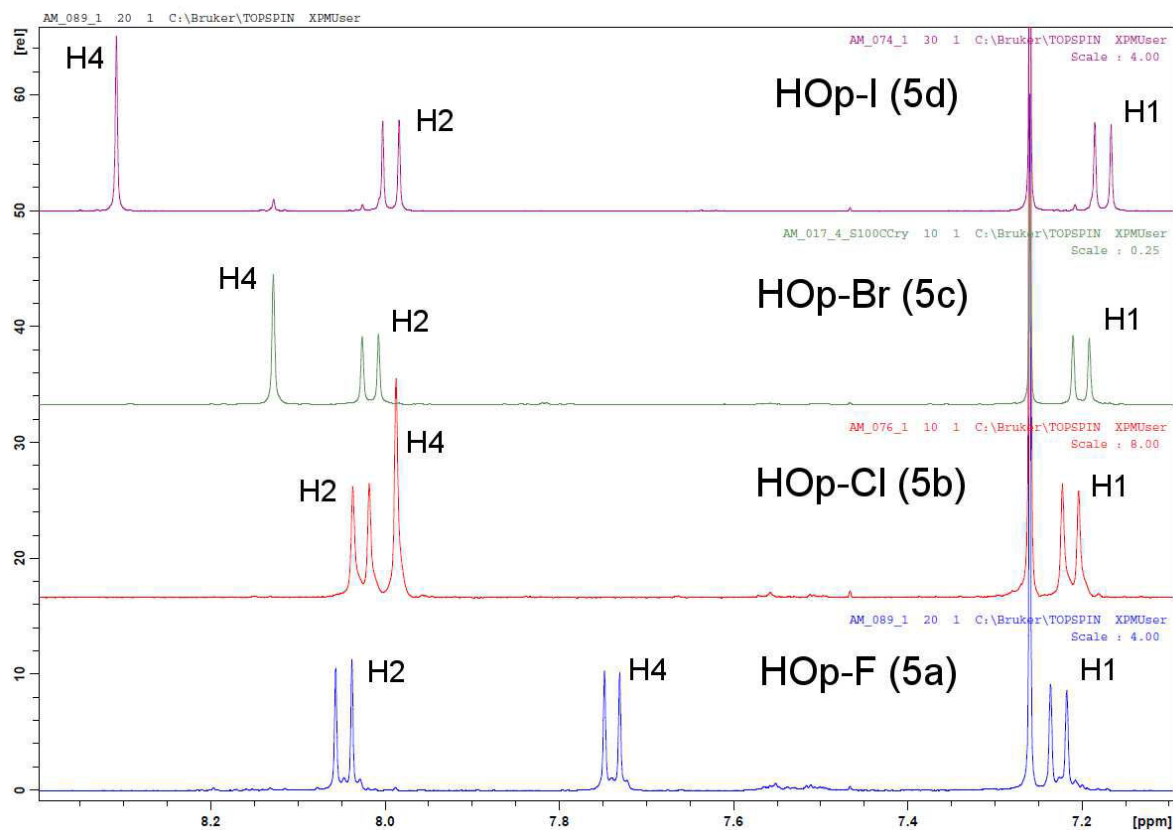
Compound	Resonances [ppm]			
	H1	H2	H4	H9
HOp−F **5a**	7.22	8.05	7.74	15.80
HOp−Cl **5b**	7.21	8.03	7.98	15.87
HOp−Br **5c**	7.20	8.02	8.13	15.83
HOp−I **5d**	7.17	7.99	8.31	15.85

Figure 3.6: ^{1}H-NMR spectra of the halogenated ligands HOp−X **5a**–**d** in CDCl$_3$. The resonances are marked accordingly to the numbering shown in Scheme 3.2.

Compound	Resonances [ppm]		
	H1	H2	H4
Al(Op−F)$_3$ **6a**	7.17	7.96	7.68
Al(Op−Cl)$_3$ **6b**	7.14	7.92	7.92
Al(Op−Br)$_3$ **6c**	7.13	7.93	8.06
Al(Op−I)$_3$ **6d**	7.11	7.91	8.24
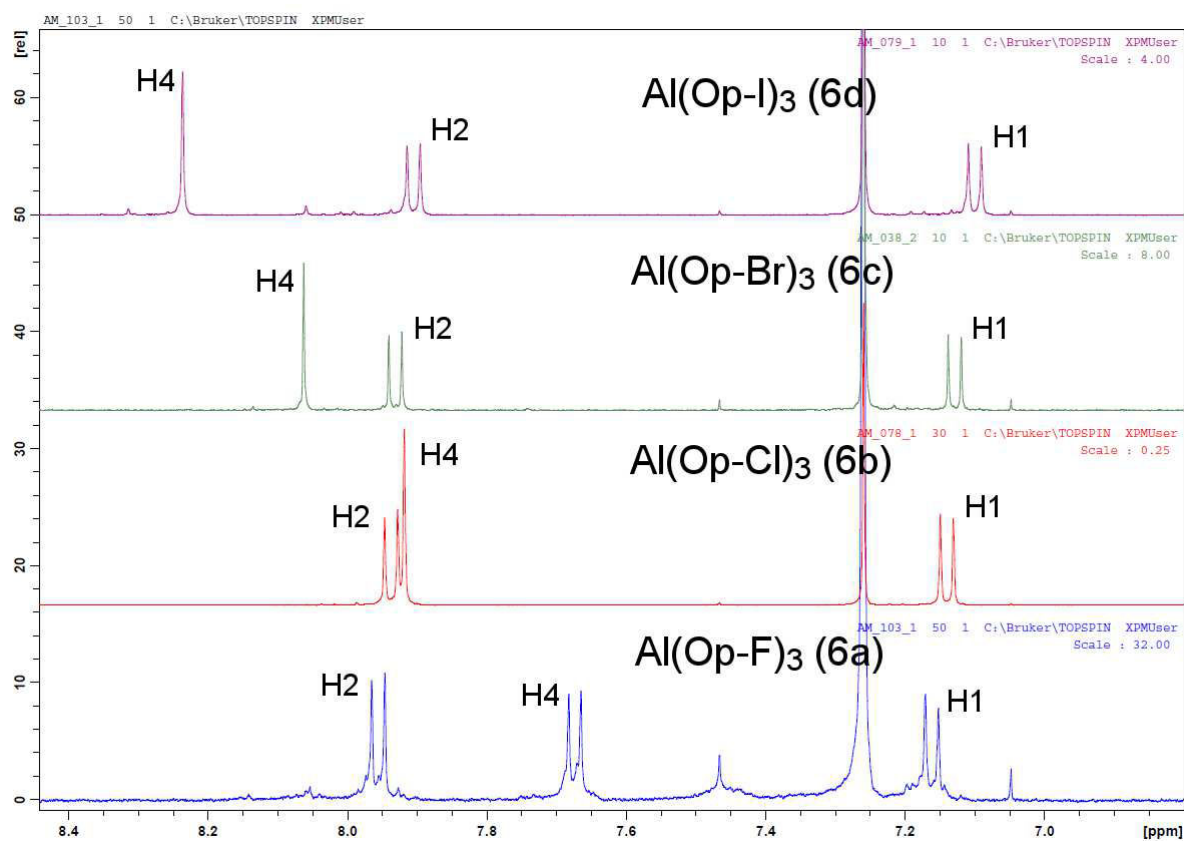
Figure 3.7: ^{1}H-NMR spectra of Al(Op−X)$_3$ **6a**–**d** in CDCl$_3$. The resonances are marked accordingly to the numbering shown in Scheme 3.2.
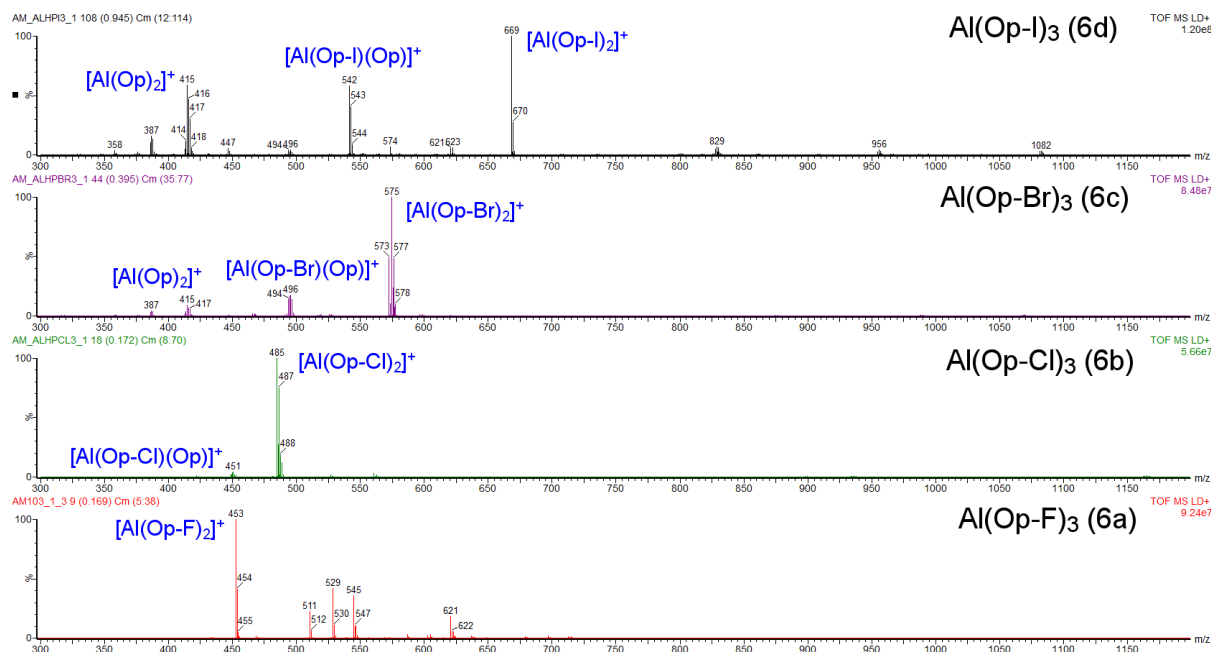
Figure 3.8: MALDI-TOF spectra of the halogenated complexes Al(Op−X)$_3$ **6a**–**d**. The fragments are marked in the figure.

The halogenated complexes Al(Op−X)$_3$ **6a**–**d** were additionally characterized by means of elemental analysis and MALDI-TOF spectrometry. Results of the carbon and hydrogen elemental analysis, listed in Table 3.3, are in fairly good agreement with the calculated values considering the adsorption of H$_2$O molecules. In detail, for Al(Op−F)$_3$ **6a** the experimental values are C= 63.97% and H= 3.53% and those calculated are C= 63.41% and H= 3.56%, for Al(Op−Cl)$_3$ **6b** the experimental values are C= 62.65% and H= 3.18% and those calculated are C= 62.29% and H= 2.96%, for Al(Op−Br)$_3$ **6c** the experimental values are C= 54.53% and H= 2.57% and those calculated are C= 54.01.41% and H= 2.33%, and for Al(Op−I)$_3$ **6d** the experimental values are C= 46.81% and H= 2.41% and those calculated are C= 46.46% and H= 2.00%. MALDI-TOF spectra of Al(Op−X)$_3$ **6a**–**d** are illustrated in Figure 3.8. In all spectra, the most intense peak is associated to the fragment [Al(Op−X)$_2$]$^+$, where the cation is formed by the cleavage of one ligand ([Al(Op−F)$_2$]$^+$ *m/z*= 453, [Al(Op−Cl)$_2$]$^+$ *m/z*= 486, [Al(Op−Br)$_2$]$^+$ *m/z*= 575 and [Al(Op−I)$_2$]$^+$ *m/z*= 669). As described in Section 3.3.1, this behavior is typical of neutral phenalenyl-based aluminum complexes. The spectrum of Al(Op−F)$_3$ **6a** presents a series of peaks at higher *m/z* which could not be assigned. Moreover, the spectra of Al(Op−Cl)$_3$, Al(Op−Br)$_3$ and Al(Op−I)$_3$ **6b**–**d** are characterized by a series of peaks at lower *m/z* corresponding to fragments in which halogens are eliminated during the MALDI process. As a result, the fragment [Al(Op−Cl)(Op)]$^+$ (*m/z*= 452) is detected in the spectrum of Al(Op−Cl)$_3$ **6b**, the fragments [Al(Op−Br)(Op)]$^+$ (*m/z*= 495) and [Al(Op)$_2$]$^+$ (*m/z*= 415) are revealed in the spectrum of Al(Op−Br)$_3$ **6c** and the fragments [Al(Op−I)(Op)]$^+$ (*m/z*= 542) and [Al(Op)$_2$]$^+$ (*m/z*= 415) are observed in the spectrum of Al(Op−I)$_3$ **6d**.

In conclusion, the formation of the halogenated complexes Al(Op−X)$_3$ **6a**–**d** is proved unambiguously by the structural characterization. However, we were unable to grow high quality single crystals suitable for single crystal X-ray diffraction. The most probable reason is that the halogen atom in the 5-position prevents the correct orientation of the molecules during the crystallization process.

3.3.3 5-Substituted Al(Op)$_3$: Al(Op−R)$_3$ (16a-c)
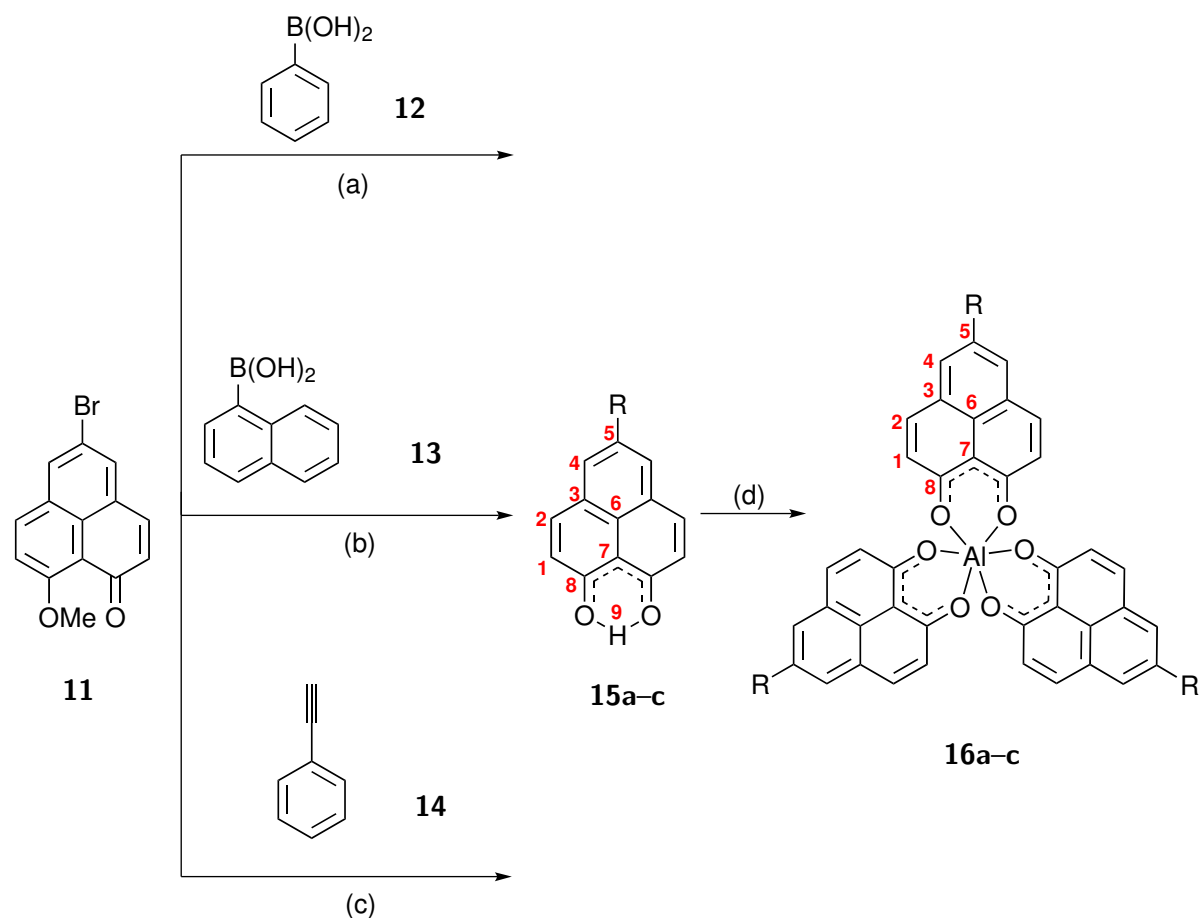
Ref.	Name	Ref.	Name	R
15a	HOp−p	**16a**	Al(Op−p)$_3$	Phenyl
15b	HOp−n	**16b**	Al(Op−n)$_3$	Naphtalen
15c	HOp−pe	**16c**	Al(Op−pe)$_3$	Phenylethynyl

Scheme 3.4: Synthesis of the substituted ligands HOp−R **15a**–**c** and complexes Al(Op−R)$_3$ **16a**–**c**. (a.1) CsF, Pd(PPh$_3$)$_4$, DME, reflux, overnight. (a.2) BBr$_3$, DCM, reflux, overnight, yield: 51%. (b.1) CsF, Pd(PPh$_3$)$_4$, DME, reflux, overnight. (b.2) BBr$_3$, DCM, reflux, overnight, yield: 53%. (c.1) CuI, Pd(PPh$_3$)$_2$Cl$_2$, PPh$_3$, THF/Et$_3$N (2:3), reflux, 48 h. (c.2) BBr$_3$, DCM, reflux, overnight, yield: 36%. (d) AlCl$_3$, toluene, reflux, yields: Al(Op−p)$_3$ **16a** 86%, Al(Op−n)$_3$ **16b** 67%, Al(Op−pe)$_3$ **16c** 83%.

A series of novel ligands and aluminum complexes was synthesized by exchanging the hydrogen in the 5-position with aromatic functionalities. 2-Methyl- and 5-methyl-HOp were previously synthesized and characterized. However, the effect on the absorption spectra was negligible [135]. As a consequence, we have implemented bulky aromatic molecules aiming to significantly modify the electronic properties of Al(Op)$_3$ **4**. The procedures to obtain the substituted ligands HOp−R **15a**–**c** and complexes Al(Op−R)$_3$ **16a**–**c** are detailed in Scheme 3.4. The synthesis of the three substituted ligands HOp−R **15a**–**c** takes place starting from the methoxy derivative **11** by coupling reactions with phenyl boronic acid **12**, naphthalen boronic

acid **13** and ethynylbenzene **14**. The hydrolysis of the methoxy group is efficiently carried out with BBr$_3$. Although this strategy involves two steps more than direct coupling with HOp−Br **5c**, overall yields and purities were higher. To form the substituted complexes Al(Op−R)$_3$ **16a**–**c**, the ligands HOp−R **15a**–**c** were reacted with AlCl$_3$. In more detail, starting from 2-bromo-6-methoxynaphthalene **7**, the overall yield of the synthesis of 9-hydroxy-5-phenyl-1H-phenalen-1-one (HOp−p) **15a** is ≈38% and tris-(1-oxo-5-phenyl-1H-phenalen-9-olate)aluminum (Al(Op−p)$_3$) **16a** was obtained with a yield of ≈32%. The yield to form (9-hydroxy-5-(naphthalen-1-yl)-1H-phenalen-1-one (HOp−n) **15b** is ≈39% and to form tris-(5-(naphthalen-1-yl)-1-oxo-1H-phenalen-9-olate)aluminum (Al(Op−n)$_3$) **16b** it is ≈26%. At last, the yield of the synthesis of 9-hydroxy-5-(phenylethynyl)-1H-phenalen-1-one (HOp−pe) **15c** is ≈26% and tris-(1-oxo-5-(phenylethynyl)-1H-phenalen-9-olate)aluminum (Al(Op−pe)$_3$) **16c** is obtained with a yield of ≈22%.

(a)   (b)   (c)
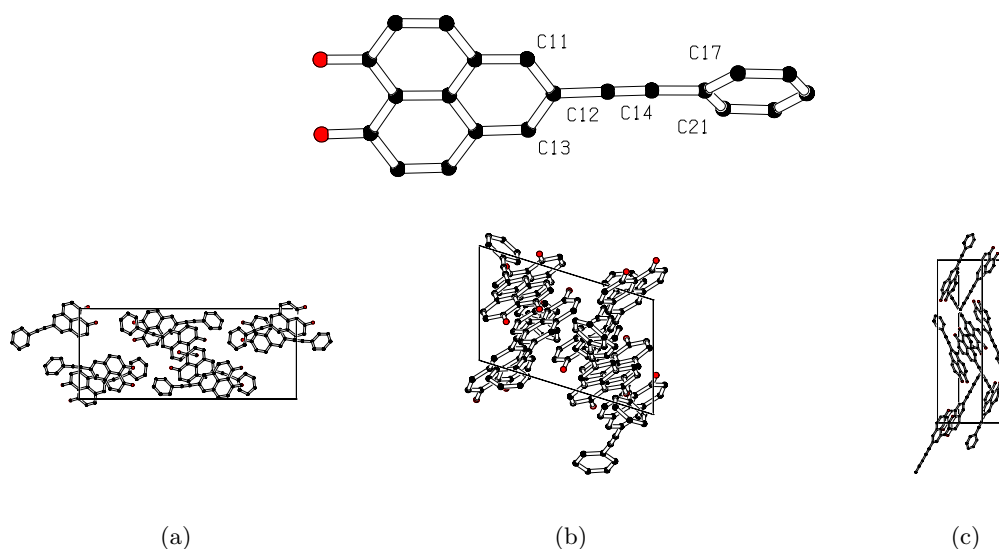
Figure 3.9: Molecular structure obtained by single crystal X-ray diffraction on a single crystal of HOp−pe **15c**. H-atoms and solvent molecules are omitted for clarity. The crystal refinement data is reported in Table C.4. The molecular packing in the single crystal of HOp−pe **15c** is illustrated in (a) yz (b) xz (c) xy perspective.

Due to the presence of bulky substituents, which prevents the correct orientation of the phenalenyl ligands, we were unable to grow high quality single crystals of the substituted complexes Al(Op−R)$_3$ **16a**–**c** for single crystal X-ray diffraction. However, we have grown single crystals of the ligand HOp−pe **15c** to investigate the effect of the ethynyl bridge on the electronic coupling between the phenalenyl core and the phenyl substituent. The molecular structure obtained by single crystal X-ray diffraction is illustrated in Figure 3.9. Obviously the phenalenyl and the phenyl rings are misaligned with torsion angles C11-C12-C14-C17 of 27.34° and C11-C12-C14-C17 of −149.70°. Additionally, C-C bond lengths in the phenalenyl moiety of HOp−pe **15c**, between 1.352 and 1.435 Å, are almost identical to C-C bond lengths in HOp **3** [149]. In conclusion, the electronic coupling between the phenalenyl core and the phenyl ring can be excluded.

The substituted ligands HOp−R **15a**–**c** were characterized by NMR spectroscopy. ^{1}H-NMR spectra of the three ligands are illustrated and compared in Figure 3.10. It can be seen that the three spectra are characterized by two sets of resonances: one corresponding to the aromatic substituent (not marked in Figure 3.10) and one belonging to the phenalenyl (marked in Fig-
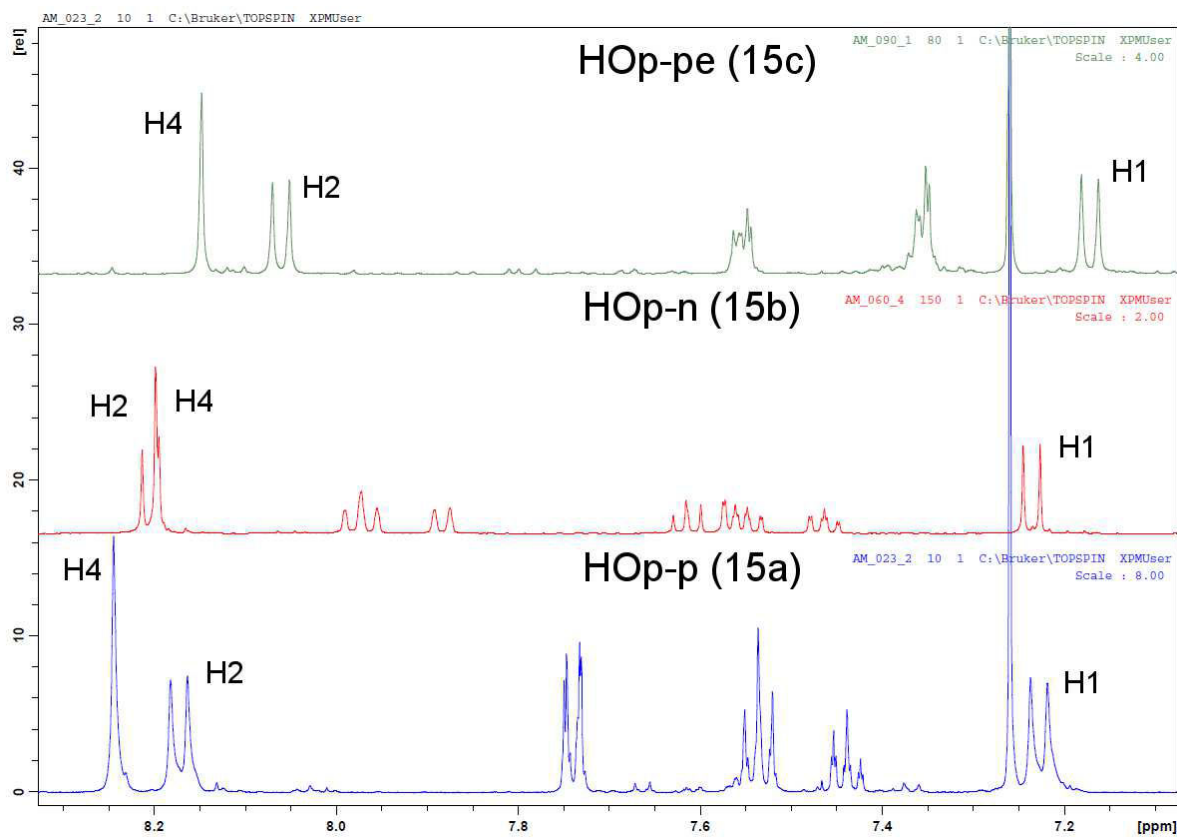
Compound	Resonances [ppm]			
	H1	H2	H4	H9
HOp−p **15a**	7.22	8.17	8.25	15.98
HOp−n **15b**	7.24	8.21	8.21	16.03
HOp−pe **15c**	7.17	8.06	8.15	15.91

Figure 3.10: ^{1}H-NMR spectra of the substituted ligands HOp−R **15a**–**c** in CDCl$_3$. The resonances are marked accordingly to the numbering shown in Scheme 3.4.
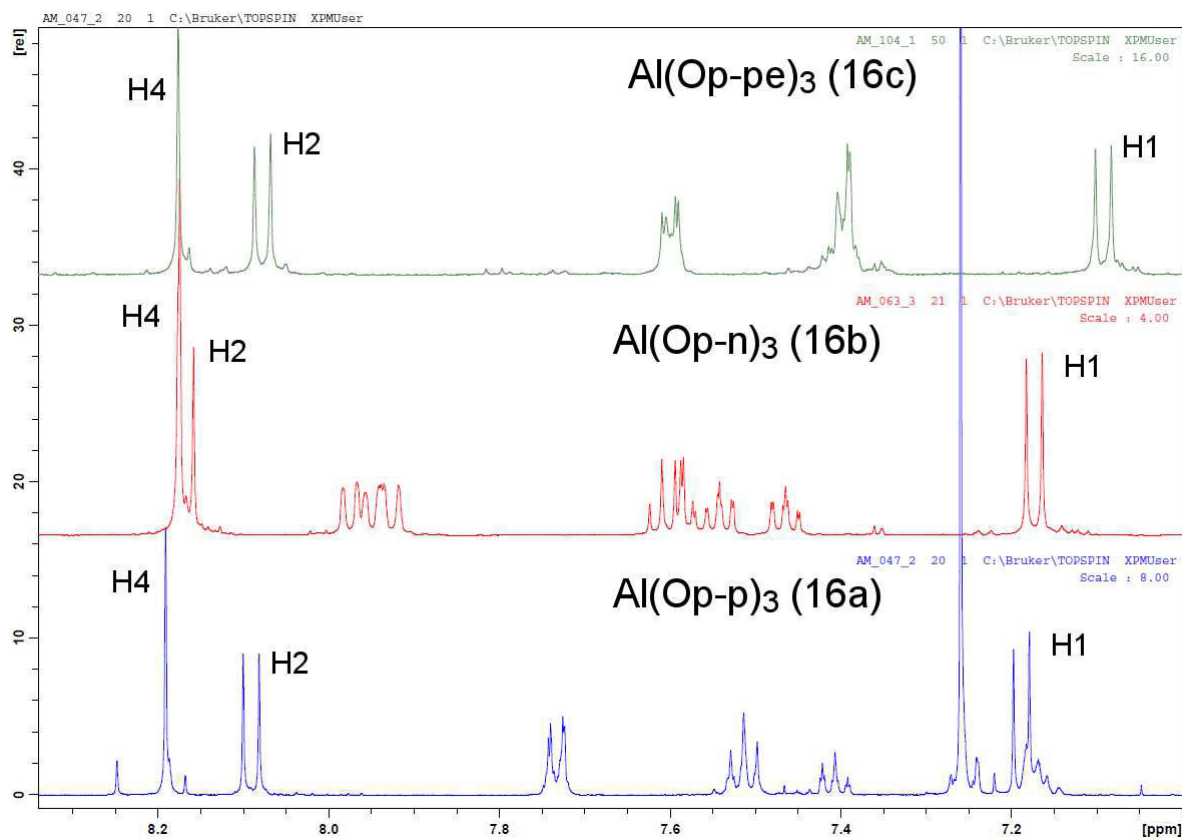
Compound	Resonances [ppm]		
	H1	H2	H4
Al(Op−p)$_3$ **16a**	7.18	8.08	8.17
Al(Op−n)$_3$ **6b**	7.17	8.17	8.17
Al(Op−pe)$_3$ **6c**	7.09	8.08	8.18

Figure 3.11: ^{1}H-NMR spectra of the substituted complexes Al(Op−R)$_3$ **16a**–**c** in CDCl$_3$. The resonances are marked accordingly to the numbering shown in Scheme 3.4.

ure 3.10). The resonances of the aromatic substituents result from their structure, and thus, they are different from each other. On the other hand, the phenalenyl, despite the substitution, gives rise to the same set of resonances. The first peak, relative to H9 (out of the range of Figure 3.10), has similar chemical shifts for all the substituted ligands HOp−R **15a**–**c**, between 15.91 and 16.03 ppm. Resonances corresponding to the hydrogen atoms of the phenalenyl moiety shift in relation with the different substituents. For instance, hydrogen H4, which is in the α position in respect to the substituent, has a chemical shift of 8.25 ppm in HOp−p **15a**, 8.21 ppm in HOp−n **15b**, and 8.15 ppm in HOp−pe **15c**. Moreover, the chemical shift of H1 and H2 are almost identical for HOp−p **15a** and HOp−n **15b**, $\approx$7.23 ppm and $\approx$8.20 ppm, respectively, whereas for HOp−pe **15c** are shifted to 7.17 ppm and 8.06 ppm, respectively. The same resonances, recorded for the ligands HOp−R **15a**–**c**, are observed in the ^{1}H-NMR spectra of the substituted complexes Al(Op−R)$_3$ **16a**–**c** illustrated in Figure 3.11. Interestingly, the resonance of H4 is almost identical for the three complexes, $\approx$8.17 ppm. In addition, the resonance of H1 is similar for Al(Op−p)$_3$ **16a** and Al(Op−n)$_3$ **16b**, $\approx$7.17 ppm, and it is shifted to 7.09 ppm for Al(Op−pe)$_3$ **16c**. In contradiction, the resonance of H2 is comparable for Al(Op−p)$_3$ **16a** and Al(Op−pe)$_3$ **16c**, $\approx$8.08 ppm, and shifted to 8.17 ppm for Al(Op−n)$_3$ **16b**.
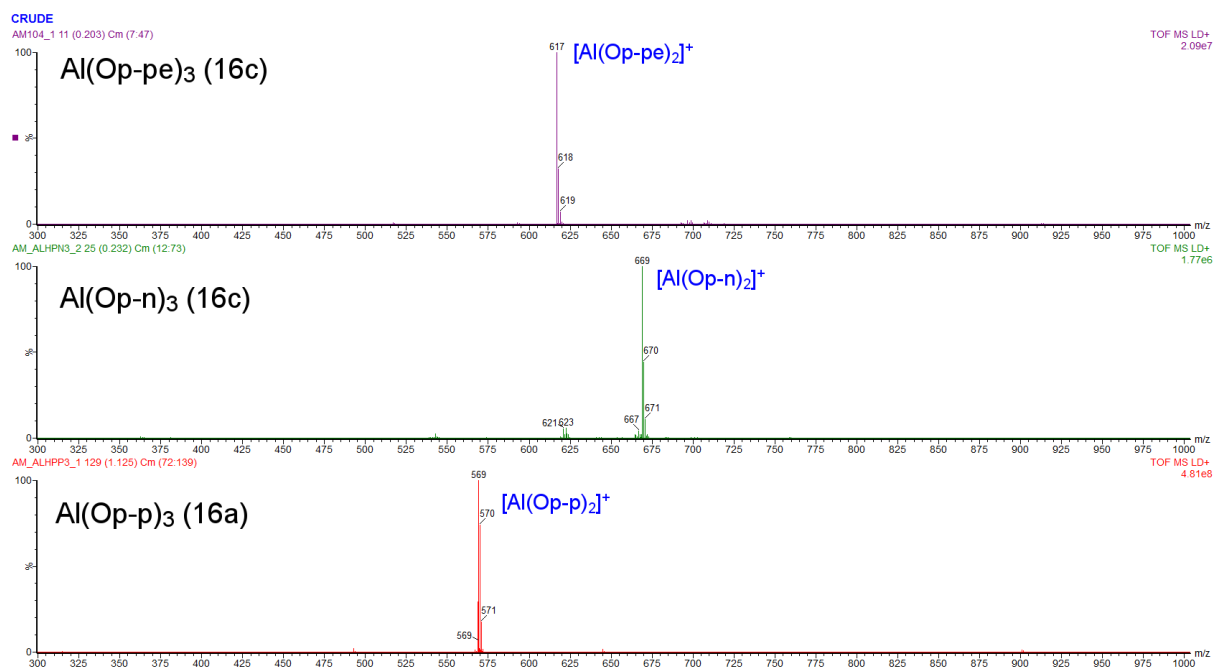
Figure 3.12: MALDI-TOF spectra of Al(Op−R)$_3$ **16a**–**c**. The main fragments are marked in the figure.

The substituted complexes Al(Op−R)$_3$ **16a**–**c** have been further characterized by means of elemental analysis and MALDI-TOF spectrometry. The results of the carbon and hydrogen elemental analysis, listed in Table 3.3, are in fairly good agreement with the calculated values considering the adsorption of additional H$_2$O molecules. In detail, for Al(Op−p)$_3$ **16a** the experimental values are C= 76.58% and H= 4.36% and those calculated are C= 76.49% and H= 4.40%, for Al(Op−n)$_3$ **16b** the experimental values are C= 76.54% and H= 4.60% and those calculated are C= 76.65% and H= 4.58% and for Al(Op−pe)$_3$ **16c** the experimental values are C= 76.43% and H= 5.79% and those calculated are C= 76.81% and H= 4.20%. In the MALDI-TOF spectra of the complexes Al(Op−R)$_3$ **16a**–**c**, illustrated in Figure 3.12, only peaks corresponding to the fragments [Al(Op−R)$_2$]$^+$ are detected. Clearly, to form the cation one ligand is eliminated ([Al(Op−p)$_2$]$^+$ *m/z*= 569, [Al(Op−n)$_2$]$^+$ *m/z*= 669 and [Al(Op−pe)$_2$]$^+$

$m/z= 617$), as previously described for Al(Op)$_3$ **4** (see Section 3.3.1). Despite the lack of single crystal X-ray diffraction experiments, the formation of the substituted complexes Al(Op−R)$_3$ **16a**–**c** is unambiguously proved by the structural characterization.

3.3.4   Tris-(7-oxo-7H-benzo(de)anthracen-6-olate)aluminum (Al(Oba)$_3$) (19)
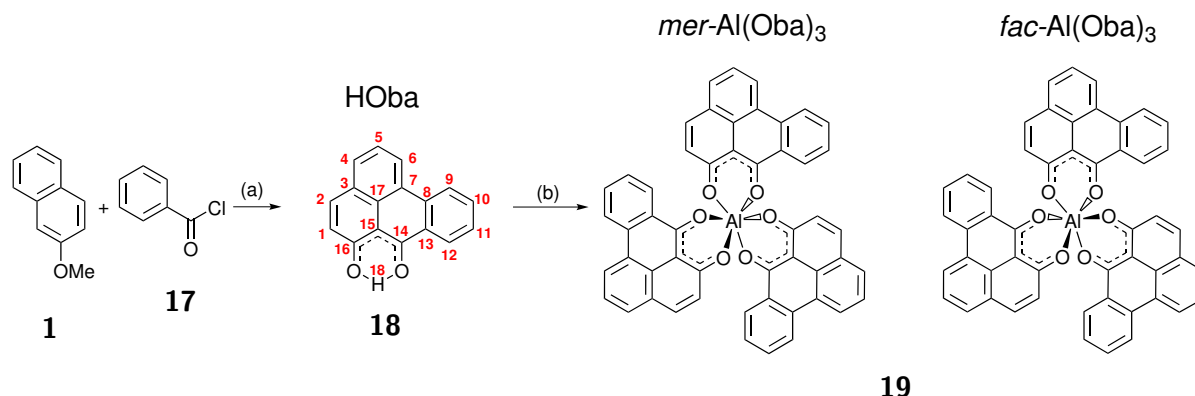
Scheme 3.5: Synthesis of Al(Oba)$_3$ **19**. (a) AlCl$_3$, DCB, 120 °C, 48 h, yield: 61%. (b) AlCl$_3$, toluene, reflux, overnight, yield: 86%. The *mer*-Al(Oba)$_3$ and *fac*-Al(Oba)$_3$ isomers are schematically depicted.

The first strategy implemented to significantly modify the electronic properties of Al(Op)$_3$ **4** was to break the symmetry of HOp **3** adding a benzene ring to form 6-hydroxy-7H-benzo[de]anthracen-7-one (HOba) **18**. Proton transfer properties of asymmetrical extensions of HOp **3**, including HOba **18**, were previously studied by Haddon *et al.* [156]. In addition, the aluminum complex Al(Oba)$_3$ **19** has been previously synthesized and studied in OLEDs for commercial applications [136]. The synthetic procedure to form Al(Oba)$_3$ **19** is illustrated in Scheme 3.5. 2-Methoxynaphthalene **1** and benzoyl chloride **17** were reacted to obtain HOba **18** with a yield of ≈61%. The ligand was mixed with AlCl$_3$ to form Al(Oba)$_3$ **19**. The overall yield to obtain Al(Oba)$_3$ **19** is ≈52%.

Despite the asymmetric nature of the ligand HOba **18**, the resonance of H18 in its ^{1}H-NMR spectrum (see Figure B.43) is at 15.87 ppm, which is similar to that of H9 in HOp **3** (see Section 3.3.1). This indicates that H18 is involved in a fast proton transfer between the two oxygens at room temperature. In the spectrum, resonances relative to the aromatic hydrogens are between 7.37 and 8.37 ppm. Due to the asymmetric nature of HOba **18**, Al(Oba)$_3$ **19** can form two different geometrical configurations, *mer*-Al(Oba)$_3$ and *fac*-Al(Oba)$_3$, which are schematically illustrated in Scheme 3.5. The purification of one isomer by separation methods was impossible, and thus, we were unable to grow high quality single crystals for single crystal X-ray diffraction. Moreover, was impossible to record clear NMR spectra of Al(Oba)$_3$ **19**. However, the carbon and proton content measured by elemental analysis, C= 76.48% and H= 5.05%, is in a fairly good agreement with the calculated values, C= 76.68% and H= 3.92% (see Table 3.3). In addition, the MALDI-TOF spectrum, illustrated in Figure 3.15, is characterized by a single peak corresponding to the fragment [Al(Oba)$_2$]$^+$. We can assume the formation of Al(Oba)$_3$ **19** is unambiguously proved.
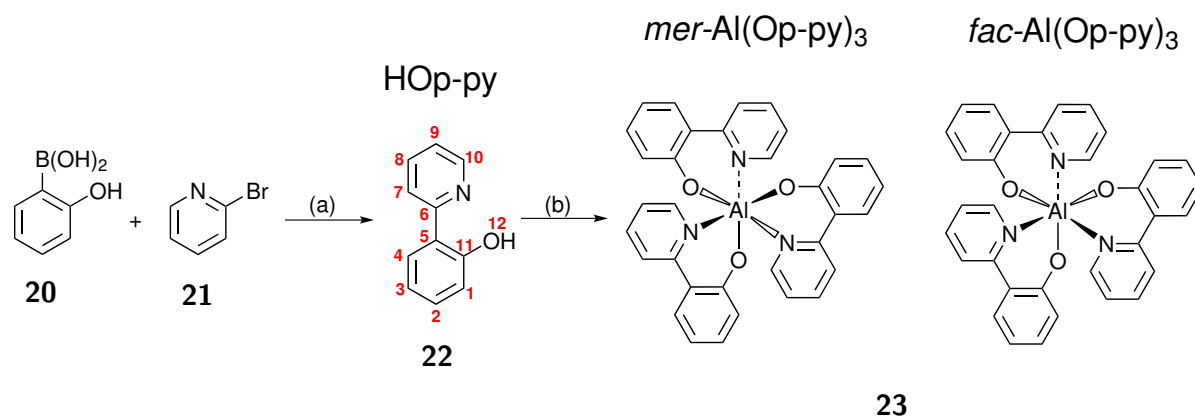
Scheme 3.6: Synthesis of $Al(Op-py)_3$ **23**. (a) $Pd(PPh_3)_4$, toluene/ethanol/K_2CO_3 (2 M) in H_2O, reflux, overnight, yield: 68%. (b) $Al(CH_3)_3$, THF, room temperature, 120 h, yield: 73%. The *mer*-$Al(Op-py)_3$ and *fac*-$Al(Op-py)_3$ are schematically depicted.

3.3.5 Tris-(2-(pyridin-2-yl)phenolate)aluminum ($Al(Op-py)_3$) (23)

The ligand 2-(pyridin-2-yl)phenol (HOp−py) **22** was selected due to its similarity to Hq. In can be considered as an extension of Hq where the two chelating atoms (nitrogen and oxygen) are inserted in two separated aromatic rings. HOp−py **22** was previously studied to investigate the intramolecular proton transfer in excited state by Basaric *et al.* [157]. Moreover, in an earlier work, the ligand HOp−py **22** was used to form lithium derivatives to be implemented as electron injection layers in OLEDs [158]. HOp−py **22** is obtained by a coupling reaction between 2-hydroxybenzenboronic acid **20** and 2-bromopyridine **21** with a yield of ≈68%. To form the aluminum complex, we reacted HOp−py **22** with $Al(CH_3)_3$, which was formerly used to obtain complexes with similar ligands [159, 160]. The overall yield of the synthesis of $Al(Op-py)_3$ **23** is ≈50%.

HOp-py **22** is characterized by a strong intramolecular hydrogen bond involving H12 (according to Scheme 3.6), and thus, in ^{1}H-NMR, its resonance is at 14.36 ppm (see Figure B.46). Additionally, resonances of aromatic hydrogens are between 6.90 and 8.42 ppm. Since HOp-py **22** is asymmetric, as Alq$_3$ (see Section 1.2), $Al(Op-py)_3$ **23** can occur in two geometrical isomers, *mer*-$Al(Op-py)_3$ and *fac*-$Al(Op-py)_3$. However, as described for Alq$_3$, and reported for HOp-py **22** complexes with trivalent metals [161–163], the *mer*-isomer is normally formed. Hence, we have assumed that *mer*-$Al(Op-py)_3$ is the predominant species. The solubility of *mer*-$Al(Op-py)_3$ in all the common solvents is too low to run solution-based characterization methods. Nonetheless, by both ESI-TOF measurements on the crude reaction (see Figure B.48) and MALDI-TOF measurements on the precipitate (see Figure 3.15), the fragment corresponding to the cation $[Al(Op-py)_2]^+$ was detected, and thus, we can assume the formation of $Al(Op-py)_3$ **23**. Furthermore, the carbon, hydrogen and nitrogen content measured by elemental analysis, C= 67.48%, H= 4.59% and N= 7.13%, is in a good agreement with the expected values for $Al(Op-py)_3$ **23**, C= 67.00%, H= 5.12% and N= 7.10% (see Table 3.3).

3.3.6 Tris-(7-oxocyclohepta-1,3,5-trienolate)aluminum ($Al(Trop)_3$) (25)

2-Hydroxycyclohepta-2,4,6-trien-1-one (tropolone) **24** was selected due to its structural analogy with HOp **3**. Similarly to HOp **3**, the chelating atoms of tropolone **24** are two oxygen atoms. On the contrary, the backbone of tropolone **24** is formed by a single seven-membered aromatic
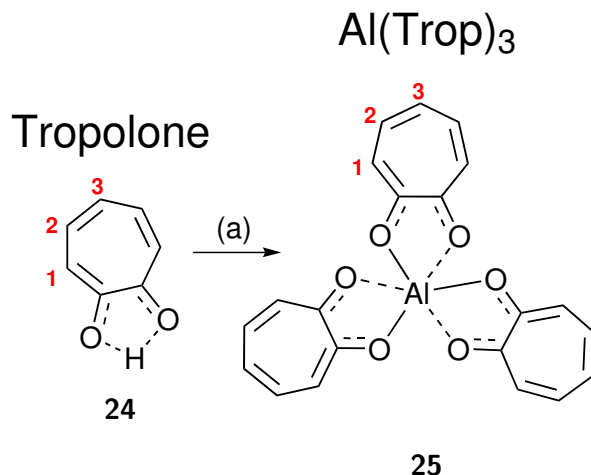
Scheme 3.7: Al(Trop)$_3$ **25**. (a) AlCl$_3$, toluene, reflux, overnight, yield: 83%.

ring. In a previous work by Ozeki *et al.*, tropolone **24** and HOp **3** were investigated to study how the aromatic structure influences the proton transfer between the two oxygen atoms [138]. In contrast to HOp **3**, which is planar [149], the aromatic ring of tropolone **24** deforms from planarity to a boat configuration of about 2° [164]. These differences are expected to significantly influence the electronic properties of Al(Trop)$_3$ **25** in comparison to Al(Op)$_3$ **4**. Al(Trop)$_3$ **25** was obtained with a yield of ≈83% by reacting tropolone **24** with AlCl$_3$. Single crystals were grown and the structure was confirmed by comparing the cell parameters obtained by single crystal X-ray diffraction with those reported in literature [165].

Molecular structure, crystal packing and selected bond lengths and angles of Al(Trop)$_3$ **25**, obtained by single crystal X-ray diffraction, are illustrated in Figure 3.13. It can be seen that the molecular structure of Al(Trop)$_3$ **25** is symmetrical, and thus, Al-O bond lengths and O-Al-O bond angles are repeating themselves. In detail, the oxygens of the top ring (O1 and O1a) are equidistant from the aluminum (1.8841 Å), indicating a plane of symmetry cutting in half the tropolonate. In contrast, the other two tropolonates are symmetrical in respect of each other, and thus, the bond lengths Al-O2 and Al-O2a (1.8894 Å) are identical as well as the bond lengths Al-O3 and Al-O3a (1.8886 Å). In the same manner, the bond angles O1-Al-O2 and O1a-Al-O2a (89.08°), O1-Al-O2a and O1a-Al-O2 (96.50°), O1-Al-O3a and O1a-Al-O3 (91.87°), O1-Al-O3 and O1a-Al-O3a (169.29°), O2-Al-O3 and O2a-Al-O3a (82.19°), and O2-Al-O3a and O2a-Al-O3 (92.75°) are equivalent. As demonstrated by the bond angles, which are 82.19-96.50° and 169.29-172.57°, the six chelating oxygens in Al(Trop)$_3$ **25** are arranged in a distorted octahedral geometry due to the narrow bite angle of tropolone **24**. Moreover, the Al-O bond lengths, between 1.8841 and 1.8894 Å, are, in average, slightly longer than those of Al(Op)$_3$ **4** (see Section 3.3.1). At last, the boat configuration of tropolone **24** is preserved in Al(Trop)$_3$ **25** with a deformation of about 3.35-3.70°. Despite the boat configuration assumed by the ligands, the $\pi - \pi$ stacking between the aromatic systems seems to drive the orientation of the molecules in the crystal lattice.

The ^{1}H-NMR spectra of tropolone **24** and Al(Trop)$_3$ **25**, illustrated in Figure 3.14, show three resonances corresponding to the aromatic protons of tropolone **24** and of Al(Trop)$_3$ **25**. Most probably, as a result of the boat configuration of tropolone, which breaks the symmetry, the resonances are slightly broadened. Due to the coordination of aluminum, the resonances of Al(Trop)$_3$ **25** are slightly shifted compared to those of tropolone **24**. However, for tropolone

(a)   (b)   (c)
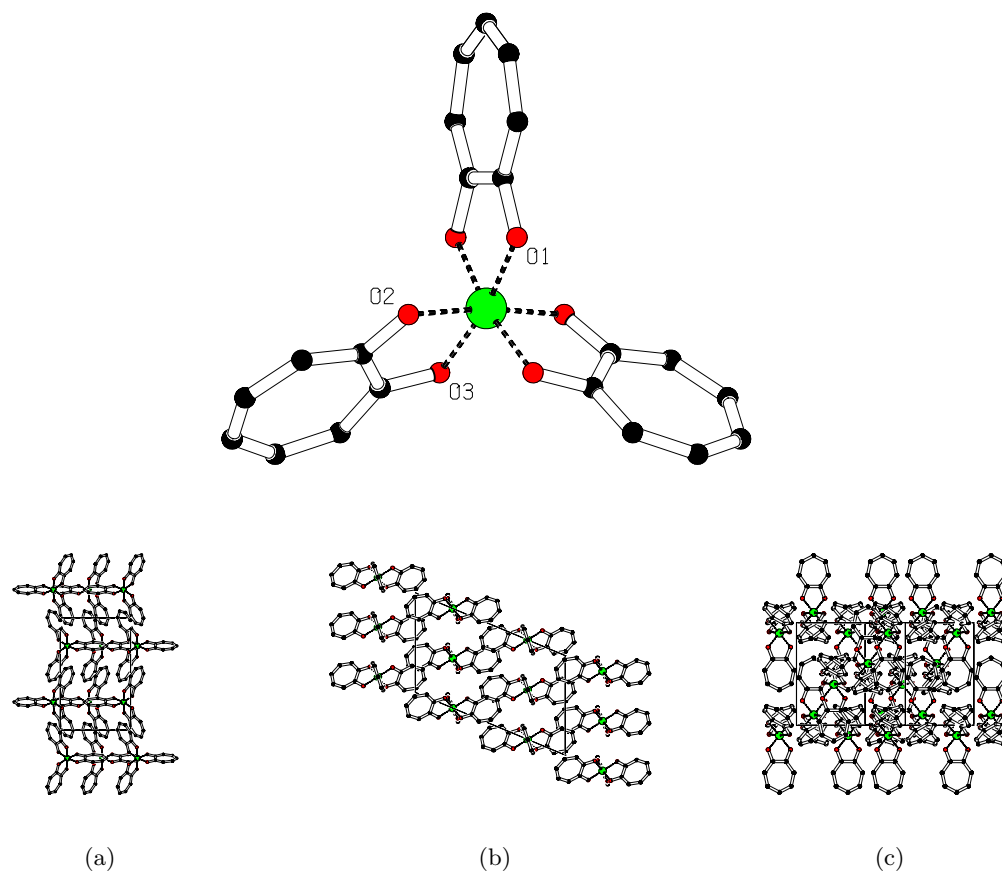
Bond	Length [Å]	Bond angle	Angle [°]	Bond angle	Angle [°]
		Al(Trop)$_3$ **25**			
Al1-O1	1.8841	O1-Al1-O1a	82.92	O1a-Al1-O3a	169.29
Al1-O1a	1.8841	O1-Al1-O2	89.08	O2-Al1-O2a	172.57
Al1-O2	1.8894	O1-Al1-O2a	96.50	O2-Al1-O3	82.19
Al1-O2a	1.8894	O1-Al1-O3	169.29	O2-Al1-O3a	92.75
Al1-O3	1.8886	O1-Al1-O3a	91.87	O2a-Al1-O3	92.75
Al1-O3a	1.8886	O1a-Al1-O2	96.50	O2a-Al1-O3a	82.19
		O1a-Al1-O2a	89.08	O3-Al1-O3a	94.73
		O1a-Al1-O3	91.87		

Figure 3.13: Molecular structure obtained by single crystal X-ray diffraction on a single crystal of Al(Trop)$_3$ **25** [165]. H-atoms and solvent molecules are omitted for clarity. The molecular packing in the single crystal of Al(Trop)$_3$ **25** is illustrated in (a) yz (b) xz (c) xy perspective. Table: selected bond distances and angles for Al(Trop)$_3$ **25**.

60

Figure 3.14: ^{1}H-NMR spectra of tropolone **24** (blue) and Al(Trop)$_3$ **25** in CDCl$_3$. The resonances are marked accordingly to the numbering shown in Scheme 3.7.
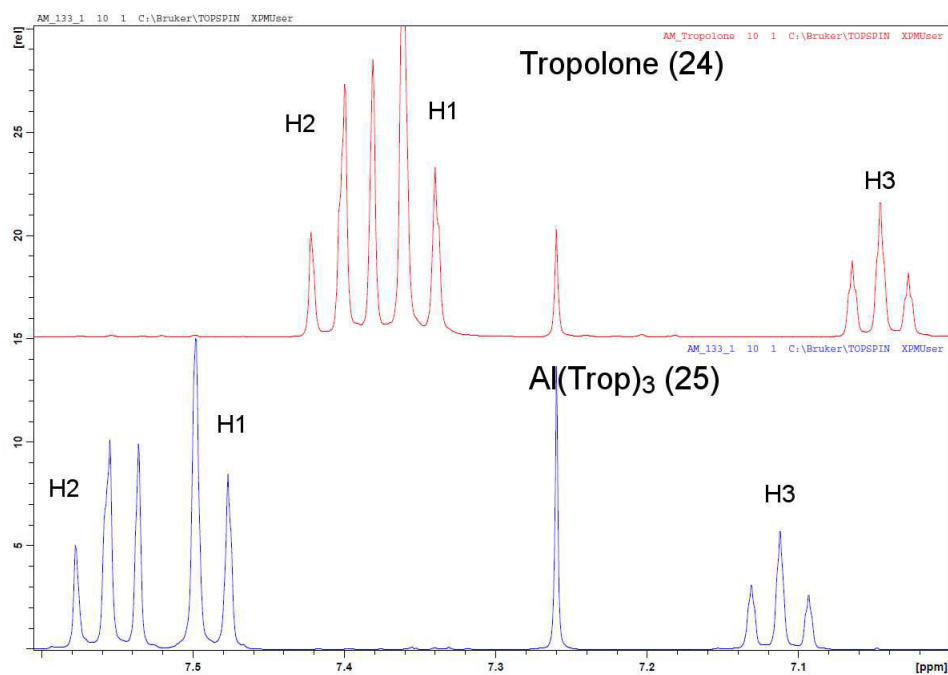
Compound	Resonances [ppm]		
	H1	H2	H3
Tropolone **24**	7.35	7.40	7.05
Al(Trop)$_3$ **25**	7.49	7.55	7.11
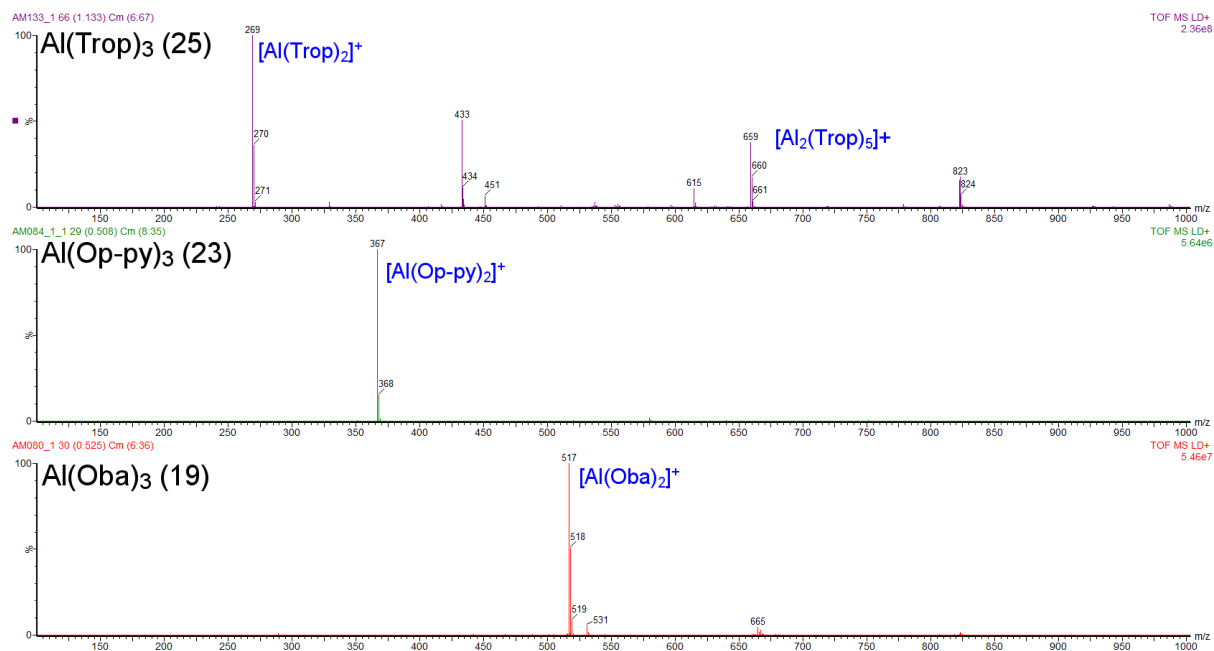
Figure 3.15: MALDI-TOF spectra of Al(Oba)$_3$ **19**, Al(Op−py)$_3$ **23** and Al(Trop)$_3$ **25**. The main fragments are marked in the figure.

61

24 no resonance relative to the proton between the two oxygen was recorded. Carbon and hydrogen content measured by elemental analysis, C= 64.57% and H= 3.83%, matches the calculated one, C= 64.61% and H= 3.88% (see Table 3.3). At last, the MALDI-TOF spectrum, shown in Figure 3.15, is characterized by a series of peaks. The most intense peak corresponds to the fragment $[Al(Trop)_2]^+$ ($m/z= 269$). Additionally, the binuclear fragment $[Al_2(Trop)_5]^+$ ($m/z= 659$), most probably produced during the MALDI process, was identified.

3.3.7 Bis-(quinolin-8-olate)-4-oxopent-2-en-2-olate aluminum (Al(q₂Acac) (28)
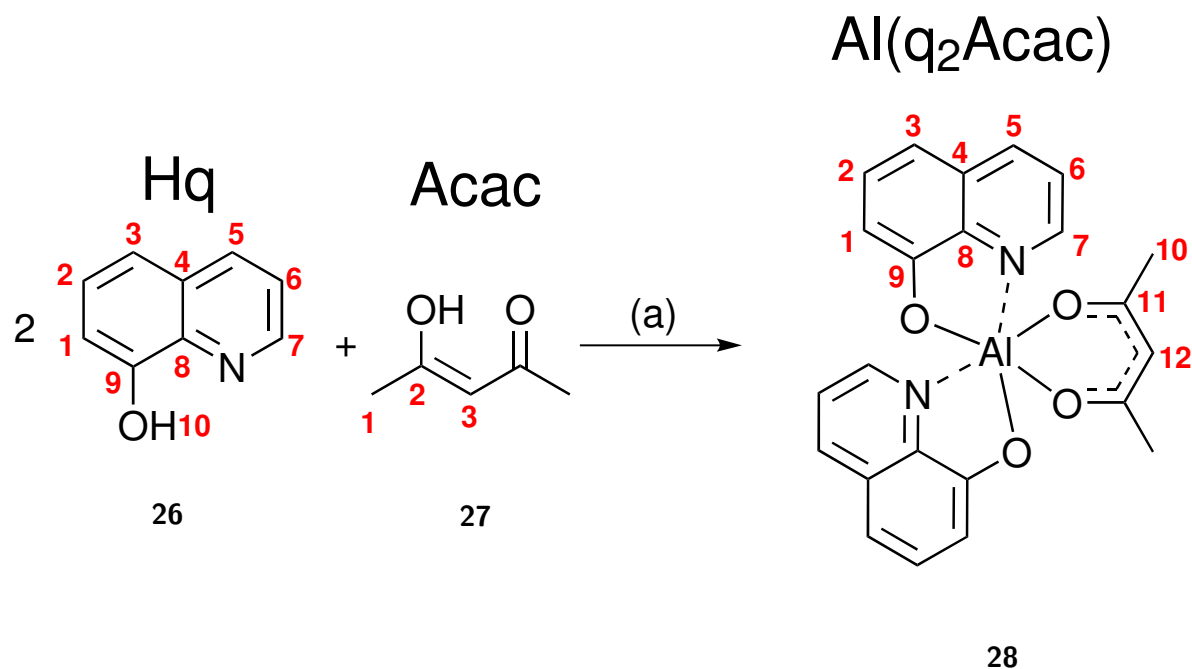
Scheme 3.8: Synthesis of Al(q₂Acac) **28**. (a) $Al(CH_3)_3$, toluene, room temperature, overnight, yield: 71%.

In order to further understand the relationship between OSCs structure and their electronic properties, we have replaced one quinolinate in Alq₃ with 4-hydroxypent-3-en-2-one (also known as acetyl acetonate, Acac) **27**. The mixed-ligand aluminum complex formed, Al(q₂Acac) **28**, was previously synthesized and studied for application in OLEDs [167, 168]. Furthermore, several quinoline-based mixed-ligands aluminum complexes have been synthesized and studied in former works [29, 169–171]. To synthesize the coordination complex Al(q₂Acac) **28**, we have implemented a modified version of the procedure described by Yamaguchi *et al.* [172]. As illustrated in Scheme 3.8, Al(q₂Acac) **28** is formed with a yield of ≈71% by the reaction between one equivalent of $Al(CH_3)_3$ and two equivalents of Hq **26**. Subsequently, the coordination sphere was completed by adding one equivalent of Acac **27**. Suitable single crystals were grown for single crystal X-ray diffraction measurements. The cell parameters were compared with those reported by Montes *et al.* to confirm the structure [166]. The molecular structure obtained single crystal X-ray diffraction is illustrated in Figure 3.16. Despite the introduction of a symmetric moiety such as Acac **27**, Al(q₂Acac) **28** can form two geometrical isomers. In the *pseudomer*-isomer the two axial nitrogens are facing each other. Conversely, in the *pseudofac*-isomer the two neighboring nitrogens are facing two oxygens. As illustrated in Figure 3.16, *pseudofac*-Al(q₂Acac) **28** is obtained by the synthetic procedure implemented. Since Hq **26**
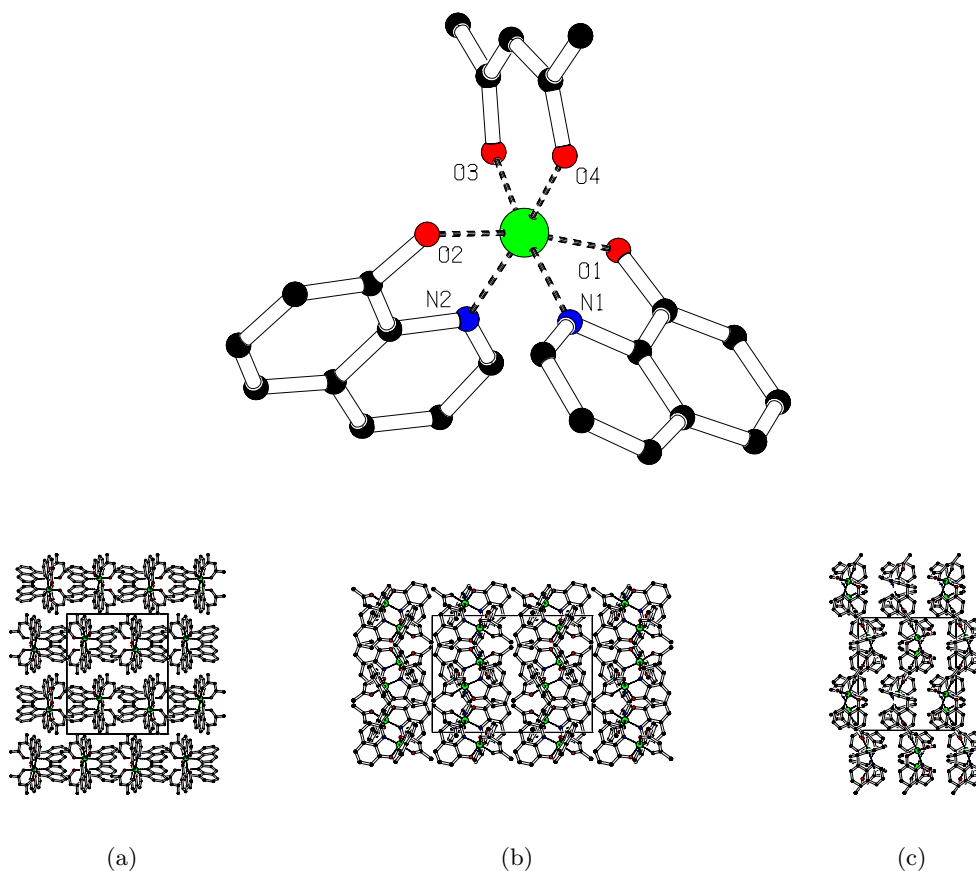
Bond	Length [Å]	Bond angle	Angle [°]	Bond angle	Angle [°]
		Al(q$_2$Acac) **28**			
Al1-O1	1.8549(14)	O1-Al1-O2	169.80(7)	O2-Al1-N2	82.32(6)
Al1-O2	1.8530(14)	O1-Al1-O3	90.36(6)	O3-Al1-O4	91.74(6)
Al1-O3	1.8765(14)	O1-Al1-O4	97.96(6)	O3-Al1-N1	173.02(7)
Al1-O4	1.8816(14)	O1-Al1-N1	82.67(6)	O3-Al1-N2	90.33(6)
Al1-N1	2.0464(16)	O1-Al1-N2	89.38(6)	O4-Al1-N1	89.17(6)
Al1-N2	2.0738(17)	O2-Al1-O3	95.58(6)	O4-Al1-N2	172.36(7)
		O2-Al1-O4	90.16(6)	N1-Al1-N2	89.67(6)
		O2-Al1-N1	91.33(6)		

Figure 3.16: Molecular structure obtained by single crystal X-ray diffraction on a single crystal of Al(q$_2$Acac) **28** [166]. H-atoms and solvent molecules are omitted for clarity. The molecular packing in the single crystal of Al(q$_2$Acac) **28** is illustrated in (a) yz (b) xz (c) xy perspective. Table: selected bond distances and angles for Al(q$_2$Acac) **28**.

is characterized by a narrower bite angle (O1-Al-N1 82.67° and O2-Al-N2 82.32°) than Acac **27** (O3-Al-O4 91.74°) and considering the electrostatic repulsion between oxygen and nitrogen atoms, the chelating atoms in *pseudofac*-Al(q$_2$Acac) **28** are arranged in a distorted octahedral geometry with bond angles of 82.32-97.96° and 169.80-173.02°. In addition, the bond lengths Al-O(quinolinate) (1.8530 Å and 1.8549 Å), are shorter than those Al-O(acetyl acetonate) (1.8765 Å and 1.8816 Å). However, the Al-O(quinolinate) and the Al-N(quinolinate) bond lengths in *pseudofac*-Al(q$_2$Acac) **28** are comparable to those of *mer*-Alq$_3$ (see Section 1.2). Similarly, the Al-O(acetyl acetonate) bond lengths are analogous to those of Al(Acac)$_3$ determined by Hon *et al.* [173]. In the crystal lattice the molecules of *pseudofac*-Al(q$_2$Acac) **28** are oriented to maximize the $\pi - \pi$ stacking between the aromatic system of the quinolinates, whereas the acetyl acetonates are not involved in any intermolecular interaction.
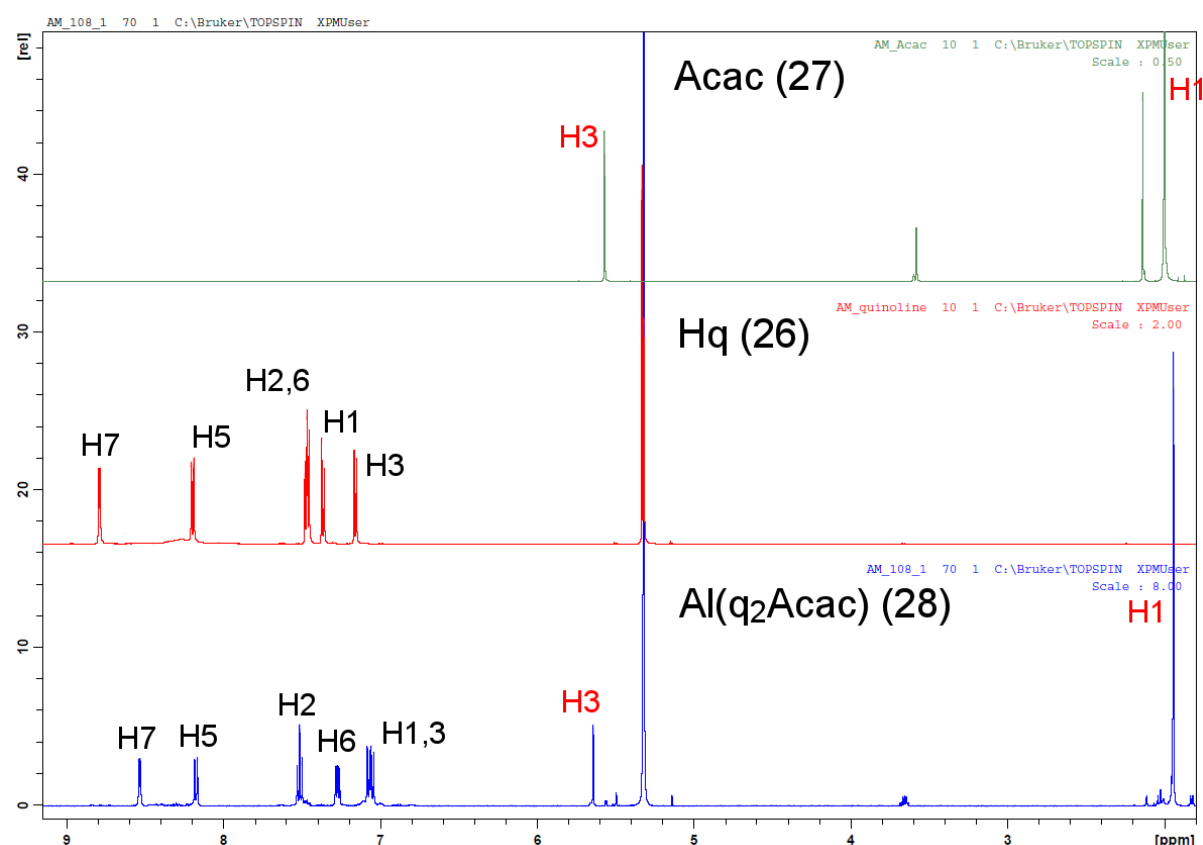
Compound	Resonances [ppm]							
	H1	H2	H3	H5	H6	H7	H1	H3
Acac **27**	-	-	-	-	-	-	2.00	5.57
Hq **26**	7.36	7.47	7.16	8.20	7.47	8.79	-	-
Al(q$_2$Acac) **28**	7.05	7.51	7.05	8.17	7.27	8.52	1.95	5.64

Figure 3.17: ^{1}H-NMR spectra of Al(q$_2$Acac) **28**, Hq **26** and Acac **27** in CD$_2$Cl$_2$. The resonances are marked accordingly to the numbering shown in Scheme 3.8.

The ^{1}H-NMR spectrum of Al(q$_2$Acac) **28**, illustrated in Figure 3.17 in comparison with the spectra of Hq **26** and Acac **27**, is composed by two sets of resonances. Between 7.00 and 8.52 ppm are the resonances of the aromatic hydrogens of quinolinate, whereas the resonances at 5.64 ppm and 1.94 ppm are relative to the hydrogens of acetyl acetonate. The elemental analysis

on Al(q$_2$Acac) **28**, C= 65.98%, H= 4.38% and N= 6.55%, fairly matches the expected values, C= 66.66%, H= 4.63% and and N= 6.76% (see Table 3.3). Mass spectrometry experiments were carried out by ESI-TOF and MALDI-TOF measurements. The main fragment in the ESI-TOF spectrum is relative to the fragment [Al(q$_2$Acac)H]$^+$ (m/z= 415.12), where an additional hydrogen forms the cation (see Figure B.55). Moreover, a series of peaks corresponding to various combinations of the ligands are observed: [Al(qAcac$_2$)H]$^+$ (m/z= 370.12), [Al(q$_2$)]$^+$ (m/z= 315.07), and [Al(qAcac)]$^+$ (m/z= 270.07). In the same manner, the MALDI-TOF spectrum displays a series of peaks relative to different combinations between the ligands (see Figure 3.21). The most intense peak corresponds to the fragment [Al(q$_2$)]$^+$ (m/z= 315). In addition, the fragment [Al(qAcac)]$^+$ (m/z= 270) and two dinuclear fragments, [Al$_2$(q$_4$Acac)]$^+$ (m/z= 729) and [Al$_2$(q$_3$Acac$_2$)]$^+$ (m/z= 684), were detected.

3.3.8 Bis-(quinolin-8-olate)-4-oxopent-2-en-2-olate aluminum (Al(q$_2$Op) (29)
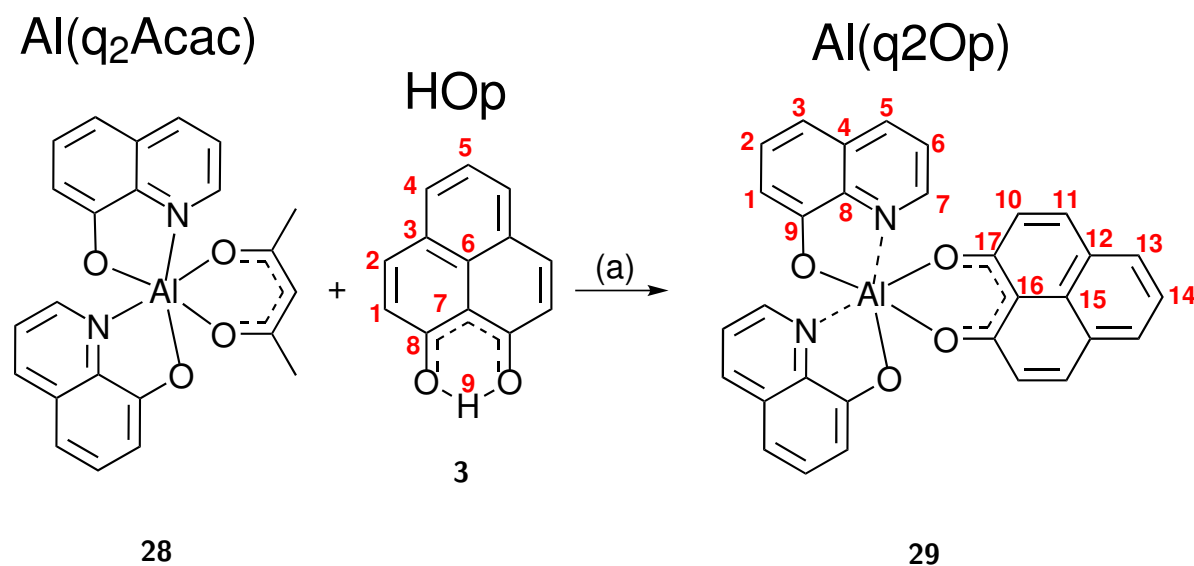
Scheme 3.9: Synthesis of Al(q$_2$Op) **29**. (a) Ethanol, reflux, overnight, yield: 73%.

The novel aluminum complex Al(q$_2$Op) **29** was obtained by the substitution of acetyl acetonate in Al(q$_2$Acac) **28** with a phenalenyl ligand. As illustrated in Scheme 3.9, Al(q$_2$Op) **29** is formed by the reaction between Al(q$_2$Acac) **28** and HOp **3** with a yield of ≈73%. High quality single crystals were grown for single crystal X-ray diffraction measurements. Hence, for the first time, the crystal structure of Al(q$_2$Op) **29** was resolved (crystal refinement data is reported in Table C.5). Similarly to Al(q$_2$Acac) **28**, Al(q$_2$Op) **29** can form two geometrical isomers: the *pseudomer*-isomer, where the two nitrogens are facing each other, and the *pseudofac*-isomer, where the two nitrogen are facing two oxygens. From the molecular structure, shown in Figure 3.18, it can be seen that the two nitrogens occupies neighboring positions in a *pseudofac* geometry. Due to the similar bite angle of HOp **3** and Acac **27**, *pseudofac*-Al(q$_2$Op) **29** is characterized by similar bond angles, 81.9-94.7° and 172.4-174.0°, in respect to those of *pseudofac*-Al(q$_2$Acac) **28** (see Section 3.3.7). Accordingly, the bond distances between the chelating atoms of quinolinate and aluminum, Al-O1 (1.844 Å), Al-O2 (1.864 Å), Al-N1 (2.050 Å), and Al-N2 (2.036 Å), are similar to those of Al(q$_2$Acac) **28** and *mer*-Alq$_3$ (see Section 1.2). Furthermore, the bond lengths between the oxygens of phenalenyl and aluminum, Al-O3 (1.867 Å) and Al-O4 (1.861 Å), are analogous to those of Al(Op)$_3$ **4** (see Section 3.3.1). In the crystal lattice, the
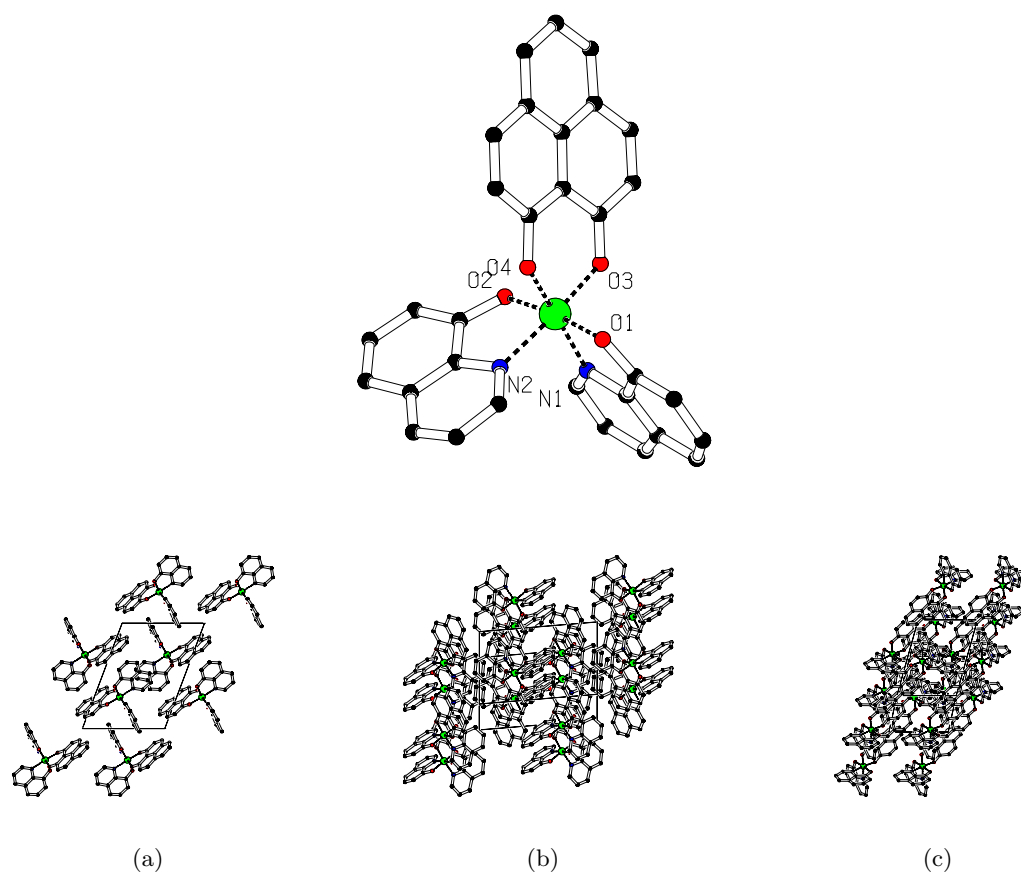
Bond	Length [Å]	Bond angle	Angle [°]	Bond angle	Angle [°]
		Al(q$_2$Op) **29**			
Al1-O1	1.844(6)	O1-Al1-O2	172.9(3)	O2-Al1-N2	81.9(3)
Al1-O2	1.864(6)	O1-Al1-O3	94.7(3)	O3-Al1-O4	92.1(3)
Al1-O3	1.867(6)	O1-Al1-O4	91.9(3)	O3-Al1-N1	91.2(3)
Al1-O4	1.861(6)	O1-Al1-N1	82.8(3)	O3-Al1-N2	172.4(3)
Al1-N1	2.050(6)	O1-Al1-N2	92.6(3)	O4-Al1-N1	174.0(3)
Al1-N2	2.036(7)	O2-Al1-O3	90.7(3)	O4-Al1-N2	89.7(3)
		O2-Al1-O4	92.5(3)	N1-Al1-N2	87.6(3)
		O2-Al1-N1	92.5(3)		

Figure 3.18: Molecular structure obtained by single crystal X-ray diffraction on a single crystal of Al(q$_2$Op) **29**. H-atoms and solvent molecules are omitted for clarity. The crystal refinement data is reported in Table C.5. The molecular packing in the single crystal of Al(q$_2$Op) **29** is illustrated in (a) yz (b) xz (c) xy perspective. Table: selected bond distances and angles for Al(q$_2$Op) **29**.

molecules of *pseudofac*-Al(q$_2$Op) **29** are oriented to maximize the interaction between quinolinates and phenalenyls. Interestingly, it can be noted that the quinolinates are only facing between themselves as well as the phenalenyls.
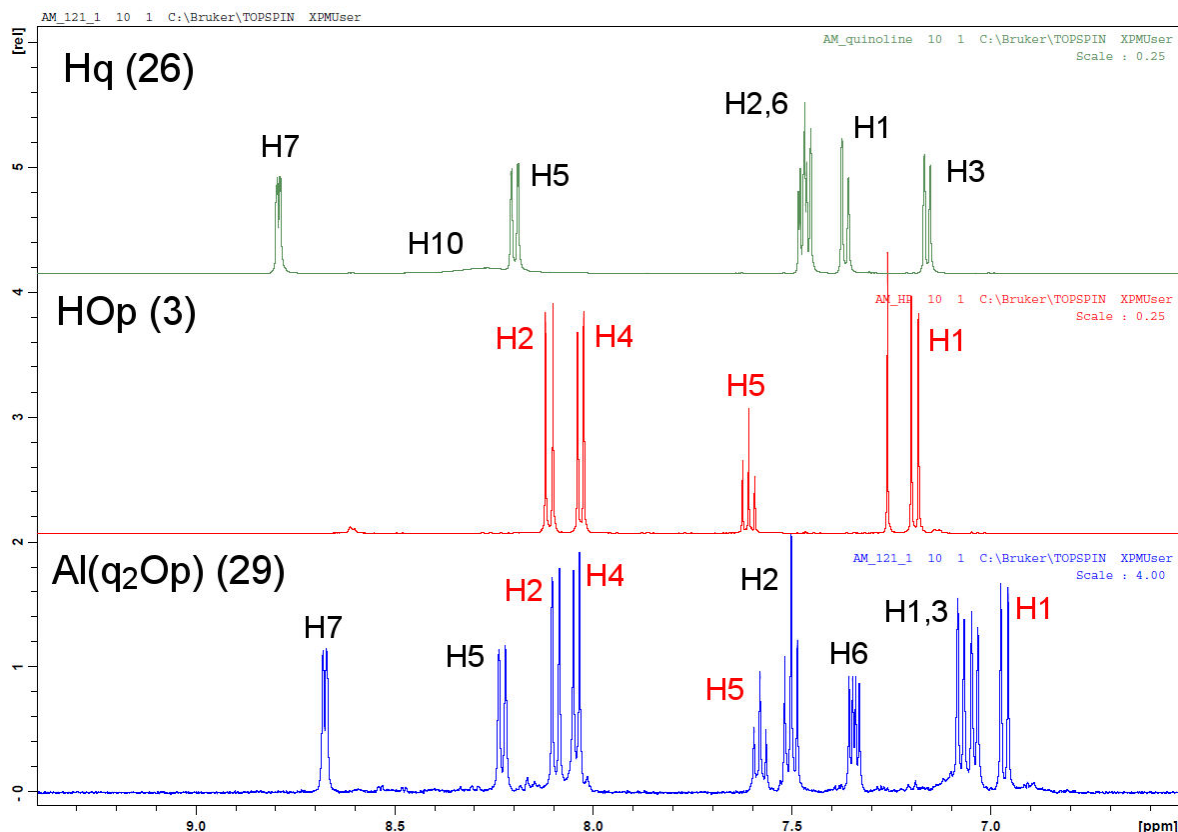
Compound	Resonances [ppm]									
	H1	H2	H3	H5	H6	H7	H1	H2	H4	H5
Hq **26**	7.36	7.47	7.16	8.20	7.47	8.79	-	-	-	-
HOp **3**	-	-	-	-	-	-	7.19	8.11	8.03	7.61
Al(q$_2$Op) **29**	7.06	7.50	7.06	8.23	7.34	8.68	6.96	8.09	8.04	7.58

Figure 3.19: ^{1}H-NMR spectra of Al(q$_2$Op) **29**, HOp **3** and Hq **26** in CD$_2$Cl$_2$ (HOp **3** in CDCl$_3$). The resonances are marked accordingly to the numbering shown in Scheme 3.9 and Scheme 3.8 (for Hq **26**).

In the ^{1}H-NMR spectrum of Al(q$_2$Op) **29**, illustrated in Figure 3.19 together with the spectra of HOp **3** and of Hq **26**, two sets of resonances are clearly visible. One set (H1, H2, H3, H5, H6, H7) is corresponding to the hydrogens of quinolinate. On the other hand, the second set (H10, H11, H13, H14) is relative to the hydrogens of phenalenyl. The elemental analysis of carbon, hydrogen and nitrogen, C= 72.17% H= 3.97% and N= 5.31%, matches the expected values, C= 72.93% H= 3.76% and N= 5.49% (see Table 3.3). In the ESI-TOF mass spectrometry two peaks are detected (see Figure B.58), the most intense peak is assigned to the fragment [Al(q$_2$Op)H]$^+$ (m/z= 511.11), where an additional proton forms the cation. The second peak is assigned to the fragment [Al(qOp)]$^+$ (m/z= 366.06), where the cation is formed by the elimination of one ligand. Diversely, the fragments [Al(Op$_2$)]$^+$ (m/z= 417), which is the most intense, and [Al(qOp)]$^+$ (m/z= 366) are detected in the MALDI-TOF experiment (see Figure 3.21). Most

probably the cation $[\text{Al}(\text{Op}_2)]^+$ is formed by the recombination of ligands during the MALDI process.

3.3.9 Bis-(quinolin-8-olate)-7-oxocyclohepta-1,3,5-trienolate aluminum (Al(q$_2$Trop) (30)
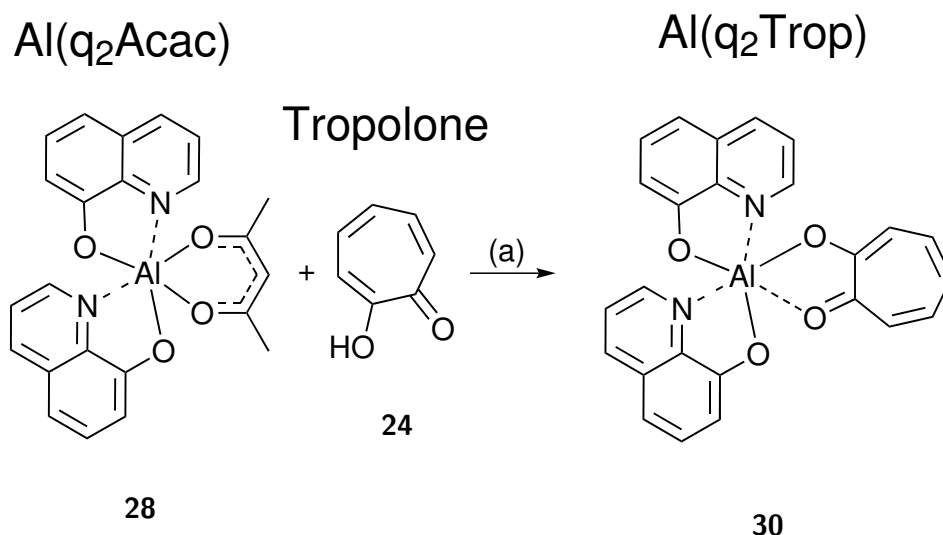
Scheme 3.10: Synthesis of Al(q$_2$Trop) **30**. (a) Ethanol, reflux, overnight, yield: 68%.

At last, we have exchanged the acetyl acetonate of Al(q$_2$Acac) **28** with a tropolonate to synthesize the unprecedented Al(q$_2$Trop) **30**. As illustrated in Scheme 3.10, the reaction takes place by mixing Al(q$_2$Acac) **28** and tropolone **24** in ethanol with a yield of ≈68%. High quality single crystals suitable for single crystal X-ray diffraction were grown, and thus, the molecular structure of Al(q$_2$Trop) **30**, depicted in Figure 3.20, was resolved (crystal refinement data is reported in Table C.6). Unexpectedly, in the molecular structure of Al(q$_2$Trop) **30**, the two nitrogens are facing each other in a *pseudomer* geometry. This is most surprising because the starting material Al(q$_2$Acac) **28** is characterized by a *pseudofac* geometry. Most probably, during the reaction between Al(q$_2$Acac) **28** and tropolone **24**, a rearrangement of the ligands takes place resulting in *pseudomer*-Al(q$_2$Trop) **30**. It might be also possible that the *pseudomer*-isomer has a higher tendency to crystallize than the *pseudofac*-isomer, and thus, we could grow only single crystals of *pseudomer*-Al(q$_2$Trop) **30** out of a mixture of both isomers. In *pseudomer*-Al(q$_2$Trop) **30** the six chelating atoms are arranged in a distorted octahedral geometry with bond angles of 81.19-98.51° and 170.60-172.81°. However, the geometry has a plane of symmetry, which lies on the N-O-N angle and cuts in half the tropolonate. As a consequence, the angles O1-Al-O2 and O1a-Al-O2a (170.60°) are identical as well as the angles O1-Al-N1 and O1a-Al-N1a (92.98°), O1-Al-O2a and O1a-Al-O2 (90.27°), O1-Al-N1a and O1a-Al-N1 (92.48°), O2-Al-N1 and O2a-Al-N1a (83.44°), and O2-Al-N1a and O2a-Al-N1 (91.85°). Similarly, the bond lengths Al-O1 and Al-O1a (1.909 Å) are equivalent as the bond lengths Al-O2 and Al-O2a (1.863 Å) and Al-N1 and Al-N1a (1.993 Å). Since in *pseudomer*-Al(q$_2$Trop) **30** the two nitrogens are facing each other, the bond lengths Al-N result shorter than those of *mer*-Alq$_3$ (see Section 1.2). Furthermore, the bond lengths Al-N in *pseudomer*-Al(q$_2$Trop) **30** are shorter than those of *pseudofac*-Al(q$_2$Acac) **28** and those of *pseudofac*-Al(q$_2$Op) **29**. On the contrary, the Al-O bond lengths in *pseudomer*-Al(q$_2$Trop) **30**, 1.863-1.909 Å, are slightly longer than those of

(a)	(b)	(c)
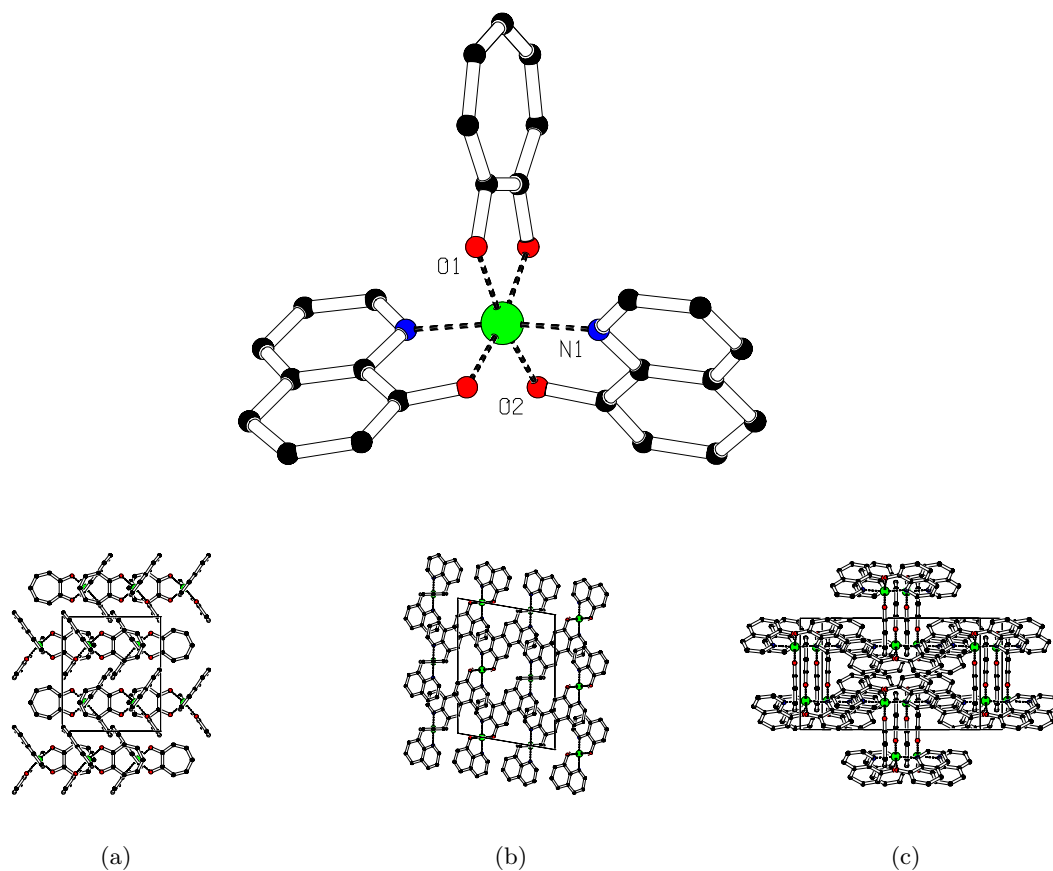
Bond	Length [Å]	Bond angle	Angle [°]	Bond angle	Angle [°]
			Al(q$_2$Trop) **30**		
Al1-O1	1.909(3)	O1-Al1-O1a	81.19(13)	O1a-Al1-N1a	92.98(13)
Al1-O1a	1.909(3)	O1-Al1-O2	170.60(14)	O2-Al1-O2a	98.51(14)
Al1-O2	1.863(3)	O1-Al1-O2a	90.27(12)	O2-Al1-N1	83.44(12)
Al1-O2a	1.863(3)	O1-Al1-N1	92.98(13)	O2-Al1-N1a	91.85(12)
Al1-N1	1.993(3)	O1-Al1-N1a	92.48(13)	O2a-Al1-N1	91.85(12)
Al1-N1a	1.993(3)	O1a-Al1-O2	90.27(12)	O2a-Al1-N1a	83.44(12)
		O1a-Al1-O2a	170.60(14)	N1-Al1-N1a	172.81(16)
		O1a-Al1-N1	92.48(13)		

Figure 3.20: Molecular structure obtained by single crystal X-ray diffraction on a single crystal of Al(q$_2$Trop) **30**. H-atoms and solvent molecules are omitted for clarity. The crystal refinement data is reported in Table C.6. The molecular packing in the single crystal of Al(q$_2$Trop) **30** is illustrated in (a) yz (b) xz (c) xy perspective. Table: selected bond distances and angles for Al(q$_2$Trop) **30**.

mer-Alq$_3$ (see Section 1.2), *pseudofac*-Al(q$_2$Acac) **28** and *pseudofac*-Al(q$_2$Op) **29**. In the crystal lattice, *pseudomer*-Al(q$_2$Trop) **30** is oriented to maximize the interaction between quinolinates and tropolonates. In particular, quinolinates are exclusively facing each other as well as the tropolonates.

Al(q$_2$Trop) **30** was partially characterized by ESI-TOF, MALDI-TOF and elemental analysis. In the ESI-TOF spectrum, illustrated in Figure B.60, the main peak is corresponding to the fragment [Al(qTrop$_2$)H]$^+$ (m/z= 414.08), in addition, two peaks relative to the fragments [Al(q$_2$Trop)H]$^+$ (m/z= 437.09) and [Al(qTrop)]$^+$ (m/z= 292.26) are detected. The MALDI-TOF spectrum, shown in Figure 3.21, is characterized by several peaks. The most intense ones correspond to the fragments [Alq$_2$]$^+$ (m/z= 315), [Al(qTrop)]$^+$ (m/z= 292), and [Al(Trop$_2$)]$^+$ (m/z= 269). An additional series of peaks, corresponding to dinuclear fragments formed by all the possible combinations of ligands from [Al$_2$(qTrop$_4$)]$^+$ (m/z= 682) to [Al$_2$q$_5$Trop]$^+$ (m/z= 774), was detected. It is clear that, besides the presence of impurities in the samples for ESI-TOF and MALDI-TOF, a recombination of ligands takes place during the ionization process to form unexpected fragments. The content of carbon, hydrogen and nitrogen, C= 69.15% H= 4.37% N= 5.69%, measured by elemental analysis is in fairly good agreement with the expected values, C= 68.80% H= 3.39% N= 6.42%.
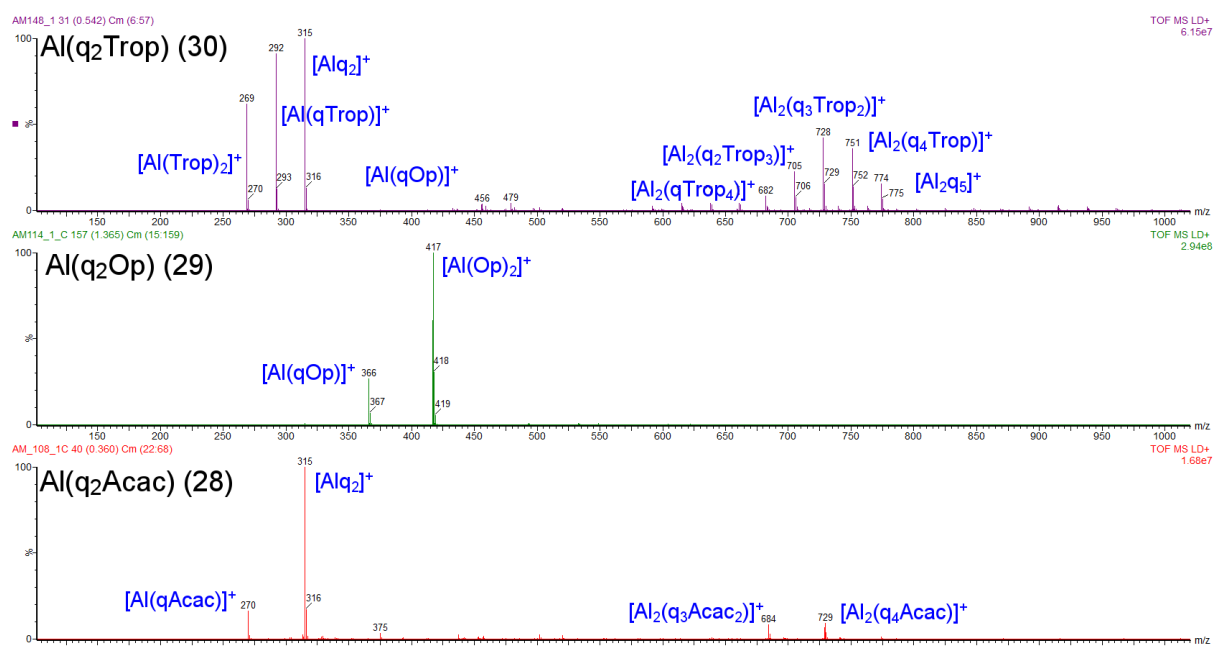
Figure 3.21: MALDI-TOF spectra of Al(q$_2$Acac) **28**, Al(q$_2$Op) **29** and Al(q$_2$Trop) **30**. The main fragments are marked in the figure.

3.3.10   A zinc complex: Bis-(1-oxo-1H-phenalen-9-olate)zinc (Zn(Op)$_2$) (31)

As mentioned in the introduction, a tetrahedral phenalenyl-based complex of zinc has been implemented in spin-valve devices (see Section 1.2.3). Hence, we have synthesized the novel Zn(Op)$_2$ **31** as the starting molecule to investigate the electronic properties of the phenalenyl-based zinc complexes class. The zinc complex was obtained through the reaction between HOp **3** and zinc acetate with a yield of ≈84%, as shown in Scheme 3.11. Suitable single crystals were grown for single crystal X-ray diffraction (crystal refinement data in Table C.7). The molecular
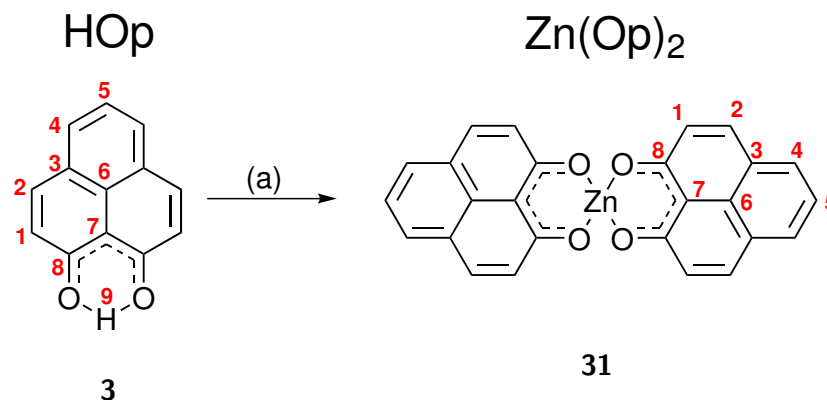
Scheme 3.11: Synthesis of Bis-(1-oxo-1H-phenalen-9-olate)zinc (Zn(Op)$_2$). (a) Zn(CH$_3$COO)$_2$, ethanol, reflux, overnight, yield: 84%.

structure, illustrated in Figure 3.22, reveals that two phenalenyls lie on a flat plane and two additional water molecules occupy the perpendicular axial positions, resulting in a symmetrical octahedral geometry with an inversion center on the zinc atom. The four chelating oxygens of the phenalenyl ligands are arranged in an almost perfect planar quadratic geometry with O-Al-O angles close to 90° and 180°. The two additional water molecules complete the coordination sphere occupying the opposite vertexes of the octahedron. Due to the different nature of the metal, the Zn-O bonds, 2.012-2.016 Å, are considerably longer than the Al-O bond in Al(Op)$_3$ **4** (see Section 3.3.1). Molecules of Zn(Op)$_2$ **31**, in the crystal lattice, are oriented to maximize the interaction between the phenalenyls and the water molecules in the axial positions.

The novel zinc complex was further characterized by ^{1}H-NMR spectroscopy, MALDI-TOF mass spectrometry and elemental analysis. The [1]NMR spectrum, shown in Figure 3.23 in comparison with the spectrum of HOp **3**, is characterized by four resonances corresponding to the aromatic hydrogens of phenalenyl. These resonances are shifted in respect to the free ligand (in the ^{1}H-NMR spectrum of Zn(Op)$_2$ **31** the resonances of residual non-reacted free ligand are visible). The fragment [Zn(Op)]$^+$ (m/z= 260) is detected in the MALDI-TOF spectrum of Zn(Op)$_2$ **31** (see Figure 3.24). As described for Al(Op)$_3$ **4** in Section 3.3.1 the cation is formed by the elimination of one phenalenyl. At last, the carbon and hydrogen content, C= 63.53% and H= 4.12%, measured by elemental analysis, is in agreement with the expected one, C= 63.49% and H= 3.70%.

The last consideration on the zinc complex Zn(Op)$_2$ **31** is concerning the presence of water molecules which complete the coordination sphere. These water molecules can affect the thermal stability of the complex during the vacuum evaporation process. In order to achieve a water-free zinc complex, reactions have to be carried out in a controlled environment, such as a glove-box using anhydrous starting materials. However, due to the nature of zinc, a water-free zinc complex would be characterized by a tetrahedral geometry. Nonetheless, in principle, all the ligands listed in Table 3.1 can be utilized to form zinc complexes for further studies. Moreover, it might be possible to obtain complexes with mixed-ligands in a similar fashion to that presented in Section 1.2.3.

| | (a) | | (b) | | (c) |
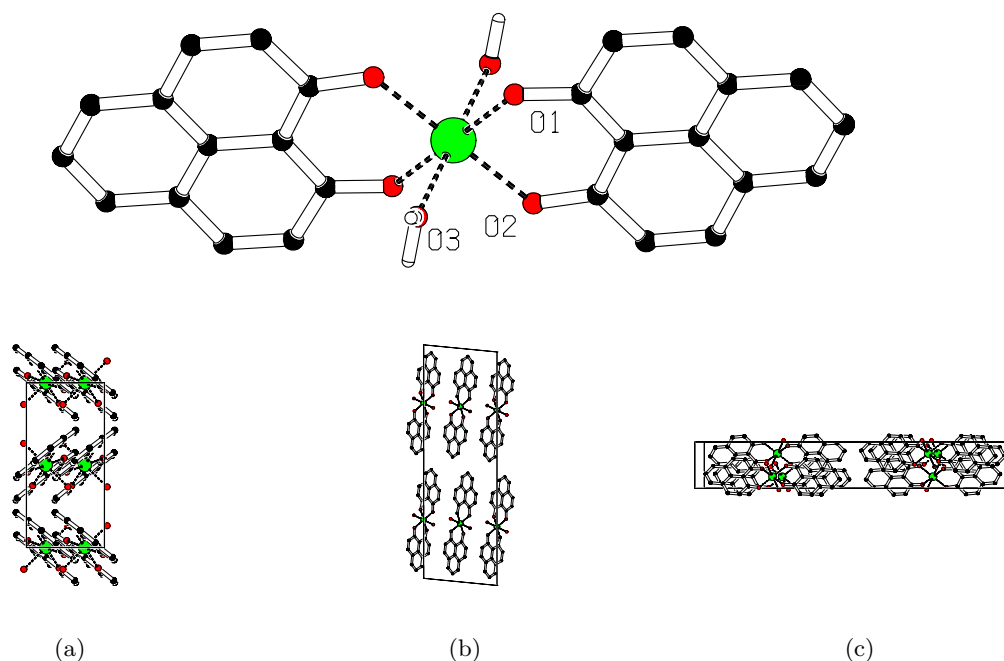
Bond	Length [Å]	Bond angle	Angle [°]	Bond angle	Angle [°]
		$Zn(Op)_2 \cdot 2\,H_2O$ **31**			
Zn1-O1	2.012(2)	O1-Zn1-O1a	180.00	O1a-Zn1-O3a	91.81(11)
Zn1-O1a	2.012(2)	O1-Zn1-O2	88.49(10)	O2-Zn1-O2a	180.00
Zn1-O2	2.016(3)	O1-Zn1-O2a	91.51(10)	O2-Zn1-O3	89.64(11)
Zn1-O2a	2.016(3)	O1-Zn1-O3	91.81(11)	O2-Zn1-O3a	90.36(11)
Zn1-O3	2.186(3)	O1-Zn1-O3a	88.19(11)	O2a-Zn1-O3	90.36(11)
Zn1-O3a	2.186(3)	O1a-Zn1-O2	91.51(10)	O2a-Zn1-O3a	89.64(11)
		O1a-Zn1-O2a	88.49(10)	O3-Zn1-O3a	180.00(16)
		O1a-Zn1-O3	88.19(11)		

Figure 3.22: Molecular structure obtained by single crystal X-ray diffraction on a single crystal of $Zn(Op)_2$ **31**. H-atoms and solvent molecules are omitted for clarity. The crystal refinement data is reported in Table C.7. The molecular packing in the single crystal of $Zn(Op)_2$ **31** is illustrated in (a) yz (b) xz (c) xy perspective. Table: selected bond distances and angles for $Zn(Op)_2$ **31**.

Compound	Resonances [ppm]				
	H1	H2	H4	H5	H9
HOp **3**	7.19	8.11	8.03	7.61	16.05
$Zn(Op)_2$ **31**	7.14	8.01	7.96	7.51	-
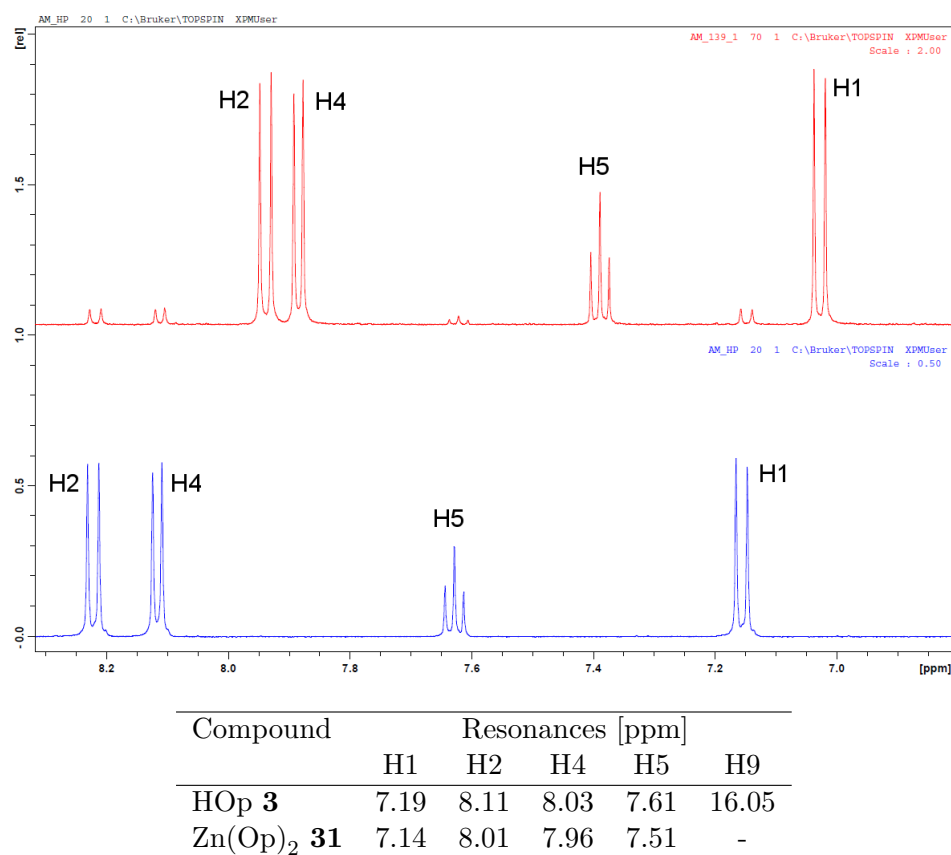
Figure 3.23: ^{1}H-NMR spectra of HOp **3** (blue) and $Zn(Op)_2$ **31** (red) in THF-d_4. The resonances are marked accordingly to the numbering shown in Scheme 3.11.
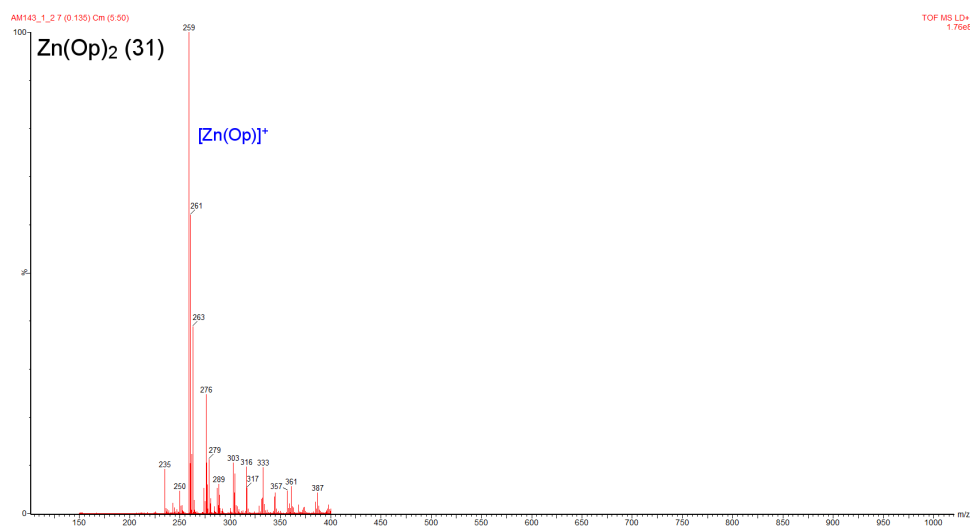
Figure 3.24: MALDI-TOF spectrum of $Zn(Op)_2$ **31**. The fragment is marked in the figure.

Table 3.3: Carbon, hydrogen and nitrogen content of the synthesized complexes measured by elemental analysis. The calculated values are listed for comparison.

Compound	Experimental			Calculated		
	C [%]	H [%]	N [%]	C [%]	H [%]	N [%]
$Al(Op)_3{}^+2H_2O$ **4**	72.29	4.01	-	72.00	4.19	-
$Al(Op-F)_3{}^+4H_2O$ **6a**	63.97	3.53	-	63.41	3.56	-
$Al(Op-Cl)_3{}^+2H_2O$ **6b**	62.65	3.18	-	62.29	2.96	-
$Al(Op-Br)_3{}^+H_2O$ **6c**	54.53	2.57	-	54.01	2.33	-
$Al(Op-I)_3{}^+H_2O$ **6d**	46.81	2.41	-	46.46	2.00	-
$Al(Op-p)_3{}^+3H_2O$ **16a**	76.58	4.36	-	76.49	4.40	-
$Al(Op-n)_3{}^+5H_2O$ **16b**	76.54	4.60	-	76.65	4.58	-
$Al(Op-pe)_3{}^+4H_2O$ **16c**	76.43	5.79	-	76.81	4.20	-
$Al(Oba)_3{}^+2H_2O$ **19**	76.84	5.05	-	76.68	3.92	-
$Al(Op-py)_3{}^+3H_2O$ **23**	67.48	4.59	7.13	67.00	5.12	7.10
$Al(Trop)_3$ **25**	64.57	3.83	-	64.61	3.88	-
$Al(q_2Acac)$ **28**	65.98	4.38	6.55	66.66	4.63	6.76
$Al(q_2Op)$ **29**	72.17	3.97	5.31	72.93	3.76	5.49
$Al(q_2Trop)$ **30**	69.15	4.37	5.69	68.80	3.39	6.42
$Zn(Op)_2 \cdot 2\,H_2O$ **31**	63.53	4.12	-	63.49	3.70	-

3.4 Spectroscopic characterization

Ligands (see Table 3.1) and complexes (see Table 3.2), synthesized in Section 3.3, were photophysically characterized. At first, a complete photophysical investigation has been carried out for $Al(Op)_3$ **4** in solution and in thin film, in comparison with the benchmark Alq_3. For all the other OSCs synthesized, the absorption and emission spectra have been recorded. Additionally, some of the OSCs have been grown on quartz substrates to measure their spectra in thin film. The findings (absorption maxima and their extinction coefficient and emission maxima) are listed in Table 3.5 for the ligands and in Table 3.6 for the OSCs. By measuring absorption and emission spectra, important information on the frontier orbitals and electronic transitions of the molecules can be inferred [174]. Furthermore, from the onset of the first band in the absorption spectra it is possible to calculate the optical HOMO-LUMO gaps listed in Table 3.7 and Table 3.8.

3.4.1 Photophysical characterization of $Al(Op)_3$ (4) in comparison with Alq_3

The photophysical properties of $Al(Op)_3$ **4** were determined by measuring the absorption and emission spectra in solution and in thin film. Additionally, photoluminescence quantum yield and luminescence lifetime were estimated. The results are reported in Table 3.4.

Table 3.4: Photophysical properties recorded at room temperature for Alq_3 and $Al(Op)_3$ **4** in solution and in thin film deposited on quartz.

Compound	λ_{max}^{abs} [a](ϵ) [nm] ([$M^{-1} cm^{-1}$])	λ_{max}^{emi} [b] [nm]	Φ [c]	τ [d] [ns]
Alq_3 solution	385 (1.1×10^4)	517	0.13	16.2
Alq_3 thin film	393	523	0.17	12.5
$Al(Op)_3$ solution	454 (4.4×10^4)	458	0.027	0.7
$Al(Op)_3$ thin film	463	583	0.014	7.1

[a] λ_{max}^{abs} = absorption maximum of the first transition band and its extinction coefficient (ϵ).   [b] λ_{max}^{emi} = emission maximum.

[c] Φ = photoluminescence quantum yield. It is determined using rhodamine 6G as a standard.   [d] τ = luminescence lifetime.

Figure 3.25 illustrates the absorption and emission spectra in diluted solution of Hq and Alq_3 and in thin film deposited onto a quartz substrate of Alq_3. There are two bands in the absorption spectrum of Alq_3, which are at 385 nm and at 250 nm. These bands correspond to $\pi \rightarrow \pi^*$ transitions localized on the quinolinate moiety [175, 176]. As a consequence, Hq shows the same bands shifted at lowered wavelength [177]. On the contrary, the band between 300 and 350 nm, which is not visible for the free ligand, is attributed to a charge transfer metal to ligand (MLCT). In addition, since Alq_3 is formed by three quinolinates, its extinction coefficient ϵ is about threefold compared to the extinction coefficient ϵ of Hq. As an example, the extinction coefficient of the first absorption band of Alq_3 is $\epsilon_{385}= 1.1 \times 10^4 \, M^{-1} cm^{-1}$ and that of the first absorption band of Hq is $\epsilon_{314}= 3.1 \times 10^3 \, M^{-1} cm^{-1}$. The absorption spectrum of Alq_3 in thin film is similar to that in solution, which confirms that the complex was successfully deposited onto the substrate. The slight shift of the peaks is caused by the solvatochromic effect [178, 179]. Furthermore, the emission spectrum of the film is almost identical to that in solution; the emission maximum λ_{max}^{emi} in solution is 517 nm and in thin film is 523 nm, only 6 nm shifted. In solution and in thin film, Alq_3 is characterized by comparable photophysical properties. In

(a)   (b)
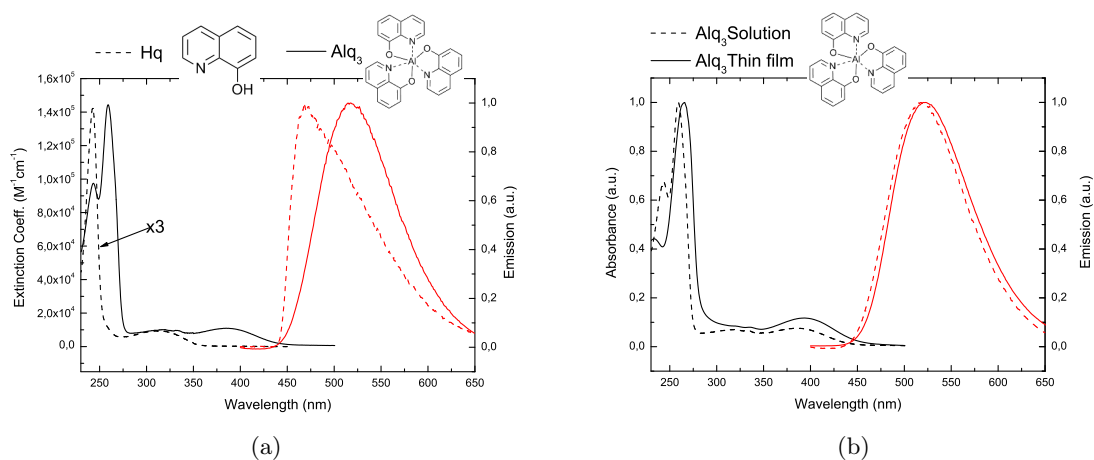
Figure 3.25: (a) Absorption (black) and fluorescence (red) spectra at room temperature in diluted DCM solution of Hq and Alq$_3$. (b) Absorption (black) and fluorescence (red) spectra at room temperature in solution and in thin film of Alq$_3$.
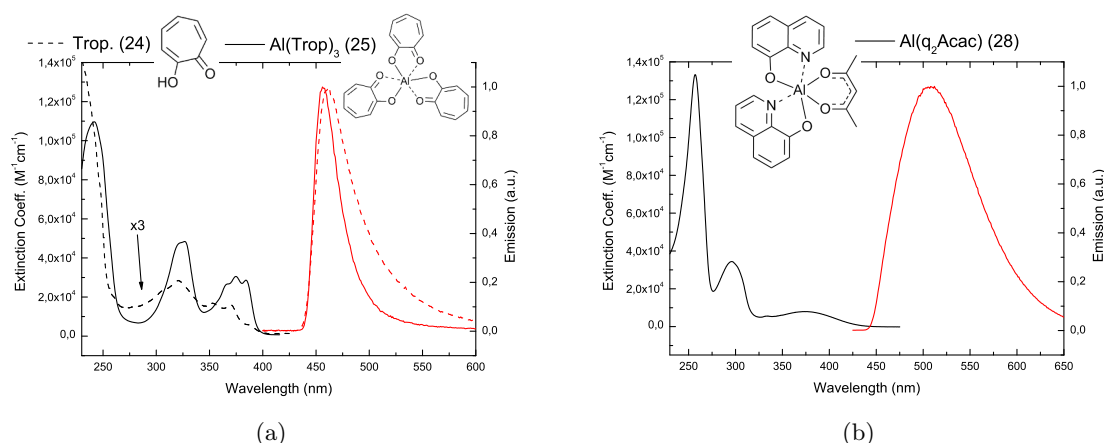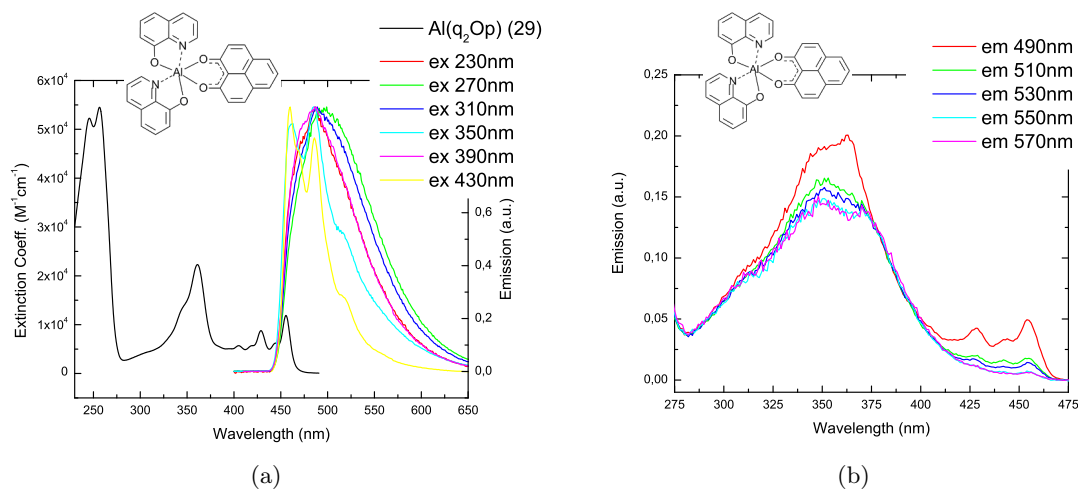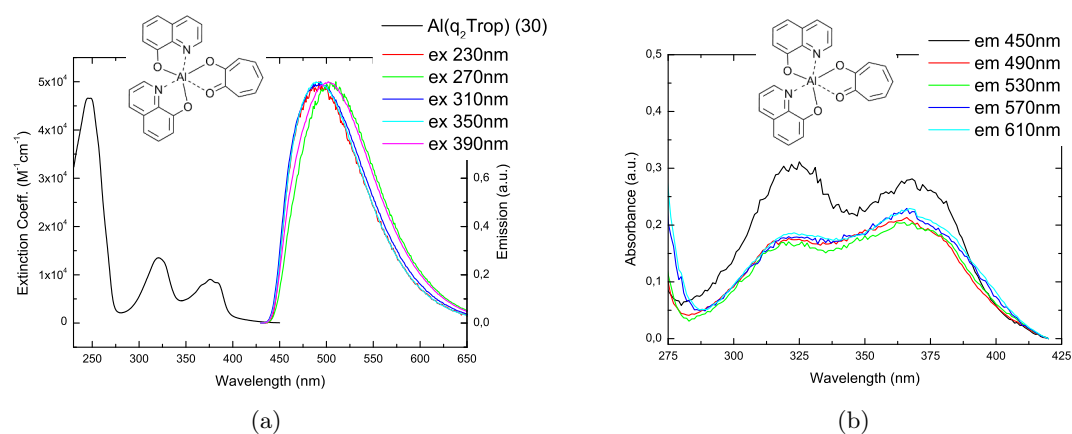

(a)   (b)
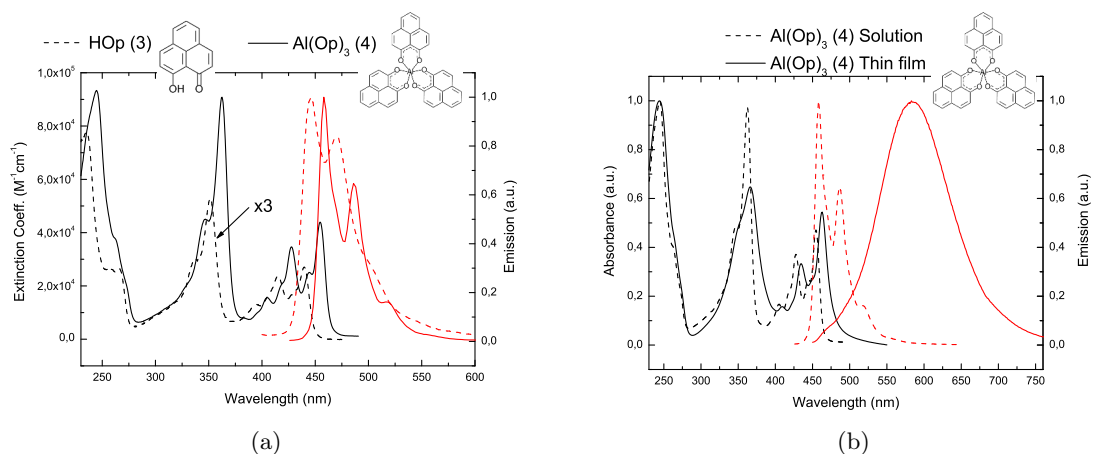
Figure 3.26: (a) Absorption (black) and fluorescence (red) spectra at room temperature in diluted DCM solution of Hp **3** and Al(Op)$_3$ **4**. (b) Absorption (black) and fluorescence (red) spectra at room temperature in solution and in thin film of Al(Op)$_3$ **4**.

detail, the photoluminescence quantum yield Φ in solution and in solid state is 0.13 and 0.17, respectively, and the luminescence lifetime τ, extracted from the photoluminescence decay, illustrated in Figure 3.27, is 16.2 ns and 12.5 ns, respectively. In both cases the photoluminescence decay is mono-exponential.

| (a) | (b) |
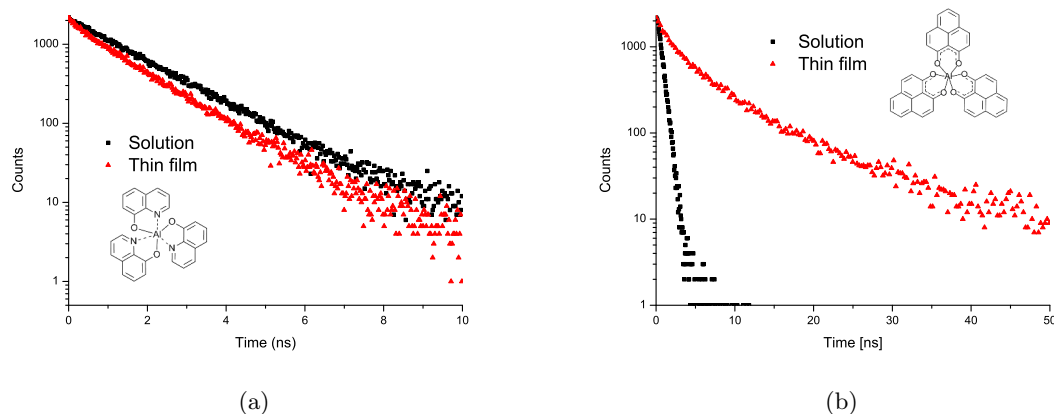
Figure 3.27: (a) Luminescence decay at room temperature in diluted DCM solution (black) and in thin film (red) of Alq$_3$. (b) Luminescence decay at room temperature in diluted DCM solution (black) and in thin film (red) of Al(Op)$_3$ **4**.

The absorption and emission spectra of HOp **3** and Al(Op)$_3$ **4** in diluted solution are illustrated Figure 3.26. The photophysical properties of HOp **3** derive from its characteristic α, β-conjugated carbonyl group [180]. Three bands are observed in the absorption spectra of Al(Op)$_3$ **4**, correlated to transitions localized on the ligands. As a result, the absorption profiles of Al(Op)$_3$ **4** and HOp **3** are strongly related exhibiting only minimal shifts of the peaks. However, the extinction coefficient ϵ of Al(Op)$_3$ **4** is about five times that of HOp **3**. As an example, the extinction coefficient of the first absorption band of Al(Op)$_3$ **4** is $\epsilon_{454}= 4.4 \times 10^4 \, \mathrm{M}^{-1} \, \mathrm{cm}^{-1}$, whereas that of HOp **3** is $\epsilon_{439}= 9.0 \times 10^4 \, \mathrm{M}^{-1} \, \mathrm{cm}^{-1}$. The structured band between 400 and 450 nm can be attributed to $n \rightarrow \pi^*$ transitions. Conversely, the bands observed between 320 and 375 nm and the in the UV region, $\approx$250 nm are associated to $\pi \rightarrow \pi^*$ transitions. The emission spectra of HOp **3** and Al(Op)$_3$ **4** are dominated by a structured band in the region between 425 and 550 nm, the shape and energy of the band clearly indicate an intense fluorescence emission. Figure 3.26 illustrates the absorption and emission spectra of Al(Op)$_3$ **4** in solution and in thin film. In thin film and in solution the absorption spectra of Al(Op)$_3$ **4** have the same pattern, indicating that the complex was successfully grown onto the quartz substrate. In contrast, the emission spectrum in solid state is dramatically red-shifted and broadened. As a result, the emission maximum λ_{max}^{emi} in solution occurs at 458 nm and in thin film at 583 nm. The formation of excimers (collision complexes at the excited state), which is well-known for molecules such as pyrene [181], is assumed to have occurred. Normally an excimer is caused by a charge-transfer interaction between an electronically excited species and a ground state molecule. Often, the excimer possesses observable properties quite distinct from those of the single molecule [180, 182]. That becomes clear observing the photoluminescence quantum yield Φ and lifetime τ of Al(Op)$_3$ **4** in solution and in thin film. In solution, the quantum yield Φ is 0.027 and in thin film is 0.014. Moreover, as it can be seen in Figure 3.27, the lifetime τ in solution is considerably shorter than in thin-film. In solution, Al(Op)$_3$ **4** is characterized by a mono-exponential decay with a lifetime $\tau= 0.7$ ns. On the contrary, the decay in thin film is multi-exponential and the average lifetime estimated is $\tau= 7.1$ ns. Interestingly, was impossible

77

to solely detect the emission from excimers in concentrated solutions of HOp **3** and Al(Op)$_3$ **4**. However, in the spectra illustrated in Figure D.1 and Figure D.2 a long tail, which can be ascribed to the formation of excimers, is observed.
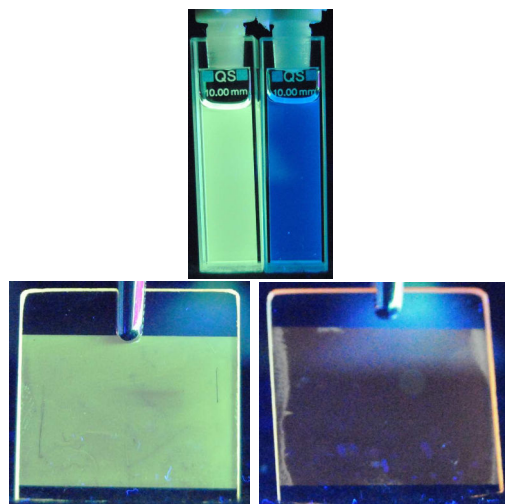
Figure 3.28: Emission in solution of Alq$_3$ (yellow) and Al(Op)$_3$ **4** (blue). Emission in thin film of Alq$_3$ (yellow) and Al(Op)$_3$ **4** (brown). The emission in thin film of Al(Op)$_3$ **4** is dramatically shifted compared to the emission in solution due to the formation of excimers.

By the photophysical characterization, we have observed how the different structure of Alq$_3$ and Al(Op)$_3$ **4** results in dramatically divergent photophysical properties in solution and in thin film. The photophysical properties of both the complexes originate mainly from the ligands with a small contribution of the central aluminum. As a result, the absorption and emission spectra of Alq$_3$ and Al(Op)$_3$ **4** in solution are similar to those of Hq and HOp **3**, respectively. However, the photophysical properties of Alq$_3$ and Al(Op)$_3$ **4** are not comparable. As an example, the absorption bands in the visible range of Al(Op)$_3$ **4** have quite higher extinction coefficients ϵ compared to those of Alq$_3$ (see Table 3.6). In addition, the florescence quantum yield Φ in solution of Alq$_3$ (0.13) is considerably larger than that of Al(Op)$_3$ **4** (0.027). In the same way, the fluorescence lifetime τ in solution of Alq$_3$ (16.2 ns) is substantially longer than that of Al(Op)$_3$ **4** (0.7 ns). Low fluorescence quantum yield and short fluorescence lifetime in solution suggest that fast non radiative decay processes take place in Al(Op)$_3$ **4**. Both the complexes were successfully deposited onto quartz substrates to measure the photophysical properties in thin film, as proved by the equivalent absorption spectra. The emission spectra of Alq$_3$ in solution and thin film are almost identical. In addition, fluorescence quantum yield Φ and lifetime τ of Alq$_3$ in thin film, 0.17 and 12.5 ns, respectively, are comparable to those in solution. In contrast, the emission spectra of Al(Op)$_3$ **4** in thin film is substantially different from that in solution. As a result, fluorescence quantum yield Φ and lifetime τ of Al(Op)$_3$ **4** in thin film, 0.014 and 7.1 ns, respectively, heavily deviate from those in solution, 0.027 and 0.7 ns. The origin of the discordant photophysical properties of Al(Op)$_3$ **4**, in solution and in thin film, is the formation of excimers in the solid state (see Figure 3.28). The extended flat aromatic system of HOp **3** is presumably the cause of the excimer formation. Conversely, the small hetero aromatic system of Hq is preventing the excimers generation in thin films of Alq$_3$.

3.4.2 Characterization of the (novel) OSCs

Absorption and emission spectra of the (novel) OSCs have been measured. To explain the features of the spectra of the (novel) OSCs, the photophysical characterization of Alq_3 and $Al(Op)_3$ **4**, described in the previous section, has been used as a reference .
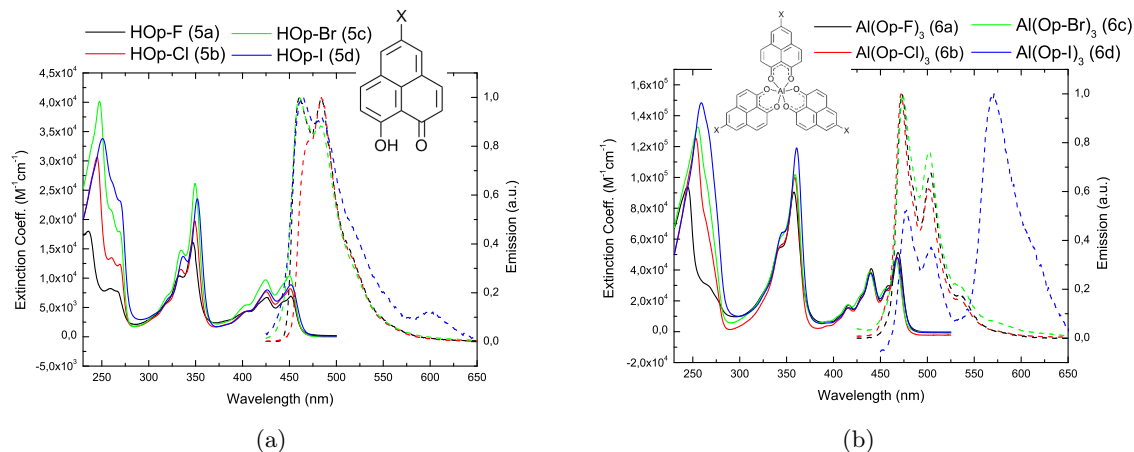
Figure 3.29: (a) Absorption (black) and fluorescence (red) spectra at room temperature in diluted DCM solution of HOp−X **5a**–**d**. (b) Absorption (black) and fluorescence (red) spectra at room temperature in diluted DCM solution of $Al(Op-X)_3$ **6a**–**d**.

The absorption and emission spectra in solution of the halogenated ligands HOp−X **5a**–**d** and complexes $Al(Op-X)_3$ **6a**–**d** are illustrated in Figure 3.29. The absorption spectra of the halogenated derivatives are characterized by the same three bands observed in the spectra of HOp **3** and $Al(Op)_3$ **4**. Here, these three bands are slightly shifted to higher wavelengths. In the emission spectra of the halogenated ligands HOp−X **5a**–**d** and complexes $Al(Op-X)_3$ **6a**–**d**, the bands are red-shifted compared to those of HOp **3** and $Al(Op)_3$ **4**. Moreover, the relative peak intensities exhibit slight variations. A second band at higher wavelength ($\approx$600 nm) is identified in the emission spectra of the iodo derivatives HOp−I **5d** and $Al(Op-I)_3$ **6d**. This band is assigned to a phosphorescence emission from the triplet state triggered by the intramolecular heavy-atom effect [183]. The presence of three iodine atoms in $Al(Op-I)_3$ **6d** results in a partially quenched fluorescence emission in favor of a more intense phosphorescence emission (see Figure 3.37).

Figure 3.30 illustrates the absorption and emission spectra in solution of the substituted ligands HOp−R **15a**–**c** and complexes $Al(Op-R)_3$ **16a**–**c**, in addition, the spectra of $Al(Op-p)_3$ **16a** in thin film are shown. In solution, the absorption spectra of the substituted ligands HOp−R **15a**–**c** and complexes $Al(Op-R)_3$ **16a**–**c** show considerably different patterns compared to those of HOp **3** and $Al(Op)_3$ **4**. In the region between 325 and 475 nm transitions localized on the phenalenyl take place. On the contrary, in the UV region, the absorption spectra of the substituted derivatives present entirely different profiles, due to $\pi \rightarrow \pi^*$ transitions localized on the aromatic substituents. In addition, the bulky substituents influence the structure of the peaks in the absorption and emission spectra. As a result, all the bands are less structured and slightly red-shifted. Out of the three substituted complexes, only $Al(Op-p)_3$ **16a** was grown onto a quartz substrate to investigate the effect of the bulky phenyl substituent on the excimers formation. The absorption spectrum in thin film resemble the spectrum in solution, confirming that the complex was deposited successfully onto the quartz substrate. In contrast, the emission in thin film is dominated by a band originating from excimers with a maximum

(a)

(b)

(c)
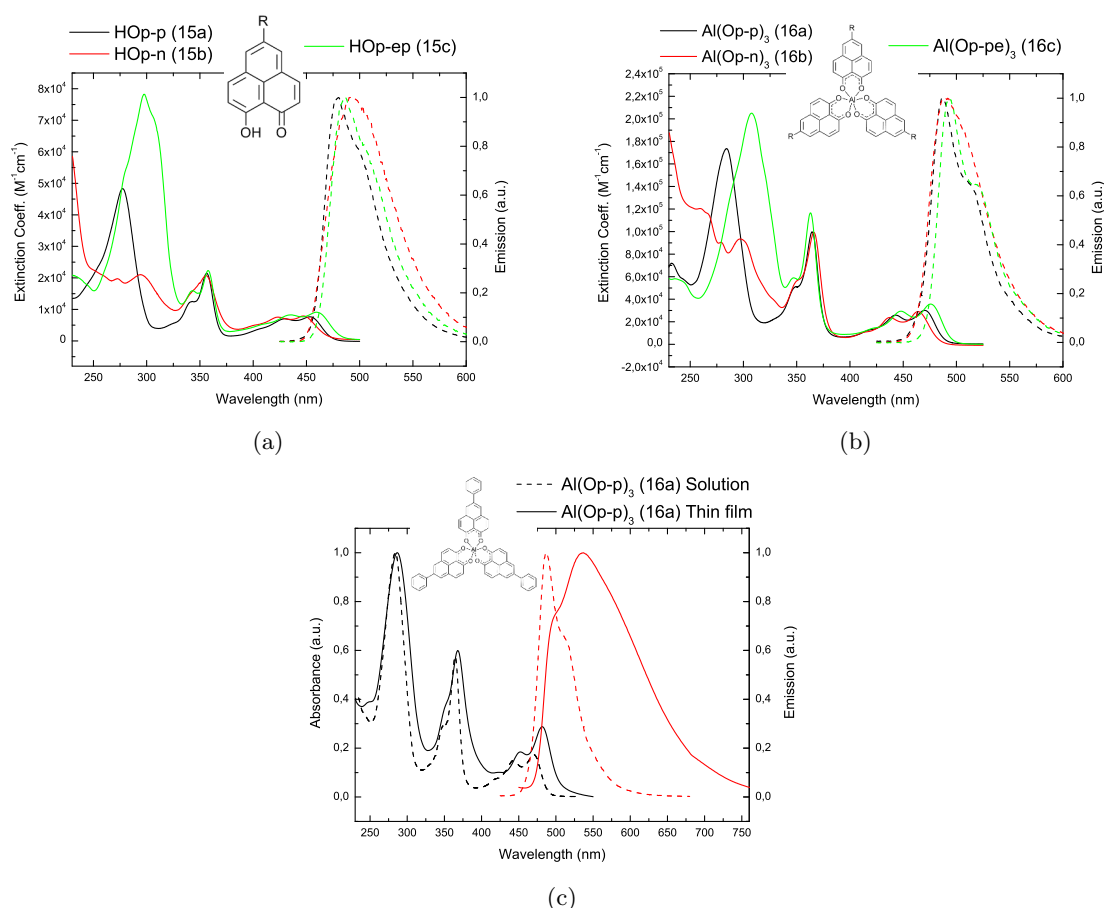
Figure 3.30: (a) Absorption (black) and fluorescence (red) spectra at room temperature in diluted DCM solution of HOp−R **15a**–**c**. (b) Absorption (black) and fluorescence (red) spectra at room temperature in diluted DCM solution of Al(Op−R)$_3$ **16a**–**c**. (c) Absorption (black) and fluorescence (red) spectra at room temperature in solution and in thin film of Al(Op−p)$_3$ **16a**.

at 537 nm. However, the formation of excimers is partially hindered as demonstrated by the shoulder at ≈475 nm, which corresponds to the emission of single complexes. By measuring the emission spectra of Al(Op−p)$_3$ **16a** in function of the concentration, the excimers formation in solution was only partially observed, as illustrated in Figure D.3.

The absorption and emission spectra in solution of HOba **18** and of Al(Oba)$_3$ **19** are illustrated in Figure 3.31. The absorption spectrum of HOba **18** and of Al(Oba)$_3$ **19** in solution has a different pattern compared to that of HOp **3** and of Al(Op)$_3$ **4**. Nonetheless, the same two bands, in the region between 325 and 475 nm, are observed. These bands are associated to $n \rightarrow \pi^*$ and $\pi \rightarrow \pi^*$ transitions localized on the phenalenyl core of HOba **18**. On the contrary, the bands observed in the UV region at ≈250 nm correspond to $\pi \rightarrow \pi^*$ transitions, most probably localized on the whole ligand. Similarly to HOp **3** and Al(Op)$_3$ **4**, an intense structured band with a maximum at 461 nm is detected in the emission spectra of HOba **18** and of Al(Oba)$_3$ **19**. Finally, Al(Oba)$_3$ **19** was grown onto a quartz substrate; the spectra are shown in Figure 3.31. The absorption spectra in solution and in thin film are identical, confirming that the molecule was deposited on quartz successfully. On the other hand, the emission spectrum of Al(Oba)$_3$ **19** is dominated by a red-shifted emission, with a maximum at 591 nm, arising from excimers.

80

(a)   (b)
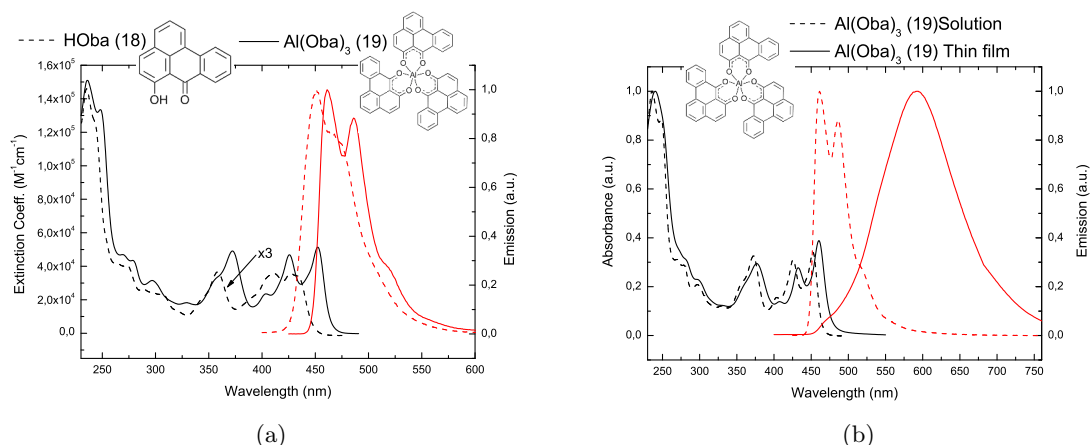
Figure 3.31: (a) Absorption (black) and fluorescence (red) spectra at room temperature in diluted DCM solution of HOba **18** and Al(Oba)$_3$ **19**. (b) Absorption (black) and fluorescence (red) spectra at room temperature in solution and in thin film of Al(Oba)$_3$ **19**.

In spite of the asymmetric geometry of HOba **18**, the excimers formation is not hindered in Al(Oba)$_3$ **19** thin film.

(a)   (b)
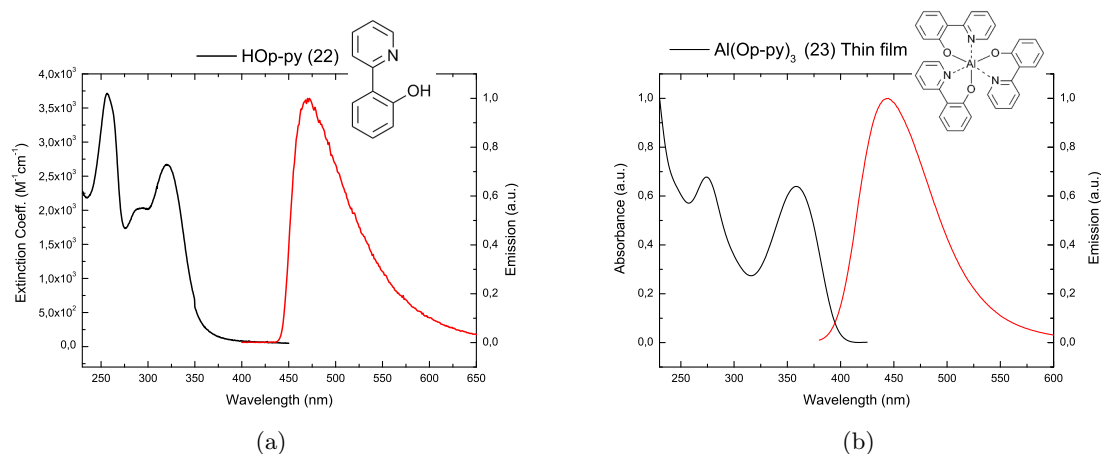
Figure 3.32: (a) Absorption (black) and fluorescence (red) spectra at room temperature in diluted DCM solution of HOp−py **22** .(b) Absorption (black) and fluorescence (red) spectra at room temperature in solid state of Al(Op−py)$_3$ **23**.

Figure 3.32 illustrates the absorption and emission spectra in solution of HOp−py **22**. Due to the structural analogy between HOp−py **22** and Hq **26**, the absorption and emission spectra of the two ligands in solution are similar. Two characteristic bands are observed in the absorption spectrum, corresponding to $\pi \rightarrow \pi^*$ transitions. The emission spectrum of HOp−py **22** shows a fluorescence band at ≈475 nm. Al(Op−py)$_3$ **23** is insoluble in all the solvents, therefore, it was impossible to measure the absorption and emission spectra in solution. Nevertheless, Al(Op−py)$_3$ **23** was grown onto a quartz substrate and its spectra, illustrated in Figure 3.32, were recorded. The two bands observed in the absorption spectrum are related to the $\pi \rightarrow \pi^*$ transitions localized on the ligands. The maximum of the emission in the thin film of Al(Op−py)$_3$ **23** is 445 nm.

The absorption and emission spectra of tropolone **24** and of Al(Trop)$_3$ **25** in solution are illus-

Figure 3.33: (a) Absorption (black) and fluorescence (red) spectra at room temperature in diluted DCM solution of Tropolone **24** and Al(Trop)$_3$ **25**. (b) Absorption (black) and fluorescence (red) spectra at room temperature in diluted DCM solution of Al(q$_2$Acac) **28**.

trated in Figure 3.33. The absorption spectrum of tropolone **24** derives from the characteristic carbonyl group [180]. Clearly, the absorption spectra of tropolone **24** and of Al(Trop)$_3$ **25** are characterized by the same three bands. As a consequence, we can presume that the absorption transitions in Al(Trop)$_3$ **25** are mainly localized on the tropolonates. In detail, the structured band between 350 and 400 nm can be attributed to $n \rightarrow \pi^*$ transitions, and the bands observed between 275 and 350 nm and in the UV region ($\approx$250 nm) are assigned to $\pi \rightarrow \pi^*$ transitions. The emission spectra of Al(Trop)$_3$ **25** is characterized by a narrow fluorescence emission peaked at 456 nm.

Figure 3.33 illustrates the absorption and emission spectra of Al(q$_2$Acac) **28** in solution. The absorption spectrum of Al(q$_2$Acac) **28** is identified by quinolinate centered bands. In detail, the first band is observed at 380 nm and the second band at 260 nm. Both the bands correspond to $\pi \rightarrow \pi^*$ transitions localized on the quinolinate. An additional band is observed at 300 nm. This band is assigned to a $n \rightarrow n^*$ transition localized on the acetyl acetonate moiety. The emission spectrum of Al(q$_2$Acac) **28** shows an intense fluorescence band with a maximum at 508 nm.

In Figure 3.34 are illustrated the absorption, emission and excitation spectra of Al(q$_2$Op) **29** in solution. The absorption spectrum is characterized by the characteristic absorption bands of Hq **26** and HOp **3**. Between 400 and 475 nm and between 325 and 375 nm is visible the phenalenyl absorption profile. In addition, between 375 and 400 nm and at 250 nm, the absorption of the quinolinates can be observed. Interestingly, as a result of the insertion of the phenalenyl, the emission profile of Al(q$_2$Op) **29** depends from the excitation wavelength. This is clear when the molecule is excited at 430 nm. Here, solely the phenalenyl moiety absorbs the excitation light, and thus, the emission pattern resembles the emission of HOp **3** and Al(Op)$_3$ **4**. At lower wavelengths both ligands absorb the incident light, hence, the overall emission arises from a combination between the emission of the quinolinate and the phenalenyl. Indeed, in the excitation spectra, at wavelengths higher than 550 nm, the emission origins only from the quinolinate, and thus, the absorption of the phenalenyl disappears.

Figure 3.35 illustrates the absorption, emission and excitation spectra of Al(q$_2$Trop) **30** in solution. The absorption spectrum of Al(q$_2$Trop) **30** is a combination of the absorptions of the quinolinate and tropolonate. As an example, the bands between 350 and 400 nm and between

Figure 3.34: (a) Absorption (black) and fluorescence (red) spectra at room temperature in diluted DCM solution of Al(q$_2$Op) **29**. (b) Excitation spectra at room temperature in diluted DCM solution of Al(q$_2$Op) **29**.

Figure 3.35: (a) Absorption (black) and fluorescence (red) spectra at room temperature in diluted DCM solution of Al(q$_2$Trop) **30**. (b) Excitation spectra at room temperature in diluted DCM solution of Al(q$_2$Trop) **30**.

300 and 350 nm are localized on the tropolonate. On the contrary, the small absorption at 400 nm is localized on the quinolinates. The emission spectrum of Al(q$_2$Trop) **30** remains almost constant in relation to the excitation wavelength. Due to the superimposition of the quinolinate and tropolonate absorption spectra, it was impossible to excite selectively one of the ligands. Therefore, the emission spectra of Al(q$_2$Trop) **30** are a combination between the emission of both moieties. In the resulting excitation spectra, the absorption bands exhibit only a slight variation of the relative intensities in function of the emission wavelength.
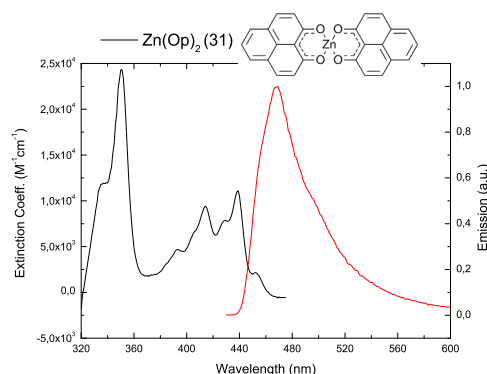
Figure 3.36: Absorption (black) and fluorescence (red) spectra at room temperature in diluted THF solution of Zn(Op)$_2$ **31**.

The absorption and emission spectra of Zn(Op)$_2$ **31** in diluted THF solution are illustrated in Figure 3.36. The absorption spectrum shows the characteristic bands of the phenalenyl. More in detail, the first band between 380 and 460 nm is assigned to $n \rightarrow \pi^*$ transitions, and the second band peaked at 350 nm is attributed to $\pi \rightarrow \pi^*$ transitions. The emission spectrum of Zn(Op)$_2$ **31** is dominated by an unstructured intense fluorescence emission band at 469 nm characterized by a long tail presumably caused by the emission of excimers which can form in solution due to the flat geometry of Zn(Op)$_2$ **31**.

In Table 3.5 are listed absorption peaks λ_{max}^{abs} with their extinction coefficient ϵ and emission peaks λ_{max}^{emi} of the ligands used in the synthesis of the (novel) OSCs. Comparing the absorption peaks of the halogenated ligands HOp$-$X **5a**–**d** with the peaks of HOp **3**, only minor differences can be noticed. The absorption peaks are few nm shifted toward higher wavelengths, and, in addition, their extinction coefficients ϵ have the same order of magnitude. As an example the extinction coefficient of the first absorption peak of the halogenated ligands HOp$-$X **5a**–**d** (ϵ_{451}^{HOp-F}, ϵ_{451}^{HOp-Cl}, ϵ_{450}^{HOp-Br}, and ϵ_{452}^{HOp-I}) is between 6.9×10^3 and $1.0 \times 10^4\,\mathrm{M^{-1}\,cm^{-1}}$, close to that of HOp **3**, $\epsilon_{439} = 9.0 \times 10^4\,\mathrm{M^{-1}\,cm^{-1}}$. Similarly, the extinction coefficient of the first absorption peak of the substituted ligands HOp$-$R **15a**–**c** (ϵ_{454}^{HOp-p}, ϵ_{448}^{HOp-n}, and ϵ_{448}^{HOp-pe}) is between 7.6×10^3 and $7.9 \times 10^3\,\mathrm{M^{-1}\,cm^{-1}}$, comparable to that of ϵ of HOp **3**, $\epsilon_{439} = 9.0 \times 10^4\,\mathrm{M^{-1}\,cm^{-1}}$. However, the absorption peaks of the substituted ligands HOp$-$R **15a**–**c** below 300 nm originate from the substituent, and thus, their extinction coefficient ϵ is not comparable with HOp **3**. Obviously, the halogenation and substitution of HOp **3** is not strongly affecting the absorption transitions localized of the phenalenyl-based ligands.

The absorption peaks of HOba **18**, in the region between 350 and 460 nm, have similar extinction coefficients ϵ to those of HOp **3** in the same region. As an example, the first absorption peak at 459 nm has an extinction coefficient, $\epsilon_{459} = 9.1 \times 10^3\,\mathrm{M^{-1}\,cm^{-1}}$, which is virtually identical to the extinction coefficient, $\epsilon_{439} = 9.0 \times 10^3\,\mathrm{M^{-1}\,cm^{-1}}$, of the first absorption peak at 439 nm of HOp **3**. This means that the absorption transition is probably located on the phenalenyl core of HOba **18**. In contrast, the peak at 235 nm has an extinction coefficient,

Table 3.5: List of the absorption and emission peaks of the studied ligands. In the parenthesis is reported the extinction coefficient ϵ relative to the absorption peak.

Compound		λ_{max}^{abs} (ϵ) [nm] ([M^{-1} cm^{-1}])	λ_{max}^{emi} [nm]
Hq, **26**	Solution	243 (4.7×10^4), 314 (3.1×10^3)	468
HOp, **3**	Solution	235 (2.6×10^4), 351 (1.8×10^4), 415 (7.9×10^3), 439 (9.0×10^3)	446, 470
HOp−F, **5a**	Solution	236 (1.8×10^4), 347 (1.6×10^4), 426 (6.7×10^3), 451 (6.9×10^3)	460, 483
HOp−Cl, **5b**	Solution	245 (3.1×10^4), 349 (2.0×10^4), 425 (7.7×10^3), 451 (8.2×10^3)	484
HOp−Br, **5c**	Solution	248 (4.0×10^4), 350 (2.6×10^4), 425 (9.7×10^3), 450 (1.0×10^4)	461, 483
Hp−I, **5d**	Solution	251 (3.4×10^4), 352 (2.3×10^4), 426 (8.0×10^3), 452 (8.9×10^3)	465, 485, 600
HOp−p, **15a**	Solution	277 (4.8×10^4), 356 (2.1×10^4), 429 (7.0×10^3), 454 (7.6×10^3)	480
HOp−n, **15b**	Solution	295 (2.1×10^4), 356 (2.1×10^4), 424 (7.5×10^3), 448 (7.9×10^3)	491
HOp−pe, **15c**	Solution	298 (7.8×10^4), 356 (2.1×10^4), 424 (7.5×10^3), 448 (7.9×10^3)	491
HOba, **18**	Solution	235 (4.9×10^4), 358 (2.2×10^4), 434 (8.2×10^3), 459 (9.1×10^3)	486
HOp−py, **22**	Solution	257 (3.7×10^3), 320 (2.7×10^3)	470
Tropolone, **24**	Solution	320 (9.5×10^3), 353 (5.6×10^3), 370 (5.3×10^3)	462

$\epsilon_{235}= 4.9 \times 10^4 \, \text{M}^{-1} \, \text{cm}^{-1}$, about two times higher than the extinction coefficient of the same absorption peak of HOp **3**, $\epsilon_{235}= 2.6 \times 10^3 \, \text{M}^{-1} \, \text{cm}^{-1}$. Hence, these absorption transitions might have a different origin. The extinction coefficient of the absorption peak of HOp−py **22** at 320 nm, $\epsilon_{320}= 2.7 \times 10^3 \, \text{M}^{-1} \, \text{cm}^{-1}$, is comparable to the extinction coefficient of the corresponding absorption peak of Hq **26** at 314 nm, $\epsilon_{314}= 3.1 \times 10^3 \, \text{M}^{-1} \, \text{cm}^{-1}$. Conversely, the extinction coefficient of the absorption peak of HOp−py **22** at 257 nm, $\epsilon_{257}= 3.7 \times 10^3 \, \text{M}^{-1} \, \text{cm}^{-1}$, is one order of magnitude lower than the the extinction coefficient of the corresponding absorption peak of Hq **26** at 243 nm, $\epsilon_{243}= 4.7 \times 10^4 \, \text{M}^{-1} \, \text{cm}^{-1}$. This suggests that the first absorption transitions of HOp-py **22** and Hq **26** have similar pathways. In contrast the second absorption transition has a different origin. At last, the extinction coefficient ϵ of the absorption peaks of tropolone **24** are ranging between 5.3×10^3 and $9.5 \times 10^3 \, \text{M}^{-1} \, \text{cm}^{-1}$, comparable with those of the other studied ligands. However, due to the different structure of tropolone **24**, a direct comparison between its extinction coefficients ϵ and those of the other ligands is impossible.

Table 3.6 lists all the absorption peaks with their extinction coefficient ϵ and the emission peaks λ_{max}^{emi} of the (novel) OSCs. The comparison between the extinction coefficients ϵ of the halogenated and substituted complexes, Al(Op−X)$_3$ **6a**–**d** and Al(Op−R)$_3$ **16a**–**c**, and of Al(Op)$_3$ **4** yields to the same observation described for the halogenated and substituted ligands, HOp−X **5a**–**d** and HOp−R **15a**–**c**, and HOp **3**. Similarly, the observations on the extinction coefficients ϵ of the peaks for the ligands HOba **18** and tropolone **24** are identical to those for Al(Oba)$_3$ **19** and Al(Trop)$_3$ **25**.

Comparing the two tables, Table 3.5 and Table 3.6, it can be noted that the extinction coefficient ϵ of an absorption peak of a complex is about 3-5 times that of the corresponding absorption peak of its ligand. Since a complex is formed by three ligands, its extinction coefficient ϵ is roughly the sum of the extinction coefficient ϵ of three ligands. As an example the first absorption peak of Alq$_3$ has an extinction coefficient, $\epsilon_{385}= 1.1 \times 10^4 \, \text{M}^{-1} \, \text{cm}^{-1}$, which is 3.5 times the extinction coefficient of the first absorption peak of Hq **26**, $\epsilon_{314}= 3.1 \times 10^3 \, \text{M}^{-1} \, \text{cm}^{-1}$. For Al(Op)$_3$ **4**, the extinction coefficient of the first absorption peak, $\epsilon_{454}= 4.4 \times 10^4 \, \text{M}^{-1} \, \text{cm}^{-1}$, is about 4.9 times the extinction coefficient of the first absorption peak of HOp **3**, $\epsilon_{439}= 9.0 \times 10^3 \, \text{M}^{-1} \, \text{cm}^{-1}$. The same trend is observable for the halogenated complexes Al(Op−X)$_3$ **6a**–**d**, which have extinction coefficient of the first absorption peak ($\epsilon_{469}^{Al(Op-F)_3}= 5.1 \times 10^4 \, \text{M}^{-1} \, \text{cm}^{-1}$, $\epsilon_{467}^{Al(Op-Cl)_3}= 4.8 \times 10^4 \, \text{M}^{-1} \, \text{cm}^{-1}$, $\epsilon_{467}^{Al(Op-Br)_3}= 4.6 \times 10^4 \, \text{M}^{-1} \, \text{cm}^{-1}$, and $\epsilon_{468}^{Al(Op-I)_3}= 4.8 \times 10^4 \, \text{M}^{-1} \, \text{cm}^{-1}$) between 4.6 and 7.4 times that of the corresponding absorption peak of their respective ligands ($\epsilon_{451}^{HOp-F}= 6.9 \times 10^3 \, \text{M}^{-1} \, \text{cm}^{-1}$, $\epsilon_{451}^{HOp-Cl}= 8.2 \times 10^3 \, \text{M}^{-1} \, \text{cm}^{-1}$, $\epsilon_{450}^{HOp-Br}= 1.0 \times 10^4 \, \text{M}^{-1} \, \text{cm}^{-1}$, and $\epsilon_{452}^{HOp-I}= 8.9 \times 10^3 \, \text{M}^{-1} \, \text{cm}^{-1}$). The extinction coefficient ϵ of the first absorption peak of the substituted complexes Al(Op−R)$_3$ **16a**–**c** ($\epsilon_{470}^{Al(Op-p)_3}= 3.0 \times 10^4 \, \text{M}^{-1} \, \text{cm}^{-1}$, $\epsilon_{464}^{Al(Op-n)_3}= 2.9 \times 10^4 \, \text{M}^{-1} \, \text{cm}^{-1}$, and $\epsilon_{475}^{Al(Op-pe)_3}= 3.6 \times 10^4 \, \text{M}^{-1} \, \text{cm}^{-1}$) is between 3.7 and 4.6 times that of the corresponding absorption peaks of their respective ligands ($\epsilon_{454}^{HOp-p}= 7.6 \times 10^3 \, \text{M}^{-1} \, \text{cm}^{-1}$, $\epsilon_{448}^{HOp-n}= 7.9 \times 10^3 \, \text{M}^{-1} \, \text{cm}^{-1}$, and $\epsilon_{448}^{HOp-pe}= 7.9 \times 10^3 \, \text{M}^{-1} \, \text{cm}^{-1}$). In the case of Al(Oba)$_3$ **19** the extinction coefficient of the first absorption peak, $\epsilon_{452}= 5.1 \times 10^4 \, \text{M}^{-1} \, \text{cm}^{-1}$, is about 5.6 times higher than the extinction coefficient of the same peak of HOba **18**, $\epsilon_{459}= 9.1 \times 10^3 \, \text{M}^{-1} \, \text{cm}^{-1}$. In the same way, the extinction coefficient of the first absorption peak of Al(Trop)$_3$ **25**, $\epsilon_{384}= 2.9 \times 10^4 \, \text{M}^{-1} \, \text{cm}^{-1}$, is about 5.5 times higher than that of the first absorption peak of tropolone **24**, $\epsilon_{370}= 5.3 \times 10^3 \, \text{M}^{-1} \, \text{cm}^{-1}$.

The mixed ligands Al(q$_2$Acac) **28**, Al(q$_2$Op) **29** and Al(q$_2$Trop) **30** are characterized by absorption spectra which are a combination between the absorption of their ligands. As an example, the spectra of Al(q$_2$Acac) **28** is composed by the absorption of the two quinolinates plus the absorption of the acetyl acetonate. Hence, the extinction coefficient ϵ of a peak in Alq$_3$ should be

Table 3.6: List of the absorption and emission peaks of the (novel) OSCs. In the parenthesis is reported the extinction coefficient of the absorption peak.

Compound		λ_{max}^{abs} (ϵ) [nm] ([$M^{-1}\,cm^{-1}$])	λ_{max}^{emi} [nm]
Alq_3	Solution	244 (9.7×10^4), 259 (1.4×10^5), 385 (1.1×10^4)	517
Alq_3	Thin film	266, 393	523
$Al(Op)_3$, **4**	Solution	244 (9.3×10^4), 362 (9.1×10^4), 427 (3.5×10^4), 454 (4.4×10^4)	458, 486
$Al(Op)_3$, **4**	Thin film	244, 366, 435, 463	583
$Al(Op-F)_3$, **6a**	Solution	244 (9.4×10^4), 358 (9.0×10^4), 440 (4.1×10^4), 469 (5.1×10^4)	473, 504
$Al(Op-Cl)_3$, **6b**	Solution	253 (1.2×10^5), 359 (1.0×10^5), 439 (4.0×10^4), 467 (4.8×10^4)	472, 502
$Al(Op-Br)_3$, **6c**	Solution	255 (1.4×10^5), 359 (1.0×10^5), 439 (3.9×10^4), 467 (4.6×10^4)	474, 502
$Al(Op-I)_3$, **6d**	Solution	259 (1.5×10^5), 361 (1.2×10^5), 440 (3.8×10^4), 468 (4.8×10^4)	478, 504, 571
$Al(Op-p)_3$, **16a**	Solution	284 (1.7×10^5), 364 (1.0×10^4), 443 (2.6×10^4), 470 (3.0×10^4)	486
$Al(Op-p)_3$, **16a**	Thin film	287, 368, 452, 470	537
$Al(Op-n)_3$, **16b**	Solution	297 (9.3×10^4), 366 (9.9×10^4), 438 (2.4×10^4), 464 (2.9×10^4)	492
$Al(Op-pe)_3$, **16c**	Solution	308 (2.0×10^5), 363 (1.2×10^5), 448 (2.9×10^4), 475 (3.6×10^4)	493
$Al(Oba)_3$, **19**	Solution	236 (1.5×10^5), 372 (4.9×10^4), 426 (4.7×10^4), 452 (5.1×10^4)	461, 486
$Al(Oba)_3$, **19**	Thin Film	240, 378, 432, 481	591
$Al(Op-py)_3$, **23**	Thin Film	274, 358	445
$Al(Trop)_3$, **25**	Solution	242 (1.1×10^5), 327 (4.8×10^4), 375 (3.0×10^4), 384 (2.9×10^4)	456
$Al(q_2Acac)$, **28**	Solution	257 (1.3×10^5), 296 (3.4×10^4), 374 (8.0×10^3)	512
$Al(q_2Op)$, **29**	Solution	246 (5.2×10^4), 256 (5.4×10^4), 361 (2.2×10^4), 429 (8.7×10^3), 456 (1.2×10^4)	463, 486[a]
$Al(q_2Trop)$, **30**	Solution	246 (4.7×10^4), 320 (1.3×10^4), 376 (9.0×10^3), 384 (8.3×10^3)	489[a]
$Zn(Op)_2$, **31**	Solution	351 (2.4×10^4), 414 (9.4×10^3), 439 (1.1×10^4)	469

. [a] Excitation at 350 nm

about 1.5 times higher of the extinction coefficient ϵ of the same peak in Al(q$_2$Acac) **28**. As an example, the peak at 385 nm has an extinction coefficient for Alq$_3$, $\epsilon_{385}= 1.1 \times 10^4$ M^{-1} cm^{-1}, which is 1.38 times higher the extinction coefficient of the same peak at 384 nm for Al(q$_2$Acac) **28**, $\epsilon_{384}= 8.0 \times 10^3$ M^{-1} cm^{-1}. Similarly, for Al(q$_2$Op) **29** and Al(q$_2$Trop) **30**, the extinction coefficient ϵ of the peaks deriving from the absorption of the phenalenyl and tropolonate is about one third of that of the corresponding peaks for Al(Op)$_3$ **4** and Al(Trop)$_3$ **25**. As an example, the absorption peak of Al(q$_2$Op) **29** at 456 nm has an extinction coefficient $\epsilon_{456}=$ 1.2×10^4 M^{-1} cm^{-1}, which is 0.27 times that of the corresponding absorption peak for Al(Op)$_3$ **4** at 454 nm, $\epsilon_{454}= 4.4 \times 10^4$ M^{-1} cm^{-1}. Likewise, for Al(q$_2$Trop) **30**, the peak at 384 nm has an extinction coefficient, $\epsilon_{384}= 8.3 \times 10^3$ M^{-1} cm^{-1}, which is 0.29 times the extinction coefficient of the corresponding peak at 384 nm for Al(Trop)$_3$ **25**, $\epsilon_{384}= 2.9 \times 10^4$ M^{-1} cm^{-1}. At last, the absorption spectrum of Zn(Op)$_2$ **31** was recorded in THF, and thus, it is not possible to compare its extinction coefficient ϵ with that of the corresponding ligand HOp **3** and of Al(Op)$_3$ **4**, which were characterized in DCM.
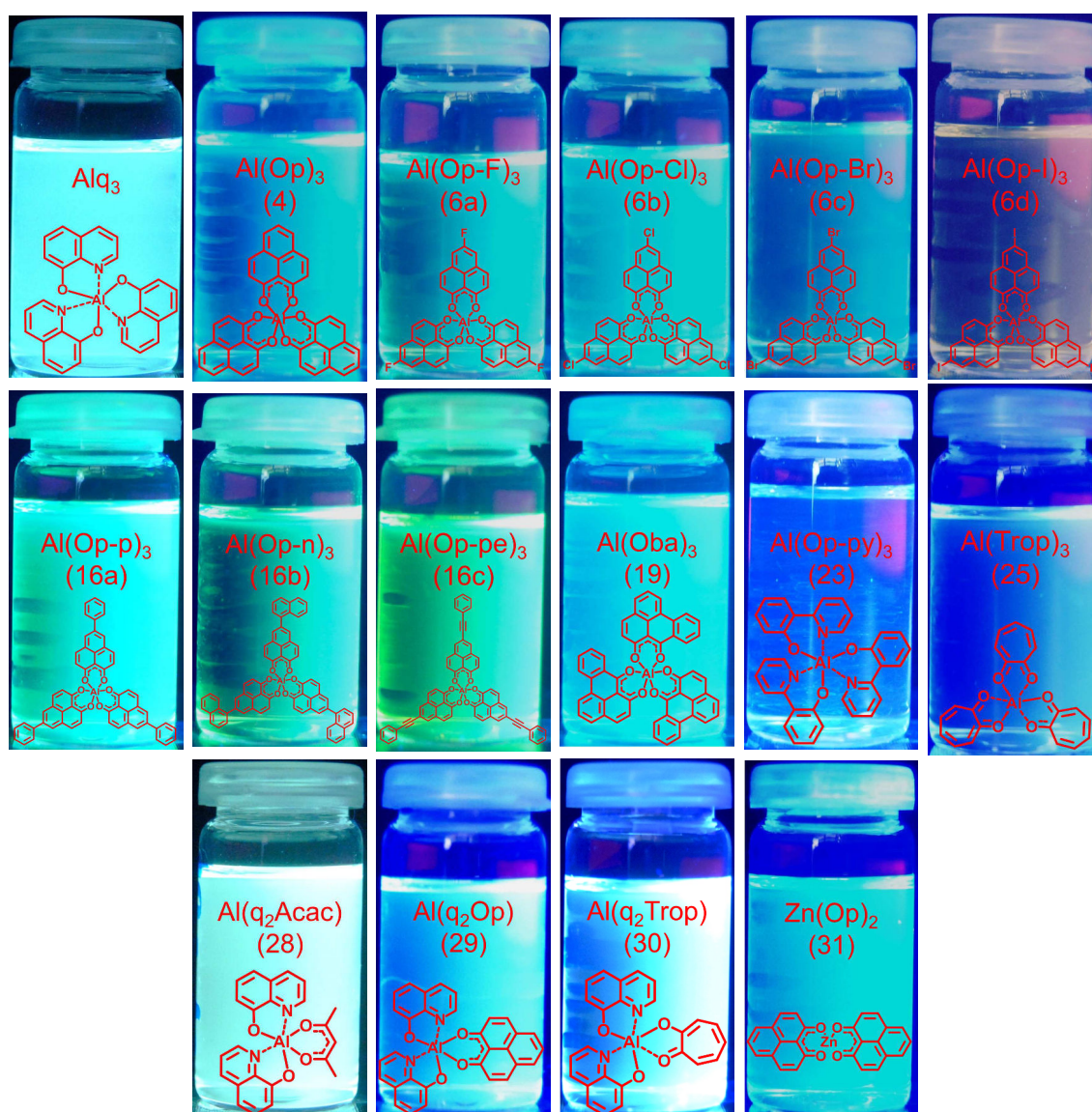
Figure 3.37: Fluorescence emission in solution of the (novel) OSCs studied.

3.5 Electrochemical characterization

Solution electrochemistry methods are known to prove insight into electron-transfer reactions in the condensed phase [184]. We have measured the cyclic voltammetries (CVs) of the ligands (see Table 3.1) and complexes (see Table 3.2) in solution to determine their reduction potentials $E_{1/2}^{red}$. CVs of the phenalenyl-based OSCs show clear reduction waves, however, no oxidation processes were recorded. Therefore, in order to compare the results we have illustrated and discussed only the cathodic processes of the CVs. In addition, from the reduction potential it is possible to estimate the LUMO energy levels. The values of the reduction potentials $E_{1/2}^{red}$ and the LUMO energies E_{LUMO} are listed in Table 3.7 and Table 3.8.
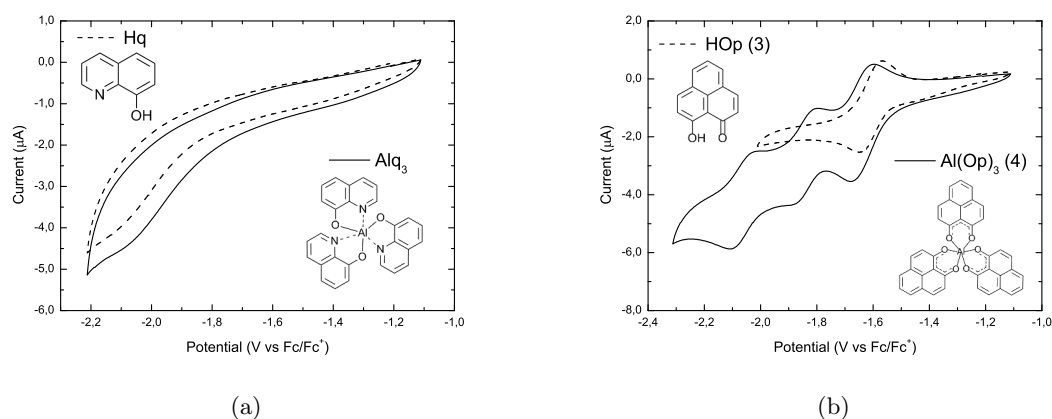
Figure 3.38: (a) Cathodic cyclic voltammogram at room temperature in DCM of Hq **26** and Alq$_3$. Electrolyte: TBAPF$_6$. Scan rate: $100\,\mathrm{mV\,s^{-1}}$. (b) Cathodic cyclic voltammogram at room temperature in DCM of HOp **3** and Al(Op)$_3$ **4**. Electrolyte: TBAPF$_6$. Scan rate: $100\,\mathrm{mV\,s^{-1}}$.

The cathodic cyclic voltammograms of Hq **26** and Alq$_3$, illustrated in Figure 3.38, are both characterized by a single irreversible reduction process. The reduction of Hp **26** and Alq$_3$ takes place at quite negative potentials. In detail, the onset of the reduction of Hp is at $-1.87\,\mathrm{V}$ and of Alq$_3$ is at $-1.79\,\mathrm{V}$. The small difference between the reduction potential of Hq **26** and Alq$_3$ clearly indicates that the electro-active species in Alq$_3$ is the quinolinate. As illustrated in Figure 3.38, the cathodic cyclic voltammogram of HOp **3** and Al(Op)$_3$ **4** is characterized by quasi-reversible reduction processes. The reduction potential of HOp **3** is $-1.60\,\mathrm{V}$, at a quite positive potential compared to that of Hq **26**. Most probably, the reason is the bigger aromatic system of HOp **3**, which can delocalize efficiently the additional electron. The cathodic cyclic voltammogram of Al(Op)$_3$ **4** shows three-quasi reversible reduction waves at -1.63, -1.84 and $-2.07\,\mathrm{V}$. These waves correspond to the formation of the mono-, di- and trianion, where the electrons are systematically transferred to each phenalenyl. Usually, the same effect is observed in molecules with several electro-active sites in resonance [185–187].

Figure 3.39 illustrates the cathodic cyclic voltammograms of the halogenated ligands HOp−X **5a**–**d**. As expected, due to the electron-withdrawing character of the halogen atoms, the reduction potentials of the halogenated ligands HOp−X **5a**–**d**, between -1.51 and $-1.47\,\mathrm{V}$, are more positive than that of HOp **3**. Interestingly, the nature of the halogen atom exhibits a negligible effect on the reduction potentials. As an example, the reduction potentials of HOp−F **5a** and HOp−I **5d** are $-1.51\,\mathrm{V}$ and $-1.48\,\mathrm{V}$, respectively. The cathodic cyclic voltammograms of the halogenated complexes Al(Op−X)$_3$ **6a**–**d** are illustrated in Figure 3.39. The three reduction

(a)

(b)
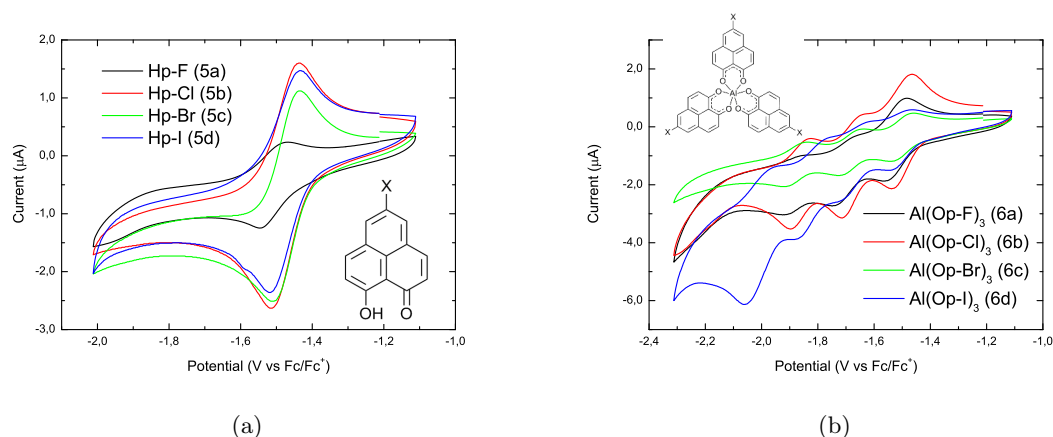
Figure 3.39: (a) Cathodic cyclic voltammogram at room temperature in DCM of the halogenated ligands HOp−X **5a**–**d**. Electrolyte: TBAPF$_6$. Scan rate: $100\,\mathrm{mV\,s^{-1}}$. (b) Cathodic cyclic voltammogram at room temperature in DCM of the halogenated complexes Al(Op−X)$_3$ **6a**–**d**. Electrolyte: TBAPF$_6$. Scan rate: $100\,\mathrm{mV\,s^{-1}}$.

waves correspond to the formation of the mono-, di- and tri-anion, as previously described for Al(Op)$_3$ **4**. In addition, the halogen atoms cause the reduction potential to shift to more positive values than those of the three reductions of Al(Op)$_3$ **4**. The first reduction potential ranges between −1.49 and −1.52 V, the second reduction potential is between −1.66 and −1.70 V, and, the third reduction potential varies from a minimum of −1.82 V and a maximum of −1.89 V. As previously observed for the halogenated ligands HOp−X **5a**–**d**, the reduction potential of the halogenated complexes Al(Op−X)$_3$ **6a**–**d** is characterized by small fluctuations in relation to the halogen atom nature. At last, Al(Op−I)$_3$ **6d** is characterized by an additional quasi-reversible wave at −2.01 V. This wave can be associated to the reduction of the C-I bonds, which can lead to the cleavage of the iodine atom [188, 189].

(a)

(b)
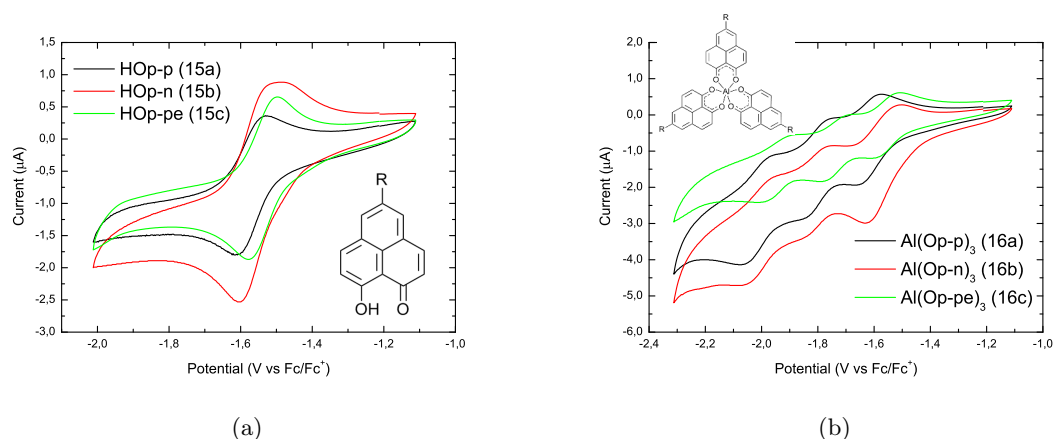
Figure 3.40: (a) Cathodic cyclic voltammogram at room temperature in DCM of the substituted ligands HOp−R **15a**–**c**. Electrolyte: TBAPF$_6$. Scan rate: $100\,\mathrm{mV\,s^{-1}}$. (b) Cathodic cyclic voltammogram at room temperature in DCM of Al(Op−R)$_3$ **16a**–**c**. Electrolyte: TBAPF$_6$. Scan rate: $100\,\mathrm{mV\,s^{-1}}$.

Figure 3.40 illustrates the cathodic cyclic voltammograms of the substituted ligands HOp−R **15a**–**c**. The reduction potential of the substituted ligands HOp−R **15a**–**c** is comprised between

a minimum of $-1.54\,\mathrm{V}$ and a maximum of $-1.57\,\mathrm{V}$. These values are close to the reduction potential of HOp **3**. Hence, we can conclude that the presence of additional aromatic system is ineffective to considerably modify the electrochemical behavior of HOp **3**. Moreover, no additional reduction wave involving the aromatic substituents is recorded. As shown in Figure 3.40, the cathodic cyclic voltammograms of the substituted complexes $\mathrm{Al(Op-R)_3}$ **16a–c** are characterized by three reduction waves. The reduction potential of the three processes is similar to that of the corresponding processes for $\mathrm{Al(Op)_3}$ **4**. In detail, the first reduction potential of the substituted complexes $\mathrm{Al(Op-R)_3}$ **16a–c** ranges between -1.55 and $-1.62\,\mathrm{V}$, the second between -1.73 and $-1.80\,\mathrm{V}$, and the third between -1.94 and $-2.02\,\mathrm{V}$. In view of these results, we can presume that the phenalenyl moiety and the aromatic substituents are electronically decoupled.

(a)   (b)
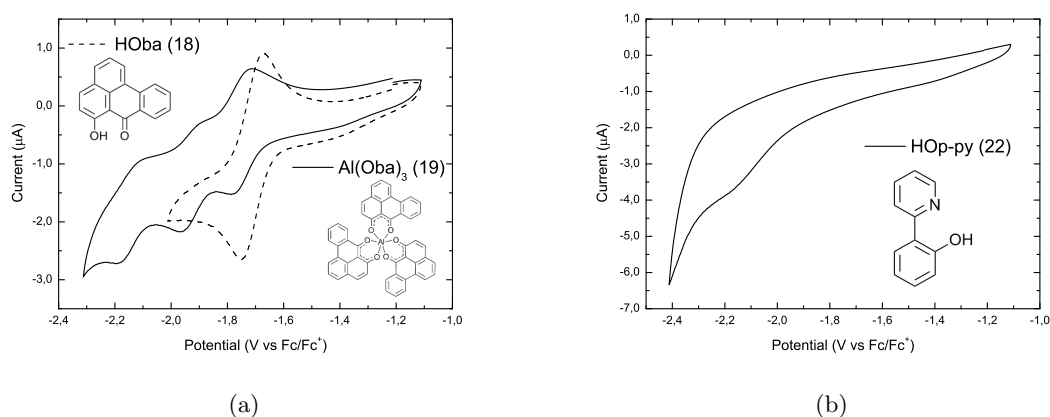
Figure 3.41: (a) Cathodic cyclic voltammogram at room temperature in DCM of HOba **18** and of $\mathrm{Al(Oba)_3}$ **19**. Electrolyte: $\mathrm{TBAPF_6}$. Scan rate: $100\,\mathrm{mV\,s^{-1}}$. (b) Cathodic cyclic voltammogram at room temperature in DCM of HOp-py **22**. Electrolyte: $\mathrm{TBAPF_6}$. Scan rate: $100\,\mathrm{mV\,s^{-1}}$.

Figure 3.41 illustrates the cathodic cyclic voltammograms of HOba **18** and $\mathrm{Al(Oba)_3}$ **19**. The cyclic voltammogram of HOba **18** is characterized by a single quasi-reversible reduction wave at $-1.71\,\mathrm{V}$, which is considerably more negative than the reduction potential of HOp **3**. This is unexpected, because, as a consequence of the bigger aromatic system, HOba **18** should be able to delocalize an electron more efficiently than HOp **3**. Hence, it should be characterized by a more positive reduction potential. Three quasi-reversible waves at -1.75, -1.93 and $-2.15\,\mathrm{V}$ are shown in the cathodic cyclic voltammogram of $\mathrm{Al(Oba)_3}$ **19**. The three consecutive reduction processes are at more negative values than those of $\mathrm{Al(Op)_3}$ **4**.

The cathodic cyclic voltammogram of HOp-py **22** is shown in Figure 3.41. Unfortunately, $\mathrm{Al(Op-py)_3}$ **23** is insoluble in all the solvents, therefore, it was impossible to record its voltammogram. Nonetheless, from the CV of HOp-py **22** in solution some observation can be drawn. The cathodic cyclic voltammogram is characterized by a single irreversible reduction wave with an onset of $-1.94\,\mathrm{V}$. The negative reduction potential, most probably, arises from the separated aromatic backbone of HOp-py **22**. In detail, the two separated aromatic rings have a scarce capability to delocalize the additional electron, as a consequence, the reduction potential of HOp-py **22** is more negative compared to the reduction potential of Hq **26**.

The cathodic cyclic voltammograms of tropolone **24** and $\mathrm{Al(Trop)_3}$ **25**, illustrated in Figure 3.42, are characterized by single reduction waves at $-2.06\,\mathrm{V}$ and $-2.10\,\mathrm{V}$, respectively. As expected, due to its small aromatic system, tropolone **24** has the most negative reduction potential.

91

(a)

(b)
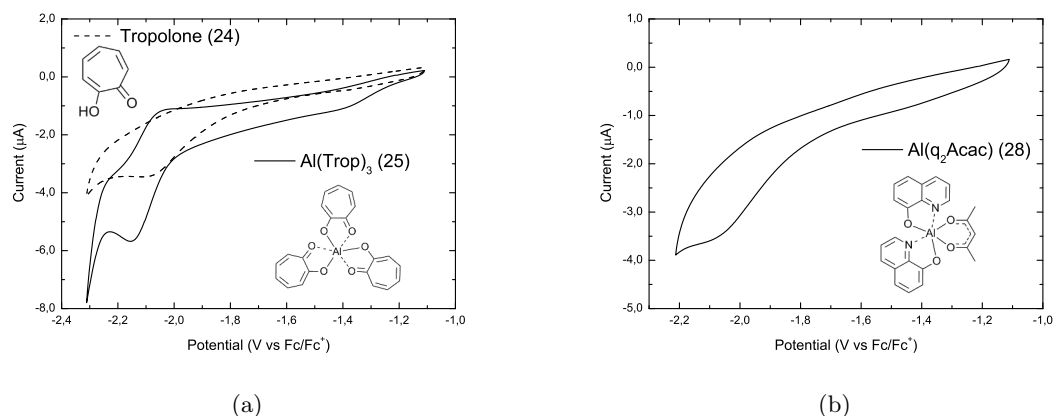
Figure 3.42: (a) Cathodic cyclic voltammogram at room temperature in DCM of tropolone **24** and of Al(Trop)$_3$ **25**. Electrolyte: TBAPF$_6$. Scan rate: $100\,\mathrm{mV\,s^{-1}}$. (b) Cathodic cyclic voltammogram at room temperature in DCM of Al(q$_2$Acac) **28**. Electrolyte: TBAPF$_6$. Scan rate: $100\,\mathrm{mV\,s^{-1}}$.

Moreover, the reduction potentials of the free ligand and the complex are almost identical. This indicates that the electro-active species in Al(Trop)$_3$ **25** is the tropolonate. Successive reductions of the complex, if any, would occur at potentials out of the redox window of our electrochemical system, and thus, they were impossible to record.

Figure 3.42 shows the cathodic cyclic voltammogram of Al(q$_2$Acac) **28**. Al(q$_2$Acac) **28** is characterized by a single irreversible reduction process with an onset of $-1.80\,\mathrm{V}$. Since the electro-active species in Al(q$_2$Acac) **28** is the quinolinate, its reduction potential is almost identical to that of Alq$_3$. Hence, we can conclude that the effect of the acetyl acetonate moiety on the electrochemical properties of Al(q$_2$Acac) **28** is negligible.

(a)

(b)
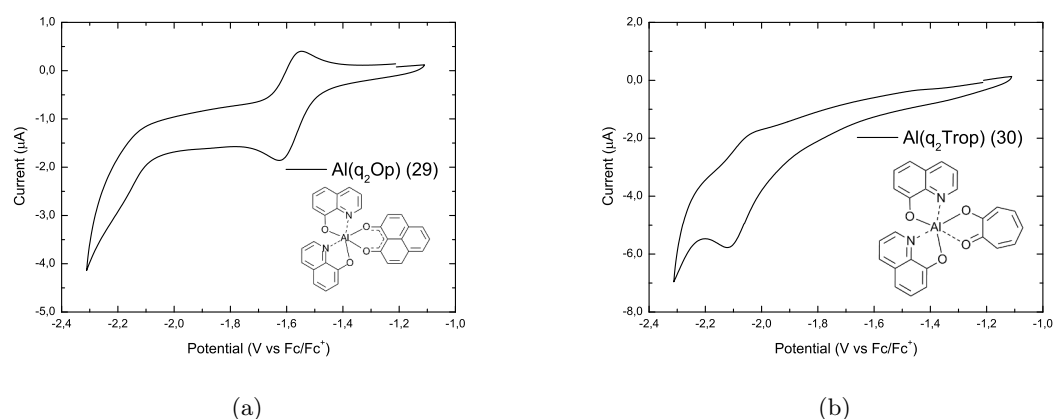
Figure 3.43: (a) Cathodic cyclic voltammogram at room temperature in DCM of Al(q$_2$Op) **29**. Electrolyte: TBAPF$_6$. Scan rate: $100\,\mathrm{mV\,s^{-1}}$. (b) Cathodic cyclic voltammogram at room temperature in DCM of Al(q$_2$Trop) **30**. Electrolyte: TBAPF$_6$. Scan rate: $100\,\mathrm{mV\,s^{-1}}$.

The cathodic cyclic voltammogram of Al(q$_2$Op) **29**, shown in Figure 3.43, is characterized by a single quasi-reversible reduction wave at $-1.58\,\mathrm{V}$ and an irreversible wave with an onset of $-2.08\,\mathrm{V}$. Since Al(q$_2$Op) **29** is formed by two quinolinates and one phenalenyl, which are both

electro-active, we can discriminate on which moiety are localized the reduction processes. The first quasi-reversible reduction process occurs at $-1.58\,\text{V}$, similar to the first reduction process of Al(Op)$_3$ **4**. The shape and the potential of the wave strongly suggest that this reduction process is localized on the phenalenyl. Therefore, the second reduction process is localized on one of the two quinolinates. Its extremely negative reduction potential, compared to the reduction of Alq$_3$, is caused by the formation of the mono-anion during the first reduction process, which shifts the second reduction process toward more negative potential.

The cathodic cyclic voltammogram of Al(q$_2$Trop) **30** is illustrated in Figure 3.43. A single quasi-reversible reduction wave at $-2.08\,\text{V}$ is recorded. Since, as previously described for Al(q$_2$Op) **29**, Al(q$_2$Trop) **30** is formed by two electro-active species, we would expect to record two distinct reduction processes. However, only one quasi-reversible wave is observed. The evidence that the wave is quasi-reversible indicates that, most probably, the reduction process takes place on the tropolonate. In addition, the reduction potential of Al(q$_2$Trop) **30** at $-2.08\,\text{V}$ is almost identical to the reduction potential of Al(Trop)$_3$ ($-2.10\,\text{V}$). Nevertheless, due to the negative potential, the simultaneous reduction of one of the two quinolinate can occur.
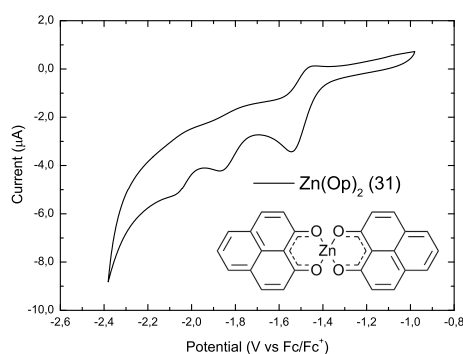
Figure 3.44: Cathodic cyclic voltammogram at room temperature in DMF of Zn(Op)$_2$. Electrolyte: TBAPF$_6$. Scan rate: $100\,\text{mV}\,\text{s}^{-1}$.

Figure 3.44 illustrates the cathodic cyclic voltammogram of Zn(Op)$_2$ in DMF. Three reduction waves are shown with potential of -1.50, -1.81 and $-2.04\,\text{V}$. The first two reduction, which have potentials similar to the potentials of the first two reduction of Al(Op)$_3$ **4**, are assigned to successive reduction processes involving the two phenalenyls. In contrast, the third wave is related to the reduction of Zn^{2+} to Zn$^+$. This reduction takes place at much more negative potential than the reduction of the free ion due to the stability of the complex and donor ability of the ligand [177].

The reduction potentials of the ligands and complexes are listed in Table 3.7 and Table 3.8. Among the studied ligands, due to their small aromatic structures, tropolone **24** and HOp$-$py **22** have the most negative reduction potentials, $-2.06\,\text{V}$ and $-1.94\,\text{V}$, respectively. Similarly, the reduction of Hq **26** occurs at $-1.87\,\text{V}$. Phenalenyl-based ligands are characterized by extended aromatic systems, and thus, their reduction occurs at a more positive potential. The reduction of HOp **3** takes place at $-1.60\,\text{V}$. The halogenated and substituted ligands, HOp$-$X **5a**–**d** and HOp$-$R **15a**–**c**, have reduction potentials between -1.47 and $-1.57\,\text{V}$, slightly more positive than that of HOp **3**. Lastly, the reduction of HOba **18** is at $-1.71\,\text{V}$. The same trend is confirmed by the reduction potentials of the (novel) OSCs studied. Al(Trop)$_3$ **25** is characterized by the most negative reduction potential, $-2.10\,\text{V}$. This value is similar to that of Al(q$_2$Trop) **30**, $-2.08\,\text{V}$, since the electro-active species is the tropolonate. The quinolinate is

Table 3.7: Reduction potentials and HOMO and LUMO energy levels determined experimentally and HOMO and LUMO energy levels calculated with a B3-LYP [83]/def2-TZVPP [90] level of theory.

Compound	Experimental				Calculated		
	$E_{1/2}^{red}$ [V]	E_{LUMO}[a] [eV]	E_{gap}[b] [eV]	E_{HOMO} [eV]	E_{LUMO} [eV]	E_{gap} [eV]	E_{HOMO} [eV]
Hq, **26**	-1.87[c]	-2.93	3.49	-6.42	-1.72	4.25	-5.97
HOp, **3**	-1.60	-3.25	2.76	-6.01	-2.71	3.57	-6.28
HOp−F, **5a**	-1.51	-3.38	2.68	-6.06	-2.91	3.42	-6.34
HOp−Cl, **5b**	-1.48	-3.39	2.67	-6.06	-2.93	3.43	-6.36
HOp−Br, **5c**	-1.47	-3.40	2.68	-6.08	-2.94	3.43	-6.37
Hp−I, **5d**	-1.48	-3.40	2.65	-6.05	-2.93	3.39	-6.32
HOp−p, **15a**	-1.57	-3.30	2.61	-5.91	-2.71	3.37	-6.09
HOp−n, **15b**	-1.55	-3.32	2.64	-5.96	-2.72	3.27	-5.99
HOp−pe, **15c**	-1.54	-3.34	2.56	-5.90	-2.79	3.13	-5.92
HOba, **18**	-1.71	-3.16	2.77	-5.93	-2.53	3.55	-6.08
HOp−py, **22**	-1.94[c]	-2.86	3.49	-6.35	-1.57	4.31	-5.88
Tropolone, **24**	-2.06[c]	-2.74	3.10	-5.84	-2.21	4.16	-6.37

[a] LUMO energy is determined by the onset of the first reduction wave recorded in the CV measurements. [b] HOMO-LUMO gap is determined by the onset of the lowest visible absorption band. [c] Onset value.

the electro-active species in Alq$_3$ and Al(q$_2$Acac) **28**, and thus, they present virtually identical reduction potentials, -1.79 V and -1.80 V, respectively. Three reduction processes are recorded for Al(Op)$_3$ **4** at -1.63 V, -1.84 V and -2.07 V. All the halogenated and substituted derivatives, Al(Op−X)$_3$ **6a**–**d** and Al(Op−R)$_3$ **16a**–**c**, show the same three reduction processes. The effect of the halogenation and substitution of the phenalenyl leads to slightly more positive reduction potentials compared to those of Al(Op)$_3$ **4**. On the contrary, the three reductions of Al(Oba)$_3$ **19**, -1.75 V, -1.93 V and -2.15 V, are at more negative potential than those of Al(Op)$_3$ **4**. Al(q$_2$Op) **29** is reduced two times at -1.58 V and -2.08 V. The first reduction occurs on the phenalenyl, hence, its value is close to the first reduction of Al(Op)$_3$ **4**, while the second reduction process involves the quinolinates. At last, Zn(Op)$_2$ **31** presents three reduction processes at -1.50 V, -1.81 V and -2.04 V which occur on the phenalenyls and, most probably, on the zinc.

3.6   HOMO and LUMO energy levels

HOMO and LUMO energy levels of OSCs play a decisive role in organic-based devices [61, 104, 190]. As described in the introduction of this thesis, the injection of charge carriers from the electrodes into organic layers is strongly affected by the mismatch between HOMO or LUMO and the work function of the electrode (anode or cathode). A large mismatch between HOMO energy level and work function of the anode results in a poor injection of holes. Similarly, a large mismatch between LUMO and work function of the cathode yields a poor injection of electrons. Additionally, in multi-layer devices, hole- and electron-transporting materials also prevent the diffusion of electrons and holes, respectively, acting as electron- and hole-blocking materials. Hence, we have estimated the HOMO and LUMO levels of the ligands and of the OSCs to investigate the relation between their molecular structure and their electronic properties.

Table 3.8: Reduction potentials and HOMO and LUMO energy levels of the (novel) OSCs.

Compound	$E^{red}_{1/2}$ [V]	E_{LUMO}[a] [eV]	E_{gap}[b] [eV]	E_{HOMO} [eV]
Alq_3	-1.79[c]	-3.01	2.82	-5.83
$Al(Op)_3$, **4**	-1.63, -1.84, -2.07	-3.26	2.67	-5.93
$Al(Op-F)_3$, **6a**	-1.52, -1.70, -1.89	-3.35	2.59	-5.94
$Al(Op-Cl)_3$, **6b**	-1.49, -1.68, -1.86	-3.37	2.60	-5.97
$Al(Op-Br)_3$, **6c**	-1.49, -1.68, -1.88	-3.36	2.60	-5.96
$Al(Op-I)_3$, **6d**	-1.50, -1.66, -1.82, -2.01	-3.35	2.58	-5.93
$Al(Op-p)_3$, **16a**	-1.62, -1.79, -2.02	-3.28	2.54	-5.82
$Al(Op-n)_3$, **16b**	-1.57, -1.80, -2.01	-3.33	2.56	-5.89
$Al(Op-pe)_3$, **16c**	-1.55, -1.73, -1.94	-3.31	2.49	-5.80
$Al(Oba)_3$, **19**	-1.75, -1.93, -2.15	-3.12	2.68	-5.80
$Al(Trop)_3$, **25**	-2.10	-2.78	3.14	-5.92
$Al(q_2Acac)$, **28**	-1.80[c]	-3.00	2.87	-5.87
$Al(q_2Op)$, **29**	-1.58, -2.08[c]	-3.31	2.67	-5.98
$Al(q_2Trop)$, **30**	-2.08	-2.84	3.11	-5.95
$Zn(Op)_2$, **31**	-1.50, -1.81, -2.04	-3.38	2.77	-6.15

[a] LUMO energy is determined by the onset of the first reduction wave recorded in the CV measurements. [b] HOMO-LUMO gap is determined by the onset of the lowest visible absorption band. [c] Onset value.

LUMO levels are computed with the empirical relation $E_{LUMO} = -(E^{red} + 4.8)$ eV, where E^{red} is the onset of the first reduction wave in the cyclic voltammogram corrected accordingly to the reduction potential of ferrocene [191]. From the onset of the first band in the absorption spectrum, the optical HOMO-LUMO gap is determined. The onset is defined as the intersection between the baseline and a tangent line that touches the point of inflection. Lastly, HOMO levels are determined by the simple relation $E_{HOMO} = E_{LUMO} - E_{gap}$. Calculated HOMO and LUMO energy levels and HOMO-LUMO gaps are listed in Table 3.7 and Table 3.8 and graphically compared in Figure 3.45.

At first we discuss the relation between structure and HOMO and LUMO energy levels of the ligands listed in Table 3.1. Ligands formed by small aromatic systems, such as Hq **26**, HOp−py **22** and tropolone **24**, have considerably higher LUMO energies than ligands formed by bigger aromatic systems, such as HOp **3** and HOba **18**. Due to its single aromatic system, tropolone **24** has the highest LUMO at −2.74 eV. HOp−py **22** and Hq **26** are structurally similar, and thus, their LUMOs are close, −2.86 eV and −2.93 eV, respectively. HOp **3** and HOba **18** have LUMOs at −3.25 eV and −3.16 eV, respectively. As expected, the extended aromatic system shifts the LUMO at a lowered energy. Surprisingly, HOba **18** has a higher LUMO than HOp **3**. Hq **26** and HOp−py **22** have the lowest HOMOs, −6.42 eV and −6.35 eV, respectively. On the other hand, HOp **3**, HOba **18** and tropolone **24** are characterized by comparable HOMOs, between −5.84 and −6.01 eV. Presumably, the carbonyl group, which characterizes the three ligands, is the reason of increased HOMOs. Halogenated and substituted ligands, HOp−X **5a**–**d** and HOp−R **15a**–**c**, have similar HOMO and LUMO compared to those of the pristine HOp **3**. Both series have slightly lowered LUMOs. The HOMO of the halogenated ligands HOp−X **5a**–**d** is slightly lowered compared to that of HOp **3**. On the contrary, the HOMO of the substituted ligands HOp−R **15a**–**c** is slightly increased compared to that of HOp **3**.

In collaboration with the group of prof. Willem Klopper (INT-KIT, Karlsruhe), the HOMO and
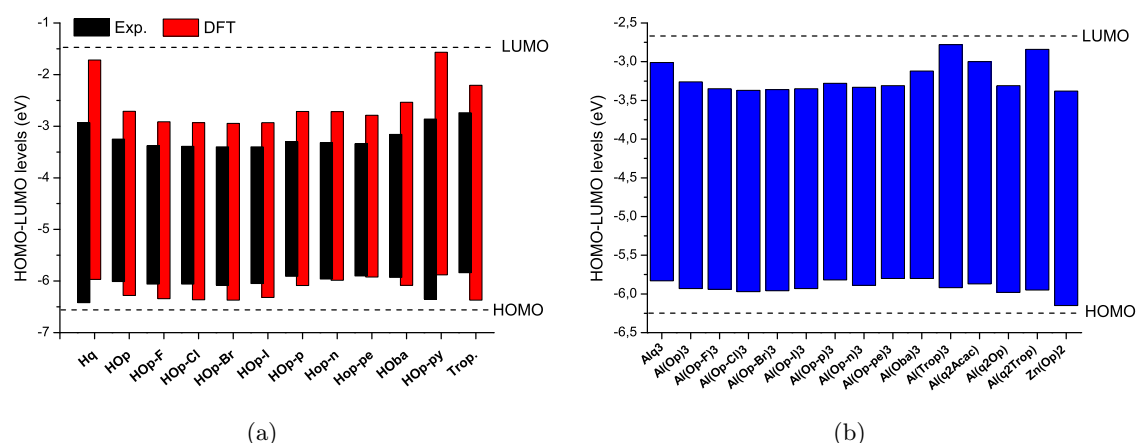
Figure 3.45: LUMO-HOMO energy levels calculated from the reduction potentials and the optical band-gaps of the ligands (a) and complexes (b).

LUMO energy levels of the ligands have been calculated at the B3-LYP [83]/def2-TZVPP [90] level of theory. The aim of this study was to evaluate the ability of the studied ligands to sensitize the emission of lanthanides. Calculated HOMO and LUMO energy levels, determined in the preliminary studies, are compared to those estimated experimentally in Table 3.7. Despite the difference between the absolute values, a general trend is identified. The calculated HOMO and LUMO energies of HOp **3**, -6.28 eV and -2.71 eV, respectively, are lowered compared to those of Hq **26**, -5.97 eV and -1.72 eV, respectively. This matches the experimental results for the LUMO, whereas the experimental HOMO of HOp **3** is higher than that of Hq **26**. As observed experimentally, HOba **18** is characterized by a calculated LUMO, -2.53 eV, lowered in respect to that of HOp **3**. Conversely to the experimental results, the theoretical HOMO level of HOba **18**, -6.08 eV, is higher compared to that of HOp **3**. Likewise, the calculated LUMO of tropolone **24**, -2.21 eV, is higher than that of HOp **3**, whereas the theoretical HOMO, -6.37 eV, is lowered compared to that of HOp **3**. In accordance with the experimental data, the HOMO and LUMO levels of HOp$-$py **22**, -5.88 eV and -1.57 eV, respectively, are higher than those of Hq **26**. Lastly, the calculated HOMO and LUMO of the halogenated ligands HOp$-$X **5a**–**d**, between -6.32 and -6.37 eV and between -2.91 and 2.94 eV, respectively, are both lowered compared to those of HOp **3**, as determined experimentally. In addition, accordingly to the experimental results, the substituted ligands HOp$-$R **15a**–**c** are characterized by slightly lowered calculated LUMO, between -2.71 and -2.79 eV, and higher calculated HOMO, between -5.92 and 6.09 eV, compared to those HOp **3**. In conclusion, the experimental HOMO and LUMO levels have been confirmed theoretically, besides few discrepancies concerning the HOMO levels. Theoretical studies on the (novel) OSCs are presented in Chapter 4.2, and thus, here, only the experimental HOMO and LUMO energy levels are discussed in the following.

HOMO and LUMO energy levels of Alq$_3$ reported in literature, -5.95 eV and -3.01 eV, respectively [36, 38], are in a fairly good agreement with the HOMO and LUMO energy levels estimated in this study, -5.83 eV and -3.01 eV, respectively. Unexpectedly, all the aluminum complexes have similar HOMOs ranging between -5.80 and -5.97 eV. On the contrary, the LUMOs follow the same trend described for those of the ligands. As an example, Al(Trop)$_3$ **25** is characterized by the highest LUMO, -2.78 eV, followed by that of Alq$_3$, -3.01 eV. The LUMOs of Al(Op)$_3$ **4** and Al(Oba)$_3$ **19** are -3.26 eV and -3.12 eV, respectively. HOMOs and LUMOs of the mixed-ligands aluminum complexes exhibit quite interesting features. Al(q$_2$Acac) **28**

presents HOMO and LUMO, $-5.87\,\text{eV}$ and $-3.00\,\text{eV}$, respectively, almost identical to those of Alq$_3$. This is expected considering that the electro- and photo-active species in Al(q$_2$Acac) **28** is the quinolinate, whereas the effect of the acetyl acetonate is negligible. In Al(q$_2$Op) **29** the predominant electro- and photo-active species is the phenalenyl, and thus, its HOMO and LUMO, $-5.98\,\text{eV}$ and $-3.31\,\text{eV}$, respectively, are similar to those of Al(Op)$_3$ **4**. At last, Al(q$_2$Trop) **30** is identified by HOMO and LUMO, $-5.95\,\text{eV}$ and $-2.84\,\text{eV}$, respectively, almost identical to those of Al(Trop)$_3$ **30**, indicating that the predominant electro- and photo-active moiety is the tropolonate. The halogenated and substituted aluminum complexes, Al(Op$-$X)$_3$ **6a**–**d** and Al(Op$-$R)$_3$ **16a**–**c**, present the same behaviors described for the halogenated and substituted ligands HOp$-$X **5a**–**d** and HOp$-$R **15a**–**c**. The LUMO of the halogenated and substituted aluminum complexes, Al(Op$-$X)$_3$ **6a**–**d** and Al(Op$-$R)$_3$ **16a**–**c**, in the range between -3.31 and $-3.37\,\text{eV}$, are lowered compared to that of Al(Op)$_3$ **4**. In addition, the halogenated complexes Al(Op$-$X)$_3$ **6a**–**d** show also a lowered HOMO, between -5.94 and $-5.97\,\text{eV}$, compared to that of Al(Op)$_3$ **4**. On the contrary, the substituted complexes Al(Op$-$R)$_3$ **16a**–**c** exhibit a higher HOMO, ranging between -5.80 and $-5.89\,\text{eV}$, compared to that of Al(Op)$_3$ **4**.

Lastly, the HOMO and LUMO energy levels of Zn(Op)$_2$ **31** are $-6.15\,\text{eV}$ and $-3.38\,\text{eV}$, respectively, comparable to those of Al(Op)$_3$ **4** (considering the different solvents used in the characterization). It is clear that, in Zn(Op)$_2$ **31**, the electro- and photo-active species are the two phenalenyls. The electronic properties of Zn(Op)$_2$ **31** are strongly determined by the ligand and are scarcely influenced by its flat structure caused by the central zinc atom.

3.7 Conclusions

In conclusion, we have designed, synthesized and characterized a series of (novel) OSCs. The goal was to determine the relationship between molecular structure and electronic properties of the (novel) OSCs in comparison to the benchmark Alq$_3$. The ligands and complexes involved in this study are listed in Table 3.1 and Table 3.2.

The first OSC synthesized was Al(Op)$_3$ **4**, which is characterized by a symmetrical structure and ligands with an extended aromatic system compared to Alq$_3$. Its molecular structure was, for the first time, resolved. Additionally, two series of halogenated and substituted derivatives of Al(Op)$_3$ **4** were synthesized, namely, Al(Op$-$X)$_3$ **6a**–**d** and Al(Op$-$R)$_3$ **16a**–**c**. The aromatic system of Al(Op)$_3$ **4** was further extended to form the aluminum complex Al(Oba)$_3$ **19**. Due to its structural similarity to Alq$_3$, Al(Op$-$py)$_3$ **23** was synthesized and studied. Because of its 7-membered aromatic backbone and its symmetrical structure, Al(Trop)$_3$ **25** was formed and investigated. The three mixed-ligands complexes Al(q$_2$Acac) **28** , Al(q$_2$Op) **29**, and Al(q$_2$Trop) **30** were obtained by the exchanging one quinolinate of Alq$_3$ with Acac **27**, HOp **3** and tropolone **24**, respectively. The molecular structure of the unprecedented Al(q$_2$Op) **29** and Al(q$_2$Trop) **30** was resolved by single crystal X-ray diffraction. At last, the flat complex Zn(Op)$_2$ **31** was synthesized as the first member of a series of complexes based on zinc, and its exact molecular structure was resolved by single crystal X-ray diffraction.

A complete photophysical characterization of Al(Op)$_3$ **4** in solution and in thin film was carried out. The results were compared to the photophysical properties of Alq$_3$. It was found that, in the solid state, Al(Op)$_3$ **4** forms excimers, and thus, the photophysical properties of Al(Op)$_3$ **4** in solution are dramatically different in relation to those in thin film. Absorption and emission spectra of the halogenated and substituted complexes, Al(Op$-$X)$_3$ **6a**–**d** and Al(Op$-$R)$_3$ **16a**–**c**, show little variations in comparison to those of the pristine Al(Op)$_3$ **4**. Interestingly, phosphorescence emission, triggered by the heavy-atom effect, was observed for Al(Op$-$I)$_3$ **6d**.

Moreover, it was demonstrated that, in spite of the bulky substituent, $Al(Op-p)_3$ **16a** forms excimers in thin film. As a consequence of its phenalenyl core, $Al(Oba)_3$ **19** presents absorption and emission spectra similar to those of $Al(Op)_3$ **4**. Moreover, it forms excimers in solid state. On the contrary, $Al(Op-py)_3$ **23**, which is insoluble in all the solvents, in solid state is characterized by an emission blue-shifted compared to the emission of Alq_3. As a result of its particular structure, the spectra of $Al(Trop)_3$ **25** are not comparable to those of Alq_3 and $Al(Op)_3$ **4**. However, the absorption bands of $Al(Trop)_3$ **25** were assigned to their respective transitions and a blue fluorescence emission was detected. Absorption and emission spectra of the mixed-ligands complexes $Al(q_2Acac)$ **28**, $Al(q_2Op)$ **29**, and $Al(q_2Trop)$ **30** result from the combination of the absorption and emission of the two moieties forming the complexes. Since Acac is not emitting, the emission of $Al(q_2Acac)$ **28** is almost identical to that of Alq_3. On the contrary, the emission of $Al(q_2Op)$ **29** is a combination between the emission of the quinolinate and the phenalenyl. It was possible to excite selectively one of the two moieties, and, as a result, the emission of $Al(q_2Op)$ **29** depends from the excitation wavelength. The same effect was observed for $Al(q_2Trop)$ **30**, however, since the absorption of the quinolinate and of the tropolonate are superimposed, it was impossible to excite selectively one of the two ligands. Lastly, absorption and emission spectra of $Zn(Op)_2$ **31** derive from the phenalenyl ligands and the flat structure of the complex has a negligible effect on its spectra.

The single irreversible electrochemical reduction of Alq_3 occurs at a quite negative potential. In contrast, $Al(Op)_3$ **4** can be reduced quasi-reversibly three times at more positive potentials. As a consequence of their structural affinity with $Al(Op)_3$ **4**, the same behavior was observed for the halogenated and substituted complexes $Al(Op-X)_3$ **6a**–**d** and $Al(Op-R)_3$ **16a**–**c** and for $Al(Oba)_3$ **19**. Due to its small aromatic structure, $Al(Trop)_3$ **25** is characterized by a single quasi-reversible reduction at a considerably negative potential. The reduction of $Al(q_2Acac)$ **28**, $Al(q_2Op)$ **29**, and $Al(q_2Trop)$ **30** is caused by their electro-active moieties. In detail, the reduction of $Al(q_2Acac)$ **28** occurs on the quinolinates, the (first) reduction of $Al(q_2Op)$ **29** takes place on the phenalenyl and the reduction of $Al(q_2Trop)$ **30** involves the tropolonate. $Zn(Op)_2$ **31** is characterized by three reduction processes which occur on the two phenalenyl and, most probably, on the zinc.

From the photophysical and electrochemical characterization the HOMO and LUMO energy levels of the (novel) OSCs were estimated. $Al(Op)_3$ **4** is characterized by both lowered HOMO and LUMO compared to Alq_3. The halogenated and substituted complexes $Al(Op-X)_3$ **6a**–**d** and $Al(Op-R)_3$ **16a**–**c** show similar HOMO and LUMO energy levels to those of $Al(Op)_3$ **4**. On the contrary, $Al(Oba)_3$ **19** presents higher HOMO and LUMO. $Al(Trop)_3$ **25** is characterized by the highest LUMO (among the studied OSCs) and a LUMO comparable to that of $Al(Op)_3$ **4**. The HOMO and LUMO of the mixed-ligands complexes $Al(q_2Acac)$ **28**, $Al(q_2Op)$ **29**, and $Al(q_2Trop)$ **30** are similar to those of Alq_3, $Al(Op)_3$ **4** and $Al(Trop)_3$ **25**, respectively. Despite the different geometry, the HOMO and LUMO of $Zn(Op)_2$ **31** are close to those of $Al(Op)_3$ $ALOP_3$.

4. Theoretical and preliminary experimental studies on the (novel) OSCs

4.1 Introduction

In this chapter, we have studied the charge carrier mobilities of the (novel) OSCs by means of theoretical and experimental methods. At first, the (novel) OSCs, $Al(Op)_3$, $Al(Op-py)_3$, $Al(Trop)_3$, $Al(q_2Acac)$, $Al(q_2Op)$, and $Al(q_2Trop)$, synthesized and characterized in Chapter 3, were investigated with newly developed theoretical methods. Alq_3 was included as a benchmark. Additionally, due to its non-aromatic structure, $Al(Acac)_3$ (tris-(4-oxopent-2-en-2-olate)aluminum) was added as comparison (Figure 4.1).
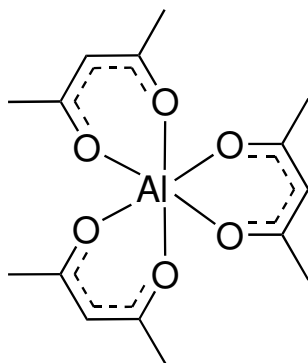
Figure 4.1: Chemical structure of $Al(Acac)_3$.

The theoretical investigation was carried out in three parts. In the first part, HOMO and LUMO energy levels and electrical dipole moment of the (novel) OSCs were investigated in vacuum. Additionally, the HOMO and LUMO energy levels computed have been compared with those obtained experimentally in Section 3.6. In the second part, morphologies of the OSCs were generated to simulate amorphous films. In the last section of the theoretical studies, implementing the morphologies in a newly developed method, the charge carrier mobility of the OSCs has been calculated. The obtained data has been compared with the structure of the OSCs aiming to infer a relation between properties and chemical structure. An additional preliminary study on the experimental charge carrier mobility of $Al(Op)_3$ is presented. In detail, the mobilities were estimated by means of field-effect transistors (FET), time of flight (TOF), and admittance spectroscopy (AS). Although the results are still inconclusive and partially unsatisfactory, sample preparation and measurement are reported.

4.2 Theoretical studies on the (novel) OSCs

Theoretical studies in collaboration with:
Dr. Velimir Meded, Pascal Friederich
INT-KIT, Karlsruhe, Germany
and Dr. Timo Strunk
Nanomatch, Eggenstein-Leopoldshafen, Germany

4.2.1 Frontier orbitals and electrical dipole moment in vacuum

In this section we have studied the complexes in vacuum with the aid of density function theory (DFT) based calculations implementing TURBOMOLE [82] on a B3-LYP [83] /SV(P) [84] level of theory. The crystal structure of the complexes, except for $Al(Op-py)_3$, was used as starting point for the atomic coordinates. HOMO and LUMO energy levels and the electrical dipole moment of the OSCs in vacuum were computed. Table 4.1 lists all the findings.
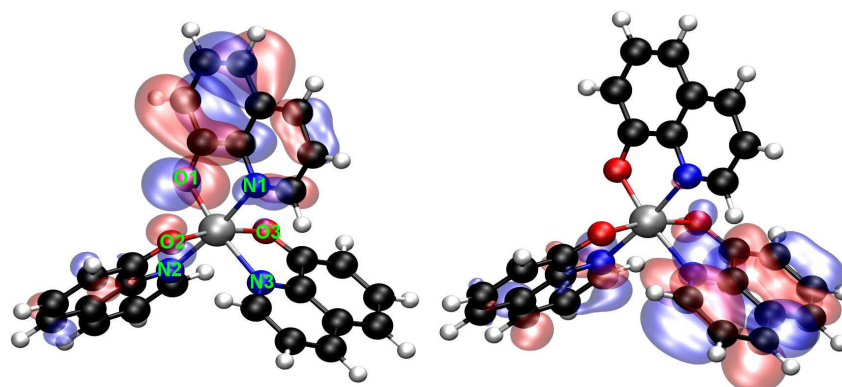
Bond	Length [Å]	Bond	Length [Å]
Al-N1	2.084	Al-O1	1.857
Al-N2	2.065	Al-O2	1.883
Al-N3	2.127	Al-O3	1.881

Figure 4.2: Molecular orbital surfaces of the HOMO (left) and LUMO (right) and list of the bond lengths of *mer*-Alq_3. The labels of the atoms are exemplary shown in green on the atoms in the molecule on the left-hand side (HOMO).

Studies on the geometry and the electronic properties of Alq_3, in neutral and charged states, as well as the bonding characteristics in metal-Alq_3 complexes, have been carried out by Andreoni and co-workers [192–194]. As reported in Section 1.2, the meridianal isomer, *mer*-Alq_3, was found to be the preferred form of Alq_3, being energetically favored than the facial isomer, *fac*-Alq_3. Therefore, we have only studied the HOMO and LUMO of the *mer*-isomer. A number of theoretical studies on the electronic structure of Alq_3 has been reported [192, 194–199], which complements the extensive experimental studies carried out using optical and ultraviolet photoelectron spectroscopies [195, 198, 200–202]. Frontier orbital levels of *mer*-Alq_3 consist of sets of closely spaced triplets. HOMOs and LUMOs largely preserve the electronic structure of the individual quinolin-8-ol (Hq) ligand with little contribution from the central aluminum.

Due to the loss of symmetry of the meridianal isomer, the highest HOMO, $-5.14\,$eV, and the lowest LUMO, $-1.91\,$eV, depicted in Figure 4.2, are mainly localized on a single ligand. A detailed analysis reveals that the HOMO is principally localized on the phenoxide side of the quinolinate, whereas the LUMO is primarily localized on the pyridyl side. The localization of the orbitals is caused by the loss of symmetry resulting in an elongation, or shrinking, of the distances between the central aluminum and the nitrogens or oxygens. As a result, in *mer*-Alq$_3$, the three oxygens and nitrogens are not equivalent. One one hand, O2 is facing O3, as well as N1 is facing N2. Conversely, O1 is facing N3. This results in a longer Al-N3 bond, 2.127 Å, compared to Al-N1 and Al-N2, 2.084 Å and 2.065 Å, respectively, and a shorter Al-O1 bond, 1.857 Å, compared to Al-O2 and Al-O3, 1.883 Å and 1.881 Å, respectively. At last, the six chelating atoms are arranged in a distorted octahedral geometry. Calculated bond lengths and coordination geometry are in agreement with the data obtained by X-ray single crystal diffraction on *mer*-Alq$_3$ single crystals reported in Section 1.2. Considering the presence of solvent molecules in the crystal lattice that slightly distort the structure of Alq$_3$, the agreement between the experimental and theoretical data is fairly good. Due to the anisotropic distribution of the molecular orbital, the ground-state dipole moment of *mer*-Alq$_3$ is predicted to be 4.45 D.

Bond	Length [Å]	Bond	Length [Å]
Al-O1	1.897	Al-O4	1.896
Al-O2	1.896	Al-O5	1.897
Al-O3	1.897	Al-O6	1.896
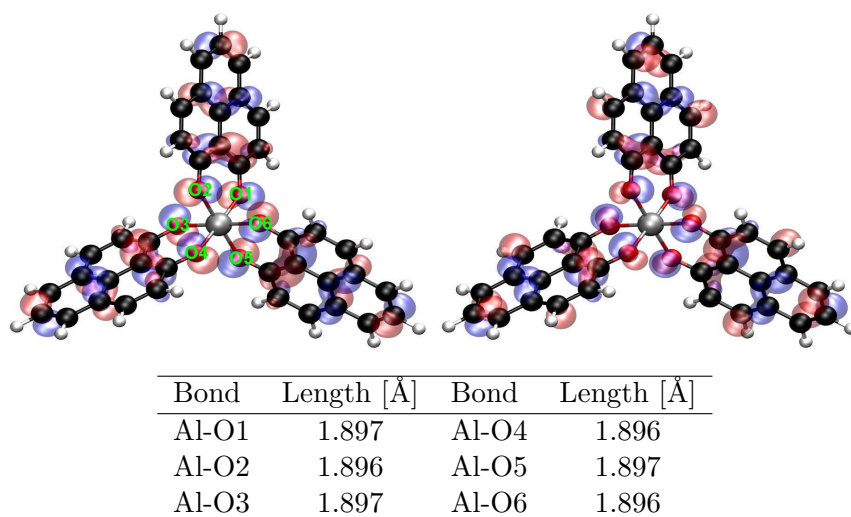
Figure 4.3: Molecular orbital surfaces of the HOMO (left) and LUMO (right) and list of the bond lengths of Al(Op)$_3$. The labels of the atoms are exemplary shown in green on the atoms in the molecule on the left-hand side (HOMO).

A study on Al(Op)$_3$ by UPS and DFT-based calculations was recently reported by Müller *et al.* [203]. As described in Section 3.3.1, in Al(Op)$_3$ the ligands solely bind to the Al^{3+} ion via oxygen donor atoms in the chelating moiety resulting in a symmetrical geometry. Consequently, the HOMO and LUMO of Al(Op)$_3$, which are illustrated in Figure 4.3, are equally distributed on the three ligands. As a result, the calculated vacuum molecular dipole of Al(Op)$_3$ turns out to be very small when compared to *mer*-Alq$_3$, namely 0.086 D versus 4.45 D. Calculated HOMO and LUMO of Al(Op)$_3$ are at lowered energies, $-5.71\,$eV and $-2.41\,$eV, respectively, compared to those of *mer*-Alq$_3$. The equivalent distribution of the molecular orbitals on the three ligands in Al(Op)$_3$ results, in the first place, from the symmetrical geometry of the ligand HOp (see Table 3.1). Consequently, the six oxygen donor atoms arrange in an almost perfect octahedral geometry with identical calculated Al-O bond lengths, 1.896-1.897 Å. This clearly indicates that the three ligands are perfectly identical and the complex is symmetrical. Taking in account the deformation caused by solvent molecules in the crystal lattice, experimental Al-O bond lengths,

determined by single crystal X-ray diffraction between 1.867 and 1.882 Å (see Section 3.3.1), are in good agreement with those calculated.

Bond	Length [Å]	Bond	Length [Å]
Al-N1	2.102	Al-O1	1.831
Al-N2	2.114	Al-O2	1.813
Al-N3	2.291	Al-O3	1.819
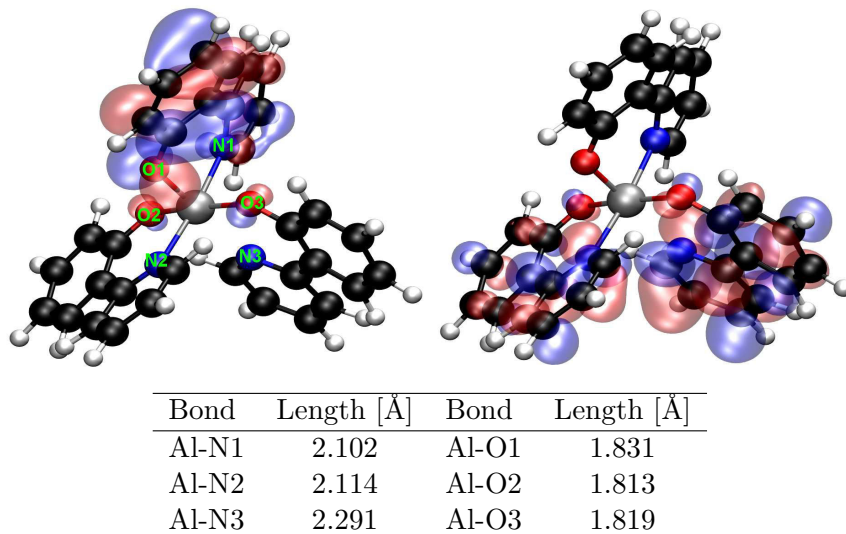
Figure 4.4: Molecular orbital surfaces of the HOMO (left) and LUMO (right) and list of the bond lengths of *mer*-Al(Op−py)$_3$. The labels of the atoms are exemplary shown in green on the atoms in the molecule on the left-hand side (HOMO).

Al(Op−py)$_3$ is formed by three asymmetrical HOp−py ligands (see Table 3.1). As described in Section 3.3.5, due to the asymmetrical structure of the ligand, two geometrical isomers can be formed *fac*-Al(Op−py)$_3$ and *mer*-Al(Op−py)$_3$. In Section 3.3.5, we have presumed that the *mer*-isomer is more stable, and thus, we have studied the HOMO and LUMO distribution exclusively of *mer*-Al(Op−py)$_3$. Both HOMO and LUMO, illustrated in Figure 4.4, are strongly localized. In more detail, the HOMO is mostly localized on the phenoxide part of one ligand, whereas the LUMO is confined unevenly on the pyridyl side of two ligands. As a result, the ground state vacuum dipole moment of *mer*-Al(Op−py)$_3$ is 4.79 D. The calculated HOMO energy, −5.07 eV, is comparable to that of *mer*-Alq$_3$. In contrast, the LUMO energy, −1.55 eV, is quite higher than that of *mer*-Alq$_3$. The localization of the orbitals is caused by the loss of symmetry resulting in an elongation or shrinking of the distances between the central aluminum and the oxygen and nitrogen atoms. In *mer*-Al(Op−py)$_3$, O2 is facing O3 and N1 is facing N2. Diversely, O1 is opposite of N3 inducing an elongation of the Al-N3 bond, 2.291 Å, in comparison to Al-N1 and Al-N2, 2.102 Å and 2.113 Å, respectively. Owing to the rotational degree of freedom of the aromatic rings around the bridging bond, and the electrostatic repulsion between the atoms, also Al-O1, 1.831 Å, is elongated in respect to Al-O2 and Al-O3, 1.813 Å and 1.819 Å, respectively. The torsion angle of the bridging bond of the ligand containing O1 and N1, 24.26°, is indeed larger than the torsion angles of the ligand including O2 and N2, 11.08°, and of the ligand including O3 and N3, 12.83°. The outcome of all these factors is a distorted octahedral geometry of the six chelating atoms. Unfortunately, we were unable to grown single crystal of *mer*-Al(Op−py)$_3$ for single crystal X-ray diffraction, and thus, theoretical results could not be compared with experimental data.

Figure 4.5 illustrates the HOMO and LUMO orbitals of Al(Trop)$_3$. Both HOMO and LUMO are equally distributed on the three ligands, and thus, the resulting ground-state dipole moment of Al(Trop)$_3$ is low, 0.12 D. In addition, the HOMO energy, −5.72 eV, is almost identical to that of Al(Op)$_3$. On the contrary, the LUMO energy, −1.79 eV, is quite higher compared to

Bond	Length [Å]	Bond	Length [Å]
Al-O1	1.912	Al-O4	1.912
Al-O2	1.911	Al-O5	1.911
Al-O3	1.911	Al-O6	1.910
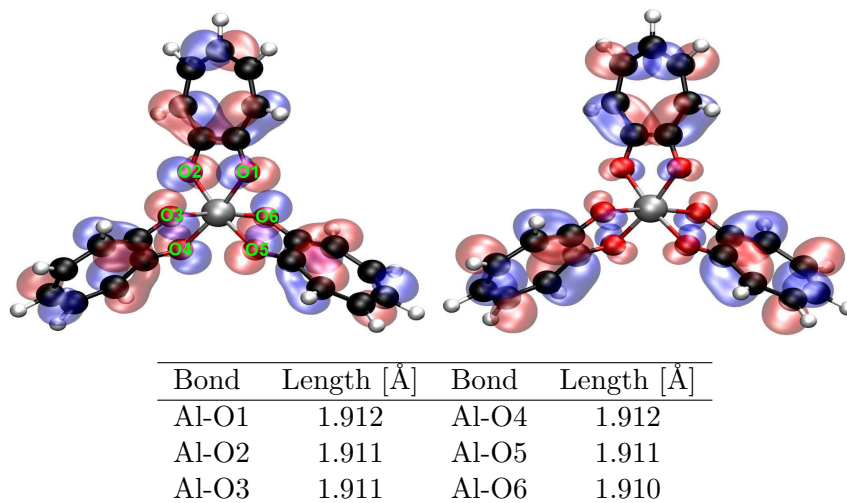
Figure 4.5: Molecular orbital surfaces of the HOMO (left) and LUMO (right) and list of the bond lengths of Al(Trop)$_3$. The labels of the atoms are exemplary shown in green on the atoms in the molecule on the left-hand side (HOMO).

that of Al(Op)$_3$. Despite its seven-membered aromatic structure, tropolone is a symmetric molecule (see Table 3.1), resulting in equal oxygen-aluminum bond lengths in Al(Trop)$_3$ (1.910-1.912 Å). However, the six oxygens are arranged in a distorted octahedral geometry due to the narrow bite angle of tropolone, as described in Section 3.3.6. The experimental Al-O bond lengths, determined by single crystal X-ray diffraction, are between 1.8841 and 1.8894 Å [165], in agreement with the theoretical results.

In view of its non-aromatic structure, Al(Acac)$_3$ was chosen to be studied theoretically to test the theoretical methods (DEPOSIT and Quantum Patch) described in Section 1.3.1. It is formed by three ligands which chelate the central aluminum atom. The symmetrical structure of Acac (see Table 3.1), and thus, of Al(Acac)$_3$, leads to evenly distributed HOMO and LUMO, as illustrated in Figure 4.6. Consequently, the calculated ground-state dipole moment of Al(Acac)$_3$ is almost neglegible, 0.053 D. The non-aromatic structure of Al(Acac)$_3$ results in a very low HOMO, -5.99 eV, and a very high LUMO, -1.19 eV. The equal distribution of the molecular orbitals is caused by the high symmetry of the complex Al(Acac)$_3$; the six oxygen donor atoms are arranged in a perfect octahedral geometry with identical Al-O bond lengths, 1.903-1.904 Å. These results are in accordance with the experimental data determined by single crystal X-ray diffraction on Al(Acac)$_3$ single crystals grown in benzene and petroleum ether [173]. Experimentally, the six oxygens occupy the vertexes of an almost perfect octahedron with Al-O bond lengths varying between 1.8720 and 1.9042 Å.

In Al(q$_2$Acac) a quinolinate is replaced by Acac, which introduces a plane of symmetry. Hence, the two quinolinate ligands are identical. In Section 3.3.7, we have observed that Al(q$_2$Acac) occurs in a *pseudofac*-geometry, for that reason, we have solely computed the HOMO and LUMO of this isomer. HOMO and LUMO, illustrated in Figure 4.7, are localized equally on the two quinolinates, giving rise to a ground state dipole moment of 1.47 D, lowered in comparison to that of *mer*-Alq$_3$. However, as previously described for *mer*-Alq$_3$, the HOMO is mainly localized on the phenoxide side of the quinolinates, whereas the LUMO is principally localized on the pyridyl side. Moreover, either the HOMO, -5.29 eV, either the LUMO, -1.74 eV, have lowered energies compared to those of *mer*-Alq$_3$. Due to the different nature of the ligands, the six chelating atoms of *pseudofac*-Al(q$_2$Acac), two nitrogens and four oxygens, are not equivalent.

Bond	Length [Å]	Bond	Length [Å]
Al-O1	1.903	Al-O4	1.903
Al-O2	1.904	Al-O5	1.904
Al-O3	1.904	Al-O6	1.904
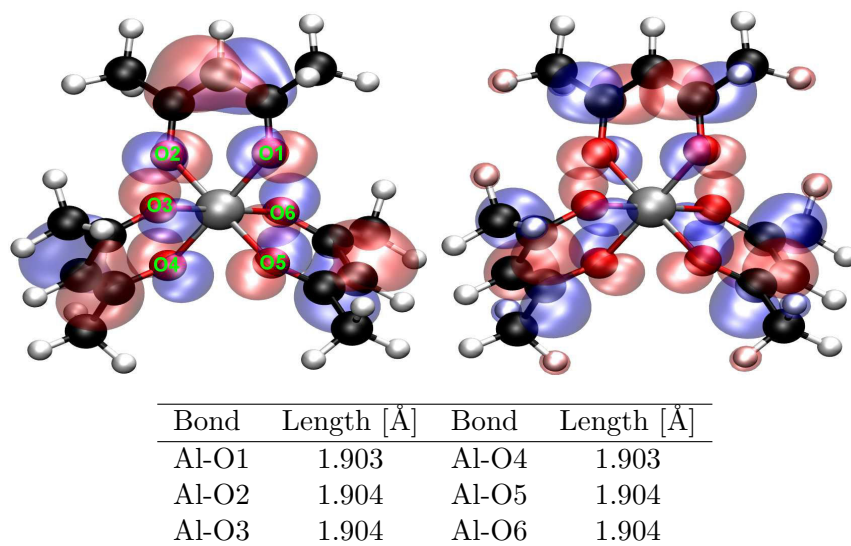
Figure 4.6: Molecular orbital surfaces of the HOMO (left) and LUMO (right) and list of the bond lengths of $Al(Acac)_3$. The labels of the atoms are exemplary shown in green on the atoms in the molecule on the left-hand side (HOMO orbital).

Bond	Length [Å]	Bond	Length [Å]
Al-N1	2.095	Al-O2	1.893
Al-N2	2.095	Al-O3	1.879
Al-O1	1.892	Al-O4	1.878
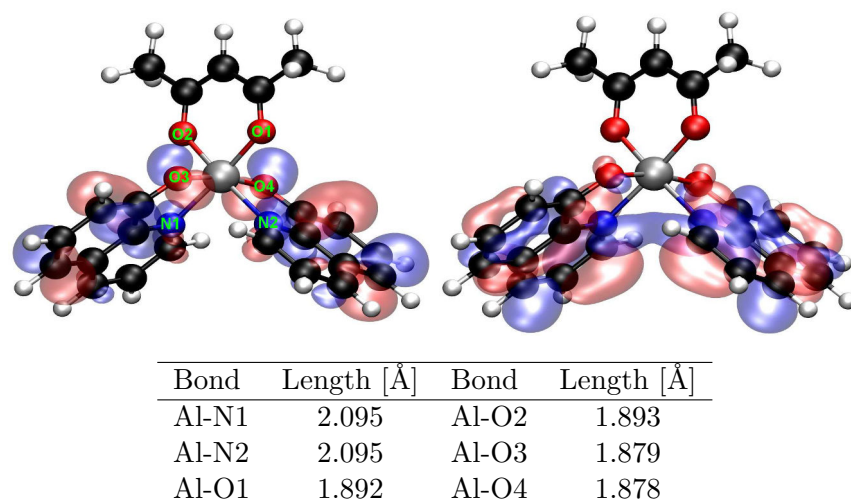
Figure 4.7: Molecular orbital surfaces of the HOMO (left) and LUMO (right) and list of the bond lengths of $Al(q_2Acac)$. The labels of the atoms are exemplary shown in green on the atoms in the molecule on the left-hand side (HOMO orbital).

In detail, O1 is facing N1 and O2 is facing N2, while O3 is facing O4. As a consequence, the bonds Al-O1 and Al-O2, 1.892 and 1.893 Å, respectively, are longer than Al-O3 and Al-O4, 1.878 and 1.879 Å, respectively. This, together with the electrostatic repulsion between the chelating atoms, results in a slightly distorted octahedral geometry. Experimentally, the O(acac)-Al bond lengths are 1.8765 and 1.8816 Å, the O(quinolinate)-Al bond lengths are 1.8549 and 1.8530 Å, the nitrogen-aluminum bond lengths are 2.0464 and 2.0738 Å, and the six chelating atoms are arranged in a distorted octahedral geometry [166] (see 3.3.7). Experimental and theoretical results are in fairly good agreement, considering the deformation effect caused by solvent molecules in the crystal lattice.

Al(q_2Op) is formed by the substitution of Acac in Al(q_2Acac) with HOp. In Section 3.3.8, we have obtained the molecular structure of *pseudofac*-Al(q_2Op) by single crystal X-ray diffraction, and thus, we have studied only the HOMO and LUMO orbitals of this geometry. The HOMO is localized uniformly on the two quinolinate moieties with a higher density on the phenoxide side. However, the LUMO is exclusively localized on the phenalenyl. The strong localization of the molecular orbitals results in a ground-state dipole moment of 6.52 D, which is the highest among all the studied OSCs. Additionally, the HOMO energy, -4.99 eV, is close to that of *mer*-Alq_3, whereas and the LUMO energy, -2.71 eV, is closer to that of Al(Op)$_3$. For the sake of understanding, we have calculated and plotted lower HOMOs and higher LUMOs of *pseudofac*-Al(q_2Op). It can be seen that the HOMO-1, HOMO, LUMO+1 and LUMO+2 are centered on the quinolinates, whereas the HOMO-2 and LUMO on the phenalenyl. The HOMO-LUMO gap of Al(q_2Op) is -2.28 eV, considerably lowered compared to that of all the other studied OSCs. However, the gap between HOMO and LUMO+1 (both centered on the quinolinates) and between the HOMO-2 and LUMO (both centered on the phenalenyl) are 3.44 eV and 3.47 eV, respectively. These values are comparable to the HOMO-LUMO gaps of *mer*-Alq_3 and Al(Op)$_3$. Due to the different nature of the ligands in *pseudofac*-Al(q_2Op), the bonds O(phenalenyl)-Al, 1.922 Å, are longer than the bonds O(quinolinate)-Al, 1.870 Å. The N(quinolinate)-Al bond lengths, 2.068 Å, are slightly shorter compared to those of *pseudofac*-Al(q_2Acac) and those of *mer*-Alq_3. As a consequence of the electrostatic repulsion between oxygens and nitrogens and of the different bond lengths, the six chelating atoms are arranged in a distorted octahedral geometry. The theoretical results are in a good agreement with the bond lengths determined experimentally in Section 3.3.8, O(phenalenyl)-Al: 1.861 and 1.867 Å; O(quinolinate)-Al: 1.844 and 1.864 Å; N(quinolinate)-Al: 2.036 and 2.050 Å.

In Al(q_2Trop), Acac is replaced with tropolone. As described in Section 3.3.9, by X-ray single diffraction, we have determined that Al(q_2Trop) assumes a *pseudomer*-geometry. Hence, we have studied the HOMO and LUMO orbitals of *pseudomer*-Al(q_2Trop). Figure 4.9 illustrates the molecular orbital surfaces of *pseudomer*-Al(q_2Trop) from HOMO-2 to LUMO+2. The HOMO is localized uniformly on the two quinolinates with a higher density on the phenoxide side. However, the LUMO is exclusively localized on the tropolonate. The strong localization of the orbitals leads to a high ground state dipole moment of 5.49 D. Whilst the HOMO-1, HOMO and LUMO+1 are localized on the two quinolinates, the HOMO-2, LUMO and LUMO+1 are centered on the tropolonate. Since the HOMO energy level is -5.09 eV and the LUMO energy level is -2.07 eV, the resulting HOMO-LUMO gap is 3.02 eV. However, the gap between HOMO-2 and LUMO, both localized on the tropolonate, is 4.09 eV, which is similar to that of Al(Trop)$_3$. On the contrary, the gap between HOMO-2 and LUMO, both localized on the quinolinates, is 3.47 eV, which is comparable to that of *mer*-Alq_3 and of *pseudofac*-Al(q_2Acac), furthermore, it is identical to that between HOMO-2 and LUMO of Al(q_2Op). The bonds O(tropolonate)-Al, 1.946 Å, are longer than those O(quinolinate)-Al, 1.864 Å. In addition, the N(quinolinate)-Al bond lengths, 2.066 Å, are similar to those of *pseudofac*-Al(q_2Op) and shorter than those of

(a)

(b)

(c)

(d)

(e)

(f)
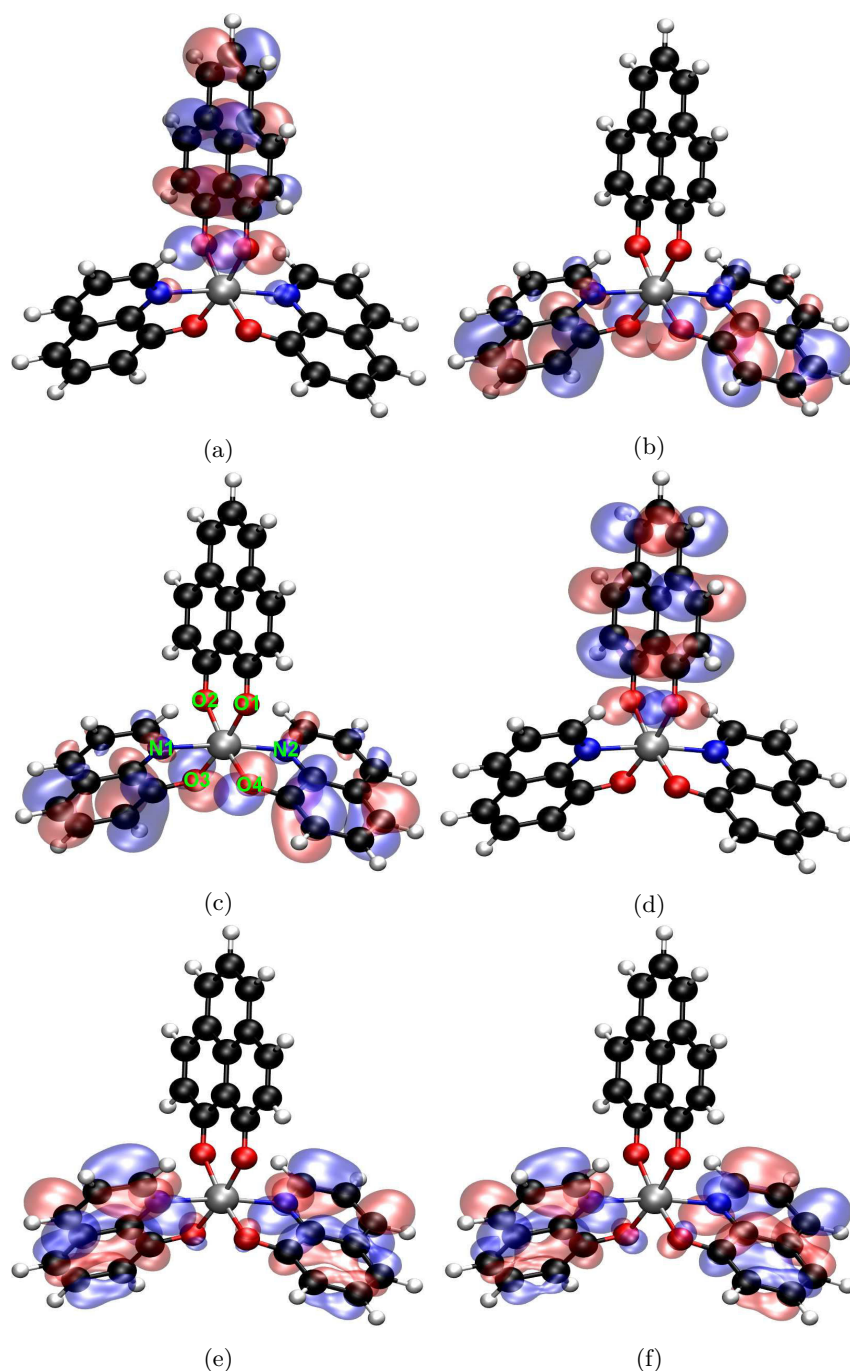
Bond	Length [Å]	Bond	Length [Å]
Al-N1	2.068	Al-O2	1.922
Al-N2	2.068	Al-O3	1.870
Al-O1	1.922	Al-O4	1.870

Figure 4.8: Molecular orbital surfaces of the HOMO-2 (a), HOMO-1 (b), HOMO (c), LUMO (d), LUMO+1 (e), LUMO+2 (f) and list of the bond lengths of Al(q$_2$Op). The labels of the atoms are exemplary shown in green on the atoms in the molecule on the left-hand side (HOMO orbital).

(a)

(b)

(c)

(d)

(e)

(f)
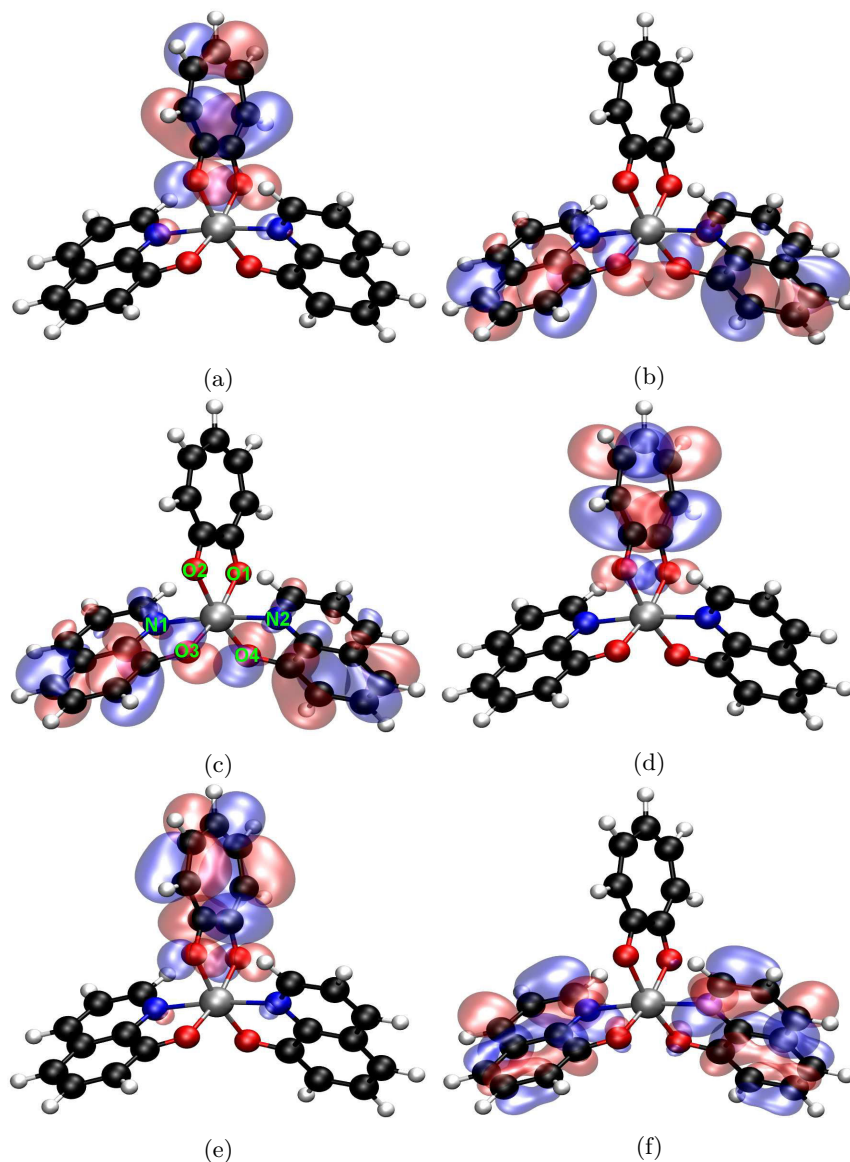
Bond	Length [Å]	Bond	Length [Å]
Al-N1	2.066	Al-O2	1.946
Al-N2	2.066	Al-O3	1.864
Al-O1	1.946	Al-O4	1.864

Figure 4.9: Molecular orbital surfaces of the HOMO-2 (a), HOMO-1 (b), HOMO (c), LUMO (d), LUMO+1 (e) LUMO+2 (f) and list of the bond lengths of Al(q$_2$Trop). The labels of the atoms are exemplary shown in green on the atoms in the molecule on the left-hand side (HOMO orbital).

pseudofac-Al(q$_2$Acac) and *mer*-Alq$_3$. The experimental data, determined by single crystal X-ray diffraction in Section 3.3.9, is in good agreement with the theoretical results, O(tropolonate)-Al: 1.909 Å; O(quinolinate)-Al: 1.863 Å; N(quinolinate)-Al: 1.993 Å.

Figure 4.12 shows the comparison between HOMO and LUMO energy levels estimated experimentally in Section 3.6 and calculated theoretically. Despite a shift of the values, caused by the underestimation of the experimental HOMO and LUMO energy levels measured by the solution-based methods, the trend of experimental and calculated HOMO and LUMO energy levels are comparable. The major differences are observed for the HOMO and LUMO energy levels of the mixed ligands complexes *pseudofac*-Al(q$_2$Op) and *pseudomer*-Al(q$_2$Trop). Experimentally, the phenalenyl and tropolonate are the photo- and electrochemical-active moieties resulting in HOMO and LUMO energy levels almost identical to those of Al(Op)$_3$ and Al(Trop)$_3$. On the contrary, the theoretical studies demonstrate that the HOMO orbitals are localized on the quinolinates, whereas the LUMO orbitals are centered on the phenalenyl or the tropolonate, as illustrated in Figure 4.8 and in Figure 4.9. As a consequence, the HOMO levels estimated experimentally are considerably underestimated than those calculated theoretically.

4.2.2   In silico morphologies

The DEPOSIT code, developed by Neumann *et al.* [85], was implemented to generate realistic morphologies based on the OSCs aforementioned. Morphologies are used to predict the microscopic parameters presented in Section 4.2.3. In addition, the degree of order of the morphologies is evaluated through the pair correlation function $g(r)$ extracted from the calculations. The prevalent morphology of a layer, produced by vapor deposition of OSCs, is an amorphous film [91, 190, 204]. The disorder in the morphology and the weak electronic coupling between the molecules lead to states described by quantum-mechanical wave functions localized on single molecules. As a result, the charge transport occurs by hopping of charge carriers from one molecule to another. Hopping probabilities depend strongly on the overlap between molecular orbitals on adjacent sites [104, 205]. Thus, the charge transport properties are extremely sensitive to the morphology of the film [206]. Morphologies have been generated using a deposition protocol that emulates vapor deposition of molecular films. In detail, the protocol consists of two steps: the first step is the deposition of a single molecule on a partially formed film, the second step consists of the selection of a neighborhood around the deposited molecule and its post-deposition relaxation via an annealing method. To reduce the trapping of the system in metastable configurations, a basing hopping approach [207–209], which comprises several simulated annealing processes [210], was used.

The setting of the DEPOSIT code, implemented to generate the morphologies, includes: 1000 molecules per morphology with the input structure of the molecules plus the partial charges (ESP) calculated as described in 4.2.1. During the simulation, standard van der Walls interaction were taken in account using the Lennard-Jones potential as an approximation. 10 simulated annealing steps for the deposited molecules were calculated. Each simulated annealing process starts at 4000 K, where the molecule can easily transverse the energy barriers separating local minima. The temperature is lowered gradually during the simulation over 60000 steps to a final temperature of 300 K. The morphologies obtained, with a size of 22 nm x 22 nm x 100-160 nm, were extended periodically in x- and y-direction to a final dimension of 9000 molecules. Three examples of the generated morphologies are shown in Figure 4.10.

The parameter, which can be extracted from the morphologies, is the so-called pair correlation function (or radial distribution function) $g(r)$, that represents the short-range order in amorphous materials. It describes the variation of the density as a function of distance from

(a)

(b)

(c)

(d)

(e)

(f)
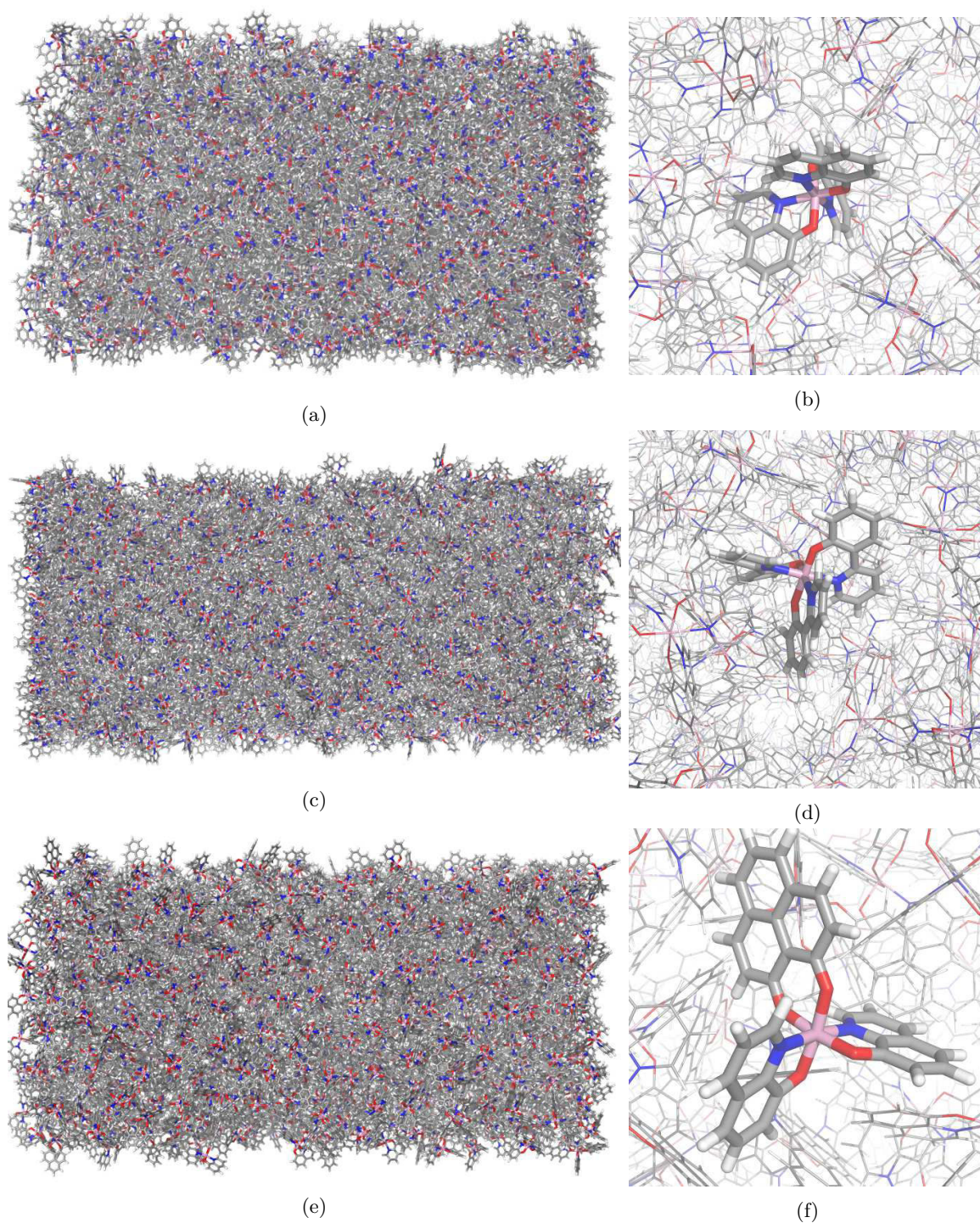
Figure 4.10: Morphologies of *mer*-Alq$_3$ (a), *mer*-Al(Op−py)$_3$ (c) and *pseudofac*-Al(q$_2$Op) (e). Particular of a single molecule embedded in the morphology for *mer*-Alq$_3$ (b), *mer*-Al(Op−py)$_3$ (d) and *pseudofac*-Al(q$_2$Op) (f).

(a) *mer*-Alq$_3$

(b) Al(Op)$_3$

(c) *mer*-Al(Op$-$py)$_3$

(d) Al(Trop)$_3$

(e) Al(Acac)$_3$

(f) *pseudofac*-Al(q$_2$Acac)

(g) *pseudofac*-Al(q$_2$Op)

(h) *pseudomer*-Al(q$_2$Trop)
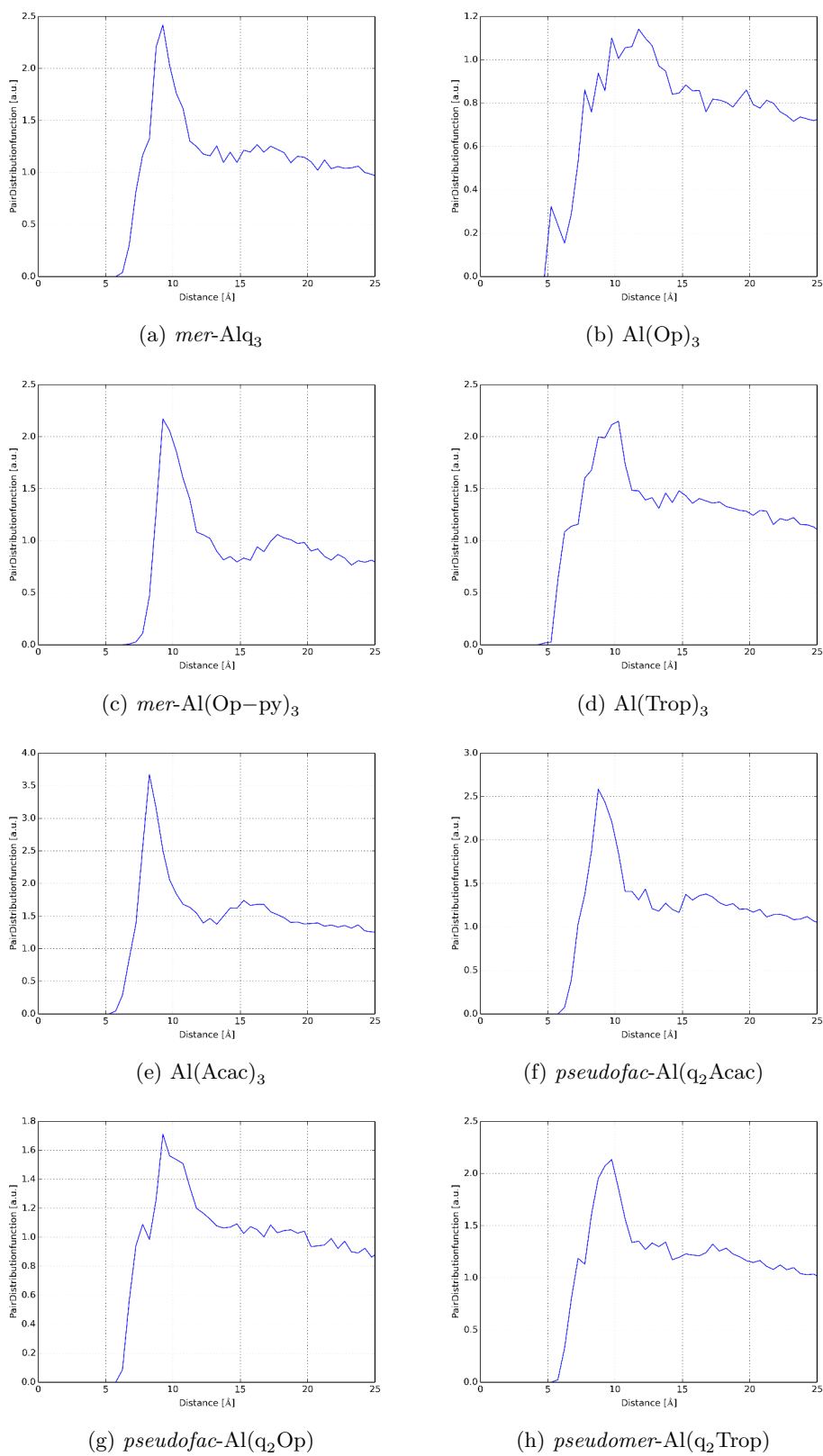
Figure 4.11: Pair correlation function $g(r)$ of the generated morphologies for the (novel) OSCs.

a reference particle (molecule). In other words, it is a measure of the probability of finding a particle (molecule) at a distance r away from a given reference particle (molecule). For amorphous films, which are anisotropic structures, the pair correlation function is an indication of the packing of the molecules in the film. In Figure 4.11, the pair distribution function $g(r)$ for all the generated morphologies is plotted. From the data, we can infer some relations between the structure (see Table 3.2) and the electrical dipole moment (see Table 4.1) of the OSCs and the degree of order of the generated films. As an example, *mer*-Alq$_3$ and *mer*-Al(Op$-$py)$_3$ are characterized by similar structures and dipole moments resulting in almost identical pair distribution functions $g(r)$, sharply peaked at nearly 10 Å. This indicates that the films have a high degree of order and the molecules are closely packed. Similarly, *pseudofac*-Al(q$_2$Acac), which is characterized by a similar structure and a lower dipole moment than those of *mer*-Alq$_3$, has a sharp pair distribution function $g(r)$. Al(Acac)$_3$ is formed by non-aromatic small ligands, as a consequence, its pair distribution function $g(r)$ is sharply peaked at ≈ 8 nm. The negligible dipole moment and the extended ligands of Al(Op)$_3$ result in a broad pair distribution function $g(r)$. Likewise, the pair distribution function $g(r)$ of Al(Trop)$_3$, although the peak is at 10 Å, is broadly distributed. The broad pair distribution function $g(r)$ of *pseudofac*-Al(q$_2$Op) and *pseudomer*-Al(q$_2$Trop), despite their high dipole moment, is induced by the introduction of bulky phenalenyl and tropolonate.

4.2.3   Calculated charge carrier mobility

In this section, the morphologies generated in Section 4.2.2 are implemented in the Quantum Patch method [86, 87]. Firstly, the HOMO and LUMO energy levels of the OSCs were re-calculated in the morphology. Subsequently, the microscopic parameters, included in the Equation 1.11, were computed. Lastly, the charge carrier mobility (for holes and electrons) of the OSCs was determined.

Table 4.1: HOMO and LUMO energy levels, HOMO-LUMO gaps and dipole moments of the OSCs calculated in vacuum and in the generated morphologies.

Compound	Vacuum				Environment			
	E_{HOMO} [eV]	E_{LUMO} [eV]	E_{gap} [eV]	P [a] [D]	E_{HOMO} [eV]	E_{LUMO} [eV]	E_{gap} [eV]	P [a] [D]
mer-Alq$_3$	-5.14	-1.91	3.22	4.45	-5.07	-1.80	3.27	5.55
Al(Op)$_3$	-5.71	-2.41	3.30	0.086	-5.41	-2.22	3.19	1.52
mer-Al(Op$-$py)$_3$	-5.07	-1.55	3.52	4.79	-4.98	-1.40	3.58	5.88
Al(Trop)$_3$	-5.72	-1.79	3.93	0.12	-5.30	-1.56	3.74	1.34
Al(Acac)$_3$	-5.99	-1.19	4.80	0.053	-5.83	-1.09	4.74	0.63
pseudofac-Al(q$_2$Acac)	-5.29	-1.74	3.55	1.47	-5.16	-1.67	3.48	2.04
pseudofac-Al(q$_2$Op)	-4.99	-2.71	2.28	6.52	-5.02	-2.54	2.49	7.89
pseudomer-Al(q$_2$Trop)	-5.09	-2.07	3.02	5.49	-4.97	-1.79	3.18	6.84

[a] Electrical dipole moment.

Table 4.1 lists the HOMO and LUMO energy levels of the studied OSCs calculated in vacuum and in the morphologies. Additionally, Figure 4.12 illustrates the comparison between the HOMO and LUMO energy levels estimated experimentally in Section 3.6 and those calculated in vacuum and in the morphology. It can be noted that HOMO and LUMO energy levels in vacuum and in the environment (amorphous film) are substantially similar. The effect of the neighboring molecules in the generated morphologies slightly shifts the orbitals to higher
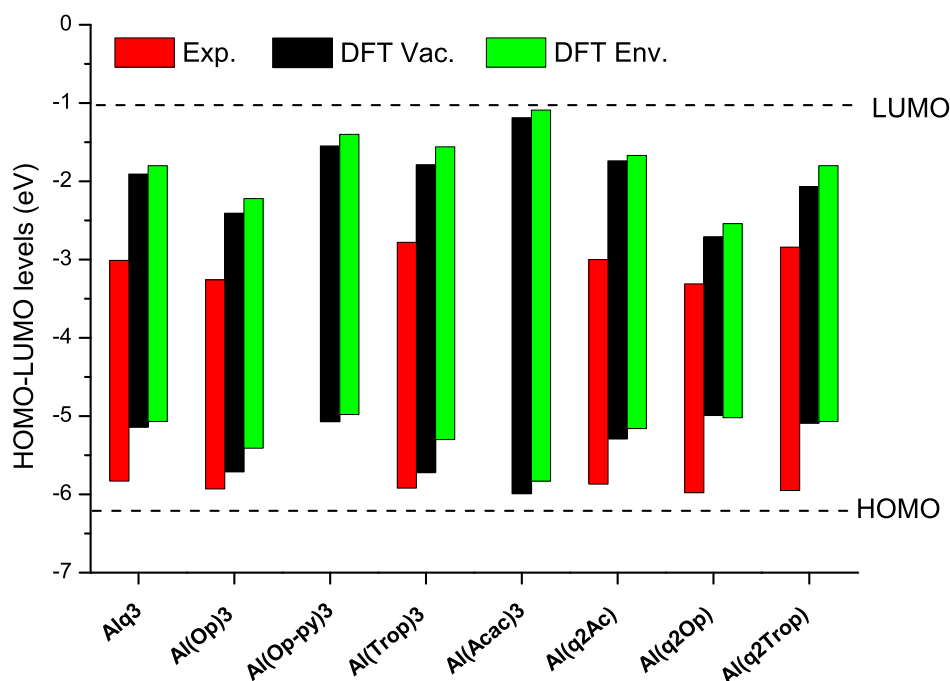
Figure 4.12: HOMO-LUMO energy levels estimated experimentally (red), theoretically in vacuum (black) and theoretically in environment (morphology) (green).

energies. Reminding that HOMO and LUMO energy levels are fundamental parameters for OSCs, because they affect the charge injection from the electrodes into the organic layers and the charge transport between the layers [61, 104, 190]. The indication that in vacuum and in amorphous film their values are comparable is most important for applications. The symmetry breaking, caused by the neighboring molecules in the morphology causes a rise in the ground state dipole moment of all the OSCs. This can be understood as a stronger localization of the molecular orbitals when the molecules are embedded in an anisotropic film.

In order to calculate μ (charge carriers mobility) of the different OSCs, as described in Equation 1.11, the microscopical parameters $\sigma(E)$ (energetic disorder), λ (reorganization energy) and $J^2 r^2$ (electronic coupling) have to be computed first. All the results for holes and electrons are listed in Table 4.2. In addition, the value of the electron and hole mobilities are summarized in Table 4.3. All the microscopic parameters are graphically compared in Figure 4.13.

The resulting mobility μ is highly sensitive to changes of the width of the density of states, or energy disorder $\sigma(E)$, as it enters the functional form in a quadratic fashion [23, 211, 212]. The energy disorder $\sigma(E)$ is defined as the width of the local on-site energy distribution of the system. It originates from the disorder of the local electronic states induced by the amorphous structure of the materials. In disordered materials, energetic disorder $\sigma(E)$ is introduced in two different ways: one effect is that molecules in amorphous structures are individually bent in a trade-off for a better alignment with other molecules, which leads to lowered intermolecular energies. The second effect is related to environmental causes. Each molecule is embedded into an individual, mainly electrostatic, environment created by all other molecules. The structure-related part is considered to be much smaller than the one caused by the electrostatic interactions with the

Table 4.2: Microscopic parameters calculated for holes and electrons in the morphologies of the studied OSCs.

Compound	Holes			Electrons		
	σ [a]	J^2r^2 [b]	λ [c]	σ [a]	J^2r^2 [b]	λ [c]
	[eV]	[eV^2 Å^2]	[eV]	[eV]	[eV^2 Å^2]	[eV]
mer-Alq$_3$	0.19	1.10×10^{-2}	0.33	0.18	1.34×10^{-2}	0.28
Al(Op)$_3$	0.14	4.42×10^{-3}	0.055	0.17	7.05×10^{-3}	0.060
mer-Al(Op−py)$_3$	0.16	6.06×10^{-3}	0.39	0.19	9.51×10^{-3}	0.25
Al(Trop)$_3$	0.21	8.32×10^{-3}	0.23	0.20	1.08×10^{-2}	0.11
Al(Acac)$_3$	0.10	1.52×10^{-2}	0.12	0.12	5.87×10^{-3}	0.12
pseudofac-Al(q$_2$Acac)	0.15	8.85×10^{-3}	0.19	0.16	1.21×10^{-2}	0.29
pseudofac-Al(q$_2$Op)	0.24	1.22×10^{-2}	0.27	0.24	6.05×10^{-3}	0.49
pseudomer-Al(q$_2$Trop)	0.23	1.10×10^{-2}	0.26	0.21	1.77×10^{-2}	0.42

[a] Energetic disorder σ.   [b] Electronic coupling J^2r^2.   [c] Reorganization energy λ.

environment [96]. Modest differences in the value of energy disorder $\sigma(E)$ lead to dramatic variation of the charge carrier mobility μ. OSCs with small energy disorder, such as Al(Acac)$_3$ and *pseudofac*-Al(q$_2$Acac), are characterized by high mobilities μ. Whereas, molecules with high energy disorder $\sigma(E)$, as *pseudofac*-Al(q$_2$Op) and *pseudomer*-Al(q$_2$Trop), yield poor mobilities μ. A relation between the dipole moment of the OSCs (see Table 4.1) and the energy disorder $\sigma(E)$ can be inferred. It appears clear that molecules characterized by low dipole moment have low energy disorder $\sigma(E)$ and *vice versa*. This is true for Al(Acac)$_3$, Al(Op)$_3$ and *pseudofac*-Al(q$_2$Acac), characterized by both low dipole moment and energy disorder $\sigma(E)$. In addition, *mer*-Alq$_3$, *mer*-Al(Op−py)$_3$, *pseudofac*-Al(q$_2$Op) and *pseudomer*-Al(q$_2$Trop) are characterized by both high dipole moment and energy disorder $\sigma(E)$. In contradiction, Al(Trop)$_3$, which has a negligible dipole moment, presents a high energy disorder $\sigma(E)$.

Table 4.3: Calculated charge carrier mobilities μ of the (novel) OSCs.

Compound	Mobility μ	
	[cm^2 V^{-1} s^{-1}]	
	Holes	Electrons
mer-Alq$_3$	3.26×10^{-8}	9.23×10^{-8}
Al(Op)$_3$	1.42×10^{-4}	9.49×10^{-6}
mer-Al(Op−py)$_3$	5.67×10^{-7}	6.64×10^{-8}
Al(Trop)$_3$	4.70×10^{-10}	2.62×10^{-8}
Al(Acac)$_3$	8.57×10^{-3}	6.31×10^{-4}
pseudofac-Al(q$_2$Acac)	1.59×10^{-5}	4.68×10^{-6}
pseudofac-Al(q$_2$Op)	8.32×10^{-12}	2.43×10^{-13}
pseudomer-Al(q$_2$Trop)	2.64×10^{-11}	3.27×10^{-10}

The reorganization energy λ is the energy obtained during the ionic relaxation of the donor and acceptor molecules as well as their environment after the charge transport process. It is usually separated in two parts: (i) the inner part λ_i includes the relaxation of the donor and acceptor, (ii) the outer part λ_o includes the relaxation of the environment. The outer part λ_o is assumed to be much smaller than the inner part λ_i, because the additional charge will cause much stronger conformational changes to the charged molecule than to the molecules in its environment. It can be noted that small differences in the reorganization energy λ do not critically affect the

charge carrier mobility μ. Nonetheless, it is clear that the reorganization energy λ is related to the dipole moment of the OSCs (see Table 4.1). Molecules with a low dipole moment, such as $Al(Acac)_3$, $Al(Op)_3$, $Al(Trop)_3$ and *pseudofac*-$Al(q_2Acac)$, have a low reorganization energy λ. On the contrary, molecules with a high dipole moment, such as *mer*-Alq_3, *mer*-$Al(Op-py)_3$, *pseudofac*-$Al(q_2Op)$ and *pseudomer*-$Al(q_2Trop)$, have also a high reorganization energy λ.
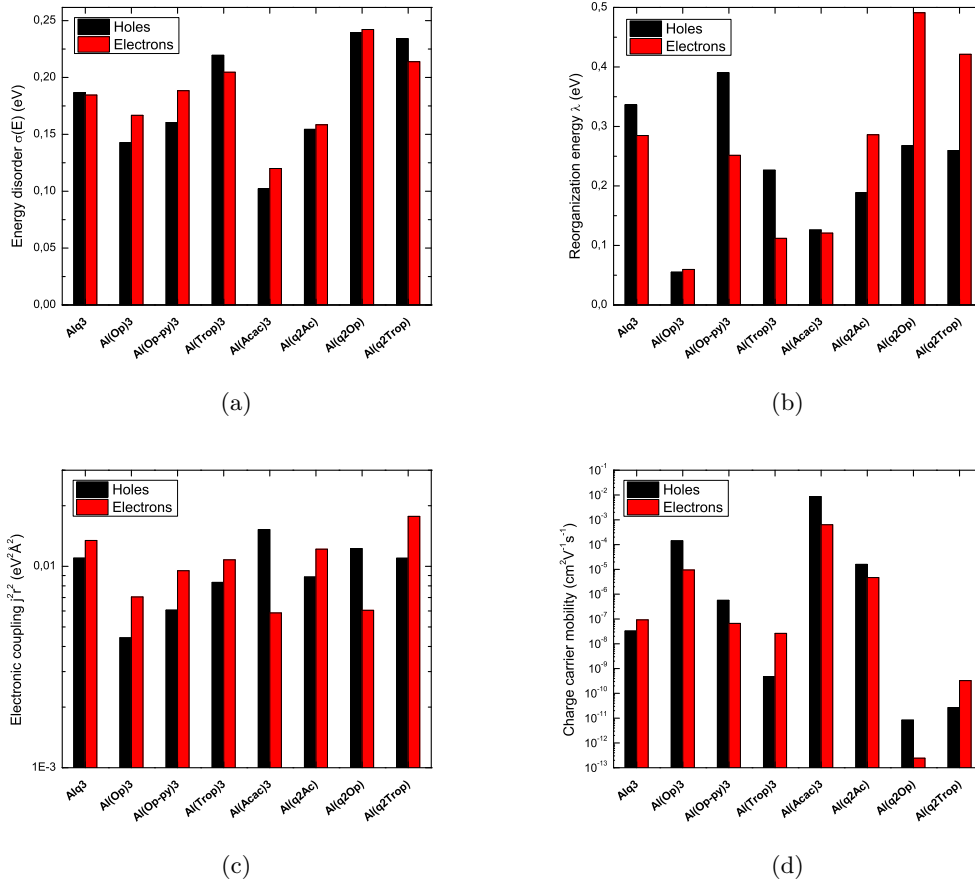
Figure 4.13: Microscopic parameters computed for holes and electrons of the OSCs in the morphologies. (a) Energy disorder $\sigma(E)$. (b) Reorganization energy λ. (c) Electronic coupling J^2r^2. (d) Charge carriers mobility μ.

The last parameter to be considered is the electronic coupling J^2r^2. As the charge carrier mobility μ depends only linearly on the electronic coupling J^2r^2, its variations are of a minor importance. The electronic coupling J^2r^2 fluctuates for all the OSCs in a narrow range between 4.4×10^{-3} and $1.1 \times 10^{-2} \, eV^2 \, Å^2$. In addition, no direct relation between the electronic couplings J^2r^2 and the OSCs structure and/or dipole moment can be inferred from the data.

Charge carrier mobilities μ, estimated for all the studied OSCs, are summarized in Table 4.3. For *mer*-Alq_3 and *pseudofac*-$Al(q_2Acac)$ it is possible to compare the results with the experimentally determined charge carrier mobilities. In addition, the hole mobility of $Al(Op)_3$, measured in thin film transistor devices (TFTs), is reported in Section 4.3.1. However, as far as the author is aware, the charge carrier mobility of the other OSCs is not reported in literature. The mobility of electrons and holes of Alq_3 has been widely studied experimentally by means of several techniques [42–49]. It has been found that the electron mobility is 10^{-5}-$10^{-6} \, cm^2 \, V^{-1} \, s^{-1}$ and the hole mobility is 10^{-8}-$10^{-9} \, cm^2 \, V^{-1} \, s^{-1}$. The calculated electron mo-

bility, $9.23 \times 10^{-8}\,\mathrm{cm^2\,V^{-1}\,s^{-1}}$, results one order of magnitude lowered than the experimental. On the other hand, the calculated hole mobility, $3.26 \times 10^{-8}\,\mathrm{cm^2\,V^{-1}\,s^{-1}}$, fairly agrees with the experimental value. The experimental electron mobility of *pseudofac*-Al(q$_2$Acac), measured via transient electroluminescence, is $2.7\text{-}4.4 \times 10^{-6}\,\mathrm{cm^2\,V^{-1}\,s^{-1}}$ [167], which matches the theoretical value of $4.68 \times 10^{-6}\,\mathrm{cm^2\,V^{-1}\,s^{-1}}$. However, no hole mobility was measured for *pseudofac*-Al(q$_2$Acac). The hole mobility of Al(Op)$_3$, measured in TFTs devices (see Section 4.3.1), is 0.6-$2.1 \times 10^{-6}\,\mathrm{cm^2\,V^{-1}\,s^{-1}}$. In contrast, no obvious electron mobility was detected. The calculated hole mobility, $1.42 \times 10^{-4}\,\mathrm{cm^2\,V^{-1}\,s^{-1}}$, is two order of magnitude higher than the experimental. In addition, with the Quantum Patch method, an electron mobility of $9.49 \times 10^{-8}\,\mathrm{cm^2\,V^{-1}\,s^{-1}}$ was computed. Obviously, the electron mobility in amorphous film of Al(Op)$_3$ is impeded by the formation of excimers in the solid state, described in Section 3.4.1. Excimers are known to be electron traps. Therefore, to obtain more realistic data on the electron mobility, the formation of excimers must be taken in account in the Quantum Patch method.

Among the studied OSCs, *pseudofac*-Al(q$_2$Acac) has a slightly higher electron mobility than *mer*-Alq$_3$. In addition, the electron mobility of *mer*-Al(Op$-$py)$_3$ and Al(Trop)$_3$ is comparable to that of *mer*-Alq$_3$. The mixed-ligands *pseudofac*-Al(q$_2$Op) and *pseudomer*-Al(q$_2$Trop) have a poor mobility of both electrons and holes. The high charge carriers mobility of Al(Acac)$_3$ is caused by its extremely low energy disorder, most probably, due to the strong localization of the orbitals on the non-aromatic ligands. However, this result is unrealistic considering that the charge transport occurs by hopping on the π orbitals of the molecules. Nevertheless, this result is most useful to further improve the Quantum Patch approach.

4.3 Experimental charge carrier mobilities

<div align="right">

TFTs in collaboration with:
Dr. Xiangnan Sun and Prof. Luis E. Hueso
CIC nanoGUNE, Donostia-San Sebastián, Spain

TOF and AS in collaboration with:
Dr. Valeria Fattori and Dr. Francesca Tinti
ISOF-CNR, Bologna, Italy

</div>

4.3.1 FET in Al(Op)$_3$-based TFTs

In this preliminary study, we have measured the charge carriers mobilities of Al(Op)$_3$ in field-effect transistors (FETs). This is most important to confirm the results obtained theoretically, and, in addition, to evaluated the performance of Al(Op)$_3$ as semiconductor (see Section 1.1). In order to do so, we have built and characterized a series of thin film transistors (TFTs) to determine the charge carriers mobility in Al(Op)$_3$ [16]. TFTs were built in a bottom contact configuration (see Section 1.2.4), using SiO$_2$ as gate dielectric, which was thermally grown onto the gate electrode of silicon. Source and drain electrodes of gold were deposited and patterned onto the gate dielectric. The OSC-based active layer was thermally evaporated onto the gate and between the source and drain electrodes, after adding a layer of trichloro(octadecyl)silane (OTS) to increment the charge carrier mobility detectability. To measure the field-effect mobility, a series of Al(Op)$_3$-based TFTs based were fabricated with channel lengths ranging from 10 to $100\,\mu\mathrm{m}$. Transfer curves were obtained by the electrical characterization of the devices.
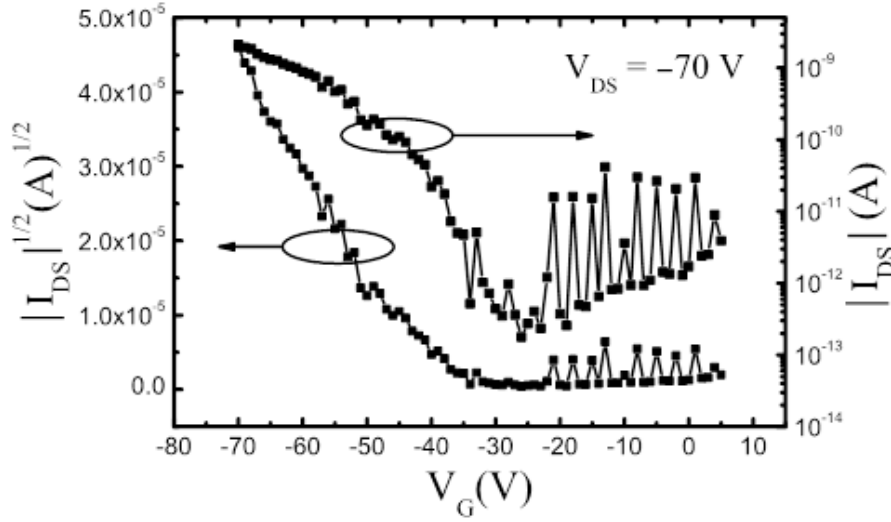
Figure 4.14: Holes transfer curve of the $Al(Op)_3$-based TFT with a channel length of $100\,\mu m$. In this image, I_{DS} and V_{DS} are the source-drain currents. V_G refers to the gate voltage. The hole mobility extrapolated by the transfer characteristics range between 0.6×10^{-6} and $2.1 \times 10^{-6}\,cm^2\,V^{-1}\,s^{-1}$
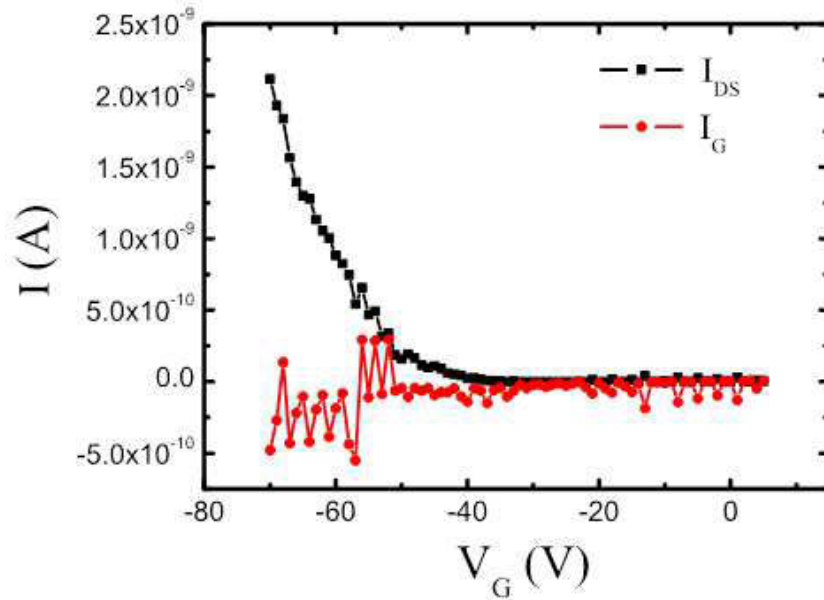
Figure 4.15: Comparison of the source-drain current I_{DS} and the leakage gate current I_G from transfer characterization of the Al(Op)3 based TFT with a channel length of $100\,\mu m$. The source-drain bias V_{DS} for this measurement is $-70\,V$.

Figure 4.14 illustrates the holes transfer curve relative to the TFT device with a channel length of $100\,\mu m$. When a negative voltage is applied to the gate electrode, the hole carriers in the organic semiconductor layer accumulate at the interface with the gate dielectric. Hence, hole transport takes place from the source to the drain electrode. The injection of the charge carriers in the organic layer is provided by a source-drain voltage (V_{DS}) of $-70\,V$. The threshold voltage V_T, necessary to measure the hole mobility, is between -35 and $-45\,V$. In addition, the on/off current ratio measured for the curve in Figure 4.15 is about 104. The on/off current ratio is defined as the ratio between the current when the TFT is in the on-state and the current when the TFT is in the off-state. The off-state is when voltage is not applied to the gate electrode and only small currents flow between source and drain electrodes. The on-state is when a negative voltage is applied to the gate electrode and hole transport takes place from the source to the drain electrode. The hole mobility is determined by the slope of the curve of $|I_{DS}|^{1/2}$ versus the gate voltage illustrated in Figure 4.14. From the characterization of the $Al(Op)_3$-based TFTs a hole mobility between 0.6 and $2.1 \times 10^{-6}\,cm^2\,V^{-1}\,s^{-1}$ was determined. As previously reported, this value is two order of magnitude lower than the hole mobility calculated in Section 4.2.3, $1.42 \times 10^{-4}\,cm^2\,V^{-1}\,s^{-1}$. No obvious electron mobility was detected, most probably, as a consequence of the excimer formation in amorphous thin films of $Al(Op)_3$, which is described in Section 3.4.1.

The hole mobility measured in $Al(Op)_3$-based TFTs is comparable to the hole mobility measured for the well-know hole transporting material α-NPD [213]. In detail, α-NPD is characterized by a hole mobility of $6.1 \times 10^{-5}\,cm^2\,V^{-1}\,s^{-1}$ [214], only one order of magnitude higher than that of $Al(Op)_3$. However, the on/off current ratio, 3.5×10^3 ($V_{SD} = -60\,V$) of the α-NPD-based devices is significantly higher compared to that of $Al(Op)_3$-based TFTs. In addition the threshold voltage V_T, $-4.4\,V$, is considerably lowered. Surprisingly, as far as the author is aware, the only report on field-effect charge carriers mobilities of Alq_3 was reported by Sakanoue *et al.*[78] (see Section 1.2.4). The measured hole mobility was $1.6 \times 10^{-7}\,cm^2\,V^{-1}\,s^{-1}$ with a threshold voltage V_T of $-43\,V$, which is comparable to that obtained for the $Al(Op)_3$-based devices. In addition, the measured electron electron mobility was $5.5 \times 10^{-7}\,cm^2\,V^{-1}\,s^{-1}$ with a threshold voltage V_T of $64\,V$.

4.3.2 Experimental techniques and instrumentation

$Al(Op)_3$ based TFTs were fabricated with a bottom-gated bottom contact geometry. In these devices, highly doped p-type silicon, which has a $150\,nm$ thermal-growth SiO_2 layer on the top, was employed as substrate and bottom gate electrode. Source and drain electrodes were patterned on the Si-SiO_2 substrates by electron beam lithography (Raith 150) method. These electrodes were deposited in high vacuum (Oerlikon evaporator) with an architecture composed by a bottom part of $1.2\,nm$ titanium and a top part of $42\,nm$ gold. Before depositing the organic layer, the substrate was cleaned by oxygen plasma for $5\,min$ and modified with OTS (Purity 90% from Aldrich) by vapor-phase modification method. This process was carried out in a vacuum oven placed inside a glove box, which has an inert N_2 atmosphere (H_2O and O_2 concentration $<0.1\,ppm$). Finally, a $40\,nm$ $Al(Op)_3$ layer was deposited on the OTS-modified substrate in a ultra-high vacuum evaporator (dual-chamber Theva system). The thickness of the $Al(Op)_3$ film in TFTs was calibrated by X-ray reflectivity (XRR) measurements. $Al(Op)_3$-based TFTs were characterized in a Lake Shore probe station with Keithley 4200 semiconductor characterization system. All the electrical measurements on TFTs were carried out in vacuum, at room temperature and in the dark, to avoid the decomposition of the organic material.
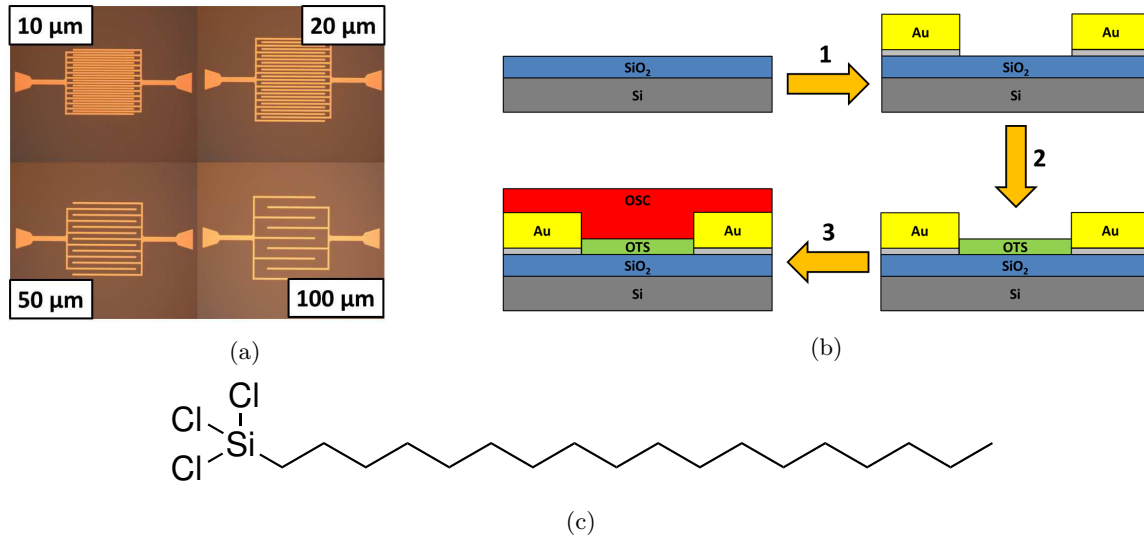
Figure 4.16: (a) Scanning electron microscopy images of the patterned source and drain electrodes. The channel length vary from $10\,\mu m$ (width to length ratio, W/L = 2000) to $100\,\mu m$ (W/L = 50). (b) Schematic procedure of the TFT fabrication. Step 1: Source and drain electrodes patterning. Step 2: OTS modification. Step 3: OSC deposition. (c) Chemical structure of OTS (trichloro(octadecyl)silane).

4.3.3 Preliminary TOF and AS studies

To measure the charge carrier mobilities of the (novel) OSCs, we have initiated a study implementing the well-known time of flight (TOF) and admittance spectroscopy (AS) techniques. Here, we present preliminary results obtained on Alq_3 and $Al(Op)_3$. A optimized configuration of the device is needed to estimate accurately the charge carrier mobilities. So far, the measurements with both the techniques were unsatisfactory. However, a description of the experiments is reported.

We prepared a series of samples with the configuration illustrated in Figure 4.17. Samples were constructed by thermal evaporation on quartz/ITO substrates using FI3 (ter(9,9'-diethylfluorene)) as CGL (charge generation layer) [215]. Due to the high absorption coefficient of FI3 at $337\,nm$, which is the emission wavelength of the used N_2 laser, the CGL allowed to deposit lowered layer thickness of the aluminum complexes. A CGL $200\,nm$ thick is needed to absorb 99.6% of the incident light, thus, the Al-complex layer must be not less than $2\,\mu m$ thick. This configuration should lead to fairly good results since the Al-complex layer is ten times thicker than the CGL. The charge carriers mobilities obtained for Alq_3 (electrons: 2.89×10^{-5}-$6.11 \times 10^{-5}\,cm^2\,V^{-1}\,s^{-1}$; holes: 1.52×10^{-9}-$2.02 \times 10^{-9}\,cm^2\,V^{-1}\,s^{-1}$), illustrated in Figure 4.19, are in good agreement with the reported data in Section 1.2, 10^{-5}-$10^{-6}\,cm^2\,V^{-1}\,s^{-1}$ (electrons) and 10^{-8}-$10^{-9}\,cm^2\,V^{-1}\,s^{-1}$ (holes) [42–49]. Implementing the same sample configuration, preliminary results on $Al(Op)_3$ were unsatisfactory. Since TOF is capable to measure low charge carrier mobilities, we expected to detect, at least, the hole mobility of $Al(Op)_3$, which was measured by FET in the previous section. In order to improve the results, a different sample configuration might be necessary.

The configuration of the samples for the AS measurements is illustrated in Figure 4.18. For holes, MoO_x was used as injecting material together with a silver cathode to prevent the electron diffusion into the organic layer. For electrons, a calcium cathode was utilized to inject the

(a)

(b)
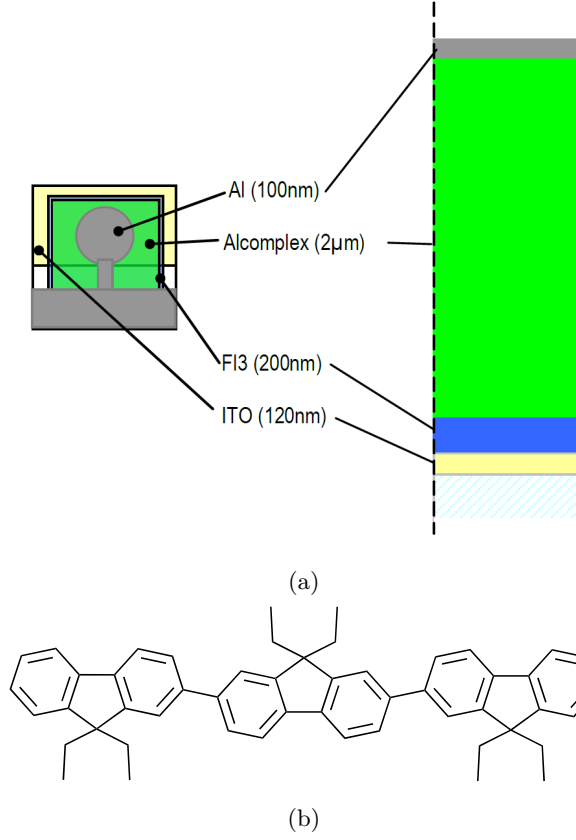
Figure 4.17: (a) Schematic representation of the ambipolar sample used in our experiments ITO/FI3 [200 nm]/Al-complex [2 μm]/Al [100 nm]. The OSC was sandwiched between a transparent ITO electrode and an aluminum electrode. A charge generation layer (CGL) of FI3 (ter(9,9'-diethylfluorene)) was inserted to increase the absorption at the N_2 laser emission wavelength (337 nm). (b) Chemical structure of FI3.

(a)

(b)
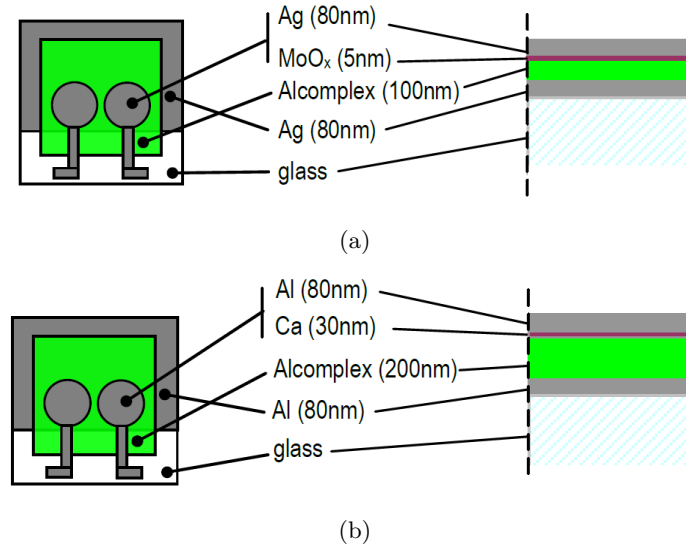
Figure 4.18: (a) Schematic representation of a hole AS setup: Ag [80 nm]/Al-complex [100 nm]/MoO_x [5 nm]/Ag [80 nm]. (b) Schematic representation of an electron AS setup: Al [80 nm]/Al-complex [200 nm]/Ca [30 nm]/Al [80 nm].
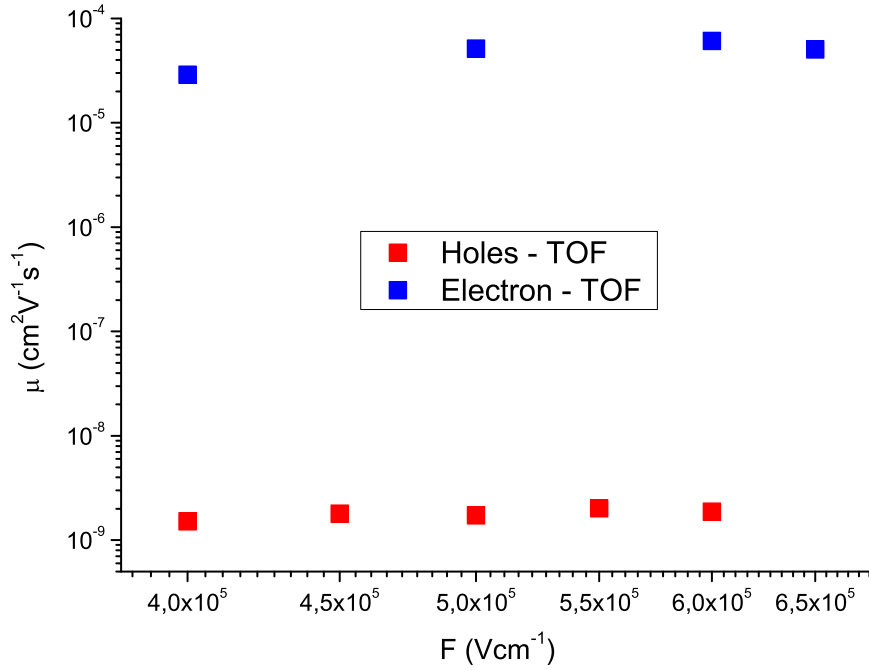
Figure 4.19: Charge carrier mobility of electrons and holes measured for the sample ITO/FI3 [200 nm]/Alq$_3$ [2 μm]/Al [100 nm]. Applied field F for electron mobility: 4.0×10^5 V cm^{-1}-6.5×10^5 V cm^{-1}; for hole mobility: 4.0×10^5 V cm^{-1}-6.0×10^5 V cm^{-1}.

carriers together with an aluminum anode to exclude the hole diffusion into the organic layer. Preliminary studies were unsuccessful in measuring charge carrier mobilities of both Alq$_3$ and Al(Op)$_3$. The reason is, most probably, a wrong choice of electrodes. Therefore, in the future measurements, different electrodes will be implemented.

4.4 Conclusions

In this chapter, we have studied, by means of theoretical and experimental methods, the charge carrier mobility of the (novel) OSCs.

In the first part, the frontier orbitals and the dipole moment were computed in vacuum. It has been shown that the localization of the HOMO and LUMO depends from the symmetry of the ligand. Asymmetric ligands, which form *mer*-Alq$_3$ and *mer*-Al(Op−py)$_3$, lead to localized HOMO and LUMO, and thus, to OSCs with a high dipole moment. Conversely, symmetric ligands, which form Al(Op)$_3$, Al(Trop)$_3$ and Al(Acac)$_3$, result in equally distributed HOMO and LUMO, and thus, to low dipole moments. HOMO and LUMO of the mixed-ligands complex *pseudofac*-Al(q$_2$Acac) are localized exclusively on the quinolinates. On the contrary, HOMO and LUMO of *pseudofac*-Al(q$_2$Op) and *pseudomer*-Al(q$_2$Trop) are strongly and alternatively localized on the different ligands yielding high dipole moments.

Via the DEPOSIT code, morphologies of the OSCs were generated. Pair distribution functions $g(r)$ of the films were plotted. Due to its small and symmetric structure, Al(Acac)$_3$ forms the most ordered and packed film. Similarly, *mer*-Alq$_3$, *mer*-Al(Op−py)$_3$ and *pseudofac*-Al(q$_2$Acac), due to their dipole moment and small ligands, form ordered and packed films. On the other hand, as a consequence of their negligible dipole moments, Al(Op)$_3$ and Al(Trop)$_3$ form quite

disordered films. Likewise, Al(q$_2$Op) and Al(q$_2$Trop), despite their high dipole moment, as a result of the bulky phenalenyl and tropolonate, form disordered films.

Through the newly developed Quantum Patch method, a number of microscopical parameters were computed. In particular we focused our attention on: energy disorder ($\sigma(E)$), reorganization energy (λ), and electronic coupling ($J^2 r^2$). These quantities were used to calculate the charge carrier mobilities μ of the OSCs in film. The theoretical and experimental data for *mer*-Alq$_3$, *pseudofac*-Al(q$_2$Acac) and Al(Op)$_3$ are in a good agreement. Nevertheless, it is necessary to take in account the formation of excimers in solid state for molecules such as Al(Op)$_3$, to compute realistic electron mobilities. In addition, as shown by the high charge carrier mobility of Al(Acac)$_3$, the Quantum Patch method needs further improvement in case of small non-aromatic molecules. Among the OSCs, *mer*-Alq$_3$, *mer*-Al(Op$-$py)$_3$, Al(Trop)$_3$ and *pseudofac*-Al(q$_2$Acac) have similar calculated electron mobility. On the contrary, the calculated hole mobility fluctuates between five orders of magnitude. The mixed-ligands *pseudofac*-Al(q$_2$Op) and *pseudomer*-Al(q$_2$Trop) have the lowest calculated electron and hole mobilities.

In the second part, Al(Op)$_3$ was implemented in TFTs devices to measure the field-effect mobility. A hole mobility between 0.6 and $2.1 \times 10^{-6}\,\mathrm{cm^2\,V^{-1}\,s^{-1}}$ was determined. However, due to the excimer formation, no obvious electron mobility was detected. Additionally, a on/off current ratio of about 104 and a threshold voltage between -35 and $-45\,\mathrm{V}$ were obtained for the Al(Op)$_3$-based TFTs. In contrast, was impossible to measure the charge carrier mobility of Al(Op)$_3$ by TOF and AS. To improve the measurements, it is necessary to reconsider the architecture of the devices.

5. Studies on Co/OSCs Hybrid Interfaces

In collaboration with:
Dr. Mirko Cinchetti and Nicolas Großmann
Prof. Martin Aeschlimann group
Department of Physics and Research center OPTIMAS
University of Kaiserslautern, Kaiserslautern, Germany

5.1 Introduction

The performance of organic spintronic devices is strongly determined by the peculiar spin-dependent properties of the hybrid interface, or *spinterface* [216], formed between the organic semiconductor and the ferromagnetic electrodes [74, 217]. As described in 1.2.3, the prototypical spinterface is Co/Alq$_3$, since it constitutes the basic building block of a large number of organic spintronic devices [15]. The existence of spin polarized hybrid interface states (HISs) has been revealed by spin- and time-resolved spectroscopy experiments. In addition, it has been suggested that Alq$_3$-based spinterfaces can be easily tuned to control the spintronic performance of organic spin valves [75, 218]. Additionally, to tailor the spin-dependent properties of the Co/Alq$_3$ interface, and thus, the performance of the related devices, a systematic chemical substitution is a possible approach.

In this work, we have studied Al(Op)$_3$ as an alternative OSC to form hybrid interfaces, exploiting the mutability of organic semiconductors [219]. As a result of the bigger ligands, compared to those of Alq$_3$ (see Table 3.1), we expect a modification of the chemisorption on cobalt, and thus, different spin-dependent properties of the Co/Al(Op)$_3$ hybrid interface with respect to those of Co/Alq$_3$. Different electronic properties of the OSCs deposited on cobalt will inevitably lead to a modified interaction, in character and strength, between the molecule and the ferromagnetic substrate, resulting in modified spin-filtering properties. The hybrid interface Co/Al(Op)$_3$ has been systematically investigated by spin-dependent spectroscopy to determine its spin-dependent properties [203]. In detail, we have made use of the photoemission spectroscopy techniques (PES) described in 1.3.3: ultraviolet photoemission spectroscopy (UPS), near threshold photoemission spectroscopy (NT-PS), and two-photon photoemission (2PPE). In addition, preliminary UPS studies on the Co/Al(Op$-$py)$_3$ hybrid interface are reported.

5.2   Experimental techniques and instrumentation

All the spectroscopic measurements were performed with an UHV-system consisting of one spectrometer chamber and two evaporator chambers. The base pressure in the spectrometer chamber was 4×10^{-11} mbar. The evaporator chamber enabled us to produce the hybrid interfaces *in situ*, which is crucial to obtain a clean and high quality surface. Cobalt was evaporated by an Omicron EFM 3 evaporator at a pressure of 10^{-10} mbar. OSCs were deposited with a Knudsen cell from Kentax Gmbh at a pressure of 9×10^{-10} mbar. The deposition rates were monitored by a quartz crystal balance calibrated with ellipsometry.

The 3.5 nm thin cobalt films were deposited by electron beam epitaxy on a Cu(001) single crystal. Afterward, the substrate was annealed at 370 K. This resulted in a metastable tetragonally distorted Co fcc structure with an in-plane magnetic uniaxial anisotropy along the (110) direction of copper [113, 114]. The Co/Cu(001) was then progressively covered with OSC to form the hybrid interface.

To detect the occupied manifold of the Co/OSCs systems, we performed UPS and NT-PS [111, 112]. UPS was performed by using an Omicron HIS 13 vacuum ultraviolet lamp, which operates at the He I line ($h\nu$=21.2 eV). The excitation source for NT-PS is a Ti:sapphire laser system with a central wavelength of 800 nm, 82 MHz repetition rate, a pulse power of 1.5 W, and a pulse duration of 100 fs. The output is frequency quadrupled, by using two β-barium borate crystals, leading to the fourth harmonic with a photon energy of 5.95 eV. For both UPS and NT-PS the light incident angle was 45°. The emitted photoelectrons were energy and spin selected by a spin detector based on spin polarized low-energy electron diffraction (Focus SPLEED) mounted on a commercial cylindrical sector analyzer (Focus CSA). The acceptance angle of the detector system is $\pm 13°$ and its energy resolution is 0.22 eV. All the measurements were performed at room temperature.

For static and dynamic detection of unoccupied electronic states we used spin- and time-resolved 2PPE. The experimental set-up for the 2PPE experiments was similar to that described by Cinchetti *et al* [220]. The pulsed light source was a Ti:sapphire laser system similar to that for NT-PS. The system delivers sech^2-shaped pulses of up to 10 nJ pulse^{-1} with a duration of approximately 40 fs at a repetition rate of 80 MHz and a varying central wavelength tunable from 750 to 850 nm. The linearly polarized laser output is frequency doubled in a 0.2 mm-thick β-barium borate crystal, to produce ultraviolet pulses at photon energy tunable between 2.91 and 3.31 eV. The frequency doubled beam is divided with a beam splitter into two equally intense p-polarized beams (Mach-Zehnder interferometer design). One of the beams is guided to a mechanical delay stage where Δt, with respect to the second beam, can be adjusted in steps of 0.67 fs, which corresponds to a change of the beam path length of 0.2 μm. Using a second beam splitter the two beams are made collinear again. The 2PPE technique was used in two modes. In the static mode, which is the 2PPE spectroscopy, the time delay between the two photons is fixed, $\Delta t = \pm 1$ fs, whereas the photon energy was varied between 2.91 and 3.31 eV. In the time-resolved mode, the time delay between the two laser pulses varies from $\Delta t = -9$ to $\Delta t = +9$ps, whereas the photon energy is tuned to 3.25 eV. In this mode, it is possible to determine the lifetime of hot electrons in the intermediate states populated in the 2PPE process [116]. As described for UPS and NT-PS, the light incident angle was 45°. The photoemitted electrons were analyzed in a normal emission geometry in an ultrahigh vacuum system equipped with a commercial cylindrical sector energy analyzer (Focus CSA) and a spin detector (Focus SPLEED).

5.3   Co/Al(Op)$_3$ UPS studies

Al(Op)$_3$ was progressively grown on a freshly deposited cobalt thin film with coverage ranging between 0.5 and 5 nm. The occupied manifold of the interfaces was investigated by UPS. For every growth step, the changes in the work function and the energetic position of the molecular orbitals, giving information about the energy level alignment, were monitored.
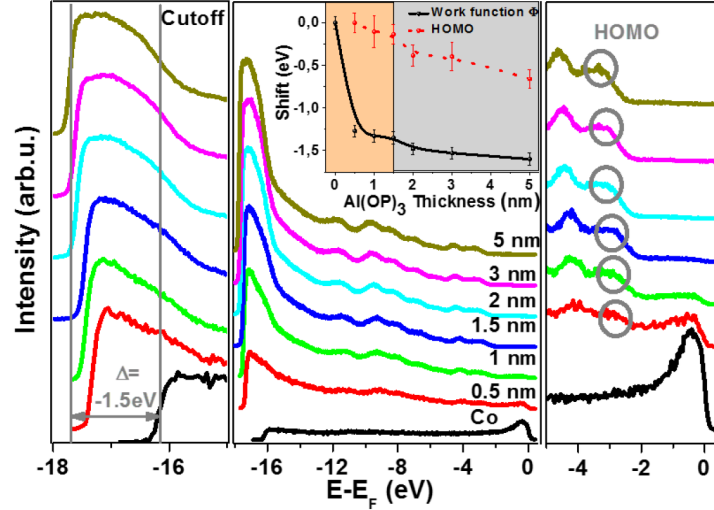
Figure 5.1: UPS spectra of the Co/[x nm] Al(Op)$_3$ system (x= 0 nm, 0.5 nm, 1 nm, 1.5 nm, 2 nm, 3 nm and 5 nm). Right panel: HOMO region; the HOMO (in circle) shifts to lower energies for increasing x. Left panel: normalized low energy cut-off region; the maximal energetic shift of the lower cut-off (Δ= −1.5 eV) is marked. Inset: shift of the work function (black) and of the HOMO (red, dashed) versus x; cobalt work function is 5.1 eV, energetic position of the HOMO for x= 5 nm is −3.3 eV.

The UPS spectra of the Co/[x nm] Al(Op)$_3$ system for x= 0 nm, 0.5 nm, 1 nm, 1.5 nm, 2 nm, 3 nm and 5 nm are shown in Figure 5.1. From the position of the low-energy cut-off (E_{cutoff}), in the left panel, the work function (Φ= 21.2-E_{cutoff} eV) is extracted. The variation of the work function with increasing Al(Op)$_3$ coverage, obtained from the UPS spectra, is plotted in the inset. In detail, we observe a reduction of the work function with increasing Al(Op)$_3$ coverage up to 1.5 nm, caused by a negative interface dipole moment with strength Δ= −1.5 eV. Interface dipole moments of Al(Op)$_3$ and of Alq$_3$ are virtually identical (Δ= −1.5 eV) [218]. In contrast, the calculated molecular dipole moment of Al(Op)$_3$ and of *mer*-Alq$_3$ is rather different either in vacuum, 0.086 D and 4.45 D, respectively, either in amorphous film, 1.52 D and 5.55 D, respectively (see Table 4.1). The identical dipole moment, detected in the UPS measurements, is caused by the symmetry breaking of the interface. The symmetry can be broken in two distinct mechanisms: firstly, interface charge transfer and hybridization, and secondly, by substantial environment symmetry lowering. The work function is almost constant for coverages above 1.5 nm, suggesting that at this nominal coverage the cobalt is completely covered by a monolayer of Al(Op)$_3$ [221, 222]. The right panel shows the magnified UPS spectra in the HOMO region. A progressive shift of the HOMO toward lower energies with increasing Al(Op)$_3$ coverage is observed (plotted in the inset as a dashed red line). The HOMO position ranges from −2.6 eV at x= 0.5 nm to −3.3 eV at x= 5 nm. In addition, the shift is almost linear in function of the Al(Op)$_3$ coverage. The shift in energy of the HOMO position is probably due to the different conditions experienced by the Al(Op)$_3$ molecules in the submonolayer, monolayer, and

bulk molecular film regime, as described by Hill *et al* [223]. Strictly speaking, the surrounding potential of the cobalt film, of neighboring molecules, and of the vacuum will vary with coverage. Since the UPS technique is surface sensitive, the UPS spectra mainly contain information about the first monolayer of organic molecules. Nonetheless, a non-vanishing contribution from the Co/Al(Op)$_3$ interface is preserved in the spectra for 2 and 3 nm Al(Op)$_3$ coverages (the cobalt Fermi energy is still slightly visible in the UPS spectra). Conversely, for 5 nm coverage we solely detect the signal of the surface of the molecular film, with contributions from the underlying molecules in the bulk.
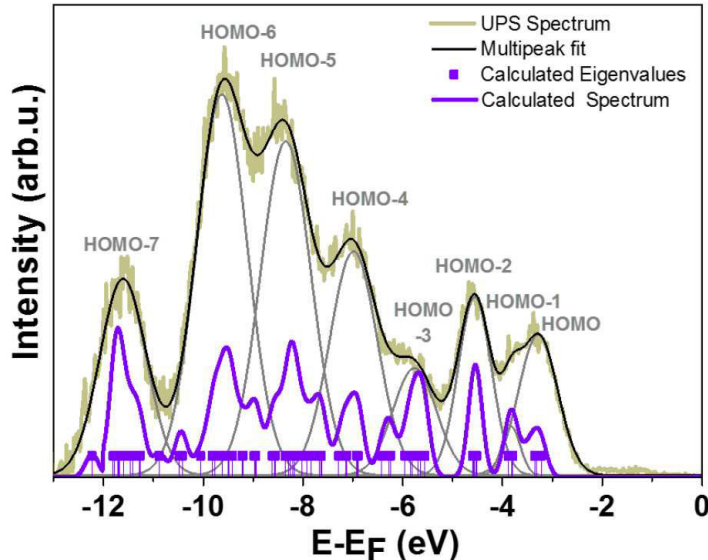
Figure 5.2: UPS spectrum of the Co/[5 nm] Al(Op)$_3$ system after subtraction of the inelastic electron background function performed according to [224] (brown). The fitting with an eight-peak function (black) provides the energetic position of the eight occupied states. The eigenvalues calculated with DFT-B3LYP are indicated with purple vertical bars. The purple continuous line represent the density of states (Gaussian broadening 0.22 eV).

The UPS spectrum of the Co/[5 nm] Al(Op)$_3$ system, after subtracting the inelastic electron background function [224], is shown in Figure 5.2. The eight occupied states have been determined by approximating the spectrum with a multi-peak function. The molecular orbitals, determined by UPS on the Co/[5 nm] Al(Op)$_3$ system, can be compared with the occupied manifold of a free Al(Op)$_3$ molecule, since the electrons originating from the cobalt substrate and from the Co/Al(Op)$_3$ interface cannot be photoemitted anymore.

DFT calculations, in collaboration with Dr. Droghetti A. and Prof. Sanvito S. (Trinity College Dublin, Dublin, Ireland), in addition to the theoretical studies reported in Section 4.2.1, have been carried out to compare the experimental UPS spectrum of the Co/[5 nm] Al(Op)$_3$ system with the DFT-B3LYP spectrum (see Figure 5.2). The NWCHEM [225] quantum chemistry package has been implemented with the exchange correlation functional B3LYP [82] and the 6-31G* basis sets. B3LYP and other hybrid functional have been successfully employed in the description of free Alq$_3$ [226, 227] and, in that case, the density of states compares quantitatively with the UPS spectrum [227, 228]. Furthermore, hybrid functionals often improve the description of molecular spectra, by partially correcting the inherent self-interaction error of local and semi-local functionals [229]. The HOMO energy computed with the ΔSCF method [230] is -6.6 eV, which is in good agreement with the HOMO position, -6.9 eV with respect to the vacuum energy, inferred from the UPS spectrum of the Co/[5 nm] Al(Op)$_3$ system. Simi-

larly, through the ΔSCF method, the calculated LUMO is -1.25 eV and the transport gap is equal to 5.35 eV, i.e. about 0.5 eV smaller than the computed Alq₃ transport gap [226]. In the DFT-B3LYP spectrum, shown in Figure 5.2, the eight-peak structure is clearly recognizable, although some differences between theoretical and experimental results are present.

5.4   Co/Al(Op)₃ NT-PS studies

The normalized NT-PS spectra of the Co/[x nm] Al(Op)₃ system (x= 0 nm, 0.5 nm, 1 nm, 1.5 nm, 2 nm, 3 nm and 5 nm) are shown in Figure 5.3. In the spectra, three main features are visible. The first, close to E_F, is originated by the excitation of a cobalt bulk state with Δ5 symmetry [114]. As expected, its intensity decreases for increasing Al(Op)₃ coverage and vanishes at x= 2 nm. Up to 3 nm coverage, two additional features are visible. Strictly speaking, with the NT-PS we detect two HISs forming at the Co/Al(Op)₃ interface confirming that NT-PS is highly sensitive to the metal/non-metal interface [112].
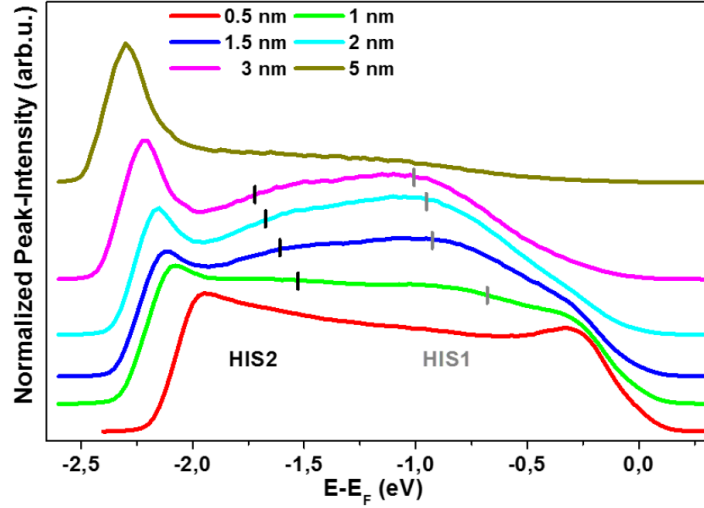
Figure 5.3: Normalized NT-PS spectra of the Co/[x nm] Al(Op)₃ system (x= 0 nm, 0.5 nm, 1 nm, 1.5 nm, 2 nm, 3 nm and 5 nm). The energetic positions of the two interface states HIS1 and HIS2, detectable for $1 \leq x \leq 3$ are marked in the spectra.

To extract the energetic position of the two HISs, a multi-peak fit was carried out for the Co/[1.5 nm] Al(Op)₃ system, as illustrated in Figure 5.4. The energetic positions of the two HISs, HIS1 and HIS2, are marked in Figure 5.3 by vertical lines. The energetic position of the two HISs shifts to lower energy with increasing coverage of Al(Op)₃. As reported for the HOMO of Al(Op)₃, described in Section 5.3, the shift is due to the interaction of the HISs with the surrounding potential of cobalt, neighboring molecules, and vacuum [223].

To compare the the spin polarization (SP) of cobalt with that of the HISs over the complete energy range of the NT-PS measurements, caesium was used to lower the work function of cobalt [114]. The SP polarization of caesiated cobalt (CsCo) ranges between 30 and 40%, in agreement with references [114, 231]. Figure 5.4 illustrates the relative SP of the Co/[x nm] Al(Op)₃ system (x= 0 nm, 0.5 nm, 1 nm, 1.5 nm, 2 nm and 3 nm). The relative SP is is calculated by normalizing the SP of Co/[x nm] Al(Op)₃ to the SP of CsCo. Clearly, the SP for x= 1.5 nm deviates from the SP measured for the other Al(Op)₃ coverages. At x= 1.5 nm the true spinterface formed in the Co/Al(Op)₃ is investigated. In detail, for x< 1.5 nm the interface dipole, and thus, the
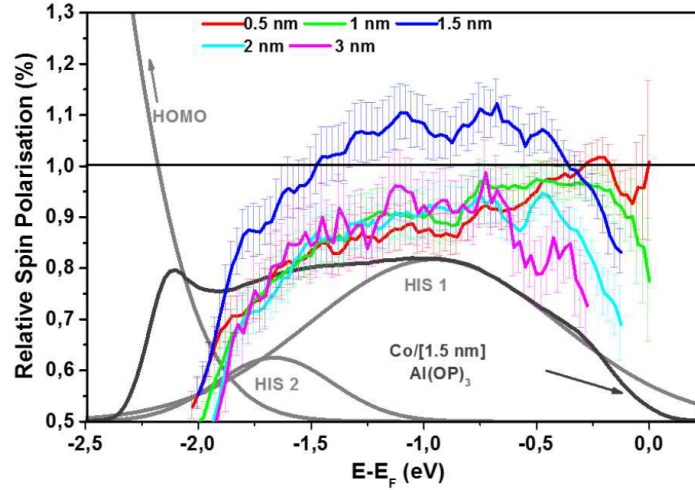
Figure 5.4: Multi-peak fit used to extract the energetic position of HIS1 and HIS2 states, shown for the NT-PS spectrum of the Co/[1.5 nm] Al(Op)$_3$ system. The right y-axis indicates the relative SP of the Co/[x nm] Al(Op)$_3$ system, calculated as the ratio between the SP of the Co/[x nm] Al(Op)$_3$ and the SP of caesiated Cobalt (CsCo), measured by spin-resolved NT-PS.

HISs are not completely formed, and as a consequence, their spectral weight is low. On the contrary, for $x > 1.5$ nm, the spectral weight of the spin-polarized electrons originating from the spinterface is much lower than the spectral weight of the unpolarized electrons excited from the HOMO in bulk Al(Op)$_3$. The measured SP of both HISs is also reduced with increasing Al(Op)$_3$ coverage, in consequence of the spin-flip processes experienced by the spin-polarized electrons, photoexcited at the Co/Al(Op)$_3$ interface, while they travel through the Al(Op)$_3$ before being photoemitted.

The relative SP for $x = 1.5$ nm at the energetic position of the HIS1 is up to 10% higher that the SP of cobalt. Averaged over the energetic region of HIS1 the observed enhancement of the SP is 8%. At the energetic position of HIS2, on average, the SP is 4% lower than the SP of cobalt. Thereby, we conclude that HIS1 has a SP parallel to the cobalt magnetization. Conversely, HIS2 is either unpolarized or polarized antiparallel to the cobalt magnetization.

5.5 Co/Al(Op)$_3$ 2PPE studies

In Figure 5.5 is illustrated the 2PPE spectra of the Co/[2 nm] Al(Op)$_3$ system, measured for photon energy ranging from 3.02 to 3.30 eV. The kinetic energy of the photoemitted electrons is chosen as energy scale. The main feature visible in the spectra, beside the secondary electron peak (SEP) at kinetic energies between 0 and 1 eV, is the LUMO peak. The origin of the LUMO peak is verified by evaluating its energetic shift as a function of the photon energy. This is shown in the inset of Figure 5.5. Clearly, the LUMO energy shifts linearly with $h\nu$, and thus, we can conclude that indeed we are probing an intermediate state (the energy of an initial state shifts with $2h\nu$, as described in Section 1.3.3) [218]. The energy dependent behavior of the unoccupied state is similar to a molecular resonance effect, resulting from a resonant excitation from an occupied state into an unoccupied molecular state (exciton). With a maximum excitation energy of 3.30 eV, no initial states in Al(Op)$_3$ exist for direct excitations into this unoccupied state, i.e. this possibility is discarded.
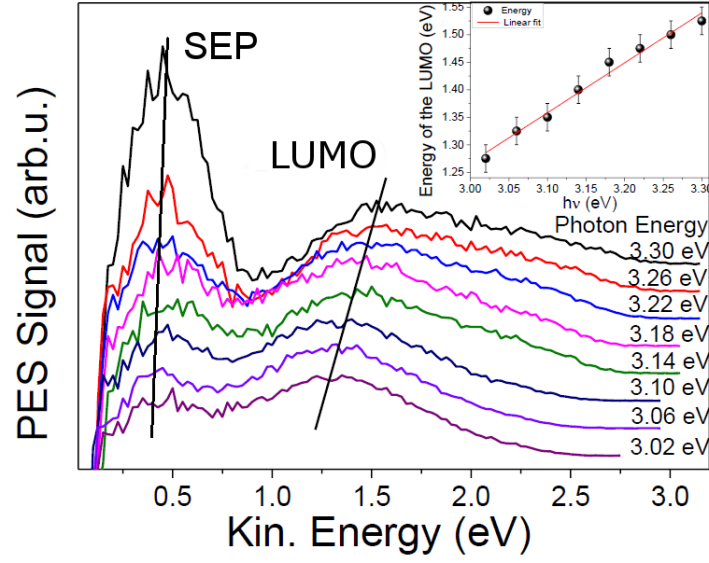
Figure 5.5: 2PPE spectra of the Co/[2 nm] Al(Op)$_3$ system measured for photon energy from 3.02 to 3.30 eV. The secondary electron peaks (SEP) and the LUMO peaks are marked in the spectra. Inset: photo energy dependence of the LUMO energy.
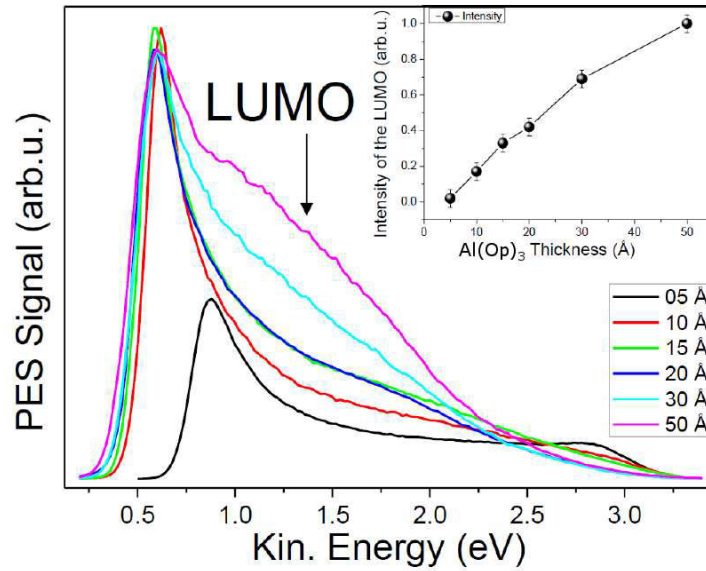
Figure 5.6: 2PPE spectra of the Co/[x nm] Al(Op)$_3$ systems (x= 0.5 nm, 1 nm, 1.5 nm, 2 nm, 3 nm and 5 nm) measured with a photon energy of 3.1 eV. The LUMO peak is marked in the spectra. Inset: thickness dependence of the spectral intensity of the LUMO.
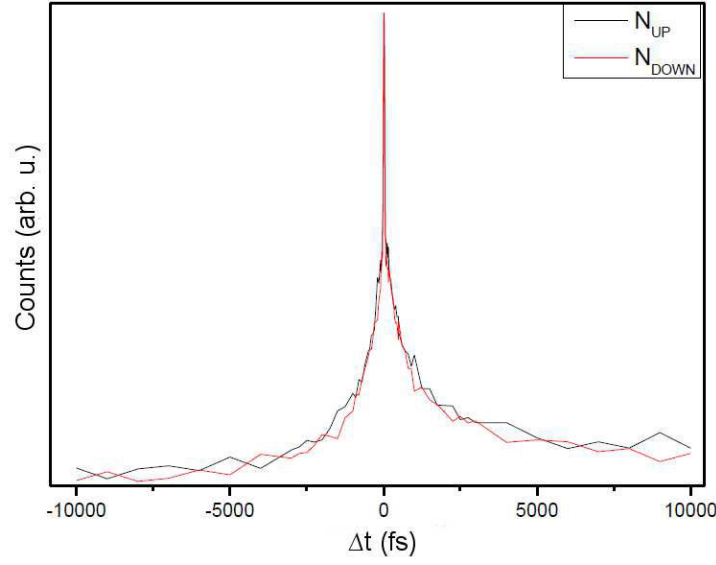
Figure 5.7: Spin- and time-resolved 2PPE spectrum of the Co/[2 nm] Al(Op)$_3$ system illustrated for the spin-up (N_{UP}) and spin-down (N_{DOWN}) electrons. The time delay varies between $-10\,000$ fs and $10\,000$ fs. The photon energy is 3.9 eV.
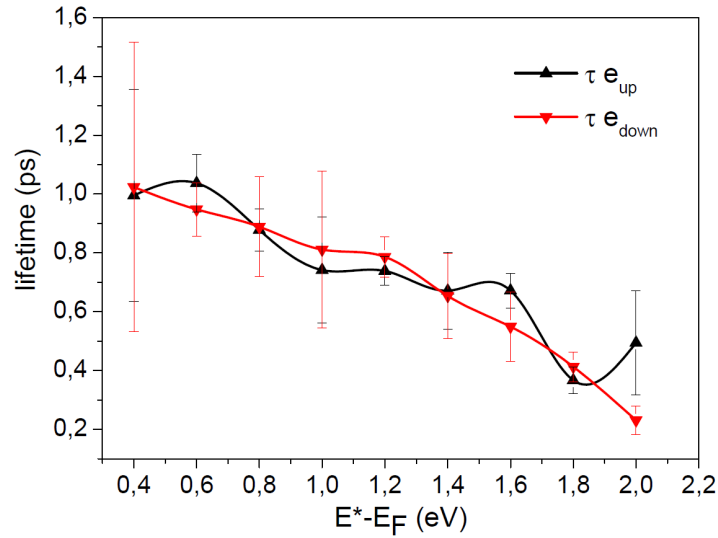
Figure 5.8: Lifetime of the spin-up and spin-down electrons (τe_{up} and τe_{down}, respectively) in the LUMO extracted from the spin- and time-resolved measurements of the Co/[2 nm] Al(Op)$_3$ system in the $E^* - E_F$ energy range between 0.4 and 2.0 eV.

Figure 5.6 illustrates the 2PPE spectra of the Co/[x nm] Al(Op)$_3$ systems ($x=$ 0.5 nm, 1 nm, 1.5 nm, 2 nm, 3 nm and 5 nm), measured with a photon energy of 3.1 eV. The detected LUMO lies 1.2 eV above the Fermi energy. Moreover, as plotted in the inset of Figure 5.6, the spectral intensity of the LUMO increases almost linearly with increasing Al(Op)$_3$ coverage. In contrast to the Co/Alq$_3$ interface, no unoccupied hybrid interface state (uHIS), which is visible only at low coverages (monolayer) and vanishes with increasing coverage (bulk), is detected [218]. Once again, the structural difference, between Alq$_3$ and Al(Op)$_3$ (see Table 3.2), results in divergent electronic properties of Co/Alq$_3$ and Co/Al(Op)$_3$ hybrid interfaces.

Spin- and time-resolved measurements were carried out on the Co/[2 nm] Al(Op)$_3$ system in the $E^* - E_F$ energies range between 0.4 and 2.0 eV. As an example, Figure 5.7 shows the spin- and time-resolved data, recorded with a photon energy of 3.9 eV and delays varying between $-10\,000$ fs and 10 000 fs, representing the population decay of the spin-up (N_{UP}) and spin-down (N_{DOWN}) electrons excited from cobalt into the LUMO of Al(Op)$_3$. The lifetime of electrons in the LUMO, extracted from the energy- spin- and time-resolved 2PPE measurements, is illustrated in Figure 5.8. It ranges between a maximum of ≈1 ps at $E^* - E_F=$ 0.4 eV to a minimum of ≈0.2 ps at $E^* - E_F=$ 2.0 eV, which is long-lived for typical metal-organic interfaces [232]. Since the LUMO orbital is not affected by the SP of the cobalt substrate as an uHIS, the lifetime of the spin-up (τe_{down}) and spin-down (τe_{up}) electrons is virtually identical (in the error range).

5.6 Co/Al(Op−py)$_3$ preliminary UPS studies

Results of the preliminary UPS studies on the Co/Al(Op−py)$_3$ hybrid interface are shown in Figure 5.9. Al(Op−py)$_3$ was progressively grown onto the cobalt surface with coverage ranging from 0.7 to 2.8 nm. Every growth step was monitored with UPS, to measure the work function and the energetic position of the molecular orbitals.
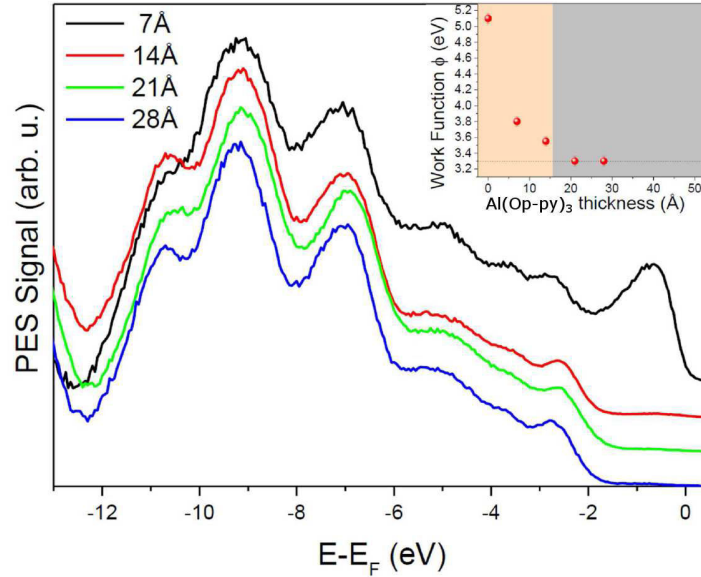
Figure 5.9: UPS spectra of the Co/[x nm] Al(Op−py)$_3$ system ($x=$ 0.7 nm, 1.4 nm, 2.1 nm and 2.8 nm). Inset: shift of the work function.

The variation of the work function with increasing Al(Op−py)$_3$ coverage is illustrated in the

inset of Figure 5.9. The work function decreases, with increasing Al(Op−py)$_3$ coverage, up to about 2 nm. An interface dipole moment with strength of Δ= −1.8 eV was measured. This value is slightly higher than the interface dipole moment observed for Alq$_3$ [218] and Al(Op)$_3$ on cobalt (see Section 5.3). Accordingly, the calculated dipole moment of *mer*-Al(Op−py)$_3$, in vacuum and in thin film, is higher than that of *mer*-Alq$_3$ and of Al(Op)$_3$ (see Table 4.1). In addition, the work function is almost constant for coverages above 2 nm, and thus, we can estimate that at this nominal coverage the cobalt substrate is completely covered by a Al(Op−py)$_3$ monolayer [221, 222]. As described for Al(Op)$_3$ in Section 5.3, a progressive shift of the HOMO to lower energies, with increasing coverage, is observed in the UPS spectra. Moreover, a non-vanishing contribution of the Co/Al(Op−py)$_3$ interface is evident for all the coverages (the cobalt Fermi energy is still slightly visible in the UPS spectra). Further studies are needed to extract accurately the occupied manifold of Al(Op−py)$_3$. In addition, NT-PS and 2PPE studies on the Co/[x nm] Al(Op−py)$_3$ system ($x=$ 0.7 nm, 1.4 nm, 2.1 nm and 2.8 nm) will give an insight on the formation of HISs states and their SP. As a result of the aromatic backbone of the HOp-py ligand (see Table 3.1), a different chemisorption on the cobalt substrate is expected, resulting in distinct HISs formation and SP properties.
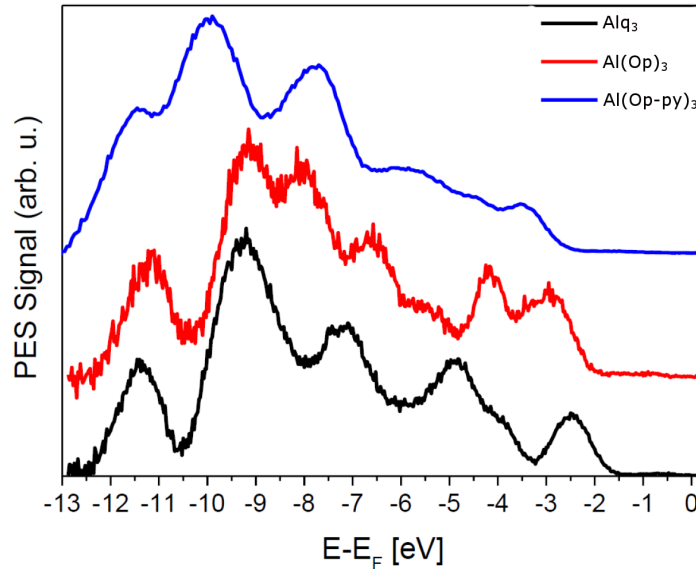
Figure 5.10: Comparison between the UPS spectra of bulk Alq$_3$, Al(Op)$_3$, and Al(Op−py)$_3$ on cobalt.

5.7   Conclusions

The findings for the Co/[5 nm] Al(Op)$_3$ system, obtained with UPS and 2PPE, and the findings for the Co/[2.8 nm] Al(Op−py)$_3$ system, extracted by UPS, are summarized in Figure 5.11, in comparison with the Co/Alq$_3$ interface. Eight occupied states and an interface dipole moment of Δ= −1.5 eV were determined for the Co/[5 nm] Al(Op)$_3$ interface. In addition, the HOMO is −3.3 eV below the Fermi energy E_F and the LUMO is 1.2 eV above the Fermi energy E_F. For the Co/[2.8 nm] Al(Op−py)$_3$ interface, a dipole moment of Δ= −1.8 eV and a HOMO −3.5 eV below the Fermi energy E_F were detected.

The results of the NT-PS measurements on the Co/[1.5 nm] Al(Op)$_3$ system are shown in Figure 5.12. The two HISs with energy $E − E_F$=−0.9 eV and $E − E_F$= −1.6 eV, formed at

the Co/Al(Op)$_3$ interface, are indicated. HIS1 presents a SP 8% higher than the SP of cobalt, whereas HIS2 is characterized by a SP 4% lower than the SP of cobalt.

The chemical tailoring of the OSCs induces different electronic properties of the metallo/organic interfaces. The HOMO of bulk Al(Op)$_3$, Al(Op$-$py)$_3$ and Alq$_3$, deposited on cobalt, is at -3.3 eV, -3.5 eV and -2.7 eV below the Fermi energy E_F, respectively. Conversely, the interface dipole moment is almost identical: $\Delta= -1.5$ eV, $\Delta= -1.8$ eV and $\Delta= -1.5$ eV, respectively.

At last, the spin- and time-resolved 2PPE measurement revealed that no unoccupied interface states (uHISs) are formed in the Co/Al(Op)$_3$ system. However, the LUMO of Al(Op)$_3$ was detected. Since the LUMO is not affected by the SP of the cobalt substrate, the lifetime of the spin-up (τe_{up}) and spin-down (τe_{down}) electrons is identical.
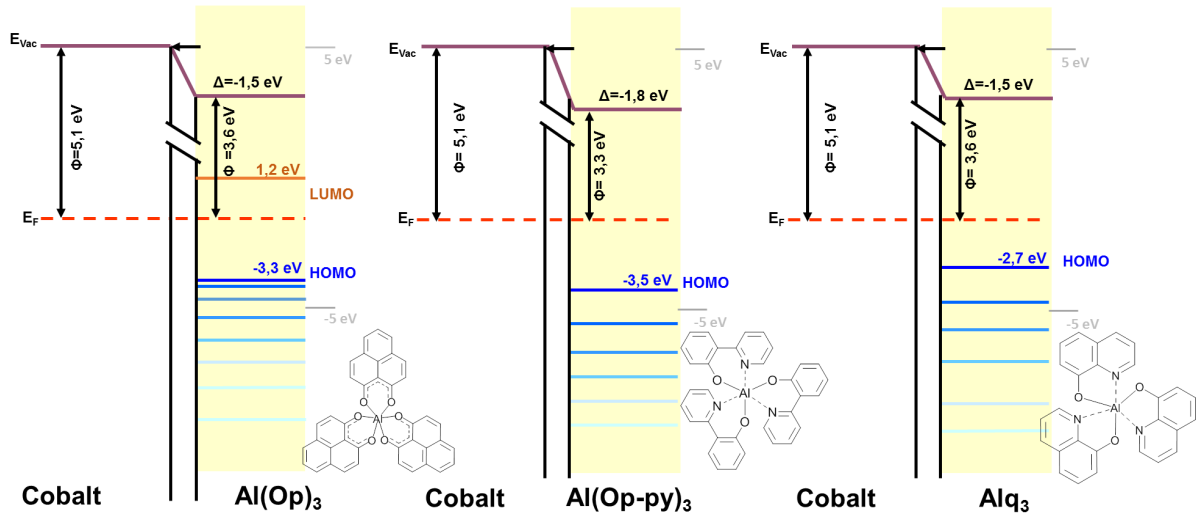
Figure 5.11: Energy level alignment of the Co/[5 nm] Al(Op)$_3$ and Co/[2.8 nm] Al(Op$-$py)$_3$ systems extracted from UPS and 2PPE spectra and compared to the energy level alignment of the Co/Alq$_3$ interface [218].
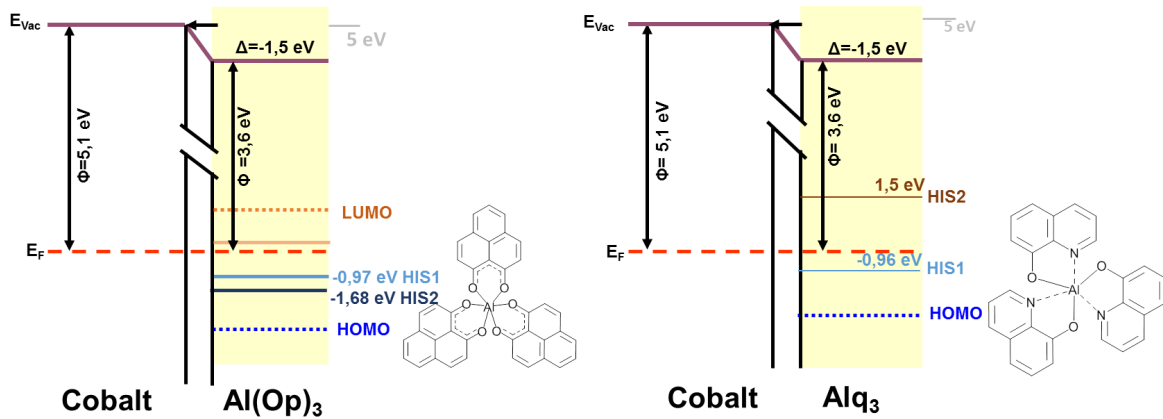
Figure 5.12: Energy level alignment of the Co/[1.5 nm] Al(Op)$_3$ system extracted from NT-PS and 2PPE spectra and compared to the energy level alignment of the Co/Alq$_3$ interface [218].

6. Phenalenyl-based SMMs

In collaboration with:
Dr. Yanhua Lan
INT-KIT, Karlsruhe, Germany

6.1 Introduction

In this chapter, we have explored the capability of the ligand 9-hydroxy-1H-phenalen-1-one (HOp) **3** to chelate paramagnetic atoms, i.e. dysprosium and terbium, to form single-molecule magnets (SMMs). As described in the Section 1.4.2 of the introduction, many lanthanide SMMs were synthesized with β-diketonate ligands. Strictly speaking, HOp **3** has the same chelating atoms and geometry of β-diketonates with the two oxygens embedded in an aromatic backbone, as illustrated in Figure 6.1.
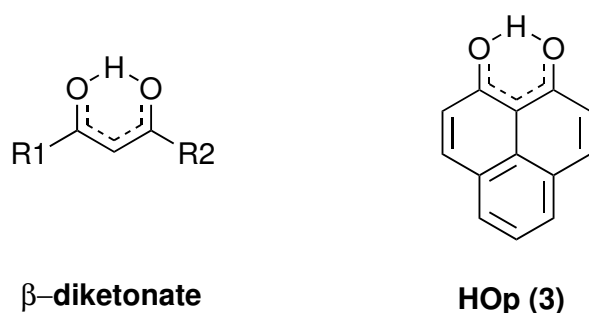
β–**diketonate**   **HOp (3)**

Figure 6.1: Chemical structure of β-diketonates and of HOp **3**.

By reacting HOp **3** with dysprosium and terbium salts we could synthesize stable complexes, which were characterized by means of paramagnetic ^{1}H-NMR, MALDI-TOF spectrometry, and UV-Vis spectrophotometry. Additionally, implementing a synthetic strategy in anhydrous conditions, we were able to form sublimable phenalenyl-based dysprosium and terbium complexes. These complexes were characterized prior and after the sublimation process.

To investigate the SMM behavior of the phenalenyl-based lanthanide complexes, magnetic measurements by SQUID are, generally, carried out on crystalline materials, and thus, at first we have grown single crystals of the complexes. In detail, single crystals of two dysprosium complexes were obtained and their exact structure was solved. The preliminary magnetic properties of these two complexes where recorded, indicating that, indeed, they might show SMM behavior. Further studies to investigate the structure of phenalenyl-based lanthanide complexes and their magnetic properties are currently ongoing.

6.2   Experimental techniques and instrumentation

All the purchased chemicals and solvents were used as received without any further purification unless otherwise stated. The reactions involving water sensitive materials were carried out with distilled THF (over Na) and implementing standard Schlenck techniques; the glassware was kept in oven at 80 °C and evacuated with argon prior use. The elemental analysis of carbon and hydrogen, was carried out in a Vario Micro Cube. Paramagnetic ^{1}H-NMR spectra were recorded in a Bruker FT-NMR Avance III 500 MHz with deuterated solvents as internal standards. Matrix-assisted laser desorption/ionization-time of flight (MALDI-TOF) mass spectrometric data were acquired on a MALDI-TOF Synapt G2-S HDMS with no additional matrix compound other than the sample itself. The absorption spectra were acquired at room temperature for diluted DMSO (spectrophotometric grade) solutions on a Cary 500 Scan Uv-Vis-NIR spectrophotometer using a 1 cm quartz cell. Emission spectra were recorded at room temperature for diluted DMSO (spectrophotometric grade) solutions on a Cary Eclipse Fluorescence spectrophotometer using a 1 cm quartz cell. Magnetic measurements were obtained with a Quantum Design SQUID magnetometer MPMS-XL. dc susceptibility measurements were carried out over the temperature range 1.8-300 K under applied an applied field of 0.1 T. Magnetization measurements were made at low temperatures with applied dc fields from 0 to 70 kOe. ac susceptibility measurements were measured in zero dc field with an oscillating ac field of 3 Oe and ac frequencies ranging from 1 to 1500 Hz. Measurements were performed on polycrystalline samples. The ground powder was restrained in Apiezon grease. The magnetic data were corrected for the sample holder. Single crystal X-ray diffraction data were collected on a STOE IPDS II diffractometer with graphite monochromated Mo Kα radiation (0.710 73 Å). Structure solution and refinement against F^2 were carried out using shelxs and shelxl software. Refinement was performed with anisotropic temperature factors for all non-hydrogen atoms (disordered atoms were refined isotropically); hydrogen atoms were calculated on idealized positions.

6.3   Synthesis of phenaleny-based Dy and Tb SMMs

The synthesis of phenalenyl-based lanthanide complexes was reported by Van Deun *et al.* [233, 234]. The authors described the synthesis of 1:3 metal-to-ligand ratio complexes using ammonia as a base, and the synthesis of 1:4 metal-to-ligand ratio complexes using a stronger base, such as NaOH. A similar approach was implemented to form phenalenyl-based europium complexes [235]. In addition, phenalenyl-based europium and gadolinium nonanuclear complexes were obtained using Et$_3$N as a base and a 1:1.8 metal-to-ligand ratio [236]. In view of these works, to obtain phenalenyl-based mononuclear dysprosium complexes, we have implemented the synthetic procedures illustrated in Scheme 6.1 and described in Section 8.3. When NaH was used as a base to deprotonate HOp in a 1:3 Dy/HOp stoichiometry , the complex bis-(1-oxo-1H-phenalen-9-olate)dysprosium chloride ([Dy(Op)$_2$Cl(HOp)(EtOH)]) **32** was formed. In [Dy(Op)$_2$Cl(HOp)(EtOH)] **32**, the coordination sphere of the dysprosium atom is completed by HOp **3** and EtOH. Conversely, using diisopropyl amine as a base, the 1:3 metal-to-ligand ratio complex was obtained. The coordination sphere of the dysprosium atom in the tris-(1-oxo-1H-phenalen-9-olate)dysprosium is filled by HOp , yielding [Dy(Op)$_3$(HOp)] **33**, or ethanol, yielding [Dy(Op)$_3$(EtOH)] **34**. The exact structure of those complexes, which is discussed in Section 6.4, was determined by single crystal X-ray diffraction experiments on single crystals grown from slow evaporation of EtOH solutions. Due to their similar structure, [Dy(Op)$_3$(HOp)] **33** and [Dy(Op)$_3$(EtOH)] **34** co-crystallized in single crystals. Since it was impossible to separate the two complexes by standard techniques, the two complexes were characterized simultaneously.
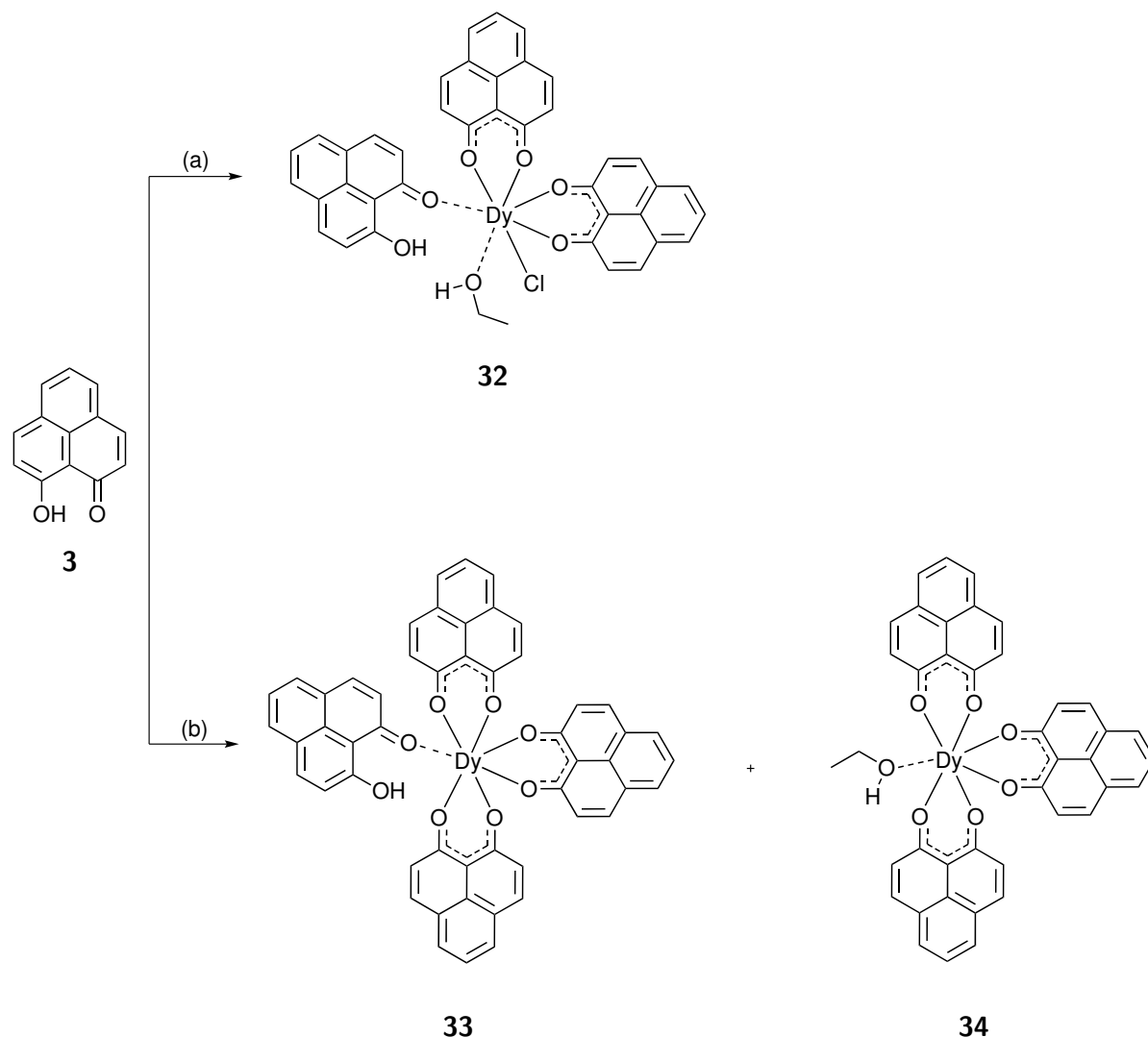
Scheme 6.1: Synthesis of $[Dy(Op)_2Cl(HOp)(EtOH)]$ **32** and of $[Dy(Op)_3(HOp)]$ **33**-$[Dy(Op)_3(EtOH)]$ **34**. (a) NaH, $DyCl_3 \cdot 6\,H_2O$, EtOH, reflux, 3 h, room temperature, overnight. (b) diisopropylamine, $DyCl_3 \cdot 6\,H_2O$, EtOH, reflux, 3 h, room temperature, overnight.

Due to the presence of HOp **3** and EtOH in the coordination sphere of $[Dy(Op)_2Cl(HOp)(EtOH)]$ **32** and of $[Dy(Op)_3(HOp)]$ **33**-$[Dy(Op)_3(EtOH)]$ **34**, the complexes decomposed at $\approx 350\,°C$, during the sublimation process in high vacuum ($10^{-6}\,mbar$). By implementing the method described by Katkova *et al.*, which makes use of bis(trimethylsilyl)amine to form sublimable lanthanides quinolinates [237–239], we synthesized a sublimable phenalenyl-based dysprosium complex **36**. The synthetic procedure, illustrated in Scheme 6.2, was carried out in anhydrous conditions, implementing standard Schlenk techniques, carefully distilled THF, anhydrous starting materials and oven-dried glassware. So far, single crystals of the dysprosium complex, obtained with this procedure, could not be grown, and thus, its exact structure it is unknown. Nevertheless, it was fully characterized by NMR spectroscopy, mass spectrometry and UV-Vis spectrophotometry. In addition, it was successfully sublimated at $\approx 300\,°C$ in high vacuum ($10^{-6}\,mbar$). To confirm the thermal stability, the dysprosium complex **36** was characterized also after the sublimation process.
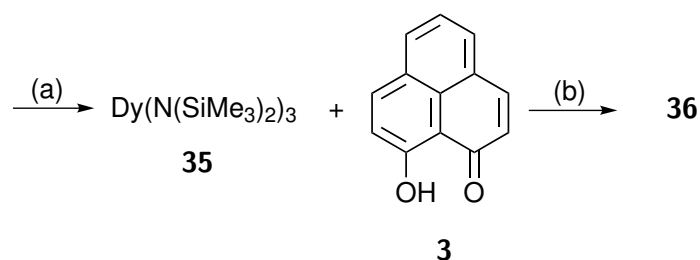
Scheme 6.2: Synthesis of a phenalenyl-based dysprosium complex **36** in anhydrous conditions. The exact structure of the complex is unknown. (a.1) $HN(SiMe_3)_2$, n-BuLi, THF, 0 °C, 1 h. (a.2) $DyCl_3$, THF, room temperature, overnight. (b) THF, reflux, overnight.
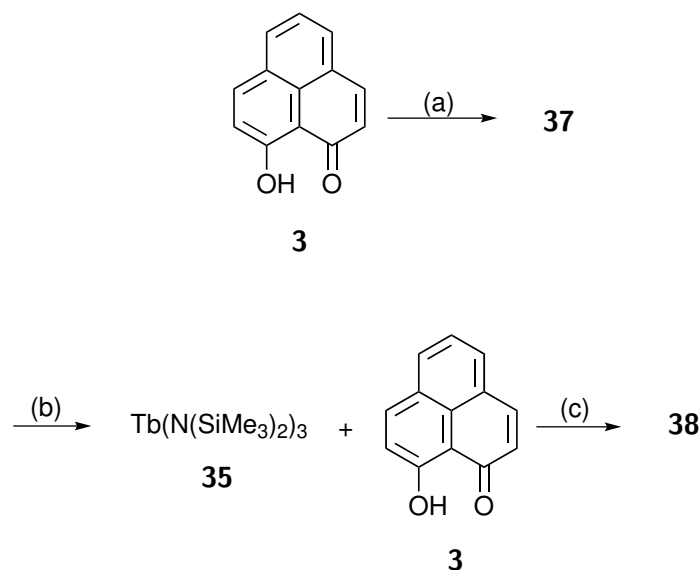
Scheme 6.3: Synthesis of phenalenyl-based terbium complexes in EtOH **37** and in anhydrous conditions **38**. The exact structures of the complexes are unknown. (a) diisopropylamine, $TbCl_3 \cdot 6\,H_2O$, EtOH, reflux, overnight. (b.1) $HN(SiMe_3)_2$, n-BuLi, THF, 0 °C, 1 h. (b.2) $DyCl_3$, THF, room temperature, overnight. (c) THF, reflux, overnight.

Phenalenyl-based terbium complexes were synthesized adopting the same synthetic strategies described to form the mononuclear phenalenyl-based dysprosium complexes. As illustrated in Scheme 6.3, at first, we have reacted the ligand HOp **3** with a terbium salt in EtOH, using diisopropylamine as base. The second procedure implemented was carried out in anhydrous conditions, using distilled THF as a solvent, anhydrous starting materials and oven-dried glassware. Single crystals of the phenalenyl-based terbium complexes **37** and **38** could not be grown, and thus, their exact structure could not be solved. Nonetheless, a structural characterization, by means of NMR spectroscopy, mass spectrometry and Uv-Vis absorption spectrophotometry was carried out. In addition, the terbium complex **38** was sublimed at $\approx 300\,^{\circ}$C in high vacuum (10^{-6} mbar); the sublimated material was additionally characterized.

6.4 Molecular structure of the dysprosium complexes

The molecular structure of $[Dy(Op)_2Cl(HOp)(EtOH)]$ **32** is illustrated in Figure 6.2 (refinement data in Table C.8). The central dysprosium is coordinated by seven atoms, six oxygens and one chloro, resulting in a mono-capped trigonal prism geometry with a symmetry lower than D_{5h} (see Table 6.1 for selected bond lengths and angles). First we discuss the bond lengths and angles between the dysprosium and the oxygen of the deprotonated phenalenyls. The bond lengths Dy-O1, Dy-O2, Dy-O3 and Dy-O4 are between 2.25 and 2.28 Å, in addition, the bond angles Dy-O1-C1, Dy-O2-C3, Dy-O3-C14, and Dy-O4-C16, are ranging between 136.8° and 138.8°. This indicates that, although the molecule is asymmetric, the two deprotonated phenalenyls are identical. On the contrary, the bond length Dy-O5 (of the protonated phenalenyl) is considerably longer, 2.38 Å, and the angle Dy-O5-C27 is wider, 148.3°. Due to the presence of HOp **3** and EtOH, $[Dy(Op)_2Cl(HOp)(EtOH)]$ **32** forms intramolecular and intermolecular hydrogen bonds. In detail, there are two intramolecular hydrogen bonds, between O6H6 and O2 (2.52 Å) and between O6H6 and O5 (1.90 Å), involving HOp, and an intermolecular hydrogen bond between O7H7 and Cl1 (2.49 Å) involving EtOH. Clearly, the intermolecular hydrogen bonds, together with the interaction between the phenalenyls, drive the molecular packing in the crystal lattice.

In an asymmetric unit, the two dysprosium complexes $[Dy(Op)_3(HOp)]$ **33** and $[Dy(Op)_3(EtOH)]$ **34** co-crystallized with two additional EtOH, as illustrated in Figure 6.3 (refinement data in Table C.9). In both the complexes, the central dysprosium is coordinated by seven oxygens in a mono-capped trigonal prism geometry (see Table 6.1 for selected bond lenghts and angles). In $[Dy(Op)_3(HOp)]$ **33**, the bond lengths between the dysprosium and the oxygens of the deprotonated phenalenyls, Dy1-O1, Dy1-O2, Dy1-O3, Dy1-O4, Dy1-O5, Dy1O6, are varying between 2.280 and 2.309 Å. The bond angles, Dy1-O1-C1, Dy1-O2-C3, Dy1-O3-C14, Dy1-O4-C16, Dy1-O5-C27 and Dy1-O6-C29, have similar values between 135.3° and 139.1°. Similar bond lengths and angles indicate that the deprotonated phenalenyls are almost identical, despite the asymmetric geometry of $[Dy(Op)_3(HOp)]$ **33**. In contrast, the bond length between Dy1 and O7 in $[Dy(Op)_3(HOp)]$ **33** is 2.381 Å, similar to Dy-O5 in $[Dy(Op)_2Cl(HOp)(EtOH)]$ **32**. Two intramolecular hydrogen bonds are formed: O8H8-O4 (2.39 Å) and O8H8-O7 (1.86 Å). The bond lengths between the deprotonated phenalenyls and the central dysprosium in $[Dy(Op)_3(EtOH)]$ **34**, Dy2-O9, Dy2-O10, Dy2-O11, Dy2-O12, Dy2-O13, Dy2O14, which vary between 2.249 and 2.324 Å, are virtually identical to those in $[Dy(Op)_3(HOp)]$ **33**. Furthermore, also the bond angles, Dy2-O9-C53, Dy2-O10-C55, Dy2-O11-C66, Dy2-O12-C68, Dy2-O13-C79 and Dy2-O14-C81, which are ranging between 137.5° and 139.1°, are comparable to those in $[Dy(Op)_3(HOp)]$ **33**. Diversely, $[Dy(Op)_3(EtOH)]$ **34** forms three intermolecular hydrogen bonds. The intermolecular hydrogen bond, O15H15-O16 (2.06 Å) involves the EtOH bonded to the dysprosium

(a)

(b)   (c)   (d)
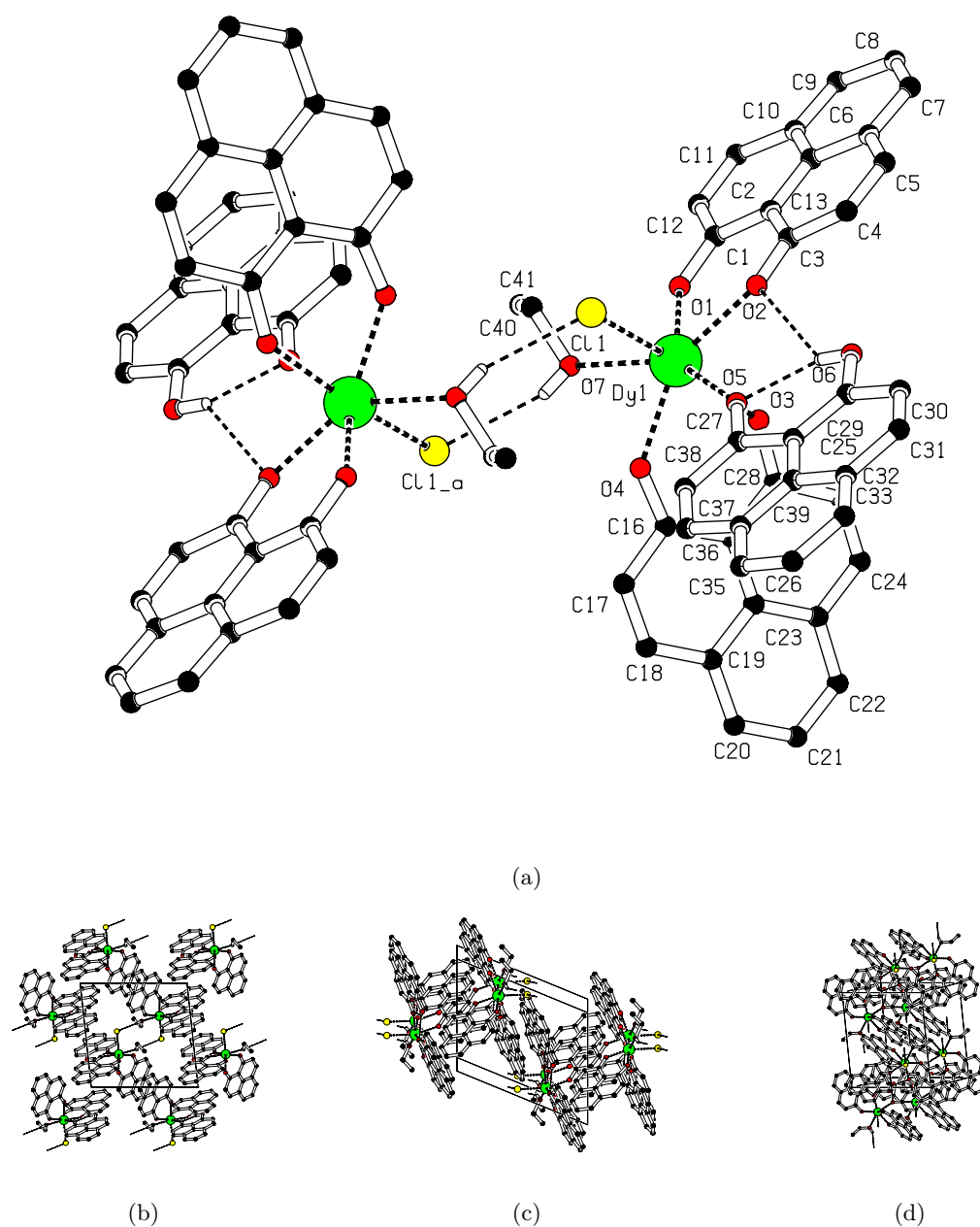
Figure 6.2: (a) Molecular structure obtained by single crystal X-ray diffraction on a single crystal of $[Dy(Op)_2Cl(HOp)(EtOH)]$ **32**. Two molecules are depicted to show the intermolecular hydrogen bond OH-Cl (2.49 Å). Hydrogen atoms non involved in hydrogen bonds are omitted for clarity. Selected bond lengths and angles are listed in Table 6.1. The crystal refinement data is reported in Table C.8. The molecular packing in the single crystal of $[Dy(Op)_2Cl(HOp)(EtOH)]$ **32** is illustrated in (a) yz (b) xz (c) xy perspective.
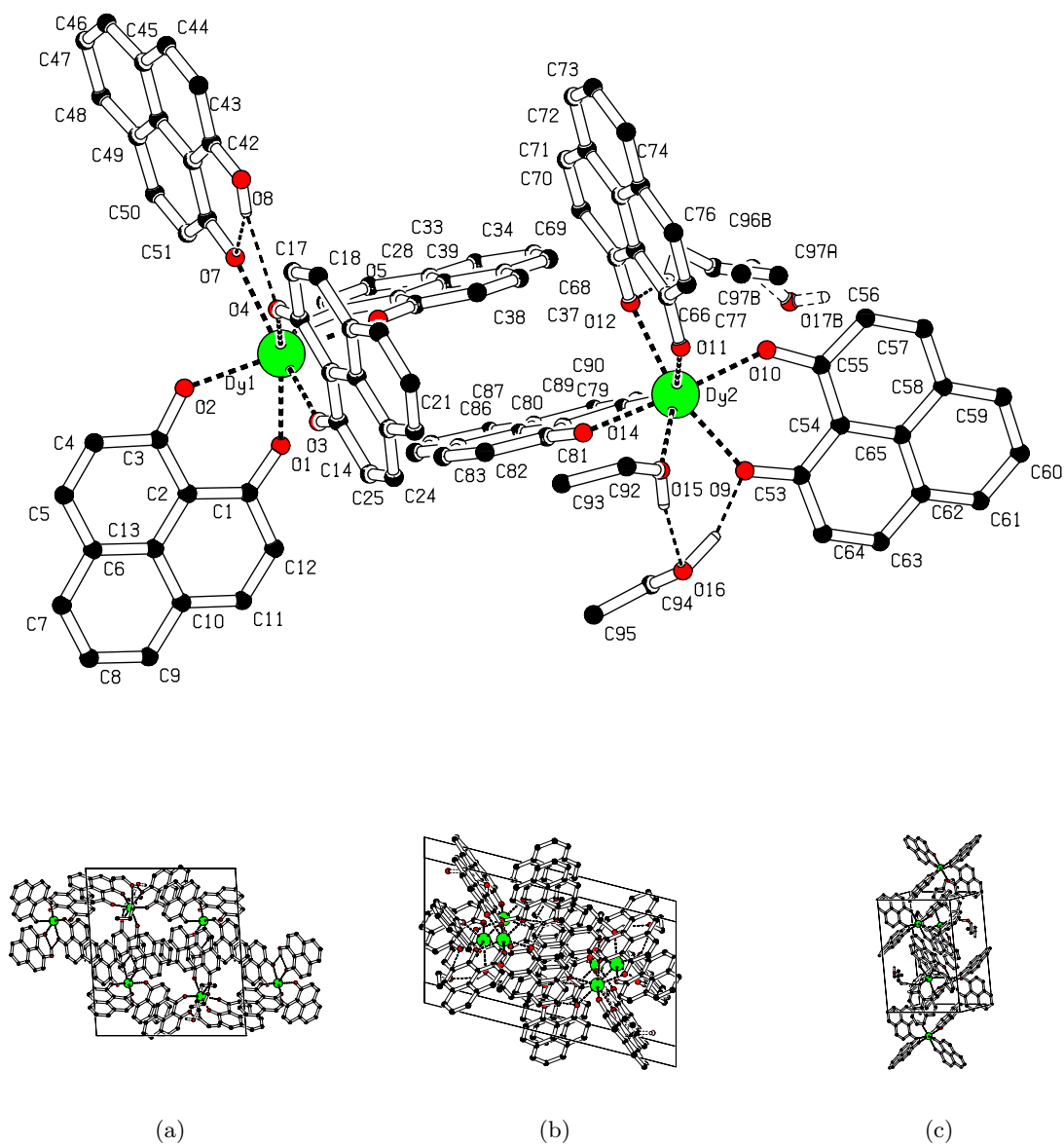
Figure 6.3: (a) Molecular structure obtained by single crystal X-ray diffraction on a single crystal of $[Dy(Op)_3(HOp)]$ **33**-$[Dy(Op)_3(EtOH)]$ **34**. Hydrogen atoms non involved in hydrogen bonds are omitted for clarity. Selected bond lengths and angles are listed in Table 6.1. The crystal refinement data is reported in Table C.9. The molecular packing in the single crystal of $[Dy(Op)_3(HOp)]$ **33**-$[Dy(Op)_3(EtOH)]$ **34** is illustrated in (a) yz (b) xz (c) xy perspective.

Table 6.1: Selected bond distances and angles for [Dy(Op)$_2$Cl(HOp)(EtOH)] **32**, [Dy(Op)$_3$(HOp)] **33**, and [Dy(Op)$_3$(EtOH)] **34**.

Bond	Length [Å]	Bond angle	Angle [°]	Bond angle	Angle [°]
		[Dy(Op)$_2$Cl(HOp)(EtOH)] **32**			
Dy1-Cl1	2.6983(5)	Dy1-O1-C1	138.85(14)	O1-Dy1-O4	127.84(5)
Dy1-O1	2.2517(18)	Dy1-O2-C3	137.87(14)	O1-Dy1-O5	143.56(5)
Dy1-O2	2.2647(14)	Dy1-O3-C14	136.81(14)	O1-Dy1-O7	72.06(6)
Dy1-O3	2.2802(15)	Dy1-O4-C16	137.62(14)	O2-Dy1-O3	85.95(5)
Dy1-O4	2.2599(16)	Dy1-O5-C27	148.28(14)	O2-Dy1-O4	149.03(6)
Dy1-O5	2.3756(16)	Dy1-O7-C40	123.20(13)	O2-Dy1-O5	72.01(6)
Dy1-O7	2.4215(17)	Cl1-Dy1-O1	108.38(4)	O2-Dy1-O7	139.73(6)
O6H6-O2	2.52(4)	Cl1-Dy1-O2	92.92(4)	O3-Dy1-O4	73.69(5)
O6H6-O5	1.90(4)	Cl1-Dy1-O3	161.85(4)	O3-Dy1-O5	78.12(5)
O7H7-Cl1	2.49(3)	Cl1-Dy1-O4	99.30(4)	O3-Dy1-O7	112.98(5)
		Cl1-Dy1-O5	84.30(4)	O4-Dy1-O5	80.97(6)
		Cl1-Dy1-O7	79.19(4)	O4-Dy1-O7	70.92(6)
		O1-Dy1-O2	73.31(5)	O5-Dy1-O7	144.33(6)
		O1-Dy1-O3	88.68(6)		
		[Dy(Op)$_3$(HOp)] **33**			
Dy1-O1	2.290(3)	Dy1-O1-C1	135.3(3)	O2-Dy1-O4	94.47(11)
Dy1-O2	2.286(3)	Dy1-O2-C3	135.8(3)	O2-Dy1-O5	176.83(12)
Dy1-O3	2.280(3)	Dy1-O3-C14	137.5(3)	O2-Dy1-O6	104.56(11)
Dy1-O4	2.280(3)	Dy1-O4-C16	137.6(3)	O2-Dy1-O7	84.20(11)
Dy1-O5	2.289(3)	Dy1-O5-C27	139.1(3)	O3-Dy1-O4	72.93(12)
Dy1-O6	2.309(3)	Dy1-O6-C29	138.5(2)	O3-Dy1-O5	86.47(12)
Dy1-O7	2.381(3)	Dy1-O7-C40	149.9(3)	O3-Dy1-O6	137.28(11)
O8H8-O4	2.39(6)	O1-Dy1-O2	73.25(11)	O3-Dy1-O7	144.34(12)
O8H8-O7	1.86(6)	O1-Dy1-O3	73.37(12)	O4-Dy1-O5	88.42(11)
		O1-Dy1-O4	142.63(12)	O4-Dy1-O6	140.20(12)
		O1-Dy1-O5	105.15(11)	O4-Dy1-O7	71.55(12)
		O1-Dy1-O6	77.00(12)	O5-Dy1-O6	72.33(11)
		O1-Dy1-O7	138.78(11)	O5-Dy1-O7	95.51(11)
		O2-Dy1-O3	95.61(12)	O6-Dy1-O7	75.94(12)
		[Dy(Op)$_3$(EtOH)] **34**			
Dy2-O9	2.324(3)	Dy2-O9-C53	137.5(3)	O9-Dy2-O11	117.23(11)
Dy2-O10	2.268(3)	Dy2-O10-C55	138.9(3)	O9-Dy2-O12	156.73(12)
Dy2-O11	2.249(3)	Dy2-O11-C66	139.1(3)	O9-Dy2-O13	82.10(11)
Dy2-O12	2.288(3)	Dy2-O12-C68	137.6(3)	O9-Dy2-O14	107.08(12)
Dy2-O13	2.290(3)	Dy2-O13-C79	137.6(3)	O9-Dy2-O15	73.15(12)
Dy2-O14	2.261(3)	Dy2-O14-C81	138.3(3)	O10-Dy2-O11	82.04(12)
Dy2-O15	2.444(3)	Dy2-O15-C92	129.7(3)	O10-Dy2-O12	89.34(12)
O15H15-O16	2.06(12)	O10-Dy2-O14	161.72(12)	O10-Dy2-O13	89.16(11)
O16H16-O9	1.64(11)	O10-Dy2-O15	120.73(12)	O12-Dy2-O14	85.15(12)
O17aH17a-O12	2.23	O11-Dy2-O12	73.47(12)	O12-Dy2-O15	129.87(12)
		O11-Dy2-O13	154.72(12)	O13-Dy2-O14	72.88(12)
		O11-Dy2-O14	112.83(12)	O13-Dy2-O15	131.41(12)
		O11-Dy2-O15	72.58(13)	O14-Dy2-O15	75.44(12)
		O9-Dy2-O10	72.83(12)	O12-Dy2-O13	82.82(12)

and one EtOH in the crystal lattice. Two more hydrogen bonds, O16H16-O9 (2.06 Å) and O17aH17a-O12 (2.23 Å), take place between the deprotonated phenalenyls and EtOH in the crystal lattice. The very similar structure of [Dy(Op)$_3$(HOp)] **33** and [Dy(Op)$_3$(EtOH)] **34** caused the co-crystallization of the complexes in single crystals. Additionally, the presence of EtOH molecules in the crystal lattice, which forms intermolecular hydrogen bonds, aids the molecular packing. Moreover, as clearly depicted in Figure 6.3, the interaction between the phenalenyls of [Dy(Op)$_3$(HOp)] **33** and of [Dy(Op)$_3$(EtOH)] **34** is driving the co-crystallization.

The bond distances between the dysprosium atom and the oxygens of the ligands can be compared to those of other dysprosium-oxygen compounds [240–246]. The average bond distance between dysprosium and oxygens of the deprotonated phenalenyls in [Dy(Op)$_2$Cl(HOp)(EtOH)] **32**, [Dy(Op)$_3$(HOp)] **33** and [Dy(Op)$_3$(EtOH)] **34** is 2.2641 Å, 2.289 Å and 2.280 Å, respectively, considerably shorter than those of other dysprosium-oxygen compounds . On the other hand, the bond distance between dysprosium and oxygen in the protonated phenalenyl is 2.3756 Å for [Dy(Op)$_2$Cl(HOp)(EtOH)] **32** and 2.381 Å for [Dy(Op)$_3$(HOp)] **33**, which is comparable to those reported in the literature. Lastly, the bond distance between dysprosium and the oxygen of EtOH is 2.4215 Å for [Dy(Op)$_2$Cl(HOp)(EtOH)] **32** and 2.444 Å for [Dy(Op)$_3$(EtOH)] **34**.

6.5 Paramagnetic ^{1}H-NMR studies
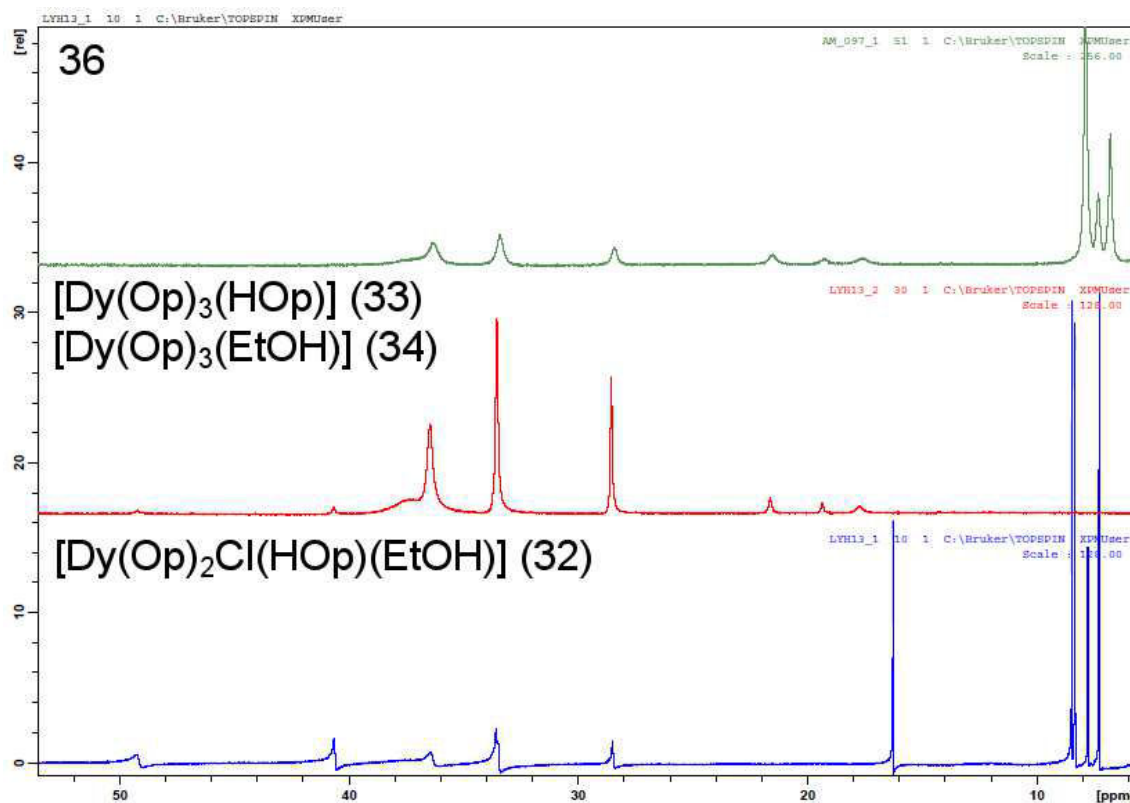
Figure 6.4: Paramagnetic ^{1}H-NMR spectra in DMSO-d_6 of the phenalenyl-based dysprosium complexes [Dy(Op)$_2$Cl(HOp)(EtOH)], **32** [Dy(Op)$_3$(HOp)] **33**-[Dy(Op)$_3$(EtOH)] **34** and **36**.

The paramagnetic ^{1}H-NMR spectra of the dysprosium complexes, obtained by the three reaction procedures described in Section 6.3, are illustrated in Figure 6.4. The spectra were

recorded on the crude precipitate obtained after the reaction. Firstly, the set of resonances between 6 and 16 ppm, in the spectrum of $[Dy(Op)_2Cl(HOp)(EtOH)]$ **32**, is clearly originating from unreacted free ligand HOp **3**. This is confirmed by two observations: (i) the peaks are not shifted to high ppm and broadened (the H-H coupling is still visible) by the paramagnetic dysprosium and (ii) the peak at ≈ 16 ppm is characteristic of the extremely de-shielded proton, which is involved in a strong intramolecular hydrogen bond with the α, β-conjugated carbonyl groups, of HOp **3**. All the three spectra present a set of peaks between 28 and 38 ppm; these peaks can be assigned to the deprotonated phenalenyls, which are in common to all the dysprosium complexes. Conversely, the peaks between 40 and 50 ppm are common only to the spectra of $[Dy(Op)_2Cl(HOp)(EtOH)]$ **32** and of $[Dy(Op)_3(HOp)]$ **33**-$[Dy(Op)_3(EtOH)]$ **34**. Since these peaks are not visible in the spectra of **36**, which is synthesized in absence of EtOH, they are assigned to the EtOH bonded to the dysprosium in $[Dy(Op)_2Cl(HOp)(EtOH)]$ **32** and in $[Dy(Op)_3(HOp)]$ **33**-$[Dy(Op)_3(EtOH)]$ **34**. In addition, the resonances between 18 and 24 ppm, which are noticeable in the spectra of $[Dy(Op)_3(HOp)]$ **33**-$[Dy(Op)_3(EtOH)]$ **34** and **36**, could be assigned to the protonated HOp. Probably, they are not detected for $[Dy(Op)_2Cl(HOp)(EtOH)]$ **32** due to the low intensity of the spectrum, or due to a partial decomposition of the complex in DMSO. At last, the spectrum of **36** is characterized by a set of resonances between 6 and 10 ppm. These resonances cannot be assigned to unreacted free ligand HOp **3**, because the peaks are broadened and the characteristic resonance at ≈ 16 ppm is missing. However, they are in region of aromatic proton signals and are not shifted at high chemical shift from the paramagnetic Dy(III) ion.
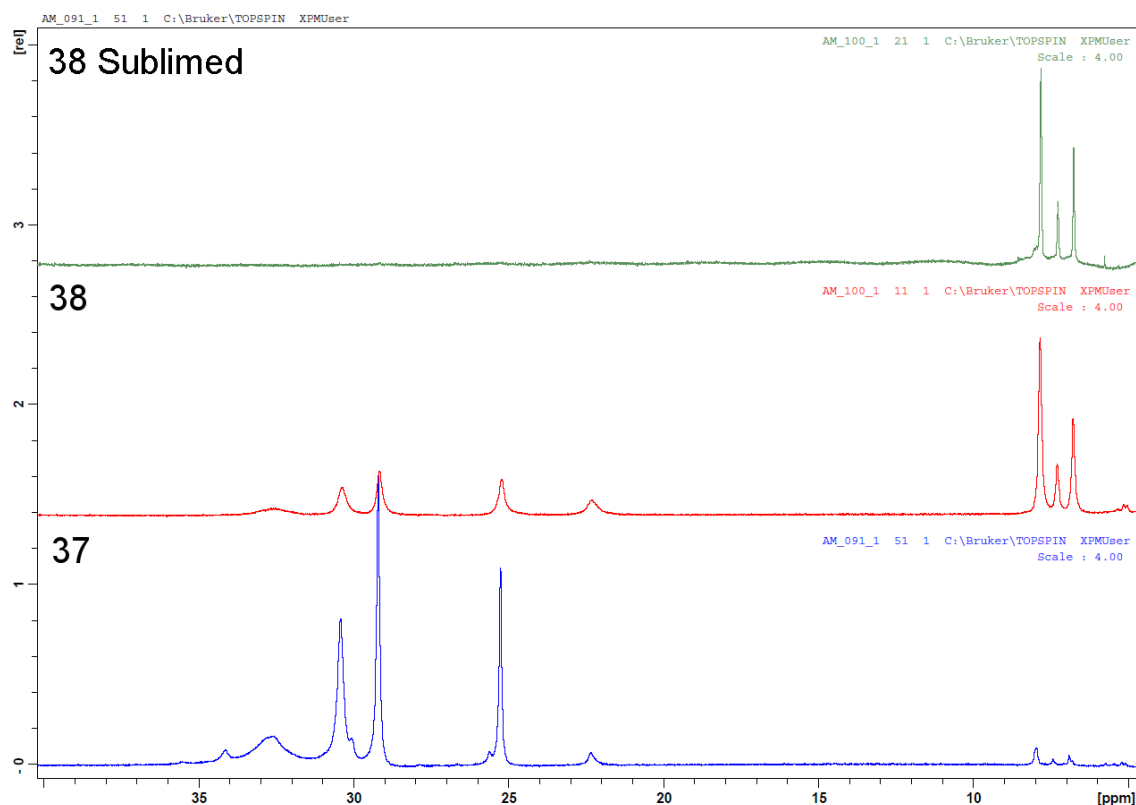
Figure 6.5: Paramagnetic ^{1}H-NMR spectra in DMSO-d_6 of the phenalenyl-based terbium complexes **37** and **38** before and after the sublimation process.

Interestingly, the same peaks were observed in the spectra of the terbium phenalenyl-based complex **38** illustrated in Figure 6.5. In addition, we were able to record a clear paramagnetic

^{1}H-NMR spectrum of **38** after the sublimation process. Surprisingly, the peaks between 4 and 8 ppm are the only peaks detected after the sublimation process. The origin of the peaks at a low chemical shift, for the dysprosium complex **36** and the terbium complex **38**, is still unclear. However, the formation of the complexes was confirmed by MALDI-TOF measurements (see Section 6.6), UV-Vis spectrophotometry (see Section 6.7) and elemental analysis (see Section 8.3). At last, in the phenalenyl-based terbium complexes **37** and **38** a sets of resonances is detected between 22 and 36 ppm. These resonances are assigned to the phenalenyls in the complexes. However, for a complete and exact assignment of the peaks, the exact structure of the complexes, obtained from single crystal X-ray diffraction, must be solved.

6.6 MALDI-TOF studies
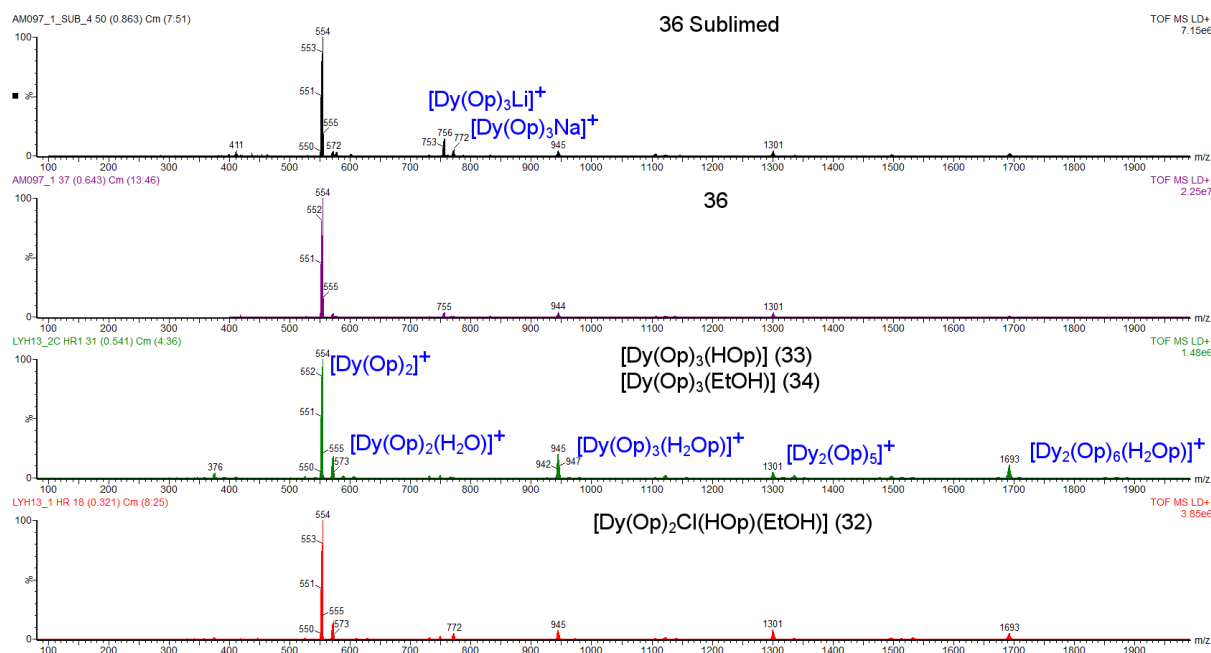
Figure 6.6: MALDI-TOF spectra of the phenalenyl-based dysprosium complexes $[Dy(Op)_2Cl(HOp)(EtOH)]$ **32**, $[Dy(Op)_3(HOp)]$ **33**-$[Dy(Op)_3(EtOH)]$ **34** and **36** before and after the sublimation process. The corresponding fragment are reported next to peak. In Table 6.2 are listed the fragments and their relative intensities.

The MALDI-TOF spectra (positive mode) of the dysprosium complexes, obtained by the three procedures described in Section 6.3, are illustrated in Figure 6.6. Additionally, the spectrum of **36** after the sublimation process is shown. The most intense peak, in all the spectra, is corresponding to $[Dy(Op)_2]^+$ (m/z= 554). This is an indication that all the complexes are, at least, including two phenalenyls around the dysprosium. The second peak, observed at m/z= 572, is relative to the fragment $[Dy(Op)_2(H_2O)]^+$. The absorption of water during the preparation of the samples is usual. However, in the spectra of the dysprosium complex **36**, which was prepared in anhydrous conditions, the relative intensity of the fragment $[Dy(Op)_2(H_2O)]^+$, before and after the sublimation process, is considerably lowered. The next two fragments found are formed by a neutral $Dy(Op)_3$ core plus a metal cation, Li^+ or Na^+ ($[Dy(Op)_3Li]^+$, m/z= 756; $[Dy(Op)_3Na]^+$, m/z= 772). As a consequence of the MALDI process, these peaks are noticeable also for $[Dy(Op)_2Cl(HOp)(EtOH)]$. These two fragments have

145
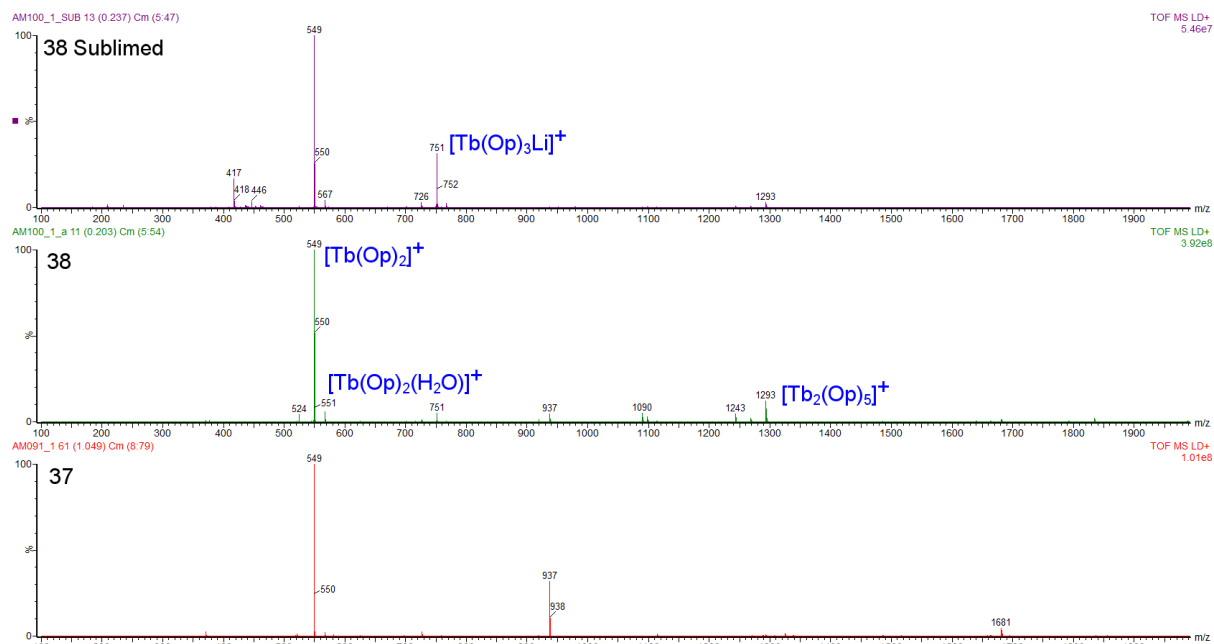
Figure 6.7: MALDI-TOF spectra of the phenalenyl-based terbium complexes **37** and **38** before and after the sublimation process. The corresponding fragment are reported next to peak. In Table 6.2 are listed the fragments and their relative intensities.

a higher relative intensity in the spectra of the dysprosium complex **36** after the sublimation process suggesting that, probably, the dysprosium is surrounded by three phenalenyls. The fragment $[\mathrm{Dy(Op)_3(H_2Op)}]^+$ (m/z= 945) is formed by a neutral $\mathrm{Dy(Op)_3}$ core plus a $[\mathrm{H_2Op}]^+$ cation. The protonation of $[\mathrm{Dy(Op)_3(HOp)}]$ **33** results in the high relative intensity, 20.2%, of the $[\mathrm{Dy(Op)_3(H_2Op)}]^+$ fragment in the MALDI-TOF spectrum of the $[\mathrm{Dy(Op)_3(HOp)}]$ **33**-$[\mathrm{Dy(Op)_3(EtOH)}]$ **34** mixture. The di-nuclear dysprosium complex fragments, $[\mathrm{Dy_2(Op)_5}]^+$ (m/z= 1301) and $[\mathrm{Dy_2(Op)_6(H_2Op)}]^+$ (m/z= 1693), are, most probably, produced during the MALDI process by the aggregation of fragments with low m/z. However, the formation of small amounts of multi-nuclear phenalenyl-based dysprosium complexes can occur during the synthetic step.

The MALDI-TOF spectra (positive mode) of the terbium complexes **37** and **38**, before and after the sublimation process, are shown in Figure 6.7. In all the spectra, the most intense peak is relative to the fragment $[\mathrm{Tb(Op)_2}]^+$ (m/z= 549). This is an indication, as previously described for the dysprosium complexes, that the terbium is coordinated by at least two phenalenyls. The second peak observed is corresponding to the fragment $[\mathrm{Tb(Op)_3(H_2O)}]^+$ (m/z= 567), where a molecule of water is absorbed during the preparation and measurement of the samples. The peak of the $[\mathrm{Tb(Op)_3Li}]^+$ fragment (m/z= 567) is also observed. Interestingly, this peak has a very high intensity in the MALDI-TOF spectrum of the terbium complex **38** after the sublimation process. This can be interpreted as an indication that the sublimable terbium complex is formed by three phenalenyls. The di-nuclear fragment $[\mathrm{Tb_2(Op)_5}]^+$ (m/z= 1293), detected in the MALDI-TOF measurements, is most probably resulting from the aggregation of fragments with smaller m/z. At last, in the spectra of **37** and **38** there are two peak at m/z= 937 and at m/z= 1681 which are unassigned. However, their m/z value is very close to that of $[\mathrm{Tb(Op)_3(H_2Op)}]^+$ (m/z= 941) and $[\mathrm{Tb_2(Op)_6(H_2Op)}]^+$ (m/z= 1685), respectively.

146

Table 6.2: List of the fragments detected in the MALDI-TOF experiments for the phenalenyl-based dysprosium complexes $[Dy(Op)_2Cl(HOp)(EtOH)]$, **32**, $[Dy(Op)_3(HOp)]$ **33**-$[Dy(Op)_3(EtOH)]$ **34** and **36** before and after the sublimation process and for the phenalenyl-based terbium complexes **37** and **38** before and after the sublimation process.

Fragment	m/z	Rel. Intensity [%]		
		32	**33**-**34**	**36** (Aft. Sub.)
$[Dy(Op)_2]^+$	554	100.0	100.0	100.0 (100.0)
$[Dy(Op)_2(H_2O)]^+$	572	14.9	18.2	2.2 (3.8)
$[Dy(Op)_3Li]^+$	756	2.5	<2.0	3.8 (14.4)
$[Dy(Op)_3Na]^+$	772	5.0	<2.0	2.0 (5.5)
$[Dy(Op)_3(H_2Op)]^+$	945	7.1	20.2	4.0 (4.4)
$[Dy_2(Op)_5]^+$	1301	7.8	5.1	3.9 (4.1)
$[Dy_2(Op)_6(H_2Op)]^+$	1693	5.0	10.1	<2.0 (2.0)
		37	**38** (Aft. Sub.)	
$[Tb(Op)_2]^+$	549	100.0	100.0 (100.0)	
$[Tb(Op)_2(H_2O)]^+$	567	2.3	5.8 (4.0)	
$[Tb(Op)_3Li]^+$	751	<2.0	4.9 (31.4)	
$[Tb_2(Op)_5]^+$	1293	<2.0	12.1 (3.0)	

6.7 Photophysical studies
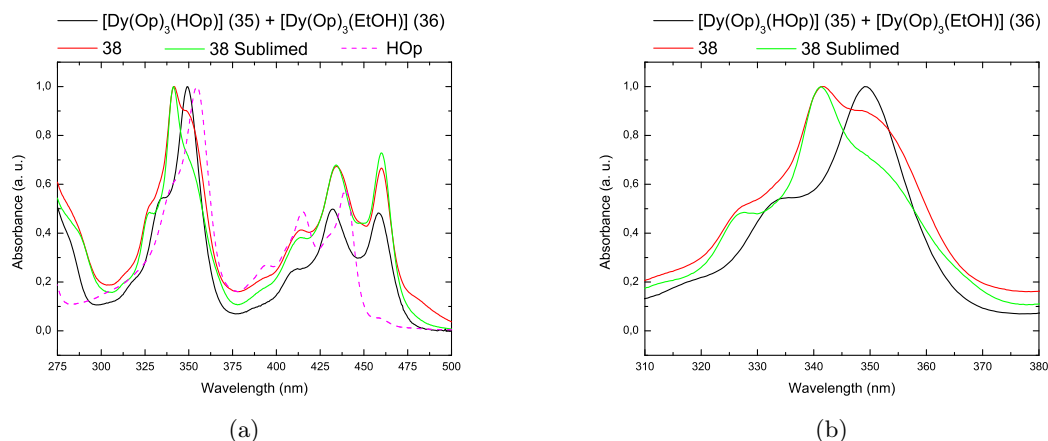
Figure 6.8: (a) Absorption spectra at room temperature of diluted DMSO solutions of $[Dy(Op)_3(HOp)]$ **33**-$[Dy(Op)_3(EtOH)]$ **34**, of **36**, before and after the sublimation process, and of HOp **3** (for comparison). (b) Magnification of the absorption spectra in the region between 310 and 380 nm. All the spectra are normalized.

To further characterize the phenalenyl-based SMMs, we have measured the absorption spectra at room temperature of diluted DMSO solutions. In detail, we were aiming to investigate the sublimable complexes. The absorption spectra of $[Dy(Op)_3(HOp)]$ **33**-$[Dy(Op)_3(EtOH)]$ **34** and of **36**, before and after the sublimation process, at room temperature are plotted in Figure 6.8. The absorption spectra of HOp **3** has been added as a comparison. Clearly all the absorption spectra are shifted in relation to that of HOp **3**, and thus, we can conclude that the spectra are not originating from the absorption of the free HOp **3**. The absorption bands between 375 and 500 nm, related to $n \rightarrow \pi^*$ transitions centered on the phenalenyl ligands (see Section 3.4.1),

are almost identical in the three spectra. However, an attentive observation of the absorption band between 300 and 375 nm reveals that this band is quite different in the spectra. The maximum of the spectrum of $[Dy(Op)_3(HOp)]$ **33**-$[Dy(Op)_3(EtOH)]$ **34** is at 349 nm, whereas the maximum of the spectra of the dysprosium complex **36** before and after the sublimation process is at 341 nm. Nevertheless, the spectra of **36**, before the sublimation, has a shoulder at 349 nm, which is less pronounced after the sublimation process. Considering that the bands between 300 and 375 nm are associated to $\pi \to \pi^*$ transitions centered on the phenalenyls (see Section 3.4.1), the shift of the band can result from slight differences in the structure of the complexes. As a consequence of the few mg of material obtained by the sublimation process, we were unable to compare the extinction coefficients of the complexes.
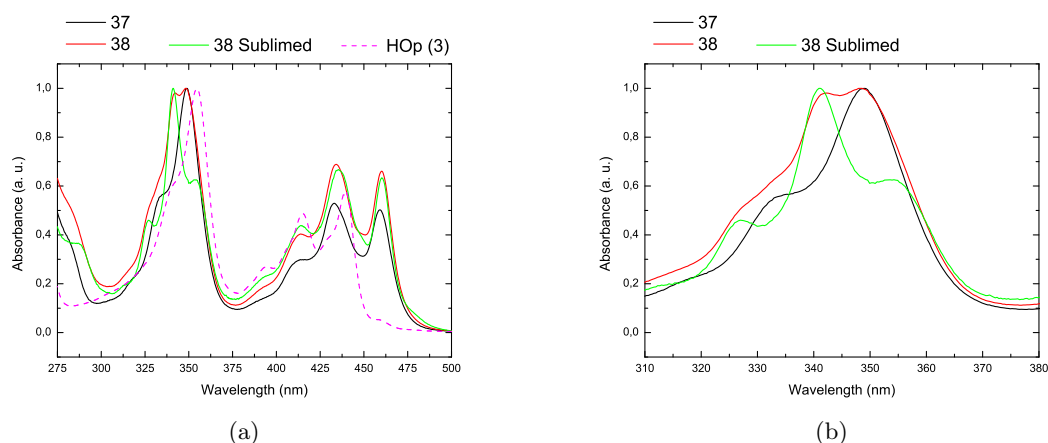
Figure 6.9: (a) Absorption spectra at room temperature of diluted DMSO solutions of **37**, **38**, before and after the sublimation process, and HOp **3** (for comparison). (b) Magnification of the absorption spectra in the region between 310 and 380 nm. All the spectra are normalized.

The absorption spectra of the phenalenyl-based terbium complexes **37** and **38**, before and after the sublimation process, are plotted in Figure 6.9. Comparing the spectra with the spectrum of HOp **3**, we can conclude that the absorption spectra are not caused by the free ligand. As observed for the dysprosium complexes, the absorption band between 375 and 500 nm, related to $n \to \pi^*$ transitions centered on the phenalenyls (see Section 3.4.1), is almost identical in the three spectra. On the contrary, the phenaleny-centered $\pi \to \pi^*$ band, between 300 and 375 nm (see Section 3.4.1), presents considerable shifts. The absorption maximum for the terbium complex **37** is at 349 nm, identical to the maximum of the terbium complex **38** before the sublimation process. However, after the sublimation process, the maximum of **38** is at 341 nm where only a shoulder is visible in the spectrum prior the sublimation. This indicates that, implementing the reaction procedure in anhydrous conditions described in Scheme 6.3, probably, two kinds of terbium complexes are formed. One is identical to the product of the reaction in EtOH, whereas the second, which is sublimable, has a different structure.

At last, we have measured the emission spectra of the phenalenyl-based lanthanide complexes illustrated in Figure 6.10. No sensitization of the lanthanide emission by the phenalenyl was observed. The emission is originating by the fluorescence transition localized on the ligands with no contribution or energy transfer to the lanthanide.
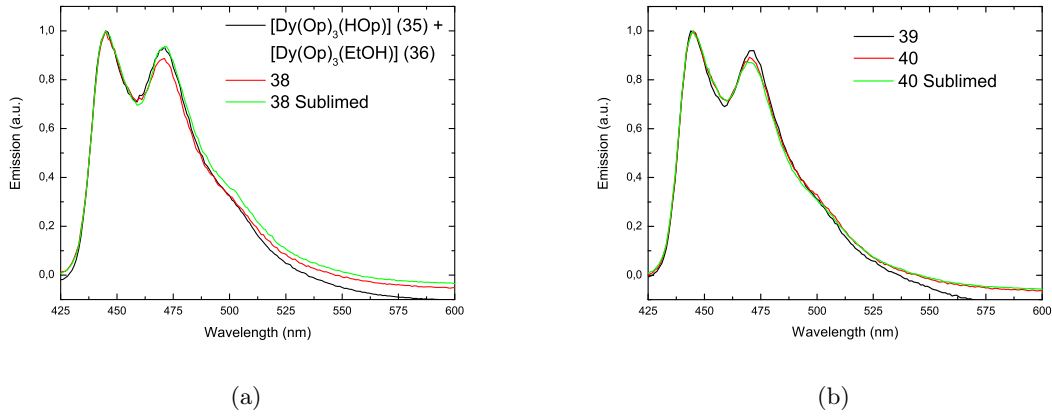
Figure 6.10: (a) Emission spectra at room temperature of diluted DMSO solutions of [Dy(Op)$_3$(HOp)] **33**-[Dy(Op)$_3$(EtOH)] **34** and **36**, before and after the sublimation process. (b) Emission spectra at room temperature of diluted DMSO solutions of **37** and **38**, before and after the sublimation process.

6.8 Magnetic properties of [Dy(Op)$_2$Cl(HOp)(EtOH)] (32)
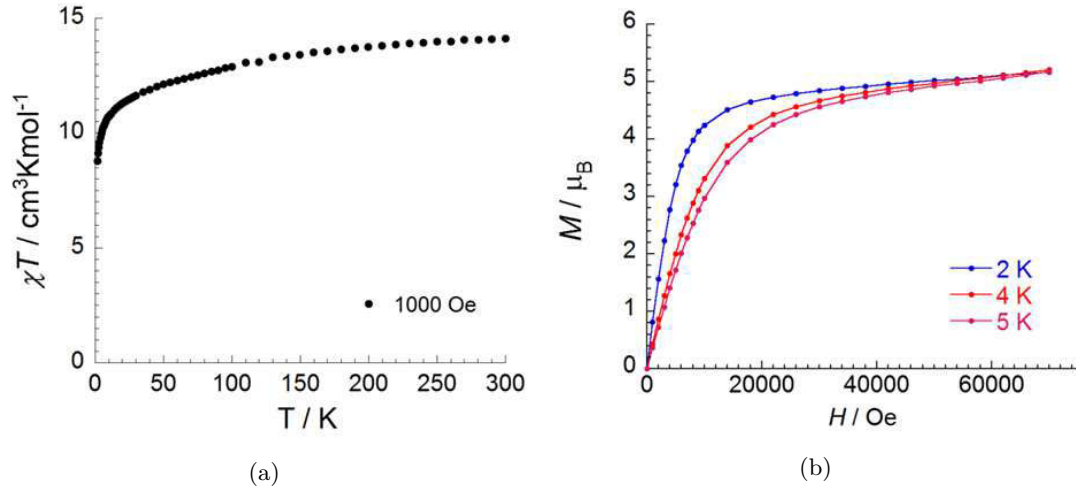
Figure 6.11: (a) Plot of χT versus T for [Dy(Op)$_2$Cl(HOp)(EtOH)] **32** in the range of 1.8-300 K at 1000 Oe. (b) Plot of M versus H for [Dy(Op)$_2$Cl(HOp)(EtOH)] **32** at 2 K, 4 K and 5 K.

The temperature dependence of the magnetic susceptibility of [Dy(Op)$_2$Cl(HOp)(EtOH)] **32** was measured in an applied magnetic field of 1000 Oe in the temperature range between 1.8 and 300 K. At 300 K, the χT product is 14.11 cm^3 K mol^{-1}, in a good agreement with the expected value of 14.17 cm^3 K mol^{-1} for one Dy(III) metal ion (S=5/2, L=5, ^{6}H$_{15/2}$, g=4/3) [121]. Decreasing the temperature, the χT product at 1000 Oe continuously diminishes to 8.78 cm^3 K mol^{-1} at 1.8 K, as illustrated in Figure 6.11. The gradual depletion of χT versus temperature is indicative of the type of paramagnetic behavior resulting from the thermal depopulation of the Stark sublevels of the ^{6}H$_{15/2}$ ground state or of low-lying excited states of the Dy(III) ion while decreasing the temperature [247–253].
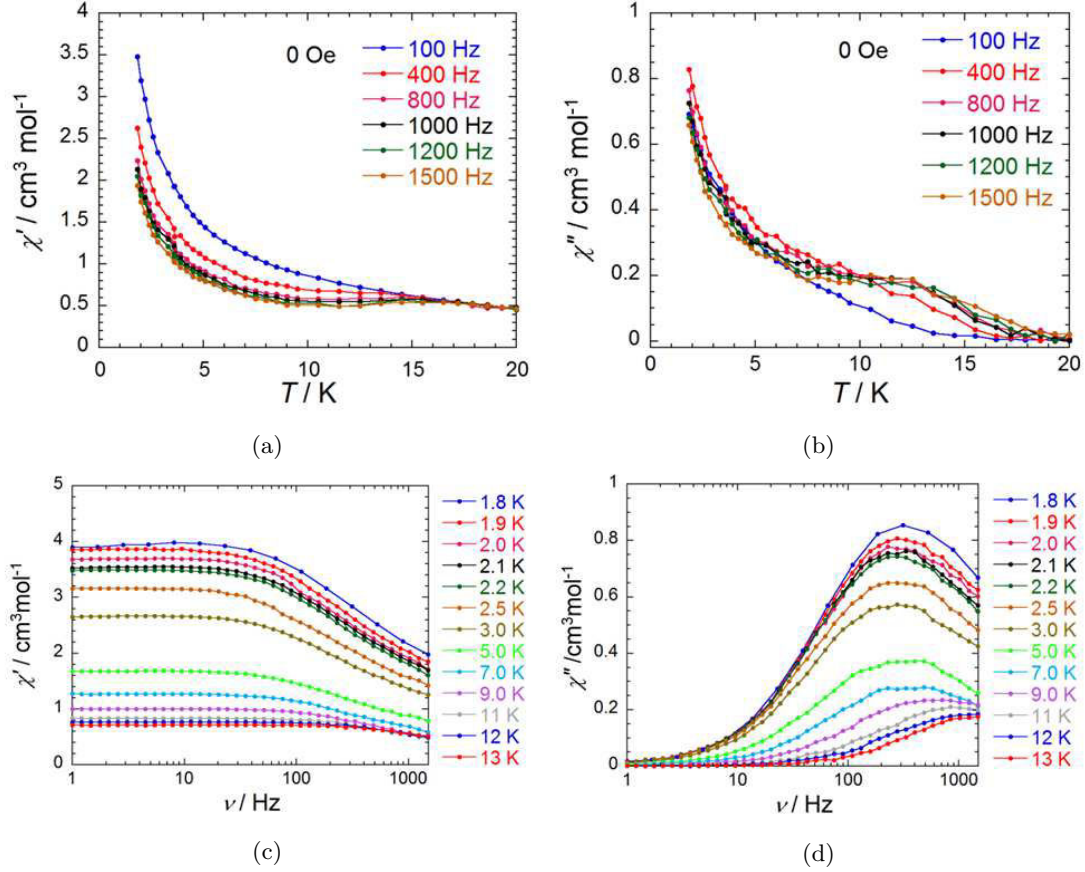
Figure 6.12: ac magnetic susceptibility measurements under zero dc field for $[Dy(Op)_2Cl(HOp)(EtOH)]$ **32**. Temperature dependence of the in-phase $\chi\prime$ (a) and of the out-of-phase $\chi\prime\prime$ (b) ac magnetic susceptibility. Frequency dependence of the in-phase $\chi\prime$ (c) and of the out-of-phase $\chi\prime\prime$ (d) ac magnetic susceptibility.

The field dependence of the magnetization at low temperatures has been measured at 2 K, 4 K and 5 K and is illustrated in Figure 6.11. At 2 K and 70 Oe the magnetization grows to $\approx 5.17\,\mu B$. However, due to the incomplete saturation of the magnetization, a residual slope is observed at high fields, indicating a small magnetic anisotropy in the material [254, 255]. Moreover, no hysteresis effect is observed under these conditions. As a consequence of the detected magnetic anisotropy, the magnetization relaxation of $[Dy(Op)_2Cl(HOp)(EtOH)]$ **32** has been probed implementing ac susceptibility measurements as a function of the temperature at different frequencies and, in addition, as a function of frequency at different temperatures. The results are plotted in Figure 6.12. Obviously, $[Dy(Op)_2Cl(HOp)(EtOH)]$ **32** is characterized by a slow relaxation of its magnetization. At zero dc field, a frequency dependent in-phase and out-of-phase signal is observed below 20 K, suggesting a slow relaxation of the magnetization. At a frequency of 1500 Hz, the out-of-phase component first reaches a maximum at 13 K and afterward steadily increases rather than decline to zero. This indicates a cross-over from a thermally activated to a temperature independent regime in the relaxation process [246, 256, 257]. The shape and frequency dependence suggests that $[Dy(Op)_2Cl(HOp)(EtOH)]$ **32** might be a SMM.

In Figure 6.13, the relaxation time was extracted, fitting the frequency sweeping data between 11 and 13 K with an Arrhenius law. As a result, the characteristic energy gap Δ has been
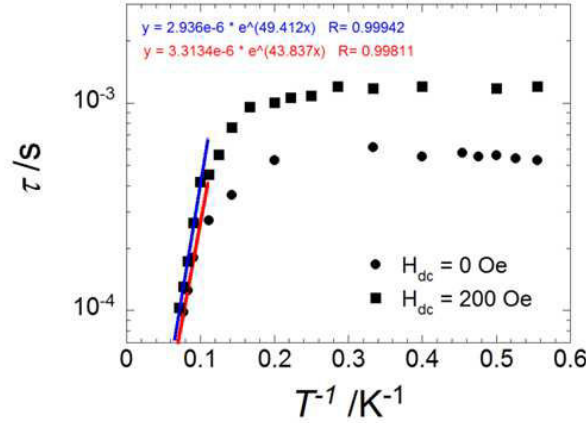
Figure 6.13: Arrhenius semilogaritmic plots of the relaxation time τ versus $1/T$ for [Dy(Op)$_2$Cl(HOp)(EtOH)] **32** from ac susceptibility measurements under a zero dc field and a dc field of 200 Oe. The solid lines represent a linear fit in the thermally activated range of temperature.

determined at 43.8 K and the pre-exponential factor τ_0 at 3.3×10^{-6} s. Additionally, a saturation of $\approx 5 \times 10^{-4}$ s, relative to the quantum relaxation time, is observed below 5 K.
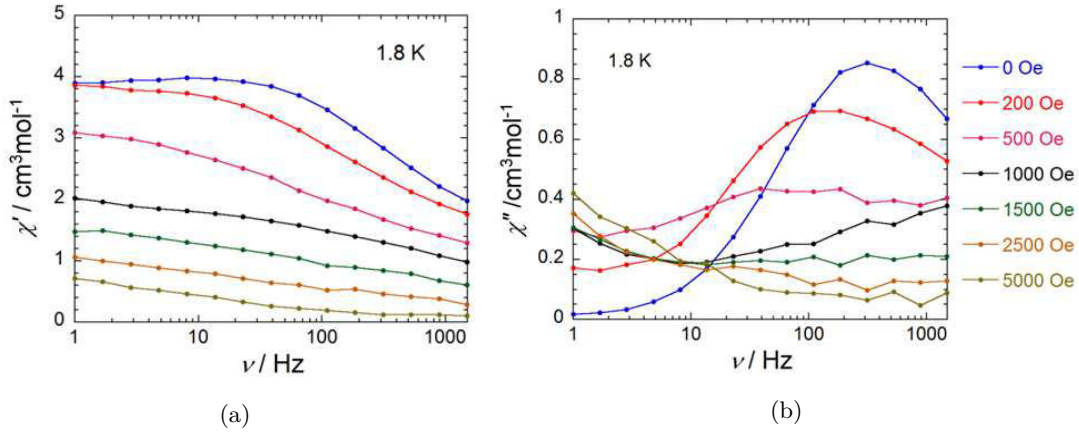
Figure 6.14: Frequency dependence of the in-phase $\chi\prime$ (a) and of the out-of-phase $\chi\prime\prime$ (b) ac magnetic susceptibility at 1.8 K and different dc-field for [Dy(Op)$_2$Cl(HOp)(EtOH)] **32**.

To further study the relaxation process and evaluate the quantum tunneling effect, the frequency dependence of the ac susceptibility at 1.8 K was measured, with the application of a small external dc field, and is illustrated in Figure 6.14. In SMMs with a relaxation partially influenced by quantum effects, the application of a small dc field removes the state degeneracy, and thus, the possibility of quantum tunneling, inducing a slowing down of the magnetization relaxation. The characteristic frequency is 315 Hz at 1.8 K in zero field, whereas with the application of a dc field, the characteristic frequency decreases to 180 Hz at $\approx$200 Oe. Therefore, a small external dc field is slowing down the relaxation time, as previously observed for some SMMs when the quantum tunneling of the magnetization is suppressed.

Lastly, ac susceptibilities as a function of temperature were measured under a dc field of 200 Oe, to estimate the effective relaxation time. The results are plotted in Figure 6.15. The data was fitted with an Arrhenius law function in the temperature range between 10 and 14 K. The

(a)   (b)
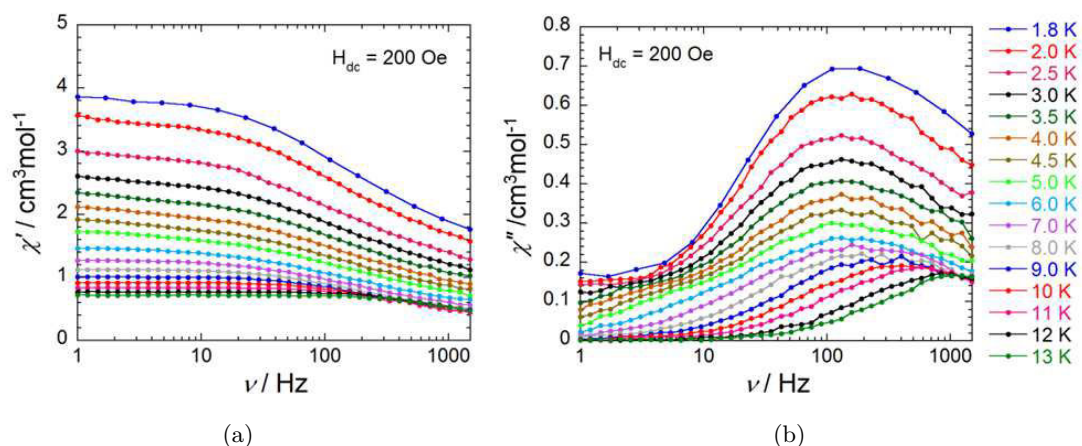
Figure 6.15: Frequency dependence at 200 Oe of the in-phase $\chi\prime$ (a) and of the out-of-phase $\chi\prime\prime$ (b) ac magnetic susceptibility at different temperatures for $[Dy(Op)_2Cl(HOp)(EtOH)]$ **32**.

characteristic SMM energy gap Δ is 49.4 K and the pre-exponential factor is τ_0 is 2.9×10^{-6} s. Additionally, a quantum relaxation time of 1×10^{-3} s is observed below 7 K. Compared to the data calculated in zero-field, the energy gap Δ and its corresponding pre-exponential factor τ_0 are fairly similar, suggesting that the quantum tunneling effect in $[Dy(Op)_2Cl(HOp)(EtOH)]$ **32** is not pronounced. However, the quantum relaxation time at low temperature under 200 Oe is two time higher than the one under zero dc field.

6.9 Magnetic properties of $[\mathbf{Dy(Op)_3(HOp)}]$ (33)-$[\mathbf{Dy(Op)_3(EtOH)}]$ (34)

(a)   (b)
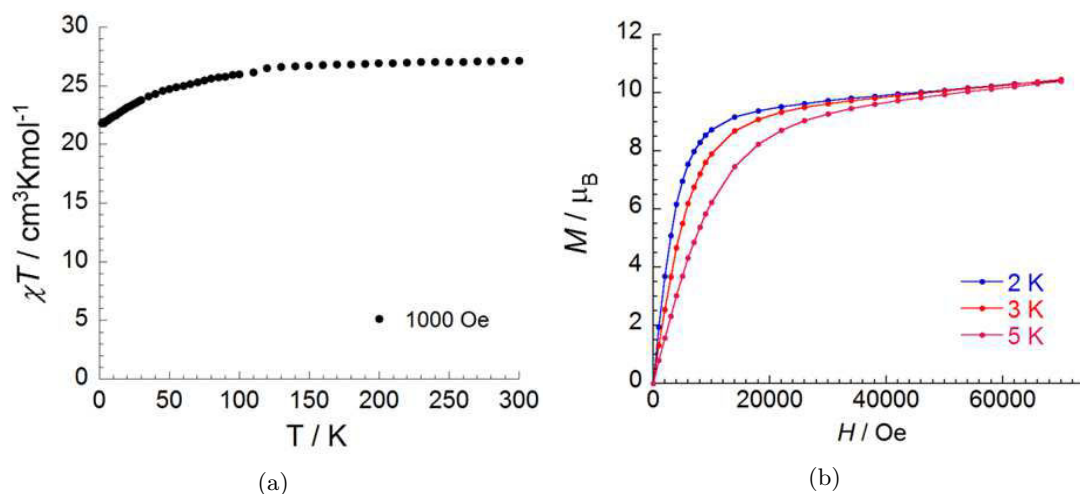
Figure 6.16: (a) Plot of χT versus T for $[Dy(Op)_3(HOp)]$ **33**-$[Dy(Op)_3(EtOH)]$ **34** in the range of 1.8-300 K at 1000 Oe. (b) Plot of M versus H for $[Dy(Op)_3(HOp)]$ **33**-$[Dy(Op)_3(EtOH)]$ **34** at 2 K, 4 K and 5 K

The temperature dependence of the magnetic susceptibility of $[Dy(Op)_3(HOp)]$ **33**-$[Dy(Op)_3(EtOH)]$ **34** was measured under an applied magnetic field of 1000 Oe in the temperature range between 1.8 and 300 K. As illustrated in Figure 6.16, the χT product at 300 K is 27.11 cm^3 K mol^{-1}

and the magnetization at $2\,\mathrm{K}$ and $70\,\mathrm{kOe}$ is $10.43\,\mu\mathrm{B}$. Both the values are in good agreement with the expected values for two isolated Dy(III) ions (S=5/2, L=5, $^6\mathrm{H}_{15/2}$, g=4/3) [121]. In addition, the χT curve decreases slowly lowering the temperature indicating a paramagnetic behavior.

(a)   (b)
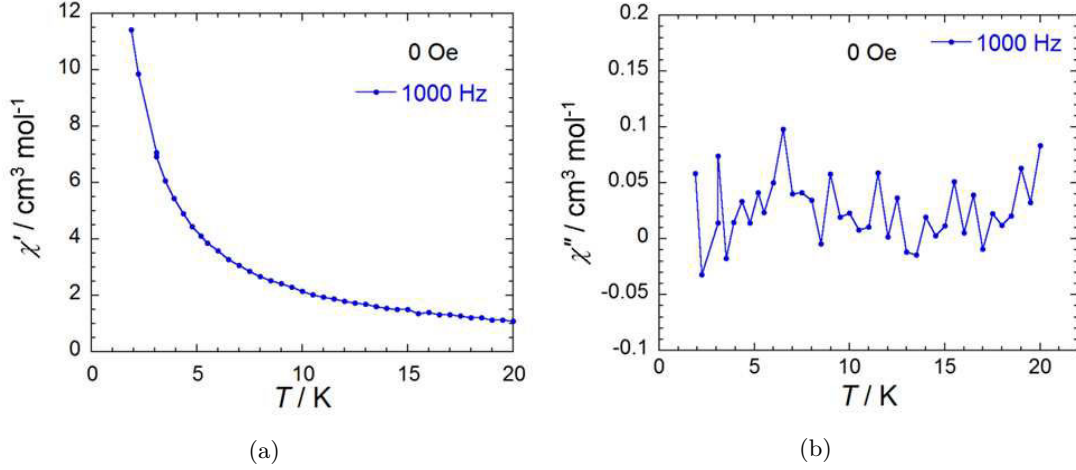
Figure 6.17: ac magnetic susceptibility measurements under zero dc field for [Dy(Op)$_3$(HOp)] **33**-[Dy(Op)$_3$(EtOH)] **34**. Temperature dependence of the in-phase $\chi\prime$ (a) and of the out-of-phase $\chi\prime\prime$ (b) ac magnetic susceptibility.

As illustrated in Figure 6.17, at a zero dc field applied, no out-of-phase component was recorded, whereas in the ac susceptibility measurements is detected at $1000\,\mathrm{Hz}$, suggesting the absence of any appreciable barrier to the relaxation of the magnetization, which could be address to a strong quantum tunneling resonance at zero dc field.

(a)   (b)
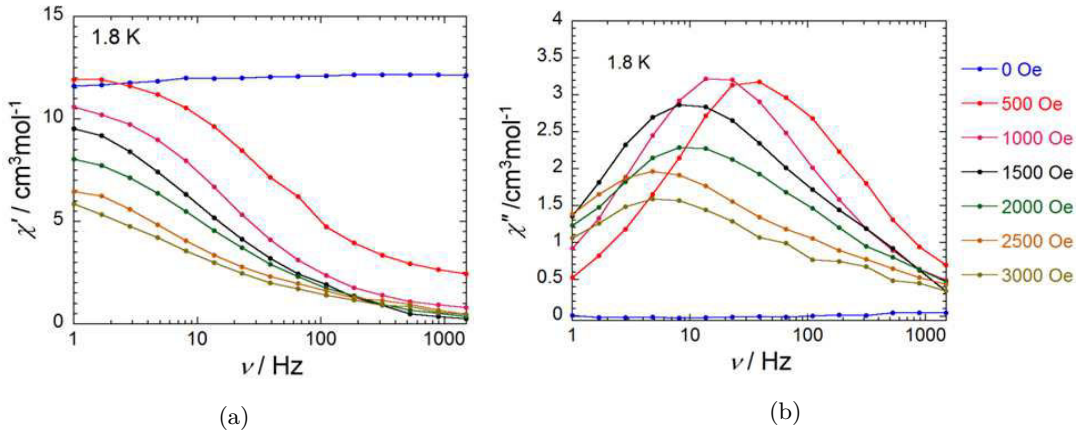
Figure 6.18: Frequency dependence of the in-phase $\chi\prime$ (a) and of the out-of-phase $\chi\prime\prime$ (b) ac magnetic susceptibility at $1.8\,\mathrm{K}$ and different dc fields for [Dy(Op)$_3$(HOp)] **33**-[Dy(Op)$_3$(EtOH)] **34**.

To further investigate the dynamic magnetic properties of [Dy(Op)$_3$(HOp)] **33**-[Dy(Op)$_3$(EtOH)] **34**, ac susceptibility measurements in the presence of a weak dc field were performed and are plotted in Figure 6.18. [Dy(Op)$_3$(HOp)] **33**-[Dy(Op)$_3$(EtOH)] **34** shows a field-induced slow relaxation of the magnetization. The intensity of the out-of-phase component of the ac susceptibility results dramatically enhanced when a dc field is applied, confirming the cooperation

between a slow magnetic relaxation and a rapid quantum tunneling. The relaxation process immediately slows down to 40 Hz when the applied field is 500 Oe, in contrast, it is faster, ≈10 Hz, at 1500 Oe. This behavior points to the fact that this compound, concerning the dynamic aspect, is characterized by a very fast tunneling process at zero dc field. When the dc field applied increases from 1500 Oe upwards, the relaxation process oscillates to a higher frequency and subsequently slows down again. This observation implies that there is more than one relaxation process in the system. Indeed, considering the presence of two Dy(III) centers with different ion anisotropy in [Dy(Op)$_3$(HOp)] **33**-[Dy(Op)$_3$(EtOH)] **34**, this observation is not surprising. Based on the present data, however, it is not possible to discriminate and assign the relaxation processes to their respective structure.

(a)

(b)

(c)

(d)
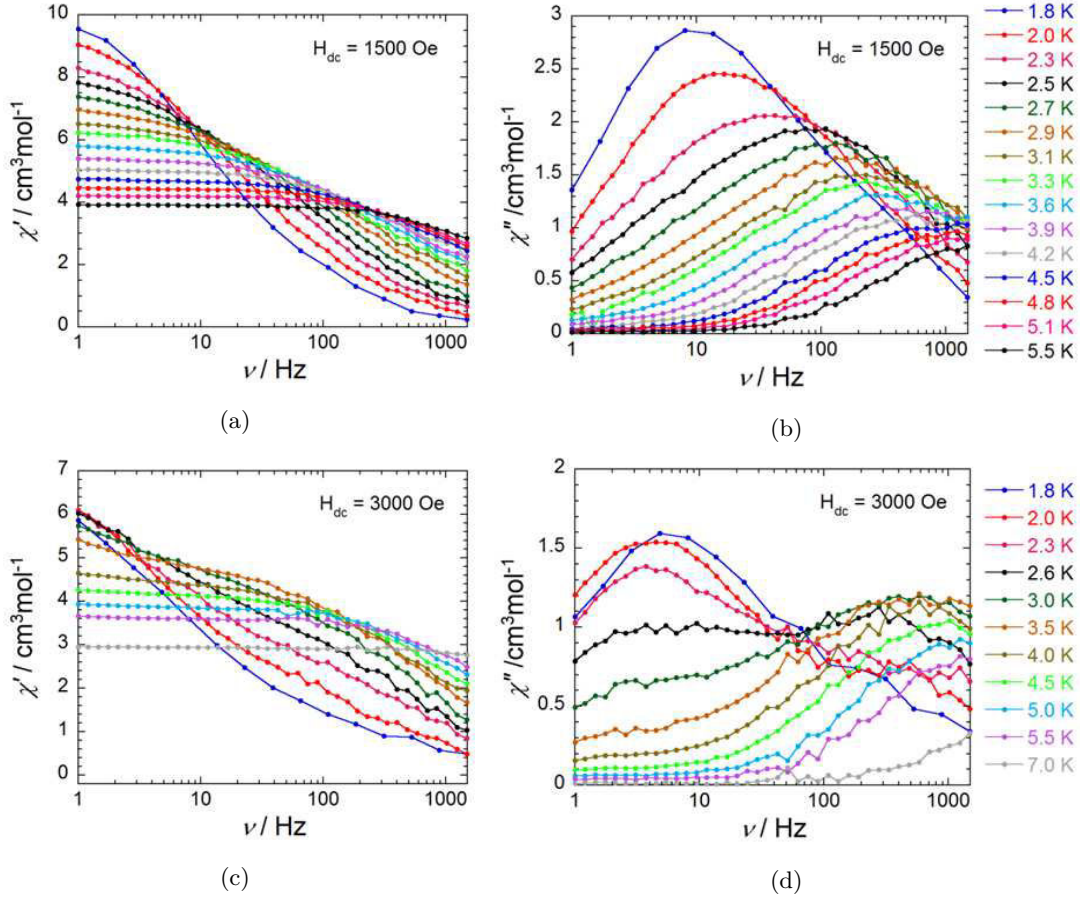
Figure 6.19: Frequency dependence at 1500 Oe of the in-phase $\chi\prime$ (a) and of the out-of-phase $\chi\prime\prime$ (b) ac magnetic susceptibility at different temperatures for [Dy(Op)$_3$(HOp)] **33**-[Dy(Op)$_3$(EtOH)] **34**. Frequency dependence at 3000 Oe of the in-phase $\chi\prime$ (c) and of the out-of-phase $\chi\prime\prime$ (d) ac magnetic susceptibility at different temperatures for [Dy(Op)$_3$(HOp)] **33**-[Dy(Op)$_3$(EtOH)] **34**.

At last, as illustrated in Figure 6.19, the frequency sweeping ac susceptibilities measurements were performed at different temperatures under two dc fields: 1500 Oe and 3000 Oe. Under a dc field of 1500 Oe, one set of peaks is observed in the out-of-phase component of the ac susceptibility. Conversely, under a dc field of 3000 Oe, two sets of peaks are clearly visible in the plot of the frequency dependence of the out-of-phase component of the ac susceptibility, indicating the presence of more than one relaxation pathway. Moreover, as a stronger dc field is applied, the smaller peak at lower frequencies increases at the expense of the larger peak

beyond the window of the measurements. The relaxation times Δ and the pre-exponential factors τ_0 of the relaxation pathways are calculated plotting the relaxation time τ versus $1/T$ (see Figure 6.20). At 1500 Oe, the relaxation time, deduced from the data between 1.8 and 5.1 K, follows an activated behavior with an energy gap Δ of 14.1 K and a pre-exponential factor τ_0 of 7.1×10^{-6} s. At 3000 Oe, the relaxation time Δ of the relaxation pathway located at higher frequencies in the temperature range between 2.6 and 5.5 K is 7.6 K and its pre-exponential factor τ_0 is 3.0×10^{-5} s. The parameters obtained under a dc field of 1500 Oe and 3000 Oe are roughly in the same order of magnitude, indicating that the mechanism of the two relaxation processes, corresponding to the two isolated Dy(III) ions in $[Dy(Op)_3(HOp)]$ **33**-$[Dy(Op)_3(EtOH)]$ **34**, is most probably the same.
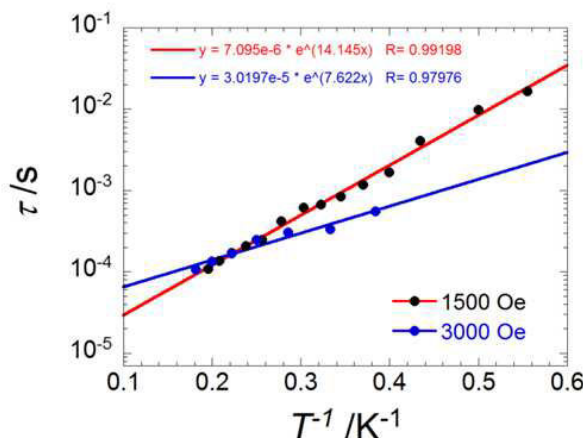
Figure 6.20: Arrhenius semilogaritmic plots of the relaxation time τ versus $1/T$ for $[Dy(Op)_3(HOp)]$ **33**-$[Dy(Op)_3(EtOH)]$ **34** from ac susceptibility measurements under dc fields of 1500 Oe and 3000 Oe. The solid lines represent a linear fit in the thermally activated range of temperature.

6.10   Conclusions

In this chapter we have studied the complexes formed by HOp **3** and paramagnetic atoms such as dysprosium and terbium. The complexes were characterized by means of ^{1}H-NMR, MALDI-TOF and UV-Vis, to determine their structure and properties. Single crystals of $[Dy(Op)_2Cl(HOp)(EtOH)]$ **32** and single co-crystals of $[Dy(Op)_3(HOp)]$ **33** and $[Dy(Op)_3(EtOH)]$ **34**, were grown. Thus, their exact molecular structures were determined.

The magnetic properties of $[Dy(Op)_2Cl(HOp)(EtOH)]$ **32** were measured. The results suggest it might be a SMM with an energy gap Δ of 43.8 K and a pre-exponential factor τ_0 of 3.3×10^{-6} s43.8 K, in addition, a quantum relaxation time of $\approx 5 \times 10^{-4}$ s was determined at zero dc field. The measurements have been carried out also under an applied dc field of 200 Oe yielding a energy gap Δ of 49.4 K and a pre-exponential factor τ_0 of 2.9×10^{-6} s, moreover, a quantum relaxation time of $\approx 1 \times 10^{-3}$ s was determined. The results indicate that the quantum tunneling effect is not pronounced. Since it was impossible to separate the two complexes, the magnetic characterization was carried out on the co-crystals of $[Dy(Op)_3(HOp)]$ **33**-$[Dy(Op)_3(EtOH)]$ **34**. At zero dc field no out-of-phase component of the susceptibility was detected which could be caused by a strong quantum tunneling resonance. The measurements have been repeated under dc fields of 1500 and 3000 Oe. The relaxation time calculated at

1500 Oe follows an activated behavior with an energy gap Δ of 14.1 K, whereas at 3000 Oe the energy gap Δ of the relaxation pathway located at higher frequencies is 7.6 K.

Lastly, further complexes of dysprosium and terbium have been synthesized and characterized. By implementing a synthetic strategy in anhydrous conditions we were able to synthesize sublimable phenalenyl-based dysprosium and terbium complexes. The molecular structure of these complexes could not be determined by single crystal X-ray diffraction. Notheless, the complex formation and thermal stability was confirmed by the analysis prior and after the sublimation process. Although this is a preliminary study, it is opening the possibility to deposit phenalenyl-based lanthanide complexes on surfaces for a variety of studies and eventually building devices.

7. Conclusions and Outlook

In this thesis I have presented a systematic study on aluminum-based OSCs. The main goal was to identify a clear relationship between the chemical structure and the electronic properties of such materials. The work was focused on the low molecular weight class of OSCs, using the well-known Alq_3 as benchmark. In an extended framework of collaborations, we were able to deeply investigate the OSCs implementing several theoretical and experimental techniques.

The rational design, synthesis and characterization of the (novel) OSCs is presented in Chapter 3. Here, the synthesis of a series of (novel) OSCs, listed in Table 3.2, has been presented. The first step was to select and synthesize, when necessary, the ligands listed in Table 3.1, which were then used to form the complexes. $Al(Op)_3$ **4** was the first aluminum complex to be synthesized. A series of halogenated and substituted derivatives of $Al(Op)_3$ **4**, namely $Al(Op-X)_3$ **6a**–**d** and $Al(Op-R)_3$ **16a**–**c**, was obtained to study the effect of halogens and substituents on the electronic properties. $Al(Oba)_3$ **19** was investigated as an asymmetric aromatic extension of $Al(Op)_3$ **4**. $Al(Op-py)_3$ **23** was chosen because it is structurally similar to Alq_3. $Al(Trop)_3$ **25** was selected as a consequence of its seven-membered aromatic structure. A series of heteroleptic aluminum complexes was synthesized: $Al(q_2Acac)$ **28** $Al(q_2Op)$ **29** and $Al(q_2Trop)$ **30**. At last, the complex $Zn(Op)_2$ **31** was characterized as the first member of a class of phenalenyl-based zinc complexes. Ligands and complexes have been further characterized by means of photophysical and electrochemical methods (findings in Table 3.5, Table 3.6, Table 3.7 and Table 3.8). $Al(Op)_3$ **4** forms excimers in the solid state, most probably due to its flat and extended aromatic system. Excimers were detected also in the thin film emission spectra of $Al(Op-p)_3$ **16a** and $Al(Oba)_3$ **19**. HOMO and LUMO energy levels of the ligands and complexes were estimated (see Figure 3.45). It can be noted that, clearly, the extension of the aromatic system influences the HOMO and LUMO energy levels. In more detail, molecules with a small aromatic system are characterized by a higher LUMO than those with a bigger aromatic system. On the other hand, the HOMO fluctuates in a narrow range with few eV of difference between the complexes.

In Chapter 4 a theoretical study on the (novel) OSCs is presented. In addition, preliminary results on the experimental charge carrier mobility of $Al(Op)_3$ are reported. The analysis of the HOMO and LUMO revealed a localization of the orbitals in asymmetric complexes, such as Alq_3, $Al(Op-py)_3$, $Al(q_2Acac)$, $Al(q_2Op)$ and $Al(q_2Trop)$. In contrast, symmetric complexes, such as $Al(Op)_3$, $Al(Trop)_3$ and $Al(Acac)_3$, are characterized by an isotropic distribution of the orbitals. This difference gives rise to a wide distribution electrical dipole moments from $6.52\,D$ of $Al(q_2Op)$ to $0.053\,D$ of $Al(Acac)_3$ (see Table 4.1). Through the newly developed DEPOSIT method, morphologies of the OSCs were generated *"in silico"*. At last, through the recently published Quantum Patch method, the charge carriers mobility of the OSCs were computed (see Table 4.3). Additionally, preliminary studies on the experimental charge carrier mobility were performed by means of FET, TOF and AS on $Al(Op)_3$. So far, only by FET was possible to measure a hole mobility of $Al(Op)_3$ between 0.6 and $2.1 \times 10^{-6}\,cm^2\,V^{-1}\,s^{-1}$.

An investigation on the $Co/Al(Op)_3$ hybrid interface is presented in Chapter 5. The occupied manifold of bulk $Al(Op)_3$ and its interface dipole moment were detected by UPS (see Figure 5.11). By NT-PS two hybrid interface states were unraveled, the SP of HIS1 is 8% higher than that of bare cobalt, whereas the SP of HIS2 is 4% lowered (see Figure 5.12). The LUMO of $Al(Op)_3$ was observed by 2PPE. Since the LUMO is not a hybrid interface state, the lifetime of the spin-up and spin-down electrons is identical. Preliminary UPS studies on the $Co/Al(Op-py)_3$ were carried out.

Lastly, the SMM behavior of phenalenyl-based lanthanide complexes was investigated. In this study we have synthesized and structurally characterized phenalenyl-based dysprosium and terbium complexes. The molecular structure of three dysprosium complexes has been resolved. $[Dy(Op)_2Cl(HOp)(EtOH)]$ **32** might be a SMM. $[Dy(Op)_3(HOp)]$ **33**-$[Dy(Op)_3(EtOH)]$ **34** outlines a strong quantum tunneling.

Asymmetric halogenation and substitution might be more effective on the electronic properties of HOp **3**, and thus, of $Al(Op)_3$ **4**. In addition, this could also hinder the formation of excimers in the solid state. The aromatic system of HOp$-$py **22** can be easily extended using isoquinoline and/or naphthalen-2-ol as backbone, in addition, by simple reactions it would be possible to insert halogens or aromatic substituents. At last, tropolone **24** can be symmetrically and asymmetrically decorated with a variety of substituents. These changes might be useful to tune the electronic properties of the OSCs. Moreover, these ligands can coordinate a variety of metals giving rise to a wide range of applications. Besides $Al(Op)_3$ **4**, the aluminum complexes obtained are currently investigated to measure the mobility and the spin filtering behavior on cobalt substrates. Although a great number of efficient materials is nowadays available for optoelectronic devices, by FET, TOF and AS measurements on the complexes, a deeper understanding on the influence of the chemical structure on the charge carrier mobility can be gained. Nonetheless, these complexes can be implemented in OSPDs to systematically investigate the chemical structure effect on the device performance. These are few studies which can be carried out on these class of materials, however, by exploiting the chemistry of the ligands and complexes, many fields of application can be identified. A clear example is the SMM behavior observed in a phenalenyl-based dysprosium complex. Studies on terbium complexes were preliminary presented, additionally, phenalenyl complexes of holmium and erbium will be investigated. Furthermore, lanthanide complexes can be obtained with the ligands implemented in the synthesis of the aluminum complexes, giving the access to a number of novel molecules. It was also demonstrated that sublimable phenalenyl-based lanthanide complexes can be synthesized, which is most important to probe these materials on surfaces and for application in devices.

8. Experimental Part

8.1 Materials and equipments

All the reactions were carried out under argon inert atmosphere using standard Schlenk techniques. All the purchased chemicals and solvents for the synthesis and column chromatography were used as received without any further purification unless otherwise stated. Elemental analysis of carbon, hydrogen, and nitrogen were carried out in a Vario Micro Cube. ^{1}H-NMR and ^{13}C-NMR were recorded in a Bruker FT-NMR Avance III 500 MHz with deuterated solvents as internal standards for proton and carbon signals. Matrix-assisted laser desorption/ionization-time of flight (MALDI-TOF) mass spectrometric data were acquired on a MALDI-TOF Synapt G2-S HDMS with no additional matrix compound other than the sample itself. Electro-spray ionization-time of flight (ESI-TOF) mass spectrometric analytical data were acquired on a Bruker microOTOF-Q II equipped with a nanospray source and on a ESI-TOF Synapt G2-S HDMS. Elemental analyses were carried out on a Vario Micro Cube. Single crystal X-ray diffraction data were collected on a STOE IPDS II diffractometer with graphite monochromated Mo Kα radiation (0.710 73 Å). Structure solution and refinement against F^2 were carried out using shelxs and shelxl software. Refinement was performed with anisotropic temperature factors for all non-hydrogen atoms (disordered atoms were refined isotropically); hydrogen atoms were calculated on idealized positions.

8.2 OSCs synthesis

Al(Op)$_3$ 4. HOp **3** (1.02 g, 5.2 mmol) was dissolved in 50 ml of freshly distilled toluene, AlCl$_3$ (0.21 g, 1.6 mmol) was added and the solution was refluxed overnight at 110 °C. The yellow precipitate was filtered and washed thoroughly with fresh toluene. The crude product was purified by column chromatography on alumina neutral grade IV with pure DCM and recrystallization from slow evaporation of a DCM/Ethanol solution (0.77 g, yield 75%). Suitable crystals for single crystal X-ray diffraction were obtained from slow evaporation at room temperature of a chloroform solution.

^{1}H-NMR (500 MHz, CDCl$_3$, 25 °C, δ(ppm)): 8.01 (d, 2H, H2), 7.96 (d, 2H, H4), 7.51 (t, 1H, H5), 7.14 (d, 2H, H1). ^{13}C-NMR (125 MHz, CDCl$_3$, 25 °C, δ(ppm)): 179.09 (C8), 141.34 (C2), 132.86 (C4), 127.94 (C1), 127.87 (C5), 125.29 (C3), 122.91 (C6), 113.40 (C7). MALDI-TOF MS (Da) m/z (rel. intensity, assigned structure): 417 (100%, C$_{26}$H$_{14}$O$_4$Al calc. = 417.07). Elemental analysis found (calc.): C$_{39}$H$_{27}$O$_8$Al (Al(C$_{39}$H$_{21}$O$_6$) $\cdot$ 2 H$_2$O, 650.64 g mol^{-1}): C 72.29 (72.00)%, H 4.01 (4.19)%.
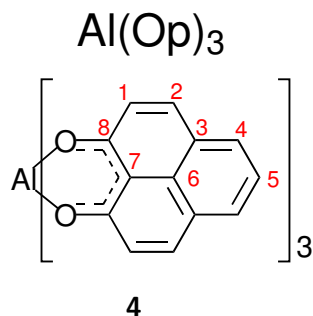
Scheme 8.1: Al(Op)$_3$ **4**. Peaks in ^{1}H-NMR and ^{13}C-NMR spectra are labeled according to the numbering shown in the figure.

6-Methoxynaphthalen-2-amine 8.   In a tube were placed 30 ml of a 2:1 solution of PEG400 and NH$_3$(28%). 2-Bromo-6-methoxynaphthalene **7** (1.20 g, 5.1 mmol), CuI (1.00 g, 5.3 mmol) and Na$_3$PO$_4$ (0.80 g, 4.9 mmol) were added and the tube was sealed. The reaction mixture was heated 24 h at 100 °C and allowed to cool to room temperature overnight. The organics were extracted with ether and purified by column chromatography on silica gel with pure DCM yielding the pure product (0.35 g, yield 40%).

^{1}H-NMR (500 MHz, CD$_2$Cl$_2$, 25 °C, δ(ppm)): 7.56 (d, 1H, H3), 7.49 (d, 1H, H4), 7.04 (m, 2H, H6,8), 6.93 (m, 2H, H1,9), 3.86 (s, 3H, H11), 1.67 (s, 2H, H12) . ^{13}C-NMR (125 MHz, CD$_2$Cl$_2$, 25 °C, δ(ppm)): 155.43 (C10), 142.86 (C5), 130.34 (C7), 128.84 (C2), 127.62 (C3), 127.20 (C8), 118.89 (C4), 118.72 (C9), 108.73 (C6), 106.10 (C1), 55.27 (C11).
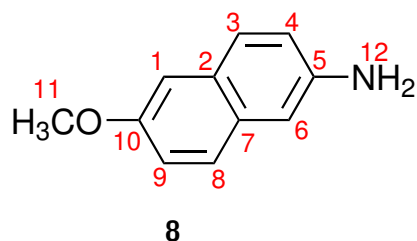
Scheme 8.2: 6-Methoxynaphthalen-2-amine **8**. Peaks in ^{1}H-NMR and ^{13}C-NMR spectra are labeled according to the numbering shown in the figure.

2-Fluoro-6-methoxynaphthalene 9.   6-Methoxynaphthalen-2-amine **8** (0.34 g, 2.0 mmol) was dissolved in 1 ml THF and cooled to 0 °C. HBF$_4$ (5 ml) and NaNO$_2$ (0.43 g, 6.0 mmol) in 2 ml of H$_2$O were added and the solution was stirred 1 h in the cold. BF$_4$Na (1.13 g, 10.0 mmol) was added and the mixture was allowed to warm up to room temperature. The solid was filtred, washed with ether, dried in vacuum and suspended in 5 ml of chlorobenzene. The suspension was refluxed 1 h at 140 °C, cooled to room temperature and 50 ml of H$_2$O were added. The organics were extracted with DCM and purified by column chromatography on silica gel with pure DCM (0.20 g, yield 58%).

^{1}H-NMR (500 MHz, CDCl$_3$, 25 °C, δ(ppm)): 7.72-7.67 (m, 2H, H3,8), 7.39 (dd, 1H, H6), 7.25-7.13 (m, 3H, H1,4,9), 3.91 (s, 3H, H11) . ^{13}C-NMR (125 MHz, CDCl$_3$, 25 °C, δ(ppm)): 160.44

(C5), 158.52 (C10), 157.23 (d, C7) , 131.57 (C2), 128.90 (d, C3), 128.75 (d, C4), 119.93 (C9), 116.65 (d, C6), 111.00 (d, C8), 106.08 (C1), 55.48 (C11).

9
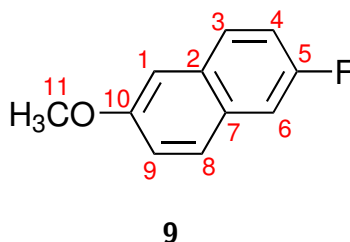
Scheme 8.3: 2-Fluoro-6-methoxynaphthalene **9**. Peaks in ^{1}H-NMR and ^{13}C-NMR spectra are labeled according to the numbering shown in the figure.

HOp−F 5a. 2-Fluoro-6-methoxynaphthalene **9** (0.25 g, 1.4 mmol) and cinnamoyl chloride **2** (0.24 g, 1.42 mmol) were dissolved in 30 ml of freshly distilled DCE and cooled down to 0 °C. AlCl$_3$ (0.19 g, 1.4 mmol) was added and the mixture was stirred 1 h in the cold. After allowing the reaction to warm up to room temperature, another aliquot of AlCl$_3$ (0.19 g, 1.4 mmol) was added and the mixture was refluxed at 90 °C overnight. The mixture was allowed to cool to room temperature, quenched with HCl 6 N 10 ml and filtered on celite. The solid was repeatedly washed with hot DCM, the organic layer of the filtrate was taken and the solvents evaporated under reduced pressure. The crude product was purified by column chromatography on silica gel with pure DCM (0.19 g ,yield 63%).

^{1}H-NMR (500 MHz, CDCl$_3$, 25 °C, δ(ppm)): 15.80 (s, 1H, H9), 8.05 (d, 2H, H2), 7.74 (d, 2H, H4), 7.22 (d, 2H, H1). ^{13}C-NMR (125 MHz, CDCl$_3$, 25 °C, δ(ppm)): 178.96 (C8), 160.29 (C5), 158.36 (C2), 140.19 (d, C3), 129.25 (d, C6), 126.93 (d, C4), 125.23 (C1), 118.77 (d, C7).

5a
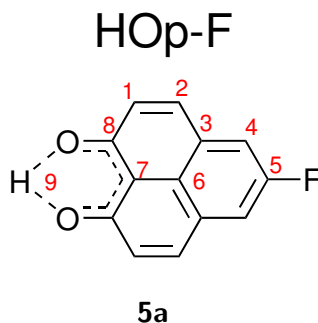
Scheme 8.4: HOp−F **5a**. Peaks in ^{1}H-NMR and ^{13}C-NMR spectra are labeled according to the numbering shown in the figure.

Al(Op−F)$_3$ 6a. HOp−F **5a** (0.16 g, 0.74 mmol) and AlCl$_3$ (32.0 mg, 0.24 mmol) were dissolved in 15 ml toluene; the solution was refluxed overnight at 110 °C. The yellow precipitate was filtered and washed thoroughly with fresh toluene. The crude product was purified by column chromatography on alumina neutral grade IV with pure DCM (0.13 g, yield 81%).

^{1}H-NMR (500 MHz, CDCl$_3$, 25 °C, δ(ppm)): 7.96 (d, 2H, H2), 7.68 (d, 2H, H4), 7.17 (d, 2H, H1). MALDI-TOF MS (Da) m/z (rel. intensity, assigned structure): 453 (100%, C$_{26}$H$_{12}$O$_4$F$_2$Al

calc. = 453.36) Elemental analysis found (calc.): $C_{39}H_{26}O_{10}F_3Al$ ($Al(C_{39}H_{18}O_6F_3) \cdot 4\,H_2O$, $738.63\,g\,mol^{-1}$): C 63.97 (63.41)%, H 3.53 (3.56)%.

Al(Op−F)₃

6a
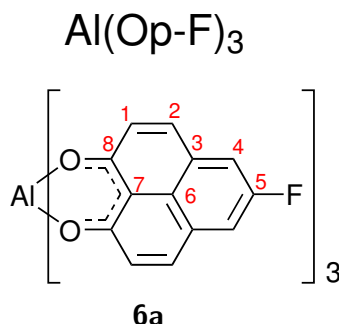
Scheme 8.5: $Al(Op-F)_3$ **6a**. Peaks in ^{1}H-NMR spectrum are labeled according to the numbering shown in the figure.

2-Chloro-6-methoxynaphthalene 10. 2-Bromo-6-methoxynaphthalene **7** (3.01 g, 12.7 mmol) was dissolved in 20 ml DMF, CuCl (1.48 g, 15.0 mmol) was added and the mixture was refluxed 24 h at 110 °C. Further CuCl (0.79 g, 7.5 mmol) was added and the mixture was refluxed 24 h more. The solvent was removed in vacuum, the solid was dissolved in ethyl acetate and washed with H_2O. The pure product was recovered by column chromatography (silica gel, DCM) (2.08 g, yield 85%).

^{1}H-NMR (500 MHz, CDCl$_3$, 25 °C, δ(ppm)): 7.74 (ds, 1H, H8), 7.66 (m, 2H, H6,3), 7.38 (dd, 1H, H4), 7.17 (dd, 1H, H4), 7.11 (ds, 1H, H1) 3.9 (s, 3H, H11). ^{13}C-NMR (125 MHz, CDCl$_3$, 25 °C, δ(ppm)): 157.96 (C10), 133.00 (C2), 129.64 (C7), 129.24 (C5), 128.68 (C8), 128.38 (C3), 127.31 (C4), 126.54 (C6), 119.95 (C9), 105.91 (C1), 55.50 (C11).

10
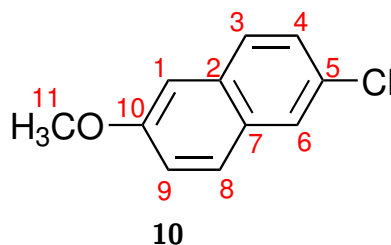
Scheme 8.6: Synthesis of 2-chloro-6-methoxynaphthalene **10**. (a) CuCl, DMF, reflux, 48 h, yield: 85%.

HOp−Cl 5b. 2-Chloro-6-methoxynaphthalene **10** (2.17 g, 11.0 mmol) and cinnamoyl chloride **2** (1.89 g, 11.0 mmol) were dissolved in 50 ml of freshly distilled DCE and cooled down to 0 °C. AlCl$_3$ (1.50 g, 11.0 mmol) was added and the mixture was stirred 1 h in the cold. After allowing the reaction to warm up to room temperature, further AlCl$_3$ (1.50 g, 11.0 mmol) was added and the mixture was refluxed at 90 °C overnight. The reaction was allowed to cool to room temperature, quenched with HCl 6 N 15 ml and filtered on celite. The solid was repeatedly washed with hot DCM and the organic layer of the filtrate was taken. The solvents were evaporated under reduced pressure and the solid was purified by column chromatography on silica gel with pure DCM yielding the pure product (1.95 g, yield 77%).

^{1}H-NMR (500 MHz, CDCl$_3$, 25 °C, δ(ppm)): 15.87 (s, 1H, H9), 8.03 (d, 2H, H2), 7.98 (s, 2H, H4), 7.21 (d, 2H, H1). ^{13}C-NMR (125 MHz, CDCl$_3$, 25 °C, δ(ppm)): 179.20 (C8), 140.12 (C2), 131.83 (C4), 129.91 (C3), 126.87 (C5), 125.18 (C1).

HOp-Cl

5b
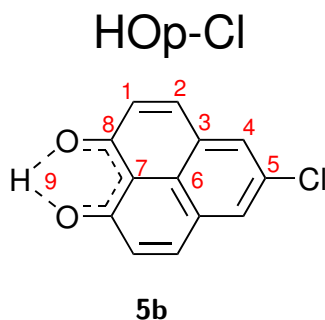
Scheme 8.7: HOp−Cl **5b**. Peaks in ^{1}H-NMR and ^{13}C-NMR spectra are labeled according to the numbering shown in the figure.

Al(Op−Cl)$_3$ 6b. HOp−Cl **5b** (0.19 g, 0.9 mmol) and AlCl$_3$ (37.4 mg, 0.28 mmol) were dissolved in 20 ml toluene; the solution was refluxed overnight at 110 °C. The yellow precipitate was filtered and washed thoroughly with fresh toluene. The crude product was purified by column chromatography on alumina neutral grade IV with pure DCM (0.17 g, yield 83%).

^{1}H-NMR (500 MHz, CDCl$_3$, 25 °C, δ(ppm)): 7.92 (m, 3H, H2,4), 7.14 (d, 2H, H1). MALDI-TOF MS (Da) m/z (rel. intensity, assigned structure): 486 (100%, C$_{26}$H$_{12}$O$_4$Cl$_2$Al calc. = 486.26), 452 (10%, C$_{26}$H$_{13}$O$_4$ClAl calc. = 451.82). Elemental analysis found (calc.): C$_{39}$H$_{22}$O$_8$Cl$_3$Al (Al(C$_{39}$H$_{18}$O$_6$Cl$_3$) · 2 H$_2$O, 743.94 g mol^{-1}): C 62.65 (62.29)%, H 3.18 (2.96)%.

Al(Op-Cl)$_3$

6b
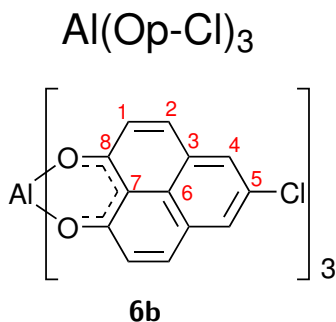
Scheme 8.8: Al(Op−Cl)$_3$ **6b**. Peaks in ^{1}H-NMR spectrum are labeled according to the numbering shown in the figure.

HOp−Br 5c. 2-Bromo-6-methoxynaphthalene **7** (1.01 g, 4.2 mmol) and cinnamoyl chloride **2** (0.71 g, 4.2 mmol) were dissolved in 20 ml of freshly distilled DCE and cooled down to 0 °C. AlCl$_3$ (0.56 g, 4.2 mmol) was added, the mixture was stirred 1 h in the cold. After allowing the reaction to warm up to room temperature, further AlCl$_3$ (0.56 g, 4.2 mmol) was added and the mixture was refluxed at 90 °C overnight. The suspension was allowed to cool to room temperature, quenched with HCl 6 N 10 ml and filtered on celite. The solid was repeatedly washed with hot DCM and the organic layer of the filtrate was taken. The solvents were

evaporated under reduced pressure and the solid was purified by column chromatography on silica gel with DCM/hexane (1:1) yielding the pure product (1.01 g, yield 87%).

^{1}H-NMR (500 MHz, CDCl$_3$, 25 °C, δ(ppm)): 15.83 (s, 1H, H9), 8.13 (s, 2H, H4), 8.02 (d, 2H, H2), 7.20 (d, 2H, H1). ^{13}C-NMR (125 MHz, CDCl$_3$, 25 °C, δ(ppm)): 179.40 (C8), 140.26 (C2), 134.88 (C4), 127.37 (C3), 125.95 (C6), 125.34 (C1), 117.57 (C5), 111.31 (C7).

HOp-Br

5c
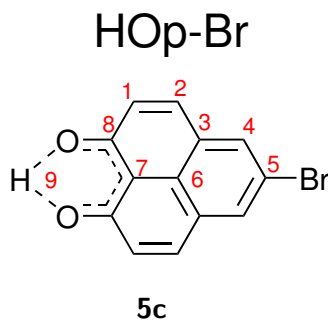
Scheme 8.9: HOp−Br **5c**. Peaks in ^{1}H-NMR and ^{13}C-NMR spectra are labeled according to the numbering shown in the figure.

Al(Op−Br)$_3$ 6c.   HOp−Br **5c** (1.01 g, 3.7 mmol) was dissolved in 40 ml toluene, AlCl$_3$ (0.15 g, 1.1 mmol) was added and the solution was refluxed overnight at 110 °C. The yellow precipitate was filtered and washed thoroughly with fresh toluene. The crude product was purified by column chromatography alumina neutral grade IV with pure DCM (0.82 g, yield 87%).

^{1}H-NMR (500 MHz, CDCl$_3$, 25 °C, δ(ppm)): 8.06 (s, 2H, H4), 7.93 (d, 2H, H2), 7.13 (d, 2H, H1) . MALDI-TOF MS (Da) m/z (rel. intensity, assigned structure): 575 (100%, C$_{26}$H$_{12}$O$_4$Br$_2$Al calc. = 575.16), 495 (20%, C$_{26}$H$_{12}$O$_4$ClAl calc. = 495.26), 415 (10%, C$_{26}$H$_{12}$O$_4$Al calc. = 415.36). Elemental analysis found (calc.): C$_{39}$H$_{20}$O$_7$Br$_3$Al (Al(C$_{39}$H$_{18}$O$_6$Br$_3$)·H$_2$O, 867.27 g mol^{-1}): C 54.53 (54.01)%, H 2.57 (2.33)%.

Al(Op-Br)$_3$

6c
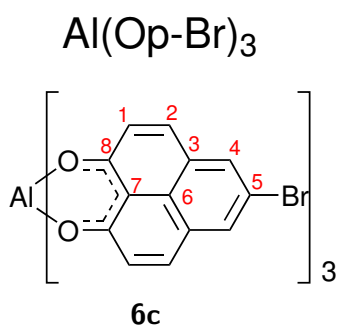
Scheme 8.10: Al(Op−Br)$_3$ **6c**. Peaks in ^{1}H-NMR spectrum are labeled according to the numbering shown in the figure.

5-bromo-9-methoxy-1H-phenalen-1-one 11.   HOp−Br **5c** (2.60 g, 9.4 mmol) and Ag$_2$O (2.21 g, 9.4 mmol) were placed in 50 ml DCM, CH$_3$I (3.5 ml, 56.0 mmol) was added dropwise and the mixture was refluxed 3 h at 50 °C. A second aliquote of CH$_3$I (3.5 ml, 56.0 mmol) was

added dropwise and the mixture was refluxed additional 3 h. After allowing the reaction to cool down to room temperature, the suspension was filtered. The clear solution was taken and the solvent was evaporated under reduced pressure (2.6 g, yield 96%).

^{1}H-NMR (500 MHz, CDCl$_3$, 25 °C, δ(ppm)): 8.13 (m, 2H, H4,8), 7.89 (ds, 1H, H6), 7.64 (d, 1H, H2), 7.52 (d, 1H, H1), 6.81 (d, 1H, H9), 4.20 (s, 3H, H14).

11
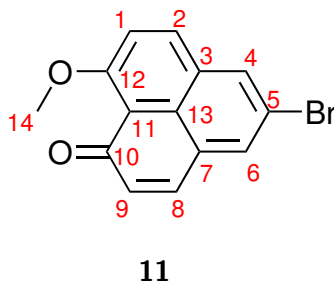
Scheme 8.11: 5-Bromo-9-methoxy-1H-phenalen-1-one **11**. Peaks in ^{1}H-NMR spectrum are labeled according to the numbering shown in the figure.

HOp−I 5d. 5-Bromo-9-methoxy-1H-phenalen-1-one **11** (2.50 g, 8.8 mmol) was dissolved in 18 ml DMSO. CuI (10.50 g, 55.0 mmol) and KI (18.30 g, 110.0 mmol) were added and the mixture was refluxed at 160 °C 40 h. The reaction was allowed to cool down to room temperature and quenched with 25 ml HCl 1 N. The mixture was filtred on celite and the filtrate was extracted with DCM. The organic layer was taken and the solvents were evaporated under vacuum. The crude product was purified by recrystallization from a DCM/ethanol solution (2.15 g, yield 76%).

^{1}H-NMR (500 MHz, CDCl$_3$, 25 °C, δ(ppm)): 15.85 (s, 1H, H9), 8.31 (s, 2H, H4), 7.99 (d, 2H, H2), 7.17 (d, 2H, H1). ^{13}C-NMR (125 MHz, CDCl$_3$, 25 °C, δ(ppm)): 179.20 (C8), 140.56 (C4), 140.00 (C2), 127.44 (C3), 124.92 (C1).

5d
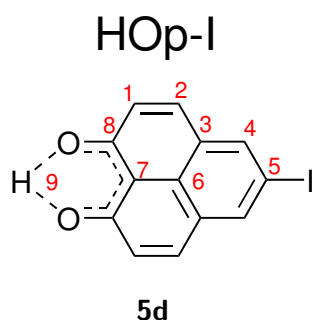
Scheme 8.12: HOp−I **5d**. Peaks in ^{1}H-NMR and ^{13}C-NMR spectra are labeled according to the numbering shown in the figure.

Al(Op−I)$_3$ 6d. HOp−I **5d** (0.56 g, 1.7 mmol) was dissolved in 40 ml toluene, AlCl$_3$ (72.0 mg, 0.54 mmol) was added and the solution was refluxed overnight at 110 °C. The yellow precipitate was filtered and washed thoroughly with fresh toluene. The crude product was purified by column chromatography (0.42 g, yield 80%).

^{1}H-NMR (500 MHz, CDCl$_3$, 25 °C, δ(ppm)): 8.24 (s, 2H, H4), 7.91 (d, 2H, H2), 7.11 (d, 2H, H1). MALDI-TOF MS (Da) m/z (rel. intensity, assigned structure): 669 (100%, C$_{26}$H$_{12}$O$_4$I$_2$Al calc. = 669.16), 542 (60%, C$_{26}$H$_{12}$O$_4$IAl calc. = 542.26), 415 (10%, C$_{26}$H$_{12}$O$_4$Al calc. = 415.36). Elemental analysis found (calc.): C$_{39}$H$_{20}$O$_7$I$_3$Al (Al(C$_{39}$H$_{18}$O$_6$I$_3$) · H$_2$O, 1008.27 g mol^{-1}): C 46.81 (46.46)%, H 2.41 (2.00)%.
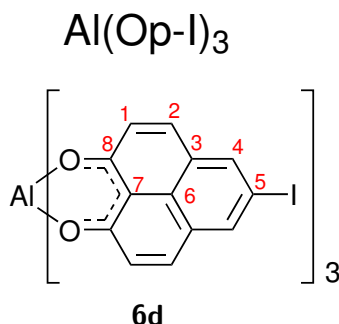
Scheme 8.13: Al(Op−I)$_3$ **6d**. Peaks in ^{1}H-NMR spectrum are labeled according to the numbering shown in the figure.

HOp−p 15a. 5-Bromo-9-methoxy-1H-phenalen-1-one **11** (2.00 g, 6.9 mmol), phenylboronic acid **12** (0.95 g, 7.8 mmol) and CsF (2.24 g, 14.7 mmol) were placed in 50 ml DME and the mixture was bubbled with argon 1 h. Pd(PPh$_3$)$_4$ (0.55 g, 0.48 mmol) was added and the reaction was refluxed overnight at 90 °C. The mixture was washed with H$_2$O after allowing it to cool to room temperature, the organic layer was taken and the solvent evaporated under reduced pressure. The crude product was partially purified by flash column chromatography on silica gel with ethyl acetate/hexane (1:1). 9-Methoxy-5-phenyl-1H-phenalen-1-one **39a** (1.30 g, 4.6 mmol) was dissolved in 200 ml DCM, BBr$_3$ 1 M in DCM (9.1 ml, 9.1 mmol) was added dropwise and the mixture was refluxed overnight at 50 °C. The reaction was cooled down to room temperature and quenched with 50 ml NaOH 2 M; the organic layer was separated, the aqueous layer acidified with HCl and extracted with DCM. All the organics were collected, the solvent was evaporated and the crude product was purified by column chromatography on silica gel with pure DCM and recrystallization from a DCM/hexane solution (0.97 g, yield 51%).

^{1}H-NMR (500 MHz, CDCl$_3$, 25 °C, δ(ppm)): 15.98 (s, 1H, H13), 8.25 (s, 2H, H4), 8.17 (d, 2H, H2), 7.74 (dt, 2H, H11), 7.53 (d, 2H, H10), 7.44 (dt, 1H, H12), 7.22 (d, 2H, H1). ^{13}C-NMR (125 MHz, CDCl$_3$, 25 °C, δ(ppm)): 141.52 (C8), 140.28 (C2), 137.82 (C4), 131.79 (C5), 129.50 (C11), 128.19 (C3), 127.70 (C10), 126.43 (C12), 124.53 (C1).

HOp-p

15a
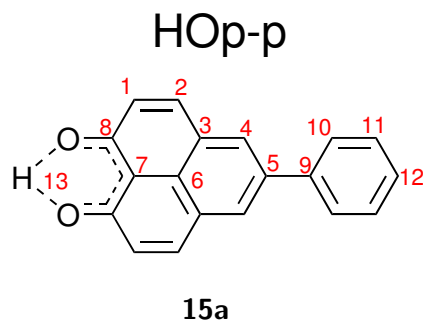
Scheme 8.14: HOp−p **15a**. Peaks in ^{1}H-NMR and ^{13}C-NMR spectra are labeled according to the numbering shown in the figure.

Al(Op−p)$_3$ 16a. HOp−p **15a** (0.97 g, 3.5 mmol) was dissolved in 15 ml toluene, AlCl$_3$ (0.16 g, 1.1 mmol) was added and the solution was refluxed overnight at 110 °C. The yellow precipitate was filtered and washed thoroughly with fresh toluene. The crude product was purified by column chromatography on alumina neutral grade IV with pure DCM (0.79 g, yield 86%).

^{1}H-NMR (500 MHz, CDCl$_3$, 25 °C, δ(ppm)): 8.17 (s, 1H, H4), 8.08 (d, 2H, H2), 7.72 (t, 2H, H11), 7.51 (d, 2H, H10), 7.40 (t, 1H, H12), 7.18 (d, 2H, H1). ^{13}C-NMR (125 MHz, CDCl$_3$, 25 °C, δ(ppm)): 179.14 (C8), 141.51 (C4), 140.34 (C9), 136.21 (C2), 131.38 (C5), 129.17 (C11), 128.23 (C10), 127.62 (C12), 127.36 (C3), 125.72 (C6), 113.31 (C7). MALDI-TOF MS (Da) m/z (rel. intensity, assigned structure): 569 (100%, C$_{38}$H$_{22}$O$_4$Al calc. = 569.58). Elemental analysis found (calc.): C$_{57}$H$_{39}$O$_9$Al (Al(C$_{57}$H$_{33}$O$_6$) · 3 H$_2$O, 894.94 g mol^{-1}): C 76.58 (76.49)%, H 4.36 (4.40)%.

Al(Op-p)$_3$

16a
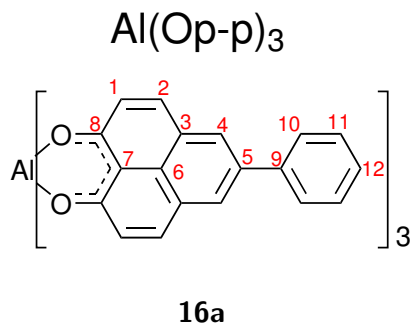
Scheme 8.15: Al(Op−p)$_3$ **16a**. Peaks in ^{1}H-NMR and ^{13}C-NMR spectra are labeled according to the numbering shown in the figure.

HOp−n 15b. 5-Bromo-9-methoxy-1H-phenalen-1-one **11** (1.01 g, 3.5 mmol), naphthalen-1-ylboronic acid **13** (0.63 g, 3.5 mmol) and CsF (1.11 g, 7.1 mmol) were placed in 40 ml DME and the mixture was bubbled with argon 1 h. Pd(PPh$_3$)$_4$ (0.16 g, 0.14 mmol) was added and the reaction was refluxed overnight at 90 °C. The reaction was cooled down to room temperature and the mixture was washed with H$_2$O, the organic layer was taken and the solvent evaporated under reduced pressure. The crude product was partially purified by flash column chromatography on silica gel with ethyl acetate/hexane (1:1). 9-Methoxy-5-(naphthalen-1-yl)-1H-phenalen-1-one **39b** (1.00 g, 3.7 mmol) was dissolved in 50 ml DCM, BBr$_3$ 1 M in DCM (10.0 ml, 10.0 mmol) was added dropwise and the reaction mixture was refluxed overnight at 50 °C. The reaction was

cooled down to room temperature and quenched with 50 ml NaOH 2 M; the organic layer was separated, the aqueous layer was acidified with HCl and extracted with DCM. All the organics were collected, the solvent was evaporated under reduced pressure and the crude product was purified by column chromatography on silica gel with pure DCM and sublimation in vacuum (0.60 g, yield 53%).

^{1}H-NMR (500 MHz, CD_2Cl_2, 25 °C, δ(ppm)): 16.03 (s, 1H, H19), 8.21 (m, 4H, H2,4), 7.97, (t, 2H, H12,14), 7.88 (d, 1H, H10), 7.61 (t, 1H, H11), 7.55 (m, 2H, H15,17), 7.46 (dt, 1H, H16), 7.24 (d, 2H, H1). ^{13}C-NMR (125 MHz, CD_2Cl_2, 25 °C, δ(ppm)): 179.57 (C8), 141.59 (C2), 139.12 (C4), 137.16 (C9), 134.68 (C13), 134.29 (C18), 131.99 (C5), 128.81 (C14,17), 128.57 (C3), 127.91 (C12), 126.82 (C15,16), 126.42 (C11), 126.04 (C10), 125.87 (C1), 124.35 (C6), 111.38 (C7).

HOp-n

15b
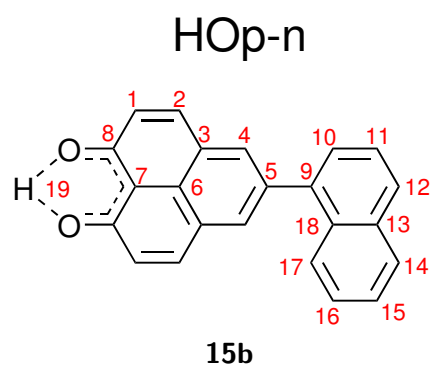
Scheme 8.16: HOp−n **15b**. Peaks in ^{1}H-NMR and ^{13}C-NMR spectra are labeled according to the numbering shown in the figure.

Al(Op−n)$_3$ 16b. HOp−n **15b** (0.30 g, 1.0 mmol) and $AlCl_3$ (40.0 mg, 0.30 mmol) were dissolved in 30 ml toluene; the solution was refluxed overnight at 110 °C. The yellow precipitate was filtered and washed thoroughly with fresh toluene. The crude product was purified by column chromatography on alumina neutral grade IV with pure DCM (0.20 g, yield 67%).

^{1}H-NMR (500 MHz, CD_2Cl_2, 25 °C, δ(ppm)): 8.17 (m, 4H, H2,4), 7.94 (m, 3H, H12,14,10), 7.58 (m, 3H, 11,15,17), 7.47 (dt, 1H, H16), 7.17 (d, 2H, H1). ^{13}C-NMR (125 MHz, CD_2Cl_2, 25 °C, δ(ppm)): 179.26 (C8), 142.23 (C2), 139.31 (C4), 135.99(C9), 134.84 (C13), 134.30 (C18), 132.06 (C5), 128.76 (C14), 128.38 (C17), 127.87 (C3), 127.85 (C12), 127.26 (C15), 126.74 (C16), 126.35 (C11), 126.00 (C10), 125.87 (C1), 125.52 (C6), 113.51 (C7). MALDI-TOF MS (Da) m/z (rel. intensity, assigned structure): 669 (100%, $C_{46}H_{26}O_4Al$ calc. = 669.70), 623 (8%, $C_{36}H_{19}O_4BrAl$ calc. = 622.43). Elemental analysis found (calc.): $C_{69}H_{49}O_{11}Al$ ($Al(C_{69}H_{39}O_6) \cdot$ 5 H_2O, 1081.16 g mol^{-1}): C 76.54 (76.65)%, H 4.60 (4.58)%.

Al(Op-n)$_3$

16b
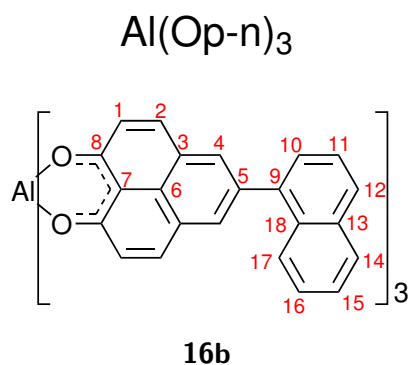
Scheme 8.17: Al(Op−n)$_3$ **16b**. Peaks in ^{1}H-NMR and ^{13}C-NMR spectra are labeled according to the numbering shown in the figure.

HOp−pe 15c. 5-Bromo-9-methoxy-1H-phenalen-1-one **11** (0.41 g, 1.4 mmol) and ethynylbenzene **14** (0.18 ml, 1.6 mmol) were dissolved in 50 ml of a mixture 2:3 THF/Et$_3$N. The solution was bubbled 1 h with argon. CuI (20.0 mg, 0.10 mmol), Pd(PPh$_3$)$_2$Cl$_2$ (20.0 mg, 0.03 mmol) and PPh$_3$ (10.0 mg, 0.04 mmol) were added. The reaction was refluxed over weekend at 75 °C and cooled down to room temperature. DCM was added and the organics were washed with H$_2$O. The organic layer was taken and the solvents were evaporated under reduced pressure. The crude product was partially purified by flash column chromatography on silica gel with ethyl acetate/hexane (1:1). 9-Methoxy-5-(phenylethynyl)-1H-phenalen-1-one **39c** (0.27 g, 0.9 mmol) was dissolved in 30 ml DCM, boron tribromide 1 M in DCM (2.0 ml, 2.0 mmol) was added dropwise and the reaction mixture was refluxed overnight at 50 °C. The reaction was cooled down to room temperature and quenched with 20 ml NaOH 2 M; the organic layer was separated, the aqueous layer was acidified with HCl and extracted with DCM. All the organics were collected, the solvent was dried and the crude product was purified by column chromatography on silica gel with pure DCM (0.15 g, yield 36%). Suitable crystals for single crystal X-ray diffraction were obtained from slow evaporation at room temperature of a DCM/ethanol solution.

^{1}H-NMR (500 MHz, CDCl$_3$, 25 °C, δ(ppm)): 15.91 (s, 1H, H15), 8.15 (s, 2H, H4), 8.06 (d, 2H, H2), 7.55 (m, 2H, H12), 7.36 (m, 3H, H13,14), 7.17 (d, 2H, H1). ^{13}C-NMR (125 MHz, CDCl$_3$, 25 °C, δ(ppm)): 179.49 (C8), 140.83 (C2), 135.42 (C4), 131.83 (C12), 128.81 (C13), 128.65 (C14), 125.73 (C3), 124.63 (C6), 122.96 (C1), 88.37 (C9,10).

HOp-pe

15c
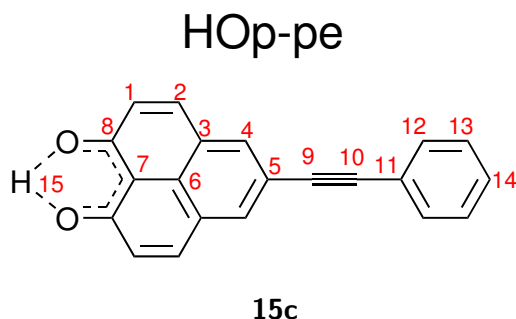
Scheme 8.18: HOp−pe **15c**. Peaks in ^{1}H-NMR and ^{13}C-NMR spectra are labeled according to the numbering shown in the figure.

Al(Op−pe)₃ 16c. HOp−pe **15c** (0.10 g, 0.3 mmol) was dissolved in 10 ml toluene, AlCl₃ (14.0 mg, 0.1 mmol) was added and the solution was refluxed overnight at 110 °C. The yellow precipitate was filtered and washed thoroughly with fresh toluene. The crude product was purified by column chromatography on alumina neutral grade IV with pure DCM (76 mg, yield 83%).

^{1}H-NMR (500 MHz, CD₂Cl₂, 25 °C, δ(ppm)): 8.18 (s, 2H, H4), 8.08 (d, 2H, H2), 7.59 (m, 2H, H12), 7.41 (m, 3H, H13,14), 7.09 (d, 2H, H1). ^{13}C-NMR (125 MHz, CD₂Cl₂, 25 °C, δ(ppm)): 179.42 (C8), 141.87 (C2), 135.87 (C4), 131.99 (C12), 128.91 (C13), 128.17 (C14), 125.52 (C3), 123.42 (C1), 113.47 (C7), 89.81(C9), 88.82 (C10). MALDI-TOF MS (Da) m/z (rel. intensity, assigned structure): 617 (100%, C₄₂H₂₂O₄Al calc. = 617.62). Elemental analysis found (calc.): C₆₃H₄₁O₁₀Al (Al(C₆₃H₃₃O₆) · 4 H₂O, 985.02 g mol^{-1}): C 76.43 (76.81)%, H 5.79 (4.20)%.

Al(Op-pe)₃

16c
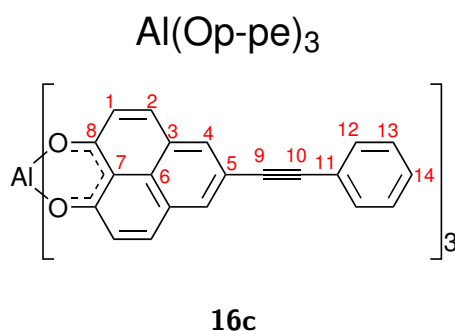
Scheme 8.19: Al(Op−pe)₃ **16c**. Peaks in ^{1}H-NMR and ^{13}C-NMR spectra are labeled according to the numbering shown in the figure.

HOba 18. 2-Methoxynaphthalene **1** (5.00 g, 32.0 mmol) and benzoyl chloride **17** (3.7 ml, 32.0 mmol) were dissolved in 60 ml DCB. The mixture was cooled to 0 °C and AlCl₃ (4.30 g, 32.0 mmol) was slowly added. The reaction was warmed up to room temperature and stirred 1 h. Another aliquote of AlCl₃ (4.30 g, 32.0 mmol) was added and the mixture was refluxed at 120 °C over 48 h. The mixture was cooled to room temperature and quenched with HCl 6 N 40 ml. The solid was filtered off on celite and washed with hot DCM; the organic layer was taken and the solvents were evaporated under vacuum. The crude product was purified by chromatography on silica gel with DCM/hexane (1:1) (4.79 g, yield 61%).

^{1}H-NMR (500 MHz, CDCl₃, 25 °C, δ(ppm)): 15.87 (s, 1H, H18), 8.67 (d, 2H, H4,6), 8.53 (d, 1H, H9), 8.20 (d, 1H, H12), 8.02 (d, 1H, H2), 7.86 (s, 1H, H5), 7.67 (t, 2H, H10,11), 7.37 (d, 1H, H1). ^{13}C-NMR (125 MHz, CDCl₃, 25 °C, δ(ppm)): 186.40 (C14,16), 140.07 (C2), 133.51 (C8), 130.97 (C10), 129.84 (C17), 128.01 (C4), 127.29 (C3), 126.74 (C11), 125.61 (C12), 124.25 (C7), 123.25 (C6), 120.58 (C5).

HOba
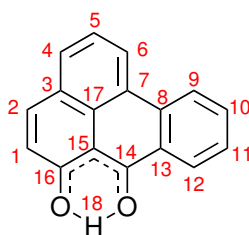
18

Scheme 8.20: HOba **18**. Peaks in ^{1}H-NMR and ^{13}C-NMR spectra are labeled according to the numbering shown in the figure.

Al(Oba)$_3$ 19. HOba **18** (0.41 g, 1.7 mmol) and AlCl$_3$ (66.7 mg, 0.5 mmol) were dissolved in 20 ml of toluene. The mixture was refluxed at 110 °C overnight, the crude precipitate was purified by column chromatography on alumina neutral grade IV with pure DCM (0.33 g, yield 86%).

MALDI-TOF MS (Da) *m/z* (rel. intensity, assigned structure): 517 (100%, C$_{35}$H$_{18}$O$_4$Al calc. = 517.50). Elemental analysis found (calc.): C$_{51}$H$_{31}$O$_8$Al (Al(C$_{51}$H$_{27}$O$_6$)·2 H$_2$O, 798.08 g mol^{-1}): C 76.84 (76.68)%, H 5.05 (3.92)%.

Al(Oba)$_3$
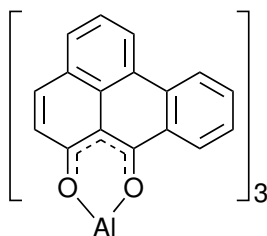
19

Scheme 8.21: Al(Oba)$_3$ **19**.

HOp−py 22. 210 ml of a mixture 4:2:1 toluene/ethanol/K$_2$CO$_3$ (2 M in H$_2$O) was prepared and 2-bromopyridine **21** (3.0 ml, 31.0 mmol) and 2-hydroxybenzenboronic acid (**20**) (4.14 g, 30.0 mmol) were dissolved in it. The mixture was bubbled with Ar 1 h and Pd(PPh$_3$)$_4$ (0.71 g, 0.63 mmol) was added. The reaction was refluxed overnight at 80 °C. The resulting solution was cooled down and extracted with ethylacetate; the organics were collected and the solvents were evaporated under reduced pressure. The crude product was purified to column chromatography on silica gel with pure DCM (3.48 g, yield 68%).

^{1}H-NMR (500 MHz, CDCl$_3$, 25 °C, δ(ppm)): 14.36 (s, 1H, H12), 8.42 (dd, 1H, H4), 7.81 (d, 1H, H10), 7.76-7.70 (m, 2H, H1,8), 7.32 (dt, 1H, H2), 7.14 (dt, 1H, H3), 7.10 (dd, 1H, H7), 6.90 (dt, 1H, H9). ^{13}C-NMR (125 MHz, CDCl$_3$, 25 °C, δ(ppm)): 159.96 (C11), 157.63 (C6), 145.61

(C10), 137.66 (C8), 131.38 (C4), 126.10(C2), 121.42 (C5), 118.92 (C9), 118.72 (C3), 118.70 (C7), 118.47 (C1).

HOp-py

22
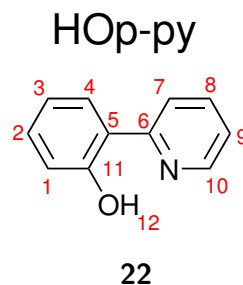
Scheme 8.22: HOp−py **22**. Peaks in ^{1}H-NMR and ^{13}C-NMR spectra are labeled according to the numbering shown in the figure.

Al(Op−py)$_3$ 23. HOp−py **22** (3.48 g, 4.0 mmol) was dissolved in 50 ml of freshly distilled THF; the solution was cooled to −78 °C and Al(CH$_3$)$_3$ (2 M in toluene) was slowly added (0.61 ml, 1.2 mmol). The reaction mixture was warmed up to room temperature and left stirring over five days. The white precipitate was filtered, washed thoroughly with fresh THF and dried under vacuum (0.47 g, yield 73%).

ESI-TOF MS (Da) *m/z* (rel. intensity, assigned structure): 367.08 (100%, C$_{22}$H$_{16}$O$_2$N$_2$Al calc. = 367.36). MALDI-TOF MS (Da) *m/z* (rel. intensity, assigned structure): 367 (100%, C$_{22}$H$_{16}$O$_2$N$_2$Al calc. = 367.36). Elemental analysis found (calc.): C$_{33}$H$_{30}$O$_6$N$_3$Al (Al(C$_{33}$H$_{24}$O$_3$N$_3$)· 3 H$_2$O, 591.19 g mol^{-1}): C 67.48 (67.00)%, H 4.59 (5.12)%, N 7.13 (7.10)%.

Al(Op-py)$_3$

23
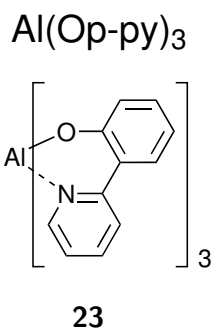
Scheme 8.23: Al(Op−py)$_3$ **23**.

Al(Trop)$_3$ 25. Tropolone **24** (1.12 g, 9.2 mmol) was dissolved in 50 ml of freshly distilled toluene, AlCl$_3$ was added (0.40 g, 3.0 mmol) and the resulting solution was refluxed overnight at 110 °C. The white precipitate was filtred and washed thoroughly with fresh toluene. The crude product was purified by column chromatography (0.97 g, yield 83%). Suitable crystals for single crystal X-ray diffraction were obtained from slow evaporation at room temperature of a DCM/ethanol solution.

^{1}H-NMR (500 MHz, CDCl$_3$, 25 °C, δ(ppm)): 7.55 (t, 2H, H2), 7.49 (d, 2H, H1), 7.11 (t, 1H, H3). ^{13}C-NMR (125 MHz, CDCl$_3$, 25 °C, δ(ppm)): 178.09 (C4), 140.28 (C2), 127.59 (C3), 125.84

(C1). MALDI-TOF MS (Da) m/z (rel. intensity, assigned structure)269 (100%, $C_{14}H_{10}O_4Al$ calc. $= 269.22$), 659 (41%, $C_{35}H_{25}O_{10}Al_2$ calc. $= 659.56$). Elemental analysis found (calc.): $C_{21}H_{15}O_6Al$ ($Al(C_{21}H_{15}O_6)$, $650.64\,g\,mol^{-1}$): C 64.57 (64.61)%, H 3.83 (3.88)%.

25
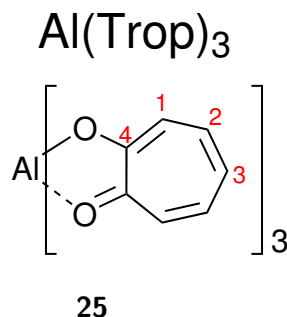
Scheme 8.24: Al(Trop)$_3$ **25**. Peaks in ^{1}H-NMR and ^{13}C-NMR spectra are labeled according to the numbering shown in the figure.

Al(q$_2$Acac) 28. Al(CH$_3$)$_3$ (2 M in toluene, 1.35 ml, 2.7 mmol) was taken in 20 ml of freshly distilled toluene and the resulting solution was cooled to 0 °C. A second solution of Hq **26** (0.78 g, 5.5 mmol) in 10 ml of freshly distilled toluene was added dropwise over 30 min. The solution was warmed up to room temperature and left stirring 3 h. Acac **27** (0.28 ml, 2.7 mmol) in 10 ml of freshly distilled toluene was added dropwise over 30 min; the resulting solution was stirred overnight at room temperature. The yellowish precipitate was filtred and washed thoroughly with fresh toluene. The crude product was purified by column chromatography on alumina neutral grade IV with pure DCM (0.79 g, yield 71%). Suitable crystals for single crystal X-ray diffraction were obtained from slow evaporation at room temperature of a acetone solution.

^{1}H-NMR (500 MHz, CD$_2$Cl$_2$, 25 °C, δ(ppm)): 8.52 (dd, 2H, H7), 8.17 (dd, 2H, H5), 7.51 (t, 2H, H2), 7.29-7.25 (m, 2H, H6), 7.10-7.00 (m, 4H, H1,3), 5.64 (s, 1H, H12), 1.94 (s, 6H, H10). ^{13}C-NMR (125 MHz, CDCl$_3$, 25 °C, δ(ppm)): 192.79 (C11), 191.76 (C9), 159.17 (C1), 144.27 (C8), 139.43 (C3), 139.11 (C4), 131.04 (C6), 129.58 (C2), 121.95 (C5), 112.01 (C7), 101.83 (C12), 27.02 (C10). ESI-TOF MS (Da) m/z (rel. intensity, assigned structure): 415.12 (100%, $C_{23}H_{20}O_4N_2Al$ calc. $= 415.43$), 370.12 (12%, $C_{19}H_{21}O_5NAl$ calc. $= 370.39$), 315.07 (12%, $C_{18}H_{12}O_2N_2Al$ calc. $= 315.28$), 270.07 (5%, $C_{14}H_{13}O_3NAl$ calc. $= 270.25$). MALDI-TOF MS (Da) m/z (rel. intensity, assigned structure): 315 (100%, $C_{18}H_{12}O_2N_2Al$ calc. $= 315.28$), 270 (22%, $C_{14}H_{13}O_3NAl$ calc. $= 270.25$), 729 (20%, $C_{41}H_{31}O_6N_4Al_2$ calc. $= 729.68$), 684 (18%, $C_{37}H_{32}O_7N_3Al_2$ calc. $= 684.65$). Elemental analysis found (calc.): $C_{23}H_{19}O_4N_2Al$ ($Al(C_{23}H_{19}O_4N_2)$, $414.12\,g\,mol^{-1}$): C 65.98 (66.66)%, H 4.38 (4.63)%, N 6.55 (6.76)%.

Al(q$_2$Acac)

28
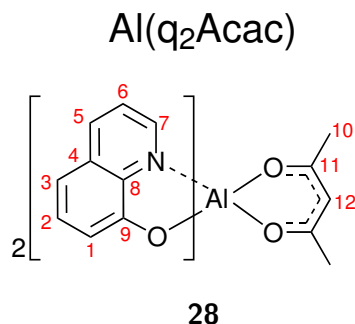
Scheme 8.25: Al(q$_2$Acac) **28**. Peaks in ^{1}H-NMR and ^{13}C-NMR spectra are labeled according to the numbering shown in the figure.

Al(q$_2$Op) 29. Al(q$_2$Acac) **28** (0.71 g, 1.7 mmol) and HOp **3** (0.30 g, 1.5 mmol) were dissolved in 100 ml on ethanol. The solution was refluxed at 90 °C overnight, cooled down to room temperature and reduced to 20 ml. The precipitate was filtered, washed with cold fresh ethanol and purified by column chromatography on alumina neutral grade IV with pure DCM (0.63 g, yield 73%). Suitable crystals for single crystal X-ray diffraction were obtained from slow evaporation at room temperature of a DCM/ethanol solution.

^{1}H-NMR (500 MHz, CD$_2$Cl$_2$, 25 °C, δ(ppm)): 8.68 (d, 2H, H7), 8.23 (d, 2H, H5), 8.09 (d, 2H, H11), 8.04 (d, 2H, H13), 7.58 (t, 1H, H14), 7.50 (t, 2H, H2), 7.34 (m, 2H, H6), 7.06 (m, 4H, H1,3), 6.96 (d, 2H, H10). ESI-TOF MS (Da) *m/z* (rel. intensity, assigned structure): 511.11 (100%, C$_{31}$H$_{20}$O$_4$N$_2$Al calc. = 511.51), 366.06 (95%, C$_{22}$H$_{13}$O$_3$NAl calc. = 366.34). MALDI-TOF MS (Da) *m/z* (rel. intensity, assigned structure): 417 (100%, C$_{26}$H$_{14}$O$_4$Al calc. = 417.38), 366 (40%, C$_{22}$H$_{13}$O$_3$NAl calc. = 366.34). Elemental analysis found (calc.): C$_{31}$H$_{19}$O$_4$N$_2$Al (Al(C$_{31}$H$_{19}$O$_4$N$_2$), 510.48 g mol^{-1}): C 72.17 (72.93)%, H 3.97 (3.76)%, N 5.31 (5.49)%.

Al(q2Op)

29
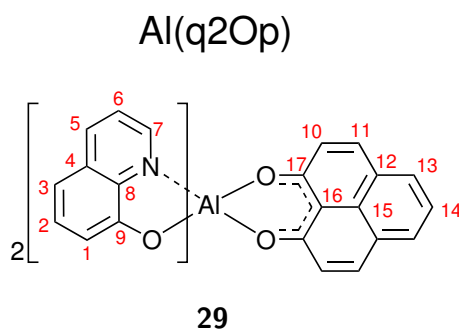
Scheme 8.26: Al(q$_2$Op) **29**. Peaks in ^{1}H-NMR spectrum are labeled according to the numbering shown in the figure.

Al(q$_2$Trop) 30. Al(q$_2$Acac) **28** (0.30 g, 0.7 mmol) and tropolone **24** (85.0 mg, 0.70 mmol) were dissolved in 60 ml of ethanol. The solution was refluxed at 90 °C overnight, cooled down to room temperature and reduced to 10 ml. The precipitate was filtred, washed with cold fresh ethanol and purified by column chromatography on alumina neutral grade IV with pure DCM (0.21 g, yield 68%). Suitable crystals for single crystal X-ray diffraction were obtained from slow evaporation at room temperature of a DCM/ethanol solution.

ESI-TOF MS (Da) *m/z* (rel. intensity, assigned structure): 414.08 (100%, $C_{23}H_{17}O_5NAl$ calc. = 414.38), 437.09 (60%, $C_{25}H_{18}O_4N_2Al$ calc. = 437.41), 292 (15%, $C_{16}H_{11}O_3NAl$ calc. = 292.26). MALDI-TOF MS (Da) *m/z* (rel. intensity, assigned structure): 315 (100%, $C_{18}H_{12}O_2N_2Al$ calc. = 315.30), 292 (80%, $C_{16}H_{11}O_3NAl$ calc. = 292.26), 269 (62%, $C_{14}H_{10}O_4Al$ calc. = 269.22), 728 (41%, $C_{41}H_{28}O_7N_3Al_2$ calc. = 728.68), 751 (38%, $C_{43}H_{29}O_6N_4Al_2$ calc. = 751.72), 705 (21%, $C_{39}H_{27}O_8N_2Al_2$ calc. = 705.64), 774 (15%, $C_{45}H_{30}O_5N_5Al_2$ calc. = 774.76), 682 (10%, $C_{37}H_{26}O_9NAl_2$ calc. = 682.60). Elemental analysis found (calc.): $C_{25}H_{17}O_4N_2Al$ ($Al(C_{25}H_{17}O_4N_2)$, 436.40 g mol^{-1}): C 69.15 (68.80)%, H 4.37 (3.39)%, N 5.69 (6.42)%.

Al(q₂Trop)

30
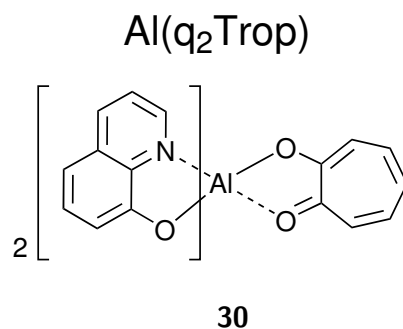
Scheme 8.27: Al(q₂Trop) **30**.

Zn(Op)₂ 31. HOp **3** (0.50 g, 2.5 mmol) was dissolved in 60 ml of ethanol, zinc acetate (0.23 g, 1.2 mmol) was added and the mixture was refluxed overnight at 90 °C. The reaction was cooled down to room temperature; the precipitate was filtred, washed thoroughly with fresh ethanol (0.46 g, yield 84%). Suitable crystals for single crystal X-ray diffraction were obtained from slow evaporation at room temperature of a DCM/ethanol solution.

^{1}H-NMR (500 MHz, THF-d_8, 25 °C, δ(ppm)): 7.99 (d, 2H, H2), 7.89 (d, 2H, H4), 7.40 (t, 1H, H5), 7.03 (d, 2H, H1). MALDI-TOF MS (Da) *m/z* (rel. intensity, assigned structure): 260 (100%, $C_{13}H_7O_2NZn$ calc. = 260.59). Elemental analysis found (calc.): $C_{26}H_{18}O_6Zn$ ($Zn(C_{26}H_{14}O_4) \cdot 2 H_2O$, 491.83 g mol^{-1}): C 63.53 (63.49)%, H 4.12 (3.70)%.

Zn(Op)₂

31
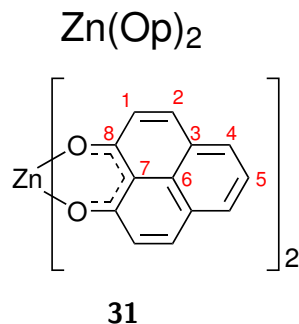
Scheme 8.28: Zn(Op)₂ **31**. Peaks in ^{1}H-NMR and ^{13}C-NMR spectra are labeled according to the numbering shown in the figure.

8.3 Phenalenyl-based SMMs

[Dy(Op)$_2$Cl(HOp)(EtOH)] 32. HOp **3** (117.7 mg, 0.6 mmol) was dissolved in 5 ml of CH$_3$Cl. An ethanol solution of NaH (14.4 mg, 0.6 mmol) was added dropwise at room temperature. A second ethanol solution of DyCl$_3 \cdot 6$ H$_2$O (75.4 g, 0.2 mmol) was added dropwise. The final mixture was stirred 2 h at room temperature and refluxed 3 h at 90 °C. After cooling the mixture overnight, the solid was filtered off and single crystals were grown by slow evaporation of the filtrate solution (18.3 mg, yield= 10%).

^{1}H-NMR (500 MHz, DMSO-d_6, 25 °C, δ(ppm)): 49.23, 40.63, 36.40, 33.58, 28.49, 16.27 (s, 1H), 8.33 (dd, 2H), 7.77 (t, 1H), 7.28 (d,2H). MALDI-TOF MS (Da) m/z (rel. intensity, assigned structure): 554 (100%, C$_{26}$H$_{14}$O$_4$Dy calc. = 552.90), 572 (15%, C$_{26}$H$_{16}$O$_5$dy calc. = 570.92), 1301 (8%, C$_{65}$H$_{35}$O$_{10}$Dy calc. = 1301.0), 945 (7%, C$_{52}$H$_{29}$O$_8$Dy calc. = 944.31), 772 (5%, C$_{39}$H$_{21}$O$_6$DyNa calc. = 771.09), 1693 (5%, C$_{91}$H$_{50}$O$_{14}$Dy$_2$ calc. = 1692.41), 756 (2%, C$_{39}$H$_{21}$O$_6$DyLi calc. = 755.04). Elemental analysis found (calc.): C$_{41}$H$_{28}$O$_7$DyCl (Dy(C$_{26}$H$_{14}$O$_4$)Cl· C$_{13}$H$_8$O$_2 \cdot$ C$_2$H$_6$O, 830.58 g mol^{-1}): C 59.87 (59.29)%, H 3.67 (3.40)%.
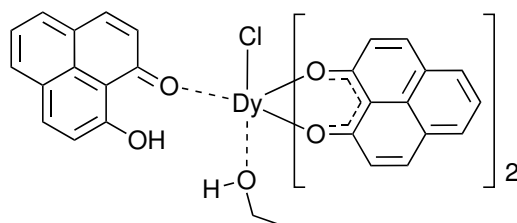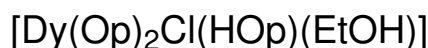
[Dy(Op)$_2$Cl(HOp)(EtOH)]

32

Scheme 8.29: [Dy(Op)$_2$Cl(HOp)(EtOH)] **32**.

[Dy(Op)$_3$(HOp)] 33-[Dy(Op)$_3$(EtOH)] 34. HOp **3** (117.7 mg, 0.6 mmol) was suspended in 5 ml of ethanol. Diisopropylamine (60.6 mg, 0.6 mmol) was added dropwise at room temperature. An ethanol solution of DyCl$_3 \cdot 6$ H$_2$O (75.4 g, 0.2 mmol) was added dropwise. The final mixture was stirred 2 h at room temperature and refluxed 3 h at 90 °C. After cooling the mixture overnight, the solid was filtered off and single crystals were grown by slow evaporation of the filtrate solution (20.8 mg, yield= 13%). The precipitate was filtered and washed thoroughly with fresh ethanol (0.15 g).

^{1}H-NMR (500 MHz, DMSO-d_6, 25 °C, δ(ppm)): 49.21, 40.67, 36.47, 33.55, 28.55, 21.63, 19.36, 17.73. MALDI-TOF MS (Da) m/z (rel. intensity, assigned structure): 554 (100%, C$_{26}$H$_{14}$O$_4$Dy calc. = 552.90), 945 (20%, C$_{52}$H$_{29}$O$_8$Dy calc. = 944.31), 572 (18%, C$_{26}$H$_{16}$O$_5$dy calc. = 570.92), 1693 (10%, C$_{91}$H$_{50}$O$_{14}$Dy$_2$ calc. = 1692.41), 1301 (5%, C$_{65}$H$_{35}$O$_{10}$Dy calc. = 1301.0). Elemental analysis found (calc.): C$_{97}$H$_{68}$O$_{17}$Dy$_2$ ([Dy(C$_{39}$H$_{21}$O$_6$) · C$_{13}$H$_8$O$_2$−Dy(C$_{39}$H$_{21}$O$_6$) · C$_2$H$_6$O]·2 C$_2$H$_6$O, 1830.51 g mol^{-1}): C 63.51 (63.64)%, H 3.66 (3.74)%. Absorption peaks (nm), DMSO solution, 25 °C: 349, 432, 458.
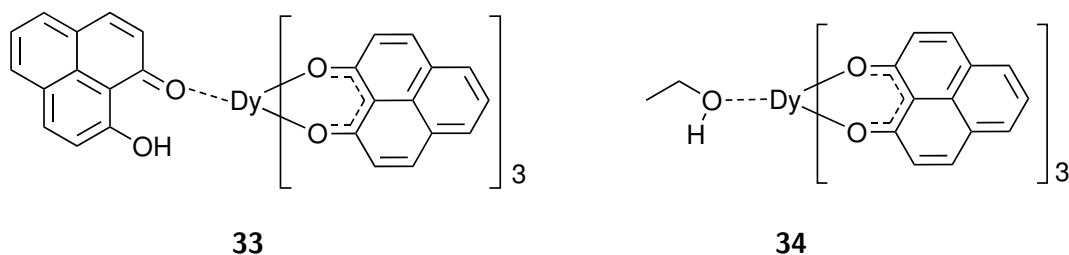
Scheme 8.30: $[\text{Dy}(\text{Op})_3(\text{HOp})]$ **33**-$[\text{Dy}(\text{Op})_3(\text{EtOH})]$ **34**.

Sublimable phenalenyl-based dysprosium complex 36. Hexamethyldisilazide (16.5 ml, 78.0 mmol) was taken in 40 ml of freshly distilled THF and the solution was cooled to 0 °C. n-Butyllithium (1.6 M in hexane, 50.0 ml, 80.0 mmol) was slowly added and the reaction was stirred 1 h. DyCl$_3$ (6.45 g, 24.0 mmol) was carefully added and the solution was stirred and allowed to warm up to room temperature overnight. The resulting product was purified by sublimation in high vacuum (2×10^{-6} mbar, 90 °C) and added (0.50 g, 0.8 mmol) to a solution of HOp **3** (0.46 g, 2.4 mmol) in 20 ml in freshly distilled THF. The mixture was refluxed at 65 °C overnight. The yellow precipitate was filtered and washed with fresh THF (0.29 g).

^{1}H-NMR (500 MHz, DMSO-d_6, 25 °C, δ(ppm)): 36.28, 33.41, 28.43, 21.51, 19.26, 17.61, 7.86, 7.31, 6.79. MALDI-TOF MS (Da) m/z (rel. intensity, assigned structure): 554 (100%, C$_{26}$H$_{14}$O$_4$Dy calc. = 552.90), 945 (4%, C$_{52}$H$_{29}$O$_8$Dy calc. = 944.31), 1301 (4%, C$_{65}$H$_{35}$O$_{10}$Dy calc. = 1301.0), 756 (4%, C$_{39}$H$_{21}$O$_6$DyLi calc. = 755.04), 572 (2%, C$_{26}$H$_{16}$O$_5$dy calc. = 570.92), 772 (2%, C$_{39}$H$_{21}$O$_6$DyNa calc. = 771.09). Absorption peaks (nm), DMSO solution, 25 °C: 341, 434, 460.

Phenalenyl-based terbium complex 37. HOp **3** (0.51 g, 2.6 mmol) was dissolved in 60 ml of ethanol, TbCl$_3 \cdot 6$ H$_2$O (0.32 g, 0.8 mmol) was added and the solution was refluxed overnight at 90 °C. The precipitate was filtered and washed thoroughly with fresh ethanol (0.44 g).

^{1}H-NMR (500 MHz, DMSO-d_6, 25 °C, δ(ppm)): 32.62, 30.42, 29.20, 25.26, 22.33, 7.97, 7.43, 6.91. MALDI-TOF MS (Da) m/z (rel. intensity, assigned structure): 549 (100%, C$_{26}$H$_{14}$O$_4$Tb calc. = 549.33), 567 (100%, C$_{39}$H$_{23}$O$_7$Tb calc. = 567.35). Elemental analysis found (calc.): C$_{39}$H$_{27}$O$_9$Tb (Tb(C$_{39}$H$_{21}$O$_6$) $\cdot$ 3 H$_2$O, 798.59 g mol^{-1}): C 58.78 (58.65)%, H 3.08 (3.41)%. Absorption peaks (nm), DMSO solution, 25 °C: 349, 434, 460.

Sublimable phenalenyl-based terbium complex 38. Hexamethyldisilazide (5.2 ml, 25.0 mmol) was taken in 20 ml of freshly distilled THF and the solution was cooled to 0 °C. n-Butyllithium (1.6 M in hexane, 17.0 ml, 27.2 mmol) was slowly added and the reaction was stirred 1 h. TbCl$_3$ (2.00 g, 7.5 mmol) was carefully added and the solution was stirred and allowed to warm up to room temperature overnight. The resulting product was purified by sublimation in high vacuum (2×10^{-6} mbar, 90 °C) and added (0.50 g, 0.8 mmol) to a solution of HOp **3** (0.46 g, 2.4 mmol) in 20 ml of freshly distilled THF. The mixture was refluxed at 65 °C overnight. The yellow precipitate was filtered and washed with fresh THF (0.33 g).

^{1}H-NMR (500 MHz, DMSO-d_6, 25 °C, δ(ppm)): 32.58, 30.36, 29.16, 25.23, 22.32, 7.84, 7.30, 6.78. MALDI-TOF MS (Da) m/z (rel. intensity, assigned structure): 549 (100%, C$_{26}$H$_{14}$O$_4$Tb

calc. = 549.33), 1293 (12%, $C_{65}H_{35}O_{10}Tb_2$ calc. = 1293.86), 567 (6%, $C_{39}H_{23}O_7Tb$ calc. = 567.35), 751 (5%, $C_{39}H_{21}O_6TbLi$ calc. = 751.47). Elemental analysis found (calc.): $C_{39}H_{25}O_8Tb$ ($Tb(C_{39}H_{21}O_6) \cdot 2\,H_2O$, 798.59 g mol^{-1}): C 60.06 (60.01)%, H 3.18 (3.26)%. Absorption peaks (nm), DMSO solution, 25 °C: 349, 434, 460.

Bibliography

(1) *The Oxford English dictionary*, 2. ed.; Clarendon Pr.: Oxford, 1989.

(2) Koenigsberger, J.; Schilling, K. *Ann. Physik* **1910**, *337*, 179–230.

(3) Volmer, M. *Ann. Physik* **1913**, *345*, 775–796.

(4) Pope, M.; Magnante, P.; Kallmann, H. *J. Chem. Phys.* **1963**, *38*, 2042–2043.

(5) Helfrich, W.; W.G., S. *Phys. Rev. Lett.* **1965**, *14*, 229–232.

(6) Silinsh, E., *Organic Molecular Crystals: Their Electronic States*; Springer: Berlin, 1980.

(7) Pope, M.; Swenberg, C., *Electronic processes in organic crystals and polymers*, 2. ed.; Oxford University Press: New York, 1999.

(8) Chiang, C.; Fincher, C.; Park, Y.; Heeger, A.; Shirakawa, H.; Louis, E.; Gau, S.; Mac-Diarmid, A. *Phys. Rev. Lett.* **1977**, *39*, 1098–1101.

(9) Tang, C.; VanSlyke, S. *Appl. Phys. Lett.* **1987**, *51*, 913–915.

(10) Tang, C.; VanSlyke, S.; Chen, C. *J. Appl. Phys.* **1989**, *65*, 3610–3616.

(11) Burroughes, J.; Bradley, D.; Brown, A.; Marks, R.; Mackay, K.; Friend, R.; Burn, P.; Holmes, A. *Nature* **1990**, *347*, 539–541.

(12) Braun, D.; Heeger, A. *Appl. Phys. Lett.* **1991**, *58*, 1982–1984.

(13) Hains, A.; Liang, Z.; Woodhouse, M.; Gregg, B. *Chem. Rev.* **2010**, *110*, 6689–6735.

(14) Clarke, T.; Durrant, J. *Chem. Rev.* **2010**, *110*, 6736–6767.

(15) Dediu, V.; Hueso, L.; Bergenti, I.; Taliani, C. *Nat. Mater.* **2009**, *8*, 707–716.

(16) Horowitz, G. *Adv. Mater.* **1998**, *10*, 365–377.

(17) *Physics of organic semiconductors*; Brütting, W., Ed.; Wiley-VCH: Weinheim, 2005.

(18) *Physics of organic semiconductors*, 2. compl. new rev. ed.; Brütting, W., Adachi, C., Eds.; Wiley-VCH: Weinheim, 2012.

(19) Schwoerer, M.; Wolf, H., *Organic molecular solids*; Wiley-VCH: Weinheim, 2007.

(20) Faupel, F.; Dimitrakopoulos, C.; Kahn, A.; Wöll, C. *J. Mater. Res.* **2004**, *19*, 1887–1888.

(21) Schmidt, T. Photophysics of organic light-emitting diodes - Device efficiency and degradation processes., Ph.D. Thesis, University of Augsburg, 2013.

(22) Kondakov, D.; Pawlik, T.; Hatwar, T.; Spindler, J. *J. Appl. Phys.* **2009**, *106*, 124510.

(23) Bässler, H. *Phys. Status Solidi B* **1993**, *175*, 15–56.

(24) Hemenger, R. *J. Chem. Phys.* **1977**, *67*, 262–264.

(25) Ruini, A.; Caldas, M.; Bussi, G.; Molinari, E. *Phys. Rev. Lett.* **2002**, *88*, 206403.

(26) Wu, Y.; Hu, B.; Howe, J. *J. Appl. Phys.* **2005**, *98*, 103510.

(27) Cölle, M.; Brütting, W. *Phys. Stat. Sol. (a)* **2004**, *201*, 1095–1115.

(28) Ohnesorge, W.; Rogers, L. *Spectrochim. Acta Part A* **1959**, *15*, 27–40.

(29) Li, Z.; Meng, H., *Organic Light-Emitting Materials and Devices*; CRC Taylor & Francis: Boca Raton, Fl., 2007.

(30) Kauffman, G. *Coord. Chem. Rev.* **1974**, *12*, 105 –149.

(31) Li, H.; Zhang, F.; Wang, Y.; Zheng, D. *Mat. Sci. Eng. B-Solid* **2003**, *100*, 40–46.

(32) Utz, M.; Chen, C.; Morton, M.; Papadimitrakopoulos, F. *J. Am. Chem. Soc.* **2003**, *125*, 1371–1375.

(33) Katakura, R.; Koide, Y. *Inorg. Chem.* **2006**, *45*, 5730–5732.

(34) Schmidbaur, H.; Lettenbauer J .and Wilkinson, D.; Müller, G.; Kumberger, O. *Z. Naturforsch. B* **1991**, *46*, 901–911.

(35) Fujii, I.; Hirayama, N.; Ohtani, J.; Kodama, K. *Anal. Sci.* **1996**, *12*, 153–154.

(36) Anderson, J. et al. *J. Am. Chem. Soc.* **1998**, *120*, 9646–9655.

(37) Thomas, K.; Lin, J.; Tao, Y.; Chuen, C. *Chem. Mat.* **2002**, *14*, 3852–3859.

(38) Montes, V.; Pohl, R.; Shinar, J.; Anzenbacher, J. *Chem. Eur. J.* **2006**, *12*, 4523–4535.

(39) Higginson, K.; Zhang, X.; Papadimitrakopoulos, F. *Chem. Mat.* **1998**, *10*, 1017–1020.

(40) Chen, C.; Shi, J. *Coord. Chem. Rev.* **1998**, *171*, 161–174.

(41) Brinkmann, M.; Gadret, G.; Muccini, M.; Taliani, C.; Masciocchi, N.; Sironi, A. *J. Am. Chem. Soc.* **2000**, *122*, 5147–5157.

(42) Kepler, R.; Beeson, P.; Jacobs, S.; Anderson, R.; Sinclair, M.; Valencia, V.; Cahill, P. *Appl. Phys. Lett.* **1995**, *66*, 3618–3620.

(43) Kalinowski, J.; Camaioni, N.; Di Marco, P.; Fattori, V.; Martelli, A. *Appl. Phys. Lett.* **1998**, *72*, 513–515.

(44) Chen, B.; Lai, W.; Gao, Z.; Lee, C.; Lee, S.; Gambling, W. *Appl. Phys. Lett.* **1999**, *75*, 4010–4012.

(45) Mückl, A.; Berleb, S.; Brütting, W.; Schwoerer, M. *Synth. Met.* **2000**, *111*, 91–94.

(46) Naka, S.; Okada, H.; Onnagawa, H.; Yamaguchi, Y.; Tsutsui, T. *Synth. Met.* **2000**, *111*, 331–333.

(47) Barth, S.; Müller, P.; Riel, H.; Seidler, P.; Rieß, W.; Vestweber, H.; Bässler, H. *J. App. Phys.* **2001**, *89*, 3711–3719.

(48) Malliaras, G.; Shen, Y.; Dunlap, D.; Murata, H.; Kafafi, Z. *Appl. Phys. Lett.* **2001**, *79*, 2582–2584.

(49) Fong, H.; So, S. *J. of Appl. Phys.* **2006**, *100*, 094502.

(50) Tsutsui, T.; Aminaka, E.; Lin, C.; Kim, D. *Philos. Trans. R. Soc. A* **1997**, *355*, 801–813.

(51) Diekmann, K. white paper on the necessity of luminous efficacy measurements standardization of OLED light sources., `http://www.hitech-projects.com/euprojects/olla/news/`.

(52) Kim, K.; Lee, D.; Jin, J. *Synth. Met.* **2000**, *114*, 49–56.

(53) Burrows, P.; Sapochak, L.; McCarty, D.; Forrest, S.; Thompson, M. *Appl. Phys. Lett.* **1994**, *64*, 2718–2720.

(54) Chen, B.; Sun, X.; Li, Y. *Appl. Phys. Lett.* **2003**, *82*, 3017–3019.

(55) Hamada, Y.; Sano, T.; Fujita, M.; Fujii, T.; Nishio, Y.; Shibata, K. *Jpn. J. Appl. Phys.* **1993**, *32*, L514–L515.

(56) Sapochak, L.; Benincasa, F.; Schofield, R.; Baker, J.; Riccio, K.; Fogarty, D.; Kohlmann, H.; Ferris, K.; Burrows, P. *J. Am. Chem. Soc.* **2002**, *124*, 6119–6125.

(57) Dónze, N.; Péchy, P.; Grätzel, M.; Schaer, M.; Zuppiroli, L. *Chem. Phys. Lett.* **1999**, *315*, 405–410.

(58) Yin, S.; Hua, Y.; Chen, X.; Yang, X.; Hou, Y.; Xu, X. *Synth. Met.* **2000**, *111*, 109–112.

(59) Jang, H.; Do, L.; Kim, Y.; Kim, J.; Zyung, T.; Do, Y. *Synth. Met.* **2001**, *121*, 1669–1670.

(60) McGhee, M.; Topinka, M. *Nat. Mater.* **2006**, *5*, 675–676.

(61) Shirota, Y.; Kageyama, H. *Chem. Rev.* **2007**, *107*, 953–1010.

(62) Sariciftci, N.; Smilowitz, L.; Heeger, A.; Wudl, F. *Science* **1992**, *258*, 1474–1476.

(63) Yu, G.; Gao, J.; Hummelen, J.; Wudl, F.; Heeger, A. *Science* **1995**, *270*, 1789–1791.

(64) Song, Q.; Li, F.; Yang, H.; Wu, H.; Wang, X.; Zhou, W.; Zhao, J.; Ding, X.; Huang, C.; Hou, X. *Chem. Phys. Lett.* **2005**, *416*, 42–46.

(65) Yu, B.; Zhu, F.; Wang, H.; Li, G.; Yan, D. *J. Appl. Phys.* **2008**, *104*, 114503.

(66) Tang, C. *Appl. Phys. Lett.* **1986**, *48*, 183–185.

(67) Julliere, M. *Phys. Lett. A* **1975**, *54*, 225–226.

(68) Moodera, J.; Kinder, L.; Wong, T.; Meservey, R. *Phys. Rev. Lett.* **1995**, *74*, 3273–3276.

(69) Xiong, Z.; Wu, D.; Vardeny, Z.; Shi, J. *Nature* **2004**, *427*, 821–824.

(70) Dediu, V.; Murgia, M.; Matacotta, F.; Taliani, C.; Barbanera, S. *Solid State Commun.* **2002**, *122*, 181–184.

(71) Wang, F.; Yang, C.; Vardeny, Z.; Li, X. *Phys. Rev. B* **2007**, *75*, 245324.

(72) Dediu, V.; Hueso, L.; Bergenti, I.; Riminucci, A.; Borgatti, F.; Graziosi, P.; Newby, C.; Casoli, F.; De Jong, M.; Taliani, C.; Zhan, Y. *Phys. Rev. B* **2008**, *78*, 115203.

(73) Majumdar, S.; Majumdar, H.; Laiho, R.; Osterbacka, R. *J. Alloy. Compd.* **2006**, *423*, 169–171.

(74) Barraud, C.; Seneor, P.; Mattana, R.; Fusil, S.; Bouzehouane, K.; Deranlot, C.; Graziosi, P.; Hueso, L.; Bergenti, I.; Dediu, V.; Petroff, F.; Fert, A. *Nat. Phys.* **2010**, *6*, 615–620.

(75) Prezioso, M.; Riminucci, A.; Graziosi, P.; Bergenti, I.; Rakshit, R.; Cecchini, R.; Vianelli, A.; Borgatti, F.; Haag, N.; Willis, M.; Drew, A.; Gillin, W.; Dediu, V. *Adv. Mater.* **2013**, *25*, 534–538.

(76) Raman, K.; Kamerbeek, A.; Mukherjee, A.; Atodiresei, N.; Sen, T.; Lazic, P.; Caciuc, V.; Michel, R.; Stalke, D.; Mandal, S.; Bluegel, S.; Muenzenberg, M.; Moodera, J. *Nature* **2013**, *493*, 509–513.

(77) Wakayama, Y.; Hayakawa, R.; Seo, H.-S. *Sci. Technol. Adv. Mater.* **2014**, *15*, 024202.

(78) Sakanoue, T.; Yahiro, M.; Adachi, C.; Takimiya, K.; Toshimitsu, A. *J. Appl. Phys.* **2008**, *103*, 094509.

(79) Di, C.; Yu, G.; Liu, Y.; Xu, X.; Wei, D.; Song, Y.; Sun, Y.; Wang, Y.; Zhu, D. *Adv. Funct. Mater.* **2007**, *17*, 1567–1573.

(80) Capelli, R.; Toffanin, S.; Generali, G.; Usta, H.; Facchetti, A.; Muccini, M. *Nat. Mater.* **2010**, *9*, 496–503.

(81)   Matsushima, T.; Adachi, C. *Appl. Phys. Lett.* **2006**, *89*, 253506.

(82)   Ahlrichs, R.; Bär, M.; Häser, M.; Horn, H.; Kölmel, C. *Chem. Phys. Lett.* **1989**, *162*, 165–169.

(83)   Becke, A. *J. Chem. Phys.* **1993**, *98*, 5648–5652.

(84)   Schäfer, A.; Horn, H.; Ahlrichs, R. *J. Chem. Phys.* **1992**, *97*, 2571–2577.

(85)   Neumann, T.; Danilov, D.; Lennartz, C.; Wenzel, W. *J. Comput. Chem.* **2013**, *34*, 2716–2725.

(86)   Friederich, P. Simulation of energetic disorder and charge transport in amorphous organic semiconductors., Ph.D. Thesis, Karlsruher Institute of Technology, 2013.

(87)   Friederich, P.; Symalla, F.; Meded, V.; Neumann, T.; Wenzel, W. *J. Chem. Theory Comput.* **2014**, *10*, 3720–3725.

(88)   Marcus, R. *Annu. Rev. Phys. Chem.* **1964**, *15*, 155–196.

(89)   Rodin, V.; Nelles, G.; von Wrochem, F.; Meded, V.; Danilov, D.; Poschlad, A.; Wenzel, W. **submitted**.

(90)   Schäfer, A.; Huber, C.; Ahlrichs, R. *J. Chem. Phys.* **1994**, *100*, 5829–5835.

(91)   Forrest, S. *Nature* **2004**, *428*, 911–918.

(92)   Kasuya, T.; Koide, S. *J. Phys. Soc. Jpn.* **1958**, *13*, 1287–1297.

(93)   Cápek, V. *Phys. Rev. B* **1987**, *36*, 7442–7447.

(94)   Cápek, V. *Phys. Rev. B* **1988**, *38*, 12983–12987.

(95)   Nagata, Y. *ChemPhysChem* **2010**, *11*, 474–479.

(96)   Rühle, V.; Lukyanov, A.; May, F.; Schrader, M.; Vehoff, T.; Kirkpatrick, J.; Baumeier, B.; Andrienko, D. *J. Chem. Theory Comput.* **2011**, *7*, 3335–3345.

(97)   Fuchs, A.; Steinbrecher, T.; Mommer, M.; Nagata, Y.; Elstner, M.; Lennartz, C. *Phys. Chem. Chem. Phys.* **2012**, *14*, 4259–4270.

(98)   Singh, U.; Kollman, P. *J. Comput. Chem.* **1984**, *5*, 129–145.

(99)   Marcus, R.; Sutin, N. *Biochim. Biophys. Acta* **1985**, *811*, 265–322.

(100)   Wesolowski, T.; Warshel, A. *J. Phys. Chem.* **1993**, *97*, 8050–8053.

(101)   Wesolowski, T.; Weber, J. *Chem. Phys. Lett.* **1996**, *248*, 71–76.

(102)   Jacob, C.; Neugebauer, J. *Comput. Mol. Sci.* **2014**, *4*, 325–362.

(103)   Stehr, V.; Pfister, J.; Fink, R. F.; Engels, B.; Deibel, C. *Phys. Rev. B* **2011**, *83*, 155208.

(104)   Coropceanu, V.; Cornil, J.; da Silva Filho, D.; Olivier, Y.; Silbey, R.; Brédas, J.-L. *Chem. Rev.* **2007**, *107*, 926–952.

(105)   Tiwari, S.; Greenham, N. *Opt. Quantum Electron.* **2009**, *41*, 69–89.

(106)   Tsung, K.; So, S. *J. Appl. Phys.* **2009**, *106*, 083710.

(107)   Borsenberger, P.; Weiss, D., *Organic Photoreceptors for Imaging Systems*; Dekker: New York, 1993.

(108)   Berleb, S.; Brütting, W. *Phys. Rev. Lett.* **2002**, *89*, 286601.

(109)   Tsang, S.; So, S.; Xu, J. *J. Appl. Phys.* **2006**, *99*, 013706.

(110)   Koopmans, T. *Physica* **1934**, *1*, 104 –113.

(111) Cinchetti, M.; Wüstenberg, J.-P.; Sanchez Albaneda, M.; Steeb, F.; Conca, A.; Jourdan, M.; Aeschlimann, M. *J. Phys. D-Appl. Phys.* **2007**, *40*, 1544–1547.

(112) Fetzer, R.; Wüestenberg, J.-P.; Taira, T.; Uemura, T.; Yamamoto, M.; Aeschlimann, M.; Cinchetti, M. *Phys. Rev. B* **2013**, *87*, 184418.

(113) Cinchetti, M.; Heimer, K.; Wüstenberg, J.-P.; Andreyev, O.; Bauer, M.; Lach, S.; Ziegler, C.; Gao, Y.; Aeschlimann, M. *Nat. Mater.* **2009**, *8*, 115–119.

(114) Andreyev, O.; Koroteev, Y.; Sanchez Albaneda, M.; Cinchetti, M.; Bihlmayer, G.; Chulkov, E. V.; Lange, J.; Steeb, F.; Bauer, M.; Echenique, P. M.; Bluegel, S.; Aeschlimann, M. *Phys. Rev. B* **2006**, *74*, 195416.

(115) Ueba, H.; Gumhalter, B. *Prog. Surf. Sci.* **2007**, *82*, 193–223.

(116) Schmuttenmaer, C.; Aeschlimann, M.; Elsayedali, H.; Miller, R.; Mantell, D.; Cao, J.; Gao, Y. *Phys. Rev. B* **1994**, *50*, 8957–8960.

(117) Woodruff, D.; Winpenny, R.; Layfield, R. *Chem. Rev.* **2013**, *113*, 5110–5148.

(118) Christou, G.; Gatteschi, D.; Hendrickson, D.; Sessoli, R. *MRS Bulletin* **2000**, *25*, 66–71.

(119) Sessoli, R.; Powell, A. *Coord. Chem. Rev.* **2009**, *253*, 2328–2341.

(120) Bogani, L.; Wernsdorfer, W. *Nat. Mater.* **2008**, *7*, 179–186.

(121) Benelli, C.; Gatteschi, D. *Chem. Rev.* **2002**, *102*, 2369–2387.

(122) Sessoli, R.; Gatteschi, D.; Caneschi, A.; Novak, M. *Nature* **1993**, *365*, 141–143.

(123) Sessoli, R.; Tsai, H.; Schake, A.; Wang, S.; Vincent, J.; Folting, K.; Gatteschi, D.; Christou, G.; Hendrickson, D. *J. Am. Chem. Soc* **1993**, *115*, 1804–1816.

(124) Thiele, S.; Balestro, F.; Ballou, R.; Klyatskaya, S.; Ruben, M.; Wernsdorfer, W. *Science* **2014**, *344*, 1135–1138.

(125) Urdampilleta, M.; Klyatskaya, S.; Cleuziou, J.-P.; Ruben, M.; Wernsdorfer, W. *Nat. Mater.* **2011**, *10*, 502–506.

(126) Ishikawa, N.; Sugita, M.; Ishikawa, T.; Koshihara, S.; Kaizu, Y. *J. Am. Chem. Soc.* **2003**, *125*, 8694–8695.

(127) Candini, A.; Klyatskaya, S.; Ruben, M.; Wernsdorfer, W.; Affronte, M. *Nano Lett.* **2011**, *11*, 2634–2639.

(128) Klyatskaya, S.; Ramon Galan-Mascaros, J.; Bogani, L.; Hennrich, F.; Kappes, M.; Wernsdorfer, W.; Ruben, M. *J. Am. Chem. Soc.* **2009**, *131*, 15143–15151.

(129) Stepanow, S.; Honolka, J.; Gambardella, P.; Vitali, L.; Abdurakhmanova, N.; Tseng, T.-C.; Rauschenbach, S.; Tait, S.; Sessi, V.; Klyatskaya, S.; Ruben, M.; Kern, K. *J. Am. Chem. Soc.* **2010**, *132*, 11900–11901.

(130) Vincent, R.; Klyatskaya, S.; Ruben, M.; Wernsdorfer, W.; Balestro, F. *Nature* **2012**, *488*, 357–360.

(131) Bindhu, C.; Harilal, S.; Nampoori, V.; Vallabhan, C. *Mod. Phys. Lett. B* **1999**, *13*, 563–576.

(132) Stürzl, N.; Lebedkin, S.; Kappes, M. *J. Phys. Chem. A* **2009**, *113*, 10238–10240.

(133) Gritzner, G.; Kuta, J. *Pure & App. Chem.* **1984**, *56*, 461–466.

(134) Greenham, N.; Samuel, I.; Hayes, G.; Phillips, R.; Kessener, Y.; Moratti, S.; Holmes, A.; Friend, R. *Chem. Phys. Lett.* **1995**, *241*, 89–96.

(135) Haddon, R.; Rayford, R.; Hirani, A. *J. Org. Chem.* **1981**, *46*, 4587–4588.

(136) Haddon, R. Electron transport material and light emitting diode that contains the electron transport material., US Patent 6428912 B1, 2002.

(137) Svensson, C.; Abrahams, S.; Bernstein, J.; Haddon, R. *J. Am. Chem. Soc.* **1979**, *101*, 5759–5764.

(138) Ozeki, H.; Takahashi, M.; Okuyama, K.; KimuraI, K. *J. Chem. Phys.* **1993**, *99*, 56–66.

(139) Kovacs, A.; Izvekov, V.; Zauer, K.; Ohta, K. *J. Phys. Chem. A* **2001**, *105*, 5000–5009.

(140) Weihrich, R.; Limage, M.; Parker, S.; Fillaux, F. *J. Mol. Struct.* **2004**, *700*, 147–149.

(141) Müller, C.; Schroeder, J.; Troe, J. *J. Phys. Chem. B* **2006**, *110*, 19820–19832.

(142) Kuwahara, D.; Koyano, H.; Manaka, T.; Nakamura, H.; Mochida, T.; Sugawara, T. *J. Phys. Chem. A* **2006**, *110*, 13731–13735.

(143) Kunze, K.; De La Vega, J. *J. Am. Chem. Soc.* **1984**, *106*, 6528–6533.

(144) Fernandez-Ramos, A.; Smedarchina, Z.; Zgierski, M.; Siebrand, W. *J. Chem. Phys.* **1998**, *109*, 1004–1013.

(145) Benderskii, V.; Vetoshkin, E.; Trommsdorff, H. *Chem. Phys.* **1999**, *244*, 299–317.

(146) Mori, H.; Sekiya, H.; Miyoshi, E.; Mogi, K.; Sakai, Y. *J. Chem. Phys.* **2003**, *119*, 4159–4165.

(147) Koelsch, C.; Anthes, J. *J. Org. Chem.* **1941**, *06*, 558–565.

(148) Demura, Y.; Kawato, T.; Kanatomi, H.; Murase, I. *B. Chem. Soc. Jpn.* **1975**, *48*, 2820–2824.

(149) Svensson, C.; Abrahams, S. *Acta Crystallogr. Sect. B-Struct. Commun.* **1986**, *42*, 280–286.

(150) Friebolin, H., *Basic one- and two-dimensional NMR spectroscopy*; Wiley-VCH: Weinheim, 2011.

(151) Nishi, K.; Sekiya, H.; Hamabe, H.; Nishimura, Y.; Mochida, T.; Sugawara, T. *Chem. Phys. Lett.* **1996**, *257*, 499–506.

(152) Mochida, T.; Suzuki, S.; Takasu, I.; Sugawara, T. *J. Phys. Chem. Solids* **2003**, *64*, 1257–1260.

(153) Chen, J.; Yuan, T.; Hao, W.; Cai, M. *Tetrahedron Lett.* **2011**, *52*, 3710–3713.

(154) Repine, J.; Johnson, D.; White, A.; Favor, D.; Stier, M.; Yip, J.; Rankin, T.; Ding, Q.; Maiti, S. *Tetrahedron Lett.* **2007**, *48*, 5539–5541.

(155) Zerbe, O.; Jurt, S., *Applied NMR spectroscopy for chemists and life scientists*; Wiley-VCH: Weinheim, 2014.

(156) Haddon, R. *Aus. J. Chem.* **1982**, *35*, 1733–1738.

(157) Basaric, N.; Wan, P. *Photochem. Photobiol. Sci.* **2006**, *5*, 656–664.

(158) Pu, Y.; Miyamoto, M.; Nakayama, K.; Oyama, T.; Masaaki, Y.; Kido, J. *Organic Electronics* **2009**, *10*, 228–232.

(159) Liu, S.; Seward, C.; Aziz, H.; Hu, N.; Popovic, Z.; Wang, S. *Organometallics* **2000**, *19*, 5709–5714.

(160) Kwong, R.; Tung, Y.; Ma, B.; Knowles, D. Materials and Structures for Enhancing the Performance of Organic Light Emitting Devices., US Patent 2005/0019605 A1, 2005.

(161) Ganis, P.; Saporito, A.; Vitagliano, A.; Valle, G. *Inorg. Chim. Acta* **1988**, *142*, 75–79.

(162) Bardwell, D.; Black, D.; Jeffery, J.; Shatz, E.; Ward, M. *J. Chem. Soc.-Dalton Trans.* **1993**, 2321–2327.

(163) Bardwell, D.; Jeffery, J.; Ward, M. *Inorg. Chim. Acta* **1995**, *236*, 125–130.

(164) Shimanouchi, H.; Sasada, Y. *Acta Crystallogr. Sect. B-Struct. Commun.* **1973**, *B 29*, 81–90.

(165) Muetterties, E.; Guggenberger, L. *J. Am. Chem. Soc.* **1972**, *94*, 8046–8055.

(166) Montes, V.; Zyryanov, G.; Danilov, E.; Agarwal, N.; Palacios, M.; Anzenbacher, J. *J. Am. Chem. Soc.* **2009**, *131*, 1787–1795.

(167) Xu, B.; Chen, L.; Liu, X.; Zhou, H.; Xu, H.; Fang, X.; Wang, Y. *App. Phys. Lett.* **2008**, *92*, 103305.

(168) Petrova, P.; Tomova, R.; Stoycheva-Topalova, R.; Kaloyanova, S. S.; Deligeorgiev, T. G. *J. Lumin.* **2012**, *132*, 495–501.

(169) Hurley, T.; Robinson, M.; Scruggs, J.; Trotz, S. *Inorg. Chem.* **1967**, *6*, 1310–1315.

(170) Lim, J.; Jeong, C.; Lee, J.; Yeom, G.; Jeong, H.; Chai, S.; Lee, I.; Lee, W. *J. Organomet. Chem.* **2006**, *691*, 2701–2707.

(171) Nayak, P.; Agarwal, N.; Ali, F.; Patankar, M.; Narasimhan, K.; Periasamy, N. *J. Chem. Sci.* **2010**, *122*, 847–855.

(172) Yamaguchi, I.; Iijima, T.; Yamamoto, T. *J. Organomet. Chem.* **2002**, *654*, 229–232.

(173) Hon, P.; Pfluger, C. *J. of Coord. Chem.* **1973**, *3*, 67–76.

(174) Birks, J., *Organic molecular photophysics*; Wiley: London, 1973; Vol. 1.

(175) Burrows, P.; Shen, Z.; Bulovic, V.; McCarty, D.; Forrest, S.; Cronin, J.; Thompson, M. *J. Appl. Phys.* **1996**, *79*, 7991–8006.

(176) Humbs, W.; van Veldhoven, E.; Zhang, H.; Glasbeek, M. *Chem. Phys. Lett.* **1999**, *304*, 10–18.

(177) Monzon, L.; Burke, F.; Coey, J. *J. OF Phys. Chem. C* **2011**, *115*, 9182–9192.

(178) Bykowski, D.; McDonald, R.; Hinkle, R.; Tykwinski, R. *J. Org. Chem.* **2002**, *67*, 2798–2804.

(179) Renger, T.; Grundkoetter, B.; Madjet, M.-A.; Mueh, F. *P. Natl. Acad. Sci. USA* **2008**, *105*, 13235–13240.

(180) N.J., T., *Modern Molecular Photochemistry*; University Science Book: California, 1991.

(181) Birks, J.; Christopohrou, L. *Spectrochim. Acta* **1963**, *19*, 401–410.

(182) Birks, J., *Photophysics of Aromatic Molecules*; Wiley-Interscience: New York, 1970.

(183) Solovyov, K.; Borisevich, E. *Phys.-Usp.* **2005**, *48*, 231–253.

(184) Bard, A.; Faulkner, L., *Electrochemical methods : fundamentals and applications*, 2. ed.; Wiley: New York, 2001.

(185) Jiao, J.; Long, G.; Rebbouh, L.; Grandjean, F.; Beatty, A.; Fehlner, T. *J. Am. Chem. Soc.* **2005**, *127*, 17819–17831.

(186) Matsuo, Y.; Tahara, K.; Nakamura, E. *J. Am. Chem. Soc.* **2006**, *128*, 7154–7155.

(187) Santi, S.; Orian, L.; Donoli, A.; Bisello, A.; Scapinello, M.; Benetollo, F.; Ganis, P.; Ceccon, A. *Angew. Chem.-Int. Edit.* **2008**, *47*, 5331–5334.

(188) Mubarak, M.; Nguyen, D.; Peters, D. *J. Org. Chem.* **1990**, *55*, 2648–2652.

185

(189) Alberti, A.; Macciantelli, D.; Naggi, A.; Urso, E.; Torri, G.; Vismara, E. *Chem.-Eur. J.* **2009**, *15*, 8005–8014.

(190) Kulkarni, A.; Tonzola, C.; Babel, A.; Jenekhe, S. *Chem. Mat.* **2004**, *16*, 4556–4573.

(191) Pommerehne, J.; Vestweber, H.; Guss, W.; Mahrt, R.; Bässler, H.; Porsch, M.; Daub, J. *Adv. Mater.* **1995**, *7*, 551–554.

(192) Curioni, A.; Boero, M.; Andreoni, W. *Chem. Phys. Lett.* **1998**, *294*, 263–271.

(193) Curioni, A.; Andreoni, W.; Treusch, R.; Himpsel, F.; Haskal, E.; Seidler, P.; Heske, C.; Kakar, S.; van Buuren, T.; Terminello, L. *Appl. Phys. Lett.* **1998**, *72*, 1575–1577.

(194) Curioni, A.; Andreoni, W. *J. Am. Chem. Soc.* **1999**, *121*, 8216–8220.

(195) Sugiyama, K.; Yoshimura, D.; Miyamae, T.; Miyazaki, T.; Ishii, H.; Ouchi, Y.; Seki, K. *J. Appl. Phys.* **1998**, *83*, 4928–4938.

(196) Zhang, R.; Lee, C.; Lee, S. *J. Chem. Phys.* **2000**, *112*, 8614–8620.

(197) Zhang, R.; Lee, C.; Lee, S. *Chem. Phys. Lett.* **2000**, *326*, 413–420.

(198) Hill, I.; Kahn, A.; Cornil, J.; dos Santos, D.; Brédas, J. *Chem. Phys. Lett.* **2000**, *317*, 444–450.

(199) Halls, M.; Schlegel, H. *Chem. Mat.* **2001**, *13*, 2632–2640.

(200) Schmidt, A.; Anderson, M.; Armstrong, N. *J. Appl. Phys.* **1995**, *78*, 5619–5625.

(201) Hopkins, T.; Meerholz, K.; Shaheen, S.; Anderson, M.; Schmidt, A.; Kippelen, B.; Padias, A.; Hall, H.; Peyghambarian, N.; Armstrong, N. *Chem. Mat.* **1996**, *8*, 344–351.

(202) Rajagopal, A.; Wu, C.; Kahn, A. *J. Appl. Phys.* **1998**, *83*, 2649–2655.

(203) Müller, S.; Steil, S.; Droghetti, A.; Grossmann, N.; Meded, V.; Magri, A.; Schäfer, B.; Fuhr, O.; Sanvito, S.; Ruben, M.; Cinchetti, M.; Aeschlimann, M. *New J. Phys.* **2013**, *15*, 113054.

(204) Pron, A.; Gawrys, P.; Zagorska, M.; Djurado, D.; Demadrille, R. *Chem. Soc. Rev.* **2010**, *39*, 2577–2632.

(205) Cornil, J.; Beljonne, D.; Calbert, J.; Brédas, J. *Adv. Mater.* **2001**, *13*, 1053–1067.

(206) Yokoyama, D. *J. Mater. Chem.* **2011**, *21*, 19187–19202.

(207) Li, Z.; Scheraga, H. *Proc. Natl. Acad. Sci. U. S. A.* **1987**, *84*, 6611–6615.

(208) Wales, D.; Doye, J. *J. Phys. Chem. A* **1997**, *101*, 5111–5116.

(209) Wales, D.; Scheraga, H. *Science* **1999**, *285*, 1368–1372.

(210) Kirkpatrick, S.; Gelatt, C.; Vecchi, M. *Science* **1983**, *220*, 671–680.

(211) Novikov, S.; Dunlap, D.; Kenkre, V.; Parris, P.; Vannikov, A. *Phys. Rev. Lett.* **1998**, *81*, 4472–4475.

(212) Pasveer, W.; Cottaar, J.; Tanase, C.; Coehoorn, R.; Bobbert, P.; Blom, P.; de Leeuw, D.; Michels, M. *Phys. Rev. Lett.* **2005**, *94*, 206601.

(213) VanSlyke, S.; Chen, C.; Tang, C. *Appl, Phys. Lett.* **1996**, *69*, 2160–2162.

(214) Saragi, T.; Fuhrmann-Lieker, T.; Salbeck, J. *Adv. Funct. Mater.* **2006**, *16*, 966–974.

(215) Hung, W.; Ke, T.; Lin, Y.; Wu, C.; Hung, T.; Chao, T.; Wong, K.; Wu, C. *Appl. Phys. Lett.* **2006**, *88*, 064102.

(216) Sanvito, S. *Nat. Phys.* **2010**, *6*, 562–564.

(217) Dediu, V. *Nat. Phys.* **2013**, *9*, 210–211.

(218) Steil, S.; Großmann, N.; Laux, M.; Ruffing, A.; Steil, D.; Wiesenmayer, M.; Mathias, S.; Monti, O.; Cinchetti, M.; Aeschlimann, M. *Nat. Phys.* **2013**, *9*, 242–247.

(219) Naber, W.; Faez, S.; van der Wiel, W. *J. Phys. D-Appl. Phys.* **2007**, *40*, R205–R228.

(220) Cinchetti, M.; Sanchez Albaneda, M.; Hoffmann, D.; Roth, T.; Wüstenberg, J.-P.; Krauss, M.; Andreyev, O.; Schneider, H. C.; Bauer, M.; Aeschlimann, M. *Phys. Rev. Lett.* **2006**, *97*, 177201.

(221) Toyoda, K.; Nakano, Y.; Hamada, I.; Lee, K.; Yanagisawa, S.; Morikawa, Y. *J. Electron Spectrosc. Relat. Phenom.* **2009**, *174*, 78–84.

(222) Shen, C.; Kahn, A. *Org. Electron.* **2001**, *2*, 89–95.

(223) Hill, I.; Mäkinen, A.; Kafafi, Z. *J. Appl. Phys.* **2000**, *88*, 889–895.

(224) Li, X.; Zhang, Z.; Henrich, V. *J. Electron Spectrosc. Relat. Phenom.* **1993**, *63*, 253–265.

(225) Valiev, M.; Bylaska, E.; Govind, N.; Kowalski, K.; Straatsma, T.; Van Dam, H.; Wang, D.; Nieplocha, J.; Apra, E.; Windus, T.; de Jong, W. *Comput. Phys. Commun.* **2010**, *181*, 1477–1489.

(226) Martin, R.; Kress, J.; Campbell, I.; Smith, D. *Phys. Rev. B* **2000**, *61*, 15804–15811.

(227) Bisti, F.; Stroppa, A.; Donarelli, M.; Picozzi, S.; Ottaviano, L. *Phys. Rev. B* **2011**, *84*, 195112.

(228) Droghetti, A.; Steil, S.; Großmann, N.; Haag, N.; Zhang, H.; Willis, M.; Gillin, W.; Drew, A.; Aeschlimann, M.; Sanvito, S.; Cinchetti, M. *Phys. Rev. B* **2014**, *89*, 94412.

(229) Dori, N.; Menon, M.; Kilian, L.; Sokolowski, M.; Kronik, L.; Umbach, E. *Phys. Rev. B* **2006**, *73*, 195208.

(230) Jones, R.; Gunnarsson, O. *Rev. Mod. Phys.* **1989**, *61*, 689–746.

(231) Steil, S.; Goedel, K.; Ruffing, A.; Sarkar, I.; Cinchetti, M.; Aeschlimann, M. *Synth. Met.* **2011**, *161*, 570–574.

(232) Zhu, X. *Surf. Sci. Rep.* **2004**, *56*, 1–83.

(233) Van Deun, R.; Nockemann, P.; Fias, P.; Van Hecke, K.; Van Meervelt, L.; Binnemans, K. *Chem. Commun.* **2005**, 590–592.

(234) Van Deun, R.; Fias, P.; Nockemann, P.; Van Hecke, K.; Van Meervelt, L.; Binnemans, K. *Inorg. Chem.* **2006**, *45*, 10416–10418.

(235) Greisch, J.-F.; Harding, M.; Schäfer, B.; Rotter, M.; Ruben, M.; Klopper, W.; Kappes, M.; Schooss, D. *J. Phys. Chem. A* **2014**, *118*, 94–102.

(236) Greisch, J.-F.; Harding, M.; Schäfer, B.; Ruben, M.; Kopper, W.; Kappes, M.; Schooss, D. *J. Phys. Chem. Lett.* **2014**, *5*, 1727–1731.

(237) Katkova, M.; Kurskii, Y.; Fukin, G.; Averyushkin, A.; Artamonov, A.; Vitukhnbovsky, A.; Bochkarev, M. *Inorg. Chim. Acta* **2005**, *358*, 3625–3632.

(238) Katkova, M.; Ilichev, V.; Konev, A.; Bochkarev, M.; Vitukhnovsky, A.; Parshin, M.; Pandey, L.; Van der Auweraer, M. *J. Appl. Phys.* **2008**, *104*, 053706.

(239) Katkova, M.; Ilichev, V.; Konev, A.; Bochkarev, M. *Russ. Chem. Bull.* **2008**, *57*, 2281–2284.

(240) Gao, Y.; Xu, G.-F.; Zhao, L.; Tang, J.; Liu, Z. *Inorg. Chem.* **2009**, *48*, 11495–11497.

(241) Prasad, T.; Ralasekharan, M. *Inor. Chem.* **2009**, *48*, 11543–11550.

(242) Feng, X.; Zhao, J.; Liu, B.; Wang, L.; Ng, S.; Zhang, G.; Wang, J.; Shi, X.; Liu, Y. *Cryst. Growth Des.* **2010**, *10*, 1399–1408.

(243) Rinck, J.; Novitchi, G.; Van den Heuvel, W.; Ungur, L.; Lan, Y.; Wernsdorfer, W.; Anson, C.; Chibotaru, L.; Powell, A. *Angew. Chem.-Int. Edit.* **2010**, *49*, 7583–7587.

(244) Ke, H.; Xu, G.-F.; Guo, Y.-N.; Gamez, P.; Beavers, C.; Teat, S.; Tang, J. *Chem. Commun.* **2010**, *46*, 6057–6059.

(245) Wang, Z.-L.; Fang, W.-H.; Yang, G.-Y. *Chem. Commun.* **2010**, *46*, 8216–8218.

(246) Liang, L.; Peng, G.; Li, G.; Lan, Y.; Powell, A.; Deng, H. *Dalton Trans.* **2012**, *41*, 5816–5823.

(247) Kahn, M.; Sutter, J.; Golhen, S.; Guionneau, P.; Ouahab, L.; Kahn, O.; Chasseau, D. *J. Am. Chem. Soc.* **2000**, *122*, 3413–3421.

(248) Kahn, M.; Ballou, R.; Porcher, P.; Kahn, O.; Sutter, J. *Chem.-Eur. J.* **2002**, *8*, 525–531.

(249) Lin, P.-H.; Burchell, T.; Clerac, R.; Murugesu, M. *Angew. Chem.-Int. Edit.* **2008**, *47*, 8848–8851.

(250) Xu, G.-F.; Wang, Q.-L.; Gamez, P.; Ma, Y.; Clerac, R.; Tang, J.; Yan, S.-P.; Cheng, P.; Liao, D.-Z. *Chem. Commun.* **2010**, *46*, 1506–1508.

(251) Rinehart, J.; Fang, M.; Evans, W.; Long, J. *Nat. Chem.* **2011**, *3*, 538–542.

(252) Long, J.; Habib, F.; Lin, P.-H.; Korobkov, I.; Enright, G.; Ungur, L.; Wernsdorfer, W.; Chibotaru, L.; Murugesu, M. *J. Am. Chem. Soc.* **2011**, *133*, 5319–5328.

(253) Guo, Y.-N.; Xu, G.-F.; Wernsdorfer, W.; Ungur, L.; Guo, Y.; Tang, J.; Zhang, H.-J.; Chibotaru, L.; Powell, A. *J. Am. Chem. Soc.* **2011**, *133*, 11948–11951.

(254) Osa, S.; Kido, T.; Matsumoto, N.; Re, N.; Pochaba, A.; Mrozinski, J. *J. Am. Chem. Soc.* **2004**, *126*, 420–421.

(255) Tang, J.; Hewitt, I.; Madhu, N.; Chastanet, G.; Wernsdorfer, W.; Anson, C.; Benelli, C.; Sessoli, R.; Powell, A. *Angew. Chem.-Int. Edit.* **2006**, *45*, 1729–1733.

(256) Car, P.-E.; Perfetti, M.; Mannini, M.; Favre, A.; Caneschi, A.; Sessoli, R. *Chem. Commun.* **2011**, *47*, 3751–3753.

(257) Watanabe, A.; Yamashita, A.; Nakano, M.; Yamamura, T.; Kajiwara, T. *Chem.-Eur. J.* **2011**, *17*, 7428–7432.

List of Figures

191

197

List of Tables

List of Schemes

A. Abbreviation of the Chemical Names

Short name	Long name

Ligands

Acac	4-Hydroxypent-3-en-2-one
HOba	6-Hydroxy-7H-benzo[de]anthracen-7-one
HOp	9-Hydroxy-1H-phenalen-1-one
HOp−Br	5-Bromo-9-hydroxy-1H-phenalen-1-one
HOp−Cl	5-Chloro-9-hydroxy-1H-phenalen-1-one
HOp−F	5-Fluoro-9-hydroxy-1H-phenalen-1-one
HOp−I	9-Hydroxy-5-iodo-1H-phenalen-1-one
HOp−n	9-Hydroxy-5-(naphthalen-1-yl)-1H-phenalen-1-one
HOp−p	9-Hydroxy-5-phenyl-1H-phenalen-1-one
HOp−pe	9-Hydroxy-5-(phenylethynyl)-1H-phenalen-1-one
HOp−py	2-(Pyridin-2-yl)phenol
Hq	Quinolin-8-ol
Tropolone	2-Hydroxycyclohepta-2,4,6-trienone

Complexes

$Al(Acac)_3$	Tris-(4-oxopent-2-en-2-olate)aluminum
$Al(Oba)_3$	Tris-(7-oxo-7H-benzo(de)anthracen-6-olate)aluminum
$Al(Op)_3$	Tris-(1-oxo-1H-phenalen-9-olate)aluminum
$Al(Op-Br)_3$	Tris-(5-bromo-1-oxo-1H-phenalen-9-olate)aluminum
$Al(Op-Cl)_3$	Tris-(5-chloro-1-oxo-1H-phenalen-9-olate)aluminum
$Al(Op-F)_3$	Tris-(5-fluoro-1-oxo-1H-phenalen-9-olate)aluminum
$Al(Op-I)_3$	Tris-(5-iodo-1-oxo-1H-phenalen-9-olate)aluminum
$Al(Op-n)_3$	Tris-(5-(naphthalen-1-yl)-1-oxo-1H-phenalen-9-olate)aluminum
$Al(Op-p)_3$	Tris-(1-oxo-5-phenyl-1H-phenalen-9-olate)aluminum
$Al(Op-pe)_3$	Tris-(1-oxo-5-(phenylethynyl)-1H-phenalen-9-olate)aluminum
$Al(Op-py)_3$	Tris-(2-(pyridin-2-yl)phenolate)aluminum
$Al(q_2Acac)$	Bis-(quinolin-8-olate)(4-oxopent-2-en-2-olate)aluminum
$Al(q_2Op)$	Bis-(quinolin-8-olate)(1-oxo-1H-phenalen-9-olate)aluminum
$Al(q_2Trop)$	Bis-(quinolin-8-olate)(7-oxocyclohepta-1,3,5-trienolate)aluminum
$Al(Trop)_3$	Tris-(7-oxocyclohepta-1,3,5-trienolate)aluminum
$Dy(Op)_2Cl$	Bis-(1-oxo-1H-phenalen-9-olate)dysprosium chloride
$Dy(Op)_3$	Tris-(1-oxo-1H-phenalen-9-olate)dysprosium
$Zn(Op)_2$	Bis-(1-oxo-1H-phenalen-9-olate)zinc

Solvents & Catalysts

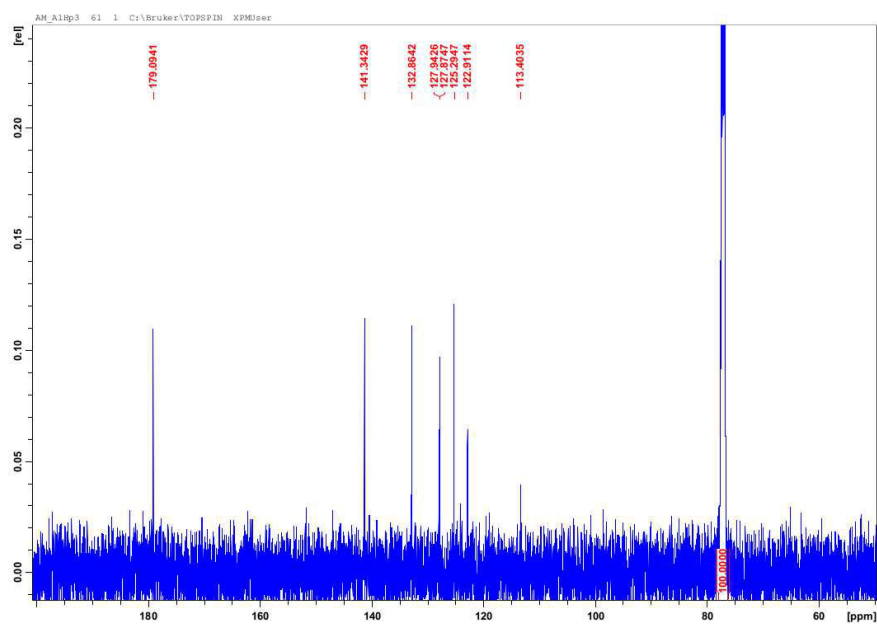|	
DCB	1,2-Dichlorobenzene
DCE	1,2-Dichloroethane
DCM	Methylenchloride
DME	1,2-Dimethoxyethane
DMF	Dimethylformamide
DMSO	Dimethylsulfoxide
Et_3N	Triethylamine
$Pd(PPh_3)_2Cl_2$	Bis-(triphenylphosphine)palladium dichloride
$Pd(PPh_3)_4$	Tetrakis-(triphenylphosphine)palladium
THF	Tetrahydrofurane

B. NMR and MS Spectra
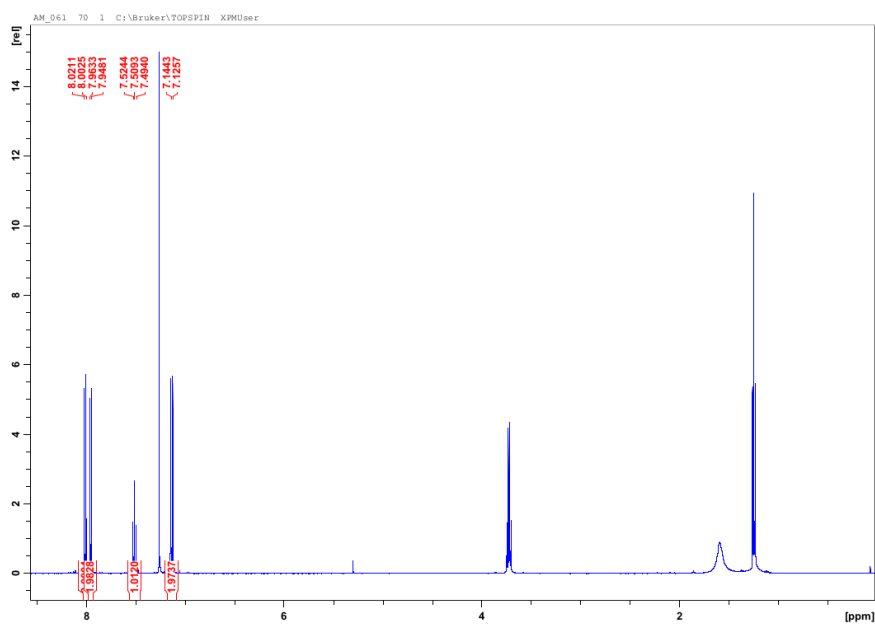
Figure B.1: ^{1}H-NMR of Al(Op)$_3$ **4**.

Figure B.2: ^{13}C-NMR of Al(Op)$_3$ **4**.
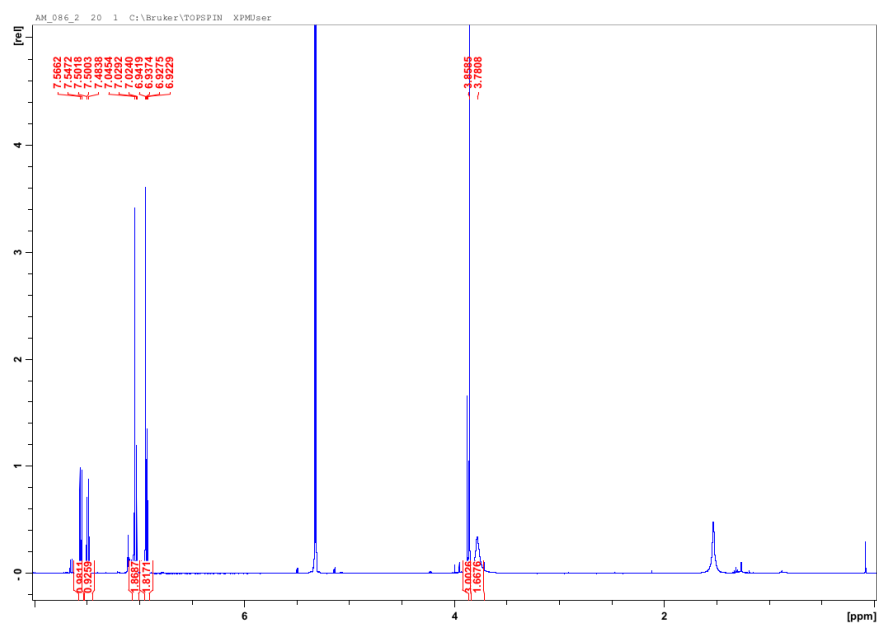

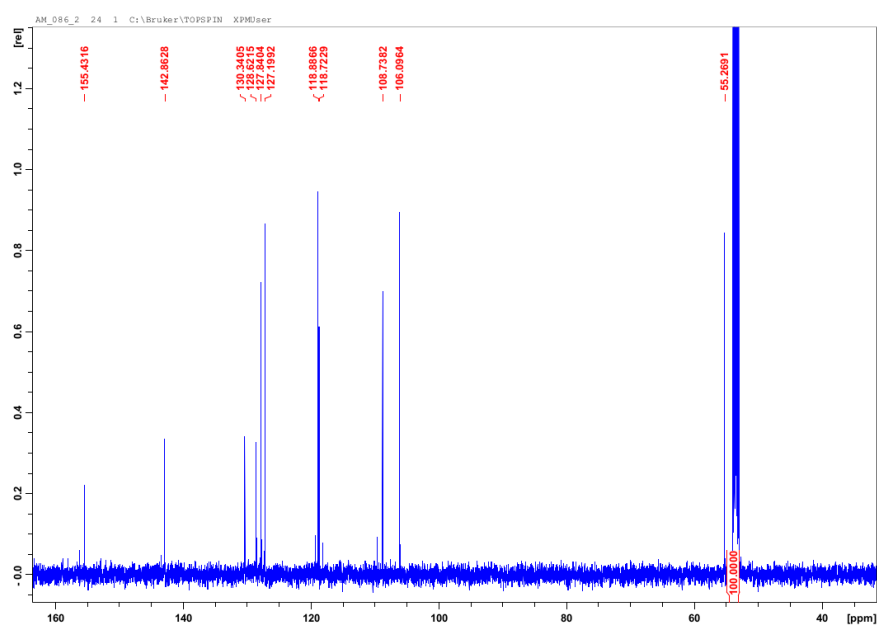Figure B.3: MALDI-TOF of Al(Op)$_3$ **4**.

Figure B.4: ^{1}H-NMR of **8**.

Figure B.5: ^{13}C-NMR of **8**.
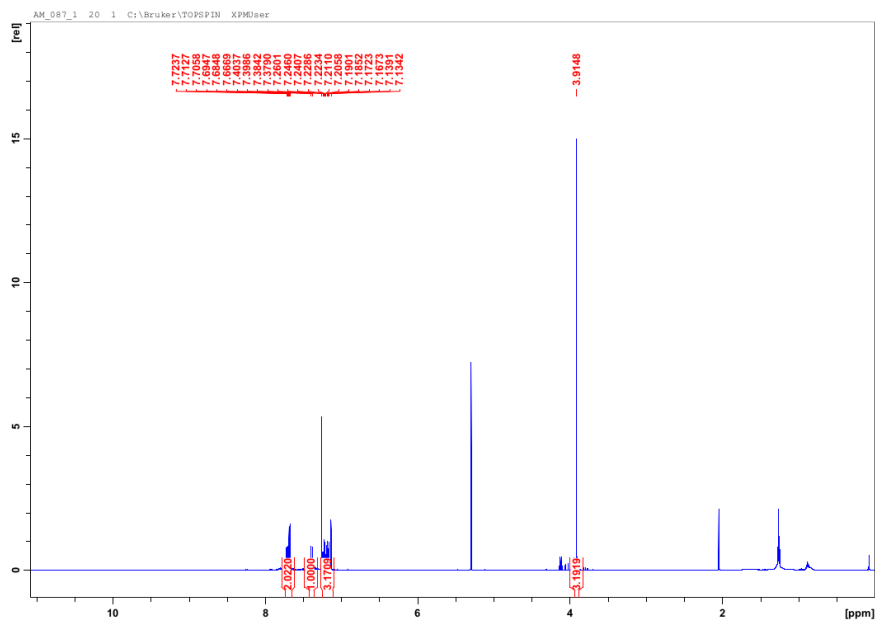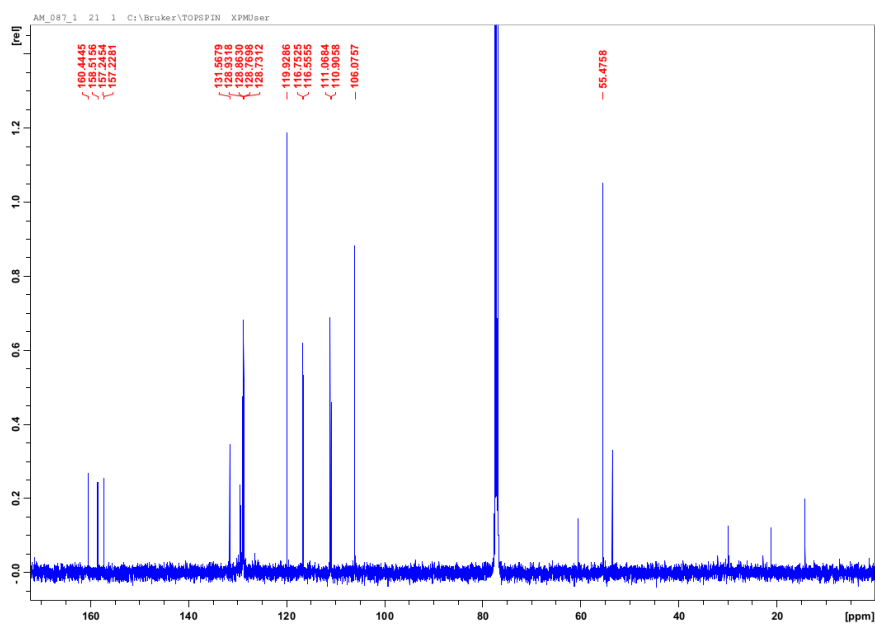
Figure B.6: ^{1}H-NMR of **9**.

Figure B.7: ^{13}C-NMR of **9**.
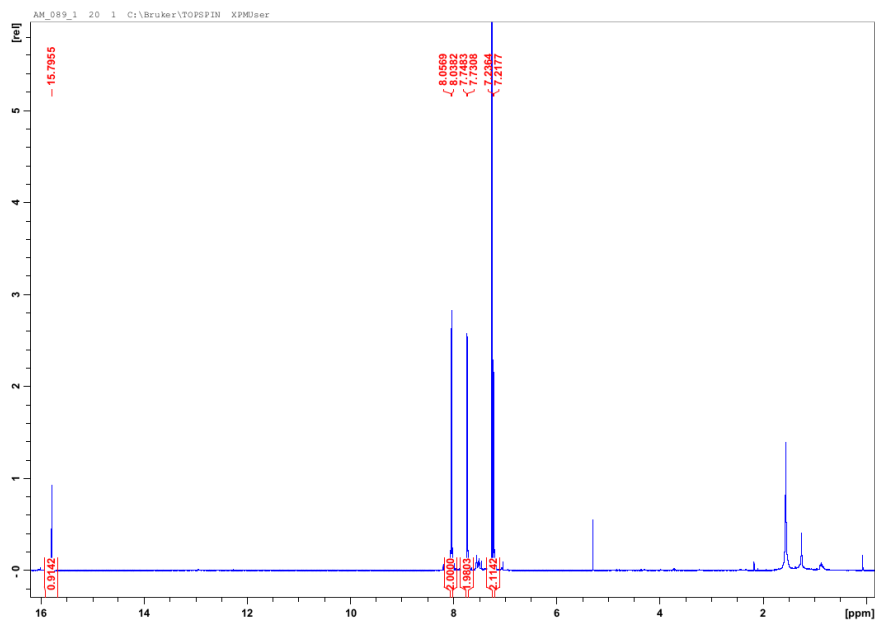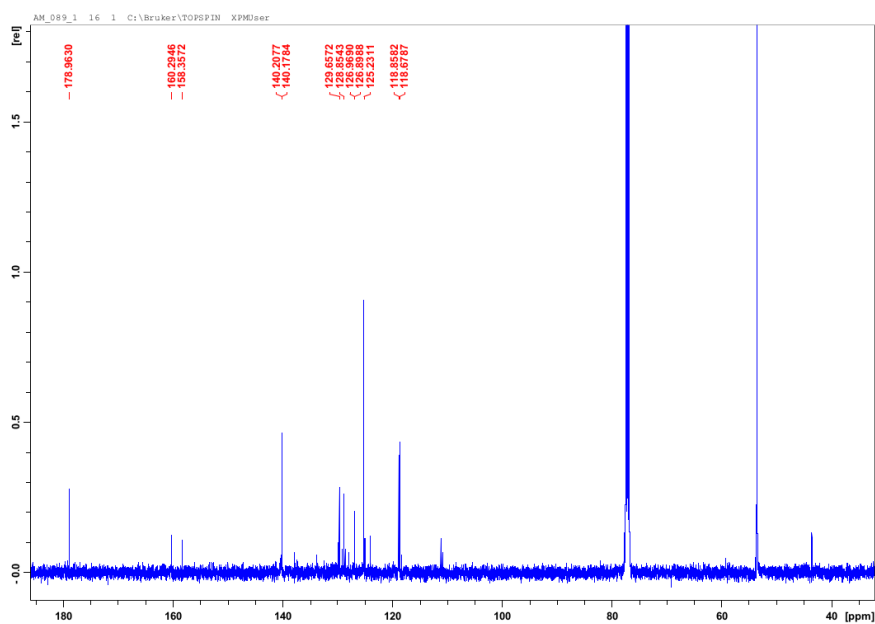
Figure B.8: ^{1}H-NMR of HOp$-$F **5a**.

Figure B.9: ^{13}C-NMR of HOp$-$F **5a**.
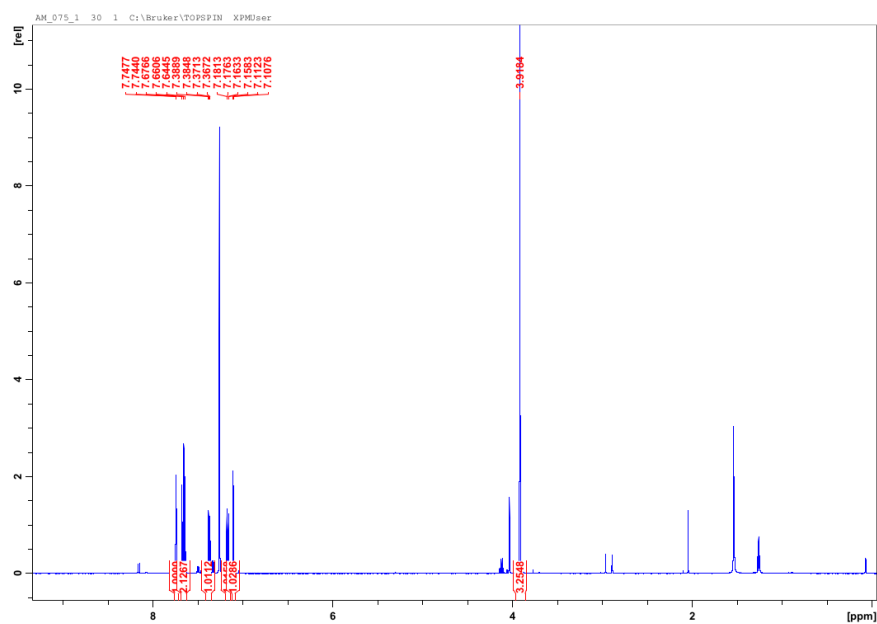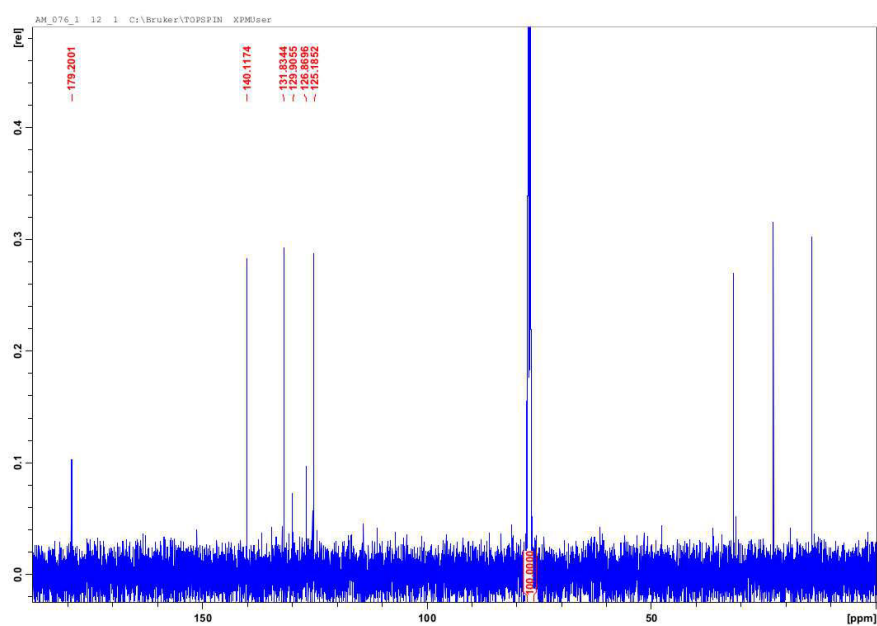
217
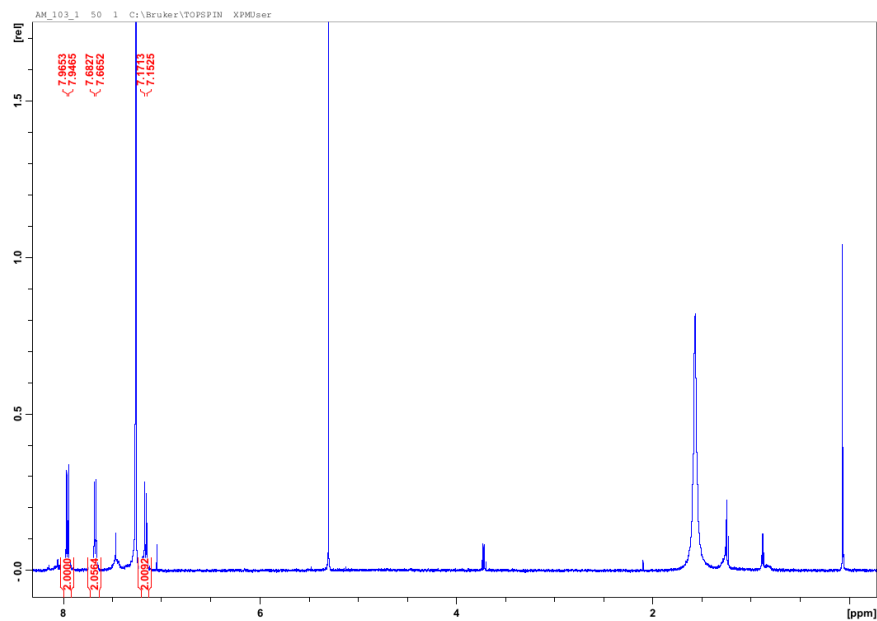
Figure B.10: ^{1}H-NMR of Al(Op−F)$_3$ **6a**.
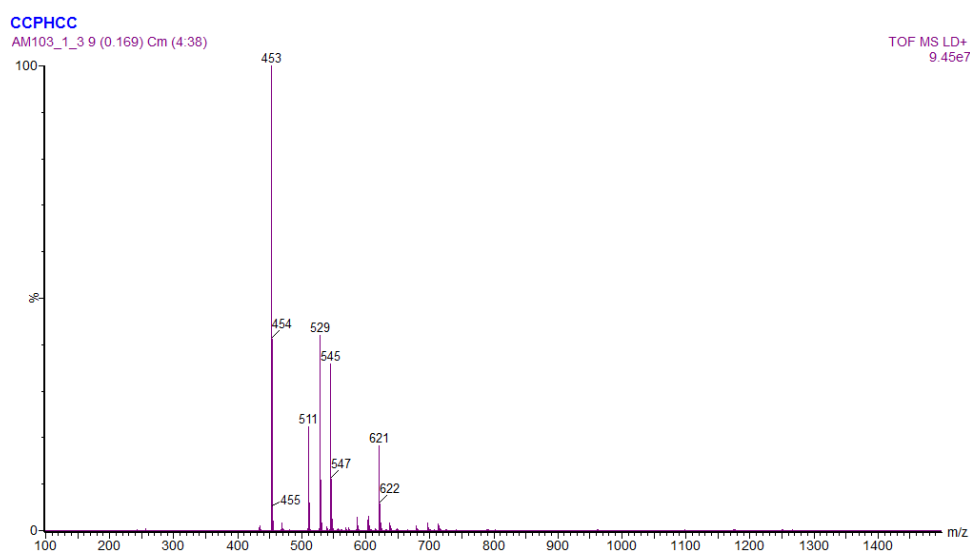
Figure B.11: MALDI-TOF of Al(Op−F)$_3$ **6a**.

Figure B.12: ^{1}H-NMR of **10**.
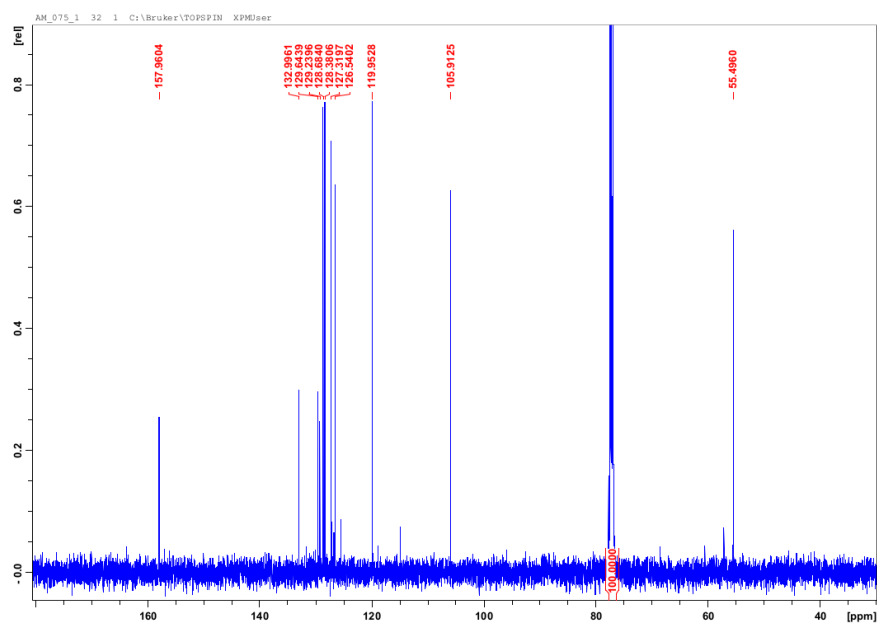
Figure B.13: ^{13}C-NMR of **10**.

219
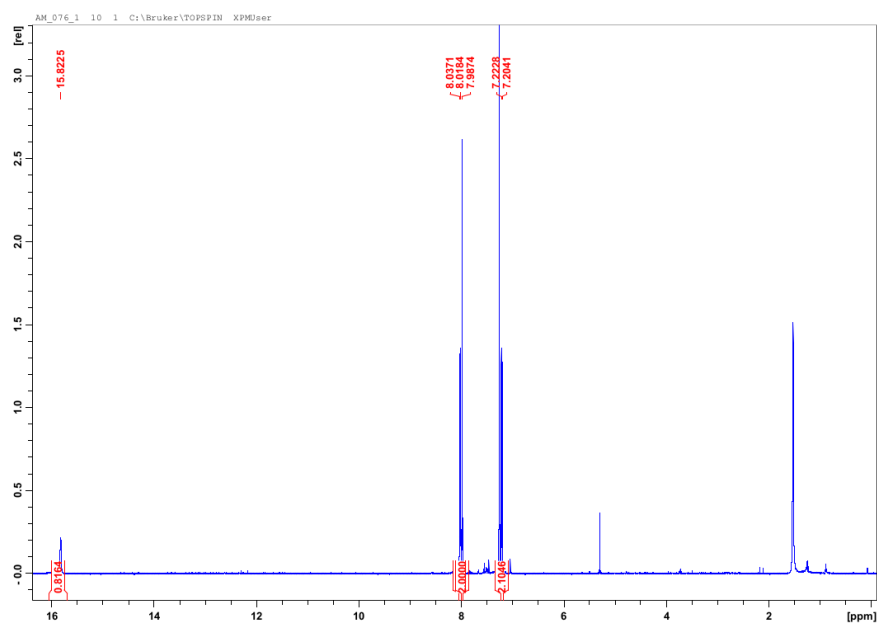
Figure B.14: ^{1}H-NMR of HOp−Cl **5b**.

Figure B.15: ^{13}C-NMR of HOp−Cl **5b**.
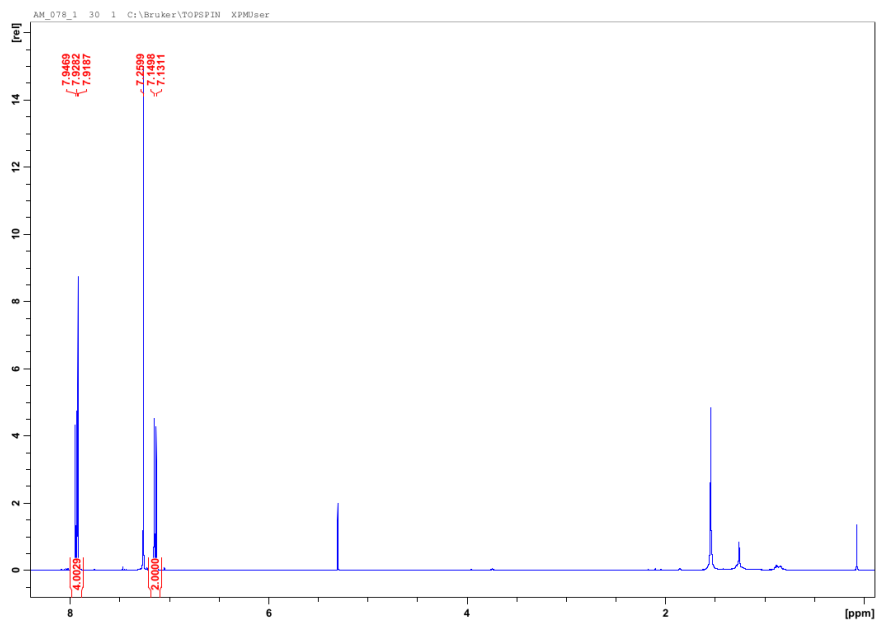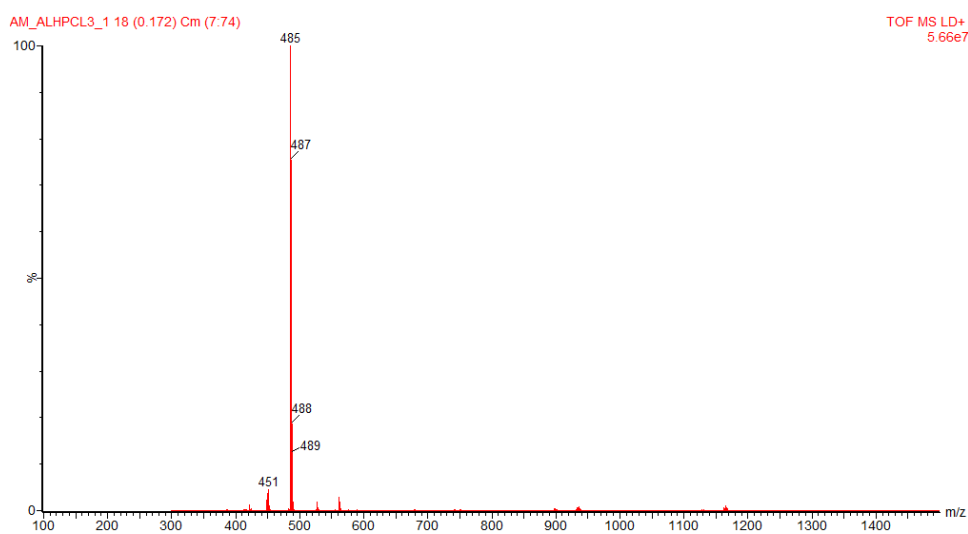
Figure B.16: ^{1}H-NMR of Al(Op−Cl)$_3$ **6b**.

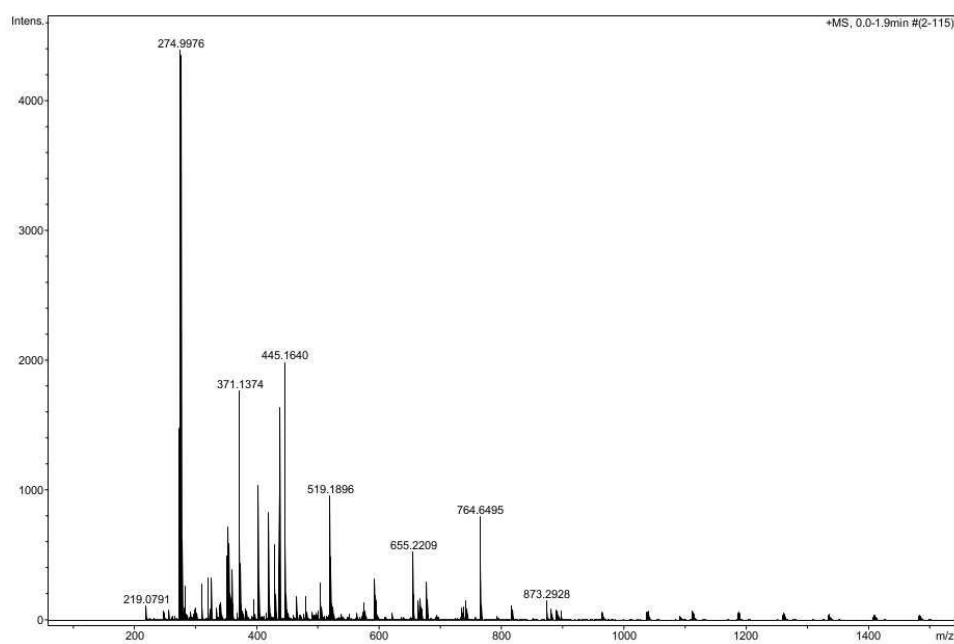Figure B.17: MALDI-TOF of Al(Op−Cl)$_3$ **6b**.
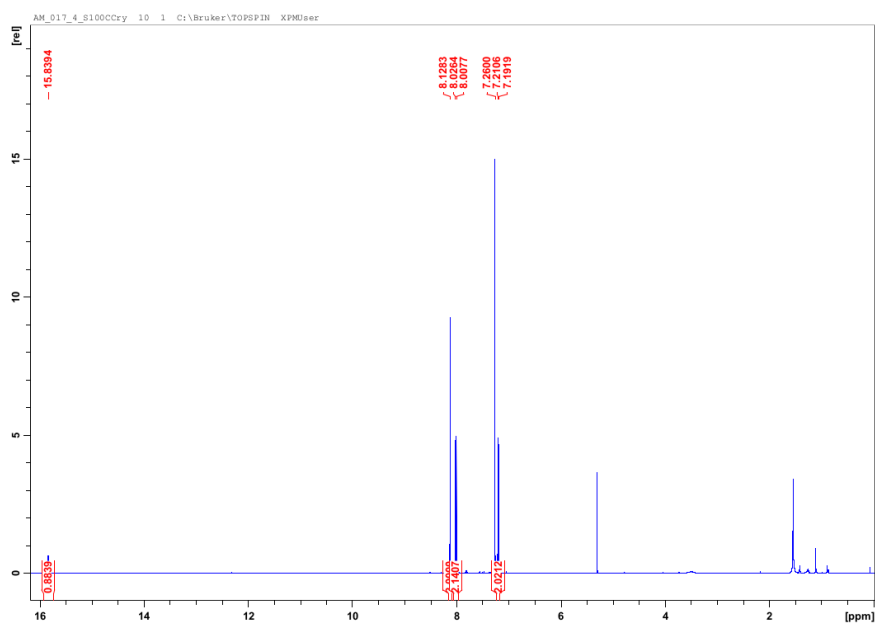
221

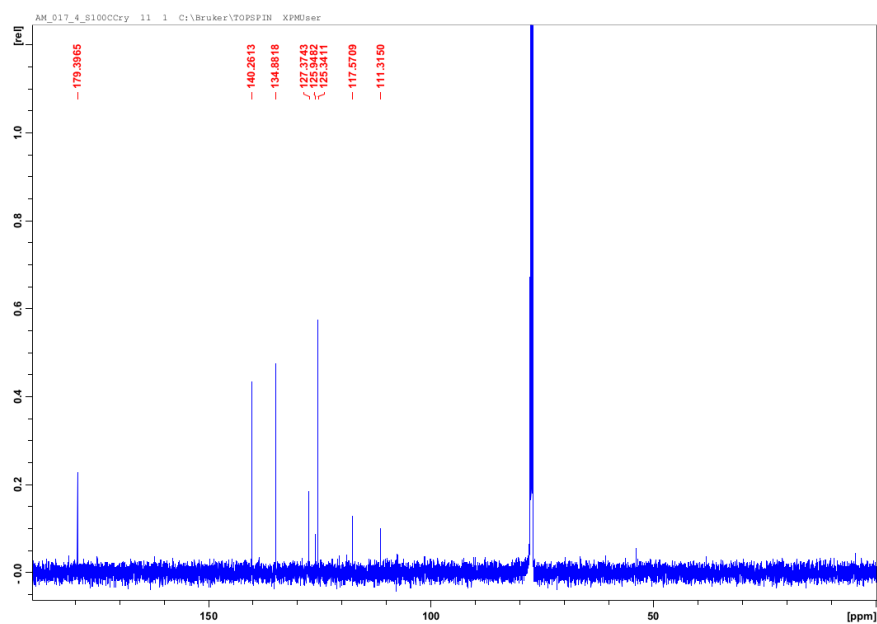Figure B.18: ESI-TOF of crude **5c**.

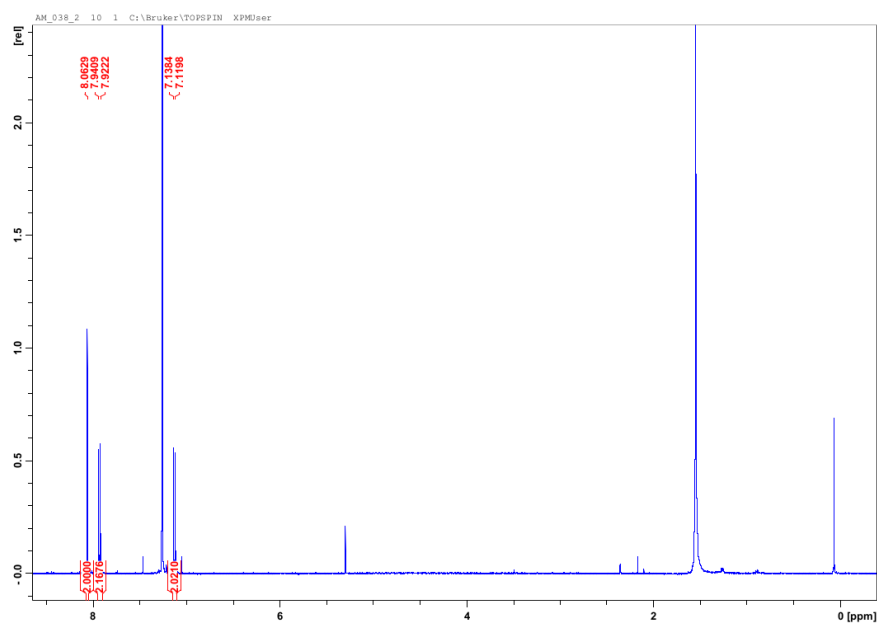Figure B.19: ^{1}H-NMR of HOp−Br **5c**.

Figure B.20: ^{13}C-NMR of HOp−Br **5c**.
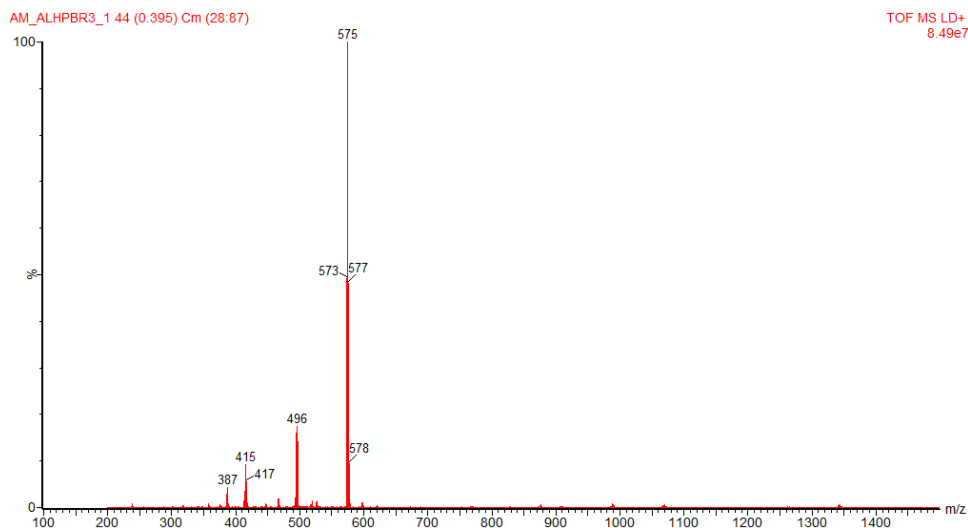

Figure B.21: ^{1}H-NMR of Al(Op−Br)$_3$ **6c**.
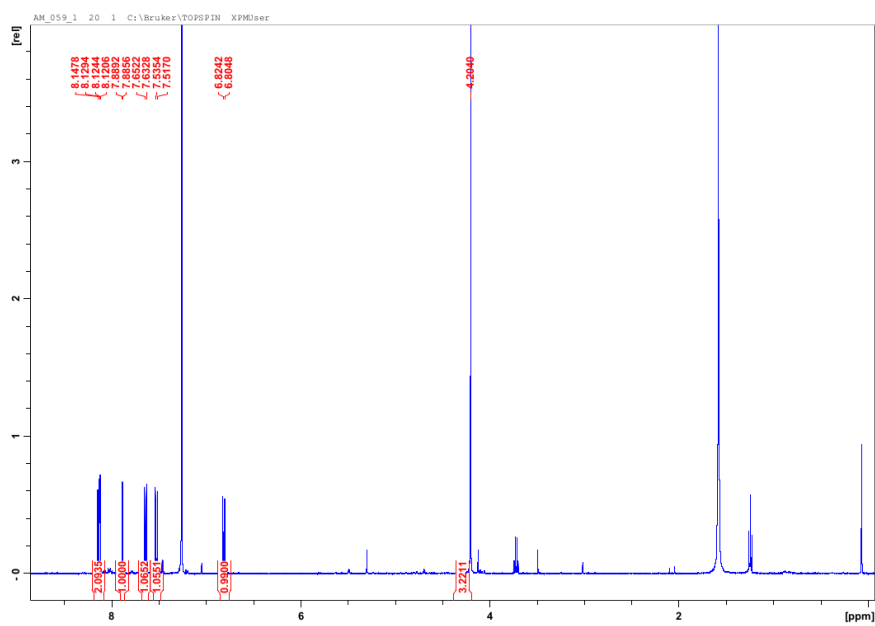
Figure B.22: MALDI-TOF of $Al(Op-Br)_3$ **6c**.

Figure B.23: ^{1}H-NMR of **11**.
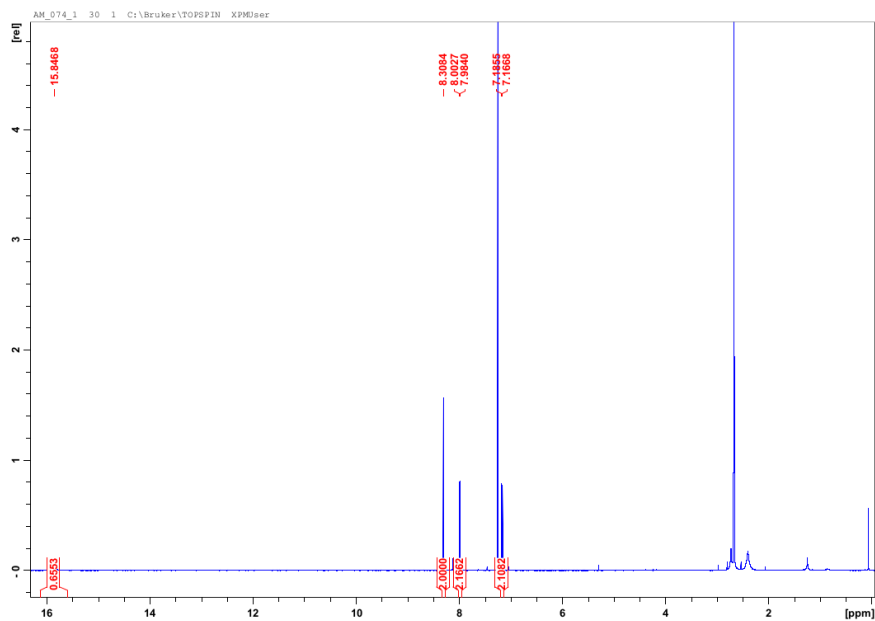
Figure B.24: ^{1}H-NMR of HOp−I **5d**.
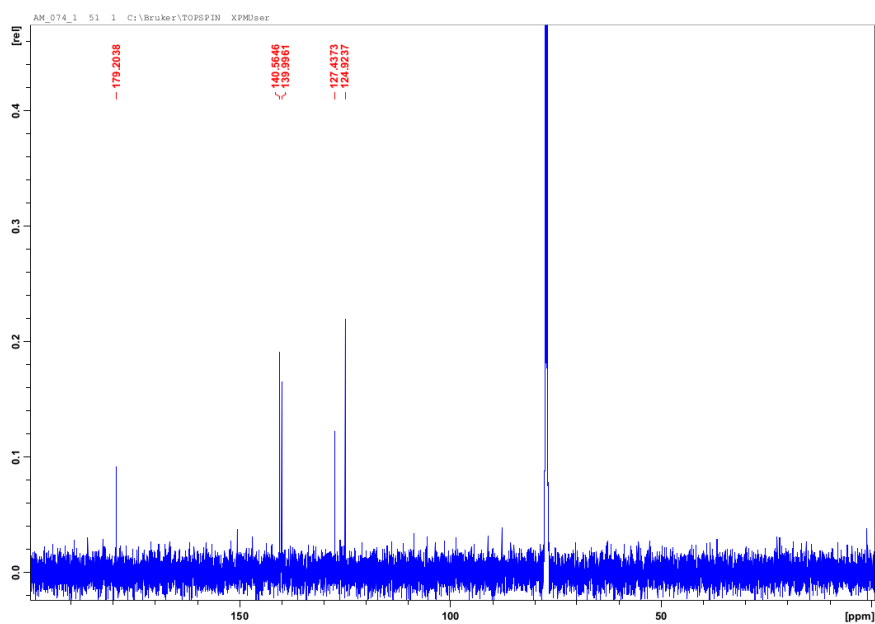
Figure B.25: ^{13}C-NMR of HOp−I **5d**.

225
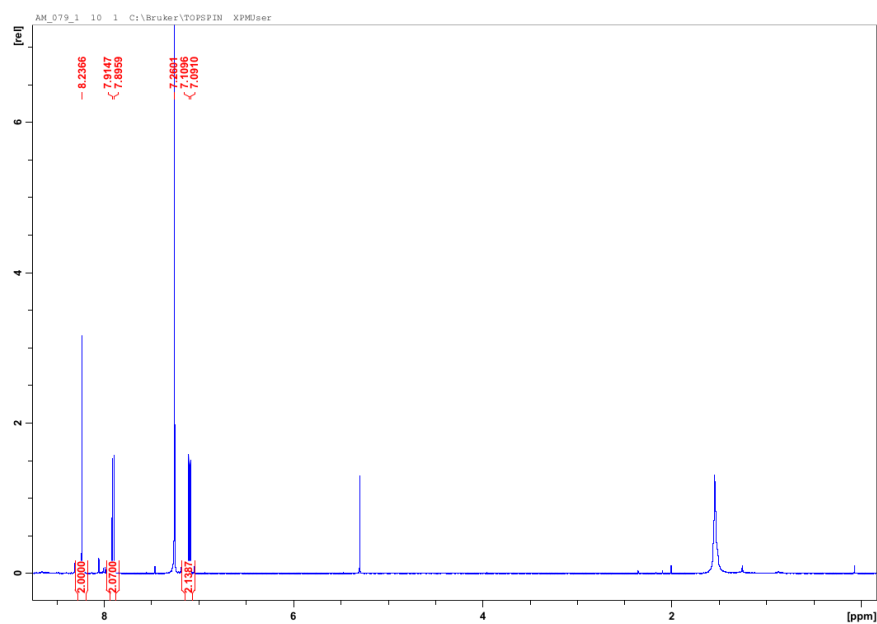
Figure B.26: ^{1}H-NMR of Al(Op$-$I)$_3$ **6d**.
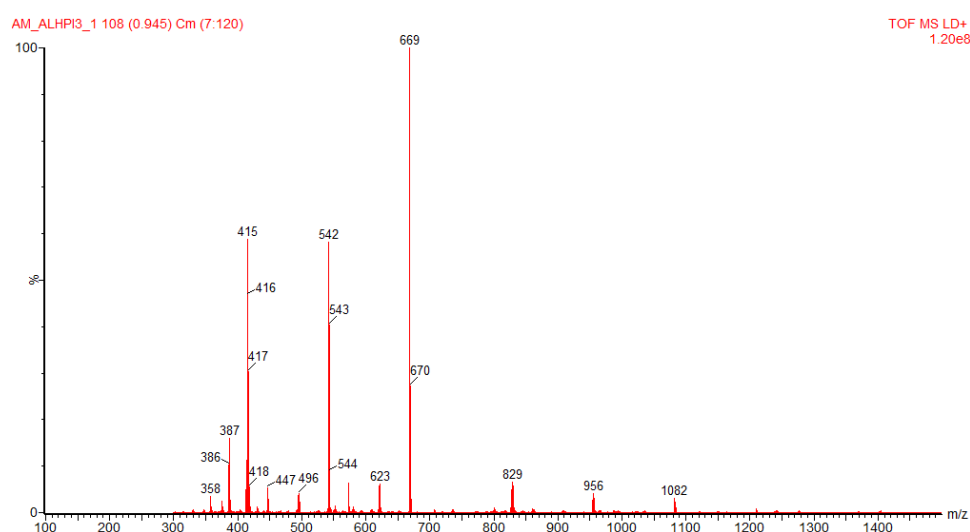
Figure B.27: MALDI-TOF of Al(Op$-$I)$_3$ **6d**.
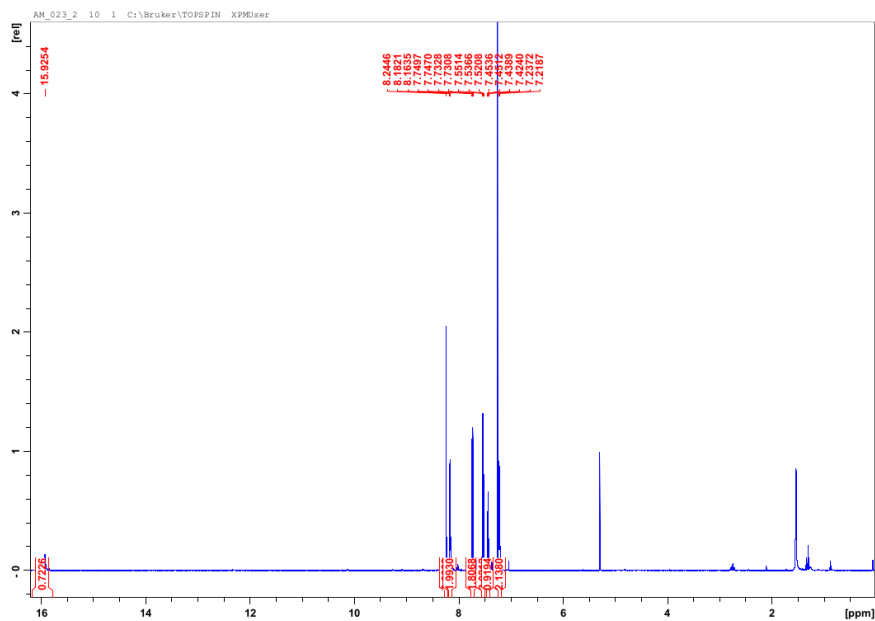
Figure B.28: ^{1}H-NMR of HOp−p **15a**.
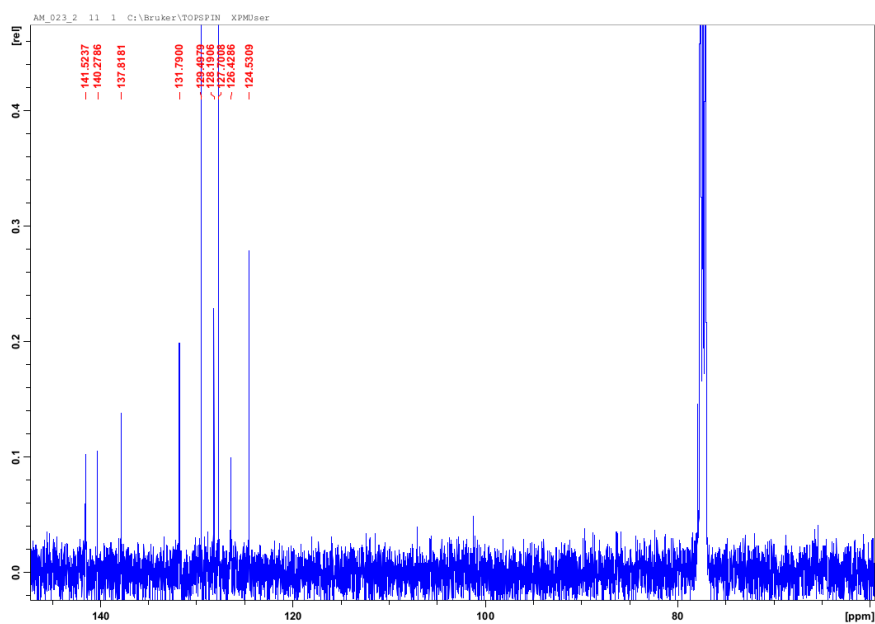
Figure B.29: ^{13}C-NMR of HOp−p **15a**.
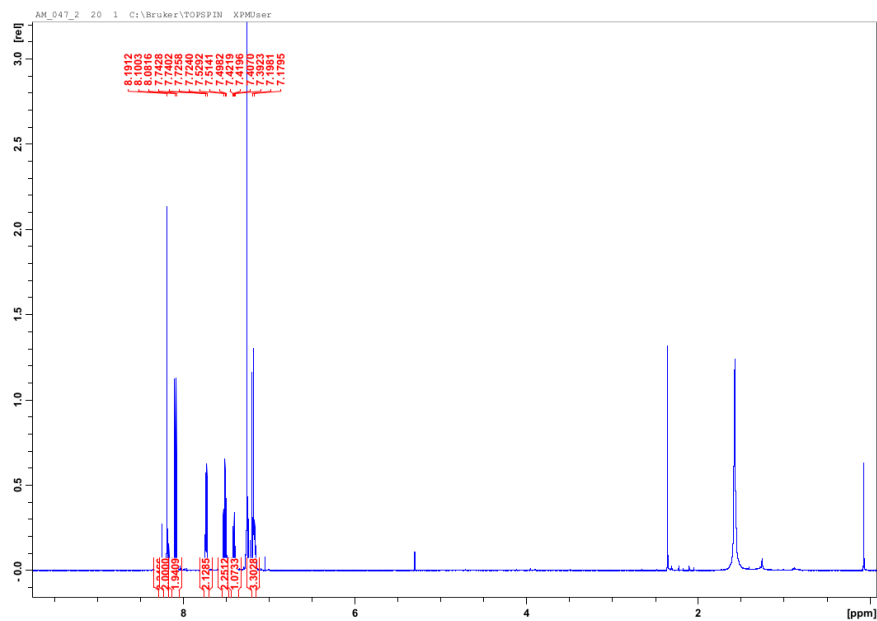
Figure B.30: ^{1}H-NMR of Al(Op$-$p)$_3$ **16a**.

Figure B.31: ^{1}H-NMR of Al(Op$-$p)$_3$ **16a**.

Figure B.32: MALDI-TOF of Al(Op−p)$_3$ **16a**.
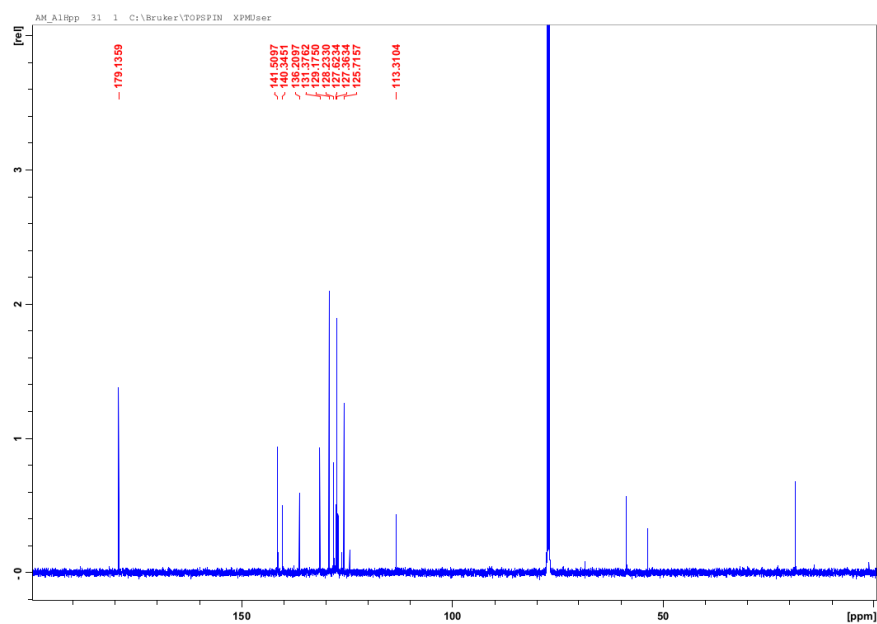
Figure B.33: ^{1}H-NMR of HOp−n **15b**.
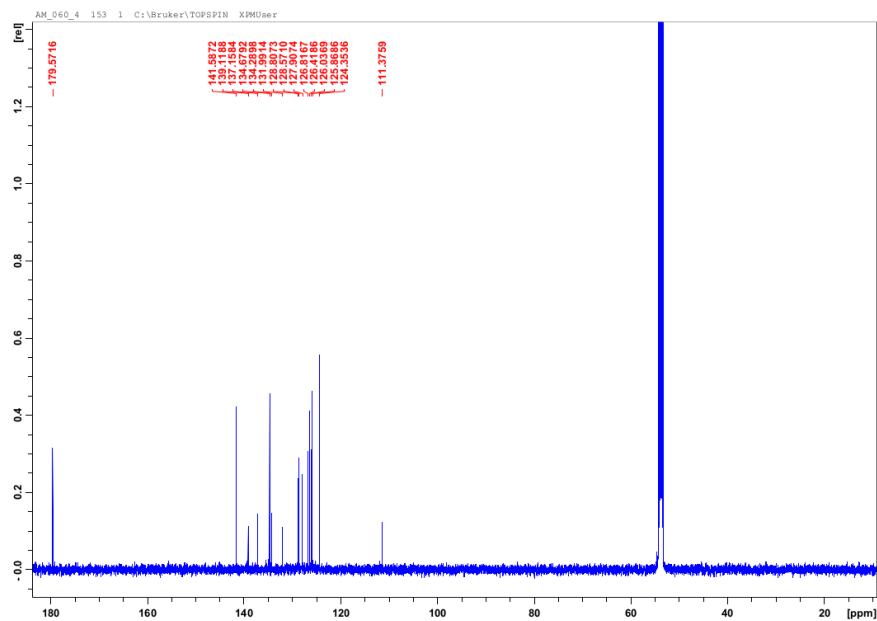
Figure B.34: ^{13}C-NMR of HOp−n **15b**.
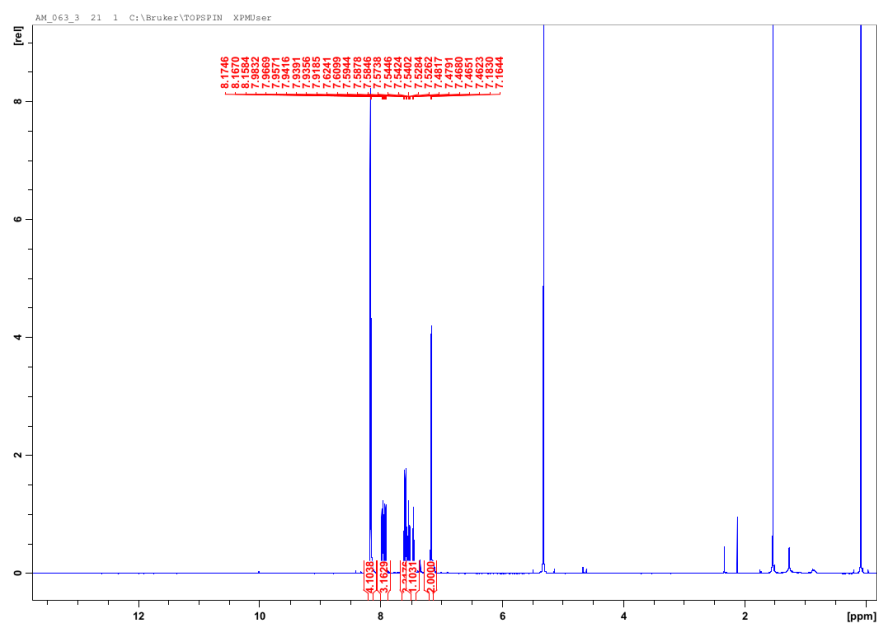
Figure B.35: ^{1}H-NMR of Al(Op−n)$_3$ **16b**.
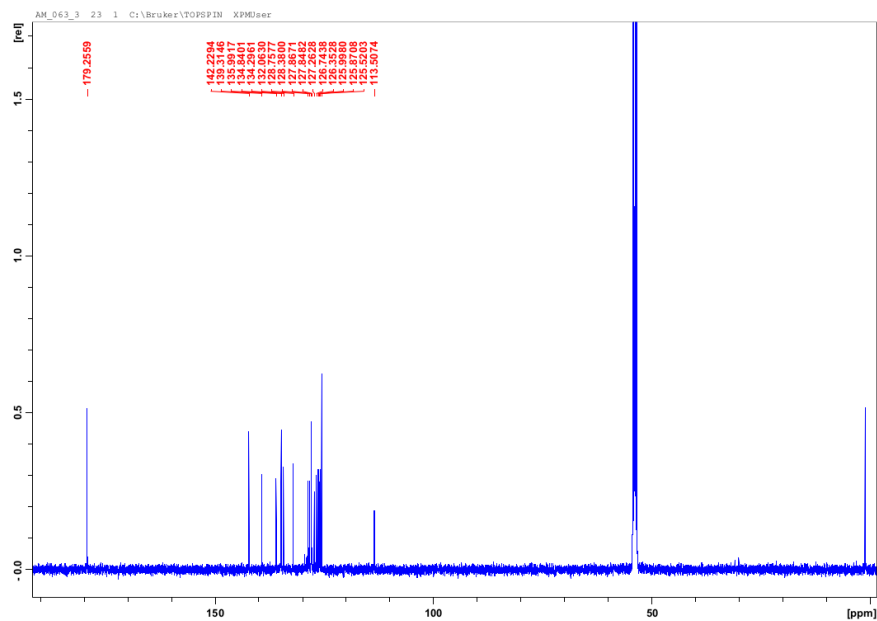
Figure B.36: ^{1}H-NMR of Al(Op−n)$_3$ **16b**.
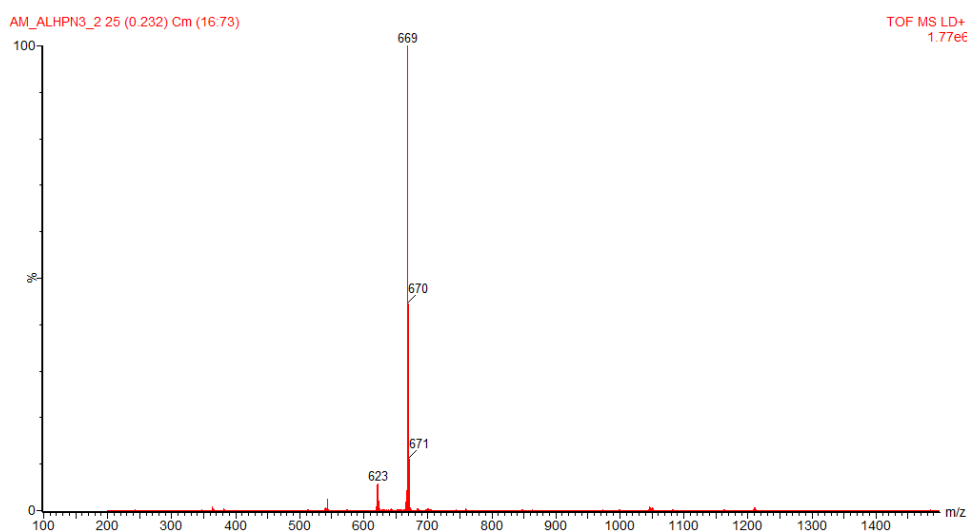
Figure B.37: MALDI-TOF of Al(Op−n)$_3$ **16b**.

231

Figure B.38: ^{1}H-NMR of HOp−pe **15c**.
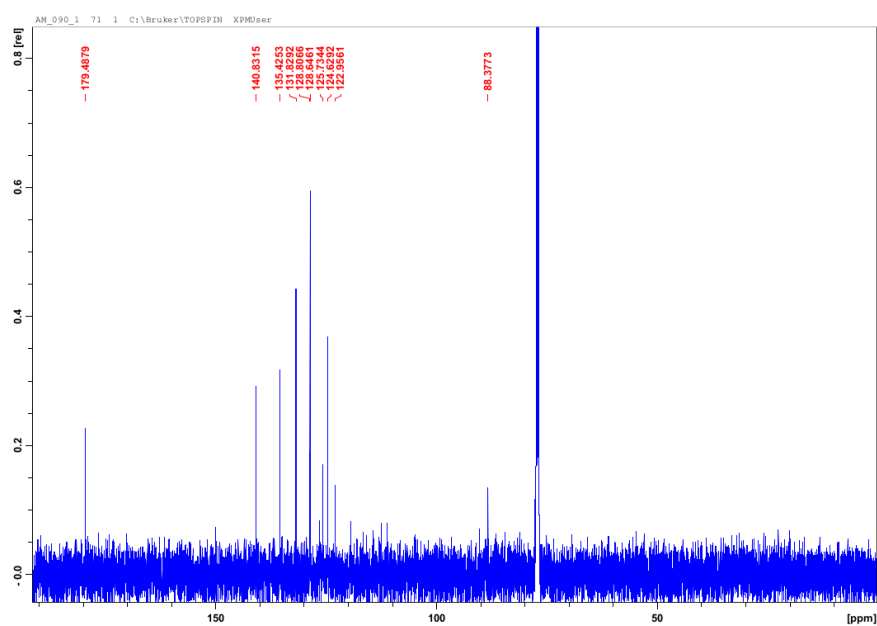
Figure B.39: ^{13}C-NMR of HOp−pe **15c**.
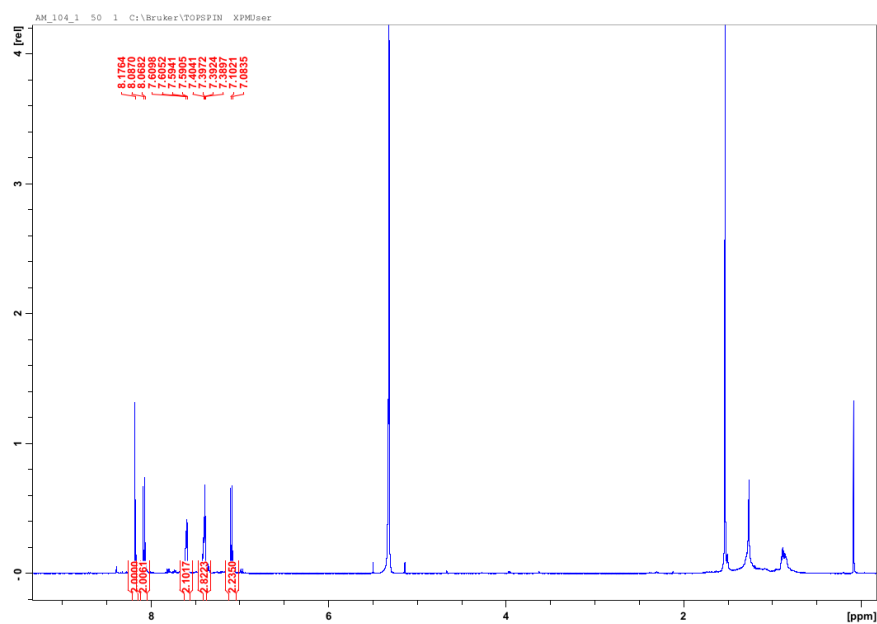
Figure B.40: ^{1}H-NMR of Al(Op−pe)$_3$ **16c**.
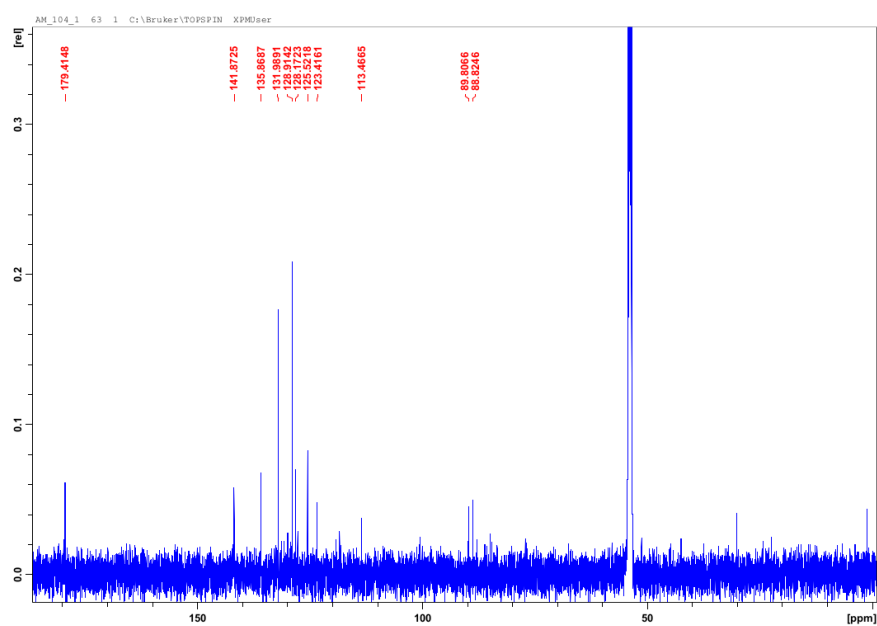
Figure B.41: ^{1}H-NMR of Al(Op−pe)$_3$ **16c**.

233
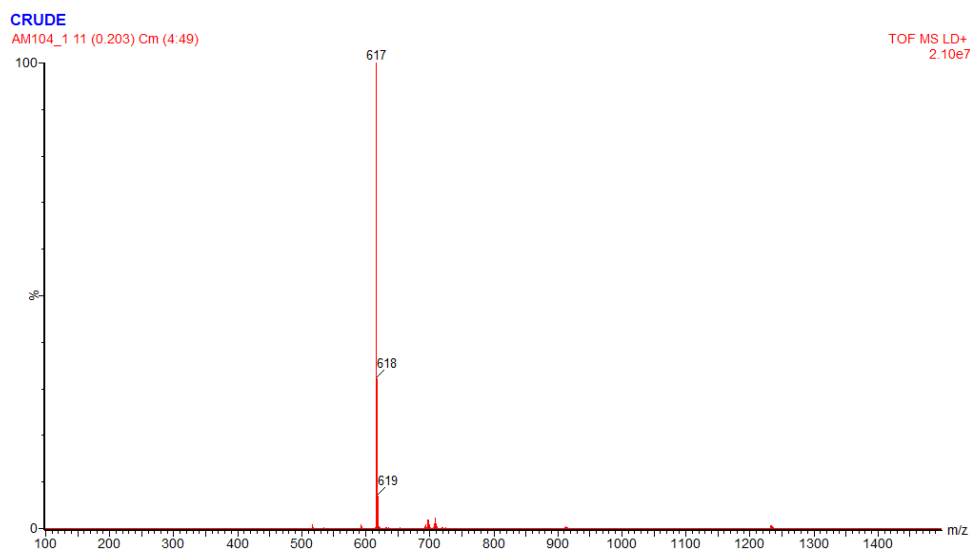
Figure B.42: MALDI-TOF of Al(Op−pe)$_3$ **16c**.
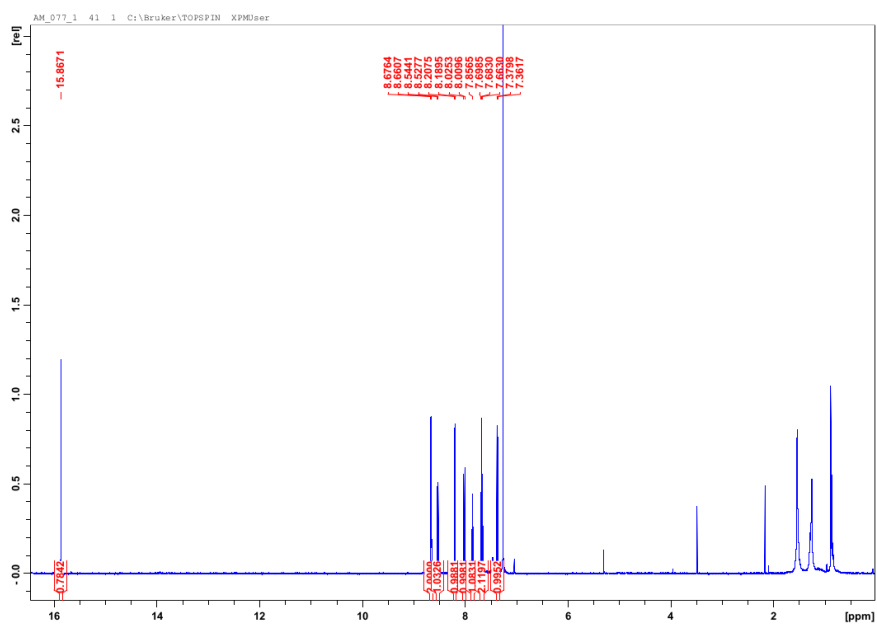
Figure B.43: ^{1}H-NMR of HOba **18**.
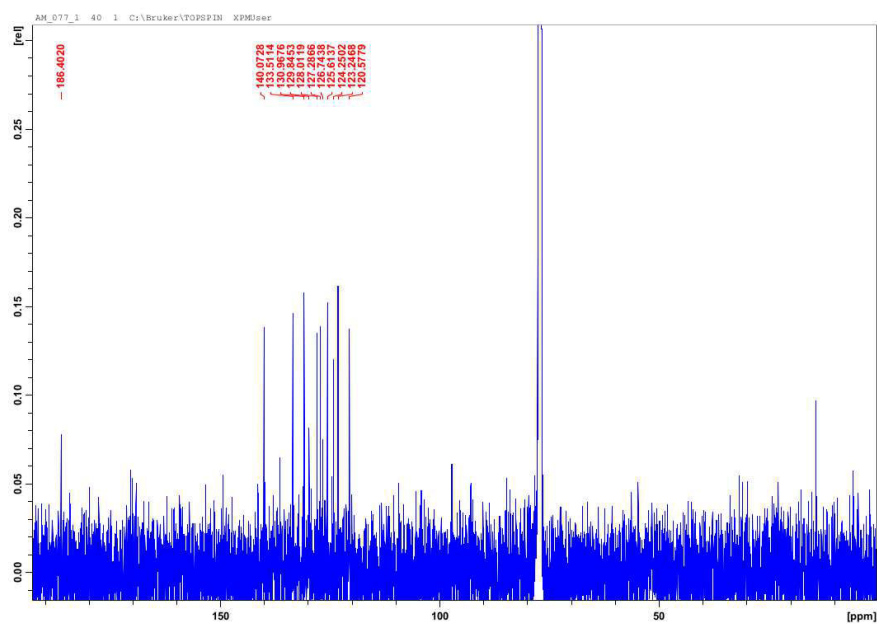
Figure B.44: ^{1}H-NMR of HOba **18**.
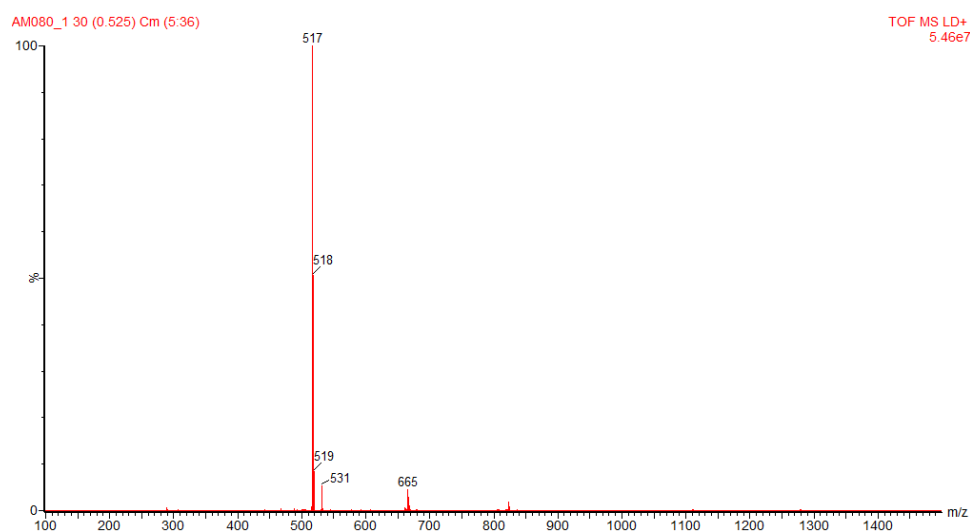
Figure B.45: MALDI-TOF of Al(Oba)$_3$ **19**.
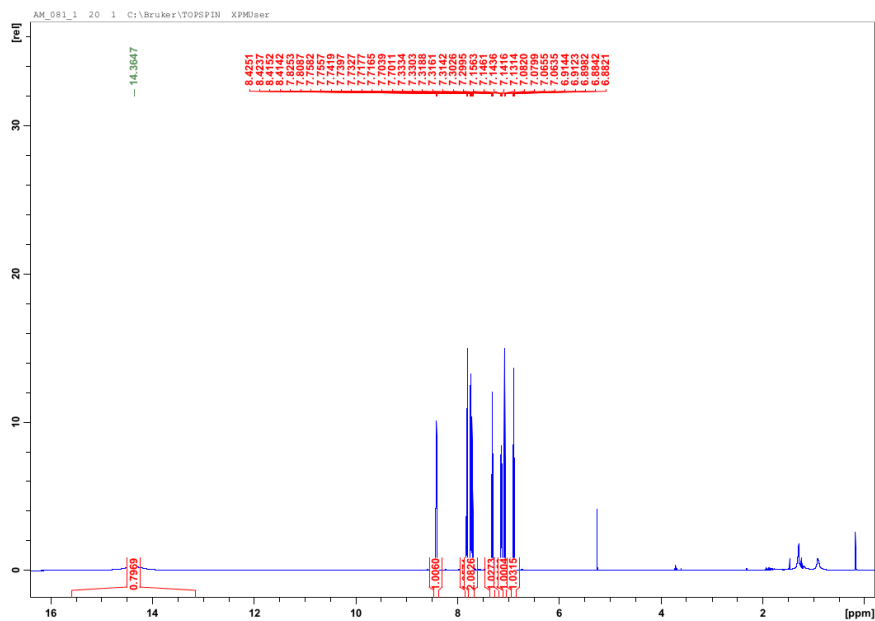
Figure B.46: ^{1}H-NMR of HOp−py **22**.
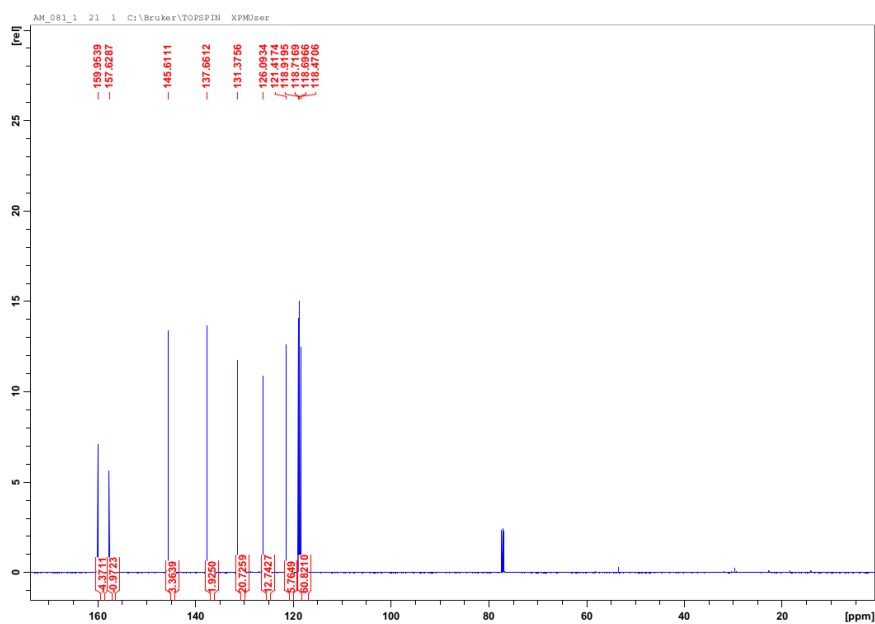
Figure B.47: ^{1}H-NMR of **22**.
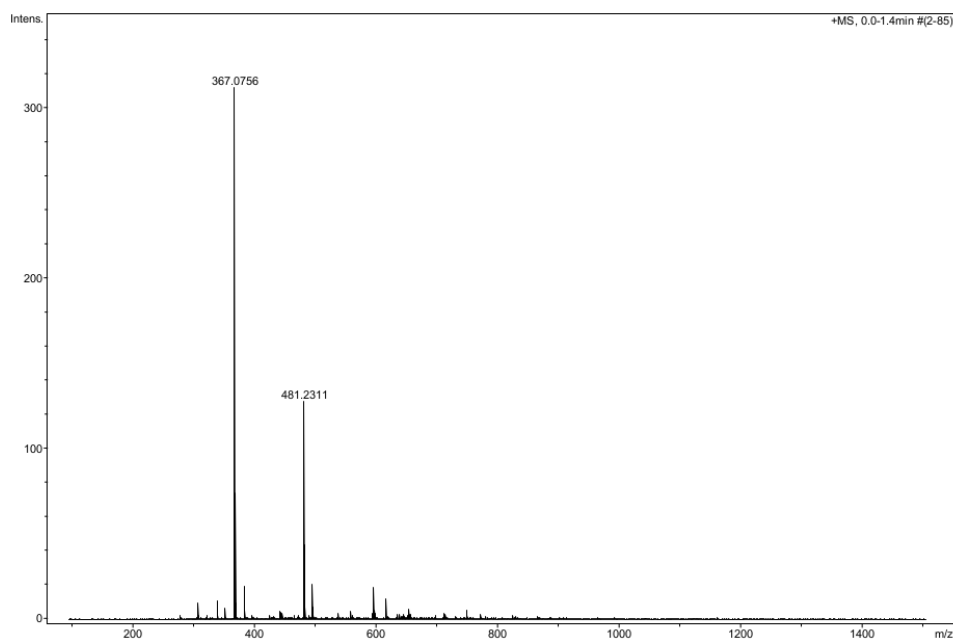
Figure B.48: ESI-TOF of Al(Op−py)$_3$ **23**.

Figure B.49: MALDI-TOF of Al(Op−py)$_3$ **23**.

237
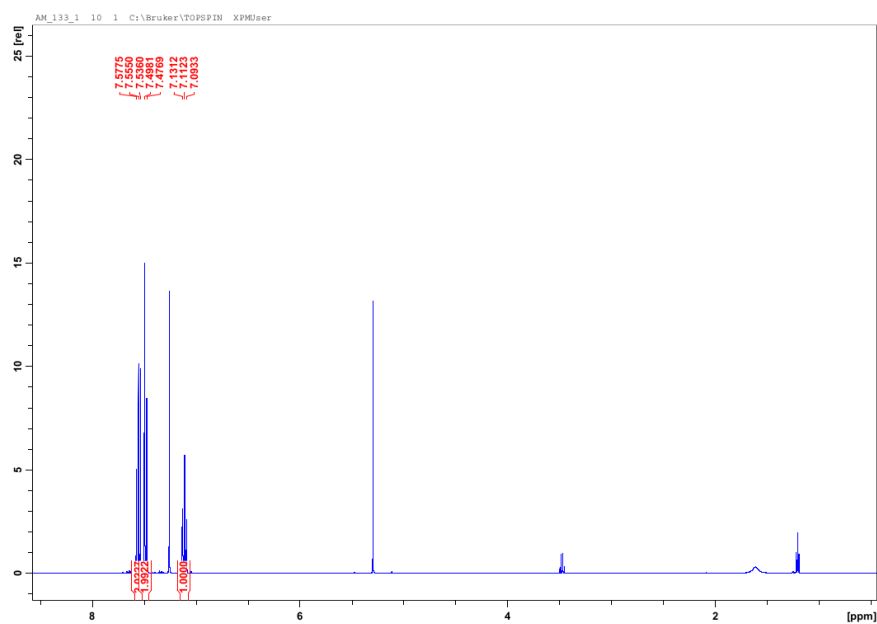
Figure B.50: ^{1}H-NMR of Al(Trop)$_3$ **25**.
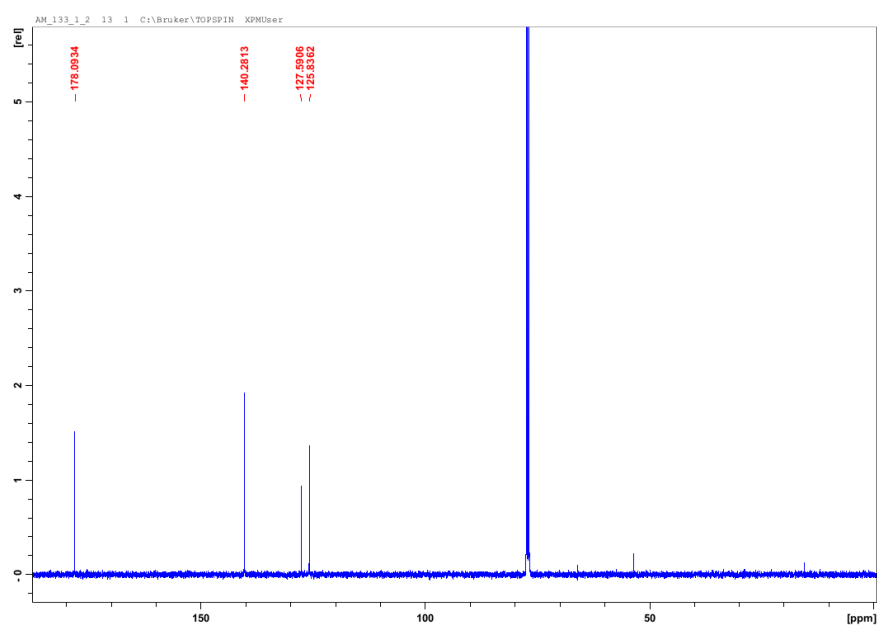
Figure B.51: ^{1}H-NMR of Al(Trop)$_3$ **25**.
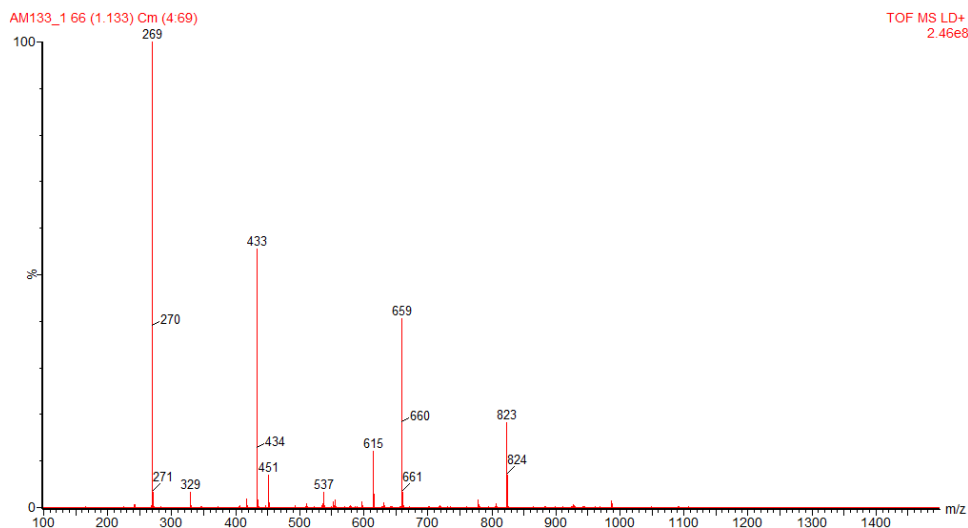
Figure B.52: MALDI-TOF of Al(Trop)$_3$ **25**.
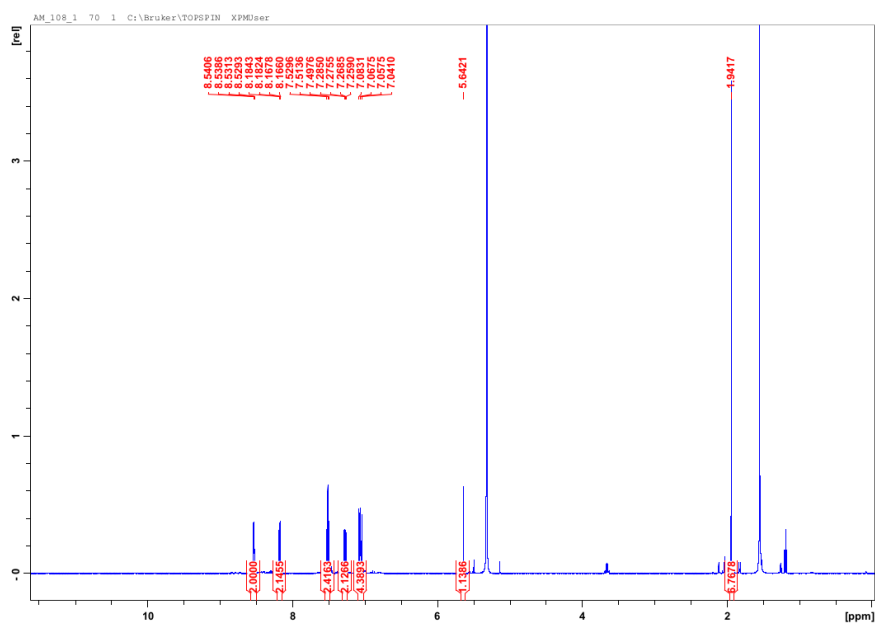
Figure B.53: ^{1}H-NMR of Al(q$_2$Acac) **28**.
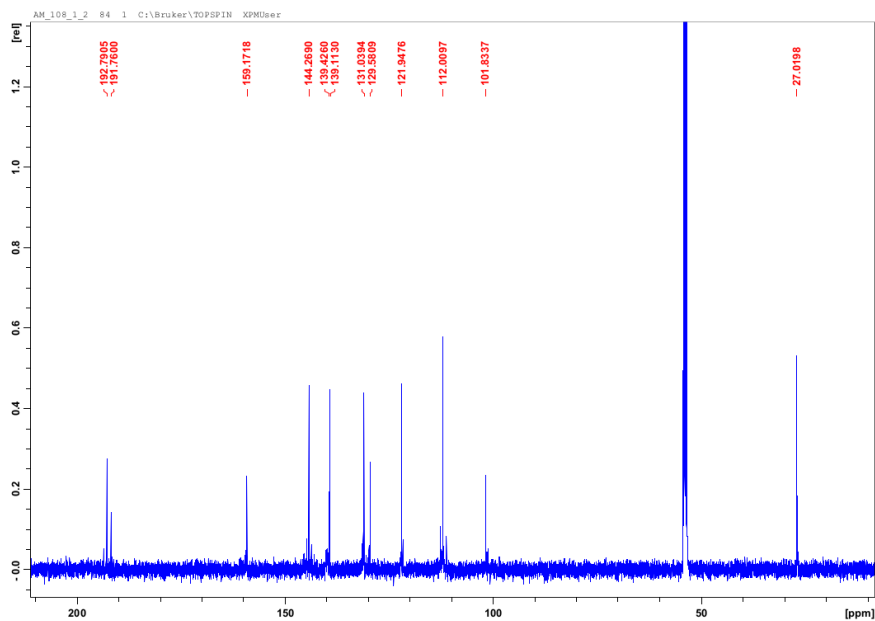
Figure B.54: ^{1}H-NMR of Al(q$_2$Acac) **28**.
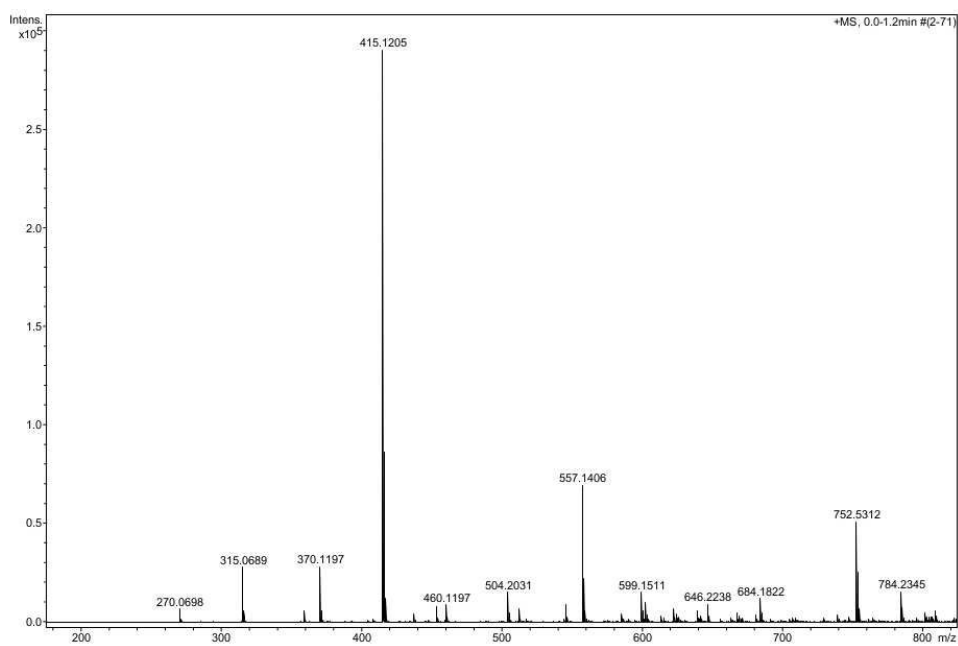
Figure B.55: ESI-TOF of Al(q$_2$Acac) **28**.
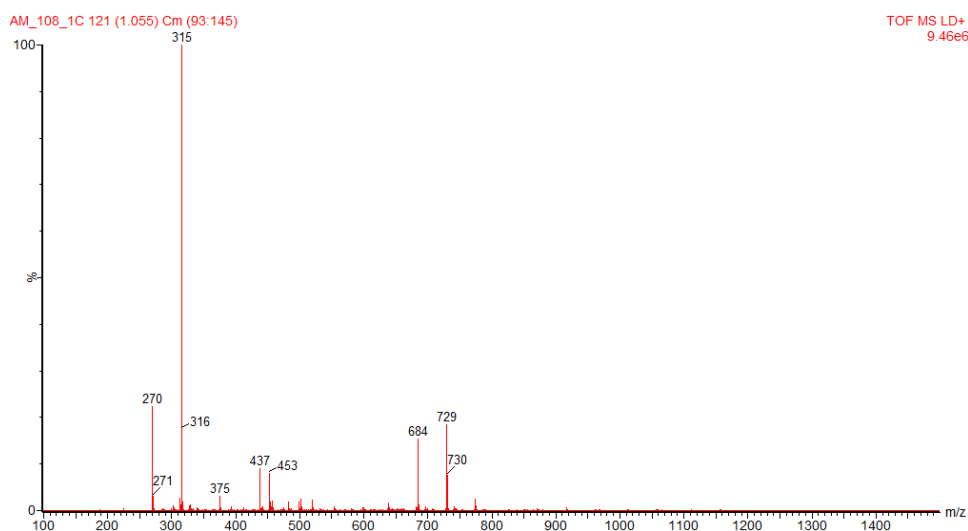
Figure B.56: MALDI-TOF of Al(q$_2$Acac) **28**.
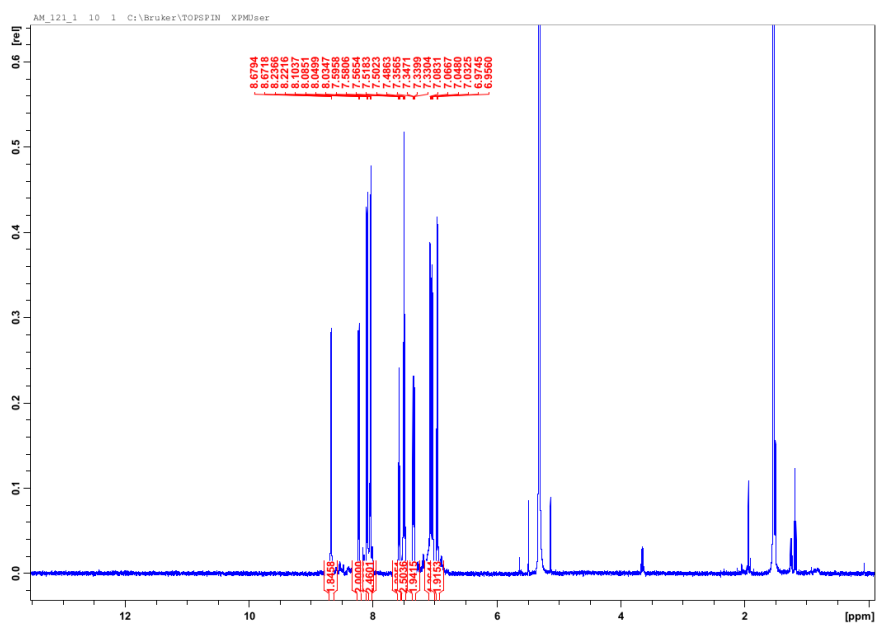
Figure B.57: ^{1}H-NMR of Al(q$_2$Op) **29**.
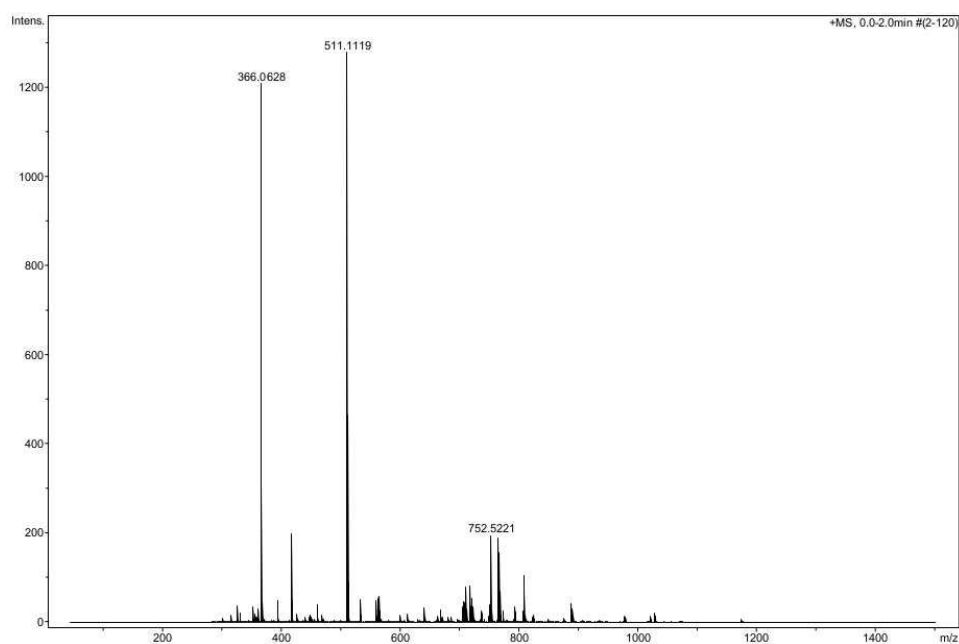
Figure B.58: ESI-TOF of Al(q$_2$Op) **29**.
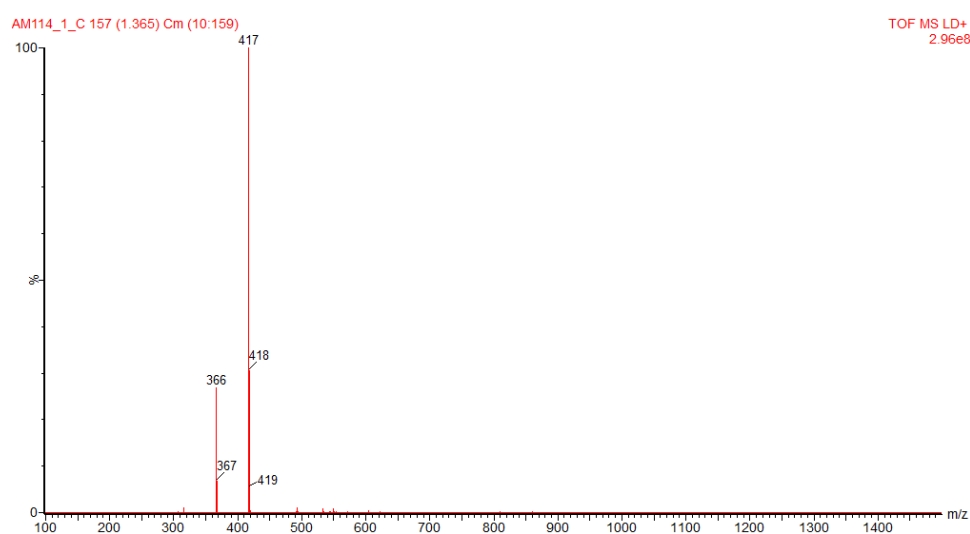
Figure B.59: MALDI-TOF of Al(q$_2$Op) **29**.
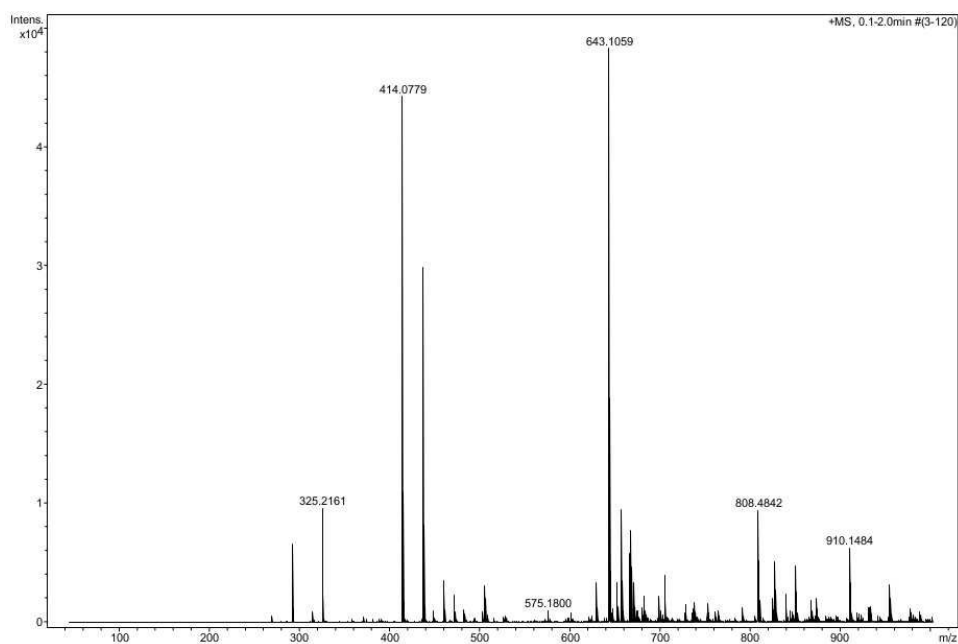
Figure B.60: ESI-TOF of Al(q$_2$Trop) **30**.
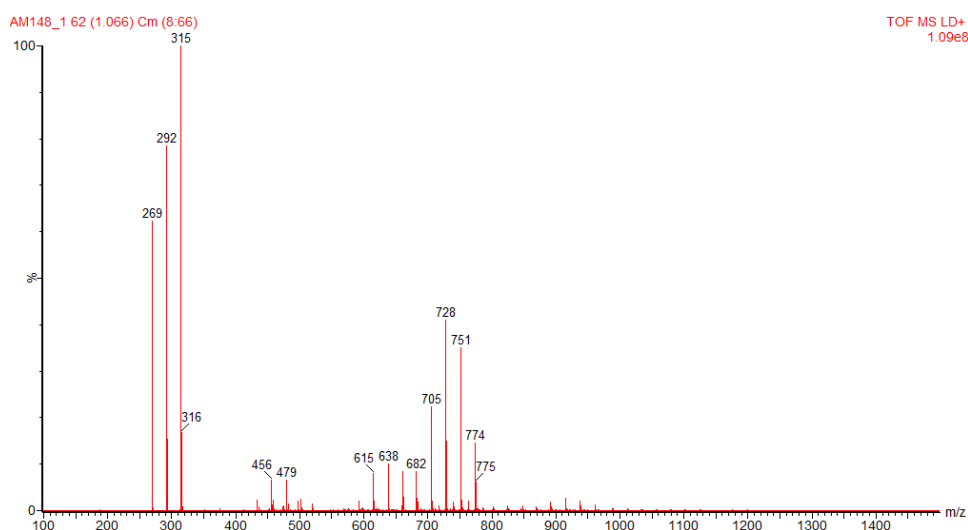
Figure B.61: MALDI-TOF of Al(q$_2$Trop) **30**.

243
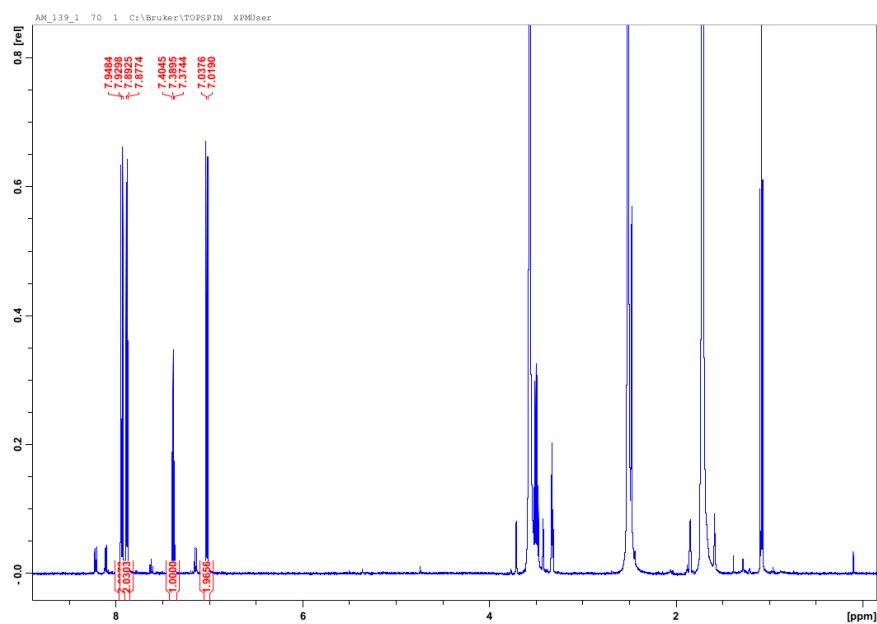
Figure B.62: ^{1}H-NMR of Zn(Op)$_2$ **31**.
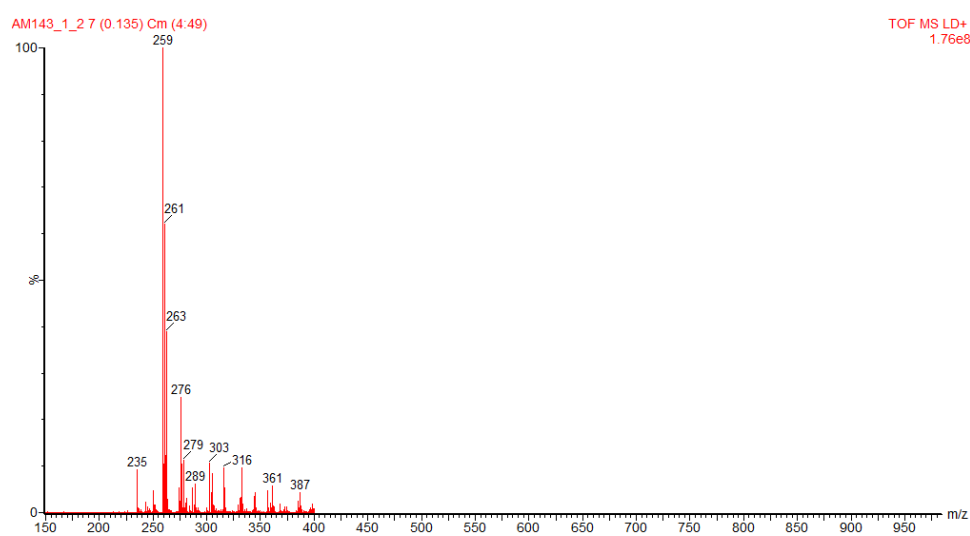
Figure B.63: MALDI-TOF of Zn(Op)$_2$ **31**.
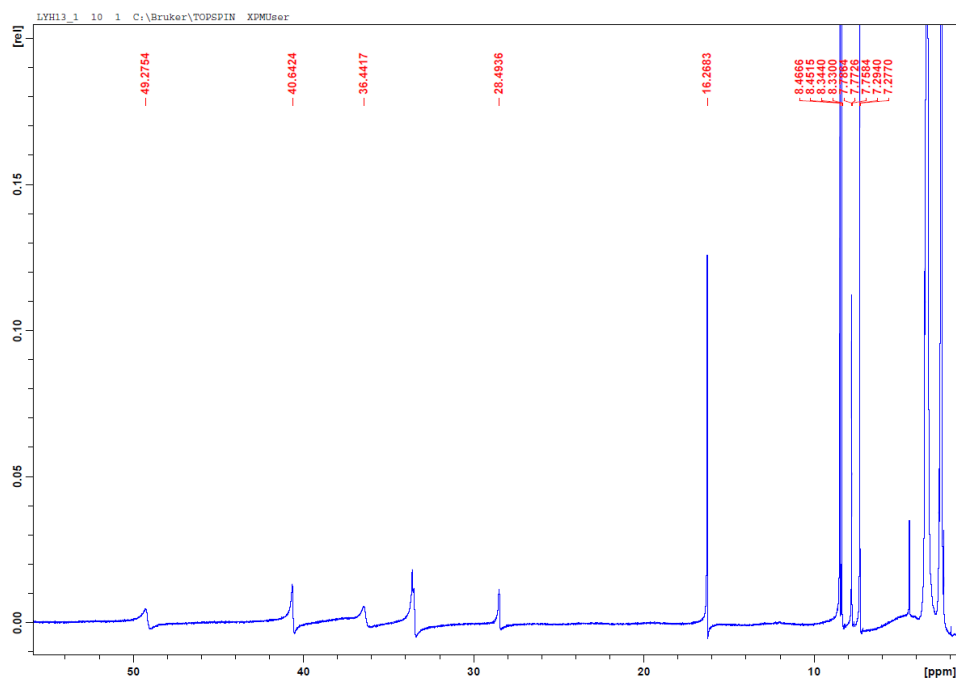
Figure B.64: ^{1}H-NMR of $\text{Dy(Op)}_2\text{Cl} \cdot \text{HOp} \cdot \text{EtOH}$ **32**.
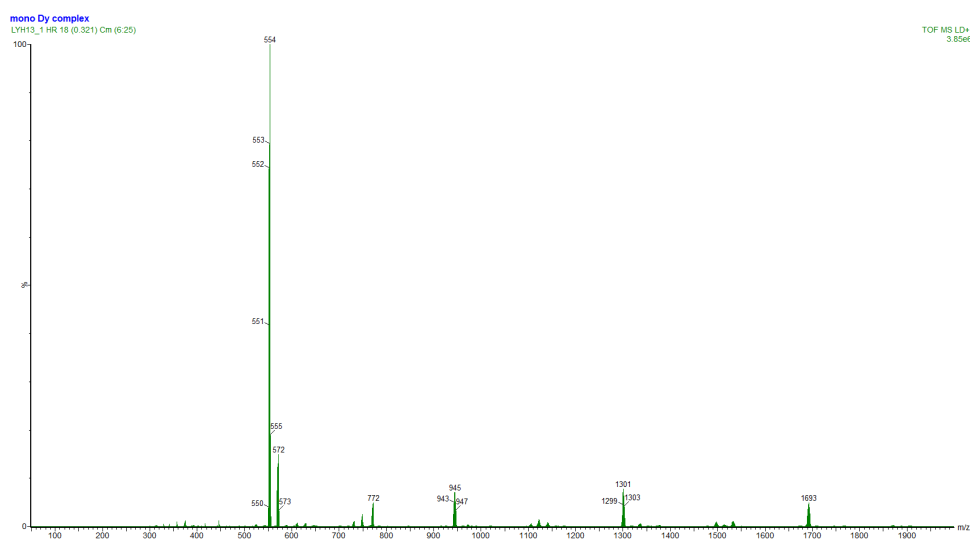
Figure B.65: MALDI-TOF of $\text{Dy(Op)}_2\text{Cl} \cdot \text{HOp} \cdot \text{EtOH}$ **32**.

245
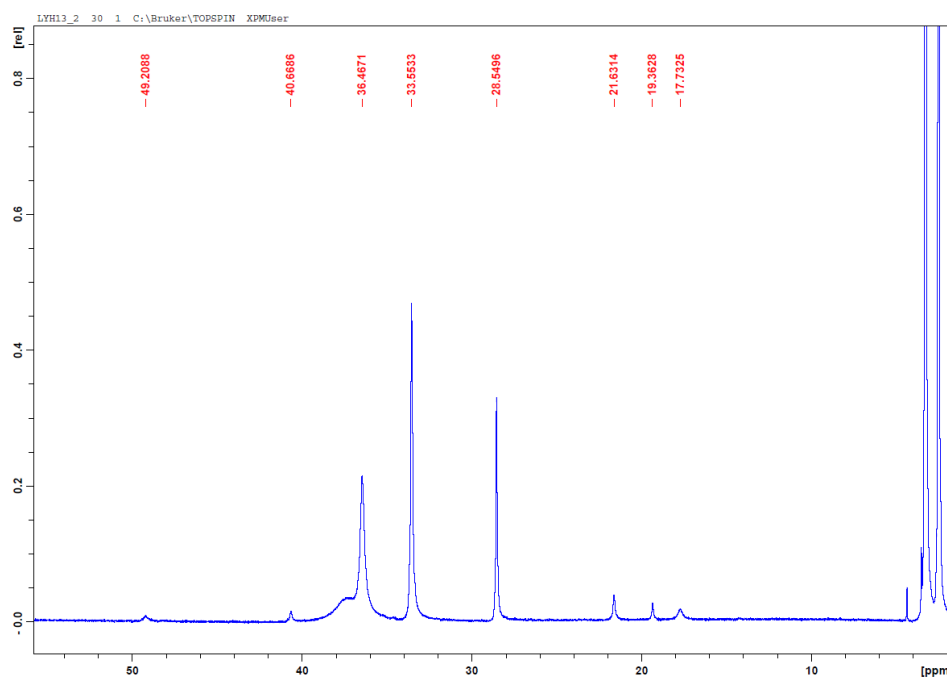
Figure B.66: ^{1}H-NMR of $Dy(Op)_3 \cdot HOp$ **33**-$Dy(Op)_3 \cdot EtOH$ **34**.
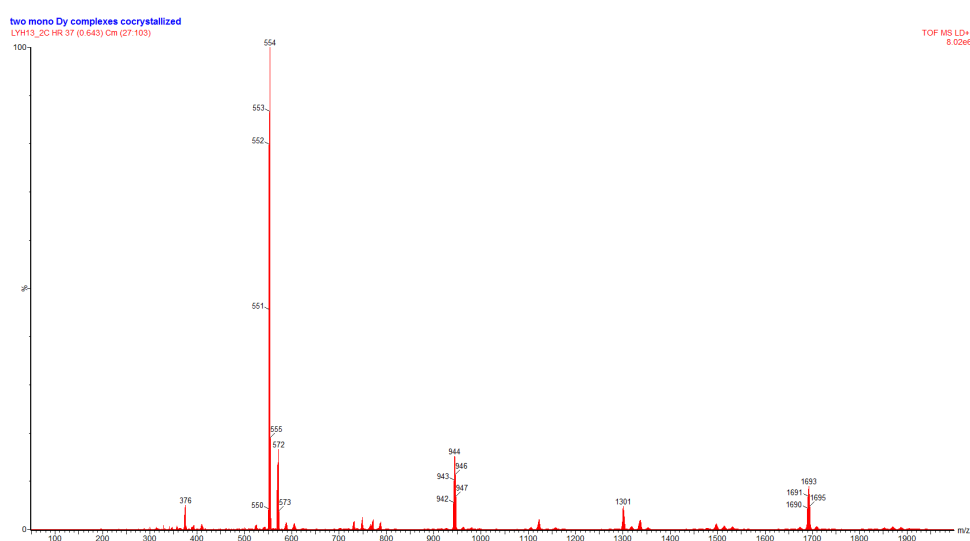
Figure B.67: MALDI-TOF of $Dy(Op)_3 \cdot HOp$ **33**-$Dy(Op)_3 \cdot EtOH$ **34**.

246
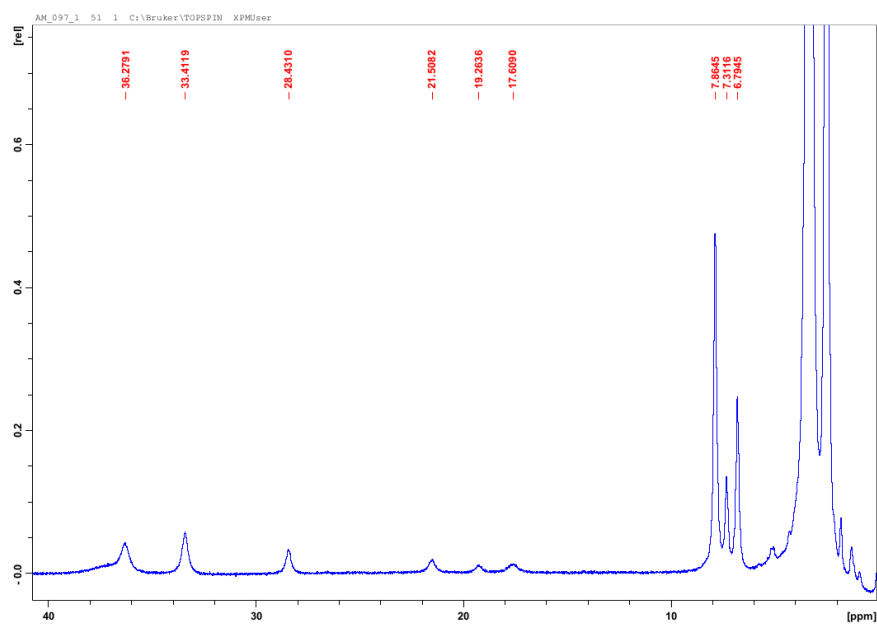
Figure B.68: ^{1}H-NMR of **36**.
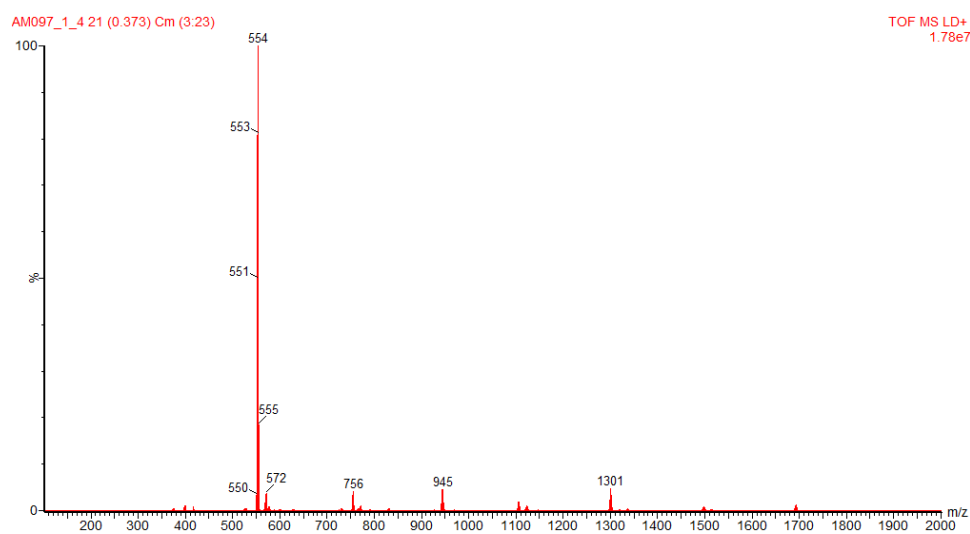
Figure B.69: MALDI-TOF of **36**.
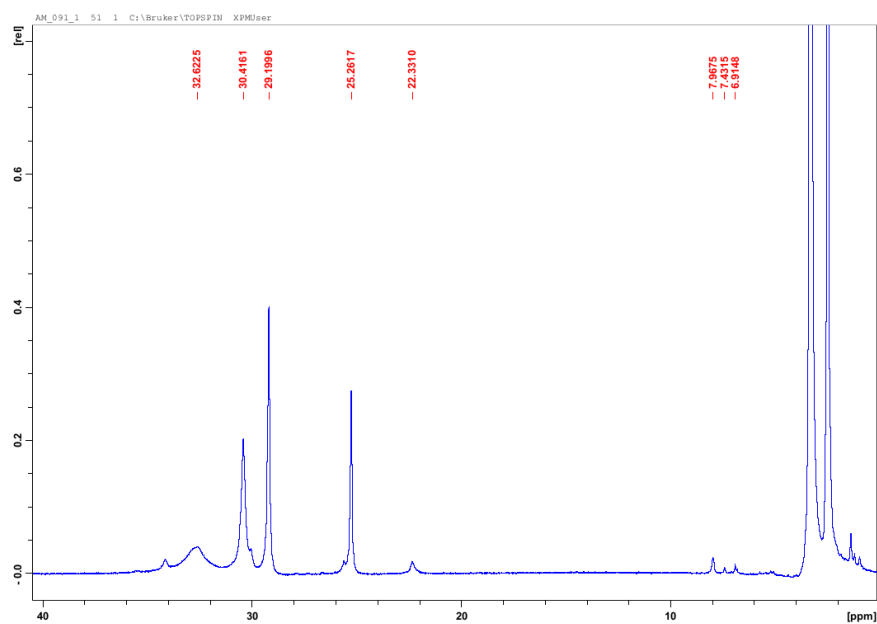
Figure B.70: ^{1}H-NMR of **37**.
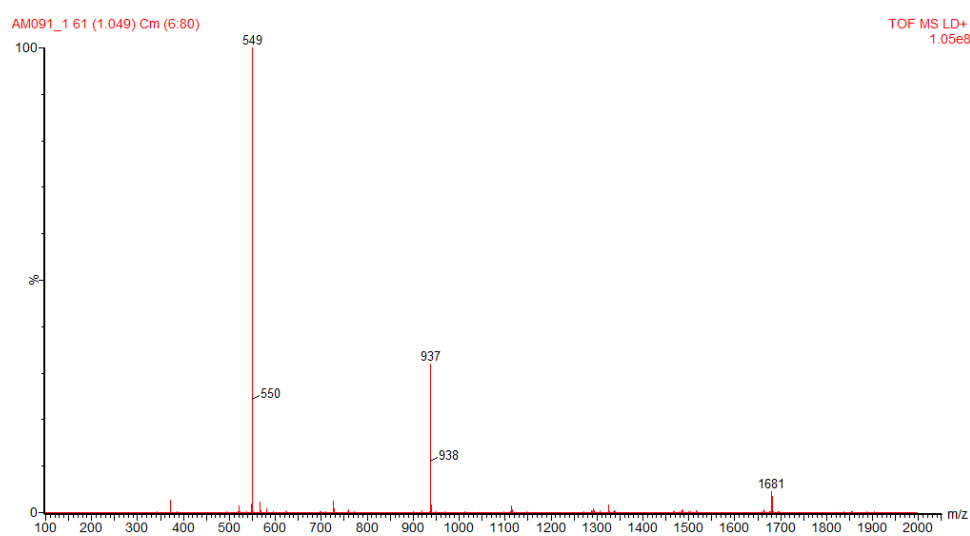
Figure B.71: MALDI-TOF of **37**.
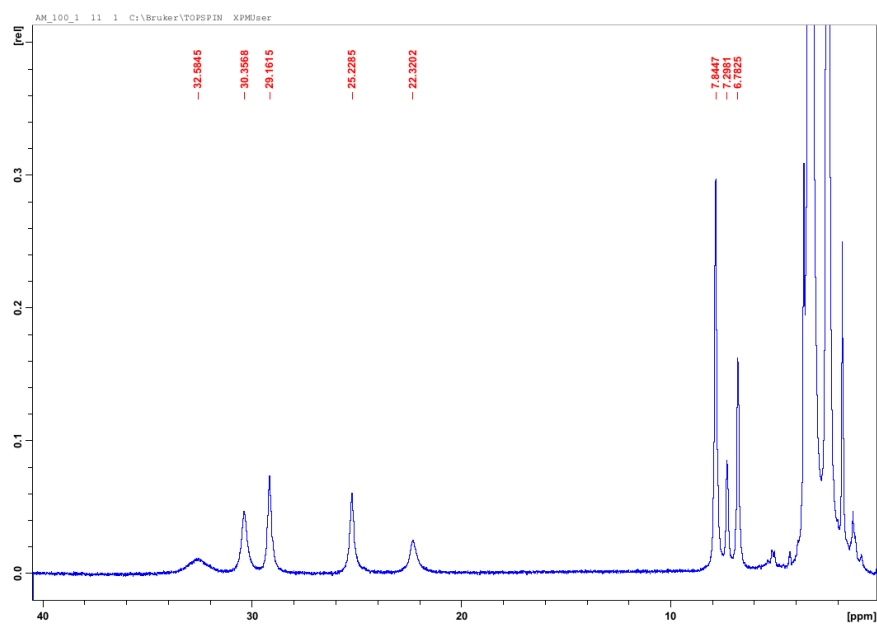
Figure B.72: ^{1}H-NMR of **38**.
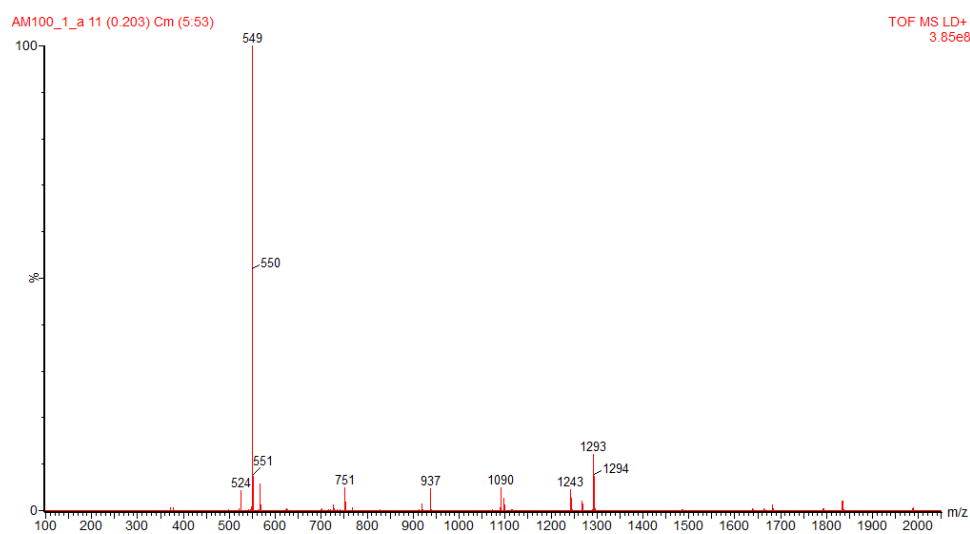
Figure B.73: MALDI-TOF of **38**.

C. Crystal Refinement Data

Table C.1: Crystallographic and refinement data of *mer*-Alq$_3$.

Compound	Alq$_3 \cdot$ EtOH
Empirical formula	C$_{29}$H$_{24}$O$_4$N$_3$Al
M [g mol^{-1}]	505.49
Crystal colour	Yellow/gree
T [K]	180.00(2)
λ [Å]	0.71073
Crystal system	Monoclinic
Space group	P21/n
a [pm]	1109.86(5)
b [pm]	1313.34(5)
c [pm]	1657.59(7)
α [°]	90.00
β [°]	94.068(3)
γ [°]	90.00
Volume [Å^3]	2410.05(18)
Z	4
$\rho_{\text{calcd.}}$ [g cm^{-3}]	1.393
μ(Mo-Kα) [mm^{-1}]	0.127
F(000)	1056
Crystal size [mm]	0.45 x 0.28 x 0.27
θ range for data collection [°]	2.140 - 25.698
Final R indices [$I2> \sigma\,(I)$]	R$_1$ = 0.0330, wR$_2$ = 0.0862
R indices (all data)	R$_1$ = 0.0394, wR$_2$ = 0.0892
GoF on F_2	1.027

Table C.2: Crystallographic and refinement data of $Al(Op)_3$ **4**.

Compound	$Al(Op)_3 \cdot 3.5\,CHCl_3$
Empirical formula	$C_{42.5}H_{24.5}Cl_{10.5}O_6Al$
M $[g\,mol^{-1}]$	1030.33
Crystal colour	Yellow
T [K]	180.00(2)
λ [Å]	0.71073
Crystal system	Monoclinic
Space group	P2(1)/n
a [pm]	934.61(4)
b [pm]	2177.32(6)
c [pm]	2133.06(9)
α [°]	90.00
β [°]	90.797(3)
γ [°]	90.00
Volume $[Å^3]$	4340.2(3)
Z	4
$\rho_{calcd.}$ $[g\,cm^{-3}]$	1.577
μ(Mo-Kα) $[mm^{-1}]$	0.742
F(000)	2076
Crystal size [mm]	0.34 x 0.31 x 0.30
θ range for data collection [°]	2.13 - 26.81
Final R indices [I2> σ (I)]	$R_1 = 0.0609$, w$R_2 = 0.1589$
R indices (all data)	$R_1 = 0.0862$, w$R_2 = 0.1757$
GoF on F_2	1.054

Table C.3: Crystallographic and refinement data of HOp−Br **5c**.

Compound	HOp−Br
Empirical formula	$C_{13}H_7O_2Br$
M [g mol^{-1}]	275.10
Crystal colour	Yellow
T [K]	180.00(2)
λ [Å]	0.71073
Crystal system	Monoclinic
Space group	C2/c
a [pm]	1212.60(14)
b [pm]	1170.76(11)
c [pm]	703.64(8)
α [°]	90.00
β [°]	98.682(9)
γ [°]	90.00
Volume [Å^3]	987.49(18)
Z	4
$\rho_{\text{calcd.}}$ [g cm^{-3}]	1.850
μ(Mo-Kα) [mm^{-1}]	4.139
F(000)	544
Crystal size [mm]	0.39 x 0.17 x 0.16
θ range for data collection [°]	2.43 - 25.61
Final R indices [$I2> \sigma (I)$]	$R_1 = 0.0198$, wR$_2 = 0.0540$
R indices (all data)	$R_1 = 0.0217$, wR$_2 = 0.0549$
GoF on F_2	1.077

Table C.4: Crystallographic and refinement data of HOp−pe **15c**.

Compound	HOp−pe
Empirical formula	$C_{21}H_{12}O_2$
M [$g\,mol^{-1}$]	296.31
Crystal colour	Yellow
T [K]	180.00(2)
λ [Å]	0.71073
Crystal system	Monoclinic
Space group	P2(1)/n
a [pm]	805.94(5)
b [pm]	2933.95(12)
c [pm]	1280.33(7)
α [°]	90.00
β [°]	107.309(5)
γ [°]	90.00
Volume [$Å^3$]	2890.4(3)
Z	8
$\rho_{calcd.}$ [$g\,cm^{-3}$]	1.362
μ(Mo-Kα) [mm^{-1}]	0.087
F(000)	1232
Crystal size [mm]	0.36 x 0.24 x 0.02
θ range for data collection [°]	2.169 - 25.271
Final R indices [$I2> \sigma (I)$]	$R_1 = 0.0463$, $wR_2 = 0.1097$
R indices (all data)	$R_1 = 0.0774$, $wR_2 = 0.1227$
GoF on F_2	0.930

Table C.5: Crystallographic and refinement data of Al(q$_2$Op) **29**.

Compound	Al(q$_2$Op)
Empirical formula	C$_{31}$H$_{19}$N$_2$O$_4$Al
M [g mol^{-1}]	510.46
Crystal colour	Yellow
T [K]	150.00
λ [Å]	0.71073
Crystal system	Triclinic
Space group	P-1
a [Å]	8.1895(17)
b [Å]	10.8580(17)
c [Å]	14.312(3)
α [°]	68.926(13)
β [°]	85.576(16)
γ [°]	74.327(14)
Volume [Å^3]	1143.1(4)
Z	2
$\rho_{\text{calcd.}}$ [g cm^{-3}]	1.483
μ(Mo-Kα) [mm^{-1}]	0.134
F(000)	528.0
Crystal size [mm]	0.07 x 0.05 x 0.01
θ range for data collection [°]	3.05 - 51.996
Final R indices [$I2> \sigma(I)$]	R$_1$ = 0.0496, wR$_2$ = 0.0618
R indices (all data)	R$_1$ = 0.3187, wR$_2$ = 0.1180
GoF on F_2	0.476

Table C.6: Crystallographic and refinement data of Al(q$_2$Trop) **30**.

Compound	Al(q$_2$Trop)
Empirical formula	C$_{25}$H$_{17}$N$_2$O$_4$Al
M [g mol^{-1}]	436.39
Crystal colour	Yellow
T [K]	180.15
λ [Å]	0.71073
Crystal system	Monoclinic
Space group	C2/c
a [Å]	16.3233(17)
b [Å]	10.0992(10)
c [Å]	11.9293(15)
α [°]	90.00
β [°]	99.621(9)
γ [°]	90.00
Volume [Å^3]	1938.9(4)
Z	4
$\rho_{\text{calcd.}}$ [g cm^{-3}]	1.495
μ(Mo-Kα) [mm^{-1}]	0.144
F(000)	904.0
Crystal size [mm]	0.18 x 0.13 x 0.10
θ range for data collection [°]	4.76 - 51.3
Final R indices [$I2> \sigma (I)$]	R$_1$ = 0.0727, wR$_2$ = 0.1896
R indices (all data)	R$_1$ = 0.1197, wR$_2$ = 0.2192
GoF on F_2	1.041

Table C.7: Crystallographic and refinement data of $Zn(Op)_2$ **31**.

Compound	$Zn(Op)_2 \cdot 2\,H_2O$
Empirical formula	$C_{26}H_{18}O_6Zn$
M $[g\,mol^{-1}]$	491.77
Crystal colour	Orange
T [K]	180.15
λ [Å]	0.71073
Crystal system	Monoclinic
Space group	C2/c
a [Å]	35.005(2)
b [Å]	5.2112(2)
c [Å]	11.0530(7)
α [°]	90.00
β [°]	95.542(5)
γ [°]	90.00
Volume $[Å^3]$	2006.9(2)
Z	4
$\rho_{calcd.}$ $[g\,cm^{-3}]$	1.628
μ(Mo-Kα) $[mm^{-1}]$	1.269
F(000)	1008.0
Crystal size [mm]	0.31 x 0.10 x 0.01
θ range for data collection [°]	4.68 - 51.34
Final R indices $[I2 > \sigma(I)]$	$R_1 = 0.0433$, $wR_2 = 0.0875$
R indices (all data)	$R_1 = 0.0796$, $wR_2 = 0.0990$
GoF on F_2	1.029

Table C.8: Crystallographic and refinement data of [Dy(Op)$_2$Cl(HOp)(EtOH)] **32**.

Compound	[Dy(Op)$_2$Cl(HOp)(EtOH)]
Empirical formula	C$_{41}$H$_{28}$O$_7$DyCl
M [g mol^{-1}]	830.58
Crystal colour	Orange
T [K]	180.15
λ [Å]	0.71073
Crystal system	Triclinic
Space group	P-1
a [Å]	10.4482(7)
b [Å]	12.5823(8)
c [Å]	13.2433(8)
α [°]	93.446(5)
β [°]	112.211(5)
γ [°]	95.762
Volume [Å^3]	1594.55(18)
Z	2
$\rho_{\text{calcd.}}$ [g cm^{-3}]	1.730
μ(Mo-Kα) [mm^{-1}]	2.483
F(000)	826.0
Crystal size [mm]	0.18 x 0.15 x 0.14
θ range for data collection [°]	4.28 - 51.20
Final R indices [$I2> \sigma (I)$]	R$_1$ = 0.0172, wR$_2$ = 0.0441
R indices (all data)	R$_1$ = 0.0194, wR$_2$ = 0.0447
GoF on F_2	1.047

Table C.9: Crystallographic and refinement data of $[Dy(Op)_3(HOp)]$ **33**-$[Dy(Op)_3(EtOH)]$ **34**.

Compound	$[Dy(Op)_3(HOp)]-[Dy(Op)_3(EtOH)] \cdot 2\,EtOH$
Empirical formula	$C_{194}H_{136}O_{34}Dy_4$
M [$g\,mol^{-1}$]	3661.03
Crystal colour	Orange
T [K]	180.15
λ [Å]	0.71073
Crystal system	Monoclinic
Space group	C2/c
a [Å]	11.0591(8)
b [Å]	17.2521(8)
c [Å]	19.8266(10)
α [°]	92.328(4)
β [°]	104.285(5)
γ [°]	95.206(5)
Volume [Å^3]	3642.9(4)
Z	1
$\rho_{calcd.}$ [$g\,cm^{-3}$]	1.669
μ(Mo-Kα) [mm^{-1}]	2.114
F(000)	1836.0
Crystal size [mm]	0.24 x 0.15 x 0.11
θ range for data collection [°]	4.28 - 51.28
Final R indices [$I2> \sigma (I)$]	$R_1 = 0.0336$, $wR_2 = 0.0639$
R indices (all data)	$R_1 = 0.0643$, $wR_2 = 0.0712$
GoF on F_2	0.914

D. Concentration Dependence Emission
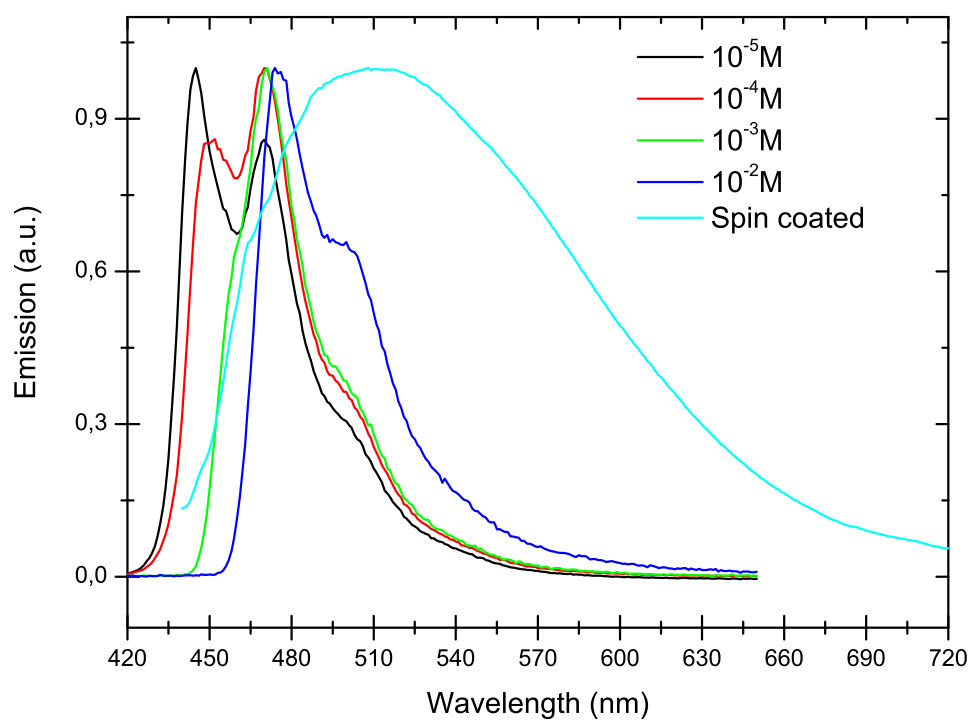
Figure D.1: Emission in function of the concentration of HOp **3**.
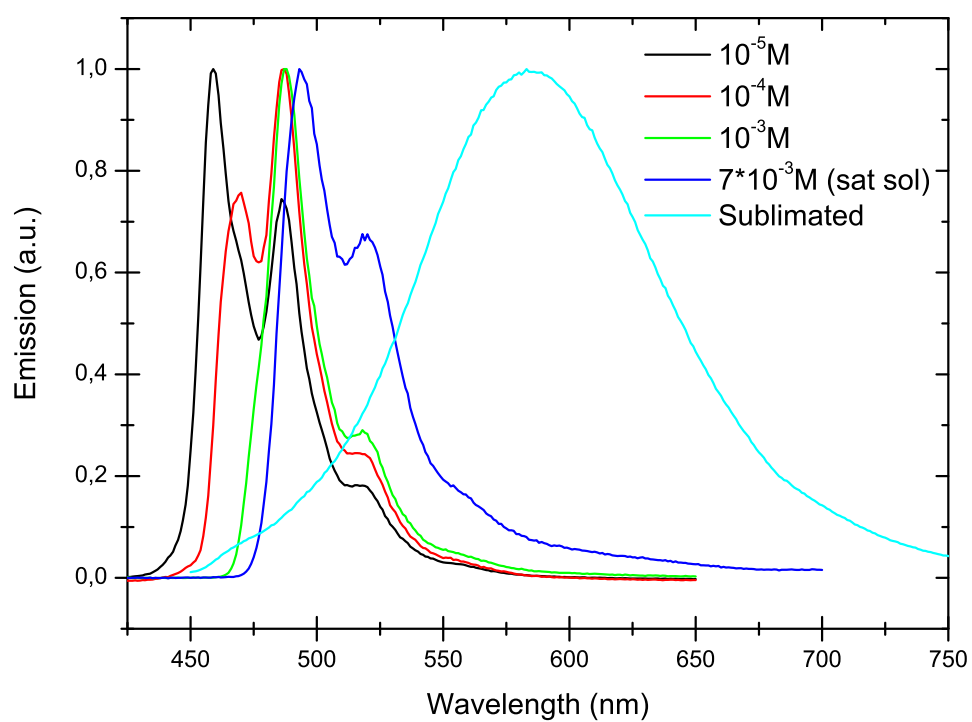
Figure D.2: Emission in function of the concentration of $Al(Op)_3$ **4**.
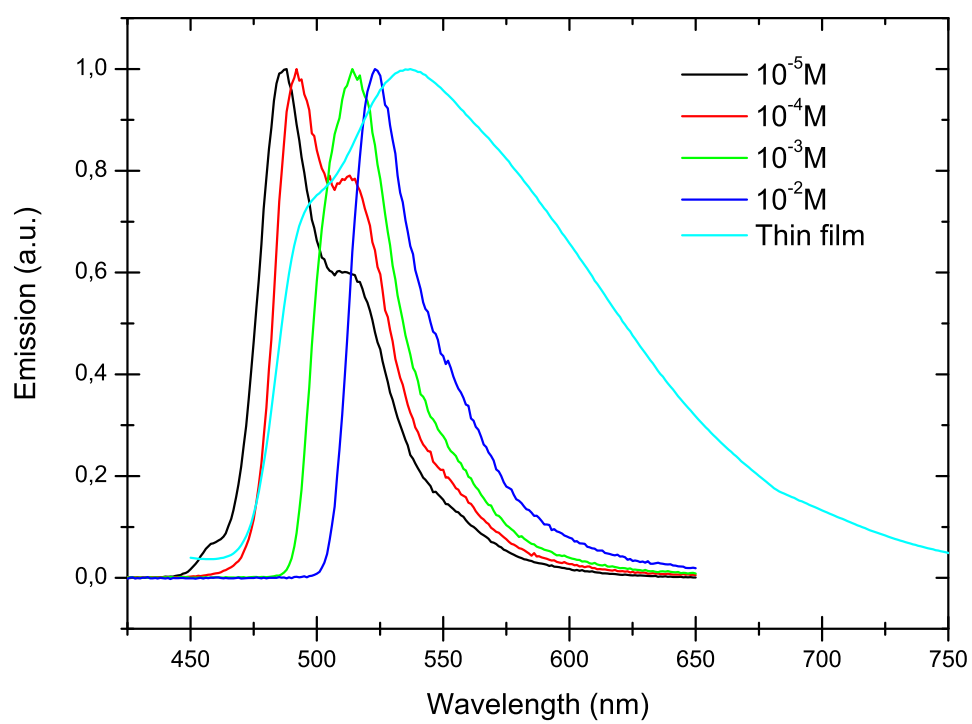
Figure D.3: Emission in function of the concentration of $Al(Op-p)_3$ **16a**.

E. Publications

- Sabine Müller, Sabine Steil, Andrea Droghetti, Nicolas Großmann, Velimir Meded, Andrea Magri, Bernhard Schäfer, Olaf Fuhr, Stefano Sanvito, Mario Ruben, Mirko Cinchetti, and Martin Aeschlimann. "Spin-dependent electronic structure of the Co/Al(OP)$_3$ interface" . *New Journal of Physics*, **2013**, *15*, 113054.

- Andrea Magri, Pascal Friederich, Bernhard Schäfer, Valeria Fattori, Xiangnan Sun, Timo Strunk, Velimir Meded, Luis E. Hueso, Wolfgang Wenzel, and Mario Ruben. "Charge carriers mobility and electronic properties of Al(Op)$_3$: impact of excimer formation". In preparation, to be submitted in *Beilstein Journal of Nanotechnology*.

- Yanhua Lan, Andrea Magri, and Mario Ruben. "Magnetic properties of phenalenyl-based dysprosium SMMs". In preparation.

New Journal of Physics
The open access journal for physics

Spin-dependent electronic structure of the Co/Al(OP)$_3$ interface

Sabine Müller[1], Sabine Steil[1], Andrea Droghetti[2], Nicolas Großmann[1], Velimir Meded[3], Andrea Magri[3], Bernhard Schäfer[3], Olaf Fuhr[3], Stefano Sanvito[2], Mario Ruben[3], Mirko Cinchetti[1,4] and Martin Aeschlimann[1]

[1] Department of Physics and Research Center OPTIMAS, University of Kaiserslautern, Erwin-Schrödinger-Strasse 46, D-67663 Kaiserslautern, Germany
[2] School of Physics and CRANN, Trinity College Dublin, Dublin 2, Ireland
[3] Institute of Nanotechnology, Karlsruhe Institute of Technology, D-76344 Eggenstein-Leopoldshafen, Germany
E-mail: cinchett@rhrk.uni-kl.de

Abstract. We have studied the spin-dependent electronic properties of the interface formed between epitaxial Co thin films deposited on Cu(001) and the experimental molecule tris-(9-oxidophenalenone)-aluminum$^{(III)}$ (Al(OP)$_3$), created as a variation of the prototypical organic semiconductor Alq$_3$ to tailor the spin filtering properties by modifying chemisorption with cobalt. The interfaces have been grown under ultra-high vacuum conditions by progressive deposition of 0.5–5 nm Al(OP)$_3$ on the freshly prepared cobalt substrate. For every growth step we have monitored the energy level alignment at the interface as well as the spin polarization of the occupied manifold by spin-resolved photoemission spectroscopy. We identify two hybrid interface states in the energy window of 2 eV below the Fermi energy. The first is at 0.9 eV below E_F and shows an 8% higher spin polarization than Co, while the second is at 1.6 eV below E_F and shows a spin polarization reduced by 4%.

[4] Author to whom any correspondence should be addressed.

Organic semiconductors constitute a very promising material class for spintronics applications [1]. The interest in the spin properties of organic semiconductors was originally stimulated by the observation of magneto-resistive effects in spin-valve structures prepared with an organic-based spacer [1–3]. Recently, it has become clear that the performance of such organic spintronic devices is strongly determined by the peculiar spin-dependent properties of the hybrid interface formed between the organic semiconductor and the ferromagnetic electrodes [4, 5]. Such *spinterfaces* [6] constitute indeed a new playground for exploiting the spin properties of organic materials, as they can be potentially used both as tunable spin filters [7] with enhanced or even inverted spin polarization (SP) with respect to the ferromagnetic electrodes [4] or as independent supramolecular layers showing interface magneto-resistive effects [8].

Co/Alq_3 is the prototypical spinterface, as it constitutes the basic building block of a large number of organic spintronics devices [1]. Recent spin- and time-resolved spectroscopy experiments have revealed the existence of spin polarized hybrid interface states (HISs) at the Co/Alq_3 interface, which act microscopically as spin traps and thus determine the spin-filtering properties of the Co/Alq_3 interface [11]. Moreover, different recent works suggest that spinterfaces formed by Alq_3 can be easily tuned to control the spintronic performance of organic spin valves [9, 10]. Another intriguing pathway to tailor the spin properties of the Co/Alq_3 interface, and thus to directly control and tune the performance of the related devices, is to systematically engineer the electronic properties of Alq_3 by chemical substitution. Different electronic properties of the molecule will inevitably lead to a modified interaction (in character and strength) between the molecule and the ferromagnetic substrate, and thus to modified spin filtering properties of the spinterface.

This is the approach that we propose in this paper. We make use of the mutability of organic semiconductors [12] to create the experimental molecule tris-(9-oxidophenalenone)-aluminum$^{(III)}$ ($Al(OP)_3$) as a variation of the aromate Alq_3. $Al(OP)_3$ was developed to produce a molecule that has bigger ligands than Alq_3. We expect a modification of the chemisorption on cobalt, and thus different spin-dependent properties of the $Co/Al(OP)_3$ spinterface with respect to Co/Alq_3. After having introduced the molecular system, we present a systematic characterization of the spin-dependent properties of the $Co/Al(OP)_3$ interface by spin-dependent spectroscopy and compare them with the well-known properties of Co/Alq_3. Our spectroscopic studies are corroborated by density functional theory (DFT) calculations. This study thus provides a full characterization of the $Co/Al(OP)_3$ system which we propose as a first step toward chemical functionalization of spinterfaces for organic spintronics applications.

The synthesis of $Al(OP)_3$ was carried out as previously described [13] (see the appendix). In order to achieve high purity of the material, several purification steps such as column chromatography and recrystallization by solvent slow evaporation were performed, purity was checked stepwise by common analysis techniques such as nuclear magnetic resonance (NMR) spectroscopy, mass spectrometry (matrix-assisted laser desorption/ionization time-of-flight experiment (MALDI-TOF)) and elemental analysis. Single crystals of the compounds were obtained, the molecular structure was resolved by x-ray single-crystal diffraction for the first time (see figure 1) and therefore reported (see the appendix, further details can be found in the Cambridge Crystallographic Data Centre, reference number: CCDC 963395). The atoms' coordinates could be extrapolated from the x-ray single-crystal diffraction and were used as the starting point for DFT optimization of the molecule structure in 'gas phase'.

3   **IOP** Institute of Physics   Φ DEUTSCHE PHYSIKALISCHE GESELLSCHAFT
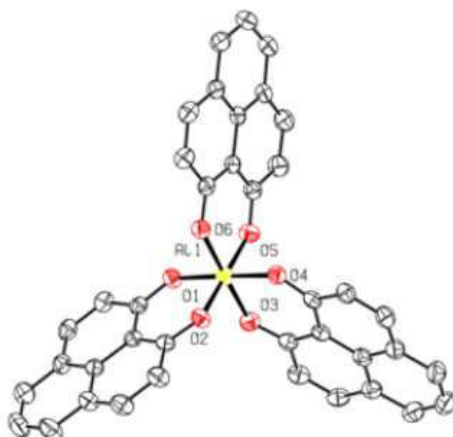
Figure 1. Molecular structure of Al(OP)$_3$ (hydrogen atoms and solvent molecules are omitted for clarity).

As a first step to the characterization of the spin-dependent properties of Co/Al(OP)$_3$, we study here the interface formed between epitaxial Co thin films deposited on Cu(001) and Al(OP)$_3$. The organic molecule was progressively grown on a freshly deposited cobalt thin film with coverage ranging between 0.5 and 5 nm. The occupied manifold of the interface was characterized by spin-resolved ultraviolet photoemission spectroscopy (UPS). For every growth step, we monitored the changes in the work function and the energetic position of the molecular orbitals, giving information about the energy level alignment, the SP and the origin of the electronic states of the interface.

All of the spectroscopic measurements were performed with an UHV-system consisting of one spectrometer chamber and two evaporator chambers. The base pressure in the spectrometer chamber is 4×10^{-11} mbar. The evaporator chambers enable us to produce the Co/Al(OP)$_3$ system *in situ*, which is crucial to obtain a clean surface and a high-quality interface. Cobalt is evaporated by an Omicron EFM 3 evaporator at a pressure of 10^{-10} mbar. Al(OP)$_3$ is deposited with a Knudsencell from Kentax GmbH evaporator at a pressure of 9×10^{-10} mbar. The deposition rates are monitored by a quartz crystal balance calibrated with ellipsometry.

The 3.5 nm thin Co films were deposited by electron beam epitaxy on a Cu(001) single crystal. Afterwards, the substrate was annealed at 370 K. This results in a metastable tetragonally distorted Co fcc structure with in-plane magnetic uniaxial anisotropy along the (110) direction of copper [15, 16]. The Co/Cu(001) film was then progressively covered with Al(OP)$_3$, to form the Co/Al(OP)$_3$ interface.

To detect the occupied manifold of the Co/Al(OP)$_3$ system, we performed UPS and near threshold photoemission spectroscopy (NT-PS) [17, 18]. UPS was performed by using an Omicron HIS 13 vacuum ultraviolet lamp, which operates at the HeI line ($h\nu = 21.2$ eV). The excitation source for NT-PS is a Ti:sapphire laser system with a central wavelength of 800 nm, 82 MHz repetition rate, a pulse power of 1.5 W and a pulse duration of 100 fs. The output is frequency quadrupled by using two beta-barium borate crystals leading to the fourth
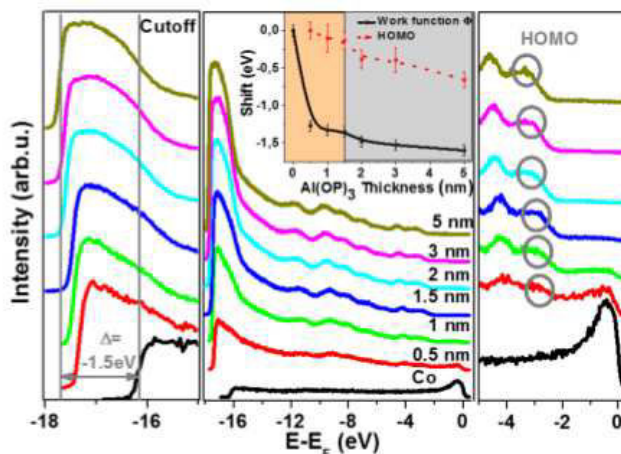
Figure 2. UPS spectra of the Co/[x nm]Al(OP)$_3$ system with $x = 0$ nm (Co substrate), 0.5, 1, 1.5, 2, 3 and 5 nm. The right panel shows the UPS spectra in the HOMO region magnified for more detail. The HOMO (marked with a circle) shifts to lower energies for increasing x. The right panel shows the region of the low-energy cutoff; here the UPS spectra have been normalized to 1. The maximal energetic shift of the low-energy cutoff ($\Delta = -1.5$ eV) is also marked. Inset: shift of the work function (black) and shift of the HOMO (red, dashed) versus Al(OP)$_3$ coverage. Cobalt work function is 5.1 eV, energetic position of the HOMO for $x = 5$ nm is -3.3 eV.

harmonic of the fundamental with a photon energy of 5.95 eV. For both the UPS and the NT-PS the light incident angle was 45°. The emitted photoelectrons are energy and spin selected by a spin detector based on spin polarized low-energy electron diffraction (Focus SPLEED) mounted on a commercial cylindrical sector analyzer (Focus CSA). The acceptance angle of the detector system is ±13° and its energy resolution is 0.22 eV. All of the presented measurements were performed at room temperature.

Figure 2 shows the UPS spectra of the Co/[x nm])Al(OP)$_3$ system for $x = 0.5$, 1, 1.5, 2, 3 and 5 nm. The left panel of figure 2 shows the low-energy cutoff of the UPS spectra, with maximum intensity normalized to 1. From the position of the cutoff (E_{cutoff}) we can extract the work function $\Phi = (21.2 - E_{cutoff})$ eV. The change in work function with increasing Al(OP)$_3$ coverage extracted from the UPS spectra is depicted in the inset of figure 2. We observe a reduction of the work function Φ with increasing Al(OP)$_3$ coverage up to 1.5 nm. This reduction is caused by a negative interface dipole with strength $\Delta = -1.5$ eV. This value is virtually identical to the interface dipole observed for the Co/Alq$_3$ system [11]. Note that the work function is almost constant for coverage above 1.5 nm (indicated by the vertical line in the graph), suggesting that at this nominal coverage the Co is completely covered by Al(OP)$_3$ molecules [19, 20]. We thus define 1 monolayer Al(OP)$_3$ as the nominal thickness of 1.5 nm.

269

5
IOP Institute of Physics Φ DEUTSCHE PHYSIKALISCHE GESELLSCHAFT
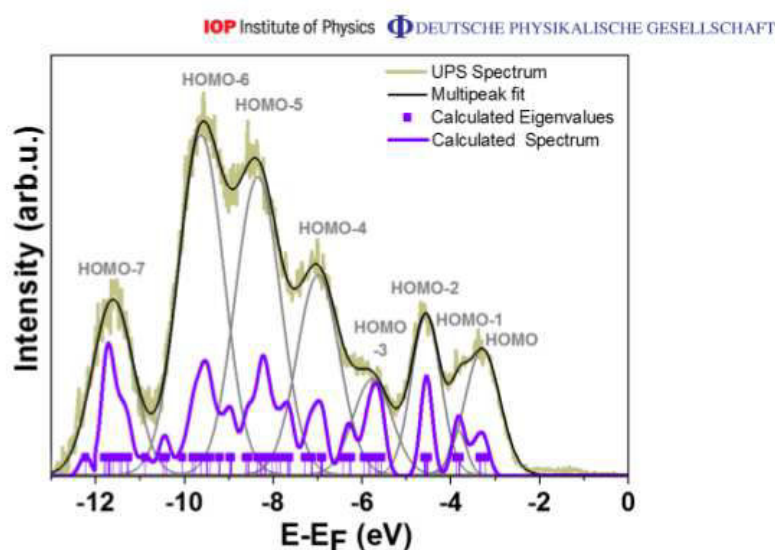
Figure 3. UPS spectrum of the Co/[5 nm]Al(OP)$_3$ system after subtraction of the inelastic electron background function performed according to [22] (brown). The spectrum is fitted with an eight-peak function (black) providing the energetic position of eight occupied states of Al(OP)$_3$ (gray: HOMO, HOMO-1,..., HOMO-7). The purple vertical bars indicate the energy of the generalized eigenvalues calculated with DFT-B3LYP, while the purple continuous lines represent the density of states with a Gaussian broadening of 0.22 eV to include the inhomogeneous broadening originating from the instrumental resolution.

The right panel of figure 2 shows the UPS spectra in the region of the highest occupied molecular orbital (HOMO) magnified for more detail. We observe a progressive shift of the HOMO of the Co/Al(OP)$_3$-system toward lower energies with increasing Al(OP)$_3$ coverage. The shift is plotted in the inset as a dashed red line. The HOMO position ranges from -2.6 eV at $x = 0.5$ nm to -3.3 eV at $x = 5$ nm, and shifts almost linearly as a function of Al(OP)$_3$ coverage. In contrast to the work function, the HOMO position does not remain constant for coverage above 1.5 nm. The shift in energy of the HOMO position is most probably due to the different conditions experienced by the Al(OP)$_3$ molecules in a submonolayer, a monolayer, a bulk molecular film and at the surface of a molecular film, as described by Hill *et al* [21]. In particular, the surrounding potential of the cobalt film of the neighboring molecules and of the vacuum will vary with coverage. As the UPS is surface sensitive, the UPS spectra contain mainly information about the first monolayer of the organic molecules. However, for 2 and 3 nm Al(OP)$_3$ coverage the spectra contain a non-vanishing contribution from the Co/Al(OP)$_3$ interface (the cobalt Fermi edge is still slightly visible in the UPS spectra), while for the 5 nm coverage we mainly detect the surface of the molecular film, with contributions from the underlying molecules in the bulk.

Figure 3 shows the UPS spectrum of the Co/[5 nm]Al(OP)$_3$ system after subtraction of the inelastic electron background function given by Henrich *et al* [22]. By approximating the

270

spectrum with a multi-peak function, we determined eight occupied states of $Al(OP)_3$. Their energetic position is listed in the table in figure 6. As already mentioned, at 5 nm $Al(OP)_3$ coverage, electrons originating from the Co and from the $Co/Al(OP)_3$ interface cannot be photoemitted anymore, since in the UPS experiment their mean free path is considerably smaller than 5 nm. This means that the molecular orbitals determined by the UPS from the $Co/[5 nm]Al(OP)_3$ system can be compared with the occupied manifold of a free $Al(OP)_3$ molecule. As, to our knowledge, neither experimental nor theoretical studies about free $Al(OP)_3$ have been reported, we have performed DFT calculations in order to obtain some insight into its electronic structure.

The DFT calculations were carried out with the NWCHEM [23] and the Turbomole [24, 25] quantum chemistry package. The hybrid exchange correlation functional B3LYP [26] was employed together with the 6–31G* basis sets, which gives well converged results for all of the quantities of interest. B3LYP and other hybrid functionals have been employed successfully in the description of the free Alq_3 molecule [27, 28] and, in that case, the density of states compares quantitatively with the UPS spectrum [28, 29]. Furthermore, hybrid functionals often improve the description of molecular spectra by partially correcting for the inherent self-interaction error of local and semi-local functionals [30].

The geometry optimization of the free molecule was carried out in two different ways: firstly, without imposing any symmetry (and using as initial condition the experimental condensed phase geometry) and, secondly, by requiring the molecule coordinates to transform according to the C_3 point group. The results of both optimizations were found to be consistent and the computed Al–O bond lengths are 1.89 Å, a value that is almost identical to that obtained for the Al–O bonds in Alq_3 [27]. We note that only minor differences between the computed geometry of the free molecule and the experimental geometry of the molecule in the crystalline phase were found. Furthermore, most of the electronic properties (HOMO–LUMO gap (LUMO: lowest occupied molecular orbital), dipole moment, etc) are predicted to be virtually identical (within the numerical uncertainties of our calculations) for the two cases.

The HOMO energy can be computed accurately by using the ΔSCF method [31] and it is found to be equal to -6.6 eV. This result is in good agreement with the HOMO position (with respect to the vacuum energy) inferred from the UPS spectra of the $Co/[5 nm]Al(OP)_3$ system. In fact, as shown in figure 6, this is about -6.9 eV. Similarly, through the ΔSCF method, the LUMO is calculated to be at -1.25 eV and the transport gap is then equal to 5.35 eV, i.e. about 0.5 eV smaller than the computed Alq_3 transport gap [27].

The DFT-B3LYP spectrum superimposed on the UPS spectrum of the $Co/[5 nm]Al(OP)_3$ system is also displayed in figure 3 (purple). Since the generalized eigenvalue corresponding to the HOMO is at -5.57 eV (i.e. about 1 eV higher in energy than the experimental HOMO position with respect to the vacuum energy), the entire theoretical spectrum was first displaced in order to align the HOMO eigenvalue with the ΔSCF HOMO and then shifted so that the 0 eV energy coincided with the Co Fermi energy. By doing that, fairly good agreement between the experimental and the theoretical spectra is obtained. The eight-peak structure is clearly recognizable, although some differences between theoretical and experimental results are present. These are mainly visible in the region between -5 and -7 eV, where the theoretical spectrum presents two symmetric peaks with a small extra feature in between, while the UPS spectrum presents a sharp peak besides a broader shoulder (called, respectively, HOMO-4 and HOMO-3). The origin of this difference between the DFT and the UPS spectra is not clear yet and a complete understanding of the problem would require comparison between various
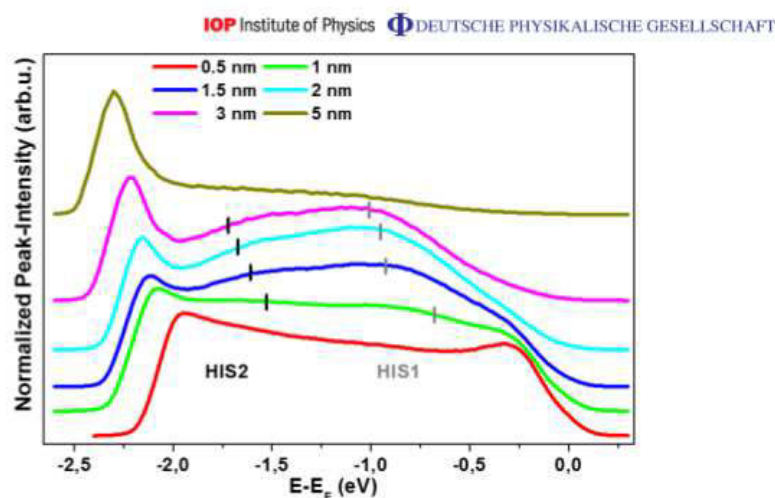
7   **IOP** Institute of Physics   Φ DEUTSCHE PHYSIKALISCHE GESELLSCHAFT

Figure 4. Normalized NT-PS spectra of the Co/[x nm]Al(OP)$_3$ system with 0.5, 1, 1.5, 2, 3 and 5 nm. The energetic positions of the two interface states HIS1 and HIS2, detectable for $1 \leqslant x \leqslant 3$ nm are marked in the spectra.

computational schemes. However, this goes beyond the goals of this work and it may be considered in future studies.

Interestingly, in Al(OP)$_3$ the ligands solely bind to the Al^{3+} ion via oxygen donor atoms in the chelating moiety. In contrast, in Alq$_3$, oxygen and nitrogen atoms connect to the metal ion in symmetrically non-equivalent positions. As a consequence, the calculated vacuum molecular dipole of Al(OP)$_3$ turns out to be very small when compared to Alq$_3$, namely 0.5 versus 4.1 Debye. Experimentally, spinterface dipole moments of Al(OP)$_3$ and Alq$_3$ are virtually identical ($\Delta = 1.5$ eV, see figure 6), which points to the fact that the interface facilitates symmetry breaking. The symmetry can be broken due to at least two distinct mechanisms: firstly, interface charge transfer and hybridization and secondly, by substantial environment symmetry lowering. The low symmetry of the environment, in its turn, can break the internal symmetry of the molecule, resulting in significant increase of the intrinsic molecular dipole. Moreover, we would like to point out that the value of the spinterface dipole is also strongly influenced by changes in the interface charge density induced by the hybridization between Al(OP)$_3$ and cobalt.

We now proceed in discussing the NT-PS experiments. Figure 4 shows the normalized NT-PS spectra for the Co/[x nm]Al(OP)$_3$ system. In the spectra, three features are visible. The first spectroscopic feature close to E_F arises from excitation of a cobalt bulk state with $\Delta 5$ symmetry [16]. Accordingly, its intensity decreases for increasing Al(OP)$_3$ coverage and has almost vanished already at $x = 2$ nm. Two further features are visible in the spectra for coverage up to 3 nm. Those two features are only present in the spectra for coverage between 0.5 and 3 nm, and disappear at $x = 5$ nm. This means that with NT-PS we detect two HISs, forming at the Co/Al(OP)$_3$ interface. This confirms the recent observation that the NT-PS performed on hybrid systems consisting of a metallic underlayer and a non-metallic top layer is highly sensitive to the metal–non-metal interface [32].
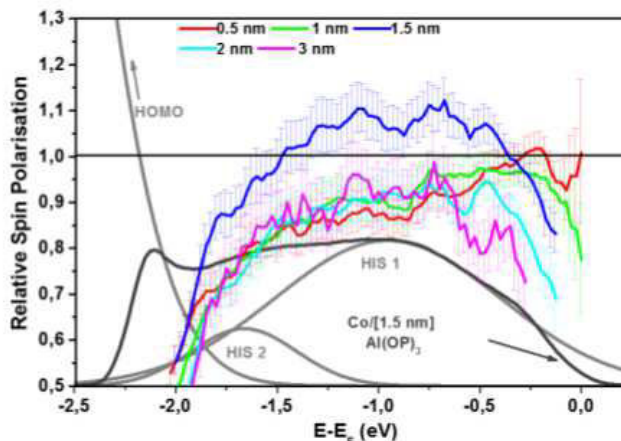
Figure 5. Multi-peak fit used to extract the energetic position of HIS1 and HIS2 states, exemplarily shown for the NT-PS spectrum of the $Co/[1.5\,nm]Al(OP)_3$ system. HIS1 and HIS2 are variables in the multi-peak function while the HOMO is at the energetic position extracted from the UPS spectra. The right y-axis indicates the relative SP of the $Co/[x\,nm]Al(OP)_3$ system, calculated as the ratio between the SP of the $Co/[x\,nm]Al(OP)_3$ and the SP of cesiated Cobalt (CsCo), measured by spin-resolved NT-PS.

In order to extract the exact energetic position of the two HISs, we performed a multi-peak fit as illustrated in figure 5 exemplarily for the $x = 1.5\,nm$ spectrum. In the fit, the position of the two peaks is a variable in the multi-peak function, while the photoemission intensity at the low-energy cutoff, arising from the $Al(OP)_3$ HOMO, is modeled by a further peak at the energetic position determined with the UPS experiments. The energetic positions of the two HISs, extracted from the multi-peak fit, are marked in figure 4 by vertical lines. The two states are named HIS1 and HIS2, respectively. In analogy with the HOMO of $Al(OP)_3$, the energetic position of the two interface states shifts to lower energy with increasing coverage of $Al(OP)_3$, which we interpret again as a result of the interaction of these states with the surrounding potential of Co, the neighboring molecules and the vacuum [21].

In the following, we evaluate and discuss the SP of the detected HISs. To be able to compare the SP of Co with that of the HISs over the complete energy range of the NT-PS measurements, we used cesium to lower the work function of cobalt. It is known that cesium does not influence significantly the SP of cobalt [16]. The SP measured by the NT-PS from the cesiated cobalt sample (CsCo in the following) ranges between 30 and 40%, in agreement with [16, 33]. Figure 5 shows the relative SP measured by the NT-PS from the $Co/[x\,nm]Al(OP)_3$ system for $x = 0.5$, 1, 1.5, 2 and 3 nm. The relative SP is calculated by normalizing the SP of $Co/[x\,nm]Al(OP)_3$ to the SP of CsCo, determined previously on a different cobalt sample. The relative SP gives thus a measure of the variation of the Co SP when the $Co/Al(OP)_3$ spinterface is formed. We observe that the relative SP for $x = 1.5\,nm$ deviates from the SP measured at the other $Al(OP)_3$ coverage; it is about 10% higher above
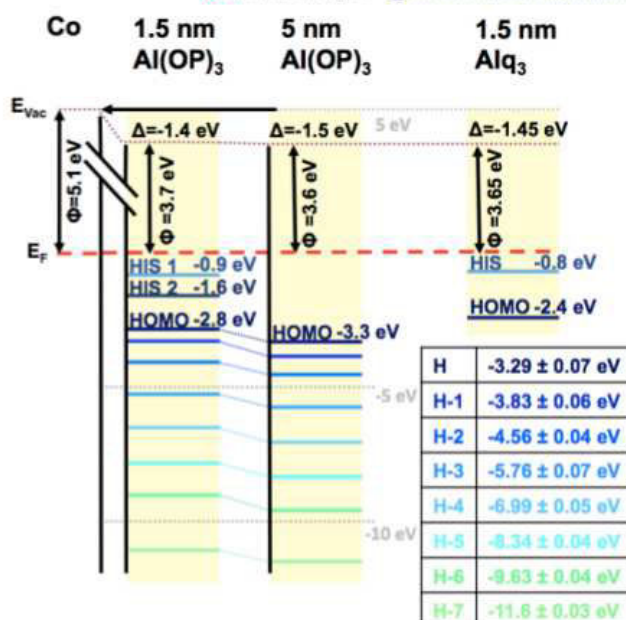
Figure 6. Energy level alignment of the Co/[x nm]Al(OP)$_3$ system for $x = 1.5$ and 5 nm compared to the energy level alignment of the Co/Alq$_3$ interface. The energy level alignment for $x = 1.5$ nm is extracted from the NT-PS spectra and reflects the alignment of the Co/Al(OP)$_3$ spinterface. The alignment for $x = 5$ nm reflects the occupied manifold of bulk Al(OP)$_3$ and is extracted from the UPS spectra. The alignment at the Co/Alq$_3$ interface is taken from [11].

the whole energetic range. Note that at $x = 1.5$ nm we are mostly sensitive to the Co/Al(OP)$_3$ spinterface, and thus we detect the true spinterface SP. In fact, for $x < 1.5$ nm the interface dipole and therefore the HISs are not completely formed and thus their spectral weight is very low. For $x > 1.5$ nm, in turn, the spectral weight of the spin-polarized electrons originating from the spinterface is much lower than the spectral weight of the unpolarized electrons excited from the HOMO in bulk Al(OP)$_3$. This artificially reduces the value of the detected SP of the HIS2 state, which decreases much more strongly with increasing Al(OP)$_3$ thickness than the SP of the HIS1 state. The measured SP of both HIS states is artificially reduced with increasing Al(OP)$_3$ thickness also as a consequence of the spin-flip processes experienced (in the final state for photoemission) by the spin-polarized electrons photoexcited at the Co/Al(OP)$_3$ interface while they travel through the Al(OP)$_3$ layer before being photoemitted.

We now analyze in detail the behavior of the relative SP for $x = 1.5$ nm, i.e. the Co/Al(OP)$_3$ spinterface SP. At the energetic position of the HIS1, the relative SP is above 100%, up to 10% higher than the SP of Co. Averaged over the energetic region of HIS1 we observe an enhancement of the SP of 8%. At the energetic position of the HIS2, the relative SP

IOP Institute of Physics **Φ** DEUTSCHE PHYSIKALISCHE GESELLSCHAFT

is below 100%, on average 4% lower than the SP of Co. We thus conclude that the HIS1 has an SP parallel to the cobalt magnetization, while the HIS2 is either unpolarized or polarized antiparallel to the cobalt magnetization.

In conclusion, we investigated the $Co/[x\,nm]Al(OP)_3$ system by spin-dependent photoemission spectroscopy. Our findings are summarized in figure 6: the left part shows the energy level alignment for $x = 1.5\,nm$, which is extracted from the NT-PS spectra and reflects the alignment of the $Co/Al(OP)_3$ spinterface. The spinterface electronic structure near E_F is dominated by two HISs, HIS1 and HIS2. HIS1 is located at $E - E_F = -0.9\,eV$ and shows on average a 8% higher SP than the Co surface. HIS2 is located at $E - E_F = -1.6\,eV$ and shows on average an SP of 4% lower than the SP of cobalt. The middle part of figure 6 shows the energy level alignment at the $Al(OP)_3$ coverage of $x = 5\,nm$, i.e. bulk $Al(OP)_3$. We determined eight occupied states of $Al(OP)_3$ and an interface dipole of $\Delta = -1.5\,eV$. For comparison to the Co/Alq_3 system, in the right part of figure 6 we present the energy level alignment reported from the Co/Alq_3 interface in [11]. As already discussed the interface dipoles are virtually identical, and moreover, the position of the HOMO is quite similar: $-2.8\,eV$ for $Al(OP)_3$ and $-2.4\,eV$ for Alq_3. However, the HISs formed for the two molecules are crucially different: two states at the $Co/Al(OP)_3$ interface versus one state at the Co/Alq_3 interface. Besides providing a full characterization of the spin-dependent electronic properties of the $Co/Al(OP)_3$ system, our results thus also demonstrate the success of the chemical tailoring approach proposed for the engineering of spinterfaces.

Acknowledgments

Appendix. Synthesis and characterization of Al(OP)₃

All of the reactions were carried out under argon inert atmosphere using standard Schlenk techniques. All of the chemicals are commercially available and were used without any further purification, toluene was distilled over Na. ^1H and ^{13}C NMR spectroscopic data were recorded on a 500 MHz NMR spectrometer with solvent-proton as internal standard. Mass spectrometric data were acquired by MALDI-TOF experiments with no additional matrix compound other than the sample itself. Elemental analysis was carried out to determine the mass fractions of carbon and hydrogen of the sample. 9-Hydroxyphenalenone (1.0203 g, 5.2 mmol) was dissolved in 50 ml of freshly distilled toluene, aluminum chloride (0.2134 g, 1.6 mmol) was added and the solution was refluxed overnight at 110 °C. The yellow precipitate was filtered and washed thoroughly with fresh toluene. The crude product was purified by column chromatography and by recrystallization from CH_2Cl_2/CH_3CH_2OH yielding to pure yellow powder (0.7673 g, yield 75%). Suitable crystals for single-crystal x-ray diffraction were obtained by slow evaporation of chloroform at room temperature. ^1H NMR (500 MHz, $CDCl_3$, 25 °C, $\delta(ppm)$): 8.01 (d, 2H, $J = 9.5\,Hz$), 7.96 (d, 2H, $J = 7.5\,Hz$), 7.51 (t, 1H, $J = 7.5\,Hz$) and 7.14 (d, 2H, $J = 9.0\,Hz$). ^{13}C NMR (125 MHz, $CDCl_3$, 25 °C, $\delta(ppm)$): 179.09, 141.34, 132.86, 127.94, 127.87, 125.29, 122.91 and 113.40. MALDI-TOF MS (Da): m/z (rel. intensity, assigned structure) = 416.87

Table A.1. Crystallographic and refinement data of Al(OP)$_3$ measured at $T = 180(2)$ K.

Compound	AlOP$_3 \cdot$ 3.5CHCl$_3$
Empirical formula	C$_{42.50}$H$_{24.50}$AlCl$_{10.50}$O$_6$
M (g mol^{-1})	1030.33
Crystal color	Yellow
λ (Å)	0.71073
Crystal system	Monoclinic
Space group	$P2(1)/n$
a (pm)	934.61(4)
b (pm)	2177.32(6)
c (pm)	2133.06(9)
β (°)	90.797(3)
V (Å)	4340.2(3)
Z	4
$\rho_{\text{calcd.}}$ (g cm^{-3})	1.577
μ(Mo $- K_\alpha$) (mm^{-1})	0.742
$F(000)$	2076
Crystal size (mm)	$0.34 \times 0.31 \times 0.30$
θ range for data collection (°)	2.13–26.81
Final R indices ($I > 2\sigma(I)$)	$R_1 = 0.0609$, $wR_2 = 0.1589$
R indices (all of the data)	$R_1 = 0.0862$, $wR_2 = 0.1757$
GoF on F_2	1.054

(100%, C$_{26}$H$_{14}$O$_2$Al calc. = 417.07). Elemental analysis found (calculated) for C$_{39}$H$_{27}$O$_8$Al (Al(C$_{39}$H$_{21}$O$_6$) $\cdot$ 2H$_2$O, 650.64 g mol^{-1}): C 72.29 (71.99)%; and H 4.01 (4.19)%.

Single-crystal x-ray diffraction data were collected on a STOE IPDS II diffractometer with graphite monochromated Mo Kα radiation (0.71073 Å). Structure solution and refinement against F2 were carried out by using shelxs and shelxl software [14]. Refinement was performed with anisotropic temperature factors for all of the non-hydrogen atoms (disordered atoms were refined isotropically); hydrogen atoms were calculated on idealized positions. Crystallographic and refinement data of Al(OP)$_3$ are summarized in table A.1.

References

[1] Dediu V A, Hueso L E, Bergenti I and Taliani C 2009 *Nature Mater.* **8** 707–16
[2] Xiong Z H, Wu D, Vardeny Z V and Shi J 2004 *Nature* **427** 821–4
[3] Santos T S, Lee J S, Migdal P, Lekshmi I C, Satpati B and Moodera J S 2007 *Phys. Rev. Lett.* **98** 16601
[4] Barraud C *et al* 2010 *Nature Phys.* **6** 1–6
[5] Dediu V A 2013 *Nature Phys.* **9** 210–1
[6] Sanvito S 2010 *Nature Phys.* **6** 562–4
[7] Cinchetti M, Neuschwander S, Fischer A, Ruffing A, Mathias S, Wüstenberg J-P and Aeschlimann M 2010 *Phys. Rev. Lett.* **104** 217602
[8] Raman K V *et al* 2013 *Nature* **493** 509–13
[9] Prezioso M *et al* 2012 *Adv. Mater.* **25** 534–8

[10] Schulz L *et al* 2010 *Nature Mater.* **10** 39–44

[11] Steil S, Großmann N, Laux M, Ruffing A, Steil D, Wiesenmayer M, Mathias S, Monti O L A, Cinchetti M and Aeschlimann M 2013 *Nature Phys.* **9** 242–7

[12] Naber W J M, Faez S and van der Weil W G 2007 *J. Phys. D: Appl. Phys.* **40** R205–28

[13] Haddon R C 2002 *US Patent* 6428912

[14] Sheldrick G M 2008 *Acta Crystallogr.* **A64** 112–22

[15] Cinchetti M, Heimer K, Wüstenberg J-P, Andreyev O, Bauer M, Lach S, Ziegler C, Gao Y and Aeschlimann M 2009 *Nature Mater.* **8** 115–9

[16] Andreyev O *et al* 2006 *Phys. Rev.* B **74** 195416

[17] Cinchetti M, Wüstenberg J-P, Sànchez-Albaneda M, Steeb F, Conca A, Jourdan M and Aeschlimann M 2007 *J. Phys. D: Appl. Phys.* **40** 1544–7

[18] Fetzer R, Wüstenberg J-P, Taira T, Uemura T, Yamamoto M, Aeschlimann M and Cinchetti M 2013 *Phys. Rev.* B **87** 184418

[19] Toyoda K, Nakano Y, Hamada I, Lee K, Yanagisawa S and Morikawa Y 2009 *J. Electron Spectrosc. Relat. Phenom.* **147** 78–84

[20] Shen C and Kahn A 2001 *Org. Electron.* **2** 89–95

[21] Hill I G, Mäkinen A J and Kafafi Z H 2000 *J. Appl. Phys.* **88** 883–95

[22] Henrich V E, Li X and Zhang Z 1993 *J. Electron Spectrosc. Relat. Phenom.* **63** 253–65

[23] Valiev M *et al* 2010 *Comput. Phys. Commun.* **181** 1477–89

[24] Ahlrichs R, Bär M, Häser M, Horn H and Kölmel C 1989 *Chem. Phys. Lett.* **162** 165

[25] Häser M and Ahlrichs R 1989 *J. Comput. Chem.* **10** 104

[26] Becke A D 1993 *J. Chem. Phys.* **98** 5648–52

[27] Martin R L, Kress J D, Campbell I H and Smith D L 2000 *Phys. Rev.* B **61** 15804–11

[28] Bisti F, Stroppa A, Donarelli M, Picozzi S and Ottaviano L 2011 *Phys. Rev.* B **84** 195112

[29] Droghetti A, Pemmaraju C D and Sanvito S 2013 Electronic structure of metal quinoline molecules from G0W0 calculations (in preparation)

[30] Dori N, Menon M, Kilian L, Sokolowski L, Kronik L and Umbach E 2006 *Phys. Rev.* B **73** 195208

[31] Jones R O and Gunnarsson O 1989 *Rev. Mod. Phys.* **61** 689–746

[32] Fetzer R *et al* 2013 Revealing the spin and symmetry properties of the buried Co$_2$MnSi/MgO interface by low energy spin-resolved photoemission arXiv:1209.4368

[33] Steil S, Goedel K, Ruffing A, Sarkar I, Cinchetti M and Aeschlimann M 2011 *Synth. Met.* **161** 570–4